

**Dynamic Recrystallization and Deformation Mechanisms
of Naturally Deformed Carrara Marble –
A Study on One- and Two-Phase Carbonate Rocks**

Inauguraldissertation

zur
Erlangung der Würde eines Doktors der Philosophie
vorgelegt der
Philosophisch-Naturwissenschaftlichen Fakultät
der Universität Basel

von

Nils Oesterling
aus Essen (Deutschland)

Basel, 2004

Genehmigt von der Philosophisch-Naturwissenschaftlichen Fakultät
auf Antrag von Prof. Dr. Renée Heilbronner

Basel, den 8.4.2003

(Datum der Fakultätssitzung)

Dekanin/Dekan

Table of Contents

| | |
|--|----|
| Abstract | 1 |
| Introduction | 3 |
| Carbonate rocks in the Earth's crust | 3 |
| Naturally deformed Carrara marble | 3 |
| Experimental rock deformation of carbonate rocks | 4 |
| Comparison of nature and experiment | 5 |
| The annealing problem | 5 |
| Aim of study | 5 |
| Structure of the thesis | 7 |
| | |
| Chapter 1: | |
| Structural geology of the Alpi Apuane tectonic window | 9 |
| 1.1 The Alpi Apuane | 9 |
| 1.2 History of Carrara marble | 12 |
| 1.3 Carrara marble in Earth Sciences | 12 |
| 1.4 Geological framework of the Alpi Apuane tectonic window | 14 |
| 1.4.1 Plate-tectonic evolution of the Northern Apennine | 14 |
| 1.4.2 Tectonic domains of the Northern Apennines | 16 |
| 1) Ligurian Domain | 17 |
| 2) Sub-Ligurian Domain (Canetolo Unit) | 17 |
| 3) Tuscan Domain | 18 |
| 4) Umbro - Marchean Domain and Cervarola Unit | 18 |
| 1.4.3 Stratigraphy of the Apuane Unit in the External Tuscan Domain | 19 |
| 1.4.4 Tectonic units and metamorphic conditions in the Alpi Apuane | 21 |
| 1) The Massa Unit | 21 |
| 2) The Apuane Unit (Apuane Autochthon and Apuane Metamorphic Sequence) | 21 |
| 3) The Panie Unit (Stamezza Unit) | 21 |
| 1.4.5 Deformation events in the Alpi Apuane | 21 |
| The first deformation event (D1) | 22 |
| The second deformation event (D2) | 26 |
| 1.5 Meso-scale structural analysis of the Arni area, Eastern Alpi Apuane | 29 |
| 1.5.1 Introduction to the mapping area | 29 |

| | |
|--|----|
| 1.5.2 Basis of mapping | 29 |
| 1.5.3 Lithologies and their structural characteristics | 29 |
| 1) Paleozoic phyllites | 31 |
| 2) Triassic ‘Grezzoni’ dolomites | 34 |
| 3) Jurassic (Lower Liassic) Carrara marble..... | 34 |
| 4) Upper Liassic to Oligocene sequences..... | 34 |
| 5) Oligocene schists..... | 35 |
| 1.5.4 Structural relationship between D1a, D1b and D2..... | 35 |
| D1a | 35 |
| D1b | 35 |
| D2 | 37 |
| 1.5.5 Summary | 38 |

Chapter 2:

Variation of deformation microstructures and temperatures of Carrara marble

| | |
|---|-----------|
| across the Alpi Apuane tectonic window..... | 39 |
| 2.1 Introduction..... | 39 |
| 2.2 Microstructures | 43 |
| 2.2.1 D1 Microstructures..... | 43 |
| 2.2.2 D2 Microstructures..... | 45 |
| 2.2.3 Statically recrystallized microstructures | 48 |
| 2.3 Temperature distribution..... | 50 |
| 2.3.1 Method | 50 |
| 2.3.2 Deformation temperatures..... | 52 |
| D1 temperature trend..... | 52 |
| D2 temperature trend..... | 55 |
| 2.4 Distribution of recrystallized grain size..... | 56 |
| 2.4.1 Method | 56 |
| 2.4.2 Recrystallized grain size | 58 |
| D1 grain size trend..... | 58 |
| D2 grain size trend..... | 59 |
| 2.4.3 Relationship between deformation temperature and recrystallized grain size..... | 60 |
| 2.5 Summary and conclusions | 62 |

Included Publication:

Molli, G., Conti, P., Giorgetti, G., Meccheri, M. & Oesterling, N. 2000.

Microfabric study on the deformational and thermal history of the Alpi Apuane marbles (Carrara marbles), Italy.

Journal of Structural Geology **22**, 1809-1825..... 63

Chapter 3:

Strain dependent variations of microstructure and texture in naturally deformed Carrara marble

(Manuscript by N. Oesterling, R. Heilbronner, H. Stünitz, A. Barnhoorn, G. Molli submitted to

| | |
|--|-----|
| Textonophysics)..... | 81 |
| Abstract | 81 |
| 1. Introduction..... | 82 |
| 2. Geological setting | 84 |
| 3. Sample description..... | 85 |
| 4 Method of analysis..... | 88 |
| 4.1 Temperature determination | 88 |
| 4.2 Microstructural analysis | 88 |
| 4.2.1 Pre-processing of microstructural data..... | 88 |
| 4.2.2 Vectorizing the grain boundaries and separating grain size classes | 89 |
| 4.2.3 Grain size analysis..... | 89 |
| 4.2.4 Determination of volume percentage of recrystallized grains..... | 89 |
| 4.2.5 Analysis of preferred orientation of grain long axes and grain boundaries..... | 90 |
| 4.2.6 Analysis of grain shape..... | 90 |
| 4.3 Analysis of crystallographic preferred orientation..... | 90 |
| 5 Results..... | 91 |
| 5.1 Shear strain..... | 91 |
| 5.2 Deformation temperature | 91 |
| 5.3 Grain size distribution..... | 93 |
| 5.4 Dynamic recrystallization and volume percentage of recrystallized grains..... | 93 |
| 5.5 Preferred orientation of grain long axes and grain boundaries | 93 |
| 5.6 Shape factors | 96 |
| 5.7 Crystallographic preferred orientation | 96 |
| 6 Discussion..... | 99 |
| 6.1 Shear strain and strain rates..... | 99 |
| 6.2 Deformation temperature | 100 |
| 6.3 Grain size distributions | 101 |
| 6.4 Volume percentage of recrystallized grains..... | 101 |
| 6.5 Preferred orientation of grain boundaries and of grain long axes..... | 102 |
| 6.6 Shape factors | 103 |
| 6.7 Textures and dominant slip systems..... | 104 |
| 6.8 Comparison with other natural shear zones and experimental data..... | 105 |
| 6.9 Summary of texture development | 107 |

| | |
|-----------------------|-----|
| Conclusions..... | 108 |
| Acknowledgements..... | 109 |
| Used software..... | 109 |
| References..... | 109 |

Chapter 4:

The influence of dolomite on the behaviour of Carrara marble during natural

| | |
|--|-----|
| deformation | 113 |
| 4.1 Introduction..... | 113 |
| 4.2 Origin of dolomite in calcite rocks of the Alpi Apuane | 115 |
| 4.3 Geological setting and sample description | 119 |
| 4.4 Methods..... | 121 |
| 4.4.1 Sample preparation..... | 121 |
| 4.4.2 Temperature determination | 121 |
| 4.4.3 Microstructural analysis | 123 |
| 4.4.4 Cathodoluminescence (CL)..... | 123 |
| 4.4.5 Crystallographic preferred orientation (CPO, texture)..... | 123 |
| 4.4.6 Phase distribution | 124 |
| 4.5 Results..... | 124 |
| 4.5.1 Deformation temperature | 124 |
| 4.5.2 General microstructural characteristics of sample A and sample B | 125 |
| Sample A..... | 125 |
| Sample B | 127 |
| 4.5.3 Detailed microstructural analysis of sample B..... | 133 |
| Grain size and grain shape..... | 133 |
| Crystallographic preferred orientation (CPO)..... | 134 |
| Phase distribution | 135 |
| 4.6 Discussion..... | 136 |
| 4.6.1 Deformation mechanism of the pure calcite layers..... | 136 |
| 4.6.2 Deformation mechanism of the mixed calcite-dolomite layers | 137 |
| 4.6.3 The influence of annealing on the microfabric..... | 139 |
| 4.6.4 Transition from dolomite veins to mixed calcite-dolomite layers | 139 |
| 4.6.5 The position of the investigated sample in the deformation mechanism map | 141 |
| 4.7 Summary | 144 |

Chapter 5:

| | |
|--|-----|
| Summary, Discussion and future work | 145 |
|--|-----|

| | |
|---|--------|
| Acknowledgements | 153 |
| References | 155 |
| Appendix A: Crystallography of calcite and dolomite | A-167 |
| Appendix B: Methods | B-173 |
| Appendix C: Samples and measurements | C1-183 |
| C1: Thin sections and sample chips | C1-183 |
| C2: CIP orientation maps, grain sizes and grain shapes | C2-197 |
| C3: EBSD orientation maps and polfigures | C3-231 |
| C4: Microstructural data | C4-239 |
| C5: Microprobe data and calculated temperatures | C5-243 |
| Appendix D: Program codes | C6-253 |
| Appendix E: Posters | C7-275 |
| Curriculum Vitae | 283 |



Abstract

Carrara marble is a greenschist facies metamorphic marble from the Alpi Apuane, Tuscany, Italy. It is widely known for its chemical purity, its homogenous microstructure and isotropic texture (crystallographic preferred orientation). During two deformation events (D1 and D2) the Liassic sedimentary precursor of Carrara marble was metamorphosed and deformed.

Besides statically recrystallized microstructures, two end members of dynamically recrystallized microstructures are preserved in Carrara marble (Molli et al. 1997, Molli & Heilbronner 1999, Molli et al. 2000). Both end members can be related either to sub grain rotation (SGR) recrystallization or to grain boundary migration (GBM) recrystallization, respectively. In order to characterize the different dynamically recrystallized microstructures and to relate them to mesoscopical structures of D1 and D2 a combined study of structural field geology and microstructural analysis was carried out. On the basis of a detailed structural mapping overprinting relationships between D1 and D2 were investigated and typical deformation structures were sampled. The microstructural analysis of these shear zones and folds revealed that D1 structures are generally characterized by GBM microstructures and D2 structures by SGR microstructures.

Systematic determination of deformation temperatures of D1 and D2 shear zones along a profile parallel to the main tectonic transport direction by calcite-dolomite thermometry shows two individual temperature trends for D1 and D2. The D1 deformation temperatures decrease from West to East from 430°C to 370°C and those of D2 decrease from 370°C in the East to 295°C in the West. This continuous temperature gradient makes it possible to study dynamic recrystallization microstructures over a temperature range of approximately 150°C.

In order to investigate the influence of strain on the formation of microstructure and texture in naturally deformed Carrara marble a mm-scaled D2 shear zone was analyzed. The shear zone was active at a constant temperature of 325°C and cross-cut the S1 main foliation, which acted as a passive strain marker. Therefore, the observed variations of microstructure and texture are solely a function of the accommodated strain and the strain rate. The protolith is characterized by a core-mantle microstructure with coarse porphyroclasts, which are embedded in a matrix of small recrystallized grains. With increasing strain the microstructure becomes progressively recrystallized, so that the center of the shear zone is completely recrystallized and a fine-grained matrix of equally shaped recrystallized grains is developed. At the same time the texture changes from an e-twinning type (single c-axes

point maximum parallel to the compression direction) in the protolith to a basal $\langle a \rangle$ texture (single c-axes maximum perpendicular to the shear plane) in the center of the shear zone. This texture transition is caused by SGR recrystallization, which forms continuously new grains with slightly rotated crystallographic orientations in the same sense as the overall shear deformation. Strain rate estimates on the basis of experimentally derived flow laws suggest that the shear zone is highly localized in space and in time.

Localization of deformation was probably caused by the presence of a pre-existing coarse-grained calcite vein. According to the Hall-Petch relationship dislocation glide is favoured by coarse-grained materials, which is why deformation may have started in the vein calcite by twinning. After a certain amount of strain twinning is exhausted and the deformation continued by dislocation creep associated by dynamic recrystallization.

Many calcite shear zones in the Alpi Apuane contain substantial amounts of dolomite, representing a second phase in 'pure' Carrara marble. Second phases are considered to influence the mechanical behaviour of a mono-mineralic rock, so that the strength of the phase mixture deviates from the one of the pure end members (Tullis et al. 1991, Dresen et al. 1998, Bruhn et al. 1999). In order to investigate the influence of dolomite on microstructure, texture and the dominant deformation mechanism of calcite a shear zone from the Eastern Alpi Apuane was analyzed. The shear zone is composed of alternating calcite and dolomite rich layers. Dolomite is presumably derived from dolomite veins, which become progressively fractured and sheared so that at the highest strains completely mixed layers of calcite and dolomite are developed. Pure calcite layers are characterized by a GBM microstructure and a strong basal $\langle a \rangle$ texture, indicating that they have deformed dominantly by dislocation creep. With increasing dolomite content the calcite grains become smaller and less lobate, while the dolomite grains maintain their initial size and shape. Also the texture of calcite becomes weaker and the initial orthorhombic symmetry (with respect to the shear plane) is almost randomized at a dolomite content of ~50 vol%. This transition suggests that the mixed layers deform dominantly by diffusion creep. Heterogeneous nucleation (Kruse & Stünitz 1999) of dolomite along calcite grain boundaries and triple junctions leads to a dispersion of calcite and dolomite, supporting the activity of diffusion creep and grain boundary sliding. The progressive addition of dolomite to calcite may lead to the transition from dislocation creep dominated deformation in the pure calcite layers to diffusion creep dominated deformation in the mixed layers. The rheological behaviour of each layer was estimated with the help of a deformation mechanism map. It turned out that the mixed layers deform either by higher strain rates and constant stresses or at lower stresses and a constant strain rate, both suggesting a localization of deformation in the mixed layers.

Introduction

Carbonate rocks in the Earth's crust

Throughout the entire earth's history large volumes of carbontic sediments have formed by organic and inorganic precipitation from seawater. These carbonate formations include, for example the Devonian reef complexes, the "Massenkalk" of the Rheno-hercynian domain, the Liassic Tethian carbonate platforms of the Helvetic Alps, the Apennines, the Dinarides and the Carpathian, the Cretaceous limestone of NW-Germany and many others. Carbonate production is still active at present day in oceanic basins, on the continental shelf and along the tropical coastlines, where carbonate reefs contribute to the global carbonate production. Carbonate rocks are therefore an important constituent of the upper to middle Earth's crust.

Because of their marine origin carbonate sediments are frequently involved in mountain building processes. Together with the subducting plates they are incorporated into accretionary wedges and subjected to metamorphism and large amounts of deformation. Already at modest metamorphic conditions the carbonate sediments are transformed to marble. Recrystallization of the fine-grained limestones and growth leads to the formation of a coarse-grained marble. Annealing produces a microstructure with straight grain boundaries and triple junctions of 120° ("foam structure"), which is typical of marbles. Later deformation may overprint an annealed marble and grain size, grain shape and crystallographic orientations characteristic of the dominant deformation may be acquired. However, such "dynamic" microstructures are only rarely preserved, because carbonate rocks are extremely sensitive to grain growth (e.g. Tullis & Yund 1981). Instead dynamically recrystallized microstructures tend to equilibrate and to form "foam-structures" as soon as deformation has ceased or during uplift and exhumation.

Naturally deformed Carrara marble

Carrara marble is of a greenschists facies metamorphic marble. It is widely known for its chemical purity, its homogeneous microstructure and isotropic texture. For a long time it was believed that all of the Carrara marble is annealed and that only statically recrystallized microstructures could be found. However, recent field studies in the Alpi Apuane (Molli et al. 1997, Molli et al. 2000) showed that a large variety of dynamically recrystallized microstructures are preserved. These "dynamic" microstructures are related to two deformation events (D1 and D2), which are related to subduction, nappe stacking and

exhumation. Folds and shear zones of these deformation events show various overprinting relationships on the meso- and the microscale. The presence of dolomite in the calcite rocks makes it possible to determine the temperature during which deformation took place, using calcite-dolomite thermometry. Thus, the dynamically recrystallized microstructures of naturally deformed Carrara marble from controlled structural positions and constrained thermal conditions can be investigated. Moreover, dolomite represents a second phase in the dominantly calcitic rocks, which has an influence on the deformation behaviour of calcite. Therefore, the study of calcite-dolomite rocks of the Alpi Apuane may elucidate the behaviour of two-phase carbonate rocks under natural conditions.

Experimental rock deformation of carbonate rocks

Carrara marble is frequently used as starting material for rock deformation experiments, because of its microstructural and textural homogeneity. Numerous studies (e.g. Rutter 1974, Schmid et al. 1980, Schmid 1981, Schmid et al. 1987, Wenk et al. 1987, De Bresser 1991, Rutter 1995) investigated the mechanical properties and the characteristics of microstructure and texture of Carrara marble under laboratory conditions. It became evident that Carrara marble deforms under experimental conditions only by dislocation creep. Dislocation glide and mechanical twinning are only active at high stresses / low temperatures and at low strains; diffusion creep has never been achieved in experiments of Carrara marble. Until recent times it was believed that the development of a microstructure and a texture is mainly controlled by temperature (e.g. Schmid et al. 1987, Wenk et al. 1987). However, high strain torsion experiments by Pieri et al. (2001a, b) and Barnhoorn et al. (2004) revealed that strain has a major influence on the development of a microstructure and a texture. In all experimental studies Carrara marble recrystallized either by sub grain rotation (SGR) and grain boundary migration (GBM) or a combination of both mechanisms. Both, SGR and GBM produce characteristic microstructures, which can be found also in naturally deformed carbonate rocks.

The mechanical properties of dolomite single crystals and dolomite aggregates was investigated by a number of studies (e.g. Neumann 1969, Wenk & Shore 1975, Barber 1977, Barber & Wenk 1979, Barber et al. 1981, Barber & Wenk 2001). However, these studies are mainly concerned with the dislocation microstructures determined in TEM and the development of textures. The characteristics of microscopical structures and dynamic recrystallization mechanisms are only investigated for naturally deformed dolomite rocks (Neumann 1994, Leiss & Barber 1999).

A large number of experimental studies consider the mechanical properties of two-phase mixtures (e.g. calcite-halite Jordan 1987, 1988, anhydrite-halite Ross et al. 1987, calcite-anhydrite Bruhn et al. 1999, Barnhoorn 2003). Experimental and theoretical studies show that the bulk strength of the phase mixture can be higher (Walker et al. 1990, Dresen

et al. 1998), situated between (Tullis et al. 1991, Handy 1992, Ji et al. 2001) or even below (Olgaard 1990, Bruhn et al. 1999) the strength of the pure endmembers. While in mono-phase materials the relation of grain size, grain shape and texture to the applied stress, strain, strain rate and temperature is relatively well known, the knowledge of their relationship in poly-phase rocks is still very limited. However, in nature it is quite obvious that the addition of a second phase influences the deformation behaviour of a single-phase rocks, because many major important thrust plane are located in impure rocks.

Comparison of nature and experiment

It is only rarely possible to determine stress, strain rate, strain and temperature from natural rock samples. For the characterization of natural deformation it is therefore essential to derive as much as possible of these parameters from rock deformation experiments. The connecting link between nature and experiment is the microstructure and texture, so that the comparison of natural deformation microstructures and textures to those from experiments of known temperature, stress, strain rate and strain may help to interpret the natural deformation behaviour. Stipp et al. (2002) applied this approach successfully to natural quartz mylonites from the Tonale line, Italy. Based on the comparison of natural microstructures to those of the experimental study of Hirth & Tullis (1992) they constructed a recrystallization mechanism map. Such a map can be used in combination with microstructural observations to infer either strain rate (at known temperature) or temperature (at known strain rate) of natural recrystallization microstructure.

The annealing problem

The comparison of nature and experiment is only applicable if the preserved natural microstructure represents the one, which was formed during the deformation of the rock. The modification of, for instance, the grain size leads to erroneous stress determinations, when applying an experimentally calibrated paleo-piezometer. Carbonate rocks are extremely sensitive to post-deformational annealing and static grain growth (Tullis & Yund 1981). The influence of 'static' recrystallization on the microstructure is not entirely clear and it may be difficult to detect it in natural samples.

Aim of study

Prior to this study the different 'dynamic' microstructures found in Carrara marble could not be related uniquely to given structural positions. In order to unravel the relationship of the different 'dynamic' microstructures (Molli et al. 2000) and meso-scale structures of the D1 and D2 deformation event in the Alpi Apuane a detailed structural mapping was

conducted. Meso-scale folds and shear zones show a variety of overprinting relationships, which were sampled and analyzed microstructurally. Calcite-dolomite thermometry revealed that the deformation temperature of D1 and D2 shear zones varies across the Alpi Apuane. It turned out that both deformation events developed characteristic microstructures, which have formed under distinct temperature conditions.

Recent experimental studies (Pieri et al. 2001a, b, Barnhoorn et al. 2004) suggest that strain influences the development of a microstructure and texture. In order to investigate the importance of strain for the development of microstructure and texture under natural conditions, a small-scale D2 shear zone from the Fondone area in the central Alpi Apuane was analyzed. The shear zone deformed under a constant temperature a pre-existing foliation, so that the variation of microstructure and texture can be investigated as a function of strain and strain rate.

The question, what has caused the localization and the formation of the above described shear zone is not entirely clear. Localization may be related to pre-existing inhomogeneities in the rock. Localization may also be related to the presence of a second phase. Shear zones in Carrara marble are frequently associated with dolomite. In order to investigate the influence of dolomite on the deformation behaviour of calcite a D1 shear zone from the Arni area in the eastern Alpi Apuane was analyzed. The presence of fine-grained layers of calcite and dolomite in the shear zone is related to pre-existing dolomite veins in the undeformed precursor rock. Continuous fracturing, shearing and the solution and precipitation of calcite and dolomite lead to the formation of the mixed layers. The volume proportion of dolomite is critical for the dominant deformation mechanism in so far that an increased dolomite content leads to a change in the deformation mechanism.

Structure of the thesis

The thesis has five chapters and five appendices. The chapters cover the major topics of research and the discussion. The appendices contain analytical data which contributed to the interpretation of the microstructures and textures but are not shown or discussed explicitly in the main part of the thesis. Since chapter 3 consists of a submitted manuscript, repetitions of text segments could not be avoided entirely.

Chapter 1: After a short introduction to the geographical position of the Alpi Apuane and the cultural and scientific importance of Carrara marble, the geological background and the plate tectonic setting of the Alpi Apuane tectonic window are summarized. The main tectonic units of the Northern Apennines and the sedimentary environment of the tectonic units of the Alpi Apuane are introduced. Macro- and mesostructures of the major deformation events are described. In the last part the relationship between the main deformation events (D1 and D2) is analyzed on the basis of a detailed structural mapping. The mapping area is located in the Arni area in the Eastern Alpi Apuane where the structures of all deformation events and their overprinting relationships are well preserved.

Chapter 2: In this chapter the deformation microstructures of D1 and D2 are described. In addition, the microstructural features of the statically recrystallized Carrara marble (“typical Carrara marble”) are presented. Six samples of D1 and D2 shear zones were collected at various localities in the Alpi Apuane, the deformation temperatures were determined using calcite-dolomite thermometry and the recrystallized grain sizes were analyzed. The results are discussed in terms of temperature dependence of recrystallization mechanisms and are compared to data from the Helvetic nappes.

Included in this chapter is the publication of Molli, G., Conti, P., Giorgetti, G., Meccheri, M. & Oesterling, N. 2000. “Microfabric study on the deformational and thermal history of the Alpi Apuane marbles (Carrara marbles), Italy.” *Journal of Structural Geology* 22, 1809-1825. This article contains a number of CIP c-axis orientation analyses including discussion, which were produced in the course of this thesis.

Chapter 3: This chapter is a manuscript, which was submitted to *Tectonophysics*. It presents a case study on the microstructural and textural variations across a small-scaled D2 shear zone. On the basis of textures determined by two different methods - Computer Integrated Polarization microscopy (CIP) and Electron Back Scattered Diffraction (EBSD) - the natural sample was compared to experimentally deformed Carrara marble.

Chapter 4: The influence of the dolomite content on the deformation mechanism of calcite

in a D1 shear zone is the topic of this chapter. The question of the origin of dolomite in Carrara marble is considered as well. Microstructural and textural observations and the analysis of the spatial distribution of calcite and dolomite are used to distinguish different deformation mechanisms. The process by which the calcite-dolomite layers have formed is also analyzed.

Chapter 5: In this chapter the previous four chapters are summarized and discussed. Future projects that are based on the present thesis are pointed out.

Appendices: Appendix A summarizes the crystallography, slip systems, Burgers vectors and flow laws of calcite and dolomite. In appendix B the preparation of ultra-thin sections and grain boundary maps are described and the calculation of sectional grain sizes from the grain boundary maps are illustrated. Appendix C contains the database of the present thesis: List of thin-sections and sample chips (C1), CIP analyses (C2), EBSD analyses (C3), grain size and grain shape analyses (C4) and microprobe measurements (C5). In the first part of appendix D, FORTRAN program codes are listed and for each program an example of a typical input and output file as well as the screen dialog is given. The second part consists of three GNU-plot scripts, which were used to calculate deformation mechanism maps. In the last appendix (E) five posters, which were presented on various conferences, illustrate the evolution of the topic of the PhD-thesis through time.

Chapter 1

Structural geology of the Alpi Apuane tectonic window

1.1 The Alpi Apuane

The Alpi Apuane are a small mountain range, which belongs to the Northern Apennines in Italy (Fig. 1.1). It is located in Northern Tuscany about 50 km North of Pisa at the border to Liguria. The Alpi Apuane have a NW-SE extension of 25 km and an extension of 15 km in SW-NE direction (Fig. 1.2 and Fig. 1.3). The mountains of this part of the Northern Apennines reach an altitude of nearly 2000 m above sea level (M. Pisanino, 1945 m; M. Tambura, 1889 m).

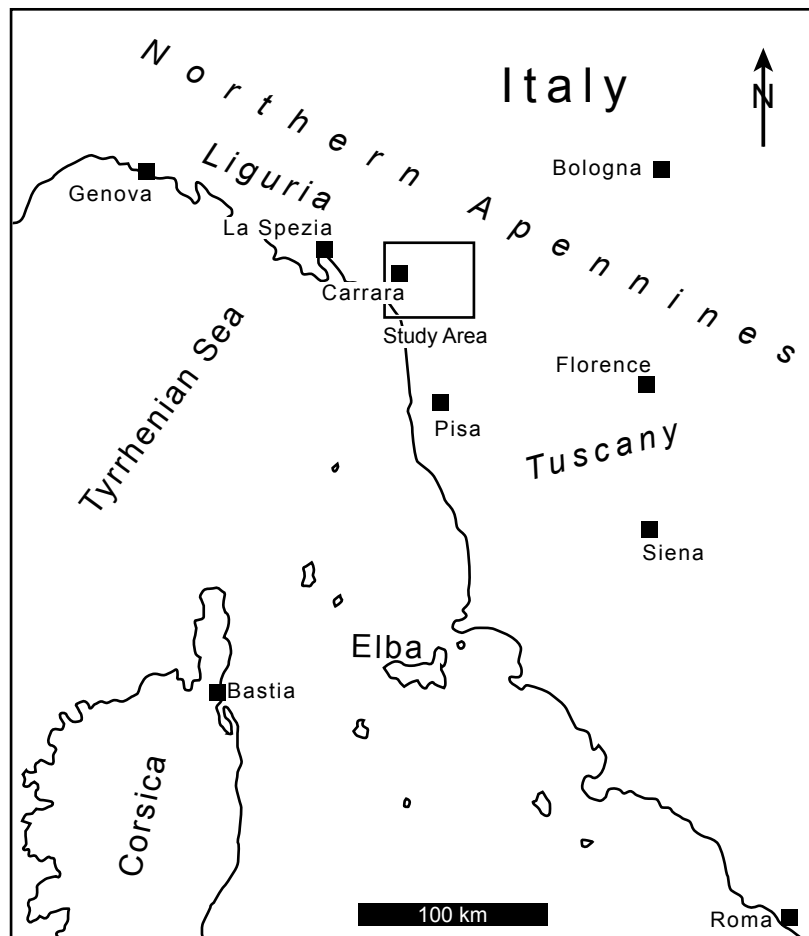


Fig. 1.1: Geographical position of the study area (box) in the Northern Apennines, Italy.

This chapter summarizes the plate-tectonic framework, in which Carrara marble was deposited, i.e. its sedimentary equivalent and the tectono-metamorphic conditions that were necessary to transform limestone to marble. The tectonic activity related to subduction and subsequent exhumation of the Alpi Apuane with particular reference to Carrara marble will be discussed and it will be shown that a polyphase deformation history has led to various structures with typical overprinting relations.

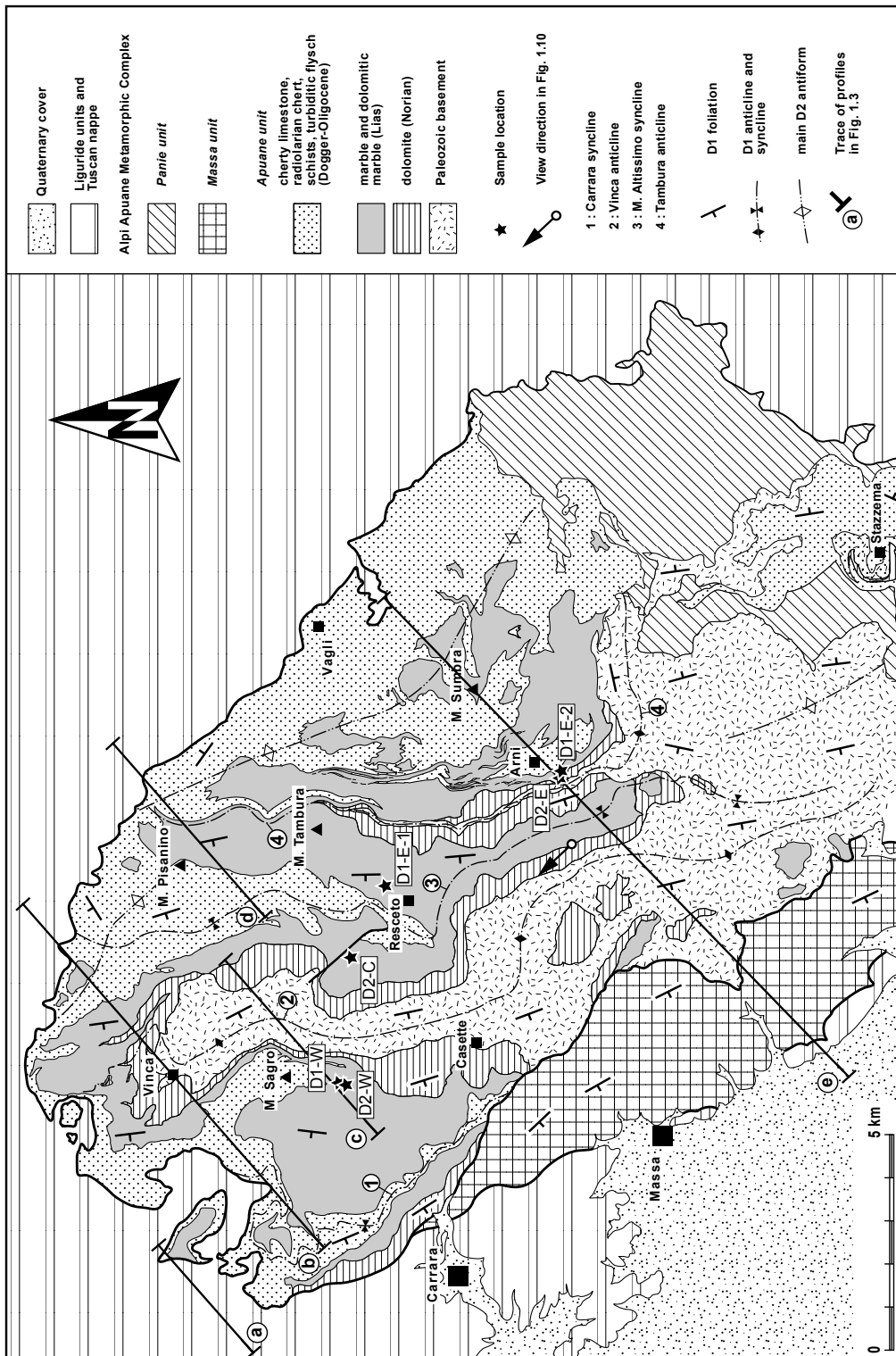


Fig. 1.2: Geological map of the Alpi Apuane tectonic window (modified after Molli et al. 2000).

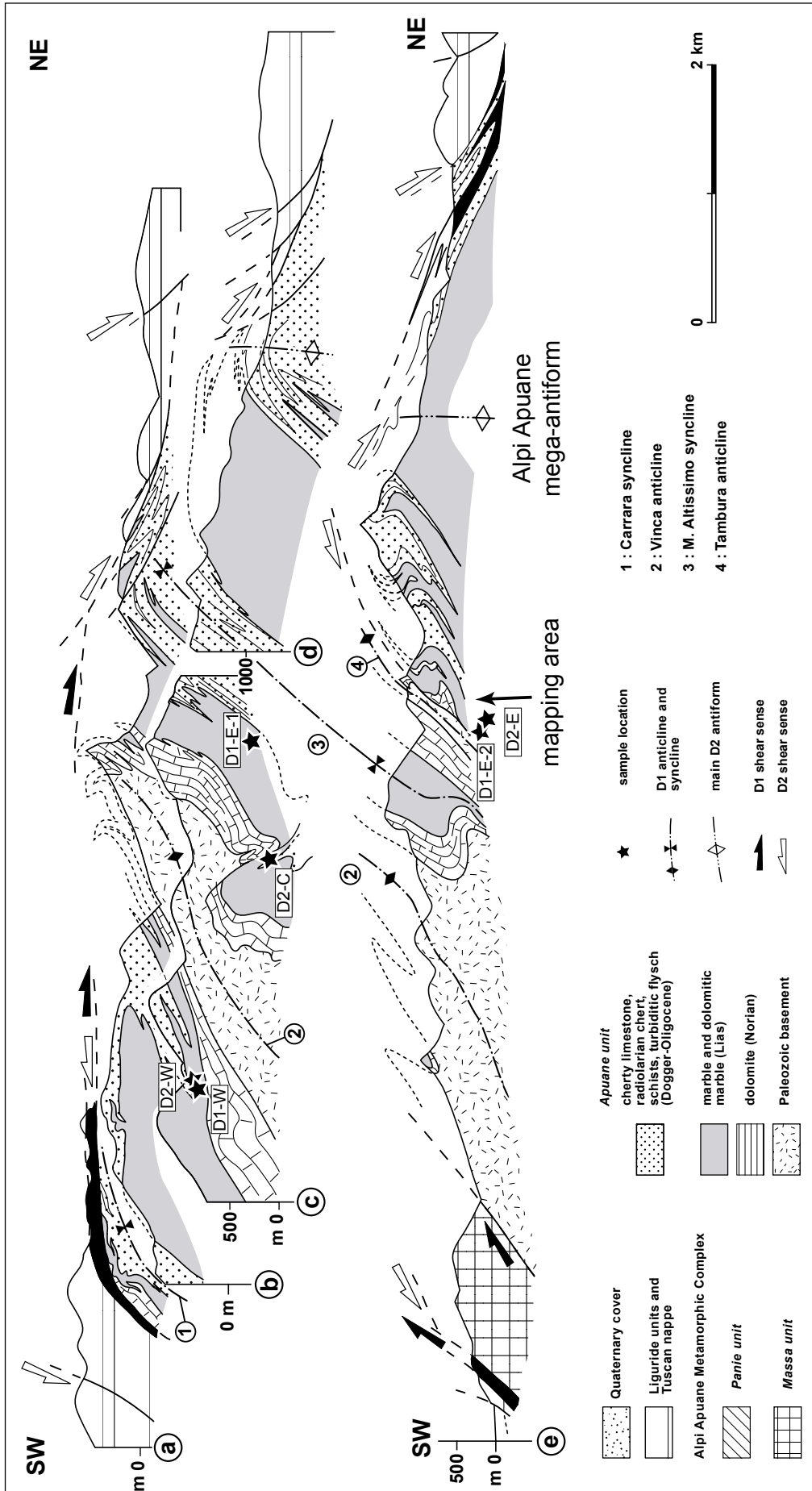


Fig. 1.3: Composite geological cross-section of the Alpi Apuane tectonic window (after Molli et al. 2000). Traces of sections are indicated in Fig. 1.2. The mapping area described in section 1.5 is indicated.

1.2 History of Carrara marble

Quarrying of marble has a long tradition in the Alpi Apuane (Technisches Handbuch des Italienischen Marmors I, 1982 a; Dolci, 1988). In the first century B.C. “Lunesian marble”, the original name of Carrara marble, was mentioned the first time by the roman writer Velleio Patercolo. The name is derived from the former harbor “Luni”, which was used by the Romans to ship the marble from the nearby Alpi Apuane throughout their empire. The climax of Roman marble production was in the time of Augustus (30 B.C. – 14 A.D.), who introduced marble as building stone for temples as well as public buildings to the Roman society. After the cultural and economic crisis of the middle ages, the need of marble increased during the Romanic and Gothic period. During the Renaissance, artists like Michelangelo (1500) used Carrara marble for plenty of sculptures. Probably the most famous example of his work is the “David” statue, which is made of a single block of Carrara marble. Carrara marble was not only used for sculpturing but also as a building stone. The Pisa tower, for example, and other famous buildings of the Italian Renaissance are made of the Apuane marbles. In modern times, especially starting from the 20th century, the quarrying activities increased exponentially. The development of new quarrying techniques, like blasting, the diamond wire saw and the chain saw, enhanced the productivity extremely (Bradley 1999). Approximately half of the total marble production of the past 2000 years was quarried in the 20th century in over one hundred active quarries. Changing commercial needs of the different marble types led to the shutdown of a large number of quarries. These closed quarries may be reopened, if the commercial needs change again. In the Alpi Apuane more than fifty different commercial marble types (i.e. different colors and patterns) are quarried (Technisches Handbuch des Italienischen Marmors II, 1982 b). These marble types are classified into three groups:

- 1) White to light grey marbles, sometimes with light grey veins with the commercial names “Ordinario”, “Venato”, “Bianco Carrara” and “Statuario”.
- 2) Mono- and polygenetic meta-breccias known as “Arabescato” and “Fantastico”.
- 3) Grey marbles named “Nuvolato” and “Bardiglio”.

At present day Carrara marble is mainly used as facade stone and for ornamental purposes. The largest part of the marble produced nowadays in the Alpi Apuane is exported to Arabian countries like Jordan and Egypt (Bradley 1999).

1.3 Carrara marble in Earth Sciences

Carrara marble has been used for a long time in experimental rock deformation. Studies on mechanical properties of Carrara marble go back to the beginning of experimental work. Von Kármán (1911) deformed Carrara marble cylinders under confining pressure to

determine the rock strength. After this early study Griggs et al. (1951), Handin & Griggs (1951), Turner et al. (1956), Heard (1968) used Yule marble in the 1950's and 1960's for their deformation tests and Carrara marble was not used for some time as experimental material. At the beginning of the 1970's Carrara marble was re-discovered as starting material for rock deformation experiments, because of its comparatively smaller grain size and its annealed microfabric. Rutter (1972, 1974) investigated the influence of temperature, strain rate and pore water on the rheological behaviour of very fine grained Solnhofen limestone and on coarser grained Carrara marble. The results of all studies mentioned above are based on the mechanical data. The microstructural and textural characteristics were neglected. Schmid et al. (1980) studied the high temperature flow and dynamic recrystallization of Carrara marble. They used light microscopy and TEM to study the microstructures at various experimental conditions and to define several rheological and microstructural regimes. Afterwards several other workers (e.g. Schmid et al. 1987; Wenk et al. 1987; Fredrich et al. 1989; De Bresser (1991); Rutter (1995); Covey-Crump et al. (1997); Paterson & Olgaard 2000) investigated the rheological, microstructural and textural evolution of Carrara marble as a function of temperature and strain rate. Depending on the experimental set-up (axial compression and extension, pre-cut simple shear) and type of deformation apparatus (Griggs type solid confining medium or Paterson type gas apparatus) only a limited amount of strain can be reached. Experiments on calcite rocks in axial compression were successfully performed to strains of 58% (e.g. Rutter 1995), pre-cut simple shear experiments attained shear strains of $\gamma < 3$ (e.g. Schmid et al. 1987), experiments in axial extension reached 1000% strain (e.g. Rutter et al. 1994). Because of these limitations the influence of strain on rheology and microfabric (microstructure and texture) could only be investigated up to low finite strains.

High strain torsion experiments help to overcome this problem. Apart from the early study of Handin et al. (1960), who deformed Yule marble and the studies on ice (e.g. Durand & Comes 1974 and Bouchez & Duval 1982) the torsion technique was only rarely applied to geological materials so far. During the past decade the torsion technique became an important tool for the understanding of the high strain behaviour of rocks. Casey et al. (1998) investigated the texture development of Solnhofen limestone as a function of strain using a Paterson type torsion apparatus. They reached a shear strain of $\gamma = 12$, which is about 10 times higher compared to the study of Schmid et al. (1987) on Solnhofen limestone. Recent studies on Carrara marble of Paterson & Olgaard (2000), Pieri et al. (2001) and Barnhoorn et al. (submitted) reached shear strains up to $\gamma = 50$. These studies revealed that strain has an important influence on the formation of microstructure and texture via the activity of dynamic recrystallization.

Besides these studies on the rheological behaviour of Carrara marble a large number of studies considered the physical properties of calcitic rocks. (e.g. Burlini & Kunze 2000, Leiss & Weiss 2000). Carrara marble is frequently used as facade stone, which is why it is subjected to extreme variations in climatic conditions (temperature, humidity, chemical

influences). Because of this reason the weathering of Carrara marble and the restoration of weathered Carrara marble is the topic of many recent studies (e.g. Siegesmund et al. 2000, Leiss & Weiss 2000, Siegesmund et al. 2003).

In contrast to the experimental deformation behaviour of Carrara marble, the natural rock is only poorly investigated in terms of microstructural development. The Alpi Apuane region has been investigated intensively during the 20th century (Zaccagna 1932, Bonatti 1938, D'Albissin 1963, Crisci et al. 1975, Di Sabatino et al. 1977, Carmignani et al. 1978, Kligfield 1979, Di Pisa et al. 1985, Coli et al. 1989, Carmignani & Kligfield 1990, Carmignani et al. 1994). Most of these studies are concerned with the tectonic and structural evolution of the Alpi Apuane, considering mainly the macro- and mesostructures. Microfabrics have been investigated only in recent times, when it became evident that besides statically recovered microstructures also dynamic recrystallization microstructures are preserved. The studies of Molli et al. (1997), Molli & Heilbronner (1999), Molli et al. (2000), Leiss et al. (2001), Rexin et al. (2000), Leiss & Molli (2003) and the ones presented in this thesis are concerned with deformation microstructures and textures of naturally deformed Carrara marble.

1.4 Geological framework of the Alpi Apuane tectonic window

1.4.1 Plate-tectonic evolution of the Northern Apennine

The Alpi Apuane are located in the internal part of the Apennines accretionary wedge, which is related to the Westward subduction of the Adriatic plate beneath the Corsica-Sardinia microplate (Fig. 1.4 and 1.5). The subduction geometry has long been a matter of debate. As summarized by Jolivet et al. (1998), Mattauer et al. (1981) and Malavieille (1982) considered an Eastward subduction, which switched its polarity during the Oligocene to form the present-day geometry. This model is supported by the presence of SE to E dipping seismic reflectors below Elba Island and the top - West sense of movement along thrusts in Alpine Corsica. Giese et al. (1982) interpreted this situation as a double-vergent wedge (Fig. 1.4b).

Alternatively Principi & Treves (1984) have assumed that the polarity of the subduction has never changed and that the West-vergent thrusts in Alpine Corsica represent back-thrusts in the Apennines accretionary wedge. The Westward subduction is still active today. In this part of the Mediterranean Sea remnant Tethyan oceanic crust was subducted during Cretaceous to Eocene times (Fig. 1.5, profile A). Rifting and the formation of oceanic crust in the Ligurian-Provençal basin due to back-arc magmatism in the Oligocene (Fig. 1.4 a) caused the counterclockwise rotation of the Corsica-Sardinia block and the convergence of the microplate and the Adriatic continent (Burrus 1984). The subsequent collision of the two continental blocks in the Late Oligocene (Fig. 1.5 profile B) led to folding and nappe

stacking in the Alpi Apuane, structures that are referred to as the first deformation event (D1) (e.g. Carmignani et al. 1978, Kligfield 1979, Carmignani & Kligfield 1990, Molli et al. 2000). Ongoing convergence and the attempted subduction of the Adriatic continental crust associated with underplating caused delamination of the Adriatic lithosphere and the retreat of the subducting slab. The consequence of the progressive attachment of crustal slices to the Corsica-Sardinian crust by underplating was the rapid thickening of the crustal segment.

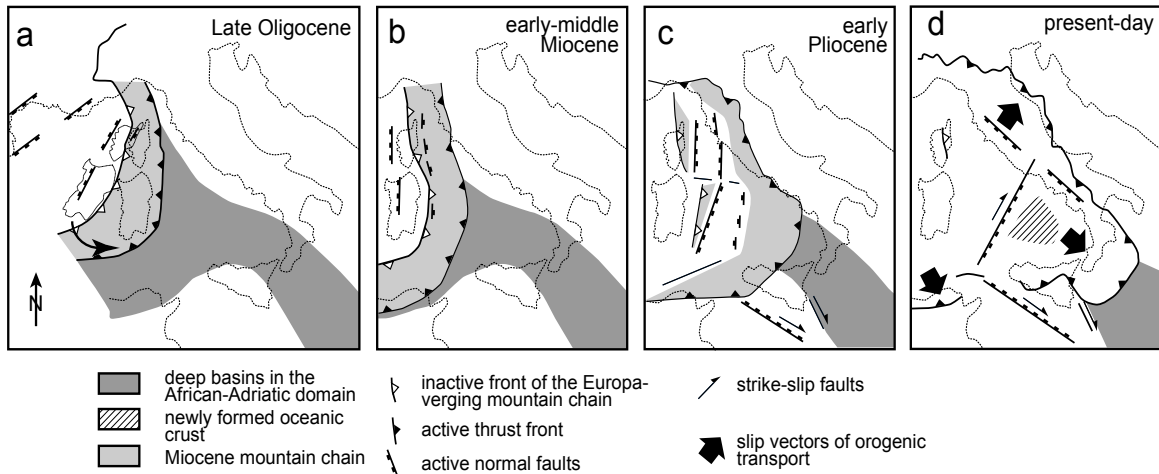


Fig. 1.4: Paleotectonic evolution and plate-tectonic framework of the Italo-Adriatic continental margin (redrawn after Jolivet et al. 1998).

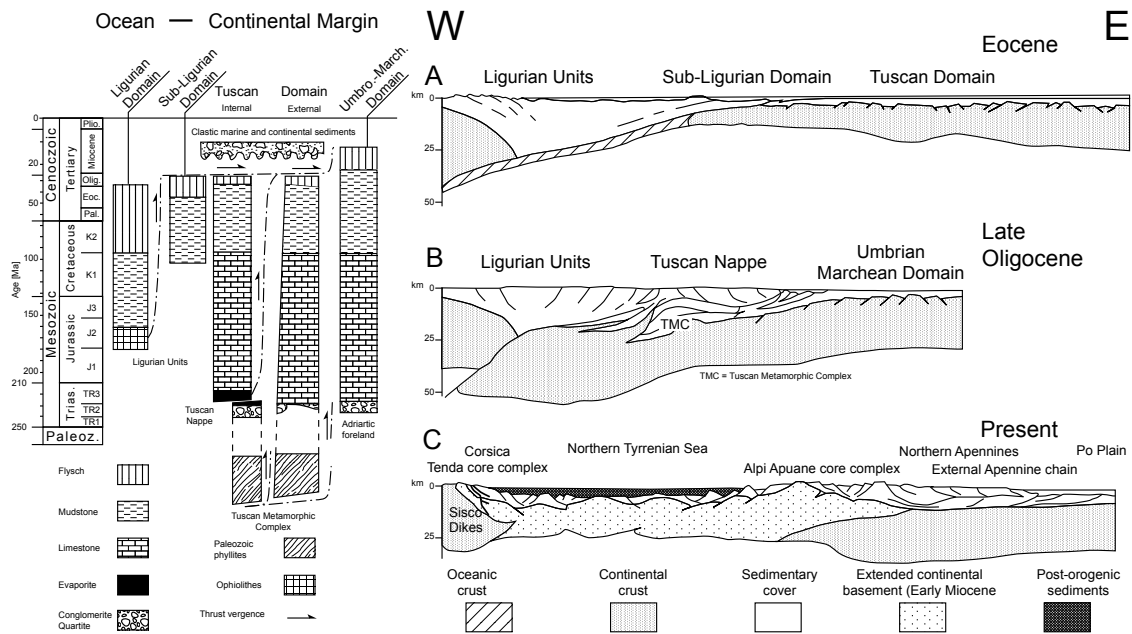


Fig. 1.5: Tectonic domains and their lithotypes in the Tyrrhenian area (redrawn after Carmignani et al. 1987). Crustal scale cross-sections (A-C) illustrate the evolution of the subduction of the Adriatic plate below the Corsica-Sardinia microplate, subsequent collision and final crustal extension.

Carmignani & Kligfield (1990) explain the extensional structures in the Alpi Apuane (D2) by the model of Platt (1986). According to this model overthickened accretionary wedges tend to change their internal stress field from compression to extension, a mechanism that leads to the gravitational stabilization of the wedge geometry. This model explains the coeval appearance of compressional structures at lower crustal levels and extensional ones at upper crustal levels. The delamination of the Adriatic lithosphere was the mechanism to start the slab rollback of the subducting Adriatic plate (Serri et al. 1993, Jolivet et al. 1998). As a result compressional and extensional deformation shifted contemporaneously Eastward (Fig. 1.4). An example for the Eastward migration of deformation are the 25 Ma old extensional structures of Corsica, which formed at approximately the same time as the compressional folds and thrusts in the Alpi Apuane (27 Ma, K/Ar data on Muscovite) (Kligfield et al. 1986). Today active thrusting can be recognized in the Eastern parts of the Northern Apennine whereas extension is active in the Tyrrhenian Sea and Alpi Apuane (Fig. 1.5, profile C). In the Southern Tyrrhenian Sea extension reached even the stage of the production of juvenile oceanic crust (Fig. 1.4 d) (Jolivet et al. 1998).

The present day lithospheric structure of the Alpi Apuane region is characterized by the transition from the attenuated continental crust (crustal thickness < 20 km) of Corsica-Sardinia to the 35 km thick crust of the Adriatic plate. Royden et al. (1993) suggest that the actual trench between the Corsica-Sardinia microplate and the underthrusting Adriatic plate is located beneath the Adriatic coast and the Po-plain (Fig. 1.4 d).

The Alpi Apuane represent a tectonic window and are interpreted by Carmignani & Kligfield (1990) as a metamorphic core complex similar to the ones in California, Utah, Idaho and Canada. Similar tectonic windows are also exposed in the Mt Pisani and Roccastrada region in Southern Tuscany (Carmignani & Kligfield 1990). Greenschist facies metamorphic rocks are exposed inside the Alpi Apuane tectonic window, which comprise Paleozoic to Tertiary sequences (Fig. 1.2). The metamorphic rocks are separated from the non-metamorphic to anchi-metamorphic ones by a brittle thrust, which lies in Triassic evaporites (Calcare Cavernoso) (Carmignani et al 1978). Non- to very low grade metamorphic sequences comprise similar lithologies as the greenschist metamorphic rocks and they are interpreted to be equivalent sedimentary series.

1.4.2 Tectonic domains of the Northern Apennines

In the Northern Apennines four tectonic domains (the Ligurian Domain, the Sub-Ligurian Domain, the Tuscan Domain and the Umbro-Marchean Domain) can be distinguished, according to their lithologies, structural position and metamorphic grade (Fig. 1.5). Paleogeographically these units represent the transition from an oceanic basin (Ligurides and Sub-Ligurides) in the West to the passive continental margin of the Italo-

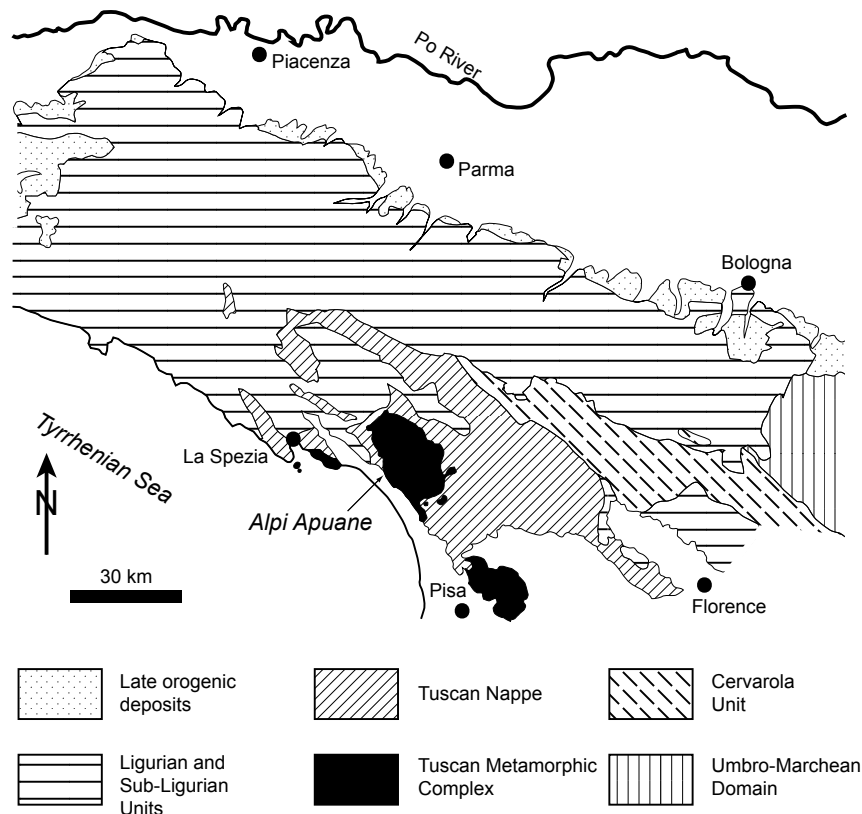


Fig. 1.6: Distribution of the tectonic domains of the Northern Apennines. The study area is located in the Alpi Apuane tectonic window (redrawn after Carmignani et al. 1987).

Adriatic plate (Sub-Ligurides, Tuscanides and Umbro-Marchian Domain) in the East. The present day distribution of these units is illustrated in Fig. 1.6.

1) Ligurian Domain

The Ligurian Domain (Fig. 1.5) comprises Jurassic ophiolites with a Jurassic - Cretaceous sedimentary cover and Cretaceous - Eocene calcareous - argillaceous flysch deposits. It is interpreted as the oceanic crust and sedimentary cover of the former Ligurian–Piemonte ocean. A detailed description of the stratigraphy of the Ligurides can be found in Elter (1975) and Giannini & Lazzarotto (1975). During the Apenninic orogeny the Ligurian sequences were thrust over the Tuscan Domain representing complete ophiolite successions.

2) Sub-Ligurian Domain (Canetolo Unit)

This domain is characterized by the transition from oceanic crust of the Ligurian Domain to continental crust of the Tuscan Domain (Fig. 1.5). It is composed of calcareous - argillaceous and arenitic sediments of Late Cretaceous – Oligocene age. Giannini & Lazzarotto (1975) and Carmignani et al. (1987) described the stratigraphy of the Sub-Ligurian Domain in more detail. Giannini & Lazzarotto (1975) refer the Sub-Ligurian Domain as “shale and limestone unit”.

3) Tuscan Domain

The Tuscan Domain can be subdivided into two parts (Internal and External Tuscan Domain) according to their structural position and their metamorphic grade (Fig. 1.5). Both units are separated from each other by the Late Triassic “Calcere Cavernoso” rauhwaacke, which acted as thrust horizon during the emplacement of the Tuscan Nappe over the Tuscan metamorphic complex.

a) The Internal Tuscanides (Tuscan Nappe) to the West are made up of non-metamorphic to very low-grade metamorphic rocks. Paleogeographically they were located East of the Sub-Ligurian Domain, representing continental margin deposits. The Tuscan Nappe is composed of Late Triassic evaporites, Early Jurassic - Early Cretaceous platform carbonates (Calcere Massiccio = low grade metamorphic equivalent of Carrara marble), an Early Cretaceous - Oligocene argillaceous sequence and a Late Oligocene arenitic flysch (Giannini & Lazzarotto (1975), Carmignani et al. (1987), Ciarapica & Passeri (1994) and reference therein).

b) The External Tuscanides (Tuscan Metamorphic Complex, TMC, Apuane Metamorphic Complex, AMC) were originally located to the East of the Internal Tuscanides. They are composed of greenschist facies metamorphic rocks of similar original lithologies as the Internal Tuscan Domain. This unit lies structurally below the Tuscan Nappe and is in the Alpi Apuane sub-divided into the Massa Unit, the Apuane Unit and the Panie Unit. Stratigraphy and structural position of these units will be discussed in section 1.4.3 and 1.4.4, respectively. Besides the Mesozoic and Tertiary sequences, which represent the sedimentary cover of the Hercynian basement, the basement itself is exposed. It is composed of Paleozoic meta-sediments and meta-volcanics (Giannini & Lazzarotto 1975, Carmignani et al. 1987).

4) Umbro - Marchean Domain and Cervarola Unit

These non-metamorphic domains represent the most external zone of the Northern Apennines to the East of the above described domains. The Umbro - Marchean domain, which was detached from its basement along Triassic evaporites, is composed of continental-margin derived sediments; from bottom to top these are: Permian - Triassic “Verrucano”, Late Triassic evaporites, Early Jurassic - Eocene carbonates (Calcere Massiccio = non-metamorphic equivalent of Carrara marble), an Eocene - Miocene argillaceous sequence and late Miocene arenitic flysch (Giannini & Lazzarotto 1975, Carmignani et al. 1987). The Cervarola Unit is a middle Miocene flysch sequence that is located between the Umbro-Marchian Domain and the overriding Tuscan Nappe. It is exposed to the East of the Alpi Apuane (Carmignani et al. 1987).

1.4.3 Stratigraphy of the Apuane Unit in the External Tuscan Domain

The stratigraphy of the Tuscan - and Umbro - Marchean Domain is similar to each other (Fig. 1.5). The Internal Tuscan (= Tuscan Nappe) and Umbro-Marchean Domain are believed to be the very low-grade or non-metamorphic equivalents of the greenschist facies rocks of the External Tuscan Domain (Ciarapica & Passeri, 1983). Fig. 1.7 correlates the lithotypes of the different tectonic units of the Tuscan Metamorphic Complex to those of the Tuscan Nappe. The thicknesses of the different Mesozoic formations vary across the Alpi Apuane due to a pre-sedimentary topography in the Paleozoic basement (Fig. 1.5, profile A). This topography formed during continental rifting, which was initiated in the Upper Triassic. An example for the variations mentioned above is the thickness increase of the Lower Liassic marbles from 200 m in the Western Alpi Apuane to about 500 m in the center of the tectonic window (Carmignani et al. 1987).

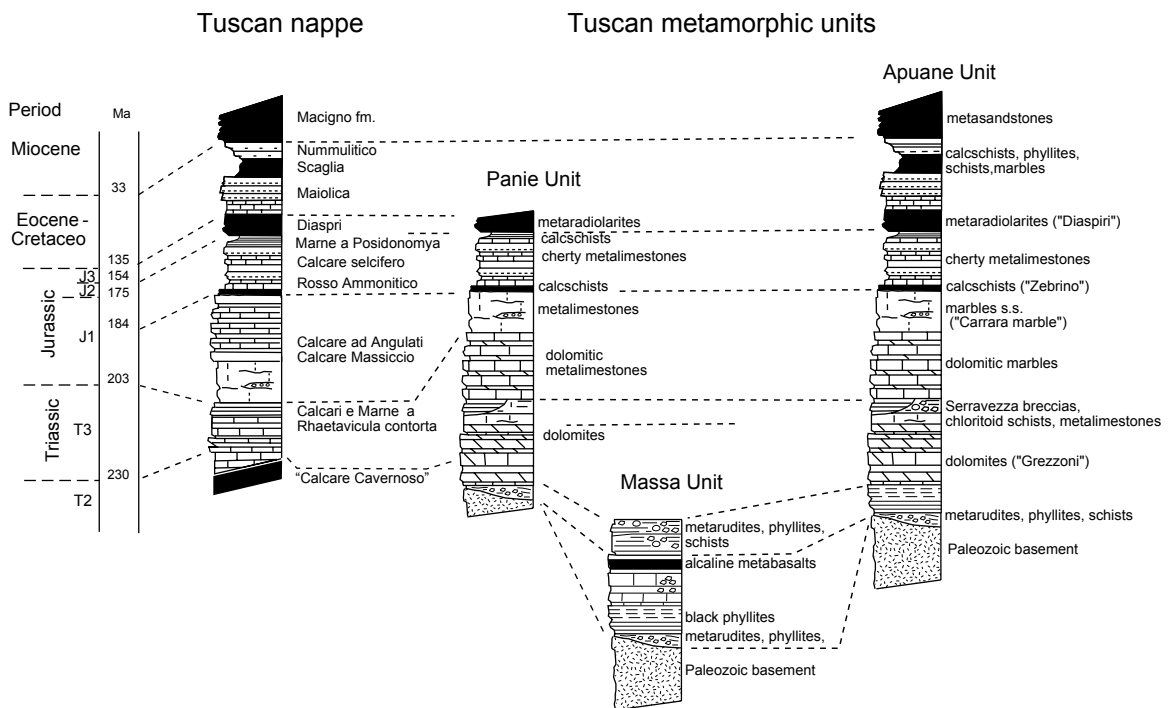


Fig. 1.7: Stratigraphic sequences of the Tuscan Domain in the Alpi Apuane region (redrawn after Molli 2002).

The oldest rocks exposed in the Alpi Apuane are of Cambrian – Devonian age. They form the continental basement of this region with many structures of a pre-Alpine, Hercynian deformation. From bottom to top the basement is made up of quartz and muscovite bearing phyllites (Middle Cambrian - Upper Ordovician) and a sequence of porphyroids and porphyritic schists (Middle Ordovician). Both units are cut by basic dikes of Upper Devonian - Upper Carboniferous age. Carmignani et al. (1987) pointed out, that the oldest rocks exposed in the Alpi Apuane (Filladi inferiori) correspond to the basement exposed in Sardinia (basamento sardo), which could be dated on the basis of Acritarche faunas to

Cambrium - Lower Ordovician. Arkoses and meta-sandstones overlie them. These clastic sediments are indicative of a transgressive phase in a shallow marine environment and could be dated to Upper Ordovician by benthic fossils. The youngest sequences in the Alpi Apuane basement are represented by crystalline dolomites, black phyllites and calcschists of Silurian to Devonian age (Giannini & Lazzarotto, 1975 and Carmignani et al., 1987)

The Mesozoic sequences of the Apuane Unit, which represent the largest part of the rocks exposed inside the tectonic window, are separated from the Paleozoic basement by a well-expressed angular discordance. Volcano-sedimentary rocks of Middle Triassic age indicate the beginning of the Mesozoic sedimentation. These rocks are only exposed in the Massa Unit and are interpreted to be the first pulse of the continental rifting of the Upper Triassic – Lower Jurassic and the subsequent opening of the Mediterranean Tethys. On top of these formations fluvio - siliciclastic sediments of the “Verrucano” were deposited. However, the “Verrucano” is only rarely exposed in the Apuane Unit. The following Upper Triassic to Paleogene sequences reflect the evolution of the passive continental margin of the Italo – Adriatic plate. Starting from the continental break-up during the Upper Carnian – Norian a first carbonate platform was formed. The so-called “Grezzoni” platform is composed of dolomite marbles with intercalated levels of siliciclastic material. It is interpreted to have formed in a marginal barrier / lagoon / tidal plain environment (Carmignani et al. 1987). This first carbonate platform is conformably overlain by a second one (Lower Liassic) with an extension that reaches from the internal Tuscan Domain in the West to the Umbro - Marchean Domain in the East. In alternating cycles supra / intertidal dolomites and subtidal limestone were formed. This formation, which is known as “Marmi dolomitici” is overlain by a level of pure calcitic marbles, the “Carrara marble sensu strictu” formation. This formation comprises calcite marbles of various sedimentary facies (Colacicchi et al. 1975, Ciarapica & Passeri 1983, Coli et al. 1989). The Carrara marble formation represents the greenschist facies metamorphic equivalent of the “Calcare Massiccio” which forms the carbonate platform in the Tuscan Nappe and the Umbro-Marchean Domain. The Upper Hettangian – Lower Pliensbachian sedimentation reflects the ongoing rifting, which caused the progressive deepening of the sedimentary basin, the fragmentation and the final drowning of the platform. The “Calcare Selciferi” (Cherty Limestone), a sequence made up of alternating levels of carbonates and cherts indicates that the depth of the basin must have approached the carbonate compensation depth (Carmignani et al. 1987). Further deepening of the sedimentary basin occurred during Callovian and Tortonian times as represented by the chert formation of the “Diaspri” sequence. The following sedimentation of the Upper Jurassic, Cretaceous and Paleocene is characterized by a progressive deepening of the sedimentary basin and the shift to a (hemi-) pelagic environment (Calcarini, Entrochi, Cipollini and Shisti Sericitici). The Cenozoic sedimentation ends with the “Pseudomacigno”, a terrigenous sequence composed of sandstone, siltite, calcarenites and micro-breccias of Upper Oligocene age (Carmignani et al. 1987).

1.4.4 Tectonic units and metamorphic conditions in the Alpi Apuane

Deformation and metamorphism of the Alpi Apuane tectonic window is caused by the Westward directed subduction of the Adriatic Plate beneath the Corsica-Sardinia microplate (Carmignani et al. 1978, 1990, 1994, Jolivet et al. 1998 and references therein) (Fig. 1.4 and 1.5). The greenschist facies metamorphic rocks of the Alpi Apuane show structures of two main deformation events (Carmignani et al. 1978, 1990, 1994), which will be described in section 1.4.5. Within the Tuscan Metamorphic Complex three main tectonic units, related to the first deformation event, can be distinguished:

1) The Massa Unit

The Massa Unit is the Westernmost unit of the Tuscan metamorphic complex (Fig. 1.2 and Fig. 1.3). During the first deformation event it was thrust Eastward over the Apuane Unit. The presence of kyanite (Franceschelli et al. 1986) indicates that the Massa Unit was deformed under the highest metamorphic conditions compared to the other units. Jolivet et al. (1998) described peak metamorphic conditions of 0.9 GPa and 450°-480°C determined by phengite barometry and chlorite thermometry.

2) The Apuane Unit (Apuane Autochthon and Apuane Metamorphic Sequence)

The Apuane Unit represents the largest part of the exposed metamorphic rocks within the Alpi Apuane tectonic window (Fig. 1.2 and Fig. 1.3). P/T estimates of Franceschelli et al. (1986, 1997), Di Pisa et al. (1985) and Schultz (1996) indicate peak metamorphic condition of 0.5 - 0.6 GPa and 300-450°C. Jolivet et al. (1998) found peak pressures of 0.8 GPa and temperatures of 390°-410°C.

3) The Panie Unit (Stamezza Unit)

The Panie Unit is exposed in the Southeastern part of the Alpi Apuane (Fig. 1.2). Carmignani et al. (1990) considered it as part of the Apuane Unit, because stratigraphy and structures are similar to the one of the Apuane Unit. However, a well expressed tectonic contact (Ciarapica et al. 1994) between the Panie Unit in the hangingwall and the Apuane Unit in the footwall indicates a different tectonic evolution of the two units. Temperature and pressure data of 300-350°C and 0.8 GPa described by Di Sabatino (1977) are still under discussion (Molli 2002).

1.4.5 Deformation events in the Alpi Apuane

The following section concentrates on the Apuane Unit and its Cenozoic deformation history, because the main part of this work was restricted to this tectonic unit. During the past 30 Ma continuous deformation related to subduction and exhumation took place in the Alpi

Apuane. The two main deformation events (D1 and D2) (Fig. 1.8) developed characteristic microstructures, which will be presented in combination with deformation temperature estimates in chapter 2.

The first deformation event (D1)

The deformation of the first event started during Eocene times (56 - 35 Ma) affecting the Westernmost units (Ligurides and Sub-Ligurides) to the W of the Italo-Adriatic continental margin. The compressive deformation shifted progressively Eastward, which is why the

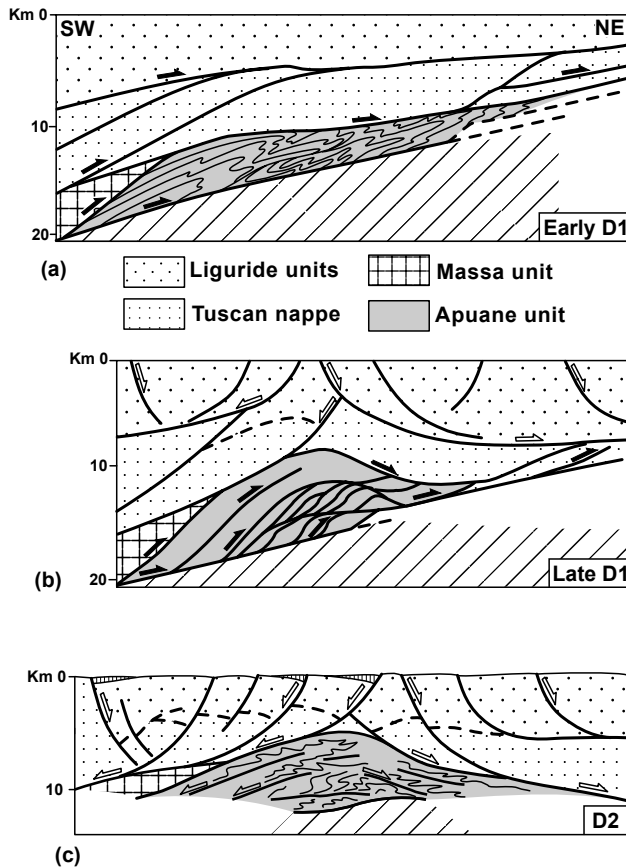


Fig. 1.8: Structural evolution of the Alpi Apuane tectonic window (modified after Molli et al. 2000). Black and white arrows mark the direction of tectonic transport during the first (D1) and the second (D2) deformation event, respectively.

a) Early stage of the compressional deformation event (D1a) led to the formation of large scale folding. After D1a the Alpi Apuane were heated statically (annealing).

b) During the late stage of the compressional deformation event (D1b) a crustal scale nappe stack formed.

c) Extensional deformation event (D2). Uplift and exhumation led to open folds and small scale shear zones.

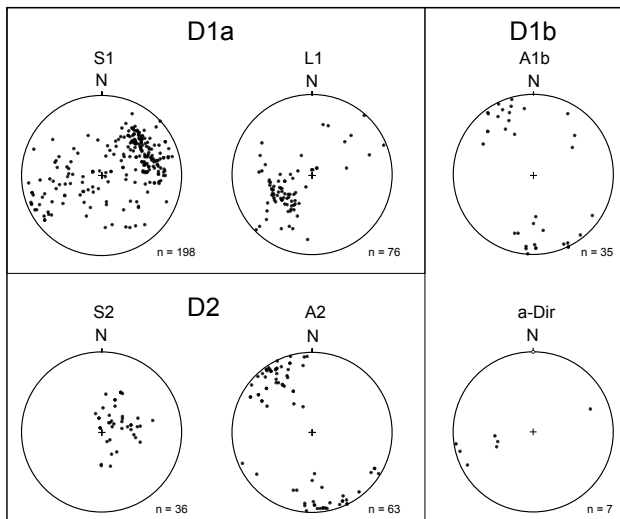


Fig. 1.9: Equal-area projection (lower hemisphere) of the most important structure elements of the Alpi Apuane. At the upper left the axial plane foliation (S1) and the L1 stretching lineation of the D1a deformation phase is shown. At the right side fold axis (A1b) and the transport direction of D1b-folds (a-Dir) are illustrated. At the bottom left the axial plane foliation of D2 folds (S2) and the corresponding axis (A2) are shown. Measurements from various sites in the Alpi Apuane.

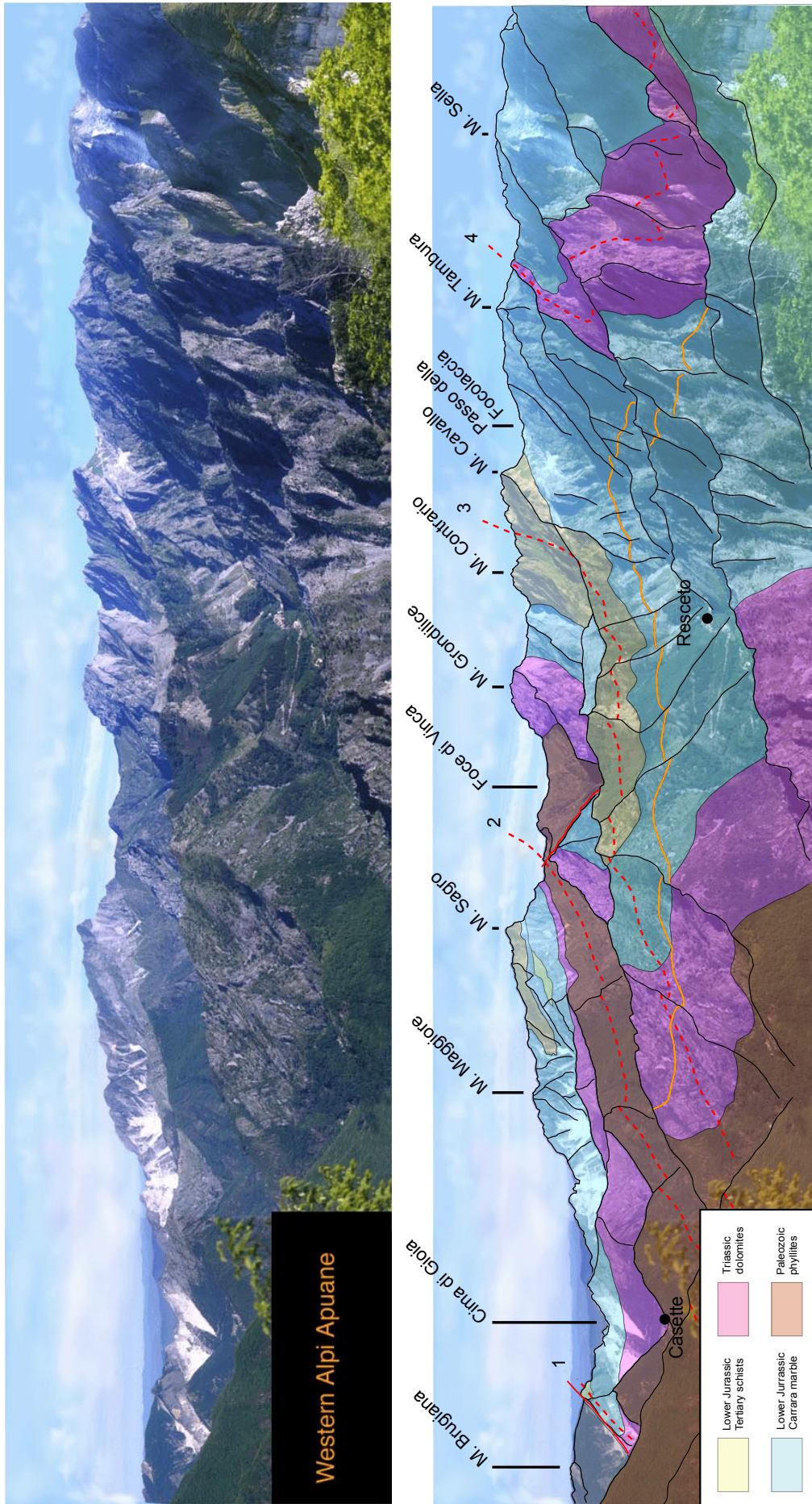


Fig. 1.10: Panoramic view of the Western Alpi Apuane (direction of view NW; for point of view see Fig. 1.2) and geological interpretation. D1 fold axial planes (dashed red lines) of Carrara Syncline (1), Vinca-Forno Anticline (2), Orto di Donna Syncline (3) and Tambura Anticline (4) are indicated. D2 fold axial line is indicated by the solid orange line. Solid red like represent traces of fault zones.

Tuscan Nappe, Massa Unit and Apuane Unit were not deformed before Late Oligocene to Miocene (27 Ma) (Kligfield et al. 1986). Calcite / Dolomite temperatures of mylonites of this event show a temperature gradient across the Alpi Apuane of 420°C in the W to 370°C in the E. This temperature trend is consistent with the one obtained from statically recrystallized microstructures (430°C in the W – 360°C in the E; Molli et al. 2000). The D1 deformation event (Carmignani et al. 1978, 1990, 1994) occurred in two phases, which will be referred to as D1a and D1b (Molli et al. 2000), respectively. D1a and D1b are not strictly separated phases but grade continuously into each other. After D1a the whole region was annealed, which caused the typical coarse grain equilibrated microstructure of Carrara marble.

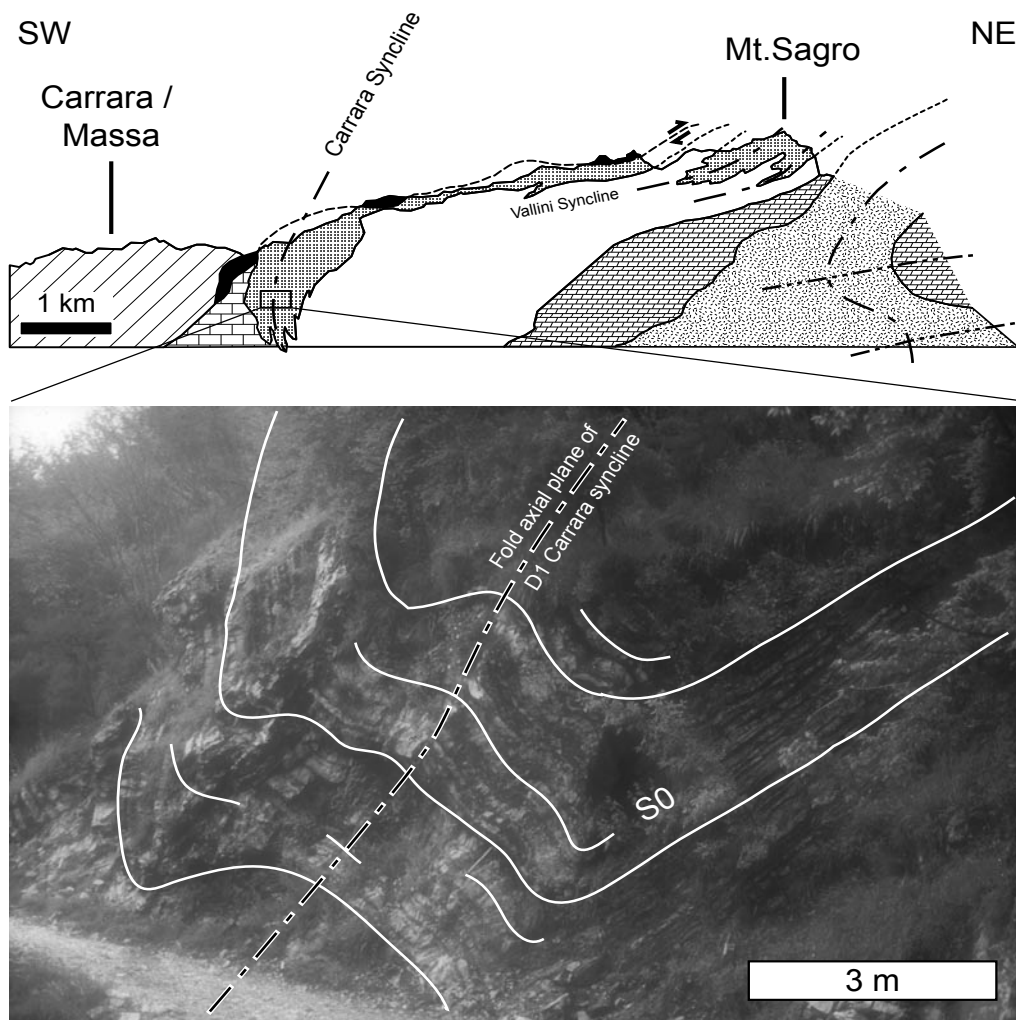


Fig. 1.11: Hinge of D1a Carrara syncline in the Western Alpi Apune. In the schematic cross-section the position of the image in the km-scale fold structure of the Western Alpi Apuane is indicated.

Early D1 (D1a): Macro- and mesostructures

During the D1a - phase, which is referred to as “main folding phase” by Molli et al. (2000), the whole region was folded isoclinally. Kilometer-scale recumbent folds with gently SW dipping axial planes and an associated axial plane foliation (S1) were developed (Fig. 1.9). S1 represents the “main foliation” of the Alpi Apuane, which is sub-parallel to the sedimentary bedding (S0). Two main NW-SE striking syncline and anticline pairs were formed (Fig. 1.2, Fig. 1.3 and Fig. 1.10). North of the line Massa – Arni the sub-horizontal axes of these structures dip slightly to the NW. The core of the km-scale Carrara Syncline with a closure of 20 m width is shown in Fig. 1.11. Considering the scale of the entire structure the attenuated isoclinal fold style becomes evident. Folding is associated with shear deformation. Mesoscopic evidence of shear deformation can be found in the limb positions of the large-scale folds. Elongated components of sedimentary marble breccias, boudinage of dolomite and chert layers (Fig. 1.12) and a pronounced down-dip stretching lineation (L1) (Fig. 1.9 and Fig. 1.13) of elongated calcite grains and strain fringes around pyrite clasts are characteristic features in the field. Millimeter scale folds of dolomite layers with stretching lineation parallel axis indicate strong deformation during this stage. The zones



Fig. 1.12: D1a shear zone in „Zebrino“ type Carrara marble. Note the boudinaged, dolomite rich layer (indicated) above the laminated marbles.

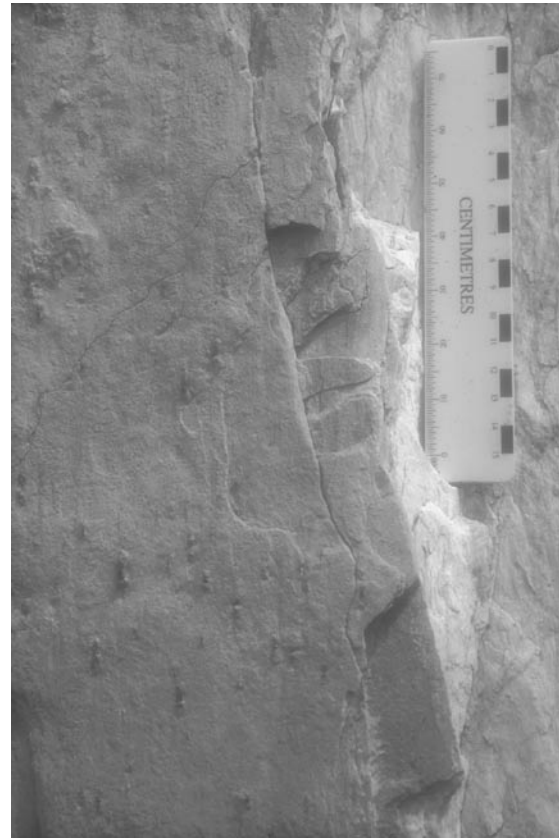


Fig. 1.13: L1 stretching lineation. Orientation of movement is indicated by strain fringes around pyrite porphyroclasts.

of strong deformation are believed to have formed after fold amplification, representing highly sheared fold limbs similar to the nappe thrusts in the Helvetic Alps (Ramsay, 1981). The “Zebrino” type of Carrara marble (Fig. 1.12) probably represents one of these “former” shear zones, which is located in the overturned limb of the Carrara syncline.

Late D1 (D1b): Macro- and mesostructures

After the annealing of the Alpi Apuane rocks the deformation continued in a compressive regime. However, the deformation, as started dominantly by folding during D1a, localized into discrete meter to deca-meter scale shear zones, which are generally located in the limbs of the km-scale folds. The lower limb of the Vallini syncline in the W, which is a parasitic fold in the normal limb of the Carrara syncline and the Tambura thrust zone in the East of the Alpi Apuane are typical examples of these shear zones. During D1b the stretching direction remains consistent with D1a in a NE-SW direction. Nappe stacking and the formation of a crustal scale duplex result from D1b, which is called “antiformal stack phase” by Molli et al. (2000) (Fig. 1.8). Besides strong mylonitization the main foliation (S1) was folded tightly, with gently inclined axial planes, dipping to the SW (Fig. 1.14). An axial plane foliation related to D1b folds is only visible in pelitic layers. The fold axes show a relatively wide scatter around a NW-SE orientation (Fig. 1.9).

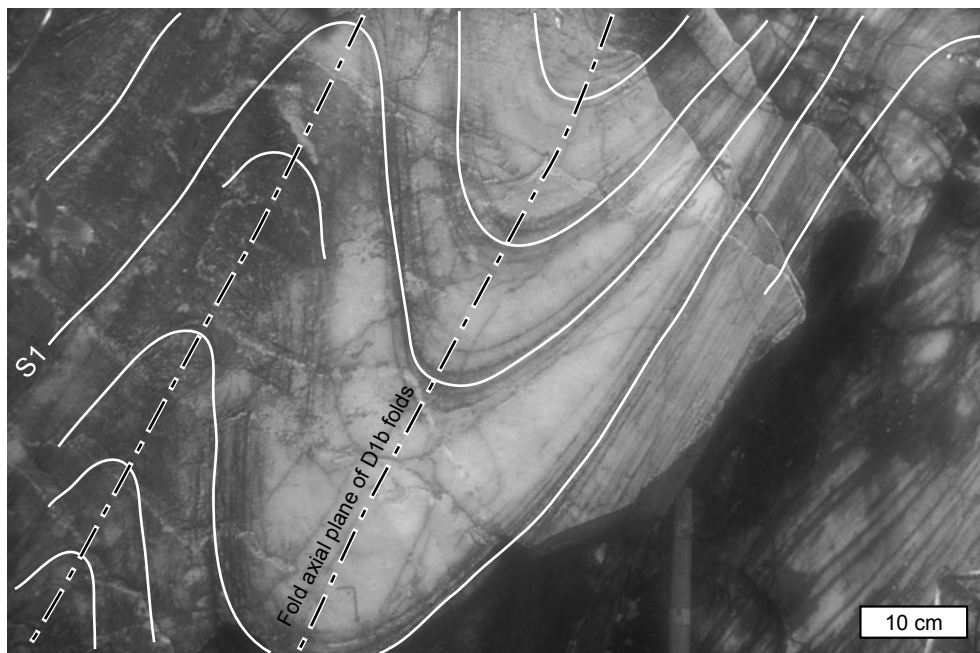


Fig. 1.14: D1b fold refolding the pre-existing S1 foliation.

The second deformation event (D2)

Progressive thrusting and nappe stacking during D1b led to instability of the nappe pile and to the collapse of the nappe stack, which was associated with uplift and exhumation (Carmignani et al. 1990, 1994, Molli et al. 2000). Similar to the D1 event two deformation

phases can be distinguished during the D2 history. The early D2 comprises the ductile part of the history, which is related to the collapse of the nappe pile. According to the structural position in the nappe pile a temperature gradient, reverse to the one present in D1 is developed. The Eastern parts of the Alpi Apuane were located in a deeper structural position in the antiformal stack and deformed at 375°C. The Western Alpi Apuane deformed at a temperature of about 295°C indicating a lower tectono-metamorphic level in comparison to the East. K/Ar and Ar/Ar dating of Kligfield et al. (1986) yield ages of 10 to 8 Ma for the end of the ductile deformation history. The late stage of D2 is related to uplift and exhumation and is characterized by brittle structures. Abbate et al. (1994) showed by apatite fission track dating that the rocks crossed the 120°C isotherm at about 4-2 Ma.

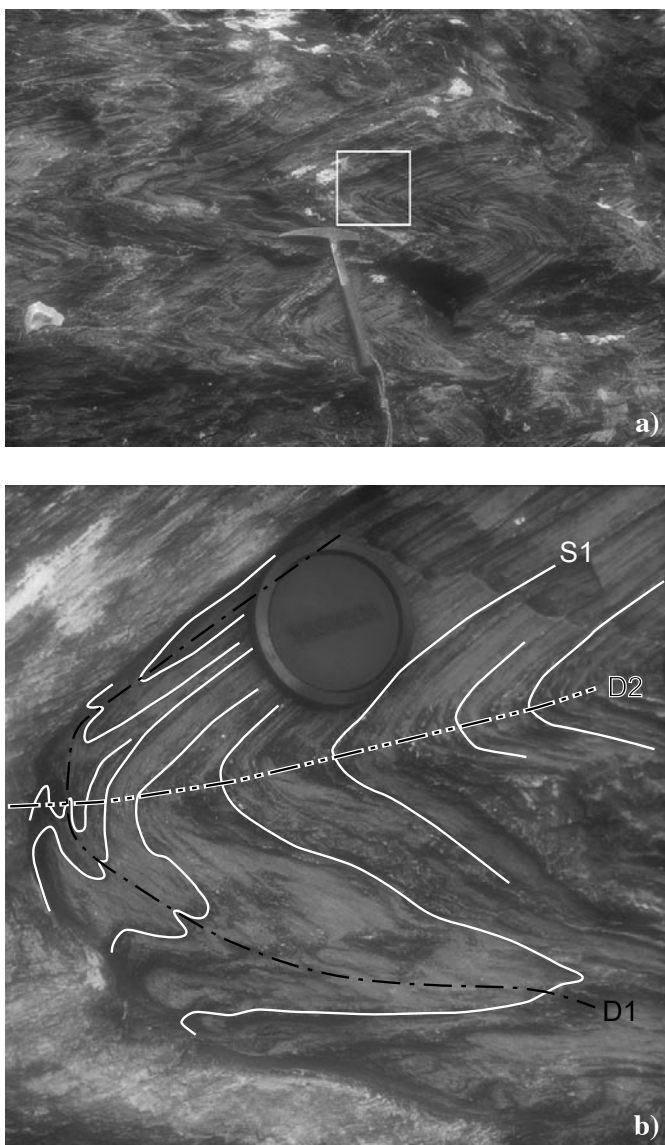


Fig. 1.15: a) D2 fold structure with a sub-horizontal axial plane. The close-up shown in b) is indicated. b) Close-up of a). S0 and tight D1 folds are refolded by D2.

Early D2: Macro- and meso-structures

The Alpi Apuane is divided asymmetrically into two parts by a kilometer scale mega-antiform with an upright fold axial plane striking in a NW-SE direction (Fig. 1.2 and Fig. 1.3). It is interpreted as the core of the collapsed antiformal stack, which was exhumed during D2 (Carmignani et al. 1990, Carmignani et al. 1994, Molli et al. 2000). However, up to now this structure is poorly understood. In contrast to the structures of the first deformation event the early D2 is characterized by folds of various scales with sub-horizontal fold axial planes (Fig. 1.15 and 1.16). An axial plane foliation (S2) (Fig. 1.9) is only visible in pelitic layers. One of the major structures is located in the central Alpi Apuane near the village of Forno, where the D1 Vinca-Forno anticline is refolded by an open D2 anticline (Fig. 1.2, Fig. 1.3 and 1.10). The fold axis of this structure trends in a NW-SE direction (Fig.

1.9). Additionally to folding mm to dm scale shear zones (Fig. 2.4 of Chapter 2) developed parallel to the D2 axial planes. Folds are developed mainly in heterogeneous and anisotropic rocktypes like the Middle - Upper Liassic cherty limestone, whereas the small-scale shear zones are dominantly located in pure calcite marbles or calcite marbles with a minor amount of dolomite (Carrara marble). D2 folding and shearing is frequently located in the necks of D1 boudins. Boudin necks represent initial points for folding or localized shearing. The fold vergence and sense of shear is opposite on either side of the Apenninic (NNW-SSE) trending mega-antiform (Fig. 1.3). A top to the SW sense of movement on the Southwestern side and a top to the NE sense of movement on the Northeastern side during the early D2 deformation is developed.

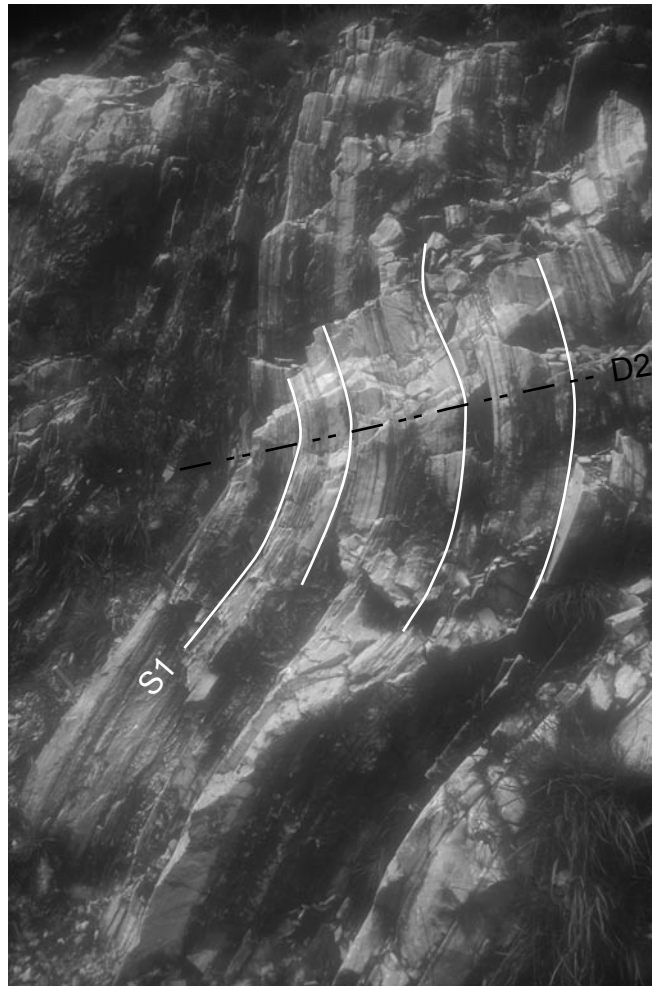


Fig. 1.16: Open D2 fold with sub-horizontal axial plane, overprinting the S1 foliation.

Late D2:

The youngest deformation phase in the Alpi Apuane area is related to brittle faulting that occurred between Pliocene and Middle Pleistocene. Ottria and Molli (2000) found that the late D2 deformation is characterized by a polyphase history with the development of co-existing strike slip and normal faults. The NE-SW oriented extension field fits well with the stress field observed in the Apenninic trending Magra graben to the West of the Alpi Apuane.

1.5 Meso-scale structural analysis of the Arni area, Eastern Alpi Apuane

1.5.1 Introduction to the mapping area

The deformation phases (cf. 1.4.5) in the Alpi Apuane are characterized by individual structures. In order to investigate the relationship between the structures of D1a, D1b and D2 a detailed mapping of the marble quarry 'Cava Landi' and its surroundings was performed (Fig. 1.17). Due to quarrying by the diamond wire saw technique (Bradley 1999) a large number of vertical to sub-vertical and horizontal cuts are present. The cuts are oriented in various directions and give insight in the spatial structure of folds and shear zones of the different deformation phases. The mapping area is located in the Eastern Alpi Apuane, close to the village of Arni. Arni lies in the 0.5 – 1km wide Tambura thrust zone, which is structurally located in the inverted limb of the Tambura anticline (Fig. 1.2 and Fig. 1.3). The Tambura anticline is one of the major fold structures, which formed during D1a (Carmignani et al. 1979, 1985, 1990, 1994; Molli et al. 2000). During D1b the deformation localized and led to the formation of the Tambura thrust zone (Molli et al. 2000). The whole structure is refolded by a series of open folds with sub-horizontal axial planes. This overprinting relationship is visible in the upper part of the Arni valley (Fig. 1.18), North of Arni, and is interpreted by Carmignani & Giglia (1979) and Carmignani et al. (1994) to have formed during D2. Cava Landi lies in the Southern prolongation of the Arni valley and exhibits a large number of overprinting relations between the different deformation phases. After a brief introduction to the mapping area and the exposed rock types the most prominent structures and their relationship are discussed.

1.5.2 Basis of mapping

Cava Landi and its surroundings were mapped on the scale 1:3500 (Fig. 1.19). A cross-section was constructed perpendicular to the average D1b fold axis with the section line oriented in a WSW-ENE direction (Fig. 1.20). Structures, which lie outside the section, were projected parallel to the average D1b-fold axis into the plane of section.

1.5.3 Lithologies and their structural characteristics

In the mapping area five different lithologies of Paleozoic to Tertiary age are exposed. These rocks belong to the sedimentary and tectonically reduced sequences of the inverted limb of the Tambura anticline. Sedimentary reduction is related to a pre-mesozoic topography in the Paleozoic basement (Carmignani et al. 1987). The presence of paleo-carst in Carrara marble and the replacement of the Upper Liassic to Cretaceous sequences (Calcare Selciferi, Diaspri, Calcare Selciferi a Entrochi) by the Cretaceous 'Cipollini' calc-schist indicate a 'paleo-high' in the carbonate platform and reduced sedimentation in the mapping area.

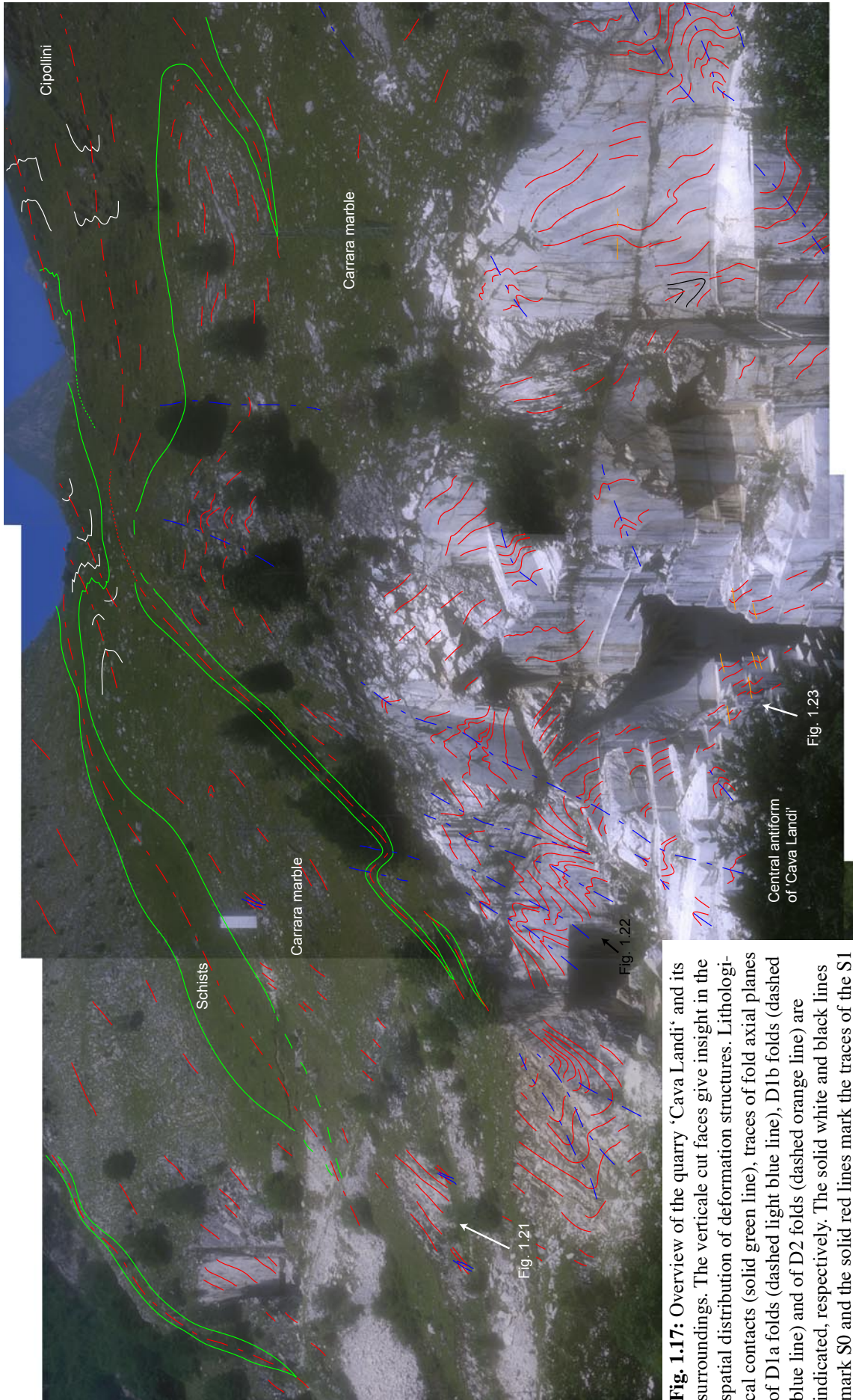


Fig. 1.17: Overview of the quarry 'Cava Landi' and its surroundings. The verticale cut faces give insight in the spatial distribution of deformation structures. Lithological contacts (solid green line), traces of fold axial planes of D1a folds (dashed light blue line), D1b folds (dashed blue line) and of D2 folds (dashed orange line) are indicated, respectively. The solid white and black lines mark S0 and the solid red lines mark the traces of the S1 foliation.



Fig. 1.18: Arni valley, North of the village of Arni, Eastern Alpi Apuane. Direction of view is North. Isoclinal D1a fold and lenses of different lithologies are refolded by open D2 folds with sub-horizontal axial planes. The quarry 'Cava Landi' is located directly to the South of the point of view.

Tectonic reduction of layer thickness is due to deformation along the Tambura thrust. Although isoclinal folding thickens Carrara marble it does not exceed 200 m. An expression of strong deformation along the Tambura thrust zone is the presence of elongated lenses of different lithologies (e.g. cherts, calc-schists) in a matrix of Carrara marble (Fig. 1.17, 1.19 and 1.20). The lenses can be interpreted as sheared-off hinges of isoclinal folds. The following lithological units can be distinguished:

1) Paleozoic phyllites

The Paleozoic phyllites are exposed at the Western border of the mapping area (Fig. 1.19 and Fig. 1.20). They represent the core of the Tambura anticline with the hinge zone located about 50 m outside the mapping area. The dominating structure in the phyllites is the SW dipping (255/50) S1 foliation, which is frequently overprinted by a sub-horizontal D2 crenulation cleavage. Compared to 700 m thickness in the West (Carmignani et al. 1987) the total thickness of the phyllites in the Arni area (< 100 m normal and inverted limb) is strongly reduced. The reason for the thickness reduction is related to the strong extension and shearing along the Tambura anticline and Tambura thrust zone.

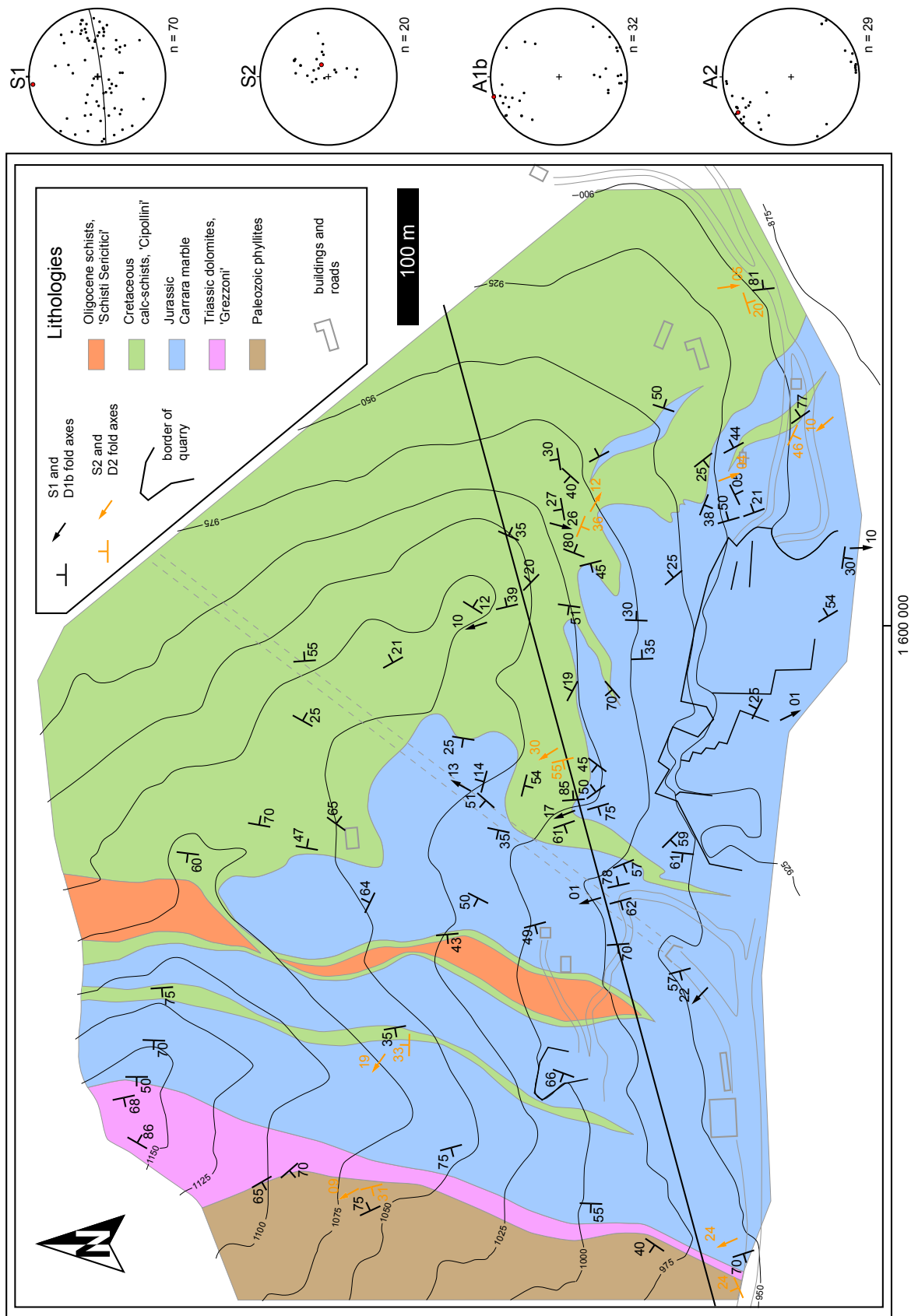


Fig. 1.19: Geological map of the surrounding of the quarry 'Cava Landi'. The NE-SW trending section line is indicated. Stereoplots (equal-area projection, lower hemisphere) to the right of the map show all structural data. Red points in the stereoplots indicate mean values.

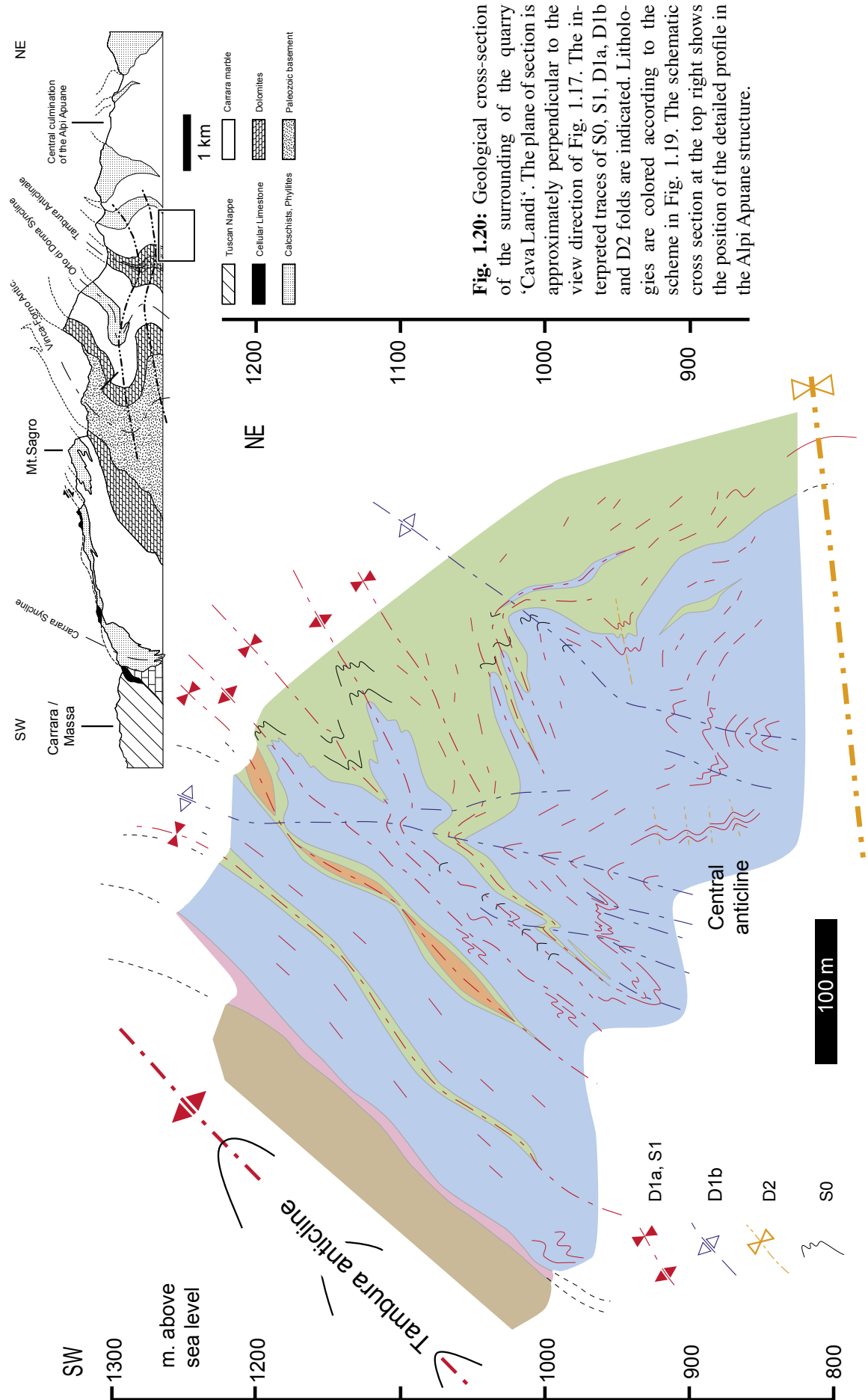


Fig. 1.20: Geological cross-section of the surrounding of the quarry 'Cava Landi'. The plane of section is approximately perpendicular to the view direction of Fig. 1.17. The interpreted traces of S0, S1, D1a, D1b and D2 folds are indicated. Lithologies are colored according to the scheme in Fig. 1.19. The schematic cross section at the top right shows the position of the detailed profile in the Alpi Apuane structure.

2) Triassic 'Grezzoni' dolomites

The Triassic is represented by the 'Grezzoni' dolomite formation (Fig. 1.19 and Fig. 1.20). Also the dolomites are strongly reduced in thickness. The 'Grezzoni' has a thickness of ~10 m, which is much less than the maximum thickness of ~200 m in the Alpi Apuane. The reason for the reduction is of sedimentary and tectonic nature. The dolomite matrix is very fine grained and dense and do not show any evidence of recrystallization during metamorphism. Neither any foliation (S1 or S2) nor other ductile deformation structure can be detected. Instead, many fractures on the mm to cm scale create a mosaic of fragments.

3) Jurassic (Lower Liassic) Carrara marble

In the largest part of the mapping area Carrara marble is exposed (Fig. 1.19 and Fig. 1.20). It is characterized by the SW-dipping S1 foliation. The foliation planes are enriched in dolomite and phyllosilicates, which cause a yellowish or greenish color and make the S1 planes visible in the field. The marble type exposed in quarry 'Cava Landi' consists of marble breccias. The components are elongated parallel to S1, so that the overprint of the D1b and D2 deformation phase on the S1 foliation can easily be detected. However, the breccias have only a limited lateral extension and are not restricted to single horizons. Thus, the breccias cannot be used as stratigraphic marker horizons to correlate different structures. The origin of these breccias is still not clear. Carmignani et al. (1987) interpreted them as infill of 'Neptunian dikes', which opened by differential movements during the fragmentation of the carbonate platform. In contrast to their origin, the deformation of the breccias is reasonably well constrained. The long axes of the breccia components lie parallel to L1 stretching lineation, which is why they must have deformed during D1a.

4) Upper Liassic to Oligocene sequences

The Upper Liassic 'Calcare Selciferi' (cherty limestones), Upper Jurassic 'Diaspri' (cherts) and Cretaceous 'Calcare Selciferi a Entrochi' formations of the Western Alpi Apuane are in this region replaced by the Cretaceous 'Cipollini' calc-schist. The 'Cipollini' is mainly composed of chloritic pelites with quartz nodules. In places, the pelitic matrix is enriched in calcite or in chert layer. Depending on the amount of calcite and cherts transitions to 'Cherty limestone' and 'Diaspri' are developed, respectively. The transitions are gradual rather than abrupt and are restricted to lenses of several meters. Therefore these rocks are represented in map and profile by only a single signature (Fig. 1.19 and Fig. 1.20).

The calc-schists are strongly foliated. Depending on the structural position it is difficult to decide whether S1 or S2 are exposed. In the limbs of D2 folds, for instance, S1 and S2 cannot be distinguished, because their orientation and intensity is the same. In the hinges of D2 folds, where S1 and S2 include a high angle, a sub-horizontal crenulation cleavage, similar to the one exposed in the Paleozoic phyllites is developed. The foliation planes show a chocolate-table boudinage, indicating pure shear deformation in the oblate field.

The thickness of the ‘Cipollini’ formation is highly variable, depending on the structural position. It ranges from a few cm to meters in the hinges of isoclinal folds to about 50 m in the limb positions.

5) Oligocene schists

The youngest rock type in the mapped area is the Oligocene ‘Schisti Sericitici’ formation. It is exposed in the central part of the investigated area only (Fig. 1.19 and Fig. 1.20). The schists are easily recognizable by their reddish-purple color and their strong foliation. The S1 foliation is concordant to the other units. Because of the mechanical weakness of the schists they form a topographic depression in the hill slope. Single lenses can be detected, which represent the stretched hinge of a D1a isoclinal fold. The quality of outcrops is not as good as of the other formations, because the schists are mostly covered by vegetation.

1.5.4 Structural relationship between D1a, D1b and D2

D1a

D1a produced highly extended isoclinal folds. If the D1a folds are not refolded by a later deformation phase, their axial planes dip gently to the SW, parallel to the axial plane of the large scale Tambura anticline. The S1 main foliation, which is the most prominent foliation the entire Alpi Apuane, is the axial plane foliation of these D1a folds. The folds are extremely amplified so that S1 is effectively parallel to the sedimentary layering (S0) and S1 represents a transposed foliation. Associated with S1 is the pronounced down-dip L1 stretching lineation. It is formed by strain fringes around pyrite porphyroclasts and elongated mineral grains. The intersection of S0 and S1 is parallel to L1. This intersection lineation coincides with the axes of mm-scale isoclinal folds. Thus, D1a isoclinal fold axes are parallel to the stretching direction.

D1b

Tight similar-type folds refold the S1 foliation and D1a fold structures. The long limbs are strongly sheared; the fold hinges and the short limbs are not sheared. Therefore, zones of low strain, represented by the hinges and short limbs, are separated from zones of high shear deformation in the long limbs. Fig. 1.21 shows the transition from a folded domain to one, which is sheared, and again to a folded domain. In the up-ward prolongation of the sheared domain of this outcrop sample D1-E-2 is located. Its microstructural and textural characteristics are discussed in chapter 2 and 4 of this thesis. A well-developed example of the D1a/D1b overprinting relation is exhibited in the Western part of ‘Cava Landi’ and its Northwestern surroundings.

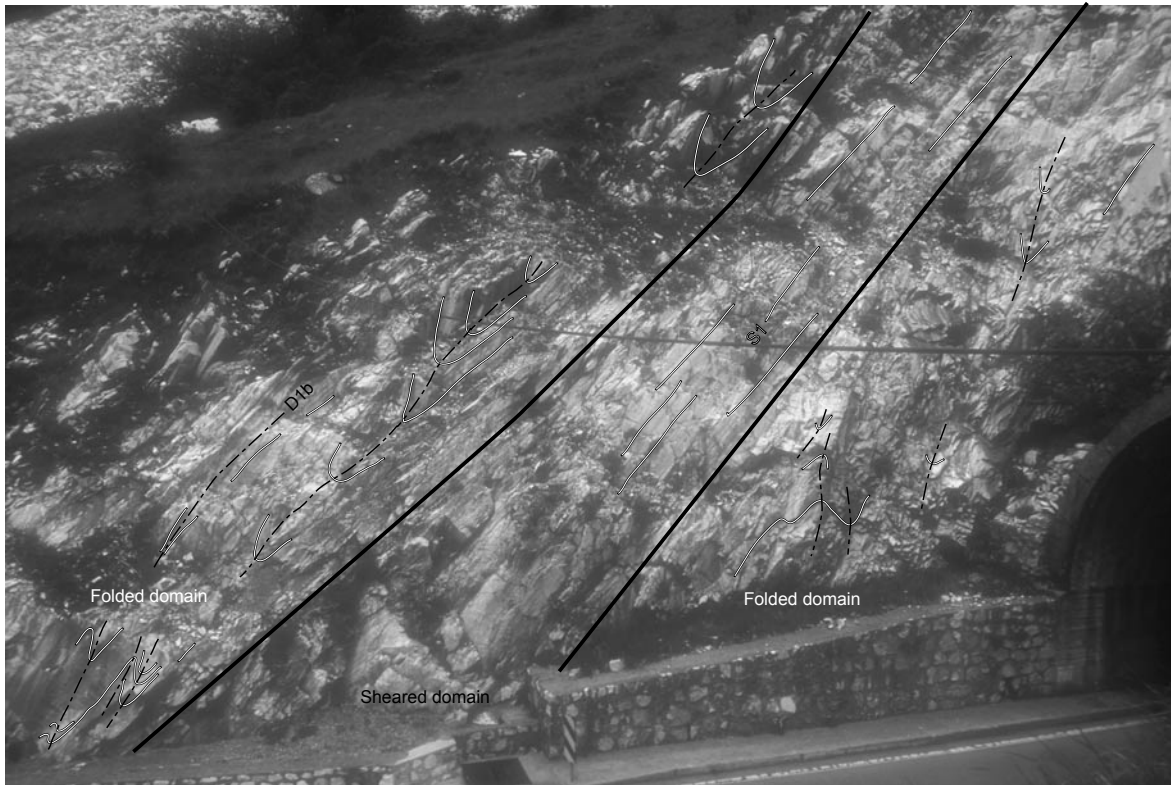


Fig. 1.21: D1b folds. The long limbs of the folds merge into shear zone (central part of the outcrop), where no folds can be detected. These domains are separated from those dominated by fold hinges and short limbs (to the right and to the left of the sheared domain).

The most prominent structure in the quarry is an up-right antiform with a $\sim 70^\circ$ inclined SW dipping axial plane (“central antiform” in Fig. 1.17). Its Western limb shows a series of similar type folds (Fig. 1.22). The fold vergence and asymmetry (gently SW dipping long limbs and steeply SW dipping short limbs) are consistent with a closure of the antiform in the East of the similar type folds so that the similar type folds and the antiform belong to the same deformation phase. Since S1 foliation and the related stretching lineation (L1) are refolded, the tight similar type folds and the antiform developed during D1b. Following the axial plane of the D1b folds in an upward direction (Fig. 1.17 and Fig. 1.20) an overprint of an isoclinal D1a fold by D1b can be detected. The determination of the a-direction (Ramsay 1960) from D1b fold axial planes and the refolded L1 reveal a transport in a NE-SW direction (Fig. 1.9). The a-direction of D1b folds coincides with the orientation of the L1 stretching lineation, which has formed during D1a. This coincidence indicates that the transport direction did not change during D1a and D1b. Therefore, it can be concluded that D1a and D1b structures belong to a continuous deformation process, rather than have formed during separated phases. The following process can be considered. The D1 deformation started by folding, producing the D1a isoclinal folds. Fold amplification was achieved by the stretching of the fold limbs and the formation of D1a shear zones like the “Zebrino”. Shear deformation continued during D1b, which was associated by the formation of D1b similar folds.

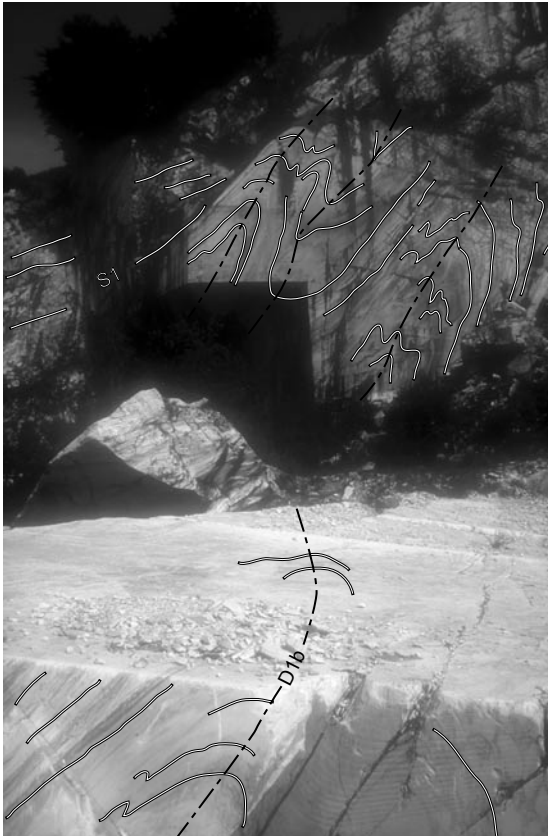


Fig. 1.22: Tight similar type D1b folds West of the central antiform of Cava Landi. Fold asymmetry and vergence are consistent with an antiformal closure to the right of the section.



Fig. 1.23: The eastern limb of the central antiform of 'Cava Landi' is refolded by open D2 folds with sub-horizontal axial planes.

D2

The Eastern limb of the D1b-antiform in 'Cava Landi' is also folded (Fig. 1.23). In contrast to the Western limb, open folds with a sub-horizontal axial plane (260/20) are developed. The short limbs dip to the SW (229/40) and the long limbs dip to the NE (070/68). The stereoplot construction indicates a fold axis plunging with 12° toward the SE. Besides the flat-lying axial plane also the fold asymmetry does not fit the D1b-antiform. Since the open folds overprint the S1 foliation and the Eastern limb of the D1b-anticline they are interpreted to have formed during the second deformation event (D2). Similar fold structures can be found all over the mapping area, but they seem to be developed only locally, because fold axial planes cannot be continuously traced. D2 folding is associated with shear deformation. Fig. 1.24 shows a typical small scale D2-fold with a sheared limb. If shear deformation continued a shear zone could have developed (cf. Fig. 2.4 of chapter 2, D2-E shear zone, note fold hinge before S1 enters the shear zone).

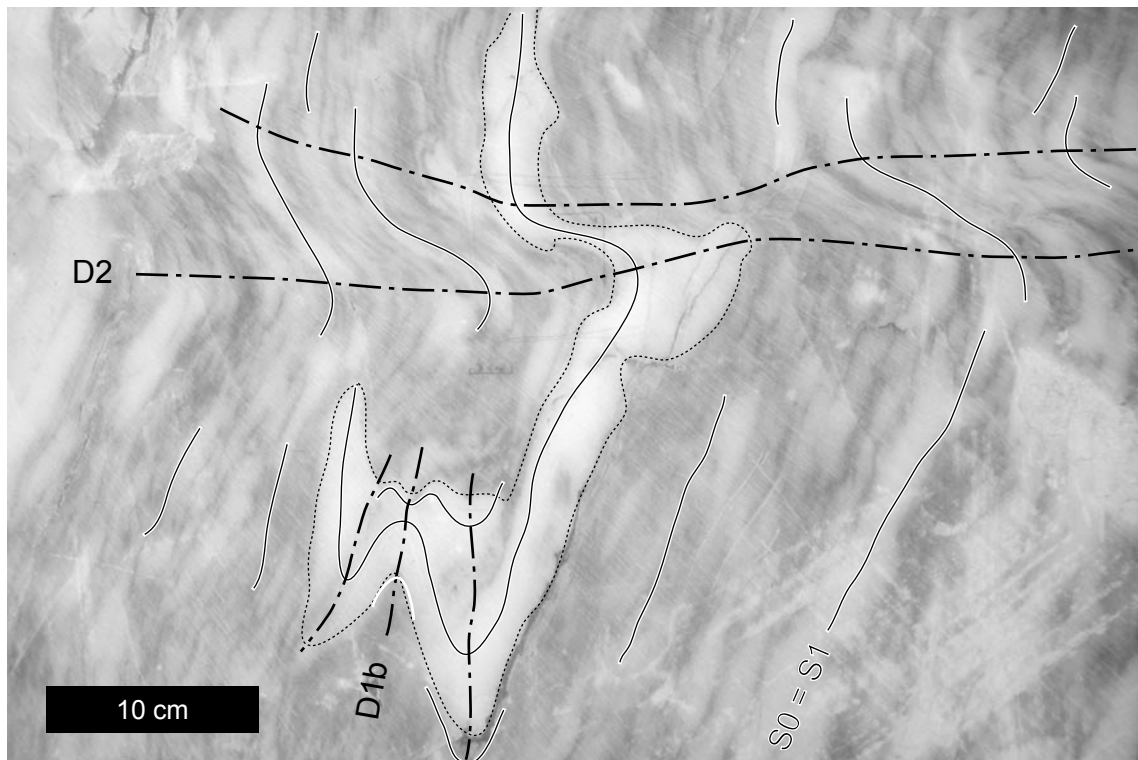


Fig. 1.24: Refolded marble breccia. A breccia component (outline by dotted line) is folded by D1b and D2. The bedding (S0) and S1 foliation (S1) are indicated by the solid line.

1.5.5 Summary

The detailed mapping of the quarry ‘Cava Landi’ revealed the following structural relationships. Due to isoclinal folding during D1a the sedimentary bedding (S0) came into parallelism to the regional main foliation (S1). S1 is the axial plane foliation of the isoclinal D1a folds. Shear deformation parallel to the L1 stretching lineation caused the formation of highly stretched lenses of different lithologies. The D1a structures are refolded during the D1b deformation phase by gently inclined axial planes. Tight similar type folds are developed with long limbs, which gradually merge into shear zones. These shear zones accommodated the largest amount of strain during the D1b deformation phase. The transport direction stayed constant during D1a and D1b, indicating a continuous deformation process rather than separated deformation phases. D1a and D1b structures are refolded along sub-horizontal axial planes of the D2 deformation event. D2 produced mainly open folds. Parallel to the axial planes shear zones are locally developed.

Chapter 2

Variation of deformation microstructures and temperatures of Carrara marble across the Alpi Apuane tectonic window

2.1 Introduction

Carrara marble is generally known for its homogeneous microstructure and isotropic texture, i.e. crystallographic preferred orientation (CPO). This microfabric with equiaxed grains of a homogeneous size, with straight boundaries and 120° triple junctions, is characteristic of a “foam structure“ (Fig. 2.1), which evolves during static grain growth (annealing)(e.g. Olgaard & Evans 1988, Passchier & Trouw 1998). Carrara marble is used frequently as starting material for rock deformation experiments (e.g. Schmid et al. 1980, De Bresser 1991, Rutter 1995, Pieri et al. 2001, Barnhoorn et al. 2004) because of this microfabric. However, dynamically recrystallized microstructures with irregular grain boundaries and a pronounced texture also exist in Carrara marble. Molli et al. (1997) describe shear zones with preserved dynamically recrystallized microstructures, which overprint the typical annealed microfabric of Carrara marble. All of these microstructures can be assigned to one of the two main deformation events (D1 and D2) of the Alpi Apuane (cf. chapter 1).

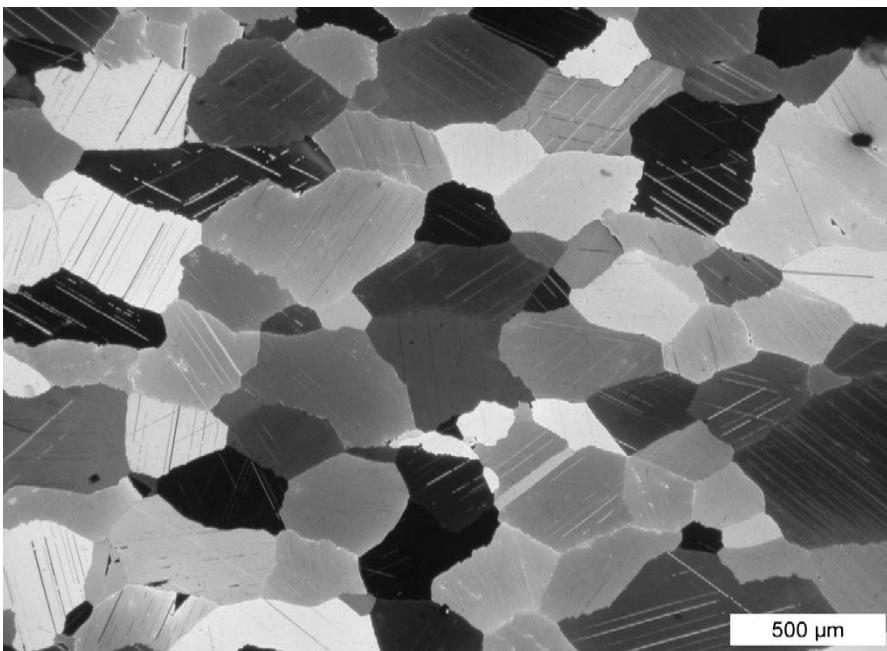


Fig. 2.1: Statically recrystallized Carrara marble. Granoblastic microstructure with large grains and straight grain boundaries. Micro-graph in crossed polarized light.

The basic features of the D1 and D2 microstructures as well as the annealed microstructure will be described in the first part of this chapter. For a more detailed description of the microstructural and textural evolution as a function of strain and the influence of a second phase on the natural deformation behaviour of Carrara marble the reader is referred to the case studies presented in chapter 3 and chapter 4. The second part of this chapter is concerned with the temperature conditions during which the different dynamic microstructures evolved and the grains sizes to which the analyzed shear zones recrystallized.

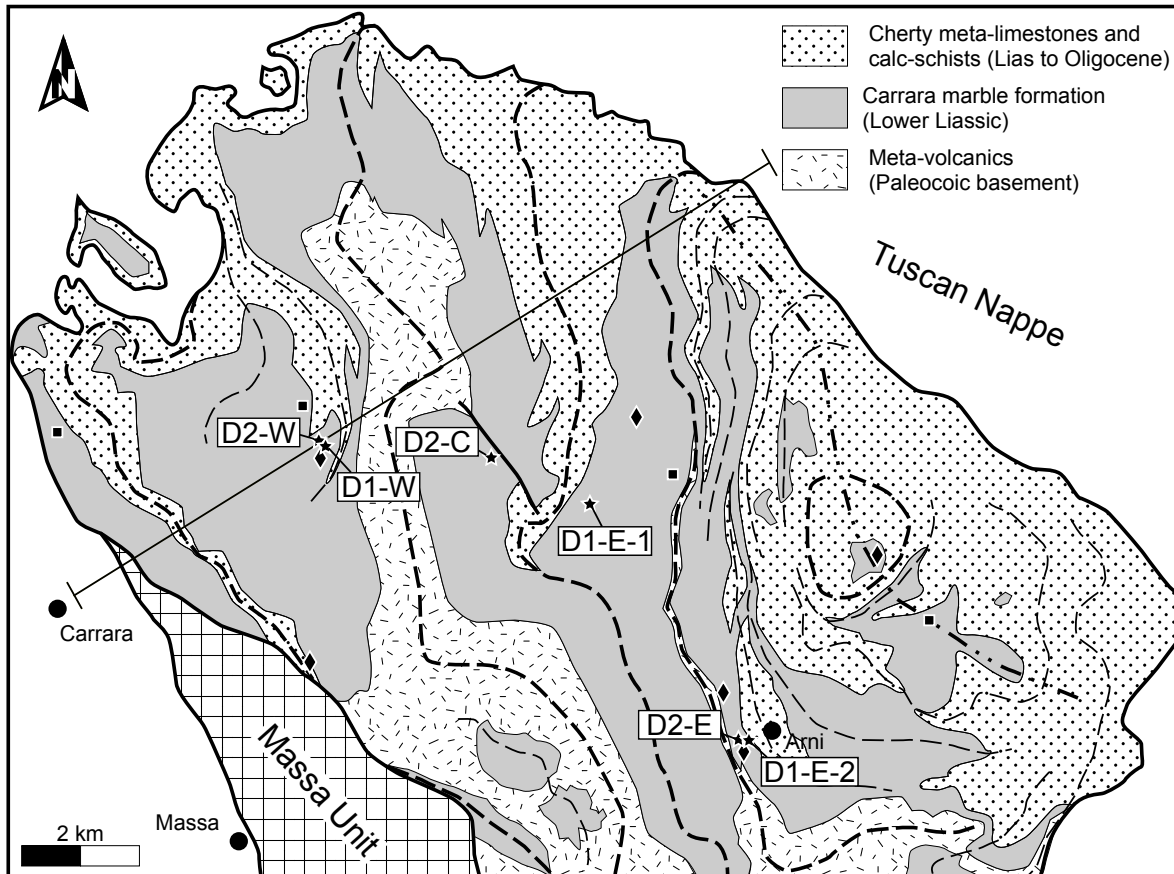


Fig. 2.2: Schematic geological map of the Northern part of the Alpi Apuane (redrawn after Carmignani et al. 1987). The section line to which the sample locations are projected in Fig. 2.17, 2.19 and 2.20 is indicated. The sample locations of the analyzed samples of this study (stars), of the studies of Di Pisa et al. (1985) (squares) and Molli et al. (2000) (diamonds) are indicated.

Three processes of dynamic recrystallization can be distinguished: slow migration recrystallization (bulging recrystallization), sub grain rotation recrystallization (SGR) and fast migration recrystallization (grain boundary migration, GBM) (Guillope & Poirier 1979, Drury et al. 1985, Urai et al. 1986, Drury & Urai 1990). The dominance of each mechanism is mainly governed by temperature and strain rate (Hirth & Tullis 1992, Hirth et al. 2001, Stipp et al. 2002). On the basis of experimentally deformed quartzite, Hirth & Tullis (1992) have introduced three dislocation creep regimes, which are characterized by distinct recrystallization microstructures. At low temperatures and fast strain rates bulging

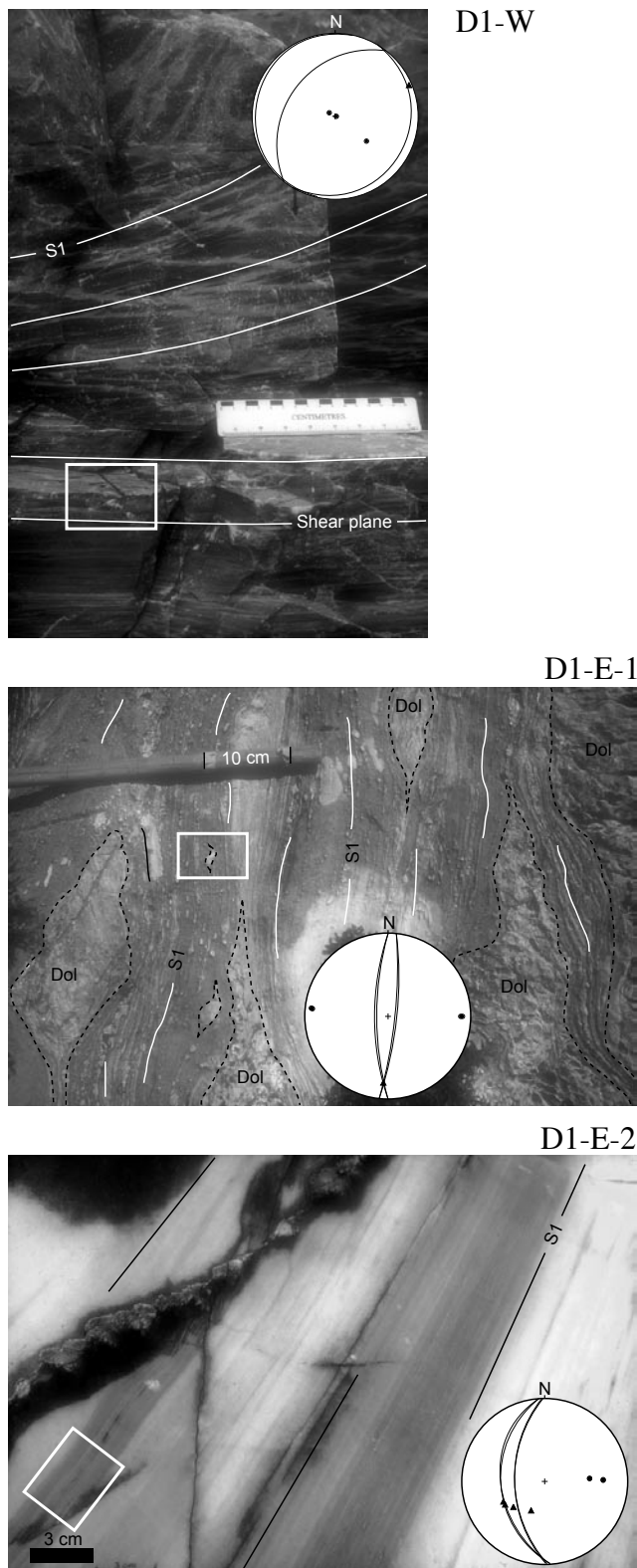


Fig. 2.3: Analyzed D1 shear zones on the outcrop scale. S1, shear plane and lithological contacts (dashed lines) are indicated. The boxes indicate the position of the analyzed sample. The stereonet diagrams (equal area projection, lower hemisphere) illustrate the orientation of S1 (circles) and L1 (triangles).

recrystallization is dominant (regime 1), at intermediate temperatures and strain rates SGR is the dominant mechanism (regime 2) and at elevated temperatures and slow strain rates GBM dominates dynamic recrystallization (regime 3). Similar differences in recrystallization microstructures are observed in deformation experiments with calcite (Schmid et al. 1987). In experiments Carrara marble recrystallizes at 700°C by sub grain rotation, whereas at 800°C and lower strain rates GBM is the dominant recrystallization mechanism. From the above examples it is clear, that temperature is an important factor for the formation of dynamically recrystallized microstructures. Therefore the determination of the deformation temperature may be used to characterize certain microstructures. For such a characterization the microstructures and deformation temperatures of the different deformation events of the Alpi Apuane were analyzed. Three shear zones representative of each deformation event were sampled to the western side of the Alpi Apuane mega-antiform (Fig. 2.2). They come from the Western (D1-W; D2-W), Central (D2-C) and Eastern Alpi Apuane (D1-E-1; D1-E-2; D2-E). Their mesoscopic appearance is illustrated in Fig. 2.3 and 2.4, respectively. For each sample the orientation of S1 and the L1 is indicated.

Based on microstructural observations Molli et al. (2000) introduced a tectonic model for the Alpi Apuane region. This study is included in this chapter, because it contains the results of analytical work, which was performed in the course of this PhD-thesis. Temperature and grain size data of Molli et al. (2000) were re-examined and may deviate from those presented in the original paper. The samples from Molli et al. (2000) are, if they are labeled, indicated by the prefix M. The aim of this chapter is to extend the work of Molli et al. (2000) in terms of the analysis of dynamic microstructures and temperatures of D1 and D2 shear zones. Moreover, the general characteristics of the different ‘dynamic’ and ‘static’ microstructures, appearing in the Alpi Apuane, are described. Detailed case studies on D1 and D2 microstructures are given in chapters 3 and 4.

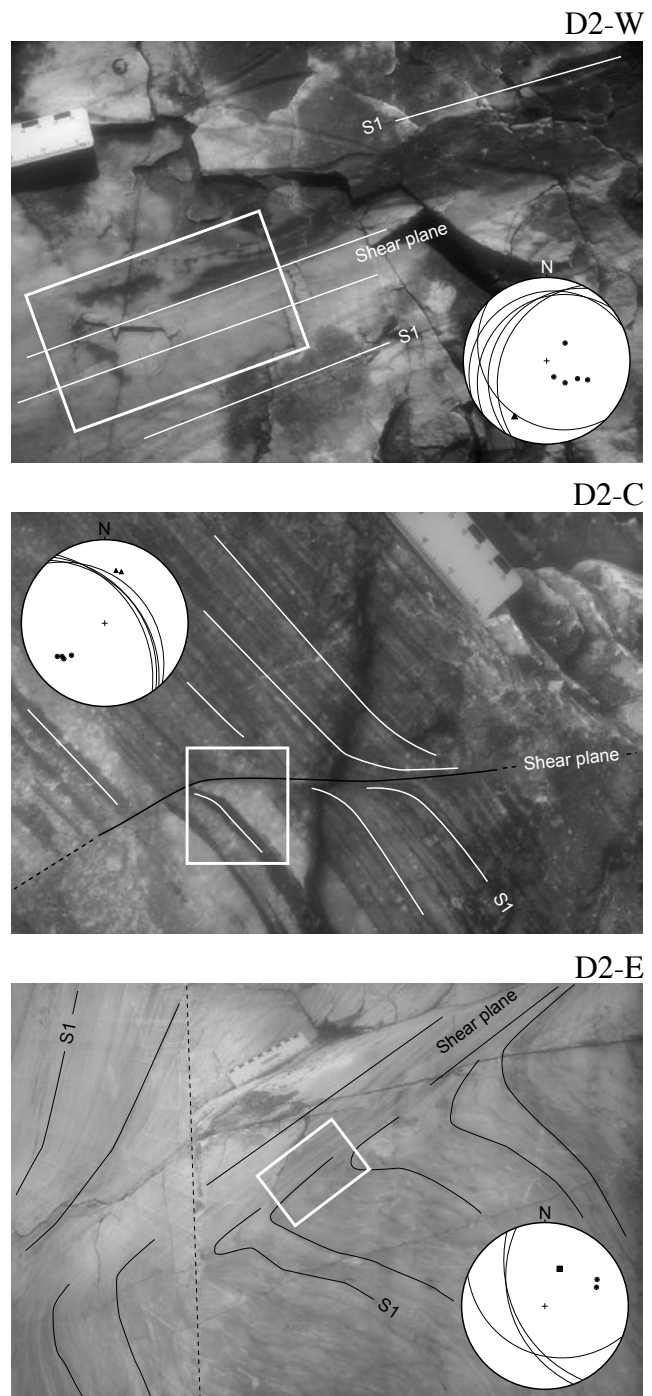


Fig. 2.4: Analyzed D2 shear zones on the outcrop scale. S1 and shear plane (SP) are indicated. The boxes indicate the position of the analyzed sample. The stereoplot diagrams (equal area projection, lower hemisphere) illustrate the orientation of the S1 (circles) and L1 (triangles). In sample D2-E the orientation of the SP (square) is plotted additionally. The dashed line in the photograph of sample D2-E indicate a vertical edge in the outcrop.

2.2 Microstructures

2.2.1 D1 Microstructures

Mesoscopically, D1a and D1b mylonites (cf. chapter 1.4.5) are indistinguishable. Only the microstructural characterization allows to distinguish these mylonites. Therefore, mesoscopical mylonites, which exhibit statically recrystallized microstructures, related to post-deformational annealing, are referred to D1a. Mylonites, which preserve dynamic recrystallization microstructures, are referred to D1b. The microstructures of the D1b mylonites show elongated grains (short/long axis, $b/a = 0.5$) with a diameter of 100-200 μm and irregular grain boundaries (Fig. 2.5). The lobate grain boundaries indicate GBM as the dominant recrystallization mechanism. Deformation by intra-crystalline processes is documented by a pronounced texture with a c-axis maximum normal to the foliation (Fig. 2.6) and an a-axis girdle within the foliation (cf. site 1 in chapter 4). This kind of crystallographic preferred orientation is typical of basal $\langle a \rangle$ slip as dominant slip system and it occurs at large finite strains (cf. chapter 4, Barnhoorn et al. 2004). On the scale of the analyzed samples the microstructure is homogeneous; no evidence of μm to mm scale localization can be detected.

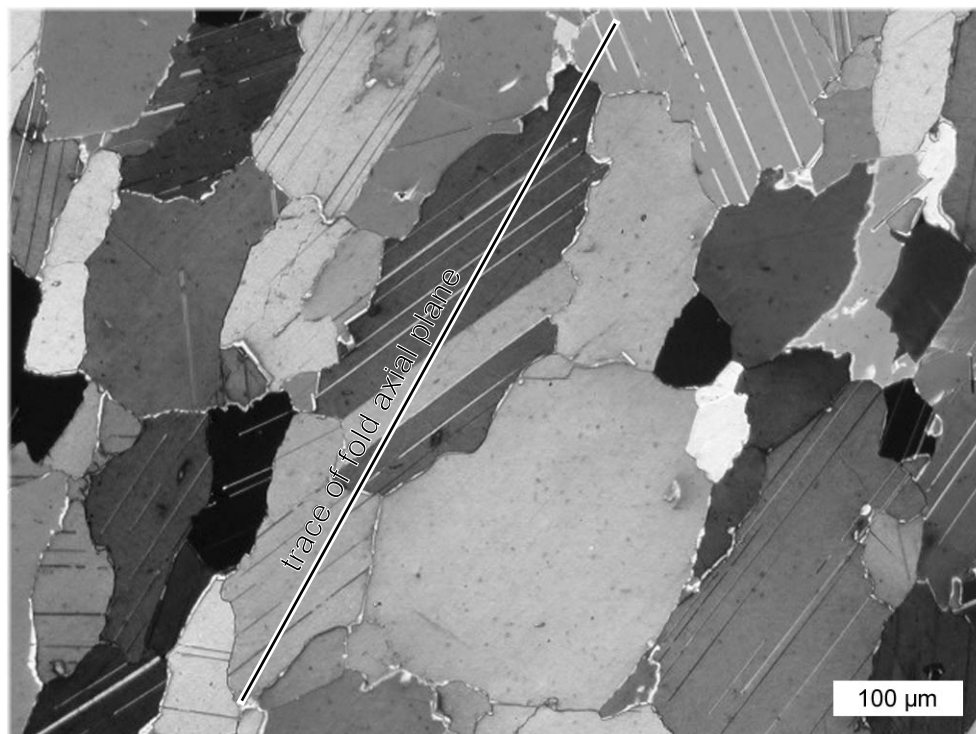


Fig. 2.5: Micrograph of D1 microstructure in crossed polarized light. Coarse grains with irregular boundaries are characteristic of GBM as dominant recrystallization mechanism. In folded samples the grain long axes correspond to the trace of the axial plane.

As described in chapter 1.4.5, D1b shearing is associated with folding. The microstructures in these folds are similar to those described previously for the D1b mylonites, with the grain long axis oriented parallel to the axial planes. Leiss et al. (2001) investigated the microstructures and textures of these meter-scale folds in detail. They found zonation patterns in cathodoluminescence and suggested that these structures may be related to grain boundary migration recrystallization. The textures in the folded samples vary between hinge and limb positions. Textures from fold limbs are consistent with those from shear zones, textures determined in the fold hinges, however, are not as simple explainable. The above-described microfabric is characteristic of deformation by dislocation creep in combination with grain boundary migration recrystallization. From field studies it became evident, that in D1b shear zones a substantial amount of dolomite is mixed with the calcite. The presence of dolomite influences the deformation behaviour of the aggregate and causes a change in deformation mechanism from dominant dislocation creep to dominant diffusion creep. This behaviour is discussed in chapter 4. After the classification of Molli et al. (2000) the microstructures and textures of the D1b mylonites and folds are called Type-B1.

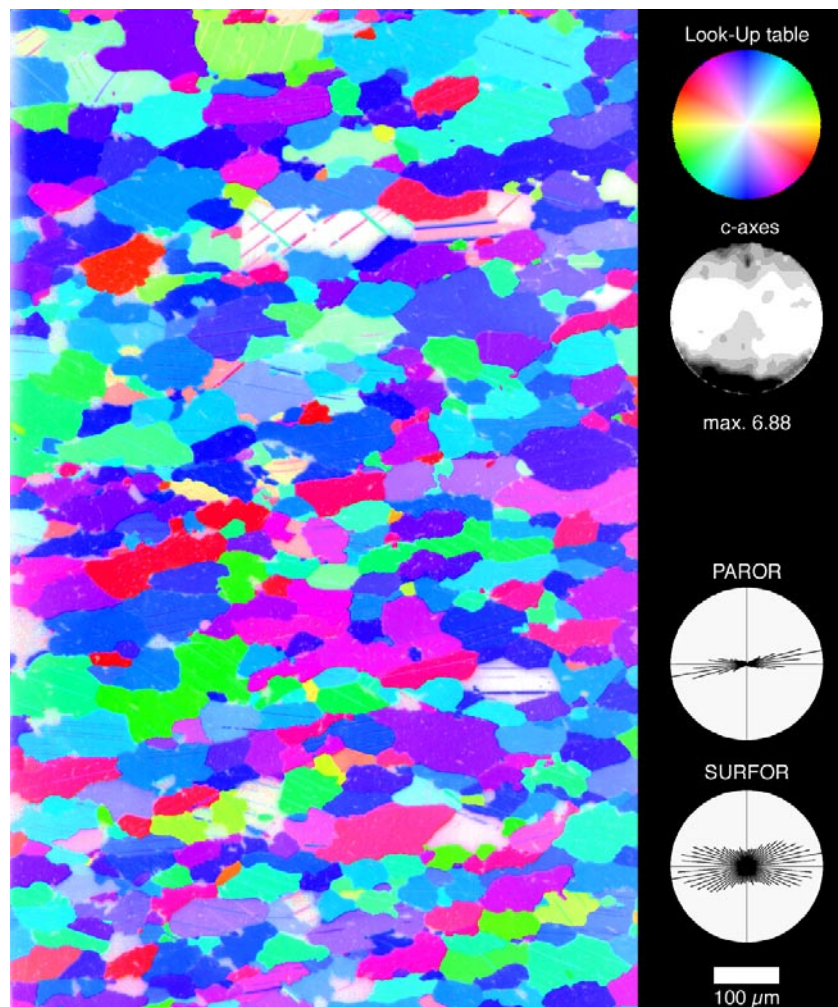


Fig. 2.6: CIP c-axes orientation image of D1 microstructure. C-axes are color coded according to the look-up table (LUT) at the upper right of the figure. C-axes polefigure on the basis of the analyzed area is shown below the LUT. Rose diagrams of particle long axes (PAROR) and grain boundary surfaces (SURFOR) are shown at the lower left.

2.2.2 D2 Microstructures

In contrast to D1, the analyzed D2 structures show stronger localization. D2 shear zones overprint annealed and dynamically recrystallized pre-existing microfabrics. In the hinges of D2 fold structures, dynamic recrystallization obliterates the folded S1 foliation. Folds and shear zones of the D2 event are characterized by core-mantle microstructures. Slightly elongated ($b/a = 0.6-0.7$), coarse porphyroclasts (100-200 μm) with irregular grain boundaries and a weak preferred orientation of grain long axes are embedded in a matrix of small equiaxed grains (20-40 μm ; $b/a = 0.8$) (Fig. 2.7). The porphyroclasts show evidence of intracrystalline deformation, like undulotonic extinction and subgrains. The subgrains and the surrounding matrix grains are of the same size and are internally strain free. The degree of recrystallization depends on the amount of strain. Not only the microstructure changes as function of strain but also the CPO. In low finite strain samples twinning textures are most common, whereas basal $\langle a \rangle$ textures (Fig. 2.8) are indicative of high strain samples. An example of the microstructural and textural variations across a D2 shear zone is given in chapter 3. The microfabric described above is characteristic of subgrain rotation recrystallization and is called Type-B2 by Molli et al. (2000).

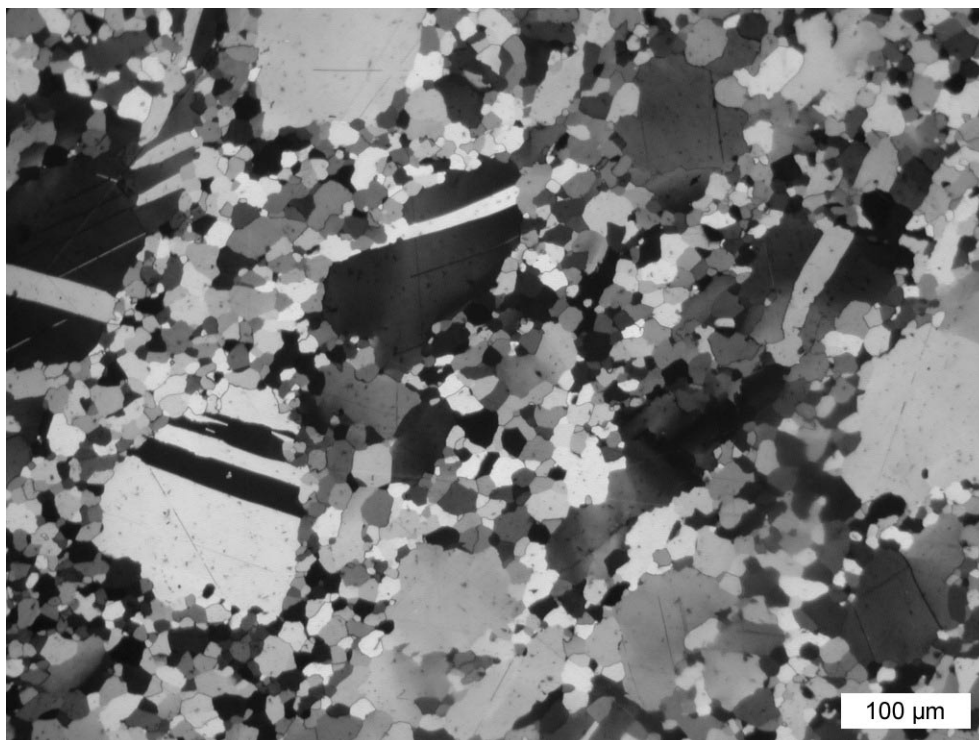
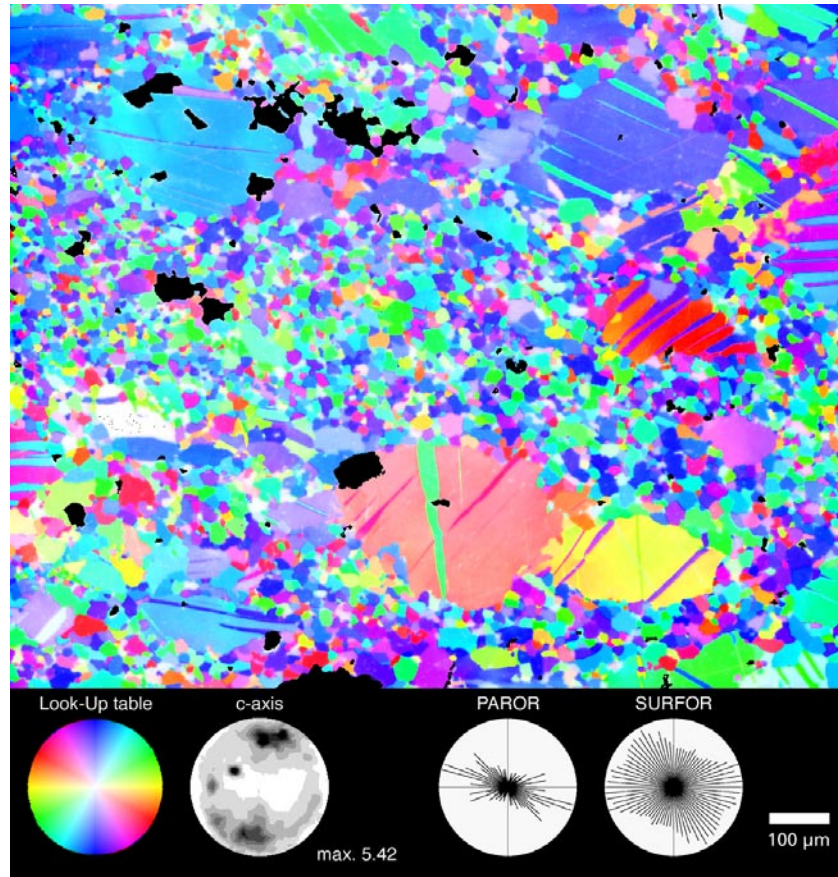


Fig. 2.7: Micrograph of D2 microstructure in crossed polarized light. Core-mantle structure in mm-scale shear zone. Coarse deformed porphyroclasts are embedded in a matrix of small new grains, which formed by sub-grain rotation recrystallization.

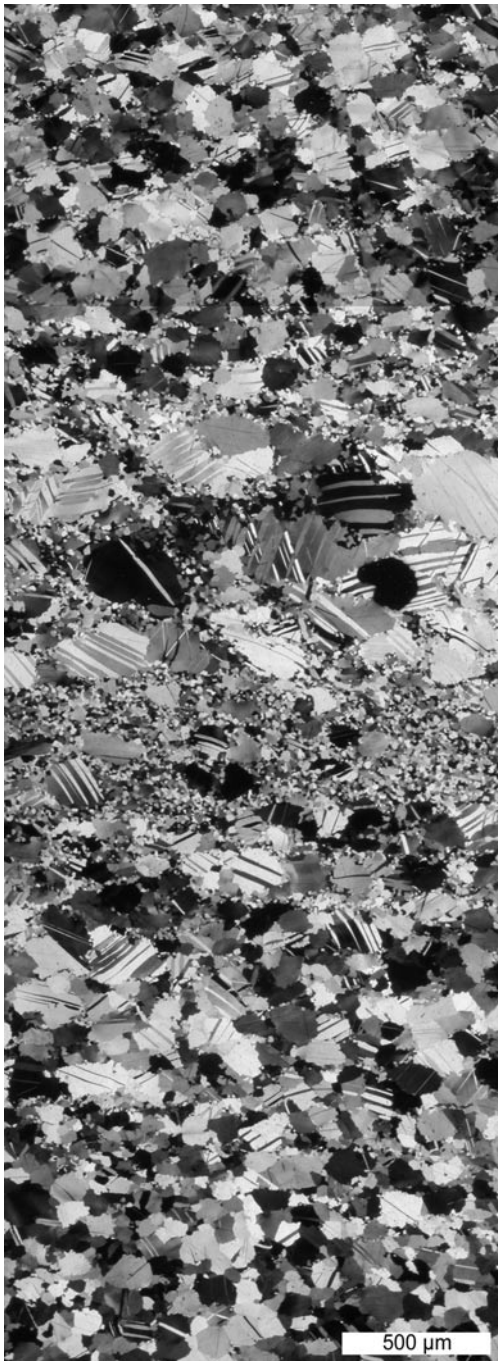
Fig. 2.8: CIP c-axes orientation image of D2 microstructure. C-axes are color coded according to the look-up table (LUT) at the lower left of the figure. C-axes polefigure on the basis of the analyzed area is shown right of the LUT. Rose diagrams of particle long axes (PAROR) and grain boundary surfaces (SURFOR) are shown at the lower right.



The center of the D2 shear zones, i.e. the domain with the largest amount of recrystallization, is frequently associated with a layer of coarse-grained calcite. The grain sizes of these crystals, which are intensively mechanically twinned, exceed the one of the protolith (Fig. 2.9, Appendix C3). There is no evidence of static grain growth, which has altered the deformation microstructure. It is most likely that the coarse grain material was already present before the deformation started. Probably, the coarse-grained calcite represents former veins. Assuming that the deformation started dominantly by dislocation glide, the coarse grained material would have deformed preferentially according to the Hall-Petch-relation (Nicolas & Poirer 1976). After the Hall-Petch relation the flow stress σ is connected to the grain size d by the following relationship:

$$\sigma = \sigma_0 + kd^{-0.5} \quad (2.1)$$

where σ_0 and k are constants. Thus, the flow stress is inversely proportional to grain size. Glide of dislocations is easier in large crystals compared to small ones, because grain boundaries represent obstacles for slip, which can only be overcome by dislocation climb. Because of the Hall-Petch relationship, the coarser grained vein material may have localized the deformation initially and thus might be responsible for the formation of the D2 shear zones. Twinning reduces effectively the grain size and twin boundaries are preferred sites



Transition to annealed
protolith; grain
diameter $\sim 100 \mu\text{m}$

Coarse-grained layer
parallel to shear zone
boundary; grain
diameter $< 300 \mu\text{m}$

Recrystallized center of
the shear zone; grain
diameter $\sim 30 \mu\text{m}$

Transition to annealed
protolith; grain
diameter $\sim 100 \mu\text{m}$

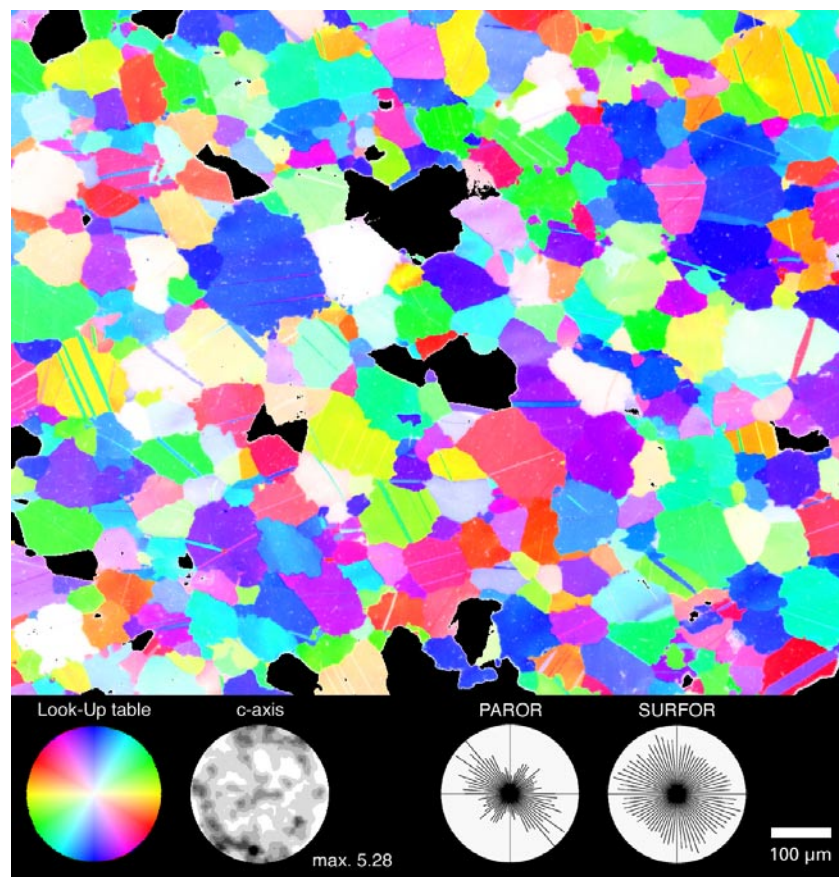
Fig. 2.9: D2 shear zone with coarse-grained layer close to its center. The coarse-grained material is strongly mechanically twinned. Probably it formed as calcite vein and may have triggered the localization of the deformation. Micrograph in crossed polarized light.

of dynamic recrystallization by GBM and SGR. Moreover twinning can only accommodate a restricted percentage of strain (e.g. Turner 1962, Schmid et al. 1987, Burkhard 1993). After $\sim 15\%$ strain dislocation glide and twinning are exhausted and dislocation climb and dynamic recrystallization have to be dominant to continue deformation. Pieri et al. (2001a, b) and Barnhoorn et al. (2004) showed recently in torsion experiments over a large range of strains that at low strains twinning contributes largely to the formation of the microstructure, whereas at higher strain dynamic recrystallization becomes dominant.

2.2.3 Statically recrystallized microstructures

The annealed microstructures correspond to the Type-A microstructures in the sense of Molli et al. (2000). Annealed marbles are characterized by a very weak texture or show even a random distribution of crystallographic axis (Fig. 2.10). The calcite grain diameters exceed 150-300 μm and the grain boundaries are straight (Fig. 2.1). In detail, however, crystallographic low index planes control the grain boundary orientation. This crystallographic control is expressed by a staircase shape of grain boundaries (Fig. 2.11). The individual faces correspond to crystallographic low index planes (e.g. rhomb planes or e-twin planes) in either of the adjacent crystals (Fig. 2.12). Further detailed analysis of crystallographic and grain boundary orientation and the determination of the misorientation relation across grain boundaries are required to answer the question of, which low index planes correspond to the individual faces. The grains are equiaxed with triple junctions of 120° angle; or only a weak preferred orientation of grain long axes and grain boundaries is developed. The above-described features correspond to the one of a “foam structure”, which evolve during thermally induced grain growth (e.g. Olgaard & Evans 1988, Covey-Crump 1997, Paschier & Trouw, 1998). A quantitative description of the Type-A microstructures is given by Molli & Heilbronner (1999) and Molli et al. (2000).

Fig. 2.10: CIP c-axes orientation image of statically recrystallized microstructure. C-axes are color coded according to the look-up table (LUT) at the lower left of the figure. C-axes polefigure on the basis of the analyzed area is shown to the right of the LUT. Rose diagrams of particle long axes (PAROR) and grain boundary surfaces (SURFOR) are shown at the lower right.



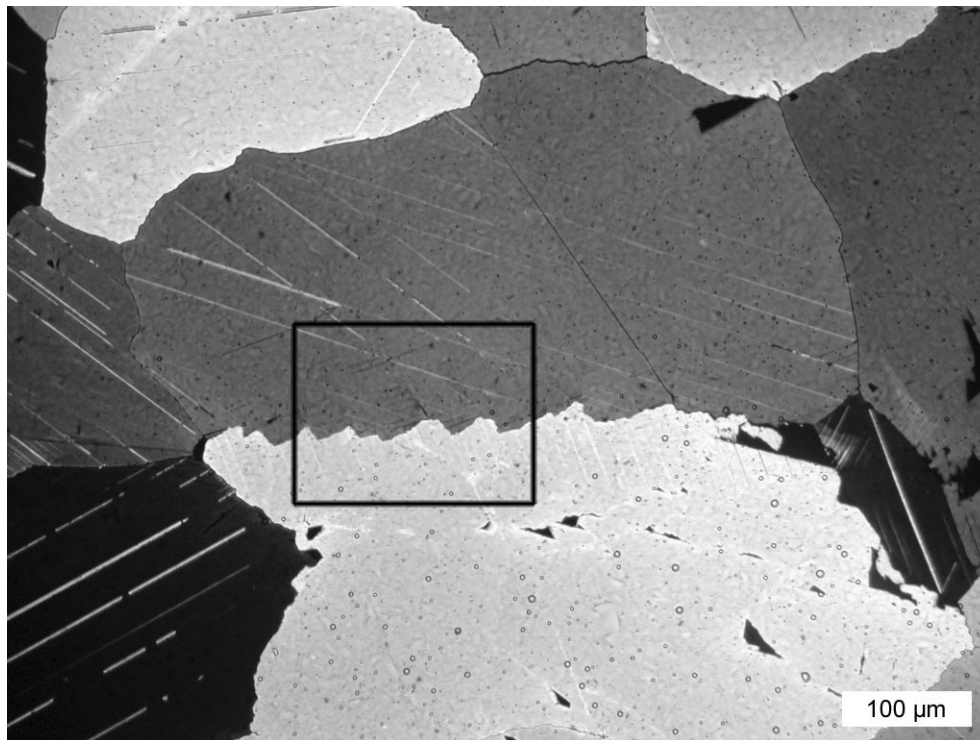


Fig. 2.11: Staircase shape of grain boundaries in annealed marbles. The outline of the close-up shown in Fig. 2.12 is indicated. Note near 120° angles at grain triple junctions are indicative of an equilibrium- or “foam”-structure. Micrograph in crossed polarized light.

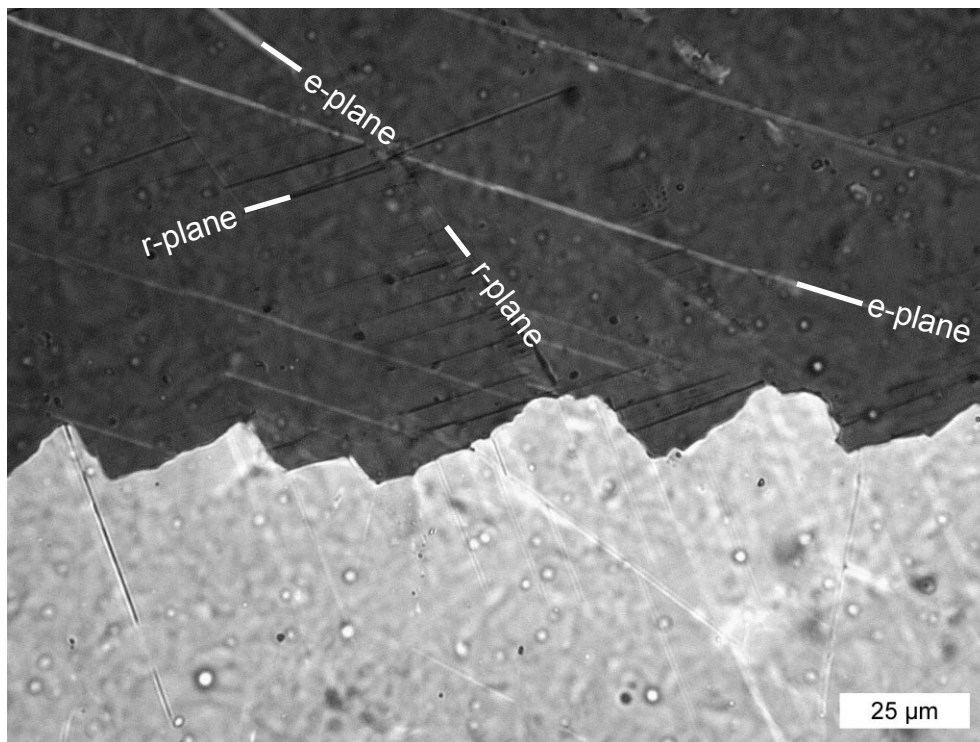


Fig. 2.12: Close-up of Fig. 2.11. Individual grain boundary segments are parallel to low index planes (rhomb planes (r), twinning planes (e)) in each of the adjacent crystals.

2.3 Temperature distribution

2.3.1 Method

In order to determine the temperature conditions during formation of the analyzed shear zones calcite-dolomite thermometry was employed. Calcite-dolomite thermometry is based on the Ca-Mg ionic exchange between co-existing calcite and dolomite (Fig. 2.13). Harker & Tuttle (1955) and Goldschmidt et al. (1961) investigated the Ca-Mg system experimentally and determined the position of the calcite-dolomite solvus. Many studies (e.g. Bickle & Powell 1977, Powell et al. 1984, Lieberman & Rice 1986 and Anovitz & Essene 1987) are based on these studies and introduced relations between the Mg-content in calcite and temperature. A major problem when applying calcite-dolomite thermometry to relatively low grade metamorphic rocks is the fact that the solvus is poorly calibrated below 500 °C (Essene 1983, Anovitz & Essene 1987) and that the system show diffusional closure below 500°C

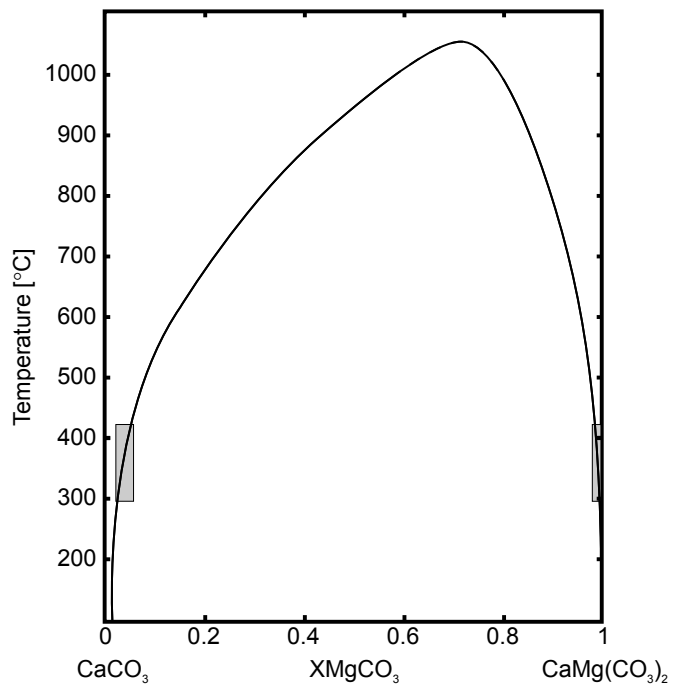


Fig. 2.13: Calcite-dolomite solvus (redrawn after Anovitz & Essene (1987)). The compositional fields of calcite and co-existing dolomite are indicated in the temperature range of this study.

(Essene 1983, Liebermann & Rice 1986, Matthews et al. 1999). However, under specific conditions calcite-dolomite thermometry may be applicable: a) dynamic recrystallization and b) the presence of dolomite grains within a matrix of calcite grains.

a) Matthews et al. (1999) investigated highly deformed HP-LT marbles from the Helinides and found temperatures of 300-400°C, which are clearly below the diffusional closure of the calcite-dolomite system. However, they pointed out that, if recrystallization is present, cation equilibration is possible even below the diffusional closure. As a consequence the determined temperatures reflect those during deformation and recrystallization.

b) Retrograde resetting of the Mg-contents complicate the application of the calcite-dolomite thermometer. Farver & Yund (1996) calculated the closure temperatures for calcite volume diffusion in calcite over a range of cooling rates and grain sizes. They showed that for 1 mm diameter calcite grains, which are cooling at a rate of 10°/Ma diffusion and therefore retrograde resetting of the calcite dolomite thermometer effectively ceases at

675°C (their fig. 7). However, temperatures of Carrara marble are in the range of 300-400°C and temperatures of other natural marbles above 600°C are seldom obtained (Essene 1982). Farver & Yund (1996) suggested that this discrepancy might be explained by the presence of dolomite inclusions in calcite. The presence of dolomite leads to a reduction of the effective diffusion radius, which in turn causes lower closure temperatures of the calcite-dolomite system. All analyzed shear zones of this study are characterized by dynamic recrystallization microstructures and contain substantial amounts of dolomite. Because of this reason the application of calcite-dolomite thermometry is appropriate. The temperature analysis of this study is therefore based on the assumption that, if a dynamically recrystallized microstructure is preserved, the determined temperature reflects the one under which the microstructure has formed. In other words, dynamic microstructures record the temperature conditions during their formation.

The composition of co-existing calcite and dolomite pairs was determined with wavelength dispersive spectrometry using a JEOL 8600 microprobe. Following the suggestion of Essene (1983) the acceleration voltage was set to 12 kV and the sample current to 7 nA on brass. Each measurement was performed in scanning mode at 30000 x magnification with a counting time of 10-20 sec. The analyzed area correspond to a beam size of $\sim 5\mu\text{m}$ in spot mode. Calcium, Magnesium, Iron, Manganese and Strontium were measured using natural standards of Wollastonite, Olivine, Graftonite, Graftonite and Celestine, respectively. The amount of carbon was calculated by assuming fixed stoichiometry. Each measurement was corrected with a ZAF routine.

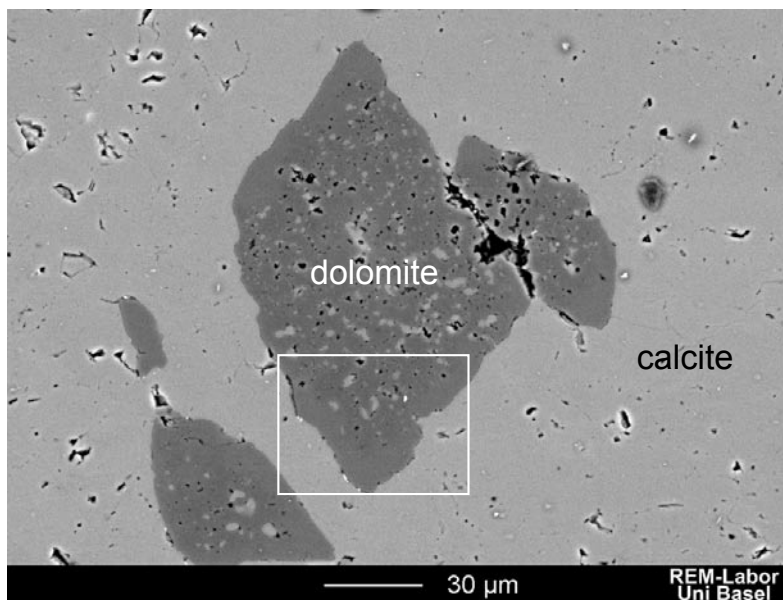


Fig. 2.14: SEM back scattered image of typical structure of dolomite present in the analyzed samples. The outline of the close-up shown in Fig. 2.15 is indicated. Note the inclusion rich core and the homogeneous rims.

Apart from sample D2-W each of the analyzed samples contain more than 10 vol-% dolomite. The dolomite crystals show a zonation with a calcite inclusion rich core and a homogeneous rim (Fig. 2.14). The presence of a rim accounts for an interaction of dolomite with a metamorphic fluid suggesting that ionic exchange was possible. The measurements

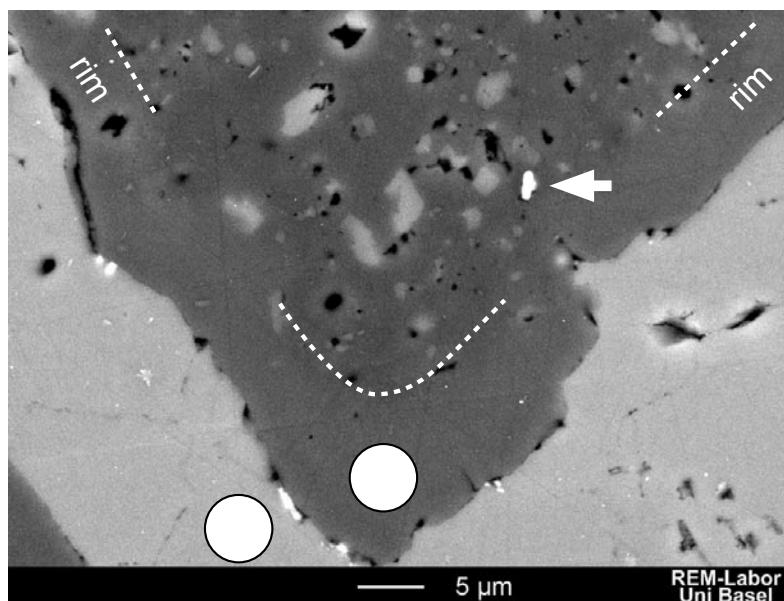


Fig. 2.15: Close-up of Fig. 2.14. The slightly lighter rim of the dolomite grain indicates interaction of dolomite with a metamorphic fluid. The location of a microprobe analysis in dolomite and the adjacent calcite is indicated. Bright white inclusions (arrow) are pyrite crystals.

were located in a homogeneous area of the calcite and dolomite crystals as close as possible to the phase boundary (Fig. 2.15). The interior of the crystals was not analyzed because the size of the calcite inclusions is smaller than the scanned area. The temperature was calculated after the approach of Anovitz & Essene (1987) without Fe-correction. Fe-correction was not applied because the Fe content is too low ($X_{\text{Fe(Cc)}} < 0.006$; $X_{\text{Fe(Dol)}} < 0.020$) to have an effect on the temperature calculation.

2.3.2 Deformation temperatures

The calculated temperatures are presented in Table 2.1 and in a series of histograms (Fig. 2.16), the corresponding measurements are listed in Appendix C5. In each sample 10-20 sites were analyzed. Apart from sample D2-W, which shows a bimodal distribution, all samples show a unimodal distribution of temperatures with a standard deviation of 20-30°C. In order to illustrate the regional distribution of deformation temperatures the data of this study were plotted versus the distance between the analyzed samples (Fig. 2.17). The orientation of the section to which the samples are projected is indicated in Fig. 2.2. It is perpendicular to the NW-SE trending D1 fold axis and parallel to the transport direction of the first deformation phase. Each deformation event is characterized by different temperatures, which are discernible even within the limits of the standard deviation. The temperature trends are marked for the two events for the mean temperature values (Fig. 2.17).

D1 temperature trend:

The mean temperature of D1-shear zones decrease from W to E from 420°C to 370 °C (Table 2.1, Fig. 2.17). Molli et al. (2000) found in D1-tectonites similar temperature values and a similar trend across the Alpi Apuane. They explained this trend by the D1 event, being related to the SW-directed subduction of the Adriatic plate below the Sardinia-Corsica micro

Table 2.1: Distances between sample locations, temperatures and grain sizes for the samples analyzed in this study in comparison to literature data.

| This study | | | | Molli et al. (2000) | | | | Di Pisa et al. (1985) | | | |
|------------------|---------------|------------------|---------------------|---------------------|---------------|------------------|---------------------|-----------------------|---------------|------------------|---------------------|
| Sample | Distance [km] | Temperature [°C] | Grain diameter [μm] | Sample | Distance [km] | Temperature [°C] | Grain diameter [μm] | Sample | Distance [km] | Temperature [°C] | Grain diameter [μm] |
| D1 | | | | D1 | | | | D1 | | | |
| D1-W | 4.83 | 420 | 85 | M45-relict | 4.80 | 420 | 125 | | | | |
| D1-E-1 | 8.30 | 395 | 65 | M 170 | 8.23 | 390 | 190 | | | | |
| D1-E-2 | 8.23 | 365 | 85 | M 107 relict | 8.73 | 400 | 85 | | | | |
| D2 | | | | D2 | | | | D2 | | | |
| D2-W | 4.75 | 295 | 25 | M 45 recry | 4.80 | 340 | 20 | | | | |
| D2-C | 7.25 | 325 | 25 | M 107 recry | 8.73 | 370 | 55 | | | | |
| D2-E | 8.43 | 375 | 55 | | | | | | | | |
| Annealing | | | | Annealing | | | | Annealing | | | |
| An-W | 4.75 | 360 | 105 | M 34 | 2.93 | 430 | 290 | W | 1.53 | 470 | |
| | | | | M 39 | 9.48 | 375 | 85 | WC | 5.00 | 445 | |
| | | | | M 190 | 12.15 | 360 | 85 | C | 9.00 | 410 | |
| | | | | | | | | E | 12.13 | 375 | |

plate (cf. chapter 1). The Alpi Apuane are located in the accretionary wedge of the orogenic system, which is why the Western part of the analyzed area is in a deeper structural position than the Eastern one. Thus, the compressional deformation occurred in the West at higher temperatures compared to the East. Additionally to dynamically recrystallized marbles, Molli et al. (2000) analyzed marbles with annealed microstructures (Fig. 2.17). They found the same temperature trend for dynamically and statically recrystallized marbles. Di Pisa et al. (1985) analyzed a series of statically recrystallized marbles of various sites in the Alpi Apuane (Fig. 2.2). They determined the composition by x-ray diffraction and by microprobe analysis. The temperatures were calculated after the approach of Bickle & Powell (1977) assuming a pressure of 5 kbar. Also the temperature trend determined by Di Pisa et al. (1985) (Fig. 2.17) is parallel to the one obtained in this study. However, their data are systematically 30°C higher than the one presented in this study, caused by the application of different measuring techniques (x-ray vs. microprobe) and thermometers (Bickle & Powell 1977 vs. Anovitz & Essene 1987).

The fact that the D1 temperature of dynamic microstructures is similar to that of annealed marbles can be explained in two ways: 1) The D1 microstructures are in fact not dynamic ones but reflect the annealing event. The analyzed shear zone would then have formed during D1a (pre-annealing). This possibility is very unlikely, because dynamic features are observed. These features include, e.g., lobate grain boundaries and a pronounced texture; reduction of recrystallized grain size towards strong particles and a preferred orientation of elongated grains. 2) The D1 deformation occurred at the same time and temperature as the annealing. This indicates that non-deforming rocks are immediately subjected to annealing and form statically recrystallized microstructures.

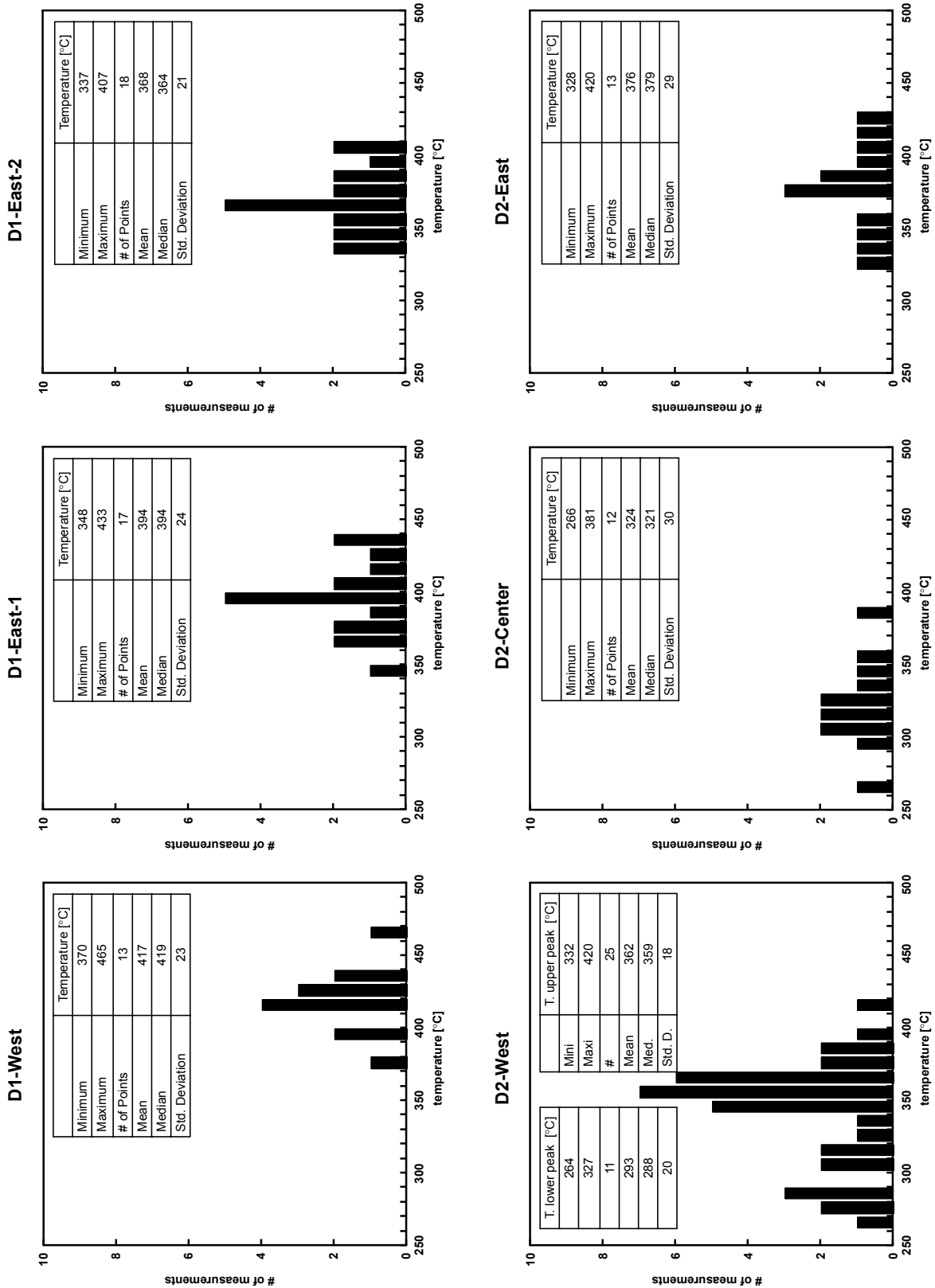


Fig. 2.16: Histograms of calculated temperatures from shear zones across the Alpi Apuane. West is on the left side, East is on the right side. Top row shows temperatures determined from D1 shear zones. Bottom row shows temperatures determined from D2 shear zones. Note that the D1 temperature decreases from West to East and the D2 temperature decreases from East to West.

For two samples (D1-E-2, D1-E-1) two different temperatures ($T = 368^{\circ}\text{C}$, $T = 394^{\circ}\text{C}$) were obtained in the same location on the section line (Table 2.1 and Fig. 2.17). The temperature difference of 26°C between the two sample can be explained by a higher structural position of the higher temperature sample (D1-E-1) compared to the lower temperature one (D1-E-2). Sample D1-E-1 comes from the inverted limb of the Vinca anticline (2 in Fig. 1.2 and 1.3) and sample D1-E-2 is located in the inverted limb of the Tambura anticline (4 in Fig. 1.2 and 1.3) When the large km-scaled D1 folding and thrusting is restored sample D1-E-1 is situated further to the West, where the Alpi Apuane rocks have been subducted to greater depth compared to the Eastern areas.

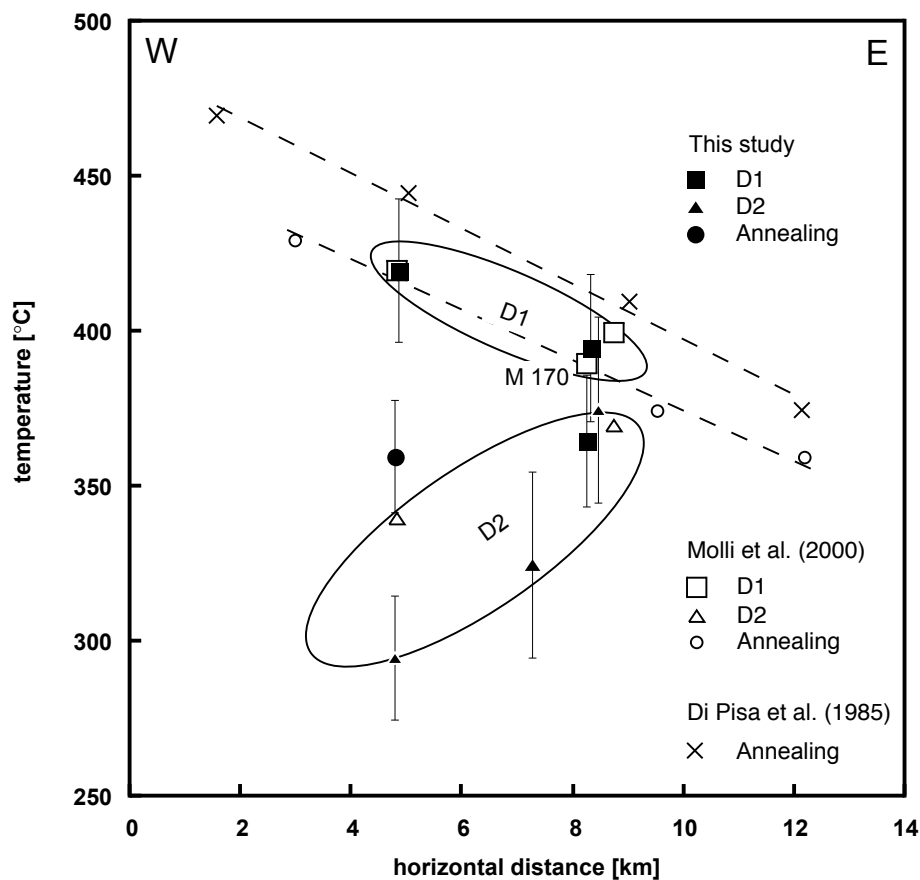


Fig. 2.17: Temperature distribution of D1, D2 shear zones and annealed marbles along a NE-SW trending section. The corresponding section line is shown in Fig. 2.2. Temperature trend for D1 and D2 (ellipses) and annealing (dashed lines) are indicated.

D2 temperature trend:

The temperatures obtained from D2-shear zones (Table 2.1 and Fig. 2.17) show a reversed trend compared to the one of the D1-shear zones, ranging from 375°C in the East to 295°C in the West. In the East, D1 and D2 shear zones were formed at similar temperature conditions within about 10°C , which is less than the standard deviation of the temperature distributions of each sample (Fig. 2.16). Molli et al. (2000) found in their study a similar temperature gradient (Fig. 2.17). They interpreted the decrease of deformation temperatures

to be related to the geometry of the nappe stack of the Alpi Apuane. The late stage of the D1 deformation event led to the formation of a nappe stack. During D2 the nappe stack collapsed, which caused the structurally upper parts to move downwards to the NE and SW side of the culmination of the structure. The culmination lies close to the Eastern border of the Alpi Apuane so that 'low temperature' shear zones from structurally high levels are located mostly to the West compared to 'high temperature' shear zones from the core of the nappe stack.

D2 samples overprint annealed microstructures. The overprint is reflected in a bimodal temperature distribution (Fig. 2.16). The two peaks can be explained when considering the microstructure of a typical D2 shear zone (sample D2-W) (Fig. 2.9). Measurements in the annealed microstructure, outside the shear zone, provide temperatures, which are located in the upper peak of the histogram (mode = 362°C). The lower peak (mode = 293°C) comprises data points obtained from the recrystallized domains in the center of the shear zone. However, it remains uncertain why the temperature of the annealed 'protolith' is about 60°C lower than annealed marbles from the same area (Fig. 2.17). Since the 'protolith' was measured close to the shear zone it might be possible that the calcite composition of the analyzed domain was altered by the proximity of the D2 deformation. Further detailed analysis including mapping of Mg-Ca ratios from core to rim is necessary to evaluate the possibility of diffusional alteration.

D1 and D2 microstructures evolved at individual temperatures. Temperatures recording D1 generally are higher than those of D2. However, temperature cannot be the only microstructure-forming factor, because in some places different microstructures have evolved at similar temperatures. For instance, in the Eastern Alpi Apuane, different D1 and D2 microstructures have formed at the same temperature. Thus, besides temperature, other factors (e.g. finite strain, strain rate) must influence the formation of a microstructure.

2.4 Distribution of recrystallized grain size

2.4.1 Method

From each sample a representative area was selected from which the grain boundaries were traced manually. Only the recrystallized domains were considered for the grain size analysis. The determination of sectional areas, the calculation of equivalent circle radii, and the conversion from 2D to 3D grain diameters were performed in the same way as described in chapter 3.

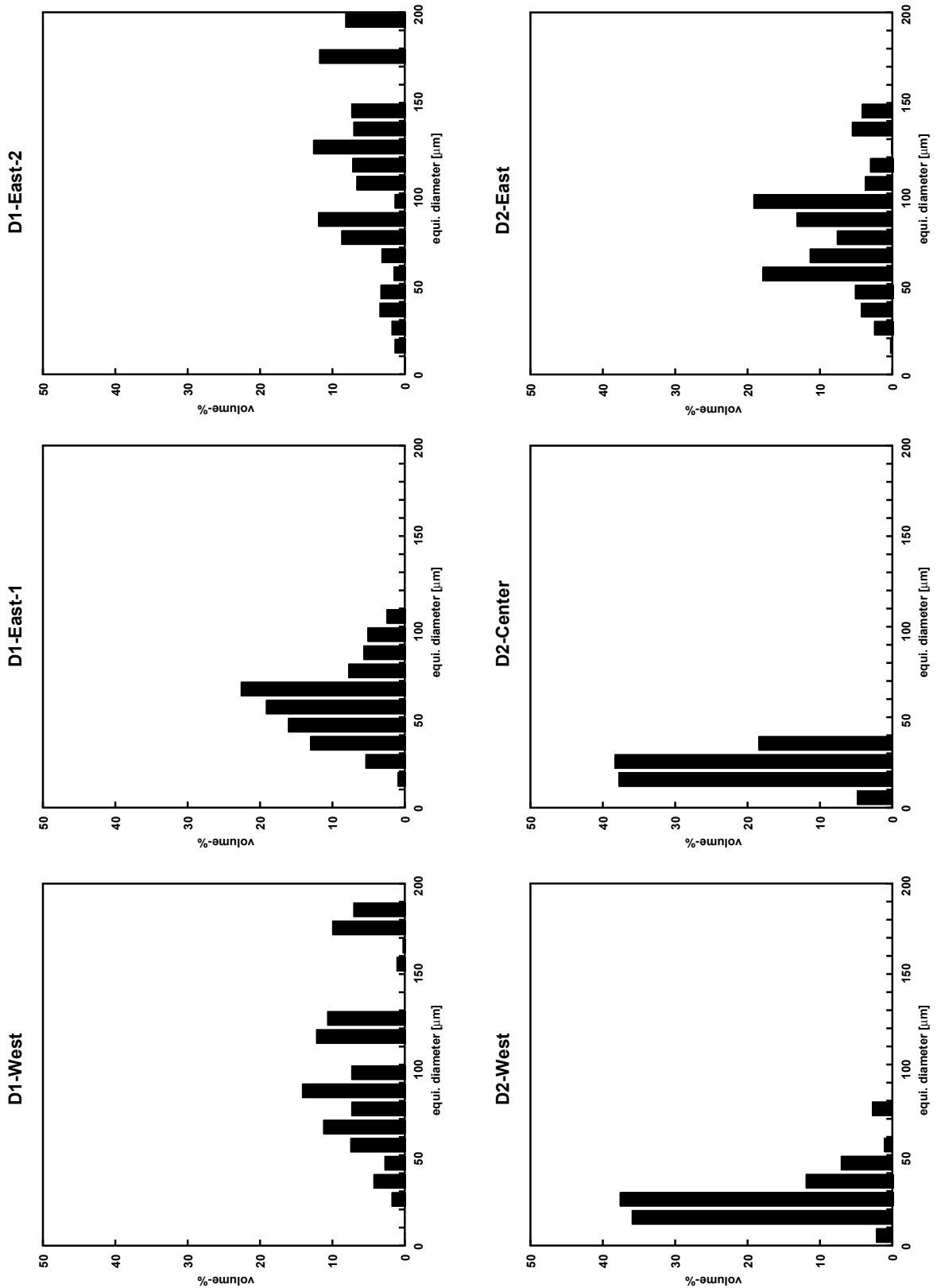


Fig. 2.18: Histograms of recrystallized grain sizes from shear zones across the Alpi Apuane. West is on the left side, East is on the right side. Top row shows the 3D grain size distributions determined from D1 shear zones. Bottom row shows 3 D grain size distributions determined from D2 shear zones.

2.4.2 Recrystallized grain size

The grain diameters of D1 and D2 shear zones are presented in Table 2.1 and as Vol-% histograms in Fig. 2.18. Each grain size distribution contains 250-750 measurements. Sample D1-E-1, D2-W and D2-C exhibit a unimodal distribution, sample D1-W and D1-E-2 a broad distribution with several minor peaks and sample D2-E a bimodal distribution. The bimodal distribution of the latter sample can be explained by its heterogeneous microstructure. Each peak of the grain size histogram corresponds to a separated domain in the bulk microstructure. The different grain sizes are related most likely to variations in the second phase content. Large amounts of second phase particles prevent grain growth effectively (Olgaard & Evans 1988) and conserve therefore an initially small grain size. Further detailed SEM analyses are required to identify the reason for the varying grain sizes. For this study, the grain diameter of the lower peak is considered to be relevant because of two reasons: 1) If post-deformational annealing has modified the microstructure, the smaller grain size (related to a higher second phases content) approaches most closely the grain size during deformation. 2) D2 shear zones are characterized by subgrain rotation recrystallization. SGR results in microstructures, which are characterized by large porphyroclasts and small recrystallized grains (core-mantle structures). Since sample D2-E is derived from a D2 shear zone, the two peaks in the grain size histogram can be related to the size of porphyroclasts and recrystallized grains, respectively. SGR consumes internally deformed porphyroclasts and produces new, strain free crystals. The fact that upper and lower peak lie closely together ($\sim 30 \mu\text{m}$) indicates that recrystallization is relatively advanced. When recrystallization approaches completion the size of porphyroclasts and recrystallized grains are indistinguishable (cf. chapter 3). Fig. 2.19 illustrates the regional distribution of the recrystallized grain diameters in the same way as Fig. 2.17 for the deformation temperature. The recrystallized grain sizes reflect basically the two separated trends of the D1 and D2 deformation temperatures. However, they are not as pronounced as the temperature trends.

D1 grain size trend:

The recrystallized grain diameter of D1 shear zones (Fig. 2.19) decrease from West to East from $85 \mu\text{m}$ (sample D1-W) to $65 \mu\text{m}$ (sample D1-E-1). However, the grain size of sample D1-E-2 is $85 \mu\text{m}$, equal to sample D1-W. Therefore, the grain size gradient is only poorly defined. When combining the data of this study with the re-examined ones of Molli et al. (2000) the regional trend becomes more evident. Only one sample (M170), which comes from the same location as sample D1-E-2 deviates significantly from the regional D1-trend. The grain diameter is $190 \mu\text{m}$ and plots closely to a trend line, which is defined by the data of statically recrystallized samples (Fig. 2.19) from Molli et al. (2000). Statically recrystallized marbles exhibit grain sizes of $290 \mu\text{m}$ in the Western Alpi Apuane, which decrease towards the East to $90 \mu\text{m}$. This gradient is related to the decreasing temperature

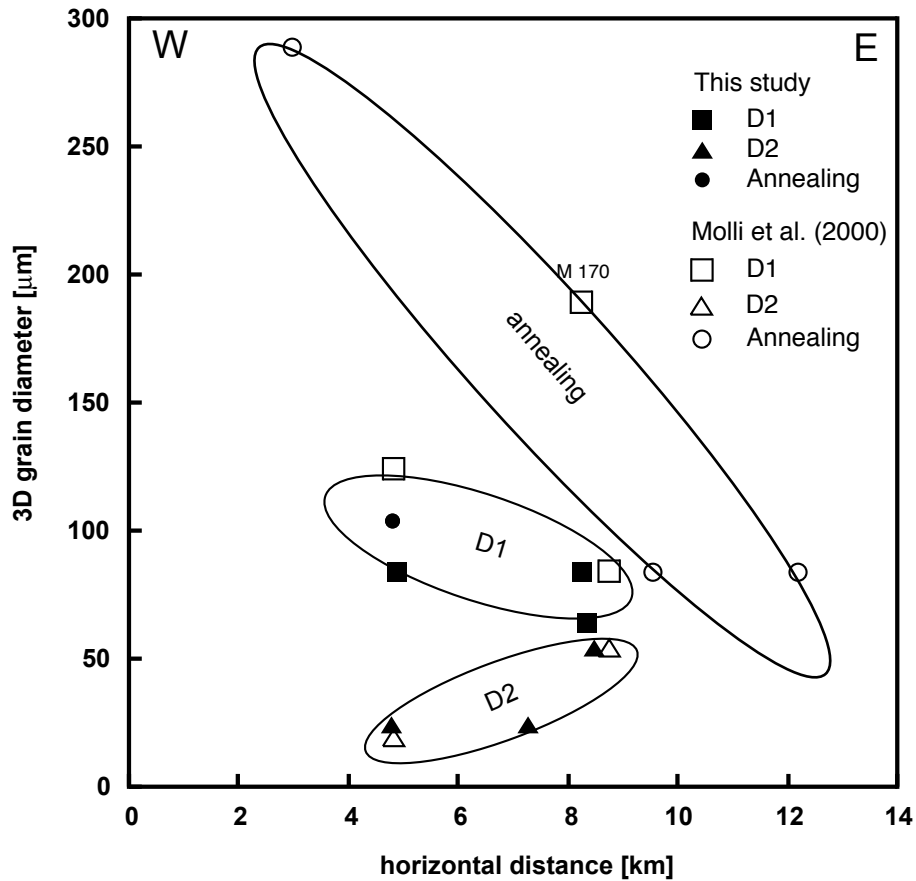


Fig. 2.19: Distribution of 3D recrystallized grain sizes of D1 and D2 shear zones and of annealed marbles across the Alpi Apuane. West is left, East is right. The corresponding section line is the same as for the temperature distribution shown in Fig. 2.17.

conditions during the annealing event (cf. 2.3.2). High temperatures lead to faster grain growth due to a greater mobility of grain boundaries. Therefore, larger grain sizes form at higher temperature conditions (Olgaard & Evans 1988, Covey-Crump 1997). Although sample M170 comes from the same location as sample D1-E-2, its grain diameter is about two times larger than the one of sample D1-E-2. This discrepancy may be explained when considering that sample M170 exhibits a higher temperature compared to the D1 sample of this study (cf. Fig. 2.17).

D2 grain size trend:

The volume weighted recrystallized grain diameter of D2 shear zones decrease from East to West from 65 μm to 25 μm , respectively. The data of Molli et al. (2000) fit well to the here obtained trend.

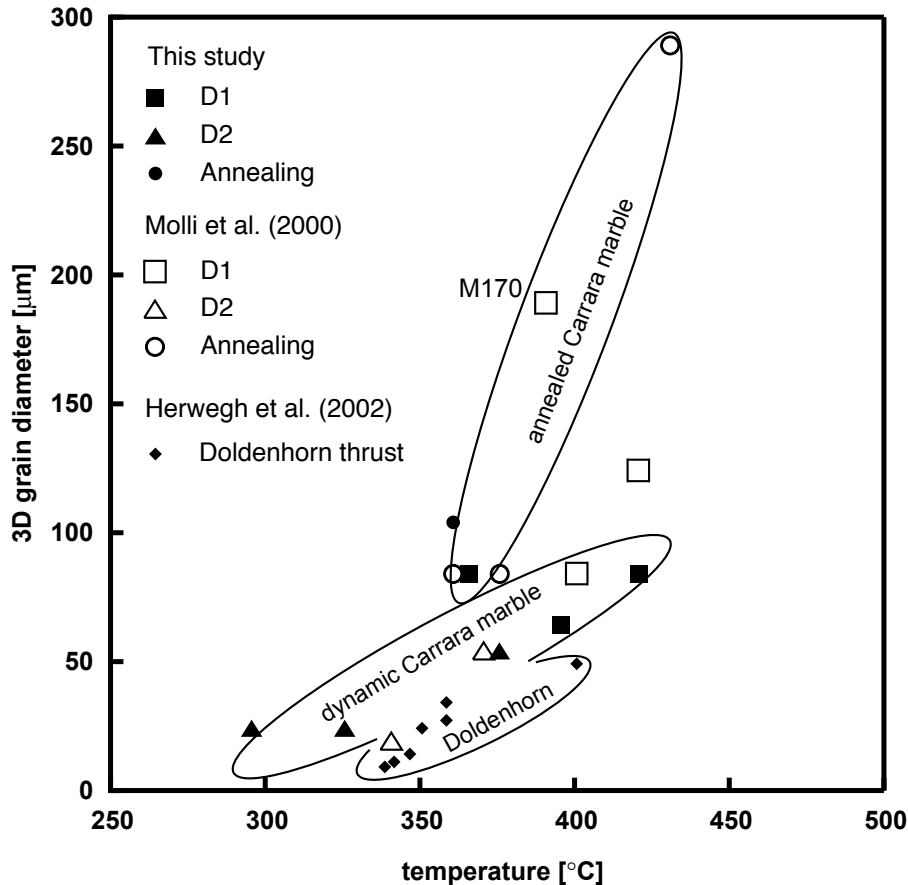


Fig. 2.20: Relationship between recrystallized grain size and temperature. The larger scatter of dynamically recrystallized Carrara marble may be related to varying strain rates from sample to sample, for discussion see text. Note that the grain size of statically recrystallized marbles increase stronger with increasing temperature compared to dynamically recrystallized ones. For comparison the data of Herwegh et al. (2002) from the Helvetic Alps are shown.

2.4.3 Relationship between deformation temperature and recrystallized grain size

For the D1 shear zones the regional gradient of recrystallized grain sizes is poorly defined (Fig. 2.19). Eliminating single data points yield in the break down of the trend. However, the grain size variation becomes clearer, when plotting the recrystallized grain diameter versus the deformation temperature (Fig. 2.20). With increasing temperature the recrystallized grain size increases. The lower part of the temperature-grain size relationship is defined by samples derived from D2 shear zones. From low to high temperatures, i.e. from small to large grain sizes the sample location changes from West to East. The upper part of the trend is defined by D1 shear zones and their location shifts from East to West with increasing temperature. At intermediate temperatures and grain sizes (370°C, 70 μm) the samples of both deformation events overlap, indicating that D1 and D2 shear zones were active at similar conditions. These conditions were achieved in the Eastern Alpi Apuane (~km 8 in Fig. 2.17 and Fig. 2.19). The scatter about the trend line is larger compared to the one of the data of Herwegh et al. (2002), abstract only; paper Deformation of Calcite

rocks in Nature: Microstructural Constraints and Rheological Implications submitted to J. Struct. Geol.) (Fig. 2.20). Herwegh et al. (2002) analyzed dynamically recrystallized meta-limestones, which are derived from the basal thrust of the Doldenhorn Nappe in the Helvetic Alps, Switzerland. Their data show in agreement with those presented in this study a positive relationship between grain size and temperature, however, the trend is shifted to slightly smaller grain sizes. The differences between the two studies can be explained by the results of the study of Tungatt & Humphreys (1981). Tungatt & Humphreys (1981) performed deformation experiments on sodium nitrate (NaNO_3), which is an analogue for calcite. They found that the recrystallized grain size depends strongly on temperature and on strain rate (their fig 8). Increasing strain rates tend to support the formation of smaller recrystallized grains at higher temperatures. On the basis of this finding it can be concluded that the Doldenhorn thrust were active at slightly higher strain rates than the average of D1 and D2 shear zones in the Alpi Apuane. However, it must be kept in mind that each Carrara marble sample comes from an individual shear zone. Consequently, variations in strain rate, from sample to sample are likely. Thus, one would predict a larger scatter in grain sizes for the Carrara marble shear zones (Fig. 2.20) compared to the Doldenhorn thrust.

Only one sample (M170) does not follow the trend defined by the dynamically recrystallized samples. It exhibits significantly higher grain sizes compared to the other samples. The position of this shear zone is located on the trend line, which is defined by statically recrystallized marbles (Fig. 2.20). Statically recrystallized marbles show an increase in grain diameters with increasing temperature. The slope of the 'annealed' trend line, however, is much steeper than the one of dynamically recrystallized samples. A steeper slope in the temperature / grain size relationship reflects faster grain growth at a constant temperature. Tullis & Yund (1981) showed in grain growth experiments on different quartzite aggregates and on Solnhofen limestone, that during static recrystallization increasing temperature lead to increasingly larger grain sizes. A similar relationship between temperature and statically recrystallized grain size was found by Covey-Crump & Rutter (1989) in naturally annealed marbles. They analyzed marbles from Naxos Island in the Hellenides, which exhibit a grain size increase as a function of the distance from the thermal dome in the center of the Naxos Island migmatite complex. However, a stable statically recrystallized grain size is not only dependent on temperature. The second phase content has a great influence on grain growth kinetics as has been shown by various studies (e.g. Rutter 1984, Olgaard & Evans 1986, Covey-Crump 1997). For the analyzed granoblastic microstructures of Molli et al. (2000), discussed in this study, this effect can be neglected, because all samples are 99% pure calcite marbles. Instead temperature dominated the grain growth behaviour of Carrara marble.

2.5 Summary and conclusions

Besides the typical statically recrystallized microstructures Carrara marble exhibits two types of dynamically recrystallized microstructures. Both microstructures can be related to one of the two deformation events. Microstructures typical of sub grain rotation recrystallization occur in samples of D2 shear zones, whereas microstructures dominated by grain boundary migration recrystallization are derived from D1 shear zones. Deformation temperature and recrystallized grain size show separated regional gradients for each deformation event. D1 temperatures and grain sizes decrease from West (420°C; 105 μm) to East (370°C, 70 μm), whereas D2 temperatures and grain sizes decrease from for East (370°C, 55 μm) to West (320°C, 20 μm).

This study confirms the general temperature and grain size trends obtained from the studies of Molli et al. (2000) and Di Pisa et al. (1985). The data of the previous studies are derived from various structures (fold and shear zones) without a clear correlation to the origin of the structure. In this study only shear zones, which can be clearly related to D1 and D2 were analyzed.

The recrystallized grain sizes of D1 and D2 shear zones increase as a function of the deformation temperature. At small grain sizes and low temperatures plot the D2 shear zones, whereas at larger grain sizes and higher temperatures D1 shear zones define the trend line. For annealed marbles the grain size temperature relationship has a steeper slope compared to the dynamically recrystallized marbles. This steeper slope can be related to faster grain growth at elevated temperatures.

Microfabric study on the deformational and thermal history of the Alpi Apuane marbles (Carrara marbles), Italy

G. Molli^{a,*}, P. Conti^b, G. Giorgetti^b, M. Meccheri^b, N. Oesterling^c

^a*Dipartimento di Scienze della Terra, Università di Pisa and C.N.R. Centro di Studio Geologia Strutturale e Dinamica App.Sett., Via S.Maria 53, I-56126 Pisa, Italy*

^b*Dipartimento di Scienze della Terra, Università di Siena, Via Laterina 8, I-53100 Siena, Italy*

^c*Department of Earth Sciences, University of Basel, Bernoullistr. 32, CH-4056 Basel, Switzerland*

Received 30 November 1999; accepted 26 June 2000

Abstract

Marbles from different geometrical and structural positions within the Alpi Apuane metamorphic complex show a large variability in microfabric types as indicated by microstructure, *c*-axis orientation and temperature analysis.

Statically recrystallized samples showing a granoblastic microstructure and polygonal grain boundaries are characterized by a grain size variation from east to west from 80–100 μm to 250–300 μm . This is correlated with an equilibration calcite-dolomite temperature from 360–380°C to 420–430°C.

Two kinds of dynamically recrystallized microstructures have been investigated: a first one exhibiting coarse grains (150–200 μm) with lobate grain boundaries and a strong shape preferred orientation and a second one characterized by a smaller grain size (40–50 μm) and predominantly straight grain boundaries. These microstructural types, associated with localized post-thermal peak shear zones and meter- to kilometer-scale folds, are interpreted as related to high strain and high temperature crystal plastic deformation mechanisms (dislocation creep) associated with predominant grain boundary migration (type-B1) or subgrain-rotation recrystallization (type-B2). These differences in dynamically recrystallized microstructures are related to equilibration temperatures higher in type-B1 (390°C) than in type-B2 (370–340°C). We have been able to relate the development of the different microfabric types to the successive stages of deformation of the Alpi Apuane metamorphic complex. © 2000 Elsevier Science Ltd. All rights reserved.

1. Introduction

The marbles from the Alpi Apuane, and in particular the white variety called “Carrara marble”, are well known geological materials due to their extensive use both as building stones and for statuary as well as in rock-deformation experiments (Rutter, 1972; Casey et al., 1978; Spiers, 1979; Schmid et al., 1980; Schmid et al., 1987; Wenk et al., 1987; Fredrich et al., 1989; De Bresser, 1991; Rutter, 1995; Covey-Crump, 1997). In the latter, Carrara marble is widely used because: a) it is an almost pure calcite marble; b) it shows a nearly homogenous fabric, with no or weak grain-shape or crystallographic preferred orientation; c) it usually develops a large grain-size; and d) a large amount of literature data about its behaviour under various experimental deformation conditions is available.

All the above features can be found in large volumes of marbles cropping out in the Carrara area, i.e. in the north-

western part of the Alpi Apuane region (Fig. 1), but are not common in marbles from other areas of the Alpi Apuane. In this paper, we illustrate the main fabric types we have recognized in marbles from the Alpi Apuane area and discuss fabric development, taking into account the role of the regional deformation history and the position of marbles in kilometer- to meter-scale geological structures. To exclude the influence of second phase particles like phyllosilicates on the microfabric development (Olgaard and Evans, 1988; Mas and Crowley, 1996), we have concentrated on the pure white calcite marbles.

In the following, “Alpi Apuane marbles” indicates the Liassic marble formation cropping out in the whole Alpi Apuane area, while “Carrara marble” stands for marbles located in the northwestern Alpi Apuane area in the surroundings of the town of Carrara (Fig. 1). Carrara marbles are the most intensely quarried marble variety within the entire Alpi Apuane. Due to their economic and cultural importance, Alpi Apuane marbles have been the object of geological investigation for a century (Zaccagna, 1932; Bonatti, 1938), with general studies

* Corresponding author.

E-mail address: gmolli@dst.unipi.it (G. Molli).

Fig. 1. Structural map of the Alpi Apuane area (from Carmignani et al., 1978, 1993, modified). See Fig. 2 for cross-sections. Locations of detailed geological maps of Fig. 6 are indicated.

appearing in the sixties and seventies (D'Albissin, 1963; Crisci et al., 1975; Di Sabatino et al., 1977). Di Pisa et al. (1985) were the first who presented calcite/dolomite thermometric estimates within the general tectonic evolution of the Alpi Apuane metamorphic complex. Later on, Coli (1989) focused on marbles from the microstructural point of view, providing a qualitative and general descrip-

tion of some microstructures. A more recent contribution by Coli and Fazzuoli (1992) tackled the problem of the Alpi Apuane marble from a lithostratigraphic point of view.

The aim of our study is to describe microfabric types in different geometrical positions in the polyphase nappe building of the Alpi Apuane metamorphic complex and

Fig. 2. Composite cross-sections in the Alpi Apuane area (from Carmignani et al., 1993).

their relationship with large- to small-scale tectonic structures. Structural data are supplemented by a calcite/dolomite investigation to constrain the thermal conditions for each microfabric type formation.

2. Geological setting

The lowermost tectonic units of the northern Apennine fold-and-thrust belt are exposed in the Alpi Apuane region (Figs. 1 and 2). According to classical interpretations (Elter, 1975; Carmignani et al., 1978, and reference therein), the following units can be recognized in this area from top to bottom.

1. The Liguride units, formed by ophiolites and deep-water sediments, representing the Mesozoic Ligurian ocean and parts of an accretionary wedge system related to the closure of the ocean itself. These units show anchimetamorphic to very low grade metamorphic conditions (Cerrina et al., 1983; Reutter et al., 1983).
2. The sub-Liguride unit (Canetolo unit), corresponding to part of the sedimentary cover of the ocean–continent transitional area.
3. The Tuscan nappe, a continent-derived unit formed by a Late Triassic to Aquitanian sedimentary sequence, deposited on the Apulia domain, detached from its original basement and characterized by a polyphase deformation associated with a very low grade metamorphism.
4. The Massa unit, with a pre-Mesozoic basement and a well developed Middle to Late Triassic sequence, associated with Middle Triassic metavolcanic rocks, deformed and metamorphosed in greenschist facies conditions.

5. The lowermost Apuane unit, made up by a Hercynian basement unconformably overlain by Triassic to Oligocene greenschist facies metamorphic rocks. The Mesozoic-tertiary succession in this unit is characterized by Triassic dolomite turning to Liassic marble and dolomitic marble. The succession (Dogger to Oligocene) continues with cherty limestones, radiolarian chert, schist and a turbiditic flysch.

In the Alpi Apuane, marbles derive from stratigraphically different levels. They are of Devonian, as well as of Liassic, Dogger and Cretaceous–Eocene age. We have focussed our attention on the Liassic marbles, which belong to the thickest and purest succession.

The northern Apennine is derived from the westernmost sector of the Apulia continental margin in the Late Jurassic paleogeography. Deformation started during Eocene times, first affecting the inner and originally westernmost domains (Liguride and sub-Liguride units), and then continuing in the Late Oligocene–Miocene to involve the more external Tuscan domain (Tuscan nappe, Massa unit and Apuane unit). Northeastward facing folding and northeastward nappe transport occurred throughout, resulting in a thick nappe stack development. Starting in the Early Miocene, contraction shifted toward more external (i.e. Umbria–Marchean) domains and the internal northern Apennines suffered extensional tectonics with uplift and tectonic denudation. In the Late Miocene the regional extensional tectonics related to the opening of the Tyrrhenian Sea affected the area (e.g. Carmignani and Kligfield, 1990; Storti, 1995 and reference therein).

In the Massa unit and the Apuane unit, two main polyphase tectono-metamorphic events can be recognized, the D_1 and D_2 events (Carmignani and Kligfield, 1990). During

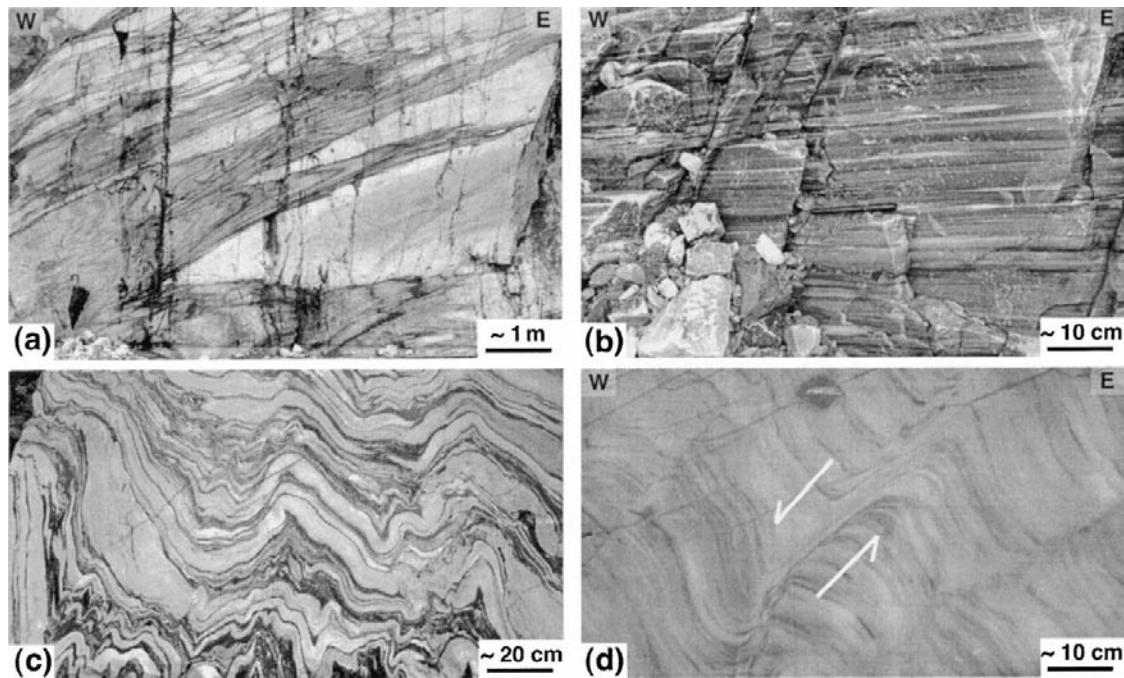


Fig. 3. (a) D_1 isoclinal folds in marbles (Vallini quarry, western Alpi Apuane). (b) D_1 shear zone in cherty limestones (Vallini, western Alpi Apuane). (c) D_2 folds refolding main foliation in marble breccia (Arni, central Alpi Apuane). (d) D_2 shear zones cutting D_1 foliation in marbles (Arni, central Alpi Apuane).

D_1 , nappe emplacement occurred, with development of kilometer-scale NE facing isoclinal folds (Fig. 3a), NE–SW oriented stretching lineations (L_1) and a greenschist facies ubiquitous regional foliation (S_1). In more detail, the D_1 event can be subdivided into: a) a “main folding phase”, in which kilometer-scale recumbent folds and an associated flat-lying axial plane foliation are formed; b) an “antiformal stack phase”, in which final nappe emplacement occurred, together with antiformal stack development and formation of shear zones (Fig. 3b). Shear zones show again top-to-the-NE/E sense of movement.

The D_2 event deforms all earlier features, developing folds (Fig. 3c) and shear zones (Fig. 3d), leading to progressive unroofing and exhumation of the metamorphic complex at higher structural levels. D_2 is characterized by retrograde metamorphic conditions and the latest stages of deformation are associated with polyphase brittle structures.

Greenschist facies conditions were achieved in the Apuane unit during D_1 and early D_2 deformation (Carmignani et al., 1978). The occurrence of the stable association pyrophyllite + quartz (Franceschelli et al., 1986, 1997) indicates temperatures between 300–450°C and pressure ranging from 0.5–0.6 GPa (Di Pisa et al., 1985; Schultz, 1996; Franceschelli et al., 1997) and 0.6–0.8 GPa (Jolivet et al., 1998). Peak of metamorphic conditions yielding to annealing was attained during the main deformational event (D_1) and before the D_2 event (Bocca-

letti and Gosso, 1980; Carmignani and Kligfield, 1990; Franceschelli et al., 1997; Molli and Giorgetti, 1999).

Radiometric K/Ar and $^{40}\text{Ar}/^{39}\text{Ar}$ data suggest that D_1 occurred approximately at 27 Ma and that early D_2 deformation ended at 10–8 Ma (Giglia and Radicati di Brozolo, 1970; Kligfield et al., 1986). Cooling through 100–120°C temperature can be constrained by fission tracks data ranging from 6 to 2 Ma (Bigazzi et al., 1988; Abbate et al., 1994).

3. Studied samples and analytical techniques

The samples analysed were collected in different geometrical positions in the Apuane unit (Figs. 1 and 2) along a SW–NE oriented transection parallel to the D_1 transport direction. Marbles are quite homogeneous, being composed of more than 99% of calcite, plus minor contributions of quartz, albite, white mica and/or opaque minerals, as confirmed by chemical analyses of major and minor elements (Table 1).

All samples were cut parallel to the stretching lineation L_1 and normal to the foliation plane S_1 . Ultra-thin sections (<4 μm thick) were prepared and analysed by optical microscopy. To quantify the grain shapes, quantitative microstructural analyses were performed using preferred orientations of the particle axes (PAROR) (Fig. 4a) and

Table 1
Whole-rock chemical analyses of a typical “granoblastic” annealed marble (Type A) and of a typical dynamically recrystallized marble (Type B). Composition was obtained using a XRF spectrometer Philips PW1414

| Wt% Oxide | Type A | Type B |
|--------------------------------|--------|--------|
| SiO ₂ | 0.15 | 0.05 |
| TiO ₂ | - | - |
| Al ₂ O ₃ | 0.08 | 0.09 |
| Fe ₂ O ₃ | 0.12 | 0.11 |
| FeO | - | - |
| MgO | 1.08 | 1.24 |
| MnO | - | - |
| CaO | 54.92 | 54.66 |
| Na ₂ O | - | - |
| K ₂ O | - | - |
| P ₂ O ₅ | 0.11 | 0.12 |
| L.O.I. | 43.50 | 43.70 |

symmetry of the orientation of the grain boundary surfaces (SURFOR) (Fig. 4b) methods (Panozzo, 1983, 1984). Grain boundary corrugation was determined using the SHAPES program (Panozzo and Hürlimann, 1983) and characterized with the PARIS factor (Panozzo and Hürlimann, 1983, see Fig. 4c), which takes into account the convexity–concavity of the grain boundary geometry.

In order to characterize the crystallographic preferred orientation (CPO, texture), universal stage measurements as well as computer integrated polarization microscopy (CIP) (Heilbronner Panozzo and Pauli, 1993) were carried out. The latter method uses the interference colour of each pixel of a series of digitally recorded thin-section images for the determination of the *c*-axis orientation. Basically, the CIP-method is similar to the “Achsenverteilunganalyse” (AVA) of Sander (1950), where the thin-section image is colour coded according to its *c*-axis orientation and a certain stereographic colour look-up table (CLUT).

The interference colour of optically uniaxial minerals is a function of the thin-section thickness and the birefringence as well as a function of the *c*-axis orientation. By the variation of the thin-section thickness, the effect of the birefringence on the interference colour can be controlled, e.g. lowering the thin-section thickness provides an interference colour. Therefore the *c*-axis orientation can be directly determined by the interference colour. The CIP-method requires interference colours of first-order grey. Since calcite has a high birefringence (0.172), thin-sections of about <2 μm thickness had to be prepared.

Dolomite-bearing marbles were carefully investigated in order to constrain the equilibrium temperatures of different calcite-dolomite relations. Calcite and dolomite grains were analyzed by wavelength-dispersive spectrometry using a Jeol JXA 8600 microprobe operating at 15 kV and 10 nA. Analyzed elements included Ca, Mg, Mn, Fe, Sr, Ba with count times of 15 s for Ca and 30 s for all the other elements. A defocused beam (up to 10 μm) was used to avoid volatilization and reintegration of possible submicroscopic exsolution of dolomite lamellae. Chemical resetting occurs easily in carbonates during retrogression and either magnesian calcite grains may exsolve dolomite lamellae or the original high Mg content is obliterated by intracrystalline diffusion (Essene, 1982). Consequently, retrograde re-equilibration produces calcite grains with Mg content lower than that attained at peak metamorphic conditions. All samples show grain-to-grain variations in Mg content, even among calcite grains with the same microstructural features and such variations are attributed to retrograde resetting (Essene, 1989). For this reason, averaging the data would obliterate this effect leading to underestimation of the peak temperature. Therefore, we consider the maximum Mg content recorded in each calcite microstructural type to calculate the actual

Fig. 4. Schematic illustration of the image analysis by means of PAROR and SURFOR method (for more details see Panozzo, 1983, 1984; Panozzo and Hürlimann, 1983). Each grain boundary is digitized and consists of short line segments. (a) Using projection method the PAROR routine presents in a rose diagram the general orientation of the grains (B) with respect to a reference line (in this study the foliation trace). (b) The SURFOR routine, using projection methods, presents the cumulative orientation of the line segments in a rose diagram; α is the orientation of the line segment with respect to a reference line. (c) The PARIS factor gives quantitative indication of corrugation of the grain boundaries and increases with migration of grain boundary.

Table 2

Chemical analyses of calcite grains; all formulae normalized to two cations per formula unit. Temperatures calculated using Anovitz and Essene (1987) calibration. A refers to granoblastic calcite grains; B refers to recrystallized calcite grains; c: core composition; r: rim composition

| | Sample n. | | | | | | | | | | |
|--------------------|-----------|-------|-------|--------|-------|-------|-------|-------|-------|-------|-------|
| | 30 | 40 | 4 | 188 | 115 | 107A | 107Bc | 107Br | 45Ac | 45Ar | 45B |
| <i>Wt.% Oxide</i> | | | | | | | | | | | |
| CaO | 55.15 | 54.02 | 53.78 | 55.15 | 54.71 | 54.30 | 53.72 | 54.65 | 53.84 | 54.49 | 54.48 |
| MgO | 1.25 | 0.92 | 0.92 | 0.85 | 0.97 | 1.09 | 1.01 | 0.91 | 0.95 | 0.87 | 0.78 |
| FeO | 0.03 | 0.02 | 0.00 | 0.02 | 0.05 | 0.00 | 0.04 | 0.04 | 0.04 | 0.04 | 0.02 |
| MnO | 0.06 | 0.3 | 0.05 | 0.04 | 0.05 | 0.00 | 0.07 | 0.00 | 0.00 | 0.01 | 0.00 |
| SrO | 0.26 | 0.15 | 0.03 | 0.09 | 0.04 | 0.04 | 0.00 | 0.00 | 0.10 | 0.05 | 0.03 |
| BaO | 0.00 | 0.00 | 0.00 | 0.00 | 0.02 | 0.03 | 0.00 | 0.00 | 0.00 | 0.03 | 0.00 |
| Sum | 56.75 | 55.14 | 54.78 | 56.15 | 55.84 | 55.46 | 54.84 | 55.60 | 54.93 | 55.49 | 55.31 |
| CO ₂ | 44.81 | 43.49 | 43.25 | 44.29 | 44.08 | 43.83 | 43.33 | 43.91 | 43.35 | 43.78 | 43.63 |
| Total | 101.56 | 98.62 | 98.03 | 100.44 | 99.93 | 99.29 | 98.17 | 99.51 | 98.28 | 99.27 | 98.94 |
| <i>No. of ions</i> | | | | | | | | | | | |
| Ca | 1.93 | 1.95 | 1.95 | 1.95 | 1.95 | 1.94 | 1.95 | 1.95 | 1.95 | 1.95 | 1.96 |
| mg | 0.06 | 0.046 | 0.05 | 0.04 | 0.05 | 0.05 | 0.05 | 0.05 | 0.05 | 0.04 | 0.04 |
| Fe | 0.00 | 0.001 | 0.00 | 0.00 | 0.00 | 0.00 | 0.00 | 0.00 | 0.00 | 0.00 | 0.00 |
| Mn | 0.00 | 0.001 | 0.00 | 0.00 | 0.00 | 0.00 | 0.00 | 0.00 | 0.00 | 0.00 | 0.00 |
| Sr | 0.01 | 0.003 | 0.00 | 0.00 | 0.00 | 0.00 | 0.00 | 0.00 | 0.00 | 0.00 | 0.00 |
| Ba | 0.00 | 0.00 | 0.00 | 0.00 | 0.00 | 0.00 | 0.00 | 0.00 | 0.00 | 0.00 | 0.00 |
| <i>Mol. %</i> | | | | | | | | | | | |
| CaCO ₃ | 98.42 | 96.41 | 95.99 | 98.44 | 97.65 | 96.91 | 95.87 | 97.54 | 96.09 | 97.25 | 97.24 |
| MgCO ₃ | 2.61 | 1.92 | 1.92 | 1.78 | 2.03 | 2.28 | 2.11 | 1.91 | 1.98 | 1.82 | 1.63 |
| FeCO ₃ | 0.06 | 0.03 | 0.00 | 0.04 | 0.08 | 0.00 | 0.06 | 0.07 | 0.07 | 0.07 | 0.03 |
| MnCO ₃ | 0.10 | 0.05 | 0.08 | 0.06 | 0.09 | 0.00 | 0.12 | 0.00 | 0.00 | 0.02 | 0.00 |
| SrCO ₃ | 0.38 | 0.21 | 0.05 | 0.18 | 0.05 | 0.06 | 0.00 | 0.00 | 0.14 | 0.07 | 0.05 |
| BaCO ₃ | 0.00 | 0.00 | 0.00 | 0.00 | 0.02 | 0.03 | 0.00 | 0.00 | 0.00 | 0.04 | 0.00 |
| <i>T°C</i> | 433 | 380 | 377 | 360 | 388 | 409 | 399 | 375 | 390 | 360 | 346 |

maximum metamorphic conditions (Essene, 1983). The reported temperatures (Table 2) were calculated using the calcite-dolomite thermometer calibrated by Anovitz and Essene (1987) which accounts for Fe in the system. The position of the solvus is well defined between 400 and 800°C with an error in the estimations of 10°C; below 400°C the solvus limb steepens and potential errors increase (Anovitz and Essene, 1987). However, even at low temperature, consistency in the relative variations in the Mg content is significant. In this case, temperatures lower than 400°C are affected by large errors, but reflect an actual trending in temperature variation.

4. Microfabrics of the Alpi Apuane marbles

Microstructural features, allow us to distinguish three main types of microfabrics in the Alpi Apuane marbles. They represent end-members of a wide range of transitional types. Each microfabric type can be found in the whole Alpi Apuane area. The three main microfabric types are: a) annealed microfabric (type-A); b) dynamically recrystallized microfabric (type-B) and c) twinned microfabric (type-C).

4.1. Annealed microfabric (type-A microfabric)

This type of microfabric is characterized by equant polygonal grains (granoblastic or “foam” microstructure, Fig. 5 a–d), with straight to slightly curved grain boundaries that meet in triple points at angles of nearly 120°. *c*-Axis orientations show a random distribution or a weak crystallographic preferred orientation. Samples showing this microstructure come from different structural and geographical positions in the Alpi Apuane unit: sample 34 from the western, sample 39 from the central and sample 190 from the eastern Alpi Apuane (Fig. 2).

The westernmost sample (sample 34) is located in the normal limb of a regional scale NE-facing D1 isoclinal fold, the Carrara syncline (Figs. 2 and 6a). This kilometer-scale syncline represents the major westernmost fold in the Apuane unit with a NW–SE trending axis, shallowly plunging to the NW. Microstructural analysis of this sample shows a unimodal grain size distribution with an average grain size of 300 μm (Molli and Heilbronner, 1999). The analysis of the preferred orientation of grain boundary surfaces (SURFOR) reveals a slightly bimodal surface distribution which can be observed in the rose diagram of Fig. 7a. This may reflect a weak grain boundary alignment

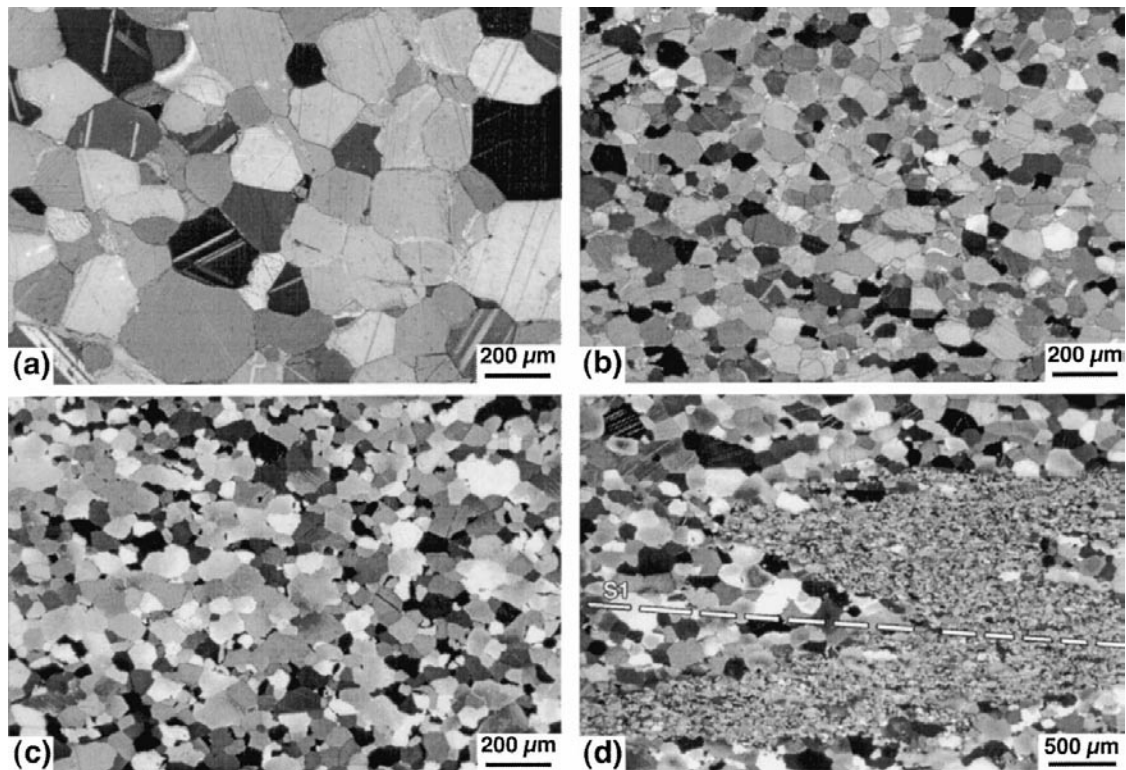


Fig. 5. Annealed microstructures in marbles: (a) Sample 34. (b) Sample 39. (c) Sample 180. (d) D_1 fold overgrown by "granoblastic" microstructure (locality Belgia, western Alpi Apuane). The folded level, made up of fine-grained, calcite dolomite and phyllosilicates, represents a former stratigraphic layer.

of rhombic symmetry, which has been already noticed for undeformed marble before (Schmid et al., 1987). The analysis of the preferred orientation of particle axes (PAROR) also shows a slightly bimodal distribution of long axis orientation, with the first maximum being inclined at approximately $20\text{--}30^\circ$ with respect to the foliation plane, and a second maximum at $20\text{--}30^\circ$ in the opposite sense (Table 3). The asymmetry of the orientation of grain boundary surfaces (SURFOR) and the preferred orientations of the particle axes (PAROR) of the sample coincide rather well. The average aspect ratios (short/long axis) of the individual grains are in the order of 0.65. The PARIS factor for this microstructure is very low (1.8), implying straight grain boundaries. The c -axis pole figure reveals a weak great circle distribution at the periphery of the pole figure. The maximum temperature calculated for a dolomite-bearing sample collected in the same outcrop (sample 30) is about 430°C (Table 2).

Sample 39 comes from the central-northern part of the Alpi Apuane, in the normal limb of the M. Altissimo Syncline (Fig. 6b). The quantitative microstructural analysis of sample 39 shows a unimodal grain size distribution with an average grain size diameter of $90\ \mu\text{m}$ (Molli and Heilbronner, 1999) (Fig. 7b). A unimodal and asymmetrical

surface orientation is revealed by the analysis of the preferred orientation of grain boundary surfaces (SURFOR) showing a maximum of orientation at an angle of approximately 30° to the foliation trace. The analysis of the preferred orientation of particle axes (PAROR) shows a weak bimodal distribution of long axis orientation, with the first maximum being inclined at approximately $20\text{--}30^\circ$ with respect to the foliation plane, and a second maximum at $20\text{--}30^\circ$ in the opposite sense. Also in this sample the symmetry of the orientation of grain boundary surfaces (SURFOR) and the preferred orientations of the particle axes (PAROR) coincide rather well. The average aspect ratios (short/long axis) of the individual grains are in the order of 0.65 and the PARIS factor of microstructures is 2.3. Sample 39 shows a nearly random distribution of c -axis. Samples 40 and 4, collected close to sample 39, show similar microfabrics and yield calcite/dolomite equilibration temperatures of $370\text{--}380^\circ\text{C}$ (Table 2).

Sample 190 comes from the geometrically lowermost marble levels of the whole Alpi Apuane complex (Fig. 2). These marbles crop out in the core of a kilometric scale upright antiform (Fig. 6c), in which the main schistosity (D_1) and all other D_1 -structures are deformed by a later subhorizontal crenulation cleavage (D_2). Sample 190

Fig. 6. Geological maps of the areas of samples locations (see Fig. 1 for the location of the maps). After Carmignani (1985), modified.

Fig. 7. Line-drawing of microstructures, *c*-axis orientation (from universal stage measurements) and results of PAROR and SURFOR analysis for calcite microfabric of samples 34, 39 and 190 (Type-A microfabric). Number of grains analysed with PAROR and SURFOR routines is more than 200.

shows an average grain size of about 100 μm (Fig. 7c) and the analysis of the preferred orientation of grain boundary surfaces (SURFOR) reveals a nearly unimodal and asymmetrical surface orientation, showing a primary orientation at a low angle to the foliation trace. The analysis of the preferred orientation of particle axes (PAROR) shows a slightly bimodal distribution of long axis orientation, with the main maximum being inclined at approximately 20–30° with respect to the foliation plane, and a second maximum at

60°. Also in this sample the symmetry/asymmetry of the surface orientation and the preferred orientations of the particle axes coincide rather well. The average aspect ratios of the individual grains are in the order of 0.7 and the PARIS factor for the grain boundary geometry is around two. No clear preferred orientation of *c*-axis can be recognized. Calcite coexisting with dolomite in a sample collected nearby (sample 188, Fig. 6c, Table 2), indicates a maximum temperature of 360°C.

Table 3
Results of microstructural analysis of representative samples of the different microfabric-types.

| Sample | Microfabric type | Grain size (μm) | Grain size distribution | α° | PARIS | SPO | T ($^\circ\text{C}$) |
|--------|------------------|------------------------------|-------------------------|--------------------------------|----------------|----------------|--------------------------|
| 34 | A | 300 | Unimodal | α_1 20° ÷ 30° | 1.8 | - | 430°* |
| 39 | A | 90 | Unimodal | α_1 20° ÷ 30° | 2.3 | - | 370° ÷ 380°* |
| | | | | α_2 20° ÷ 30° | | | |
| 190 | A | 100 | Unimodal | α_1 20° ÷ 30° | 2 | - | 360°* |
| 170 | B1 | 150 ÷ 200 | Unimodal | α_1 10° | 9 | Parallel S1 | 390°* |
| 107 | B2 | Relict 150 | Bimodal | α_1 15° | Relict 8 ÷ 15 | Parallel S2 | Relict 400° |
| | | Recryst. 40 ÷ 50 | | | Recryst. 2 ÷ 3 | Recryst. 370° | |
| 45 | B2 | Relict 150 | Bimodal | α_{relict} 15° | Relict 10 ÷ 23 | Parallel shear | Relict 420° |
| | | Recryst. 40 ÷ 50 | | $\alpha_{\text{recryst.}}$ 15° | Recryst. 2 ÷ 3 | Zone boundary | Recryst. 340° |

* Temperature of a nearby sample.

4.2. Dynamically recrystallized microfibrils (type-B microfibrils)

Within type-B microfibrils two end-members of microstructures can be recognized: a) microstructures exhibiting strong shape preferred orientation, coarse grains and lobate grain boundaries (type-B1); b) microstructures with shape preferred orientation, smaller grain size and predominantly straight grain boundaries (type-B2). The two microstructures are quite different, but in a lot of samples lobate and straight grain boundaries occur at the same time. Samples showing type-B microfibrils are found in different structural positions in the nappe stack. In the following, we discuss sample 170 (type-B1 microfibril) and sample 107 (type-B2 microfibril) that come from the central Alpi Apuane, whereas sample 45 (type-B2 microfibril) comes from the western Alpi Apuane.

Sample 170 is derived from the highly sheared inverted limb of the kilometer-scale NE-facing D_1 Tambura anticline (see profile in Figs. 2 and 6d). It shows coarse grain size, lobate grain boundaries, strong shape preferred orientation parallel to the main mesoscopic foliation, and a strong crystallographic preferred orientation (Fig. 8a). In mica-rich layers, pinning and window microstructures similar to that described by Jessell (1987) in quartzite are sometimes visible. Quantitative microstructural analysis (Fig. 9a) shows an average grain size of 150–200 μm and a unimodal nearly symmetrical surface orientation with an orientation subparallel to the foliation trace. The analysis of the preferred orientation of particle axes (PAROR) shows a unimodal distribution of long axis orientation, with a maximum inclined at low angle approximately 10° with respect to the foliation plane. Individual grains are characterized by an average aspect ratio in the order of 0.50. A strong c -axis preferred orientation with a maximum normal to the foliation plane can be observed in this sample (Figs. 8b and 9a). Calcite/dolomite thermometry on sample 115, which was collected close to sample 170, shows the same microstructural features and indicates a temperature of about 390°C (Table 2).

Microstructure with straight grain boundaries (type-B2) is found in sample 107, that comes from the core of a kilometer-scale SW-verging D_2 fold (Figs. 2 and 6d), refolding bedding and the D_1 foliation (S_1). This sample shows small recrystallized grains (40–50 μm), diffuse subgrains and core-mantle-like structures (Fig. 8c). Larger relict grains of the earlier microfibril are preserved. Quantitative analysis (Fig. 9b) shows preferred orientation of long axis particle orientation (PAROR) defining the foliation recognizable in thin section. Crystallographic preferred orientation shows a maximum of the c -axis at a low-angle and normal to the foliation plane (Fig. 9b). In contrast to the larger relict grains, which yield a calcite/dolomite equilibration temperature of about 410°C (sample 107A in Table 2), recrystallized grains are slightly zoned with Mg content, decreasing from

core to rim. Maximum temperatures calculated from the cores are about 400°C (sample 107Bc in Table 2); temperatures in the rims decrease to about 370°C (sample 107Br in Table 2).

Another kind of type-B microfibrils is found in sample 45, collected along mm- to dm-scale D_2 shear zones (Fig. 8d–h), in the western Alpi Apuane (Figs. 2 and 6e). Approaching these shear zones, a gradual change in marble microfibril can be observed. In the low strain domains, the granoblastic protolith (mean grain diameter approximately 150 μm) shows type-A microfibril, even if low-temperature intracrystalline deformation (mainly undulatory extinction and deformation twins) can be observed. Towards the high strain zone (Fig. 9c), the grain boundary corrugation of the relict calcite, i.e. the PARIS factor, increases from about 10 to 23 (Table 3). Recrystallization occurs preferentially at the grain boundaries and a progressive localization of recrystallized grains in layers, subparallel to the shear zone boundaries, is observed (Fig. 8d). This transition is sketched in Fig. 10d. The recrystallized layers show a bimodal grain size distribution. Coarse, twinned relict grains (modal grain diameter about 200 μm) are embedded in a matrix of recrystallized grains with a diameter of approximately 40 μm (Fig. 9d).

Sample 80, which shows the same microstructural type as sample 45, is characterized by a texture with c -axis small circle distribution oriented normal to the shear zone boundary (Fig. 8f). As illustrated in Fig. 8g, where recrystallized grains are masked, the few randomly distributed maxima can be related to the c -axis orientations of the relict grains. Due to bad sample statistics and a coarse grain size, a maximum of about 12 times uniform is obtained. The analysis of the completely recrystallized domain (Fig. 8h) of this type-B2 microfibril reveals that the c -axis orientations of the new grains are closely related to the relict c -axis orientations. Its small circle c -axis distribution is located in the same place as the maxima of the relict grains, shown in Fig. 8g. It is possible to interpret this feature as the result of a progressive reorientation of subgrains.

The calcite-dolomite thermometry applied in the fine-grained recrystallized calcite crystals of sample 45 yields maximum temperatures of about 340°C (sample 45B in Table 2). Granoblastic calcite grains in the low strain domains are zoned, showing Mg-rich cores and Mg-poorer rims. The maximum temperature calculated for the cores is 390°C (sample 45Ac in Table 2), whereas the Mg-content at the rim yields temperatures of 360°C (sample 45Ar in Table 2). Temperature distribution in these shear zones is sketched in Fig. 10d.

4.3. Twinned microfibril (type-C microfibril)

The third type of microfibril is related to low-strain and low-temperature crystal plastic deformation mechanisms.

Characterized by thin straight e -twins (Fig. 10e), it occurs

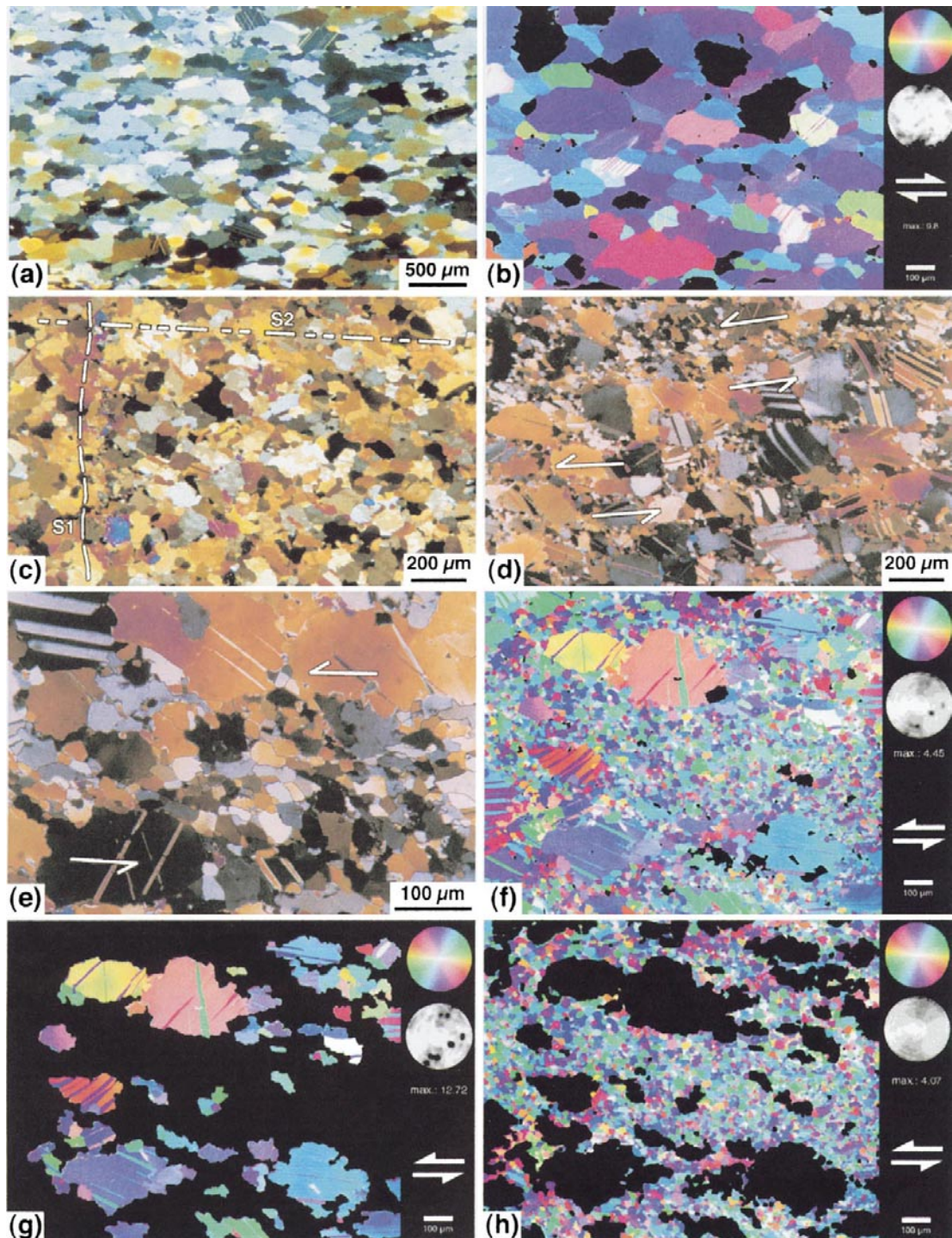


Fig. 8. Microstructures of dynamically recrystallized marbles. (a) Sample 170. (b) *c*-Axis orientations image (COI) revealed by CIP (Heilbronner Panozzo and Pauli, 1993) of sample 170. Strong *c*-axis maximum is located normal to the foliation plane. (c) Sample 107. (d) and (e) Sample 45. (f) COI of sample 80. (g) COI of relict grains in sample 80. Randomly distributed *c*-axis maxima can be related to single relict grains. (h) COI of recrystallized domain. The small circle *c*-axis maximum is located in the same place as the *c*-axis of the relict grains. Therefore subgrain rotation can be considered as the dominant recrystallization mechanism.

Fig. 9. Line-drawing of microstructures, *c*-axis orientation (from universal stage measurements) and results of PAROR and SURFOR analysis for calcite microfabric of samples 170, 107 and 45 (Type-B microfabric). For sample 45 grain size distribution, *c*-axis orientation for a similar microstructural type see sample 80 in Fig. 8f, g and h. Grain size distributions of samples 170, 107 and 45 (Type-B microfabric). Sample 45a shows an area with only limited reworking during D_2 ; sample 45b shows an area that experienced more intense recrystallization during D_2 . Number of grains analysed with PAROR and SURFOR routines is more than 200.

with different intensities in all the marble outcrops of the Alpi Apuane region, overprinting both type-A and type-B microfabrics.

It is well developed where large calcite grains are present.

In the case of type-B microstructures, where large and smaller grains are present (Fig. 8e), twinning affects only larger grains and not finer ones. This is in agreement with experimental studies indicating that twinning is easier in

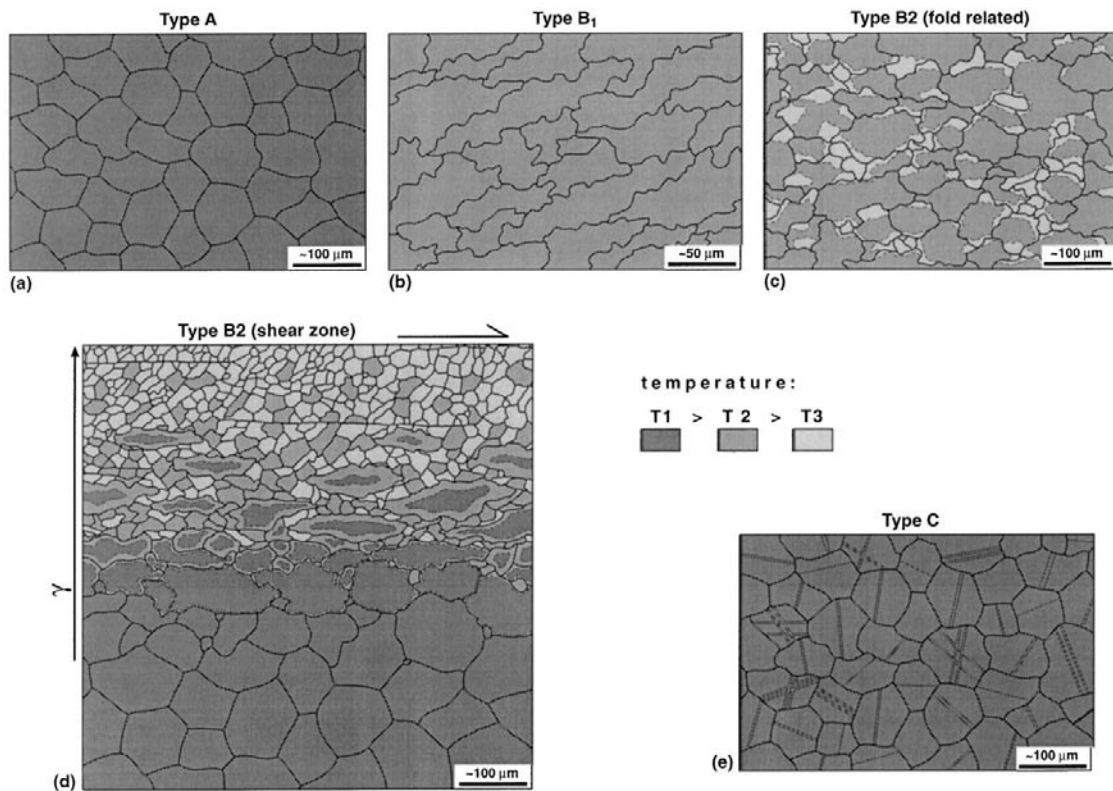


Fig. 10. Sketch showing the three types of microfabric described in this paper. (a) Type-A annealed microfabric. (b) Type-B1 dynamically recrystallized microfabric developed during late D_1 deformation. (c) Type-B2 dynamically recrystallized microfabrics formed during folding. (d) Type-B2 dynamically recrystallized microfabrics formed along shear zone. Increasing strain is associated with grain size reduction. Different grey tones represent different calcite/dolomite temperatures (γ = strain). (e) Type-C twinned microfabric.

coarse grained than in fine grained-rocks, because the spreading and widening of twin lamellae are hampered by grain boundaries (Casey et al., 1978; Rowe and Rutter, 1990).

5. Carrara marble microfabrics and the tectonic evolution of the Alpi Apuane metamorphic complex: a discussion

5.1. Microfabric evolution and thermal history

The common microstructural features of samples 34, 39 and 190, such as the granoblastic polygonal grains with straight to slightly curved boundaries (very low PARIS factor ranging from 1.8 to 2.3), the unimodal grain size distribution, the absence of any optical evidence of internal strain and the weak or absent c -axis orientation, allowed us to interpret the type-A microfabric as developed during static recrystallization (annealing). This microstructure is sketched in Fig. 10a. The statically recrystallized micro-

fabrics are observable even though samples are collected in marble levels within kilometer-scale D_1 isoclinal folds, where also minor parasitic folds developed. The presence of annealed microstructures within D_1 folds (Fig. 5d) clearly indicates that the grain growth which produced type-A microfabric occurred after the main D_1 folding phase, and obliterated all earlier syntectonic microstructures associated with folding. However, the presence of a weak texture in some samples can be possibly related to the pre-annealing deformation history.

The statically recrystallized marbles show an increase in grain size from the eastern to the western part of the Alpi Apuane complex, as already noticed by Zaccagna (1932) and Di Pisa et al. (1985). The latter authors interpreted the variation in grain size as related to a metamorphic paleogradient from the root zone (south west) to the front (north-east) during the D_1 deformation affecting the metamorphic complex. The results of our thermometric studies confirm that the grain size variation in type-A microfabrics is associated with a temperature increase from east to west from 80–100 μm and 360–380°C to 250–300 μm and

420–430°C, but in our view static recrystallization occurred after main D_1 folding. During static recrystallization history, one would expect that the structurally lower marbles experienced higher temperature than the structurally higher ones and should develop larger calcite grains. On the contrary, the composite cross sections of Fig. 2 show that coarse grained marbles of the western Alpi Apuane (samples 34–39) occur in a higher tectonic position with respect to the marbles of the central and eastern Alpi Apuane (sample 190). To explain this, we have to consider the tectonic evolution of the Alpi Apuane. If we restore the NE-directed transport of the late D_1 phase, the higher portions of the nappe stack have to be located in a more westward and deeper position with respect to their present location. It is therefore more likely that annealing occurred at the time when the marbles of the western Alpi Apuane were in a deeper position than the marbles of the eastern Alpi Apuane.

The second type of microfibrils (type-B), characterized by: a) microstructures exhibiting coarse grains with lobate grain boundaries and strong shape preferred orientation (type-B1, sample 170, sketched in Fig. 10b); and b) microstructures with shape preferred orientation, smaller grain size and predominantly straight grain boundaries (type-B2, samples 45 and 107, sketched in Fig. 10c, d), are both interpreted as related to high strain and high temperature (350–400°C) crystal plastic deformation mechanisms (dislocation creep). Whereas grain boundary migration recrystallization can be considered as predominant in type-B1 microfibril, an important contribution of both rotation recrystallization and grain boundary migration can be inferred to prevail in type-B2 microfibril.

Sample 170, which shows a type-B1 microfibril, is characterised by a single c -axis maximum subperpendicular to the foliation plane (Figs. 8b and 9a). The interpretation of the texture-forming mechanism, quite common in naturally deformed marble, is still under discussion (Lafrance et al., 1994 and references therein). A similar texture was obtained in experimental deformation (Schmid et al., 1987), both in the twinning regime (where it is related to twin gliding and a substantial amount of r - and f -glide) and in grain boundary migration regime. The microstructural features of our sample point out that a comparison with the experimental grain boundaries migration regime appears more likely.

In samples 107 and 45 (type-B2 microfibril), syntectonic recrystallization of earlier large calcite grains is suggested by the presence of core-mantle structures, the progressive reorientation of subgrains c -axis, the polymodal grain size distribution, with larger relict grains associated with smaller new recrystallized ones, and by the wavelength of the grain boundary bulges that corresponds to the grain size of the newly formed recrystallized grains. We infer therefore that syntectonic recrystallization through rotation recrystallization and grain boundary migration postdate static recrystallization, i.e. type-B2 microfibrils overprint type-A microfibrils.

All type-B microfibrils show a shape preferred orienta-

tion of the grains which has allowed us to study the relationships between the development of such microstructures and meter- to kilometer-scale tectonic structures.

Sample 170 comes from a late D_1 high strain zone (Tambura thrust) in the inverted limb of the Tambura anticline (Figs. 2 and 6d). The shape preferred orientation of grains is parallel to the main foliation recognizable in the field (S_1) and refolded by the D_2 folds. For this area, we therefore infer, that the development of type-B1 microfibrils is coeval with late D_1 NE-directed transport along the inverted limb of the Tambura anticline.

Sample 107 comes from the core of a kilometer-scale SW-verging D_2 fold (Figs. 2 and 6d), which refolds bedding and the D_1 foliation (S_1). The shape preferred orientation of the recrystallized grains is parallel to the mesoscopic axial-plane foliation (S_2 in Fig. 8c) of D_2 folds. This implies that D_2 deformation can lead to crystal plasticity in marbles, too.

Late D_1 and D_2 deformations lead therefore to reworking of type-A microfibrils producing type-B microfibrils. These overprinting relationships are easily observable where S_1 or S_2 foliations are evident and type-B microfibrils develop a foliation recognizable at outcrop-scale. Nevertheless, most of the Alpi Apuane marbles are pure calcite marbles with no phyllosilicates or impurities, which mark a macroscopic foliation. In this case, it is difficult to determine if the dynamic microfibrils overprint an early annealed fabric or if they are related to earlier stages of D_1 deformation surviving the static recrystallization and grain growth as proposed by Coli (1989). However, the investigated evolution of microstructures (sample 45) in pure marbles witnessing the transition from type-A to type-B microfibrils, points to the interpretation here proposed.

Analyses performed with the Dietrich and Song (1984) method on type-C microfibril (twinning) point out that in some samples where twinning is associated with type B microfibrils, it is kinematically coherent with stress field related to the microfibril-producing event. In other samples, this relationship is not so straightforward, and it is difficult to demonstrate in the case of twinning affecting type-A microfibrils. Therefore, we suggest that at least a part of the twinning occurred at low temperature (minor than 200°C according to Ferril, 1991 and Burkhard, 1993), and has to be related to the most recent exhumation history of the metamorphic complex (cfr. Lacombe and Laurent, 1996).

5.2. Microfibril evolution and tectonic history

In the present study, the variability of statically and dynamically recrystallized microfibrils in the Liassic Alpi Apuane marbles has been emphasised. According to our microstructural observations the following evolutionary tectonic model can be proposed.

During the main regional deformation phase (early D_1 , Fig. 11a), nappe emplacement, isoclinal folding producing

Fig. 11. Development of the Alpi Apuane structure (from Carmignani and Kligfield, 1990, modified) and marble microstructures. (a) D_1 main folding phase, with top-NE nappe emplacement. During this phase main foliation and kilometer-scale isoclinal folds developed. (b) After D_1 main folding phase annealing occurred, with complete obliteration of earlier microfabrics. In marbles polygonal granoblastic microstructures develop (type-A microfabrics). (c) D_1 antiformal stack phase, with final NE transport along thrusts. Annealed microstructures are passively transported toward NE or reworked in shear zones along thrusts (type-B1 microfabrics). (d) D_2 deformation leading to extension and exhumation. D_1 features are folded or cut by later shear zones developed along low angle normal faults. Earlier microstructures can be reworked in D_2 shear zones or along D_2 fold axial planes (type-B2 microfabrics).

kilometer-scale NE-facing folds, stretching lineations and main foliation developed in the Apuane unit. After early D_1 deformation (Fig. 11b), thermal relaxation and heating produced statically recrystallized fabrics (type-A microfabrics). The westernmost rocks were located in the deepest positions, and marbles developed the largest grain sizes and higher calcite/dolomite equilibrium temperature; easternmost marbles were in a higher position, and developed smaller grain sizes at lower temperature.

During the late stage of the D_1 event (antiformal stack phase, Fig. 11c), further shortening was accomplished. In this phase, dynamic recrystallized microstructures (type-B1 microfabrics) were produced in localized, meter to decimeter-thick shear zones, where earlier type-A annealed fabrics were reworked. These shear zones accommodate the transport of the originally deeper westernmost tectonic levels toward NE in higher positions within the nappe stack.

The D_2 history was associated with exhumation in retrograde metamorphic conditions (Fig. 11d). During this event, narrow millimeter- to decimeter-thick shear zones developed in the higher levels of the Alpi Apuane metamorphic complex (Carrara area), whereas folding occurred at lower levels (Arni area). The temperature was lower during D_2 deformation than during D_1 , but high enough to

produce syntectonic recrystallization (type B2 microfabric). This is testified by fine-grained calcite in D_2 shear zones (sample 45), and recrystallized calcite grains elongated parallel to the axial surface of D_2 folds (sample 107).

The difference in the temperature during the D_2 event (380°C in the east, 340°C in the west) can be related to the deeper position of rocks from the eastern area relative to rocks from the western area at the beginning of D_2 deformation (Fig. 11d). This frame fits well with the different styles of D_2 marble deformation, with predominant structures represented by large scale folding in the east as opposed to localized shear zones in the west. It is important to remember that not everywhere D_2 folding produced dynamic recrystallization with shape preferred orientation tracing the axial plane of folding. In the case of open D_2 folds, no significant reworking of earlier microstructures occurred, but only a passive reorientation of the previous microstructures.

Although the Carrara marble is widely used in experimental rock-deformation because of its nearly homogeneous fabric, with neither shape preferred orientation nor texture, our microfabric investigations at the scale of the whole Alpi Apuane area has pointed out a large variability of marble calcite microfabric originated during

static recrystallization as well as during various stages of the dynamic recrystallization which overprinted the “granoblastic” annealed fabric.

Presently running texture investigations on marbles at the scale of the whole Alpi Apuane region (Leiss and Molli, 1999; Oesterling et al., 1999; Rexin et al., 1999) will help to further develop the model of microfabric evolution and deformation history here presented.

Acknowledgements

The authors want to acknowledge R. Heilbronner, H. Stünitz and L. Carmignani for the valuable suggestions. Many thanks are also due to E. Tavarnelli and B. Leiss for helpful and constructive reviews. G. Saviozzi is thanked for the ultra-thin section. Financial support from P.A.R. (Piano di Ateneo per la Ricerca) 1999—Prof. A. Larracotto is gratefully acknowledged.

References

- Abbate, E., Balestrieri, M.L., Bigazzi, G., Norelli, P., Quercioli, C., 1994. Fission-track dating and recent rapid denudation in Northern Apennines, Italy. *Memorie della Società Geologica Italiana* 48, 579–585.
- Anovitz, L.M., Essene, E.J., 1987. Phase equilibria in the system $\text{CaCO}_3\text{-MgCO}_3\text{-FeCO}_3$. *Journal of Petrology* 28, 389–414.
- Bigazzi, G., Di Pisa, A., Gattiglio, M., Meccheri, M., Norelli, P., 1988. La struttura cataclastico-milonitica di Foce di Mosca, Alpi Apuane sud-orientali (M. Corchia, Gruppo delle Panie). *Atti della Società Toscana di Scienze Naturali, Memorie, Serie A* 95, 105–116.
- Boccaletti, M., Gosso, G., 1980. Analisi della deformazione plicativa e rapporti con lo sviluppo della blastesi metamorfica nell’area di Campo Cecina-M. Pisanino delle Alpi Apuane settentrionali. *Memorie della Società Geologica Italiana* 21, 101–110.
- Bonatti, S., 1938. Studio petrografico delle Alpi Apuane. *Memorie Descrittive della Carta Geologica d’Italia* 26, 116.
- Burkhard, M., 1993. Calcite twins, their geometry, appearance and significance as stress and strain markers and indicators of tectonic regime: a review. *Journal of Structural Geology* 15, 351–368.
- Carmignani, L., 1985. Carta geologico-strutturale del Complesso Metamorfico delle Alpi Apuane, scala 1:25.000. Foglio nord. Litografia Artistica Cartografica, Firenze.
- Carmignani, L., Fantozzi, P.L., Giglia, G., Meccheri, M., 1993. Pieghe associate alla distensione duttile del Complesso Metamorfico Apuano. *Memorie della Società Geologica Italiana* 49, 99–124.
- Carmignani, L., Giglia, G., Kligfield, R., 1978. Structural evolution of the Apuane Alps; an example of continental margin deformation in the northern Apennines, Italy. *Journal of Geology* 86, 487–504.
- Carmignani, L., Kligfield, R., 1990. Crustal extension in the Northern Apennines: the transition from compression to extension in the Alpi Apuane core complex. *Tectonics* 9, 1275–1303.
- Casey, M.S., Rutter, E.H., Schmid, S.M., Siddans, A.W.B., Whalley, J.S., 1978. Texture development in experimentally deformed calcite rocks. In: Gottstein, G., Lücke, K. (Eds.), *Proceedings 5th International Conference on Textures of Materials*. Springer Verlag, pp. 231–240.
- Cerrina, F.A., Plesi, G., Fanelli, G., Leoni, L., Martinelli, P., 1983. Contributo alla conoscenza dei processi metamorfici di grado molto basso (anchimetamorfismo) a carico della falda toscana nell’area del ricoprimento apuano. *Bollettino della Società Geologica Italiana* 102, 269–280.
- Coli, M., 1989. Litho-structural assemblage and deformation history of “Carrara marble”. *Bollettino della Società Geologica Italiana* 108, 581–590.
- Coli, M., Fazzuoli, M., 1992. Considerazioni sulla litostratigrafia e sull’evoluzione sedimentaria delle formazioni retico-liassiche del nucleo metamorfico apuano. *Atti Ticinensi di Scienze della Terra* 35, 43–60.
- Covey-Crump, S.P., 1997. The high temperature static recovery and recrystallization behaviour of cold-worked Carrara marble. *Journal of Structural Geology* 19, 225–241.
- Crisci, G.M., Leoni, L., Sbrana, A., 1975. La formazione dei marmi delle Alpi Apuane (Toscana); studio petrografico, mineralogico e chimico. *Atti della Società Toscana di Scienze Naturali, Memorie, Serie A* 82, 199–236.
- D’Albissin, M., 1963. Les traces de la déformation dans les roches calcaires. *Revue de géogr. physique et de géologie dynamique (fascicule supplémentaire)*, 174 pp.
- De Bresser, J.H.P., 1991. Intracrystalline deformation of calcite. *Geologica ultraiectina* 79, 191.
- Dietrich, D., Song, H., 1984. Calcite fabrics in a natural shear environment. The Helvetic nappes of western Switzerland. *Journal of Structural Geology* 6, 19–32.
- Di Pisa, A., Franceschelli, M., Leoni, L., Meccheri, M., 1985. Regional variation of the metamorphic temperatures across the Tuscanid 1 Unit and its implications on the alpine metamorphism (Apuan Alps, N-Tuscany). *Neues Jahrbuch für Mineralogie, Abhandlungen* 151, 197–211.
- Di Sabatino, B., Giampalo, C., Potenza, P.L., 1977. Metamorfismo di “very low grade” ed altissima pressione nella “Unità delle Panie”. *Periodico di Mineralogia* 46, 79–89.
- Elter, P., 1975. Introduction à la géologie de l’Apennin septentrional. *Bulletin de la Société Géologique de France* 7, 956–962.
- Essene, E.J., 1982. Geologic thermometry and barometry. In: Ferry, J.M. (Ed.), *Characterization of Metamorphism Through Mineral Equilibria. Reviews in Mineralogy*, pp. 153–206.
- Essene, E.J., 1983. Solid solutions and solvi among metamorphic carbonates with applications to geologic thermobarometry. In: Reeder, R.J. (Ed.), *Carbonates: Mineralogy and Chemistry. Reviews in Mineralogy*, pp. 77–96.
- Essene, E.J., 1989. The current status of thermobarometry in metamorphic rocks. In: Daly, J.S., Cliff, R.A., Yardley, B.W.D. (Eds.), *Evolution of Metamorphic Belts. Geological Society of London Special Publications*, pp. 1–44.
- Ferril, D.A., 1991. Calcite twin widths and intensities as metamorphic indicators in natural low-temperature deformation of limestone. *Journal of Structural Geology* 13, 667–675.
- Franceschelli, M., Leoni, L., Memmi, M., Puxeddu, M., 1986. Regional distribution of Al-silicates and metamorphic zonation in the low-grade Verrucano metasediments from the Northern Apennines, Italy. *Journal of Metamorphic Geology* 4, 309–321.
- Franceschelli, M., Memmi, I., Carcangiu, G., Gianelli, G., 1997. Prograde and retrograde chloritoid zoning in low temperature metamorphism, Alpi Apuane, Italy. *Schweizerische Mineralogische und Petrographische Mitteilungen* 77, 41–50.
- Fredrich, J.T., Evans, B., Wong, T.F., 1989. Micromechanics of the brittle to plastic transition in Carrara Marble. *Journal of Geophysical Research* 94, 4129–4145.
- Giglia, G., Radicati di Brozolo, F., 1970. K/Ar age of metamorphism in the Apuane Alps (Northern Tuscany). *Bollettino della Società Geologica Italiana* 89, 485–497.
- Heilbronner Panozzo, P.R., Pauli, C., 1993. Integrated spatial and orientation analysis of quartz c-axis by computer-aided microscopy. *Journal of Structural Geology* 15, 369–382.
- Jessell, M.W., 1987. Grain boundary migration microstructures in a naturally deformed quartzite. *Journal of Structural Geology* 9, 1007–1014.
- Jolivet, L., Faccenna, C., Goffé, B., Mattei, M., Rossetti, F., Brunet, C., Storti, F., Funicello, R., Cadet, J.P., D’Agostino, N., Parra, T., 1998.

- Midcrustal shear zones in postorogenic extension: example from the northern Tyrrhenian Sea. *Journal of Geophysical Research* 103, 12123–12160.
- Kligfield, R., Hunziker, J., Dallmeyer, R.D., Schamel, S., 1986. Dating of deformation phases using K-Ar and $^{40}\text{Ar}/^{39}\text{Ar}$ techniques; results from the Northern Apennines. *Journal of Structural Geology* 8, 781–798.
- Leiss, B., Molli, G., 1999. Natural “High Temperature” texture in Calcite from the Alpi Apuane, Italy. *Göttinger Arb. Geol. Paläont. SB4*, 100–101.
- Lacombe, O., Laurent, P., 1996. Determination of deviatoric stress tensors based on inversion of calcite data from experimentally deformed monophase samples: preliminary results. *Tectonophysics* 255, 189–202.
- Lafrance, B., White, J.C., Williams, P.F., 1994. Natural calcite c-axis fabrics: an alternative interpretation. *Tectonophysics* 229, 1–18.
- Mas, D.L., Crowley, P.D., 1996. The effect of second-phase particles on stable grain-size in regionally metamorphosed polyphase calcite marbles. *Journal of Metamorphic Geology* 14, 155–162.
- Molli, G., Giorgetti, G., 1999. Meso, microstructural and petrological constraints on the tectono-metamorphic evolution of the Alpi Apuane Complex (NW Tuscany, Italy). *Exhumation of metamorphic terranes. Rennes Meeting, Abstract volume*, pp. 54–55.
- Molli, G., Heilbronner, P.R., 1999. Microstructures associated with static and dynamic recrystallization of Carrara marble (Alpi Apuane, NW Tuscany Italy). *Geologie en Mijnbouw* 78, 119–126.
- Olgaard, D.L., Evans, B., 1988. Grain growth in synthetic marbles with added mica and water. *Contributions to Mineralogy and Petrology* 100, 246–260.
- Oesterling, N., Heilbronner, R., Molli, G., 1999. Textures of Calcite-Mylonites in Carrara Marble. Comparison of Computer Integrated Polarization Microscopy (CIP) and Universal Stage-Measurements. *Göttinger Arb. Geol. Paläont. SB4*, 144–145.
- Panozzo, R., 1983. Two-dimensional analysis of shape fabric using projection of lines in a plane. *Tectonophysics* 95, 279–294.
- Panozzo, R., 1984. Two-dimensional strain from the orientation of lines in a plane. *Journal of Structural Geology* 6, 215–221.
- Panozzo, R., Hürlimann, H., 1983. A simple method for the quantitative discrimination of convex and convex-concave lines. *Microscopica Acta* 87, 169–176.
- Rexin, E., Leiss, B., Molli, G., 1999. Microstructures and textures of the Carrara Syncline, Alpi Apuane Italy. *Göttinger Arb. Geol. Paläont. SB4*, 163–164.
- Reutter, K., Teichmüller, M., Teichmüller, R., Zanzucchi, G., 1983. The coalification pattern in the Northern Apennines and its paleogeothermic and tectonic significance. *Geologische Rundschau* 72, 861–894.
- Rowe, K.J., Rutter, E.H., 1990. Paleostress estimation using calcite twinning: experimental calibration and application to nature. *Journal of Structural Geology* 12, 1–17.
- Rutter, E.H., 1972. The influence of interstitial water on the rheological behaviour of calcite rocks. *Tectonophysics* 14, 13–33.
- Rutter, E.H., 1995. Experimental study of the influence of stress, temperature, and strain on the dynamic recrystallization of Carrara marble. *Journal of Geophysical Research* 100, 24651–24663.
- Sander, B., 1950. *Einführung in die Gefügekunde der geologischen Körper, zweiter Teil: Die Korngefüge*. Springer, Wien.
- Schmid, S.M., Panozzo, R., Bauer, S., 1987. Simple shear experiments on calcite rocks: rheology and microfabric. *Journal of Structural Geology* 9, 747–778.
- Schmid, S.M., Paterson, M.S., Boland, J.N., 1980. High temperature flow and dynamic recrystallization in Carrara marble. *Tectonophysics* 65, 245–280.
- Schultz, H., 1996. *Analyse der variszisch-apenninischen Deformationsgeschichte des paläozoischen Basements der Apuaner Alpen (Toskana, Italien)*, *Berliner Geowissenschaftliche Abhandlungen. Reihe A: Geologie und Paläontologie* 188, 108.
- Spiers, C.J., 1979. Fabric development in calcite polycrystals deformed at 400°C. *Bulletin de Minéralogie* 102, 282–289.
- Storti, F., 1995. Tectonics of the Punta Bianca promontory: Insights for the evolution of the Northern Apennines-Northern Tyrrhenian Sea basin. *Tectonics* 14, 832–847.
- Wenk, H.-R., Takeshita, T., Bechler, E., Erskine, B.G., Matthies, S., 1987. Pure shear and simple shear calcite textures. Comparison of experimental, theoretical and natural data. *Journal of Structural Geology* 9, 731–745.
- Zaccagna, D., 1932. *Descrizione Geologica delle Alpi Apuane. Memorie Descrittive della Carta Geologica d'Italia* 25, 440.



Chapter 3

Strain dependent variations of microstructure and texture in naturally deformed Carrara marble*

Nils Oesterling (1) Renée Heilbronner (1) Holger Stünitz (1) Auke Barnhoorn (2) Giancarlo Molli (3)

(1) Department of Earth Sciences, University of Basel, CH-4056 Basel, Switzerland

(2) Department of Earth Sciences, ETH Zürich, CH-8092 Zürich, Switzerland

(3) Department of Earth Sciences, University of Pisa, I-56126 Pisa, Italy

Key words: calcite deformation, Carrara marble, shear zones, dynamic recrystallization, crystallographic preferred orientation, image analysis

*) Manuscript submitted for publication in Tectonophysics

Abstract

Carrara marble is well known for its purity and annealed microstructures. Recent field investigations in the Alpi Apuane tectonic window, however, have revealed that shear zones with dynamically recrystallized microstructures and well developed textures (crystallographic preferred orientation, CPO) crosscut the annealed rocks. This study investigates the microstructural and textural variations across a mm-scale shear zone. The deformation of the shear zone, which post-dates an earlier deformation phase and subsequent annealing, is highly localized in space and time. Assuming an inferred strain rate of about 10^{-11}sec^{-1} , the finite average shear strain of $\gamma = 20$ is produced in the shear zone within a period of only ~ 23000 years. The microstructures have been investigated for grain size, preferred orientation of grain long axis and grain boundaries, and texture. Computer-Integrated Polarization Microscopy (CIP) was employed to investigate the c-axis preferred orientation of the bulk samples as well as of porphyroclasts and recrystallized grains, separately. An interpretation of the slip systems and texture development is made based on the complete CPO determined by Electron Back Scattered Diffraction (EBSD).

The protomylonite is characterized by a core mantle structure with a bimodal grain size distribution, which changes gradually to a microstructure with an unimodal grain size distribution in the completely dynamically recrystallized center of the shear zone. The image analysis of grain boundaries shows that with increasing strain the porphyroclasts become smaller and less lobate, whereas the recrystallized grains maintain their size and shape. This microstructural transition is produced by rotation recrystallization accompanied by some grain boundary migration. The microstructural transition from protomylonite to mylonite coincides with a change in texture type. A single c-axis maximum (e-twinning type) texture in the protomylonite becomes replaced by a texture that is consistent with dominant basal $\langle a \rangle$ slip. It is inferred that rotation recrystallization is responsible for this replacement. Grain boundary migration probably leads to a preferential removal of grains with an orientation unsuitable for slip. Basal $\langle a \rangle$ -slip is frequently found in natural calcite tectonites and only occurs in the highest shear strain domains of the investigated shear zone. Since the deformation temperature, determined by calcite-dolomite thermometry, is about 325 ± 30 °C and stays constant across the shear zone, the microstructural and textural variation depends on the finite strain gradient rather than on temperature variation. The comparison of the natural microstructures and textures to experimental ones indicates the importance of dynamic recrystallization for the texture development.

1. Introduction

The development of microstructures, shape fabrics, and textures (crystallographic preferred orientation, CPO) during progressive deformation can directly be studied in analogue “see-through” experiments (Burg & Wilson 1987, Herwegh & Handy 1998, Means 1983, Wilson 1981). Another way to study the development of deformation fabrics is to perform rock deformation experiments to different finite strains under constant P, T, strain rate conditions and measure the textures and microstructural parameters (i.e. grain size and grain shape) for the individual “deformation increments” (for calcite see e.g. Pieri et al. 2001 a, Pieri et al. 2001 b, Rutter 1995, Schmid et al. 1987).

Natural deformation usually only leaves an end product at a certain finite strain, and only under special conditions a detailed record of the fabric development during progressive deformation is preserved. Shear zones with finite strain gradients sometimes provide a record of progressive deformation under conditions, where several important parameters (e.g. T, P, stress, strain rate) can be assumed to be constant. In these cases one can demonstrate (and one needs to verify) that the strain gradient reflects a temporal sequence of the stages of the deformation, i.e., that the strain variations are due to the localization of the deformation in certain portions of the shear zone (type 2 shear zone of (Means 1995) rather than being the result of strain rate variations. Often, this condition is a tacit assumption in studies of progressive deformation in natural shear zones.

There are a number of studies concerning the development of microstructure and texture in natural calcite shear zones under certain temperature, strain and/or strain rate conditions (e.g. Behrmann 1983, Bestmann et al. 2000, Busch & Van der Pluijm 1995, de Bresser 1989, Dietrich & Song 1984, Erskine et al. 1993, Heitzmann 1987, Schmid 1981, Van der Pluijm 1991). All studies show consistent microstructural and textural variations, however, the absence of passive strain markers makes their investigation as a function of strain impossible.

Experimental studies on calcite marbles in the dislocation creep field and computer simulations show orthorhombic textures with a c-axis point maximum normal to the flattening plane for pure shear and a single c-axis point maximum oblique with respect to the shear plane rotated towards the maximum principal stress direction (monoclinic symmetry with respect to the shear plane) for simple shear deformation (Wenk et al. 1987, Wenk et al. 1986). The consequent application of these simulations to natural rocks has led several authors to infer partitioning of large components of pure shear deformation into calcite rocks (de Bresser 1989, Erskine et al. 1993, Ratschbacher et al. 1991) because a c-axis maximum normal to the mylonitic foliation is frequently observed. However, such an interpretation is often in contrast to macroscopically determined shear sense and other structural criteria, and the distinction of pure and simple shear deformation on the basis of c-axis distributions alone seems to be impossible (Bestmann et al. 2000, Lafrance et al. 1994).

Dynamic recrystallization is a key factor for the development of a texture and is not satisfactorily incorporated into texture simulations. Furthermore, twinning, pressure solution, and grain boundary sliding may also contribute to the deformation of calcite mylonites (Burkhard 1990, Busch & Van der Pluijm 1995, Kennedy & White 2001, Schmid 1975) to an extent that is difficult to quantify. Thus, given the partially controversial observations and models, there is need for a better data basis to compare textures of natural calcite deformation with experimental and model textures. Shear zones displaying clear and easy to interpret strain gradients may provide cases of progressive deformation. In order to use such data, information is required on the deformation temperature, strain type (pure or simple shear dominated deformation), strain and strain rate. Carrara marble is an excellent example for such studies because of the following reasons:

Carrara marble has been regarded as a completely annealed, relatively fine grained (in comparison to Yule marble), randomly textured, pure calcite marble which is why it has been used for many experimental studies of calcite deformation. However, over the past years, regional structural studies in the Alpi Apuane have shown that there is substantial deformation that postdates the annealing phase so that numerous shear zones and folds can be found, which display dynamic microstructures (Molli et al. 2000, Molli & Heilbronner 1999). Such post-annealing structures are well suited examples to study calcite deformation, because they either overprint earlier deformation and/or annealed microstructures. We have studied a small shear zone of the later stage deformation completely embedded in a matrix

of earlier deformation fabrics. The shear zone displays a clearly visible strain gradient. The curved shape of the pre-existing foliation (S1) allows the microstructural (grain size, PAROR, SURFOR and Paris factor) and texture (CPO) analysis of samples deformed to different finite shear strains.

2. Geological setting

Carrara marble is part of the lower to middle Liassic carbonate platform sequence of the former Italo-Adriatic continental margin, which was deformed and metamorphosed under greenschist facies conditions during the Apennine orogeny. The metamorphic rocks are exposed in the Alpi Apuane tectonic window in northern Tuscany, Italy.

Two deformation events can be distinguished (Carmignani et al. 1994, Carmignani & Giglia 1979, Carmignani & Kligfield 1990, Molli et al. 2000). The main deformation (D1) started in Late Oligocene times (25-27 my) in a compressional regime and a second deformation event (D2) started in the Early Miocene (12-14 my) and was the result of crustal extension (Kligfield et al. 1986).

During the first part of D1, regional scale isoclinal folds were generated with inclined axial planes dipping to the SW (Fig. 1). Folding was terminated by a thermal event, during which annealing obliterated all dynamic microstructures. During the second part of the D1-history, the deformation was localized in discrete shear zones, which overprinted the annealed microstructures. The nappe stacking at the end of the first deformation event produced an antiformal stack geometry.

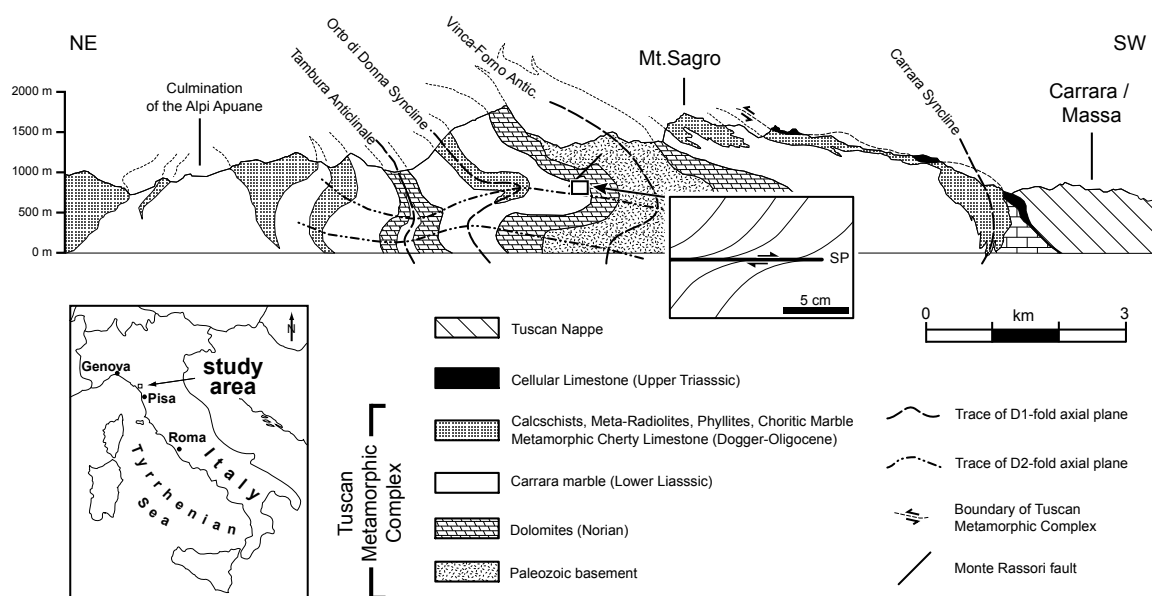


Fig. 1: Schematic geological cross section and stratigraphic section of the Alpi Apuane tectonic window (modified after Carmignani & Giglia, 1979). The sample location is marked by the rectangular box. The details in the box show the orientation of the shear plane (SP) and the S1 layering. Note that the section is oriented with NE at the left.

The nappe stack was extended during D2 and open folds with sub-horizontal axial planes and micro-scale shear zones developed (Fig. 1). Folding is restricted to heterogeneous sequences such as the middle to upper Liassic cherty limestone, which is composed of alternating layers of quartzite and impure limestone. Micro-scale shear zones occur mainly in the pure and homogeneous calcite marble (Carrara marble). Vergence of minor folds as well as the sense of shear are directed to the SW on the SW-side of the culmination of the Alpi Apuane and to the NE on the NE-side of the culmination. A detailed description of the macro- and mesoscopic deformation structures and related microstructures can be found in (Coli 1989, Molli et al. 2000, Molli & Heilbronner 1999).

3. Sample description

The shear zone analyzed in this paper formed during the D2 deformation. Samples were collected in the upper part of the Frigido valley in the central Alpi Apuane (N: 44° 40'15"; W: 2° 15'45"; Italian coordinate system) (Fig. 1). This region is characterized by a large scale D2-fold structure, which refolds the regional scale D1-Vinca-Forno anticline (Boccaletti et al. 1982, Carmignani 1985). During the initial stage of the D2-folding the overturned limb of the D1-fold, which generally dips to the SW, is overprinted by a reactivated pre-existing fault (Monte Rassori fault, indicated in Fig. 1) to such an extent that, locally, the tight S1 foliation and layering are re-oriented causing them to dip to the NE in the vicinity of the analyzed sample.

The sampled shear zone is located in the Liassic marble (Carrara marble) and its shear plane (SP) is parallel to the sub-horizontal axial plane of the large scale D2-fold structure. A top-to-the-SW sense of shear is indicated by the re-orientation of the pre-existing calcite and dolomite layers in the vicinity of the shear zone, which are otherwise parallel to the isoclinal S1 axial planes. Since no stretching lineation can be observed, the sample was cut perpendicularly to the maximum curvature of the deformed S1 foliation and perpendicularly to SP. The layering (Fig. 2a) is easily visible in hand specimen by the color contrast of creamy yellow dolomite and white translucent calcite. The shear zone length is less than 10 cm long when measured along SP, and significant shear strain is confined to the central 5 mm (Fig. 2a). Laterally the shear zone grades into a discontinuity, where the offset of S1 remains constant, but bending of S1 is absent.

The shear zone is symmetric about the central plane displaying the geometry of a ductile shear zone (Ramsay & Graham 1970) displaying heterogeneous shear with the highest shear strain values in the center. At any given distance from the central plane the shear strain is calculated using the equation (Ramsay 1967):

$$\gamma = \cot \alpha - \cot \alpha' \quad (1)$$

where γ is the shear strain at the position of interest, α is the angle between shear plane (SP) and the undeformed markers (in this case S1 foliation) and α' is the angle between SP and the deformed markers at the position of interest (Fig. 2b).

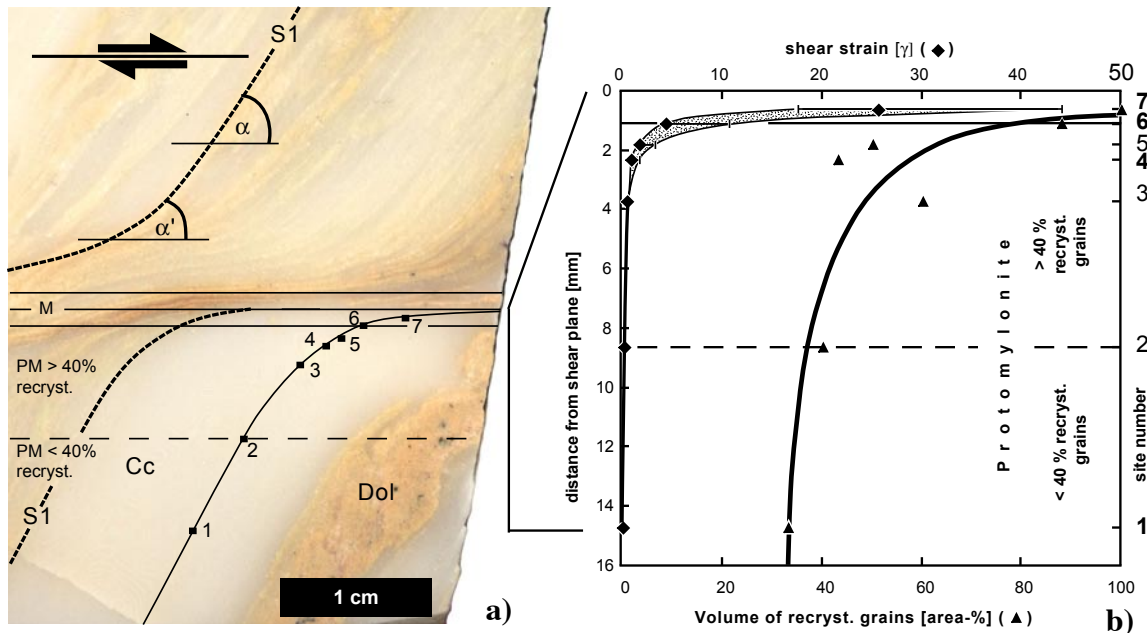


Fig. 2a: Polished hand specimen of the analyzed shear zone. The section is normal to the shear plane (SP) and parallel to the shear direction. White areas are calcite (Cc); yellowish areas dominantly dolomite (Dol). The compositional layering is parallel to the pre-existing main foliation (S1), (short dashed line). α and α' are angles between S1 layering and SP. The solid line separates mylonite (M) from protomylonite (PM), the long dashed line in protomylonite marks the limit between < 40 % recrystallization outside and > 40 % inside. The mylonite is more than 90 % recrystallized. **b)** Calculated shear strain (diamonds) and percentages of recrystallized grains (triangles) across the shear zone. Stippled area corresponds to the range of calculated shear strain values for a measuring error of $\pm 1^\circ$ in α' . The dashed and solid lines are the same as in Fig.2a. Bold numbers highlight sites discussed in the text.

There is a continuous increase of recrystallized material from the marble outside the shear zone (protolith) with an estimated 20-40 vol. % recrystallized grains to the mylonite with more than 90 vol. % recrystallized grains (Fig. 3). Microstructures with more than 90% recrystallized grains are called mylonite (they could be called ultramylonite following Heitzmann (1987) or Sibson (1977)). The present study focusses on the central part which consists of protomylonites and mylonites (with > 40 vol. % recrystallized). In the protomylonite distinct core-mantle microstructures are pre-dominant, i.e., porphyroclasts and recrystallized grains co-exist. Porphyroclasts are surrounded by recrystallized grains, they have lobate grain boundaries, and subgrains of the same size as the recrystallized grains. Twins with migrated boundaries are frequent. The recrystallized grains are isometric and internally strain free, i.e. they display neither undulatory extinction, twins nor subgrains. The mylonite is usually completely recrystallized and only few relicts of twinned porphyroclasts can be observed.

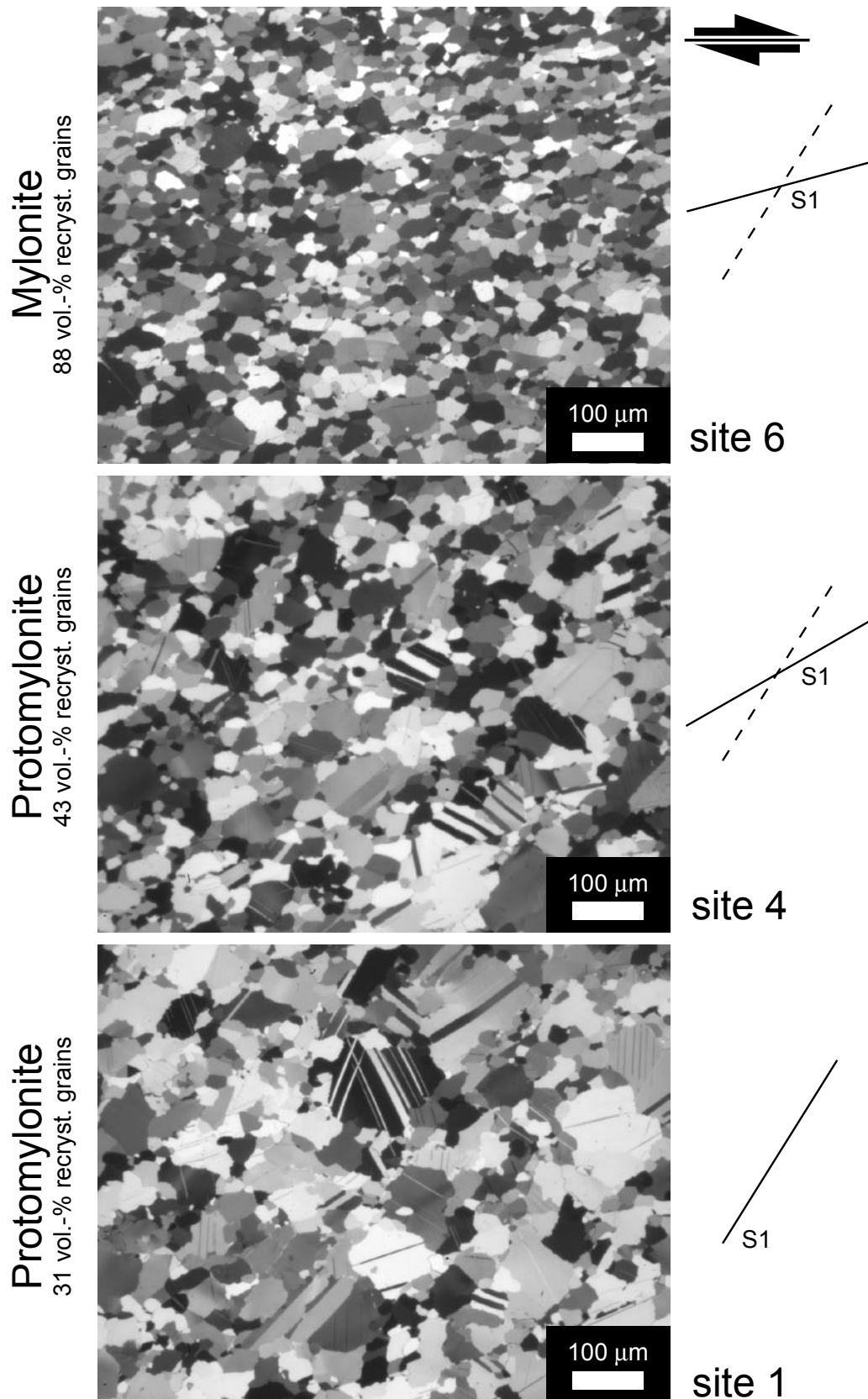


Fig. 3: Characteristic microstructures of protomylonite with $< 40\%$ recrystallized grains (site 1), protomylonite with $> 40\%$ recrystallized grains (site 4) and mylonite (site 6). The D2 shear plane (SP) is horizontal, the sense of shear is dextral. The orientation of the S1 layering at each site (solid line) and its initial orientation (dashed line) is indicated.

4 Method of analysis

4.1 Temperature determination

The deformation temperature of the analyzed shear zone was determined using calcite-dolomite thermometry. Outside the temperature range of 500° - 800° C the position of the calcite-dolomite solvus is uncertain due to sluggish ionic exchange, so that substantial errors in temperature determination may arise (Anovitz & Essene 1987). However, (Matthews et al. 1999) pointed out that, if recrystallization takes place, cation equilibration is possible at temperatures below the diffusional closure of the calcite-dolomite system. In the case of the analyzed shear zone evidence of ubiquitous dynamic recrystallization is visible. Consequently, cation equilibration is very likely, and the application of calcite-dolomite thermometry appears appropriate. Since the equilibration is assumed to occur during dynamic recrystallization, the obtained temperatures represent deformation temperatures.

We measured the Mg- and Fe-content in calcite and dolomite pairs which are located in a calcite-dolomite layer adjacent to the analyzed calcite layer from outside the shear zone into the shear zone and parallel to the central shear plane (SP, Fig. 4). Rims of dolomite grains and their immediately adjacent calcite matrix were analyzed. We used a JEOL 8600 microprobe at an acceleration voltage of 12 kV and a beam current of 7 nA. Natural standards, counting times of 10 - 20 s and a ZAF correction were used.

The temperatures were calculated after (Anovitz & Essene 1987). The approach of Anovitz & Essene uses the Mg- and Fe-content in calcite according to a ternary solution model for the determination of the deformation temperature. (Powell et al. 1984) introduced a correction for Fe-content in calcite and dolomite. Because of the low Fe-content measured in calcite and dolomite ($X_{Fe} Cc < 0.006$; $X_{Fe} Dol < 0.02$) in the analyzed sample we have used the thermometer of (Anovitz & Essene 1987) without any Fe-correction. The measurements are listed in Table I; error bars are the standard deviation of the respective measurements.

4.2 Microstructural analysis

4.2.1 Pre-processing of microstructural data

Digital micrographs and c-axis orientation images calculated by the CIP method [1] were used as a basis for image analysis. The grain outlines were traced manually directly on the digital images. With the help of NIH-Image, a public domain software [2], and the “Lazy Grain Boundary”- macro (Heilbronner 2000), the images were converted to binary grain boundary maps. The same magnification, i.e., a constant resolution of 1 pixel = 0.35 μm was used for all images. The sectional areas were measured and the size distributions, $h(de)$, of the diameters of the equivalent circles (de) were calculated.

4.2.2 Vectorizing the grain boundaries and separating grain size classes

For the determination of shape factors, the outlines of the grain boundary maps were vectorized. We used the program Ime d'Ouline [3], which is a variant of NIH-Image. A minimal distance of 10 pixel was selected in order to adequately resolve the shape details of the grain boundaries. After vectorization the grain outlines were separated into two sets on the basis of the size of the sectional areas. Set 1 consists of outlines of grains with $de < 40 \mu\text{m}$, representing predominantly recrystallized grains. Set 2 consists of outlines of grains with $de > 40 \mu\text{m}$, corresponding to the size range of porphyroclasts. The coordinate-files were analyzed separately.

Separating the outlines on the basis of sectional size implies a certain error in so far as large grains also generate small sections, and thus contribute outlines to set 1. However, the recrystallized grains cannot have $de > 40 \mu\text{m}$, so that at least set 2 cannot contain outlines of that belong to the recrystallized grains. In other words, set 2 is a “pure” set containing only sections that originate from porphyroclasts while set 1 is “contaminated” including sections of recrystallized grains and a few porphyroclasts. However, the number of porphyroclasts is small compared to that of the recrystallized grains and thus the “contamination” can safely be considered negligible.

4.2.3 Grain size analysis

From the numerical densities of equivalent diameters, $h(de)$, of sections the volumetric densities of the diameters of equivalent diameters of spheres, $V(D)$, were calculated (Fig. 5), where D is the diameter of a volume-equivalent sphere and V is the volume percentage of a given size class. For the conversion from 2-D to 3-D we used the program StripStar [4] which is based on the Schwartz-Saltykov approach (Underwood 1970). In this calculation it is assumed that grains are spherical and widely dispersed in space, no corrections for potential influences of grain shape or packing are applied. Details on the application of the program can be found in Heilbronner & Bruhn (1998) and on the web [4].

4.2.4 Determination of volume percentage of recrystallized grains

There are two ways of estimating the volume percentage of recrystallized grains. One is to estimate it via the area percentage: the ratio of the area covered by sections with $de < 40 \mu\text{m}$ divided by the area of the total image. The second way is to estimate it from the 3-D grain size distribution by integrating the densities from 0 to $40 \mu\text{m}$. The estimate from the area percentage involves the error discussed in section 4.2.2; the estimate from the histogram depends on the number of grains used for the 2-D to 3-D conversion. Because of the relatively low number of measurements we used the area estimates for the volume fractions indicated in Figs. 2b and 3 and Table II).

4.2.5 Analysis of preferred orientation of grain long axes and grain boundaries

The particle and surface fabrics were measured using the PAROR and SURFOR method (Panozzo 1983, Panozzo 1984); the corresponding programs are part of the program package FABRIC 2.0 [5]. The results are shown in Figs. 5, 6 and 7. The long and short axes of individual grains were derived and rose diagrams representing the orientation distribution functions (ODFs) of particle long axes and grain boundary segments were plotted (Fig. 5). From the projection curves $B(\alpha)$ of particles (Fig. 6), the bulk fabric anisotropy in the form of an axial ratio (b/a), and the preferred orientation of the fabric (α_p) was determined. For comparison with the CPO (see later) the rose diagram of grain long axes of porphyroclasts and recrystallized grains were calculated separately (Fig. 7).

4.2.6 Analysis of grain shape

The lobateness (convexity/concavity) of grain boundaries was quantified using the PARIS factor (percentage of the average relative indented surface fraction) as described by Panozzo & Hürlimann (1983). A PARIS factor of 0% signifies a strictly convex shape, increasing values signify increasing lobateness; there is no upper limit to the values of the PARIS factor. Separate PARIS factors for the recrystallized grains and for the porphyroclasts are shown in Fig. 8.

4.3 Analysis of crystallographic preferred orientation

The c-axes distribution was determined using the CIP method (CIP = Computer-Integrated Polarization Microscopy, Panozzo Heilbronner & Pauli, 1993) and the complete crystallographic orientation (CPO) was determined using EBSD (Electron Back Scattered Diffraction). The results are shown in Fig. 9. Due to the high birefringence of calcite ($\Delta n = 0.172$) it was necessary to prepare ultra-thin sections of less than 4 μm thickness in order to obtain first order grey as required for CIP. In each case the cut-off part of the specimen chip was used for EBSD measurements. Thus, a closest possible coincidence of the sampling sites of CIP and EBSD measurements was realized.

EBSD spot set size was 5 μm . Measuring points on grain boundaries yielded low confidence index ($CI < 0.2$) and were excluded. For the calculation of the pole figures, more than 15000 measurements were used.

The CIP method calculates area-weighted (i.e., volume-weighted) c-axis pole figures. Masking the appropriate part of the image, partial pole figures for recrystallized grains and porphyroclasts were calculated separately (Fig.10). For the same reason as given earlier, it is possible that the c-axes pole figures of the recrystallized grains include contributions from the porphyroclasts, and only the pole figures of the larger grains are truly the CPO

of porphyroclasts. CIP and EBSD pole figures are characterized by strong c-axes maxima, which are due to the relatively small number of grains per measured area.

In Figs. 9 and 10, the maxima of the pole figures are not indicated. The reason being that the evaluated area is too small for a statistically meaningful evaluation. Even though the number of evaluated pixels is large, the number of grains per analyzed section, i.e., the number of independent measurements is small. As a consequence the resulting pole figures display so-called single crystal orientations with highly exaggerated maxima. However, for the purpose of this study these artefacts present no problem since the main interest here is the symmetry – not the intensity - of the pole figures.

5 Results

5.1 Shear strain

On a traverse from the less deformed parts of the shear zone to the center (Figs. 2a and 3) one finds a complete transition from protomylonite to mylonite. Since the shear strain goes asymptotically to zero with distance from the center, the shear zone boundary is difficult to define. A major part of the shear zone discussed here is composed of the so-called protomylonite, i.e. of material which is dynamically recrystallized (up to 90 vol%) but with shear strains below $\gamma = 2$.

Shear strain values of $\gamma > 2$ are found only in the mylonite, i.e., only within the central 2 mm of the shear zone. The closer to the central plane the more difficult it is to determine the shear strain. The stippled area in Fig. 2b shows the range of calculated shear strain values if a measuring error of $\pm 1^\circ$ for α' is assumed. Note that the error of the derived shear strain values is not symmetrically disposed about the estimated value.

5.2 Deformation temperature

The dolomite grains which were used for temperature determinations, are preferentially arranged along S1 layers. The deformation temperatures, measured by applying the thermometer of Anovitz & Essene (1987), show no systematic trend from the median shear plane (SP) to the wallrock rock (Table I). The average temperature is $324 \pm 30^\circ$ C standard deviation; the total range of temperatures is 115° C. No obvious temperature trend (Fig. 4) is discernible, neither parallel to SP nor along S1. The range of temperatures determined in the center of the shear zone is 56° (Table I, Site I-L) reflecting a relatively large measuring error. Using an F-test, it can be demonstrated that the slope of the linear fit to the temperature measurements (Fig. 4) proves to be statistically insignificant. We therefore cannot confirm – on a statistically found basis - that the variations of temperature reflect increasing temperature in the course of localization.

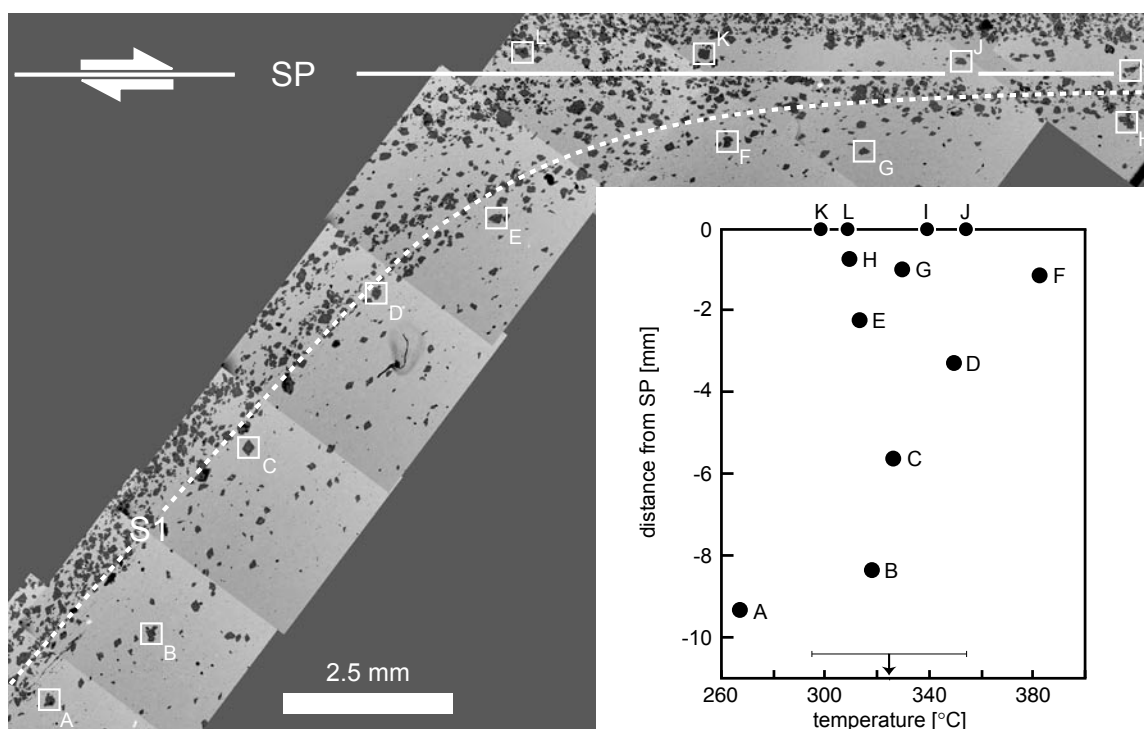


Fig. 4: Mosaic of back scattered electron images of the analyzed shear zone. Dolomite grains appear black. White boxes mark sites analyzed by the microprobe. The solid line is the shear plane (SP), the dotted line is the trace of the S1 layering. The inset shows the calculated temperatures (Anovitz & Essene, 1987) for the analyzed sites, the average temperature and standard deviation is indicated as arrow and error bar.

Table I: Calcite-dolomite temperatures of the analyzed sites and their distances to SP. Mean temperature and standard deviation is indicated.

Table I Temperature determination of the method of Anovitz & Essene (1987)

| Site ¹⁾ | Distance from SP [mm] | Temperature |
|-----------------------|-----------------------|-------------|
| L | 0.00 | 298 |
| K | 0.00 | 354 |
| J | 0.00 | 307 |
| I | 0.00 | 338 |
| H | 0.07 | 308 |
| G | 0.11 | 381 |
| F | 0.97 | 329 |
| E | 2.20 | 312 |
| D | 3.25 | 348 |
| C | 5.61 | 326 |
| B | 8.33 | 317 |
| A | 9.30 | 266 |
| Mean | | 324 |
| Std. Deviation | | 30 |

1) Location of measuring sites is shown in Fig. 4.

5.3 Grain size distribution

The protomylonite (site 1, Fig. 5) shows a broad grain size distribution ranging from a grain size of 10 to 150 μm . There is one maximum at 30-40 μm corresponding to the recrystallized grains, and a second one at 120-130 μm corresponds to the porphyroclasts. Close to the shear zone center (site 4), the porphyroclasts are consumed by recrystallization, accordingly, the porphyroclast peak is decreased and shifted towards smaller size classes while the peak of the recrystallized grains is increased. Finally, in the mylonite (site 6 and 7; close to 100% recrystallization), the distribution is unimodal, and nearly all grains are within a range of 0-40 μm . From the border of the shearzone to the center, the peak of the recrystallized grain size shifts from \sim 30-40 μm in the protomylonite to 20-30 μm in the mylonite.

5.4 Dynamic recrystallization and volume percentage of recrystallized grains

The core mantle microstructures are a clear indication that progressive subgrain rotation is the dominant process of dynamic recrystallization in the shear zone. Most grain- and some twin boundaries are slightly lobate and indicate that some grain and twin boundary migration has accompanied the rotation mechanism during recrystallization (Fig. 3). However, the migrating boundaries do not sweep whole grains and thus, boundary migration does not dominate the microstructure evolution. It does not constitute grain boundary migration recrystallization as defined by (Guillope & Poirier 1979).

Using the area percentage of small grains ($d_e < 40 \mu\text{m}$) the volume percentage of recrystallization is estimated. According to this estimate, the protomylonite contains \sim 35 vol% of recrystallized grains (site 1, Fig. 2b), a value which can also be found in the protolith at sampling sites several meters away from the shear zone. The increase of recrystallized volume from \sim 50% to 100% in the shear zone center occurs within the central 1 to 2 mm.

We estimate that approximately at a shear strain of $\gamma \approx 10$ (between site 6 and 7), the mylonite is 100 % recrystallized. With further increase of the shear strain ($\gamma > 10$), the microstructure and the grain size distribution remain constant even for increasing shear strain values (site 7, Fig. 2b) – indicating a steady-state microstructure. Below $\gamma \approx 5$, in the protomylonite, a weak correlation between shear strain and the amount of recrystallization may be inferred.

5.5 Preferred orientation of grain long axes and grain boundaries

The preferred orientation of particle long axes and grain boundary segments is represented as rose diagrams (Fig. 5). The S1 layering rotates steadily in a clockwise sense from \sim 60° with respect to SP in the protomylonite at site 1 to approximately 0° at the shear zone center (site 7).

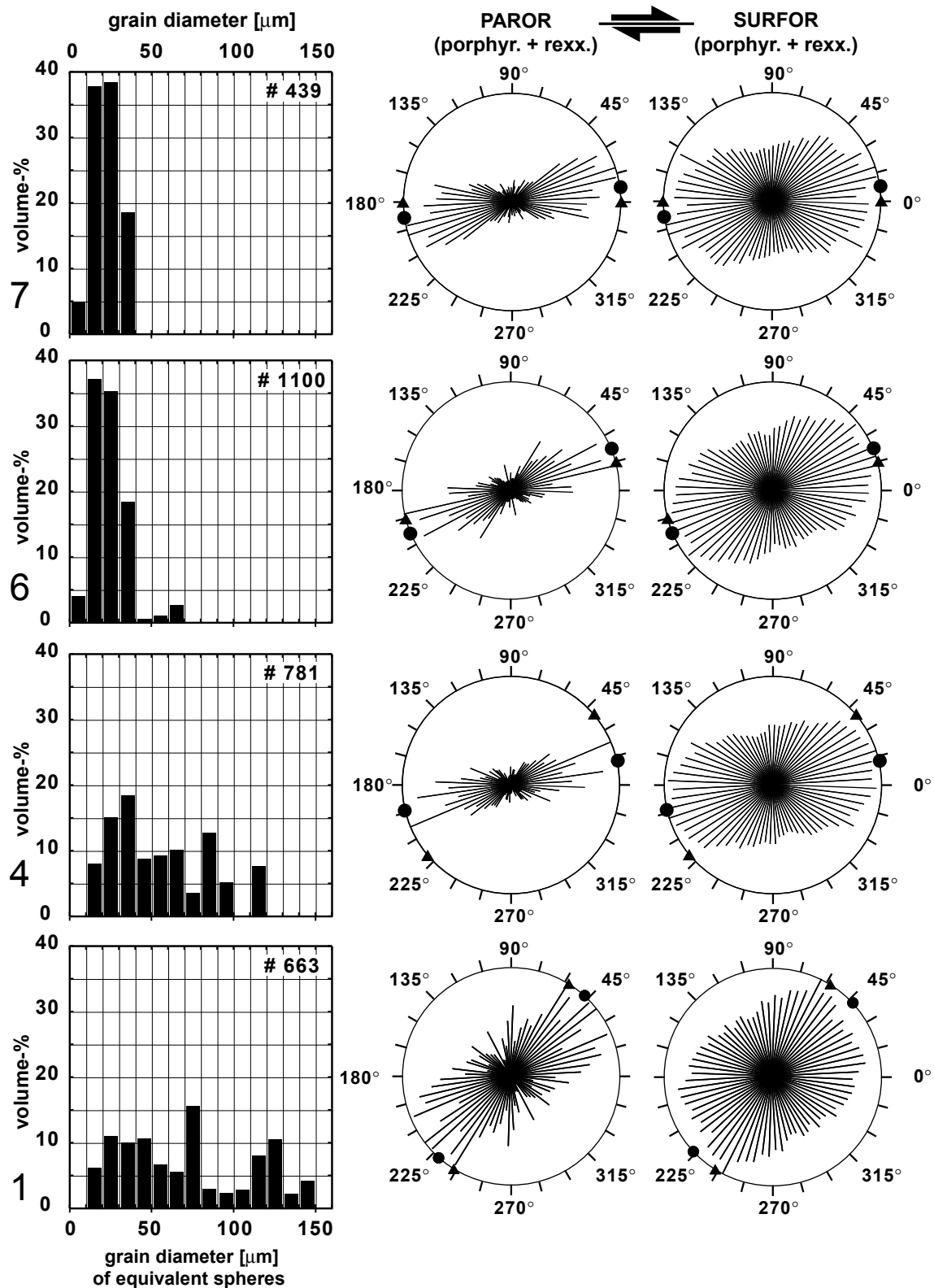


Fig. 5: Histograms of volume weighted grain size distributions and rose diagrams of grain long axes (PAROR) and grain boundaries (SURFOR) of the protomylonite (site 1+ 4), and the mylonite (site 6 + 7). In the rose diagrams, the trace of the SP is horizontal. The orientation of S1 (triangles) and of the preferred orientations of the surface and particle fabrics (circles) are indicated.

Table II: Microstructural data.

| Site | Distance to SP [mm] | Orientation of S1 | Shear strain (γ) | Area-% Recryst. | Mean-2D-grain size Porphy. | Mean-2D-grain size Recryst. | No. of Measure. |
|------|---|-------------------|--|-----------------|--|-----------------------------|-----------------|
| 7 | 0.6 | 0 | >20 | 100 | – | 13.94 | 466 |
| 6 | 1.1 | 15 | 4.7 | 88 | 47.4 | 15.78 | 645 |
| 5 | 1.8 | | 1.6 | 50 | 56.84 | 16.42 | 768 |
| 4 | 2.3 | 40 | 0.8 | 43 | 58.76 | 20.86 | 840 |
| 3 | 3.7 | | 0.4 | 60 | 56.12 | 17.26 | 819 |
| 2 | 8.6 | | 0.1 | 40 | 60.34 | 17.78 | 1003 |
| 1 | 14.7 | 58 | 0 | 31 | 61.2 | 15.12 | 707 |
| Site | SURFOR (Fig.5) A(α min) α_p | | PAROR (Fig. 5, 6) B(α min) α_p | | PARIS (%) (Fig.7) Porphy. Recryst. | | |
| 7 | 0.81 | 8 | 0.77 | 8 | – | 1.68 | |
| 6 | 0.81 | 23 | 0.80 | 23 | 12.8 | 1.74 | |
| 5 | 0.81 | 18 | 0.79 | 18 | 15.7 | 1.36 | |
| 4 | 0.80 | 13 | 0.78 | 13 | 16.4 | 1.8 | |
| 3 | 0.81 | 13 | 0.80 | 13 | 12.7 | 1.64 | |
| 2 | 0.85 | 8 | 0.84 | 13 | 15.6 | 1.72 | |
| 1 | 0.89 | 43 | 0.87 | 48 | 23.7 | 2.73 | |

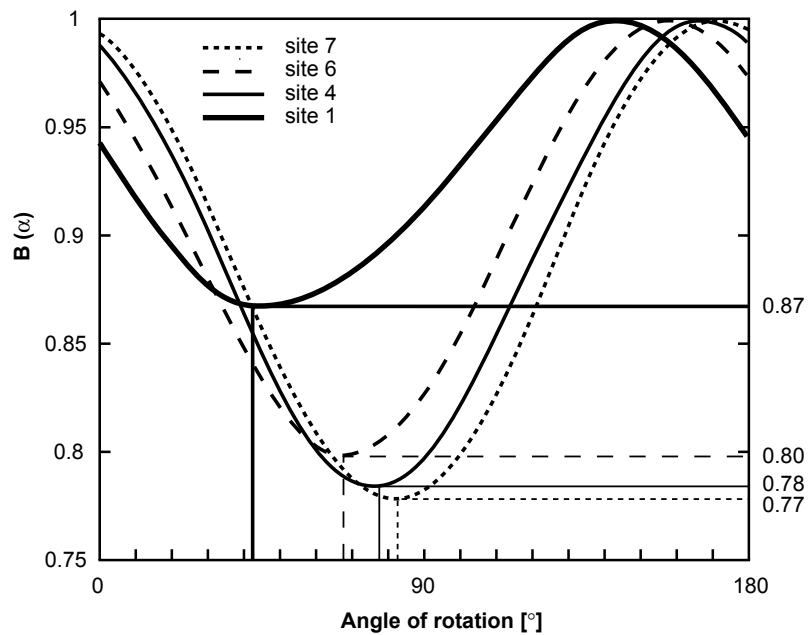
Solid line separates protomylonite from mylonite; Dashed line marks the shear zone boundary

The preferred orientation of the fabric (α_p , filled circles, Fig. 5) determined from the projection curves B(α) and A(α), do not follow this trend exactly. From site 1 to site 4, α_p rotates clockwise from 48° to 13°, from site 4 to 6, anticlockwise to 23°, and from site 6 to 7 clockwise again until α_p is at an angle of 8° (at this point S1 is parallel to SP).

The preferred orientation of the surface fabric follows that of the volume fabric very closely (compare values of α_p shown in Table II). The orientation distribution functions of the grain boundary surface (SURFOR rose diagrams on Fig. 5) of the protomylonite (site 1) is asymmetric with one maximum approximately parallel to S1 and a second one parallel to the shear plane SP. At slightly higher shear strain (site 4), the surface ODF develops a single maximum at an angle half way in between S1 and SP. At high strains (site 6), the surface ODF of the mylonite is at 23° with respect to S1. In the center of the shear zone (site 7) the grain boundaries are, similar to the bulk particle preferred orientation, aligned in a small angle (8°) the SP.

The average value of the axial ratios of the individual particles (0.63) remains constant from the protomylonite to the mylonite. This is not in conflict with an increasing fabric intensity, i.e., a decreasing “bulk” axial ratio b/a of the entire fabric from 0.87 in the protomylonite to 0.78 in the mylonite (decrease of B(α)min in Fig.6). Because the axial ratio (anisotropy) of the fabric as a whole depends on the individual axial ratio of the particles and the dispersion of the ODF of the particle long axes. A decreasing width of the ODF can be seen in the PAROR rose diagrams (Fig. 5) from site 1 to 7 indicating that particles with constant aspect ratios becoming more closely aligned as recrystallization progresses.

Fig. 6: Particle projection $B(\alpha)$ for protomylonite (site 1 and 4) and mylonite (site 6 and 7). $B(\alpha)$ is normalized: $B(\alpha)_{\max} = 1.00$. The fabric anisotropy (b/a) is derived from the minimum: $b/a = B(\alpha)_{\min}$. The angle of preferred orientation (α_p) is derived from the phase angle: $\alpha_p = 90^\circ - \alpha_{\min}$ where α_{\min} is the angle of rotation where $B(\alpha) = B(\alpha)_{\min}$.



Separate PAROR and SURFOR analyses of recrystallized grains and porphyroclasts were determined; results for site 1 and 4 are shown in Fig. 7. At site 1, the particle preferred orientation of the recrystallized grains is rotated in a clockwise sense with respect to that of the porphyroclasts, at site 4 they are aligned. The surface fabric of the porphyroclasts is parallel to S1 and to the bulk fabric at site 1 (being dominated by the stronger maximum of the bimodal surface ODF), but rotates in advance of S1 (in a clockwise sense) at site 4.

5.6 Shape factors

The PARIS-factors of recrystallized grains and porphyroclasts were determined separately (Fig. 8). Along a profile towards the center of the shear zone, set 1 (recrystallized grains) shows a constant value for the PARIS-factors (~2 %) indicating that the recrystallized grains are predominantly convex. In contrast, the PARIS-factors of set 2 (porphyroclasts) decrease towards the shear zone center (from 23 to 13 %) indicating that the shape of the porphyroclasts becomes less concave (less lobate) as recrystallization progresses.

5.7 Crystallographic preferred orientation

The c-axis pole figures measured by the CIP method, the EBSD measurements (c-, r- and a-axis pole figures) and c-axes pole figures from experimentally deformed calcite (Schmid et al., 1987) are shown in Fig. 9. For site 4, separate pole figures were calculated for twinned porphyroclasts and recrystallized grains (Fig. 10).

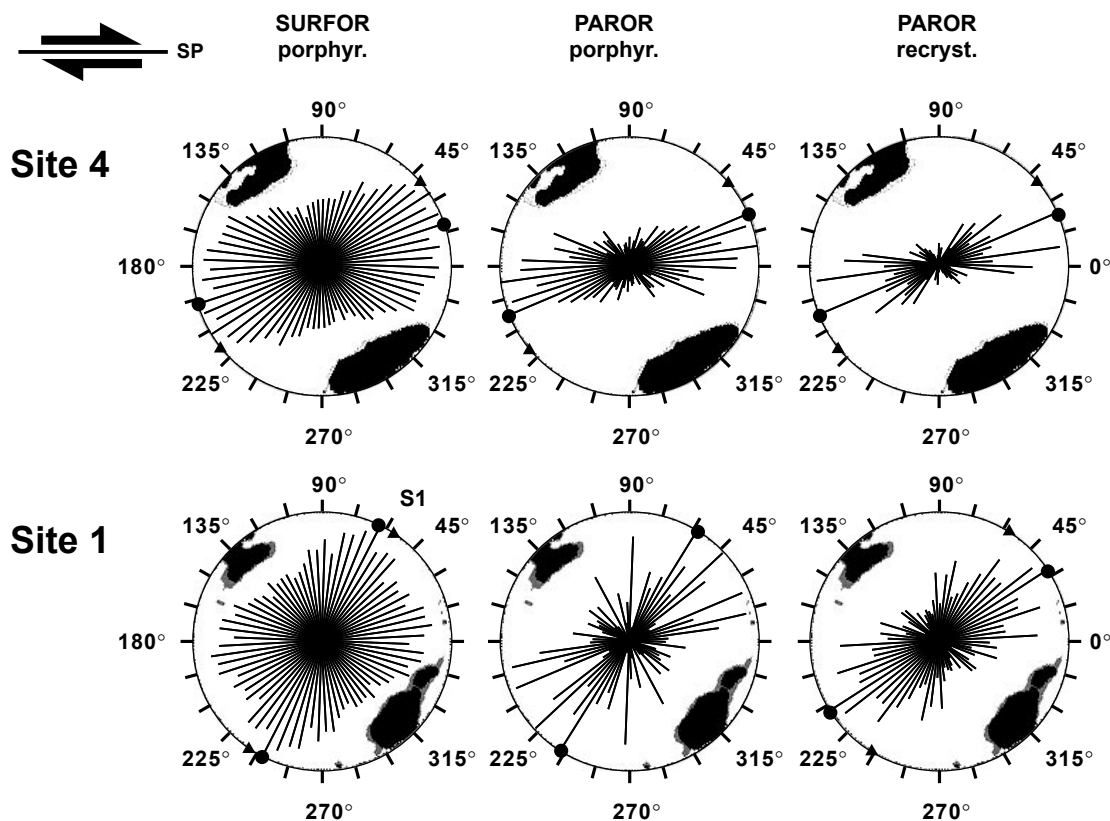


Fig. 7: Separate rose diagrams of grain long axes (PAROR) for porphyroclasts (middle) and recrystallized grains (right) for sites 1 and 4. The rose diagram of grain surfaces (SURFOR) of porphyroclasts is shown on the left side. High density regions (> 4 times uniform) of the bulk c-axis pole figure are superimposed on the rose diagrams.

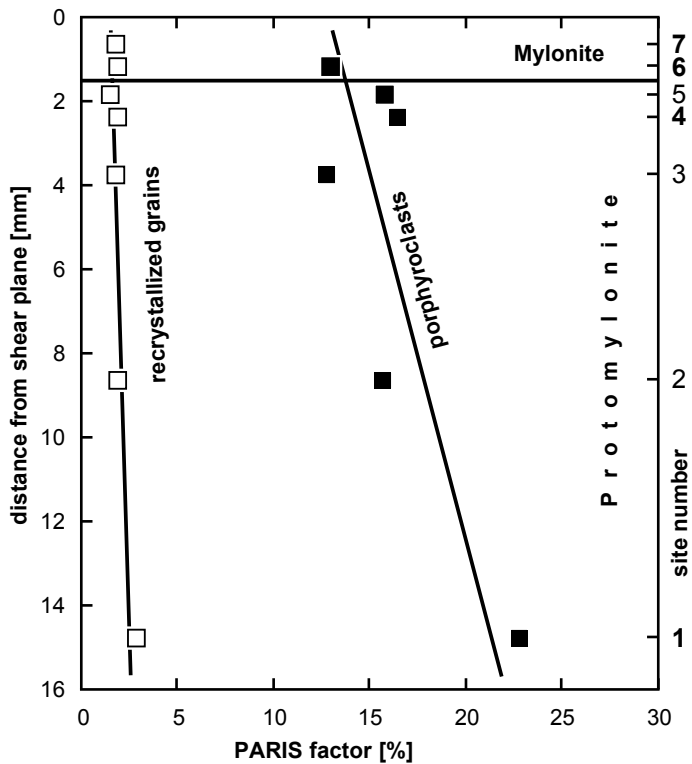


Fig. 8: PARIS factor for recrystallized grains (open squares) and porphyroclasts (filled squares). Bold numbers highlight sites discussed in the text.

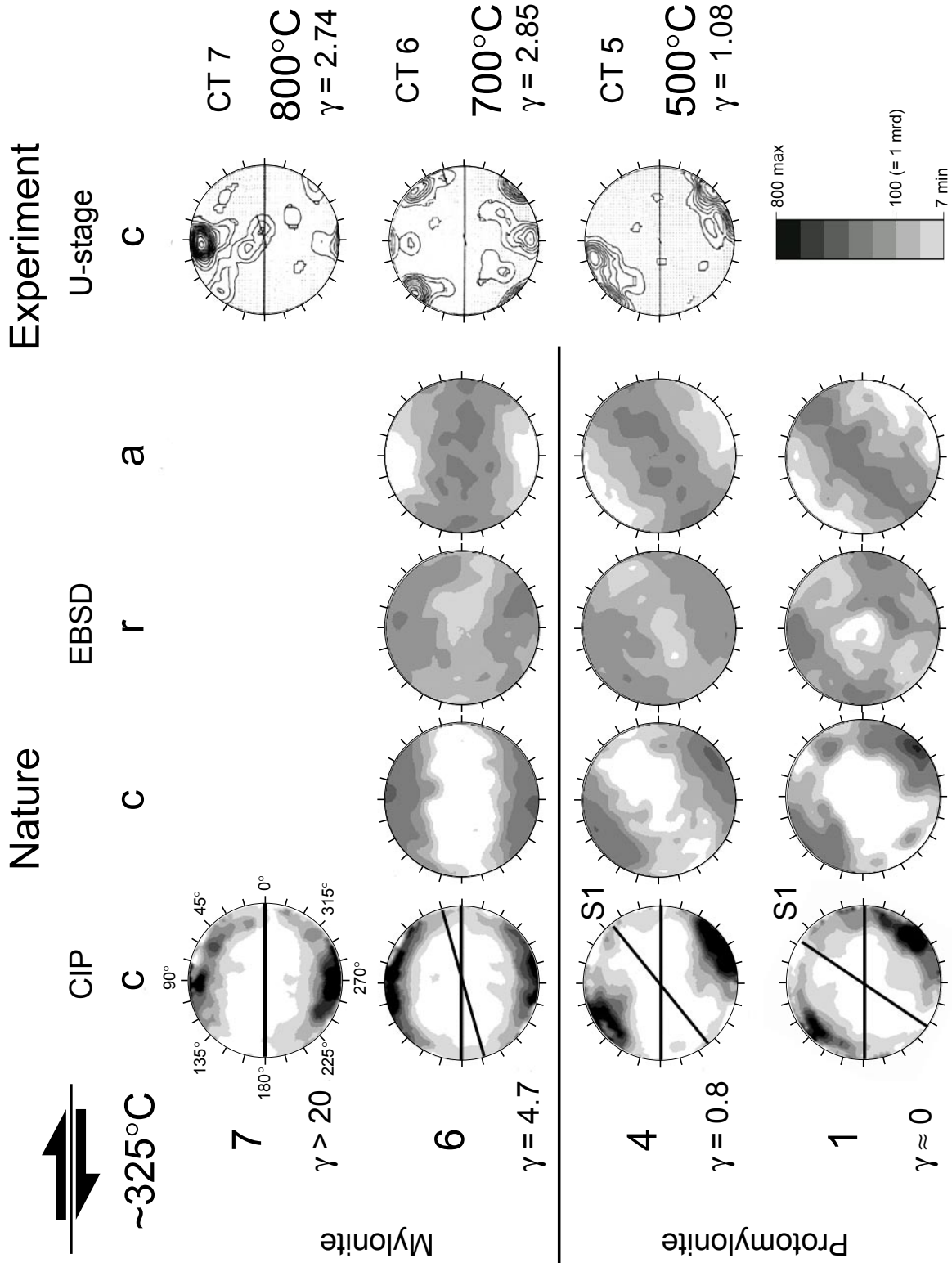


Fig. 9: Crystallographic preferred orientation determined by CIP (left) and EBSD (center), c-axis pole figures (right) of experimentally deformed Carrara marble (Schmid et al., 1987). Dextral sense of shear applies to all pole figures. Inclined lines in CIP pole figures mark the orientation of the progressively rotated S1-foliation. Contours of CIP pole figures are 0.5 times uniform, for contours of EBSD pole figures see logarithmic scale, where 100 = 1 m.r.d.; contours of Carrara marble pole figures are 1.0 times uniform. For pole figure maxima, see text.

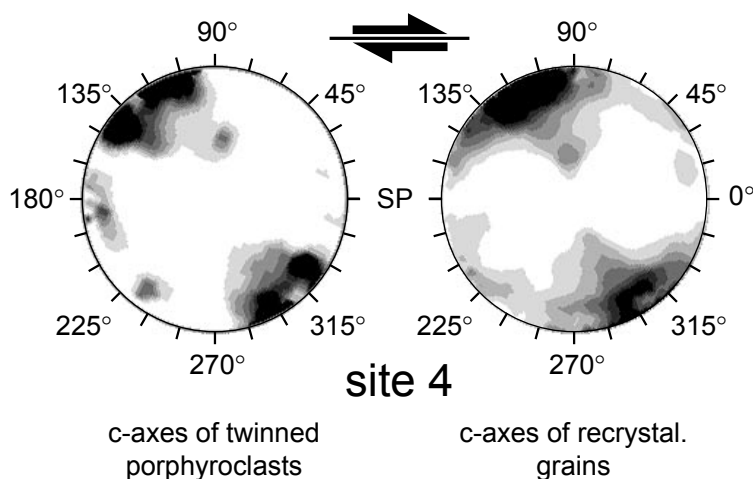


Fig. 10: Separate c-axis pole figures of twinned porphyroclasts (left) and recrystallized grains (right) of site 4 determined by CIP. For pole figure maxima, see text.

The texture of the protomylonite (site 1 and 4) is characterized by an elongated c-axis maximum, which is dispersed along the periphery of the pole figure. The dispersion decreases from site 1 to site 4. The center of the maximum is oriented oblique to SP and approximately normal to S1 with a clockwise component of rotation ($\sim 13^\circ$) corresponding to the dextral shear along SP.

In the mylonite (site 6) the c-axis maximum is normal to the SP. High pole densities lie within a range of 45° along the periphery, symmetrically disposed with respect to the shear zone normal. In the center of the shear zone (site 7) high pole densities are found within a range of 25° along the periphery of the pole figure inclined clockwise with respect to the shear zone normal, i.e. in the same rotation sense as the overall shear sense.

The internal symmetry of the CIP and EBSD pole figures is approximately constant for all microstructural domains: elongated c-axis maxima and weak r-maxima normal to S1 (protomylonite) and to the shear plane (SP) (mylonite). All sites are characterized by a-axes girdles parallel to S1. The a-axes single girdle of the mylonite is oriented parallel to the SP with one high density region close to the shear direction.

6 Discussion

6.1 Shear strain and strain rates

The total displacement across the shear zone is ~ 40 mm; this value is measured from S1-layering-offsets along the shear zone. Thus, averaged over the entire shear zone (total width ~ 10 mm), the bulk shear strain is $\gamma \approx 4$. If only the fully recrystallized mylonite is considered, $\gamma \approx 20$ or more. From the different shear strains calculated for site 3 where $\gamma = 0.4$ to site 7, we can estimate that the ratio of local shear strains from the center to the boundary is at least 50:1.

If during the formation of the shear zone all parts of the shear zone had continued to deform, the ratio between the shear strain rate along the central plane compared to that of the protolith would have exceeded 50:1. In contrast, if the shear strain rate was the same everywhere in the shear zone, the deformation must have concentrated into the central plane and continued at least 50 times as long in the center as it did near the boundaries. Even though we measured a slight grain size decrease, which accounts for a strain rate ratio of 1:4 of the recrystallized grains from the protomylonite to the mylonite (see below) (Fig. 5), we assume that for the major part the shear strain gradient is due to localization (see below).

6.2 Deformation temperature

A deformation temperature of about 325° C agrees well with other D1 and D2 temperature determinations of the region: For D1, a gradual decrease from West to East from 420 to 370° C and for D2, a decrease from East to West from 430 to 295° C is recognized. The shear zone discussed here is located in the central part of the Alpi Apuane; the calculated D2 temperature fits well into the general D2 temperature distribution of the region. The timing of the D1 and D2 deformation is not very well constrained (Kligfield et al. 1986); we assume that D1 started during the Late Oligocene (25-27 my) and had terminated with the beginning of D2 in 12-14 my. D2 stopped at Late Miocene times (8-10 my). This age range yields a gross cooling rate of approximately 70° C over 11-15 my from D1 to D2 and approximately 200° C over ~2-6 my from the ductile D2 to the beginning of shallow level brittle deformation (120°C).

The absence of any significant temperature gradient parallel to S1 (Fig. 4) indicates either that the localization took place under constant temperature conditions (at least that the localization rate was faster than the temperature decay rate) or that the entire shear zone kept deforming, with lower strain rates at the shear zone boundary compared to the center, throughout the entire time of deformation equilibrating to the temperature at all sites equally. Even though this possibility cannot be excluded with absolute certainty, it is very unlikely that a strain rate gradient can be maintained over an extended period of time in a single shear zone, and suggests that here the deformation probably is localized in space and ceased to operate in the low strain parts of the shear zone rather than operating pervasively at different rates.

Spatially localized deformation and constant temperature leads us to believe that the investigated shear zone may have been active only for a relatively short time. From this we develop the idea that deformation may be highly localized both in space and in time – a phenomenon that may be typical for the deformation of the marbles of the Alpi Apuane.

6.3 Grain size distributions

The grain size peak which corresponds to the recrystallized grains decreases from ~35 μm in the protomylonite to ~25 μm in the mylonite. From the arguments presented above this decrease cannot be explained by assuming that pre-existing recrystallized grains (35 μm) are progressively replaced by newly recrystallized grains whose typical grain size is 25 μm . Instead, it can be assumed that the strain rate increased (higher stresses will produce higher strain rates) when the localization into the central 2 mm wide mylonites of the shear zone took place.

Applying the piezometer of Rutter (1995) for rotation recrystallization of calcite (which yields slightly higher stresses as that of Schmid et al. (1980) for rotation recrystallization), flow stresses for 25 μm and 35 μm grain sizes are 48 MPa and 36 MPa, respectively. These estimates represent a minimum value of the stresses because some grain boundary migration is observed in the microstructures and the stress values for migration recrystallization are higher for a given grain size. Using the stresses from piezometry and the calculated deformation temperature (325° C) of the shear zone we can make a few crude strain rate estimates from flow laws by Walker et al. (1990) for dislocation creep (stress exponent $n = 3.3$ and grain size exponent $m = -1.3$). Strain rates as fast as $1.4 \times 10^{-11} \text{ s}^{-1}$ are possible at the center of the shear zone and $3.4 \times 10^{-12} \text{ s}^{-1}$ in the protomylonite. To achieve a total shear strain of $\gamma = 20$ (center of the shear zone), about 45000 years would be required. This period is significantly shorter than the time span available for cooling (2-6 my), and supports our idea of rather constant temperature deformation and temporal localization. The strain rate ratio for protomylonite to mylonite (for 35 μm to 25 μm grain size the strain rate ratio is 1 : 4.1) is smaller than the corresponding 1 : 50 shear strain ratio, suggesting that a pervasive deformation at differing strain rates throughout the entire time of the shear zone deformation cannot have produced the gradient in shear strain. Instead, one rather concludes that, given a fixed strain rate, deformation selects a region where it is localized at a higher shear strain rate (smaller grain size, center of the shear zone) and abandons the rest.

6.4 Volume percentage of recrystallized grains

Since we cannot find any marble with less than 30% recrystallized grains anywhere in the vicinity of the shear zone (outcrop scale is a few meters), we conclude that the D2 deformation associated with the shear zone formation has initially permeated the entire rock volume, probably during the formation of the large scale D2-fold structure (Fig. 1). The abrupt increase of recrystallization within the ~2 mm of the shear zone center is an indication of localization, after which deformation of the bulk rock ceased in favor of localized deformation.

We do not associate the recrystallization with the D1 deformation (e.g. relict recrystallized grains of D1) because the shear zone is a D2 shear zone and the syn-deformational temperatures in the host rock and in the shear zone are the same indicating that the D2 shear zone and the surrounding recrystallization must have occurred during the same event.

6.5 Preferred orientation of grain boundaries and of grain long axes

The surface orientations of the natural shear zone are similar to those of the samples of the experimental study of Schmid et al. (1987). The rose diagram (surface ODF) of site 1 (Fig. 5) shows two maxima and has an internal monoclinic symmetry. Similar bimodal patterns have been found in completely annealed Carrara marble (the undeformed sample of Schmid et al. 1987, their fig. 22) where the pattern reflect the rhombic grain boundary alignment with the strongly developed crystal faces, and at high temperature conditions (samples CT2 and CT7 of Schmid et al. 1987, their fig. 24) where the maxima are more discrete and the stronger maximum is aligned with the shear direction. We could therefore interpret the surface ODF of site 1 either as completely annealed or as the relict of D1 deformation. Because of the conspicuous alignment of the stronger of the peaks with S1 (external monoclinic symmetry with respect to the relevant shear direction) one could associate the rose diagram with the high temperature deformation of D1 (sinistral simple shear parallel to S1). However, as this study shows, bimodal patterns are not very long-lived and it is difficult to reconcile the c-axis pole figure of site 1 which indicates large shear strains parallel to S1 with this pattern. If one assumes that the pattern is due to annealing the internally symmetric annealed surface ODF would be still oblique with respect to S1 and by this external monoclinic symmetry reflect sinistral shear parallel S1.

In clear contrast to this is the orthorhombic symmetry of the surface ODF of the experimentally deformed Solnhofen limestone (ST2, ST5; Schmid et al., 1987, their Fig. 25). These experimental samples can be compared to the protomylonite (site 4) and the mylonite (site 6 and 7) of the naturally deformed sample. It is often argued that complete recrystallization is necessary for steady state deformation. If the rock starts with a small grain size (Solnhofen limestone) it rapidly acquires the final microstructure, whereas if the grain size is too large (Carrara marble), the “inappropriate” grain size is modified, starting with the formation of transient microstructures (CT2, CT7 and protomylonite) until the final state (ST2, ST5, mylonite) is reached by complete recrystallization. Transient microstructures (protomylonite) only survive because they represent sites of aborted deformation.

It has been mentioned that the separate SURFOR analyses for porphyroclasts and recrystallized grains yield the same result - the reason being that, due to the core mantle structure, in both cases the same surface is being analyzed. Separate PAROR analyses, in contrast, reveal distinct rotational behaviour of recrystallized grains and porphyroclast (Fig.

7). From site 1 to site 4 the preferred orientation of recrystallized grains rotates from 33° to 23° in a clockwise sense. The results from site 6 and 7, which are 100% recrystallized, represent a smooth continuation with bulk PAROR preferred orientation of 23° and 8° .

6.6 Shape factors

A major problem in analyzing natural microstructures is the effect of post-deformational annealing on a microstructure. In the case of the studied example, dynamic microstructural features such as undulatory extinction, subgrains and lobate grain boundaries are still ubiquitous. We therefore assume only a minor influence of annealing on microstructure and texture.

In order to analyze the annealing aspect in more detail, we compare the PARIS factors of the protomylonite to those of the naturally deformed Carrara marble studied by Molli & Heilbronner (1999). Bulk PARIS factors of the entire microstructures of Molli & Heilbronner (1999) are 1.8 % and 2.3 % for samples 34 and 39 (“completely recovered white marbles”), and up to 24 % for their dynamically recrystallized ones (sample 45 with an estimated 50 % recrystallization). The PARIS factors of the porphyroclasts of the shear zone in this study are ~20%, a value which coincides well with the dynamically recrystallized case of Molli & Heilbronner (1999). Since these values are much higher than those of the annealed samples 34 and 39, complete annealing of the microstructure (after D2) can be excluded.

Measuring the PARIS factors of the experimentally deformed Carrara marble (Schmid et al. 1987) described above also yields increased PARIS factors: 17 % for the samples deformed at 800°C (CT2 and CT7). The samples only suffered low strains and recrystallized grains are absent which may explain the somewhat lower value.

A separate analysis of the recrystallized grains of sample 45 of the naturally deformed Carrara marble (Molli & Heilbronner 1999) yields a PARIS factor of 5.5%. This value is slightly higher than the typical 2-3 % of recrystallized grains in the shear zone analysed here.

Very low absolute values of the PARIS factor may be an artefact of the relatively low magnification used here. In this situation fine details of grain boundary surface indentations are not resolved and grains appear more convex than they are. In principle, however, the same picture emerges: the protomylonite of the shear zone is characterized by a bimodal microstructure with highly lobate, large porphyroclasts, which are embedded in a matrix of isometric, small recrystallized grains.

The observation that the subgrains in the porphyroclasts are of the same size as the surrounding recrystallized grains indicates that subgrain rotation may be the dominant recrystallization mechanism. The following process is envisaged: Up to ~30 vol% recrystallization, i.e., at low strains, the originally convex porphyroclasts (low PARIS factors) become more lobate as the (convex) recrystallized grains form around them. With

increasing shear strain the highly lobate porphyroclasts (high PARIS factors) continue to recrystallize by subgrain rotation. After passing through a stage of maximum lobateness they become smaller and less lobate, as indicated by a decreasing PARIS factor (Fig. 8). In contrast the recrystallized grains (constant low PARIS factors) maintain their small size and equant shape with increasing strain.

6.7 Textures and dominant slip systems

Textures with a pronounced c-axis maximum normal to the main foliation have been found frequently in natural calcite tectonites (e.g. Turner & Weiss 1963, Lafrance et al. 1994, Bestmann, 2000). It is likely that they have formed by basal $\langle a \rangle$ slip as the dominant slip system and they are typical of D1-structures in the Alpi Apuane (Molli et al. 2000). We interpret the textures of site 1 and 4 of the protomylonite (Fig. 9) to have developed during the first deformation event prior to the formation of the shear zone. In both cases the c-axis maxima are inclined 77° with respect to S1. From site 1 to 4 S1 and the c-axis maxima together rotate through 20° in a clockwise sense. From the regional geological context it is evident that large strains are accumulated in D1 tectonites. The textures acquired may persist - if weakened - even if the annealing of the microstructure is complete (Heilbronner & Tullis 2002). Also, Rutter et al. (1994) argue that pre-existing textures survive dynamic recrystallization and may be very long-lived. Therefore, it may be concluded that the textures of the protomylonite are relict textures of D1. However, it is very conspicuous that the orientation of the D2 shear zone with respect to S1 is such that the texture is ideal for e-twinning and $r\text{-}20\text{-}2\text{-}1\text{-}$ slip. This coincidence is so fortuitous, that it may be possible that the reason for the formation of the shear zone along this particular orientation may in some way be related to the pre-existing texture of D1.

Since e-twinning is pervasive in the host rock, it may be assumed that D2 started with twinning. Twinning only produces small strains and has to be abandoned in favor of more stable dislocation creep. From site 1 to 4, the dispersion of c-axes along the periphery of the pole figure decreases. The decrease may be caused by twinning of those grains which have a c-axis dispersed along the periphery (the c-axis becomes re-oriented towards the σ_1 -direction during twinning, i.e. towards the main c-axis maximum in this case). In this way, the c-axis maximum, which is typical for twinning deformation with respect to the D2 shear plane, may be enhanced.

The c-axis maximum of site 1 is stretched out between $135\text{-}150^\circ$ and the S1 foliation is at 58° . The texture of site 4 is rotated 20° clockwise (in the sense of the dextral shear) with respect to site 1. If the separated pole figures (Fig. 10) are considered it is obvious that the c-axes of the recrystallized grains are rotated in a clockwise sense (which is the sense of D2 shear) with respect to the porphyroclasts. Such a rotation would bring them closer to the ideal orientation for basal $\langle a \rangle$ slip with respect to the SP. This is in agreement with the

clockwise rotation of the recrystallized grains long axis with increasing strain, as discussed previously (Fig. 7).

Thus the slight rotation and amplification of the c-axis maximum of a pre-existing basal $\langle a \rangle$ texture may be caused by the replacement (or gradual superposition) of the S1-originated basal $\langle a \rangle$ texture by, first, a transient D2-related e-twinning texture accompanied by a rotation of the c-axis maximum through dynamic recrystallization. In this shear zone, dynamic recrystallization occurs through subgrain rotation accompanied by some grain boundary migration. For a basal slip plane oriented favorably for slip, tilt walls are expected to produce a dispersion of the c-axis maximum along the periphery of the pole figure. If kinematically favorably oriented grains grow by boundary migration and unfavorably oriented grains are progressively consumed, the effect of the recrystallization will be a rotation of the c-axis maximum in a synthetic sense with respect to the overall shear sense until a c-axis maximum position normal to the shear plane is reached.

In the transient e-twinning texture additional r-slip may occur. The activity of the r-slip system is supported by the r-pole figure, determined by EBSD, which shows a maximum approximately normal to the SP (Fig. 9). Under easy slip conditions the transition from the texture of site 1 to that of site 4 can be explained in terms of a progressive alignment of r-planes parallel to the SP due to twinning, so that twinning rotates the crystals into an orientation, which is favored by r-slip (For a detailed description of r- and r⁺-slip see De Bresser 1991). After a certain amount of strain twinning is not possible any more and r-slip may become dominant. Inspection of separated pole figures (Fig. 10) confirms that the CPO is mainly influenced by porphyroclasts for which e-twinning is effective.

In terms of easy slip conditions, the mylonite texture (site 6 in Fig. 9) can be interpreted as a combination of an orientation favorable for dominant r- and r⁺-slip and basal $\langle a \rangle$ -slip. This interpretation is supported by the pole figures of the r-planes and the a-axis, determined by EBSD: Most of the r-planes are oriented parallel to the SP as indicated by a high density region of r-poles close to the normal of the SP. The a-axis pole figure is characterized by a broad girdle with a high density region parallel to the shear direction, indicating that a large number of grains have their $\langle a \rangle$ -Burgers vector parallel to the shear direction of the shear zone. We interpret this orientation in terms of dominant basal $\langle a \rangle$ -slip and additional r-slip.

In the center of the mylonite (site 7) only one set of r-planes (r⁺-slip) is active in addition to the basal plane which leads to a slightly inclined c-axis maximum in the sense of the overall shear. Barnhoorn (2004) found in high strain torsion experiments similar c-axis pole figures with an inclined maximum.

6.8 Comparison with other natural shear zones and experimental data

Many studies of natural calcite mylonites (Behrmann 1983, Dietrich & Song 1984, de Bresser 1989, Ratschbacher et al. 1991, Lafrance et al. 1994, Bestmann et al. 2000) show

textures, which are characterized by c-axis distributions with a single maximum normal to the shear plane or slightly inclined to its normal. The shear plane corresponds approximately to the mesoscopically visible mylonite foliation.

Such textures are similar to the low temperature texture type (LT) described by Wenk et al. (1987). In simple shear (so-called monoclinic texture symmetry) the direction and angle of the deviation of the c-axes maxima from the normal to the shear plane indicates the sense of shear and the deviation from pure shear, respectively (Wenk et al. 1987). The pure shear textures are orthorhombic; no sense of shear can be inferred.

The analyzed samples of the present study show a transition from monoclinic (with respect to the shear plane) textures in the low strain domain to orthorhombic textures at high strains. However, the curved shape of the passive strain marker (pre-existing foliation) indicates clearly a dominant non-coaxial deformation mode. Therefore the change in texture symmetry cannot be explained by a switch from simple shear to pure shear but has to be the result of a different process. This result is consistent with previous observations by Lafrance et al. (1984) and Bestmann et al. (2000).

As the deformation temperature (325° C) stays constant across the shear zone during the entire deformation history the texture development is only dependent on strain magnitude. This may appear to be in contrast to experimental results of Wenk et al. (1987) and Schmid et al. (1987) who found the texture variations to be temperature dependent. The transition in the texture type in the experiments occurs with increasing deformation temperature but always at approximately the same amount of strain ($\gamma \sim 3$). This strain magnitude is considerably lower than the finite strains in our mylonite samples and might not be sufficient to produce a stable end orientation of crystals. Hence, the influence of strain magnitude on the texture development needs to be considered.

We correlate the textures of our study with those of the experimental study of Schmid et al. (1987) as follows: protomylonite (site 4) - 500° C sample (twinning regime); mylonite (site 6) - 700° C sample (intra-crystalline slip regime); mylonite (site 7) - 800° C sample (grain boundary migration regime). Schmid et al. (1987) explained the texture variations in terms of different temperature regimes, in which different slip systems are dominantly active (twinning regime - e-twinning; intra-crystalline slip regime - r-slip and basal $\langle a \rangle$ -slip; grain boundary migration regime - basal $\langle a \rangle$ -slip). However, the occurrence of e-twinning, combined r- and basal $\langle a \rangle$ -slip textures and basal $\langle a \rangle$ -slip textures at approximately the same strain but different temperatures in the experiments suggest to us that the increased temperature is merely responsible for a faster transition to a stable end-texture (the formation of a basal $\langle a \rangle$ texture). The reason for reaching an end orientation texture at lower finite strains for increased temperature may be the faster kinetics of recrystallization at higher temperature.

For the comparatively low strains of $\gamma = 3$ in the experiments, the higher temperatures during dynamic recrystallization may be a key factor. In the natural shear zone analyzed in

this study deformation temperature was constant during deformation. The different texture types observed at different finite strain magnitude represent successive stages of texture development, because it has been inferred that the high strains in the center of the shear zone have been achieved by a localization of deformation - the margins of the shear zone probably represent earlier stages of deformation. The higher finite strain acquired in the center of the analyzed natural example coincides with complete dynamic recrystallization and probably is responsible for reaching a stable (steady state) texture.

The idea of a faster texture formation with increased temperature is supported by the results of the work of Pieri et al. (2001 a, b), who performed high strain torsion experiments at temperatures of 727° C and 927° C and increasing strain. The results of their study show the same texture development as in the natural sample (this study) and the experiments of Schmid et al. (1987). In the experiments at 927° C the stable end texture (for details see Pieri et al. 2001 a, b) is reached at lower strains compared to the experiments at 727° C.

From the arguments presented above we tend to believe that strain magnitude may be important for the progressive change in texture symmetry. Increased temperature accelerates the formation of a specific texture, i.e. higher temperatures produce the stable end texture faster (at lower amounts of strain).

6.9 Summary of texture development

For the texture development across a natural shear zone we consider a process in successive stages with progressively increasing strain magnitude and recrystallization. First, at low finite strain, twinning rotates some c-axes into parallelism with the compression direction. As a result of the lattice rotation during twinning, more crystals obtain an orientation which is favoured by r^- -slip. The corresponding c-axis orientation is shown by point 1 in Fig. 11. Progressive subgrain rotation and some grain boundary migration rotate the recrystallized grains into an orientation with their basal plans parallel to the SP (Fig. 11; point 2). The new orientation is favorable for basal $\langle a \rangle$ slip. Further subgrain rotation may lead to an orientation of grains favorable for r^+ -slip (Fig. 11; point 3).

The activity of dislocations in the operative slip system in combination with subgrain rotation recrystallization leads to the formation of tilt wall boundaries. The rotation axis of these tilt wall boundaries lies in the slip plane and normal to the slip direction. Under conditions of easy slip progressive subgrain rotation recrystallization may translate a crystal orientation at position 1 into position 2. This mechanism may change a twinning texture into a texture typical of basal $\langle a \rangle$ -slip.

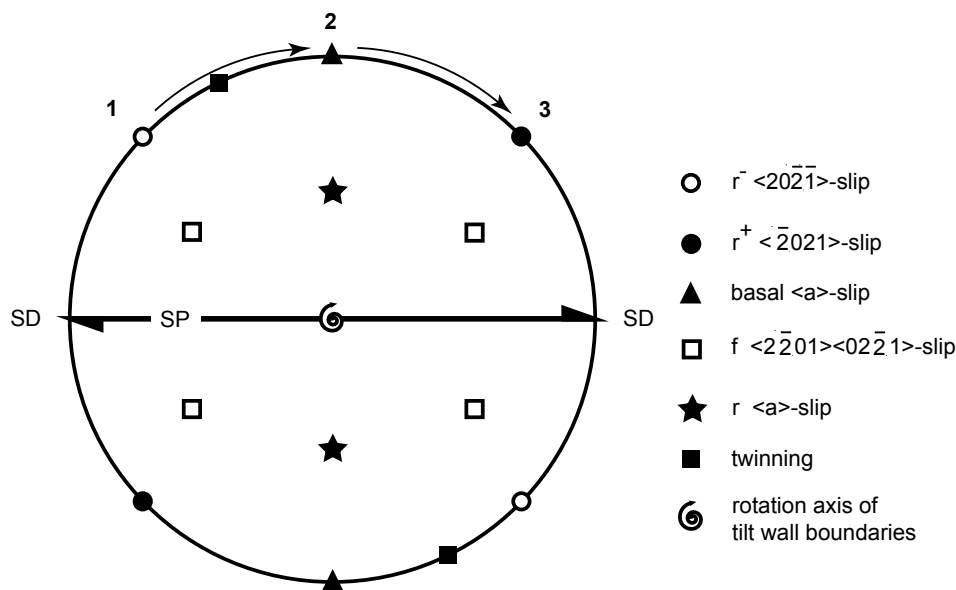


Fig. 11: Schematic presentation of ideal orientations of c-axis for different slip systems in a calcite crystal. The slip plane of the given slip system is oriented parallel to the shear plane (SP) and the slip direction parallel to the shear direction (SD) (easy slip conditions). Arrows from point 1 to 2 to 3 indicate the development of the preferred c-axis orientation with increasing shear strain as discussed in the text.

Conclusions

The microstructure, shape fabric, texture, and chemical analysis of a small shear zone in Carrara marble in the Alpi Apuane tectonic window demonstrates that progressive deformation took place at constant temperature. During the extensional stage of the Apuane deformation, the shear zone formed at a temperature of $324^{\circ}\text{C} \pm 30^{\circ}\text{C}$. The finite strain gradient is caused by a localization of deformation in the central part, so that the outer parts of the shear zone preserve earlier stages of the deformation history. Due to this development of the shear zone, the different pole figures measured across the shear zone represent progressive stages in the evolution of a calcite texture during mylonitization. The textures outside the shear zone resemble an e-twinning type pole figure with respect to the kinematic framework of the shear zone. These pre-deformational textures become strengthened near the margin within the shear zone. With increasing finite shear strain, the texture is overprinted by a single c-axis maximum oriented normal to the shear plane. In the central mylonitic, completely recrystallized parts of the shear zone with the highest finite shear strain, the single c-axis texture is synthetically rotated with respect to the shear plane. The apparent synthetic rotation of the texture is explained by a dispersion of the c-axis maximum along the periphery of the pole figure due to rotation recrystallization, accompanied by a preferential removal of kinematically unfavorably oriented grains by grain boundary migration. The comparison with experimental results (Schmid et al. 1987, Wenk et al. 1987) would suggest a temperature-dependence for the development of the different textures. As constant temperature during deformation of the shear zone is established, it is inferred that

the texture development is recrystallization-dependent. Thus, the differences in texture and shape fabrics are caused by a progressive increase in the volume fraction of dynamically recrystallized grains with increasing shear strain from less than 40 % outside the shear to 100% in the shear zone center. Because the increasing volume fraction of recrystallized grains correlates with strain magnitude, an apparent finite strain-dependence of the texture development is observed.

Acknowledgements

We wish to thank Stefan Schmid and Hans De Bresser for many fruitful and stimulating discussions on calcite deformation. We also like to thank Willi Tschudin, who prepared excellent ultra-thin sections, without which this study would have been impossible. The Swiss National Science Foundation grants NF 20-49562.96, NF 2000-055420.98 and NF 2000-063662.00 are gratefully acknowledged.

Used software

- [1] CIP, <http://www.unibas.ch/earth/micro/downloads/downloads.html>
http://www.unibas.ch/earth/micro/manuals/CIP_site/CIPsite.htm
- [2] NIH-Image, <http://rsb.info.nih.gov/nih-image/download.html>
- [3] Ime d'Ouline, <http://www.unibas.ch/earth/micro/downloads/downloads.html>
- [4] Strip Star, http://www.unibas.ch/earth/micro/downloads/StripStar/stripstar_download.html
- [5] Fabric 2.0, <http://www.unibas.ch/earth/micro/downloads/FABRIC/FABRIC.html>

References

- Anovitz, L.M. & Essene, E.J., 1987. Phase Equilibria in the System $\text{CaCO}_3\text{-MgCO}_3\text{-FeCO}_3$. *J. Petrol.*, 28(2): 389-414.
- Barnhoorn, A., 2003. Rheological and microstructural evolution of carbonate rocks during large. PhD-Thesis Thesis, ETH Zurich, 141 pp.
- Barnhoorn, A., Bystricky, M., Burlini, L. & Kunze, K., 2004. The role of recrystallization on the deformation behaviour of calcite rocks: Large strain torsion experiments on Carrara marble. *J. Struct. Geol.*, 26: 885-903.
- Behrmann, J., 1983. Micostructure and fabric transitions in calcite tectonites from the Sierra Alhamilla (Spain). *Geol. Rundsch.*, 72(2): 605-618.
- Bestmann, M., Kunze, K. & Matthews, A., 2000. Evolution of a calcite marble shear zone complex on Thassos Island, Greece: microstructural and textural fabrics and their kinematic significance. *J. Struct. Geol.*, 22: 1789-1807.
- Boccaletti, M., Coli, M. & Gosso, G., 1982. Strutture di interferenza a scala megascopica nel settore Nord delle Alpi Apuane. *Mem. Soc. Geol. Ital.*, 24: 289-292.
- Burg, J.-P. & Wilson, C.J.L., 1987. Deformation of two phase systems with contrasting

- rheologies. *Tectonophysics*, 135: 199-205.
- Burkhard, M., 1990. Ductile deformation mechanisms in micritic limestones naturally deformed at low temperatures (150–350°C). In: R.J. Knipe and E.H. Rutter (Editors), *Deformation Mechanisms, Rheology and Tectonics*. Geol. Soc. London Spec. Publ., pp. 241-257.
- Busch, J.P. & Van der Pluijm, B.A., 1995. Calcite textures, microstructures and rheological properties of marble mylonites in the Bancroft shear zone, Ontario, Canada. *J. Struct. Geol.*, 17(5): 667-688.
- Carmignani, L., 1985. Carta geologico-strutturale delle Alpi Apuane, Foglio Nord, *Litografia Artistica Cartografica*, Firenze, scala 1:25.000.
- Carmignani, L., Decandia, F.A., Fantozzi, P.L., Lazzarotto, A., Liotta, D. & Meccheri, M., 1994. Tertiary extensional tectonics in Tuscany (Northern Apennines, Italy). *Tectonophysics*, 238: 295-315.
- Carmignani, L. & Giglia, G., 1979. Large scale reverse <<drag folds>> in the late alpine building of the Apuane Alps (N. Apennines). *Atti Soc. Toc. Sci. Mem.*, 86: 109-125.
- Carmignani, L. & Kligfield, R., 1990. Crustal extension in the Northern Apennines: the transition from compression to extension in the Alpi Apuane core complex. *Tectonics*, 9(6): 1275-1303.
- Coli, M., 1989. Litho-structural assemblage and deformation history of “Carrara marble”. *Boll. Soc. Geol. Ital.*, 108: 581-590.
- De Bresser, J.H.P., 1989. Calcite c-axis textures along the Gavarnie thrust zone, Central Pyrenees. *Geol. Mijnbouw*, 68: 367-375.
- De Bresser, J.H.P., 1991. Intracrystalline deformation of calcite. PhD Thesis, University of Utrecht, Utrecht, 191 pp.
- Dietrich, D. & Song, H., 1984. Calcite fabrics in a natural shear environment, the Helvetic nappes of western Switzerland. *J. Struct. Geol.*, 6(1/2): 19-32.
- Erskine, B.G., Heidelbach, F. & Wenk, H.-R., 1993. Lattice preferred orientations and microstructures of deformed Cordilleran marbles: correlation of shear indicators and determination of strain path. *J. Geol.*, 15(9/10): 1189-1205.
- Guillope, M. & Poirier, J.-P., 1979. Dynamic recrystallization during creep of single-crystalline halite; an experimental study. *Journal of Geophysical Research*, 84: 5557-5567.
- Heilbronner, R., 2000. Automatic grain boundary detection and grain size analysis using polarization micrographs or orientation images. *J. Struct. Geol.*, 22: 969-981.
- Heilbronner, R. & Bruhn, D., 1998. The influence of three-dimensional grain size distributions on the rheology of polyphase rocks. *J. Struct. Geol.*, 20(6): 695-705.
- Heilbronner, R. & Tullis, J. 2002. The effect of static annealing on microstructure and crystallographic preferred orientations of quartzites experimentally deformed in axial compression and shear. In: *Deformation Mechanisms, Rheology and Tectonics: Current Status and Future Perspectives* (edited by de Meer, S., Drury, M. R., de Bresser, J. H. P. & Pennock, G.). Special Publication 200. Geological Society, London, 191-218.
- Heitzmann, P., 1987. Calcite mylonites in the Central Alpine “root zone”. *Tectonophysics*, 135: 207-215.
- Herwegh, M. & Handy, M.R., 1998. The origin of shape preferred orientations in mylonite: inferences from *in-situ* experiments on polycrystalline norcamphor. *J. Struct. Geol.*, 20(6): 681-694.
- Kennedy, L.A. & White, J.C., 2001. Low-temperature recrystallization in calcite: Mechanisms and consequences. *Geology*, 29(11): 1027-1030.
- Kligfield, R., Hunziker, J., Dallmeyer, R.D. & Schamel, S., 1986. Dating of deformation

- phases using K-Ar and $^{40}\text{Ar}/^{39}\text{Ar}$ techniques: results from the Northern Apennines. *J. Struct. Geol.*, 8(7): 781-798.
- Lafrance, B., White, J.C. & Williams, P.F., 1994. Natural calcite *c*-axis fabrics: an alternative interpretation. *Tectonophysics*, 229: 1-18.
- Matthews, A., Lieberman, J., Avigad, D. & Garfunkel, Z., 1999. Fluid-rock interaction and thermal evolution during thrusting of an Alpine metamorphic complex (Tinos island, Greece). *Contrib. Mineral. Petrol.*, 135: 212-224.
- Means, W.D., 1983. Microstructure and micromotion in recrystallization flow of octochloropropane, a first look. *Geol. Rundsch.*, 72: 511-528.
- Means, W.D., 1995. Shear zones and rock history. *Tectonophysics*, 247: 157-160.
- Molli, G., Conti, P., Giorgetti, G., Meccheri, M. & Oesterling, N., 2000. Microfabric study on the deformational and thermal history of the Alpi Apuane marbles (Carrara marbles), Italy. *J. Struct. Geol.*, 22: 1809-1825.
- Molli, G. & Heilbronner, R., 1999. Microstructures associated with static and dynamic recrystallization of Carrara marble (Alpi Apuane, NW Tuscany, Italy). *Geol. Mijnb.*, 78: 119-126.
- Panozzo Heilbronner, R. & Pauli, C., 1993. Integrated spatial and orientation analysis of quartz *c*-axis by computer-aided microscopy. *J. Struct. Geol.*, 15(3-5): 369-382.
- Panozzo, R., 1983. Two-dimensional analysis of shape-fabric using projections of digitized lines in a plane. *Tectonophysics*, 95: 279-294.
- Panozzo, R., 1984. Two-dimensional strain from the orientation of lines in a plane. *J. Struct. Geol.*, 6(1/2): 215-221.
- Panozzo, R. & Hürlimann, H., 1983. A simple method for the quantitative discrimination of convex and convex-concave lines. *Microscopica Acta*, 87(2): 169-176.
- Pieri, M., Burlini, L., Kunze, K., Stretton, I. & Olgaard, D.L., 2001 a. Rheological and microstructural evolution of Carrara marble with high shear strain: results from high temperature torsion experiments. *J. Struct. Geol.*, 23: 1393-1413.
- Pieri, M., Kunze, K., Burlini, L., Stretton, I., Olgaard, D.L., Burg, J.-P. & Wenk, H.-R., 2001 b. Texture development of calcite by deformation and dynamic recrystallization at 1000 K during torsion experiments of marble to large strains. *Tectonophysics*, 330: 119-140.
- Powell, R., Condliffe, D.M. & Condliffe, E., 1984. Calcite-dolomite geothermometry in the system $\text{CaCO}_3\text{-MgCO}_3\text{-FeCO}_3$: an experimental study. *J. Metam. Geol.*, 2: 33-41.
- Ramsay, J., 1967. *Folding and fracturing of rocks*. McGraw-Hill, New York.
- Ramsay, J. & Graham, R.H., 1970. Strain variation in shear belts. *Can. J. Earth Sci.*, 7: 786-813.
- Ratschbacher, L., Wenk, H.-R. & Sintubin, M., 1991. Calcite textures: examples from nappes with strain-path partitioning. *J. Struct. Geol.*, 13(4): 369-384.
- Rutter, E.H., Casey, M. & Burlini, L., 1994. Preferred crystallographic orientation development during plastic and superplastic flow of calcite rocks. *J. Struct. Geol.*, 16(10): 1431-1446.
- Rutter, E.H., 1995. Experimental study of the influence of stress, temperature, and strain on the dynamic recrystallization of Carrara marble. *Journal of Geophysical Research*, 100(B12): 24,651-24,663.
- Schmid, S.M., 1975. The Glarus overthrust: Field evidence and mechanical modal. *Eclogae geol. Helv.*, 68/2: 247-280.
- Schmid, S.M., Paterson, M., S. & Boland, J.N., 1980. High temperature flow and dynamic recrystallization in Carrara marble. *Tectonophysics*, 65: 245-280.
- Schmid, S.M., 1981. Laboratory experiments on rheology and deformation mechanisms in

-
- calcite rocks and their application to studies in the field. Habilitationsschrift Thesis, Eth Zürich, Zürich, 105 pp.
- Schmid, S.M., Panozzo, R. & Bauer, S., 1987. Simple shear experiments on calcite rocks: rheology and microstructure. *J. Struct. Geol.*, 9(5/6): 747-778.
- Sibson, R.H., 1977. Fault rocks and mechanisms. *J. Geol. Soc. London*, 133: 191-213.
- Turner, F.J. & Weiss, L.E., 1963. Structural analysis of metamorphic tectonites. McGraw-Hill, New York.
- Underwood, E.E., 1970. Quantitative Stereology. Addison-Wesley, London, 228 ff. pp.
- Van der Pluijm, B.A., 1991. Marble mylonites in the Bancroft shear zone, Ontario, Canada: microstructures and deformation mechanisms. *J. Struct. Geol.*, 13(10): 1125-1135.
- Walker, A.N., Rutter, E.H. & Brodie, K.H., 1990. Experimental study of grain-size sensitive flow of synthetic, hot-pressed calcite rocks. In: R.J. Knipe and E.H. Rutter (Editors), *Deformation Mechanisms, Rheology and Tectonics*. Geological Society of London Special Publication, pp. 259-284.
- Wenk, H.-R., Takeshita, T., Bechler, E., Erskine, B.G. & Matthies, S., 1987. Pure shear and simple shear calcite textures. Comparison of experimental, theoretical and natural data. *J. Struct. Geol.*, 9(5/6): 731-745.
- Wenk, H.-R., Takeshita, T., Van Houtte, P. & Wagner, F., 1986. Plastic Anisotropy and Texture Development in Calcite Polycrystals. *J. Geophys. Res.*, 91(B3): 3861-3869.
- Wilson, C.J.L., 1981. Experimental folding and fabric development in multilayered ice. *Tectonophysics*, 78: 139-159.

Chapter 4

The influence of dolomite on the behaviour of Carrara marble during natural deformation

4.1 Introduction

Deformation tends to localize in carbonate rocks, because their strength is significantly lower than that of other rock types, such as sandstones, granites or mafic rocks. Large amounts of deformation along thrusts in the Alps, e.g. along the ‘Glarner Überschiebung’ (e.g. Schmid 1975) and the ‘Doldenhorn Überschiebung’ (Herwegh 2000, Herwegh & Kunze 2002), are accommodated by calcite mylonites, which typically possess a fine grain size and a weak texture. Such a microfabric is typical of diffusion creep and of grain boundary sliding, two processes, which are inferred to be the dominant deformation mechanism of these rocks. Since calcite is very sensitive to post-deformational grain growth (annealing), such fine-grained microstructures have to be stabilized to be preserved. Stabilization can be achieved either by continuous deformation during rapid exhumation and cooling or by the presence of second phase particles, which prevent static grain growth.

Many carbonate mylonites are not simply composed of calcite but contain substantial amounts of phyllosilicates, dolomite, quartz and other phases. Thus, the fine-grained microstructure, which favours diffusion creep can be stabilized and be preserved. Experimental studies on Solnhofen limestone (Schmid et al. 1977) and on fine-grained synthetic calcite rocks (Walker et al. 1990) have shown that diffusion creep is active at low stresses (< 25 to 100 MPa, depending on experimental conditions). Therefore, localization of deformation into shear zones at low stress by diffusion creep may be caused by the presence of a second phase.

In order to investigate the rheological behaviour and the microstructural characteristics of two-phase rocks, a number of experimental studies (e.g. on calcite-halite (Jordan 1987), anhydrite-halite (Ross et al. 1987), calcite-anhydrite (Bruhn et al. 1999, Barnhoorn 2003) and on pure and impure calcite aggregates (Olgaard et al. 1990)) were performed during the past two decades. Each study has revealed that the phase mixture behaves rheologically differently from the pure phases. Bruhn et al. (1999), for instance, showed, that the strength of calcite-anhydrite mixtures may be significantly lower than those of the endmember phases. On the other hand, synthetic calcite rocks with added quartz particles are almost 5 times stronger than the same rock without quartz (Dresen et al. 1998).

Most studies on the rheological behaviour of two-phase rocks were performed under conditions where one or both phases deform by dislocation creep. Jordan (1987) and Ross et al. (1987), for instance, have shown that the rheology of calcite-halite and anhydrite-halite aggregates is controlled by the weak phase, which is halite and anhydrite, respectively. Depending on its volume proportion, the strong phase deforms by brittle processes or behaves like rigid inclusions, contributing only little to the bulk deformation. A critical aspect of the deformation under such conditions is the coalescence of the weak phase into layers (Jordan 1988, Handy 1990), so that the rheological properties may depend on the initial stages of the deformation history.

Experimental studies elucidating the role of diffusion creep during the deformation of two-phase rocks are rare. Bruhn et al. (1999) have studied the rheological behaviour of calcite-anhydrite mixtures at conditions where the pure phases deform dominantly by dislocation creep. The phase mixtures, however, deform dominantly by diffusion creep. One of their interpretation is based on a theoretical model (Chen 1983), which predict that diffusion rates are faster along phase boundaries than along grain boundaries. A higher degree of mixing produces more phase boundaries, which in turn leads to enhanced diffusion. Therefore, diffusion creep may be enhanced in two-phase rocks and may lead to strain weakening and localization.

Few workers investigated the rheology of naturally deformed two-phase rocks. Kruse & Stünitz (1999), for instance, showed for highly deformed gabbroic rocks differences in deformation mechanism between mono-mineralic and two-phase domains. Their microstructural analysis revealed that pure hornblende and plagioclase domains deform dominantly by dislocation creep, while domains composed of a mixture of both phases deform by granular flow. They suggested that heterogeneous nucleation of hornblende may lead to a dispersion of phases and therefore to enhanced diffusion creep, i.e. granular flow.

The deformation mechanisms in impure limestones were recently investigated by Herwegh & Berger (submitted). Their study reveals, that the presence of a second phase stabilizes the microstructure and the dominant deformation mechanism depends on the volume fraction and size of second phase particles. Consistent with Kruse & Stünitz (1999) samples with low second phase content deform by dislocation creep, while samples with a larger amount of second phases deform by diffusion creep, indicating a strong influence of second phases on the active deformation mechanism.

In order to investigate the influence of dolomite on the deformation mechanism of calcite a mixed calcite-dolomite shear zone from the Alpi Apuane was analyzed. The process, which led to the formation of calcite-dolomite layers in the shear zone is inferred from the comparison of the shear zone to its undeformed precursor. Microstructural and textural parameters determined from five layers in the shear zone of different calcite-dolomite proportions are used to investigate the deformation mechanisms of calcite. Applying these parameters to the flow laws derived from experimentally deformed Carrara marble (Schmid

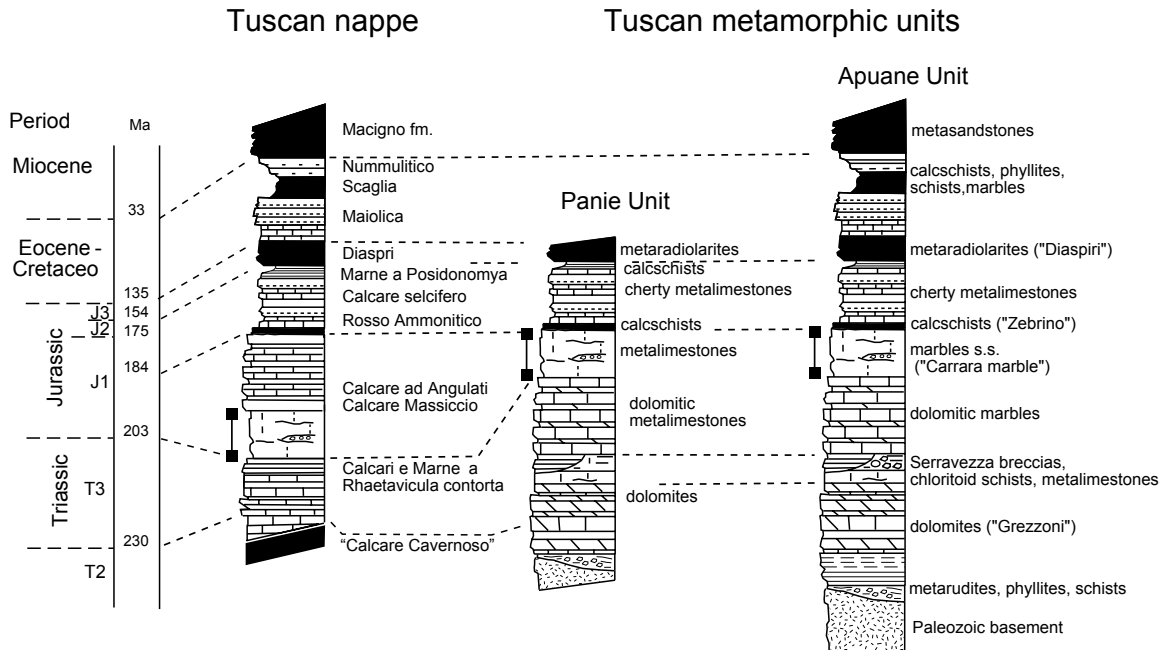


Fig. 4.1: Stratigraphic column of the Tuscan Nappe, Panie Unit and Apuane Unit, modified after Carmignani et al. (1987). Carrara marble and its non- and lowgrade metamorphic equivalents from the Tuscan nappe and Apuane Unit are indicated.

et al. 1977, Schmid et al. 1980) the rheological behaviour of calcite in each layer were estimated.

4.2 Origin of dolomite in calcite rocks of the Alpi Apuane

In the Alpi Apuane dolomite appears at different stratigraphic levels. The largest volume can be found in the Triassic "Grezzoni" formation (Fig. 4.1), which represents a dolomitized carbonate platform. During the Lower Liassic a second carbonate platform formed on top of the "Grezzoni". It is sub-divided into a lower part ("Marmi dolomitici") and an upper part ("Carrara marble sensu strictu"). The "Marmi dolomitici" formation is composed of alternating layers of calcite and dolomite marbles. The dolomitization is related to the environment of their sedimentary precursor (Carmignani et al. 1987). "Carrara marble s.s." is mainly composed of calcite, dolomite occurs only locally, either dispersed in the calcite matrix and/or enriched along the S1-foliation planes. "Calcare Massiccio" is the non- to low grade metamorphic equivalent of Carrara marble. It is widely exposed in the Tuscan Nappe, the Ligurian domain and Umbro-Marchean domain. In the Tuscan Nappe of the Alpi Apuane, "Calcare Massiccio" does not show evidence of dolomitization. Therefore, the environment of the sedimentary precursor of the analyzed shear zone does not account for the origin of dolomite.

In the Panie Unit, which is structurally located between the Apuane Unit and the Tuscan nappe (cf. chapter 1.4.4) “Calcarea Massiccio” is represented by a dark gray meta-limestone containing dolomite (Fig. 4.2). Two types of dolomite can be distinguished. The first type consists of dispersed dolomite grains of a rhombic shape containing a large number of calcite inclusions (Fig. 4.3a and Fig. 4.3b). Coli (1989) detected similar dolomite crystals in Carrara marble and Miller & Folk (1994) in meta-limestones from the Triassic ‘Portoro’ formation in Liguria. The calcite inclusions in the dolomite grains of Miller & Folk (1994) are of the same size as the surrounding microsparitic calcite matrix. They concluded that during late diagenetic dolomite growth the crystallites of the calcite matrix were incorporated into the growing dolomite grains.



Fig. 4.2: Polished sample chip from the Panie Unit. Note the fragmentation of the calcite (dark gray) matrix and the large number of dolomite veins (light gray, yellow).

The second type consists of coarse, rhombic-shaped dolomite grains, which are restricted to fractures in the matrix of the meta-limestone (Fig. 4.3c). The crystals show a concentric zonation, with calcite inclusion rich cores and rims containing few or no inclusions (Fig. 4.3d). Variations in dolomite growth rate or fluid composition may have controlled the formation of the zonation. Tectonically controlled dolomitization is described by Miller & Folk (1994) in the Portoro formation. They showed that dolomitization takes place along faults, i.e. it is structurally controlled.

The dolomite veins are fractured themselves. Calcite precipitates in the fractures and causes the disintegration and separation of dolomite veins (Fig. 4.3e). Further deformation by fragmentation, shearing and the precipitation of calcite and dolomite may lead to the complete destruction of the initial vein structure (see below).

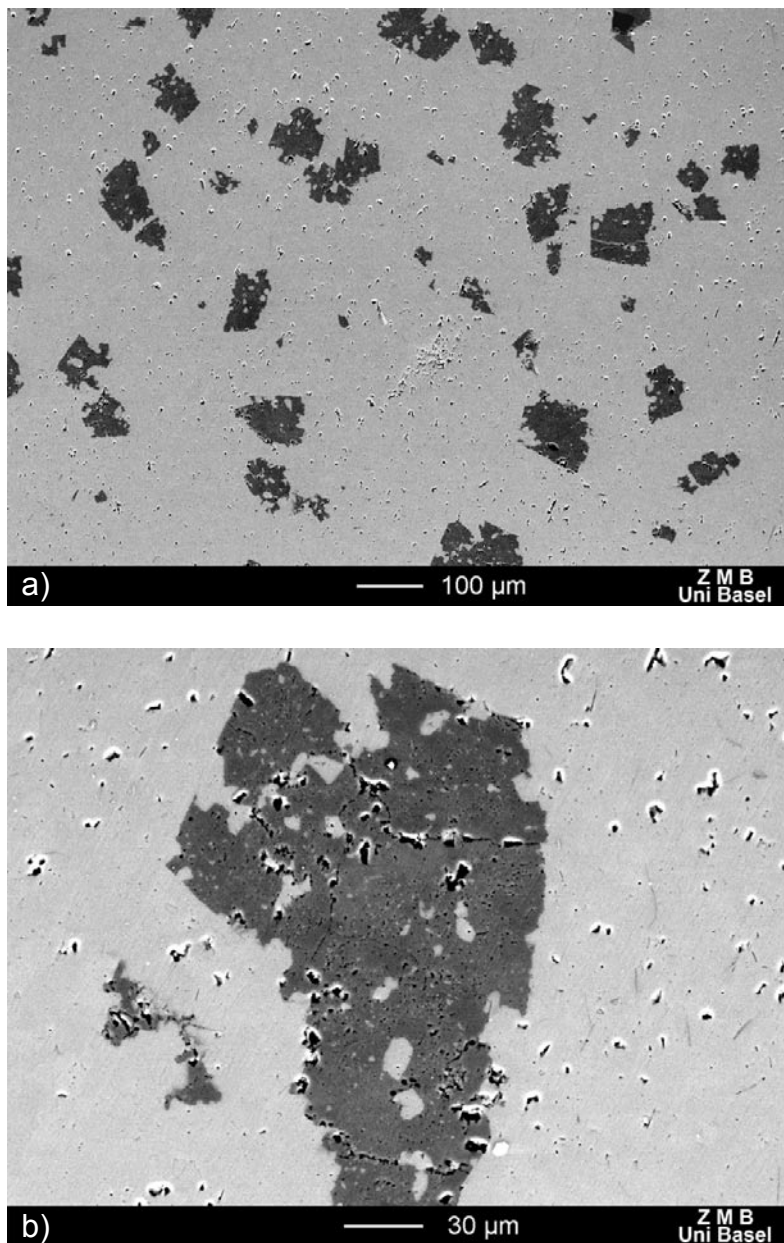


Fig. 4.3: BSEM images of the sample shown in Fig. 4.2. Dark gray is dolomite, light gray is calcite. **a)** Late diagenetic dolomite grains are dispersed in the calcite matrix. **b)** Close-up of dolomite clast from a). Calcite inclusions are visible throughout the entire crystal.

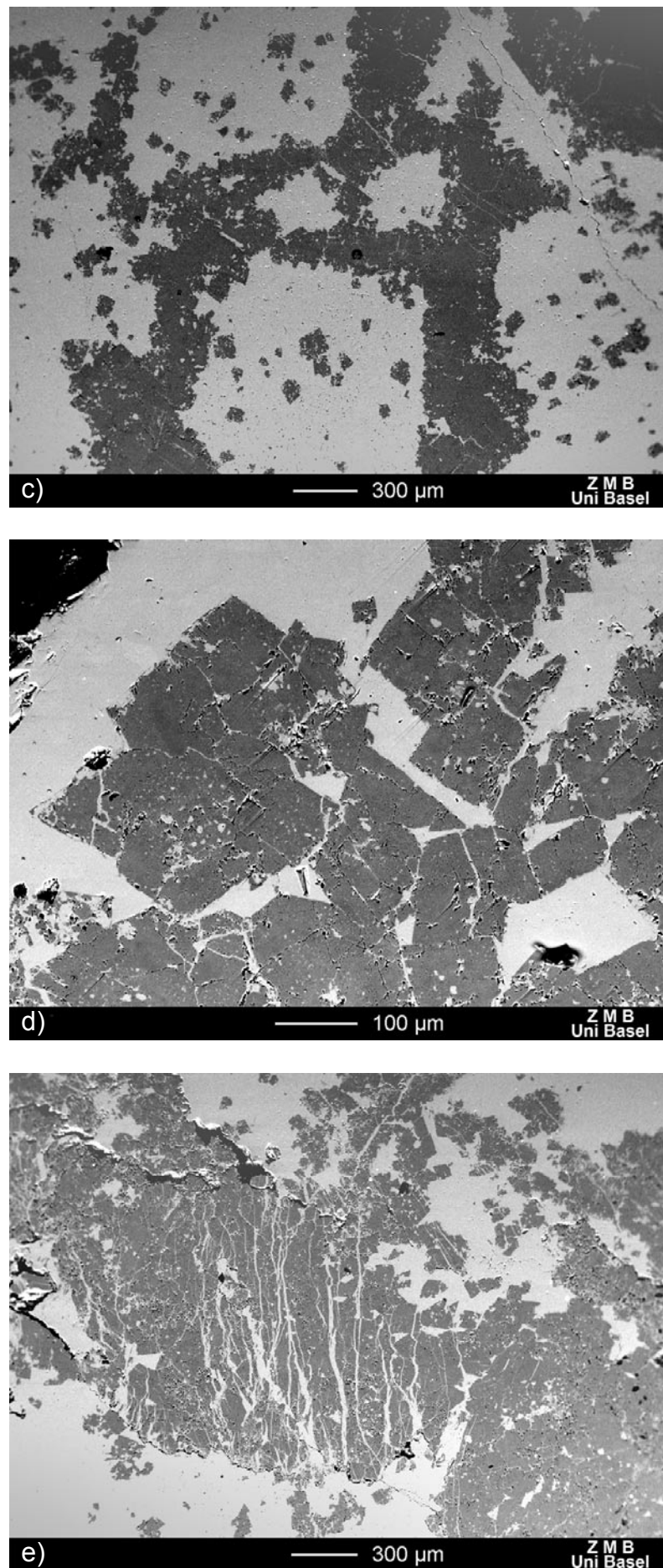


Fig. 4.3 continued **c)** Precipitation of dolomite in fractured calcite (vein dolomite). In the calcite matrix late diagenetic dolomite is visible. **d)** Vein dolomite with concentric zonation. The zonation is probably related to crystal growth. Fragmentation and precipitation of calcite in the opening fractures are visible. **e)** Fragmentation of dolomite veins. Continuous fragmentation and shearing leads to the formation of the calcite-dolomite layers of the Carrara marble shear zone (sample A and B, Fig. 4.5).

4.3 Geological setting and sample description

The analyzed shear zone is located in the Eastern Alpi Apuane, close to the village of Arni (N: 44°03'35"; W: 02°12'27"; Italian coordinate system) (Fig. 4.4). The exposed rocks are part of the 0.5 – 1 km wide Tambura thrust zone, which is located in the overturned limb of the Tambura anticline. Isoclinal folding and the interfingering of lenses of different lithologies are the expression of strong D1b deformation (Carmignani & Giglia 1979). The different deformation phases are described in chapter 1.4.5. Molli et al. (2000) discuss the relationship between the different deformation events and their meso- to microstructural appearance.

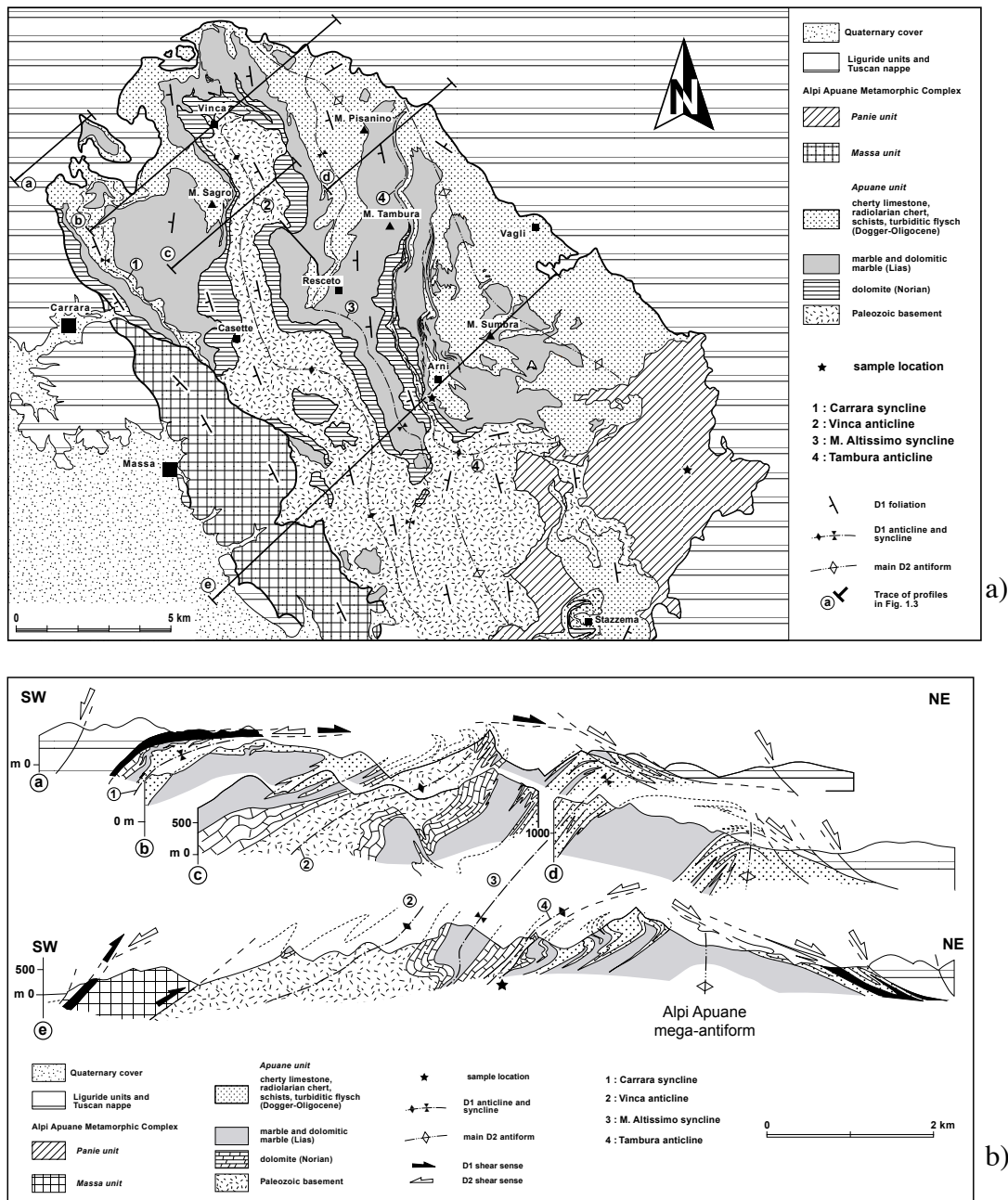
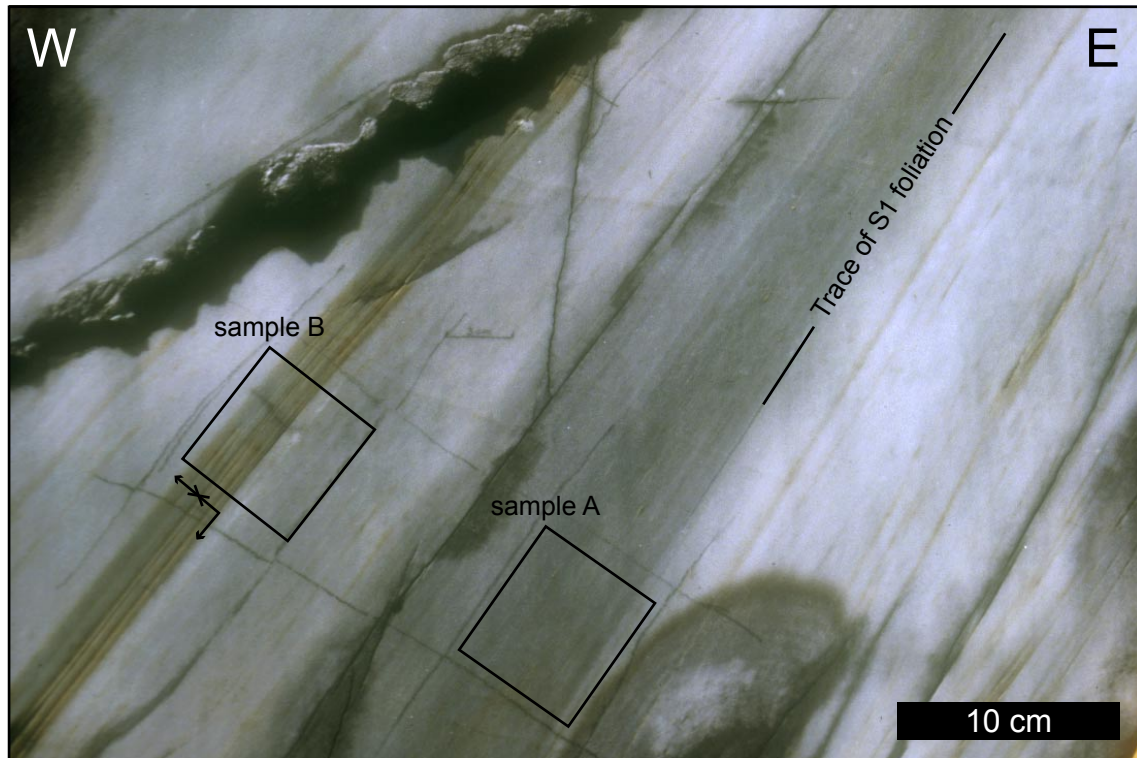
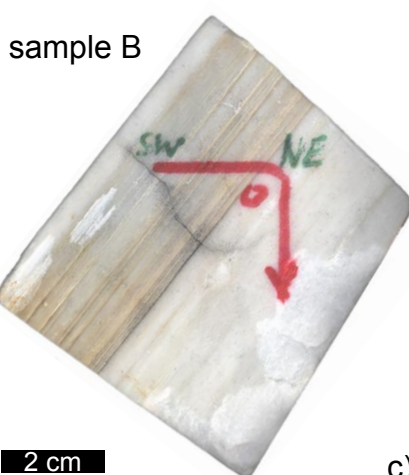


Fig. 4.4: Geological map **a)** and composite profile **b)** of the Alpi Apuane, modified after Molli et al. (2000). The position of the investigated sample in the regional geological structure is indicated.

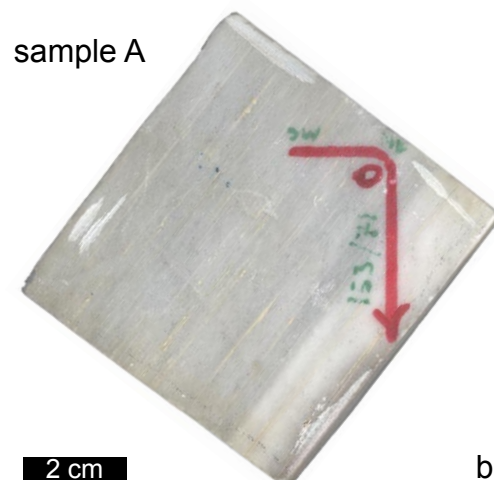
On the outcrop scale the SW-dipping S1-foliation, which is sub-parallel to the sedimentary stratification is the most prominent structural element (Fig. 4.5a). Strain fringes around pyrite porphyroclasts and elongated dolomite clasts define the SW-dipping stretching lineation. The dolomite clasts have a sigmoidal shape, however, their asymmetry is inconsistent, so that no bulk sense of shear can be inferred, neither on the outcrop scale nor in thin section.



a)



c)



b)

Fig. 4.5: a) Naturally polished outcrop face. The trace of the S1 foliation dips to the SW. The outlines of the samples shown in b) and c) are indicated. A late calcite vein crosscuts the main foliation (top left). b) Hand specimen of sample A. Elongated dolomite clasts are visible in pale yellow. c) Hand specimen of sample B. The yellowish laminated domain is composed of alternating calcite- and dolomite rich layers.

Two samples were analyzed. Sample A is characterized by mm-scale dolomite clasts, which grade laterally into thin tails (Fig. 4.5b). The clasts themselves are fractured and the fragments are slightly separated. Sample B is located 10 cm away from sample A. It is derived from a 3 cm thick laminated band, composed of pure calcite and calcite-dolomite layers (Fig. 4.5c). The mixed layers are approximately 1 mm thick and are more strongly weathered than the pure calcite ones. Similar bands are present throughout the entire area and can be recognized by their laminar appearance and their yellow color. Since no strain markers exist the amount of strain accommodated by sample A and sample B cannot be determined.

4.4 Methods

4.4.1 Sample preparation

Normal thin sections (~30 μm), ultra-thin sections (< 4 μm) and polished rock chips were prepared perpendicular to the S1-foliation and parallel to the stretching lineation. One sample was prepared for EBSD investigations by polishing with mechano-chemical silica suspension, which further reduces damage in the upper part of the sample (~100 nm).

In the light microscope it is difficult to distinguish calcite and dolomite in ultra-thin sections, because of the small difference in birefringence ($\Delta n_{\text{Cc}} = 0.172$; $\Delta n_{\text{Dol}} = 0.177 - 0.185$) and refractive index ($n_{\text{Cc}} = 1.486 - 1.658$; $n_{\text{Dol}} = 1.500 - 1.679$). Scanning electron microscopy in back scattered mode (BSEM) was used to observe the compositional difference of the two phases (e.g. Fig. 4.3). Grain boundaries within each phase were difficult to detect. In order to visualize the grain boundaries the sampled surfaces had to be etched (e.g. Fig. 4.6b). We largely followed the etching technique introduced by Herwegh (2000) with etching durations of 60 sec. using diluted hydrochloric acid (0.37% HCl) and 3 min. using diluted acetic acid (0.1 % $\text{CH}_3\text{CO}_2\text{H}$).

4.4.2 Temperature determination

The deformation temperature of the analyzed specimen was determined using calcite-dolomite thermometry after the approach of (Anovitz & Essene, 1987). We used a JEOL 8600 microprobe at an acceleration voltage of 12 kV and a beam current of 7 nA. Natural standards, counting times of 10 - 20 s and a ZAF correction were used. The approach of Anovitz & Essene uses the Mg- and Fe-content in calcite according to a ternary solution model for the determination of the deformation temperature. The temperatures were not corrected for the influence of iron because of the low Fe-content in calcite and dolomite ($X_{\text{Fe}(\text{Cc})} < 0.003$; $X_{\text{Fe}(\text{Dol})} < 0.05$) in the analyzed sample. The individual measurements, mean values and standard

deviation are listed in Appendix C5. Details of the procedure are described in chapter 3. Fine-grained dolomites were selected for the temperature determination because coarse-grained dolomites are rare and usually rich in calcite inclusions. Fine-grained dolomites are assumed to be the product of fracturing and precipitation during the deformation process, thus the estimated temperature represents the one during deformation.

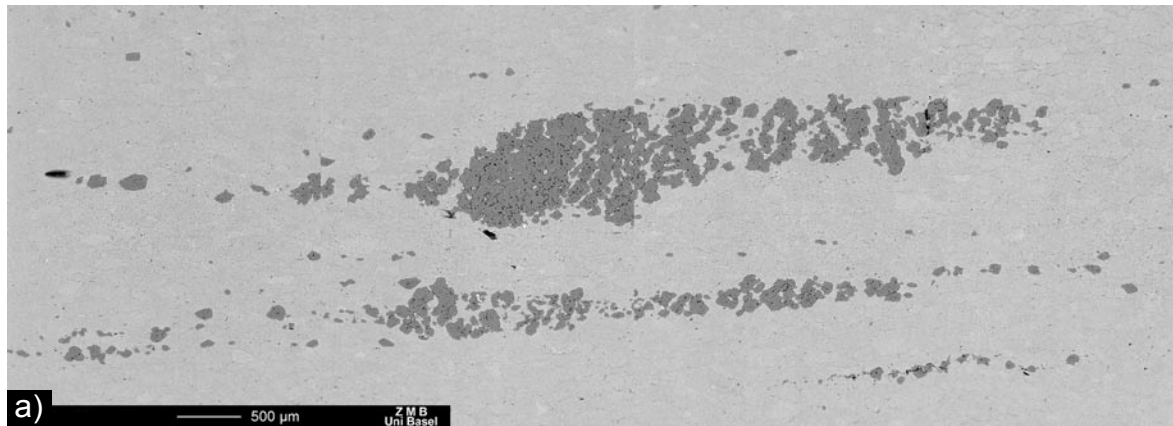
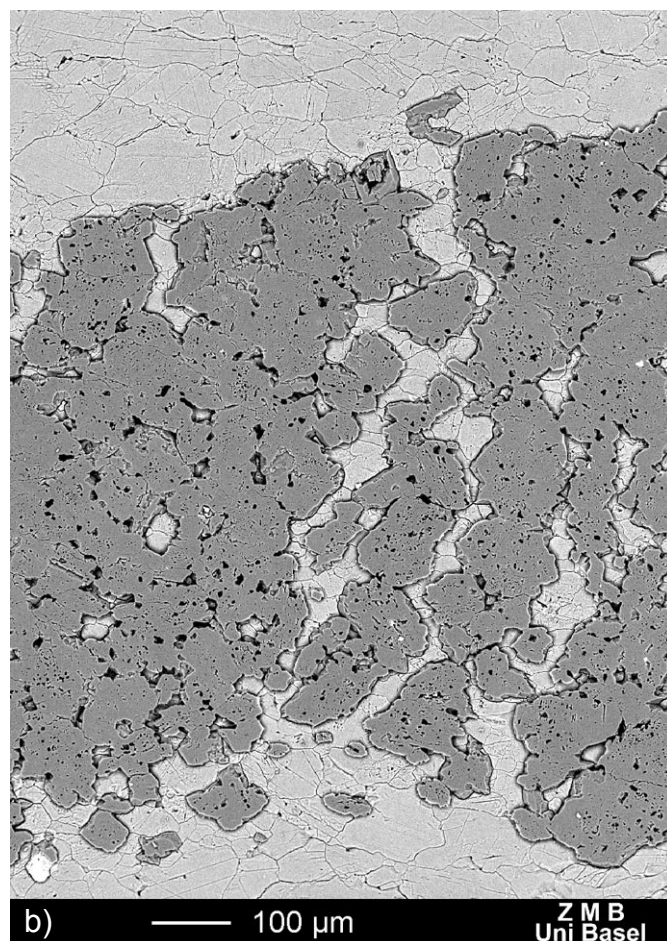


Fig. 4.6: a) BSEM image of typical dolomite clasts in sample A. Dolomite is dark gray, calcite is light gray. The clasts are strongly fractured, with fractures inclined $\sim 60^\circ$ to the foliation plane (horizontal). The fractures follow the cleavage faces of the dolomite crystals. Close-up shown in Fig. 4.6 b is outlined. b) Close-up of the area indicated in Fig. 4.6 a. Dolomite is dark gray, calcite is light gray. The orientation of fractures is controlled by the rhomb faces of the dolomite crystals. The grain and phase boundaries are visible due to acid treatment.



4.4.3 Microstructural analysis

Five sites of sample B with different proportions of calcite and dolomite were analyzed. In each case the volume proportions of calcite and dolomite were determined using NIH-Image for gray level thresholding of SEM back scattered (BSEM) images. The quantitative analysis of grain size and grain shape is based on digital BSEM images of the etched specimen. The grain boundaries were traced manually on the digital image-files using constant magnification for all images (1 pixel = 0.42 μm) and then converted to grain boundary maps. Each phase (calcite and dolomite) was analyzed separately. The size distribution of equivalent radii of sectional areas was measured and the three-dimensional grain diameters were calculated by the StripStar program (Heilbronner & Bruhn 1998). The preferred orientations of grain long axes and grain boundaries and the axial ratios ($b/a = \text{short} / \text{long axis}$) were determined using the PAROR and the SURFOR method (Panozzo, 1983; Panozzo, 1984). The program Ime d'Outline was used for vectorization of the grain boundary maps (cf. chapter 3). The lobateness of grain boundaries, i.e. the deviation of a grain shape from the strictly convex shape, was quantified using the PARIS factor (Panozzo & Hürlimann, 1983).

4.4.4 Cathodoluminescence (CL)

In order to better understand the optical microstructure, i.e. grain and phase boundaries, all analyzed regions were recorded in plain and crossed polarized light and in CL mode. A "hot-cathode" (Walker & Burley 1991) in the CL-Lab of Karl Ramseyer at Geological Department of the University of Bern was used to investigate the cathodoluminescence of calcite and of dolomite. An acceleration voltage of 15 kV for ultra-thin section and 25 kV for normal sections was used.

4.4.5 Crystallographic preferred orientation (CPO, texture)

In order to determine the crystallographic preferred orientation of the analyzed specimens two techniques were applied: Computer-Integrated Polarization microscopy (CIP) (Panozzo Heilbronner & Pauli, 1993) and Electron Back Scattered Diffraction (EBSD) (Venables et al. 1973, Dingley & Randle (1992), Adams et al. 1993, Kunze et al. 1993). The first technique calculates the c-axis orientation of uni-axial minerals from digitally recorded polarization micrographs. Since this technique requires first order gray interference ultra-thin sections with a thickness of less than 2 μm were prepared. Calcite and dolomite textures were separated, using masks derived from the CL-images. EBSD measurements were performed in collaboration with Auke Barnhoorn at the SEM-Unit of the ETH-Zurich. Complete crystallographic orientations of calcite were determined. The measuring step-sizes were adjusted to the sectional grain diameter of calcite in each layer (Site 1: 60 μm ; Site 9:

30 μm ; Site 2: 20 μm ; Site 4: 15 μm ; Site 6: 15 μm). The EBSD patterns of both calcite and dolomite were separated by the following filtering technique. The chemical composition of each data point was determined by an EDX detector. All points with less than 50% Ca and more than 20% Mg of the maximum EDX counts correspond to dolomite and were excluded. Both thresholds were determined empirically (cf. Appendix C3). Points on grain boundaries were characterized by a bad image quality (IQ) and low confidence index (CI). Points with $\text{CI} < 0.2$ were excluded. For the calculation of the calcite pole figures, 1100 measurements were used.

4.4.6 Phase distribution

In order to determine the spatial distribution of calcite and dolomite in each of the analyzed layers calcite-calcite (cc) and dolomite-dolomite (dd) grain boundaries and calcite-dolomite (cd) phase boundaries were separated. The length of each boundary type was counted and normalized by the total length of the bulk outline. These fractions are $o(\text{cc})$, $o(\text{dd})$ and $o(\text{cd})$. The expected proportion $p(\text{cc})$, $p(\text{dd})$ and $p(\text{cd})$ in a random distribution of calcite and dolomite is calculated after the following equations:

$$p(\text{cc}) = (a_c)^2 \quad (4.1)$$

$$p(\text{dd}) = (a_d)^2 \quad (4.2)$$

$$p(\text{cd}) = 2 (a_c) (a_d) \quad (4.3)$$

where a_c and a_d are the volume fractions of calcite and dolomite, respectively. Departure from randomness towards aggregation will cause an increase in the amount of grain boundaries (cc) and (dd) relative to the expected amount, while the departure towards regularity will increase the amount of phase boundaries (cd) (Roger & Bogy 1958).

4.5 Results

4.5.1 Deformation temperature

The temperature condition during deformation was determined from sample B. Because of the short distance between the two samples temperature variations from sample A to sample B are unlikely. The temperature values scatter around an average of 366°C, with a standard deviation of 20°C. The total spread in temperature is 69°C (Table I. and cf. Appendix C5).

Table I: Deformation temperatures determined by calcite-dolomite thermometry after the approach of Anovitz & Essene (1987). The temperature values of individual co-existing calcite-dolomite is listed on the left, the average temperature and standard deviation on the right. The corresponding microprobe analysis is shown in Appendix C5.

| Measure. No. | Temperature [°C] | Measure. No. | Temperature [°C] |
|--------------|------------------|---------------|------------------|
| 1 | 370 | 10 | 384 |
| 2 | 398 | 11 | 361 |
| 3 | 361 | 12 | 386 |
| 4 | 373 | 13 | 348 |
| 5 | 338 | 14 | 373 |
| 6 | 337 | 15 | 365 |
| 7 | 406 | 16 | 351 |
| 8 | 347 | 17 | 353 |
| 9 | 363 | | |
| Maximum | 406 | Mean | 365.5 |
| Minimum | 337 | Std Deviation | 19.7 |
| Range | 69 | | |

4.5.2 General microstructural characteristics of sample A and sample B

Sample A

Sample A is characterized by 1-3 mm long dolomite clasts (Fig. 4.6a), which are embedded in a matrix of calcite. The diameter of the calcite grains is 100–200 μm . Most grains have lobate grain boundaries and an axial ratio, b/a , of 0.5. The elongated dolomite clasts ($b/a = 0.3$) grade laterally into thin tails. After a few mm the tails terminate in the calcite matrix. From BSEM and CL images it becomes evident that the clasts are fractured. The fractures include an angle of 60° with the foliation plane and do not continue visibly in the surrounding calcite matrix. On the grain scale the fractures seem to follow crystallographic low index planes, developing a zig-zag pattern of fractures (Fig. 4.6b). Individual dolomite fragments have a grain diameter of 50–200 μm and are of rhombic shape. Size, shape and internal structure of these dolomite clasts are similar to those of crystals of the fractured veins from the Panie Unit (cf. Fig. 4.3d). The elongated, fractured dolomite clasts might represent relicts of former veins, so that the Panie Unit sample might be the undeformed precursor of sample A. Calcite and dolomite exhibit different CL colors (Fig. 4.7). Dolomite shows zonations with bright orange cores and pale red rims. The width of the rims is in the range of 10–30 μm . Variations in rim width are due to section effects. In contrast to the

bright CL colors of dolomite, calcite is characterized by a dull luminescence of a brownish color or is even non-luminescent. The non-luminescent crystal volume corresponds to the cores of the calcite grains, whereas the dull luminescence appears in the rims. However, the zonation is not concentric as in many diagenetic carbonate cements (Machel & Burton 1991). Frequently the non-luminescent parts of the crystals are impinged directly on the grain boundaries, so that the width of the rims varies between 0-100 μm . Non-luminescence and dull luminescence is visible in separated, S1-parallel domains. Dull luminescence occurs mostly close to dolomite clasts or in layers, which are enriched in single dolomite crystals. Dominantly non-luminescent domains are restricted to pure calcite layers. The fraction of dull luminescent calcite in the non-luminescent domains forms an interconnected framework. It shows an alignment, which is 25° inclined to the foliation plane (Fig. 4.7).

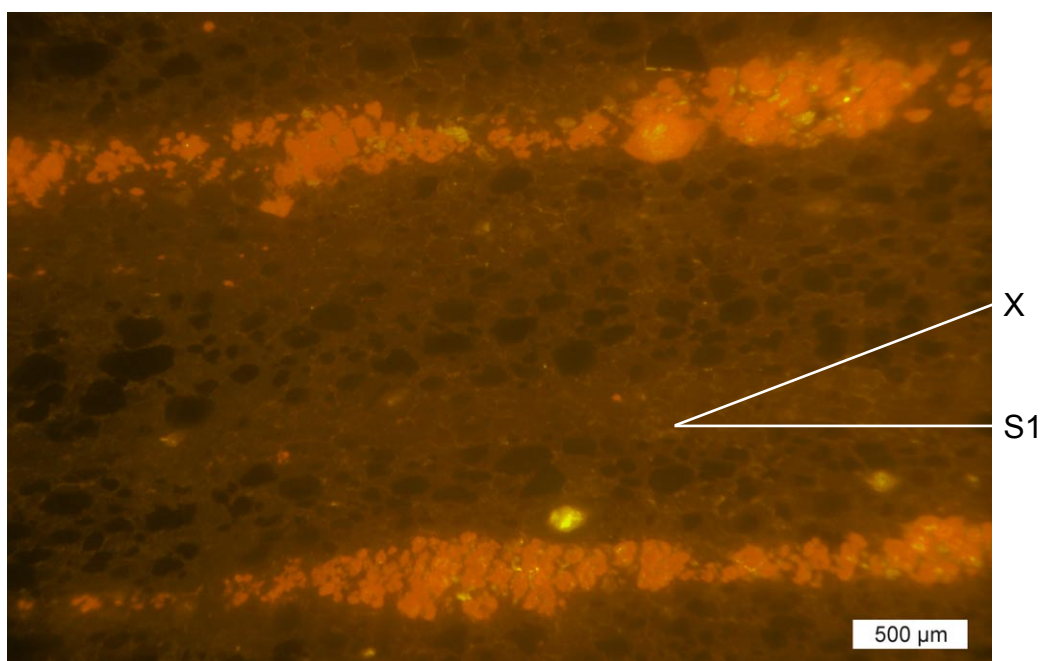


Fig. 4.7: CL image of sample A. Dolomite exhibit bright orange colors. The calcite matrix is brownish or non-luminescent. S1 and the preferred alignment of dull luminescent calcite (X) is indicated.

The CL-zonation of calcite may be explained by grain boundary migration recrystallization. Ionic exchange along migrating grain boundaries modifies the trace element content of calcite possibly by the interaction with a metamorphic fluid. The trace element content influences the CL of a given material (Machel et al. 1991). Thus, GBM may lead to the development of a dull CL of initially non-luminescent calcite. The fact that the dull calcite CL is related to the presence of dolomite suggests that the trace elements causing the luminescence are partly derived from dolomite grains. Thus, trace element transport may have taken place in a more or less closed system of the calcite-dolomite layers. Alternatively to the process described above the dull luminescent domains might represent dominant diffusion pathways, indicating that diffusion was active along grain boundaries and might

have altered the rims of calcite crystals. Since diffusion is probably enhanced along phase boundaries (Bruhn et al. 1999) the dull CL in contact to dolomite crystals may indicate that diffusion occurs preferentially parallel to calcite-dolomite interfaces.

Sample B

Sample B is characterized by alternating layers of pure calcite and mixtures of calcite and dolomite (Fig. 4.8, 4.9). The volume proportion of phyllosilicates, pyrite, quartz and feldspar is less than 2.5 %. Mixed layers are up to 1mm thick and pure calcite layers exceed a thickness of several millimeters. The results of the microstructural analysis of all investigated layers are listed in Table II and Appendix C4. The layers are parallel to each other and to the shear plane, which in turn is parallel to the main foliation (S1). Boudinage and pinch and swell structures are absent in layers with low dolomite volume proportions. Only layers with a dolomite content of approximately 50 vol-% exhibit minor perturbations in their laminar structure (Fig. 4.9).

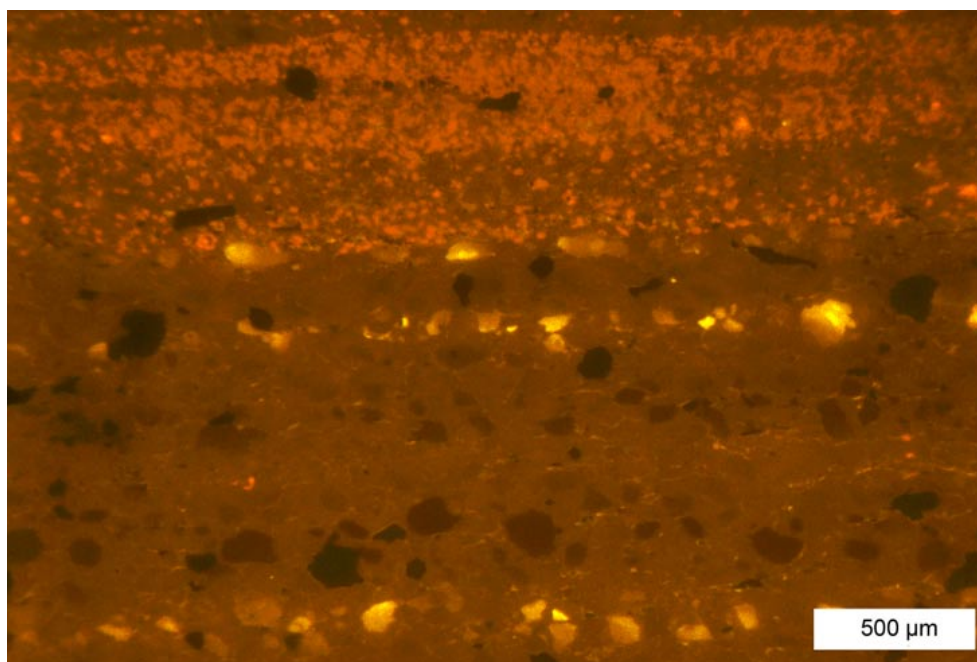


Fig. 4.8: CL image of sample B. Dolomite layers (orange CL) alternate with calcite layers (brownish CL, non-luminescent). Compared to sample A (Fig. 4.7) calcite shows fewer non-luminescent grains. Bright yellow calcite appears only in a few layers.

Based on grain size, shape and CL two types of dolomite can be distinguished. First, coarse-grained ($\sim 150 \mu\text{m}$) crystals of rhombic shape and an internal zonation, which is visible in BSEM and CL (Fig. 4.10). Their cores exhibit a bright orange CL and are rich in calcite inclusions of $\sim 5 \mu\text{m}$ diameter. The rims show pale red luminescence colors and are inclusion free. Shape and zonation are similar to those of the dolomites in sample A, suggesting a co-genetic formation. Furthermore, shape and internal structure resemble those of dolomite crystals from veins in the Panie Unit, so that this type of dolomite may be interpreted to represent relicts of vein dolomite.

Table II: Results of microstructural and textural analysis. The vol-%, grain size and grain shape is shown for calcite and dolomite. b/a is the average axial ratio of short / long particle axes, A (min) and B(min) represents the minimum of the PAROR and SURFOR projection function, which indicate the intensity of the fabric anisotropy. α (Amin) and α (Bmin) is the angle between the shear plane and the preferred orientation of grain long axes and grain boundaries. (for details see Panozzo 1983, Panozzo 1984). For the calcite texture, symmetry and J-index are given. Average deformation temperature and standard deviation is indicated at the bottom right.

| Site | Vol-% | Grain diameter [μm] | | | Texture (CPO) | |
|---------|-------|----------------------------------|-----------|---------|---------------|---------|
| | | 2D-Mean | 2D-Median | 3D-Mode | Symmetry | J-index |
| 1 : Cc | 99.58 | 42.94 | 30.25 | 125 | orthorh. | 2.9 |
| 1 : Dol | 0.09 | – | – | – | | |
| 2 : Cc | 86.17 | 18.03 | 12.84 | 65 | orthorh. | 2.1 |
| 2 : Dol | 12.89 | 12.78 | 11.75 | 15 | | |
| 3 : Cc | 71.52 | 16.26 | 11.91 | 25 | ortho./rand. | 2.3 |
| 3 : Dol | 25.90 | 15.35 | 14.45 | 15 | | |
| 4 : Cc | 57.40 | 11.93 | 9.44 | 25 | rando/axial. | 1.7 |
| 4 : Dol | 40.01 | 13.60 | 13.19 | 15 | | |
| 5 : Cc | 48.43 | 10.75 | 8.72 | 15 | rando/axial. | 1.6 |
| 5 : Dol | 50.14 | 12.44 | 11.39 | 15 | | |

| Site | Vol-% | Grain shape | | | | | |
|---------|-------|-------------|------|---------------------|------|---------------------|-----------|
| | | b/a | Amin | α (Amin) [°] | Bmin | α (Bmin) [°] | PARIS [%] |
| 1 : Cc | 99.58 | 0.55 | 0.66 | 0 | 0.62 | 5 | 8.10 |
| 1 : Dol | 0.09 | – | – | – | – | – | – |
| 2 : Cc | 86.17 | 0.55 | 0.65 | 0 | 0.61 | 0 | 6.32 |
| 2 : Dol | 12.89 | 0.61 | 0.73 | 0 | 0.72 | 0 | 0.84 |
| 3 : Cc | 71.52 | 0.53 | 0.61 | 0 | 0.58 | 0 | 2.57 |
| 3 : Dol | 25.90 | 0.64 | 0.73 | 0 | 0.73 | 0 | 2.46 |
| 4 : Cc | 57.40 | 0.54 | 0.64 | 0 | 0.60 | 0 | 4.78 |
| 4 : Dol | 40.01 | 0.62 | 0.72 | 0 | 0.72 | 0 | 1.74 |
| 5 : Cc | 48.43 | 0.54 | 0.65 | 0 | 0.62 | 0 | 4.38 |
| 5 : Dol | 50.14 | 0.63 | 0.75 | 0 | 0.76 | 0 | 2.50 |

Av. T (°C): 365.54 °C Std. Dev.: 19.58 °

Second, small (~20 μm), convex shaped crystals with a homogeneous interior and a pale red CL (Fig. 4.11). The CL is similar to that of the rims of the larger dolomite grains in sample B. This similarity suggests that both dolomite species formed probably simultaneously. Dolomite nucleation in the calcite matrix leads to small dispersed crystals, while overgrowth of dolomite caused the formation of the homogeneous rims of the pre-existing coarse dolomite rhombs. The small dolomite crystals represent the largest fraction of dolomite in the sample and coarse-grained dolomite can be detected only sporadically.

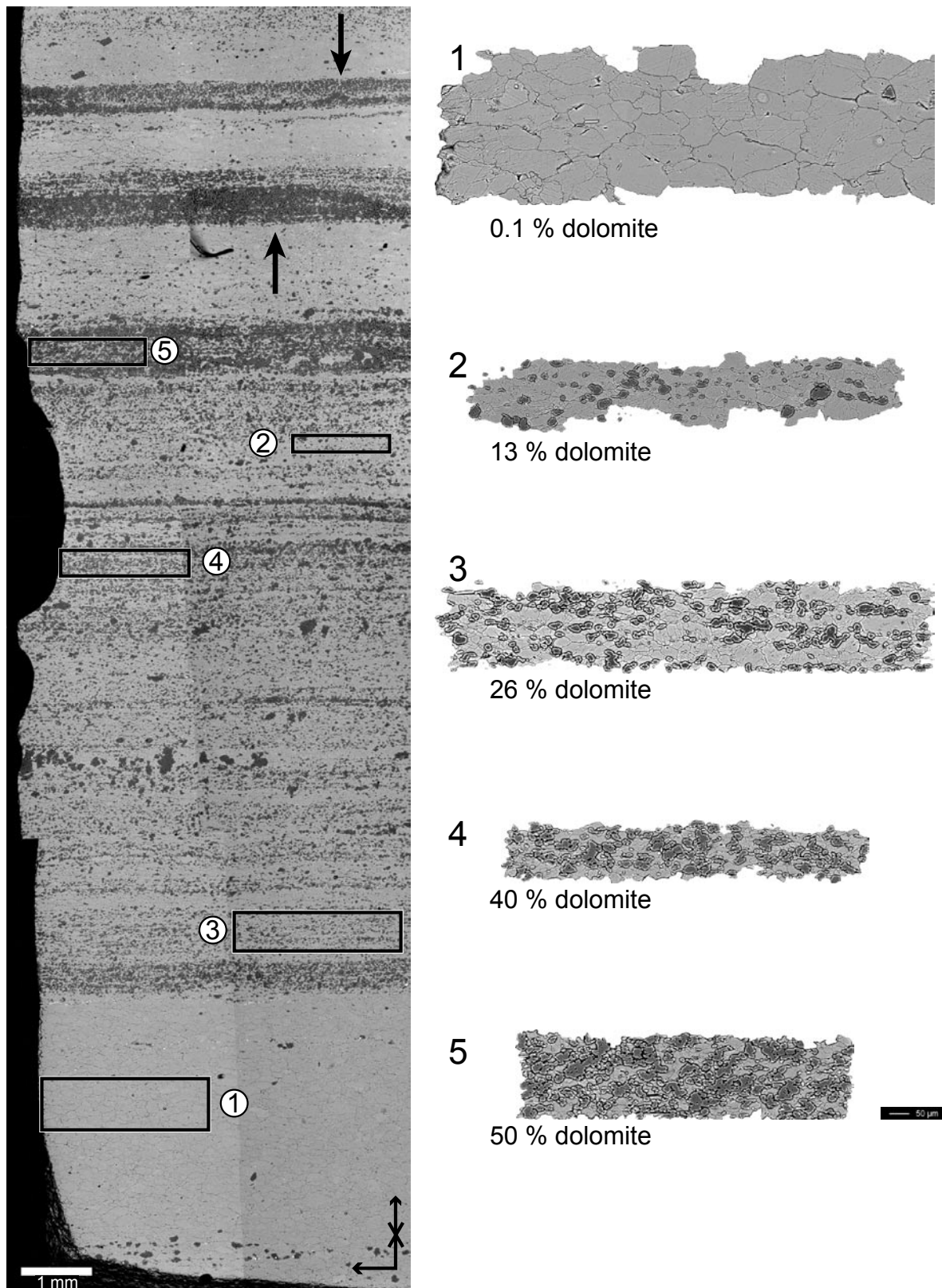


Fig. 4.9: BSEM overview image of sample B (left side). The analyzed sites are outlined and the respective microstructures are shown on the right side (scalebar = 50 μm). From top to bottom the dolomite content increases. Dolomite is dark gray, calcite is light gray. Arrows indicate perturbations of layers with more than ~ 50 vol-% dolomite.

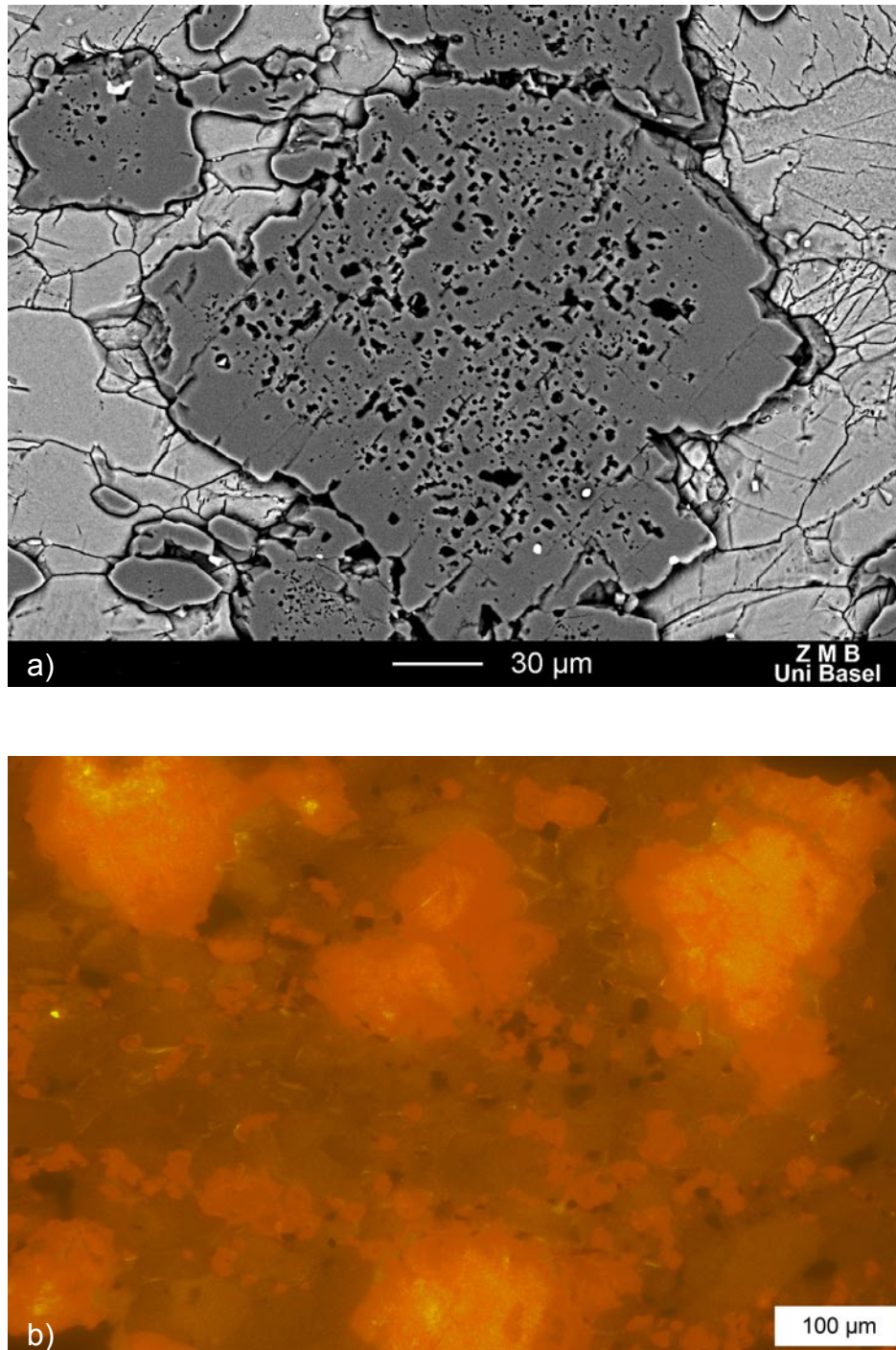


Fig. 4.10: **a)** BSEM image of a large rhomb shaped dolomite clast. An inclusion rich core and a homogeneous rim is visible. The dark spots in the interior of the dolomite clast correspond to calcite inclusion, which were exsolved during acid treatment. **b)** CL image of large dolomite crystals (orange color) in sample B. Calcite exhibits a monotonous brownish CL-color.

Calcite exhibits a monotonous dull CL, only along grain- and phase boundaries secondary calcite with a bright yellow CL has precipitated. The fraction of non-luminescent calcite, which is ~50 % in sample A, decreased extremely in sample B, so that only a few grains (< 10 %) are non-luminescent (Fig. 4.8). This decrease might be caused by GBM

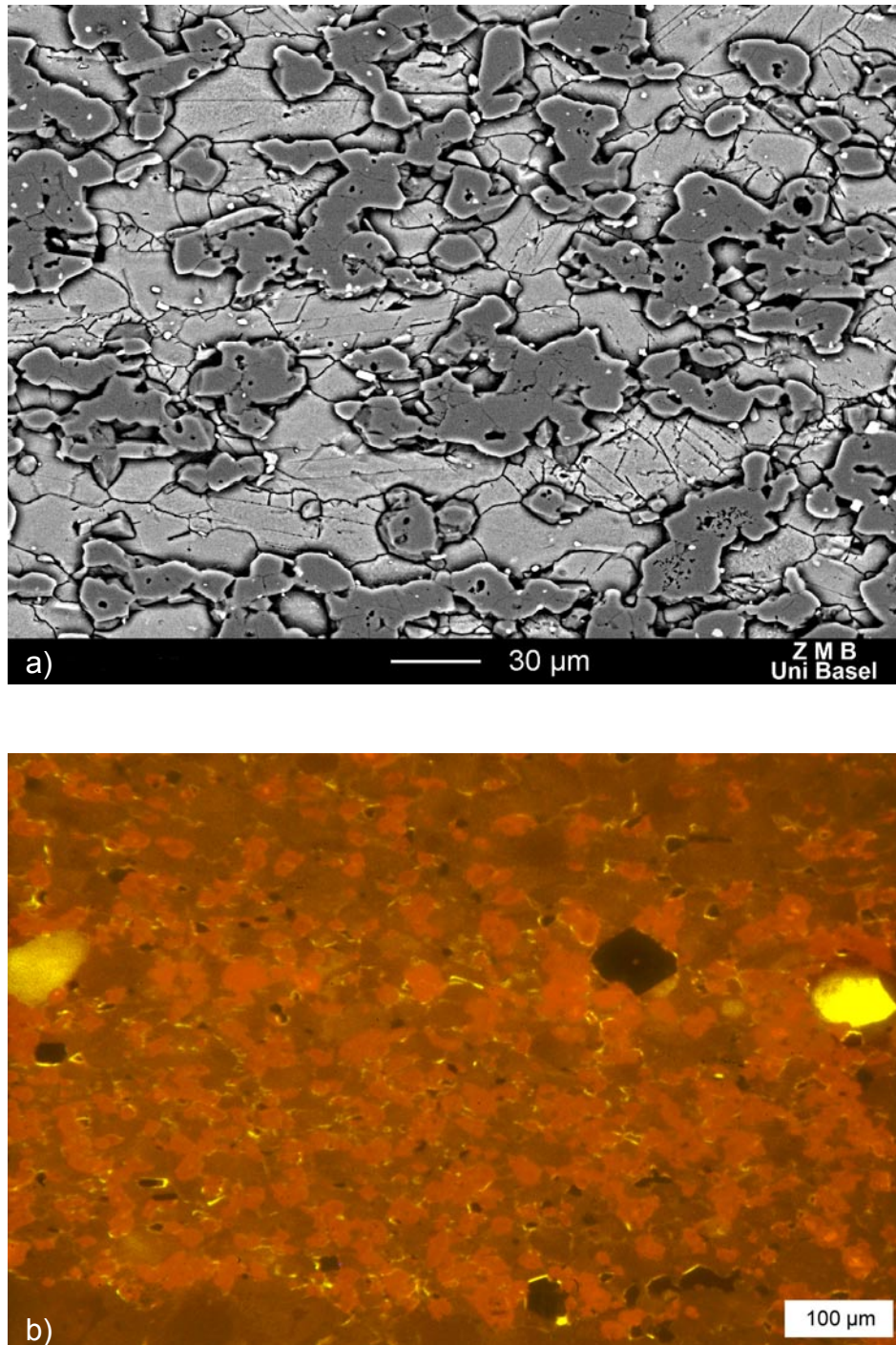


Fig. 4.11: **a)** BSEM image of a typical microstructure in a 50:50 calcite-dolomite layer of sample B. Dolomite is dark gray and calcite is light gray. Note calcite and dolomite have approximately the same grain size. **b)** CL image of a 50:50 calcite-dolomite layer of sample B. Note the secondary calcite (bright yellow CL color) along many grain and phase boundaries.

recrystallization affecting a larger crystal volume or by enhanced diffusion affecting and altering entire crystals. Both possibilities suggest that sample B accommodated more strain either by dislocation creep associated with GBM recrystallization or by diffusion creep.

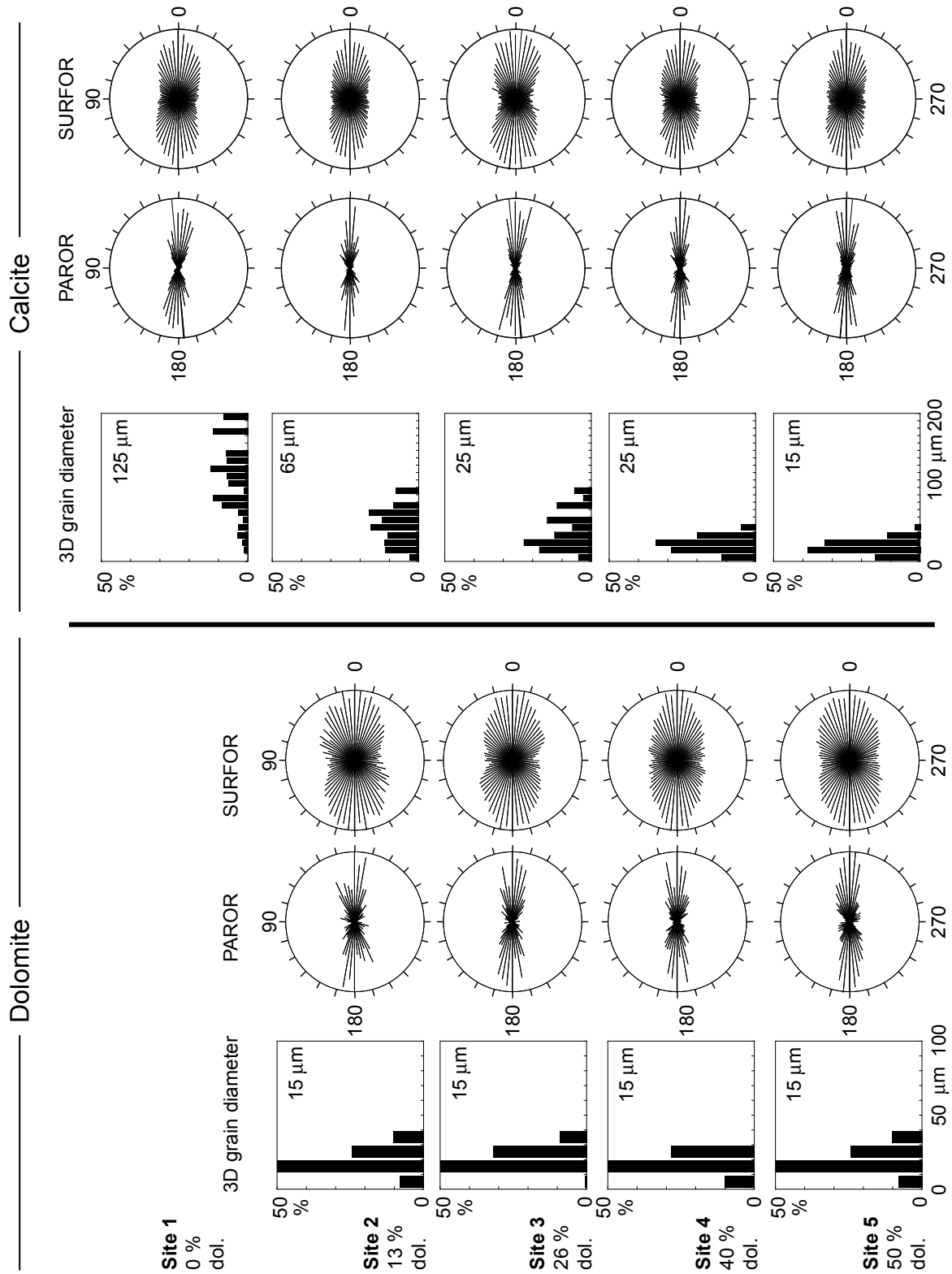


Fig. 4.12: Volume weighted grain size distribution and PAROR and SURFOR rose diagrams for dolomite (left) and for calcite (right). From top to bottom the dolomite content increases. Numbers and dolomite content of each site is indicated on the left. The modal grain size of calcite and dolomite is indicated for each site at the upper right of the corresponding histogram.

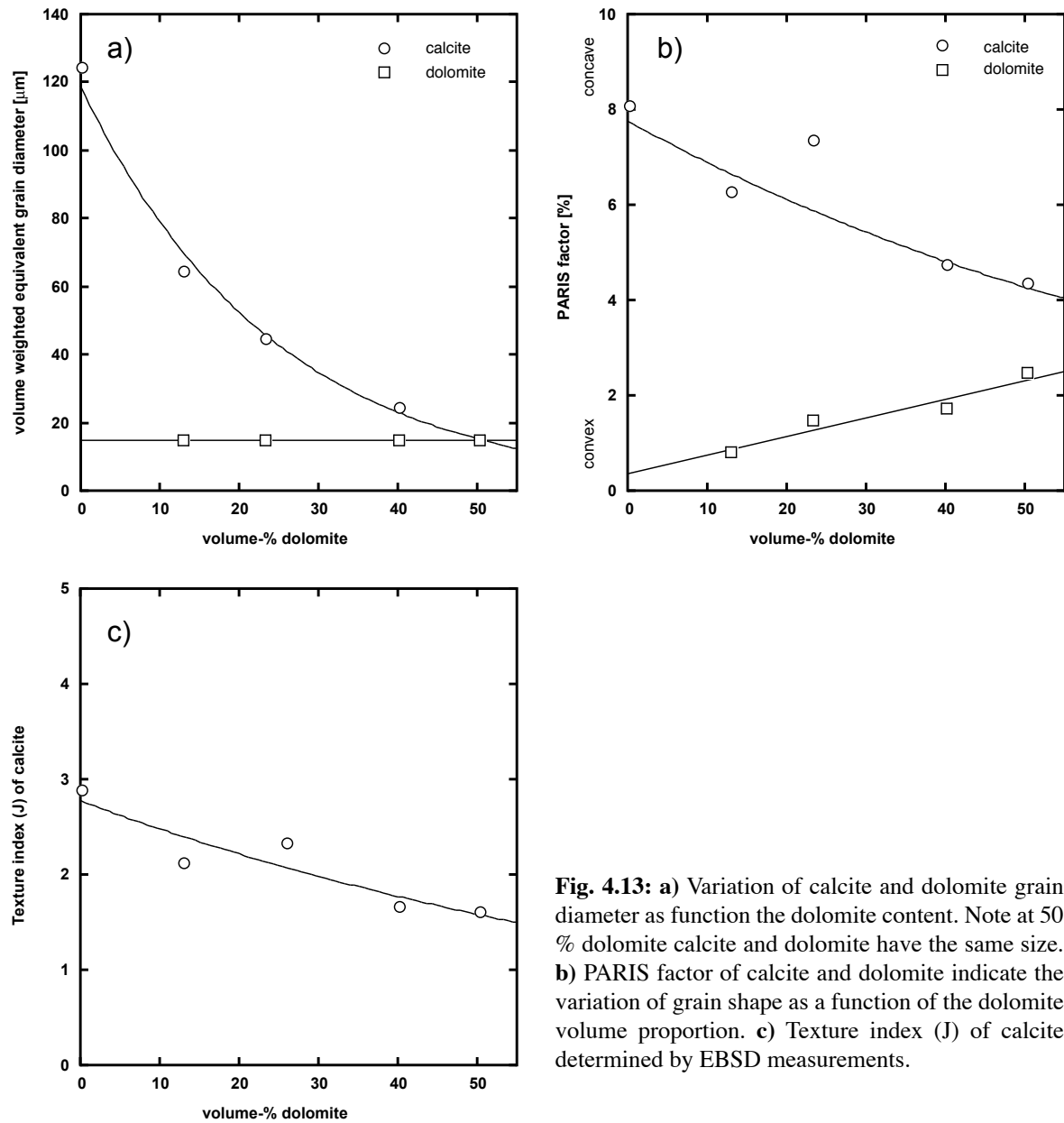


Fig. 4.13: **a)** Variation of calcite and dolomite grain diameter as function the dolomite content. Note at 50 % dolomite calcite and dolomite have the same size. **b)** PARIS factor of calcite and dolomite indicate the variation of grain shape as a function of the dolomite volume proportion. **c)** Texture index (J) of calcite determined by EBSD measurements.

Layers with 0, 13, 24, 40 and 50 vol-% dolomite content were analyzed in detail. The results of the analysis of grain size and shape, crystallographic preferred orientation and distribution of both, calcite and dolomite are described below.

4.5.3 Detailed microstructural analysis of sample B

Grain size and grain shape

The grain diameter of dolomite is constant (15 μm) irrespective of the dolomite volume proportion (Fig. 4.12 and Fig. 4.13a). In each layer, the grains are slightly elongated with an average axial ratio of 0.62 (Table II, Appendix C4). The anisotropy of the particle fabric,

determined by PAROR is ~ 0.73 for all layers. In combination with the low PARIS factor values of 0.8-2.5 % (Fig. 4.13b) these data reflect the slightly elongated shape of dolomite grains with dominantly convex grain boundaries.

The grain diameter of calcite decreases from 125 μm in a pure calcite layer to 15 μm in a layer with 50% dolomite (Fig. 4.12 and Fig. 4.13a). Lobate calcite grain boundaries become more straight with increasing dolomite contents, causing a decrease of the PARIS factor from 8.1 % in pure calcite layers to 4.4 % in layers containing 50 vol-% dolomite (Fig. 4.13b and Table II). At 50 vol-% dolomite, both phases approach similar values in grain diameter (15 μm) and PARIS factor (2 - 4 %). The average axial ratio of the grains and the anisotropy of the particle and surface fabric are approximately constant for all layers. Similar to dolomite, calcite is weakly flattened. Grain long axis and grain boundaries are oriented preferentially within 5° to the S1-foliation and do not show systematic variations as a function of the dolomite content (Fig. 4.12).

Crystallographic preferred orientation (CPO)

CIP as well as EBSD measurements reveal that the pure calcite layers have a preferred crystallographic orientation with a broad c-axis maximum normal to the foliation plane. EBSD shows additionally a girdle distribution of a-axes within the foliation plane (Fig. 4.14). The a-axes pole figure of site 1 reveals a slight increase in pole density close to the shear direction, possibly indicating basal $\langle a \rangle$ slip. The r-planes are slightly concentrated in the plane perpendicular to the shear direction at an angle of approximately 40° from the periphery. At a dolomite content of ~ 10 vol-% (site 2) the c-axis maximum, the a-axis girdle and the preferred orientation of r-planes are much weaker. The CPO decreases in intensity with increasing dolomite content and at 50 vol-% dolomite (site 5) the r- and a-pole figures hardly show any preferred orientation. Only the c-axes texture is characterized by a girdle distribution at the periphery of the pole figure. Thus, with increasing dolomite content the CPO of calcite becomes progressively weaker and shows a transition from an orthorhombic texture (with respect to an internal and external reference system) to a nearly random one, which is axial symmetric around direction normal to the section.

For dolomite, CIP c-axis pole figures at ~ 50 vol-% dolomite shows no significant preferred c-axis orientation, whereas at low dolomite volume proportions a strong c-axis texture with a maximum in the center of the pole figure is developed (Fig. 4.14). However, the strong texture is related to the presence of large dolomite crystals in the microstructure, occupying a large area fraction (cf. Appendix C2). Consequently poor sample statistics produce this strong maxima in the pole figure.

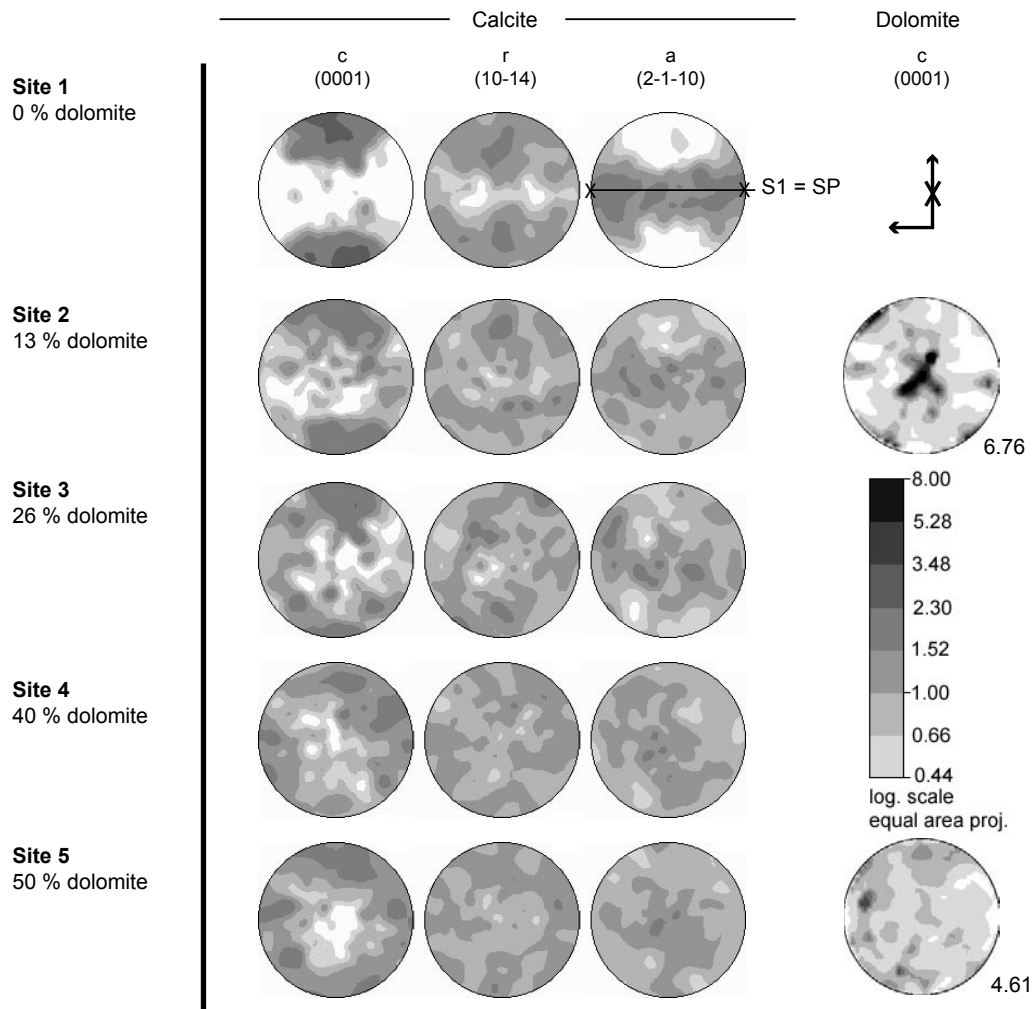


Fig. 4.14: EBSD textures of calcite (left) and CIP c-axes pole figures of dolomite (right). From top to bottom the dolomite content increases. The sample orientation is indicated (top right). The contouring intervals for calcite pole figures are indicated. The maxima (J-Index) of calcite are shown in Fig. 4.13 c and Table II. The shear direction (X) is shown in the a-axes pole figure of site 1.

Phase distribution

The expected and measured proportions of calcite-calcite, dolomite-dolomite and calcite-dolomite boundaries are shown in Fig. 4.15. Below a dolomite volume fraction of ~50%, there are less calcite-calcite boundaries and more dolomite-dolomite boundaries than would be expected. Above ~50% dolomite there are more calcite-calcite and less dolomite-dolomite boundaries than expected. The observed length of calcite-dolomite phase boundaries is always longer than the expected one. In order to analyze the phase distribution in the vertical and horizontal direction, the entire outline of the grain fabric was separated in two sets. Set 1 contains the vertical fraction and set 2 the horizontal fraction of grain- and phase boundaries. The results are shown in (Fig. 4.16). There are less vertical calcite-calcite boundaries than horizontal ones, while dolomite appears to behave more isotropically. Calcite-dolomite boundaries are more frequent in the vertical than in the horizontal direction.

4.6 Discussion

4.6.1 Deformation mechanism of the pure calcite layers

The pure calcite layers exhibit coarse grains with lobate grain boundaries (Fig. 4.13, site 1), which usually develop by GBM recrystallization (Urai et al. 1986). The crystallographic preferred orientation of calcite (Fig. 4.14, site 1) indicates an alignment of crystal slip planes caused by the deformation by dislocation creep (e.g. Law 1990). The texture type in the pure calcite layers is consistent with basal $\langle a \rangle$ slip, if easy slip conditions are assumed. Recent studies of experimentally (Barnhoorn et al. 2004) and naturally (chapter 3 of this thesis) deformed Carrara marble revealed that the basal $\langle a \rangle$ slip system becomes increasingly important with increasing finite strain. Therefore it seems to be likely that also this sample accommodated a large amount of strain.

The microstructure and texture of the pure calcite layer suggest that they might have deformed dominantly by dislocation creep associated by GBM recrystallization.

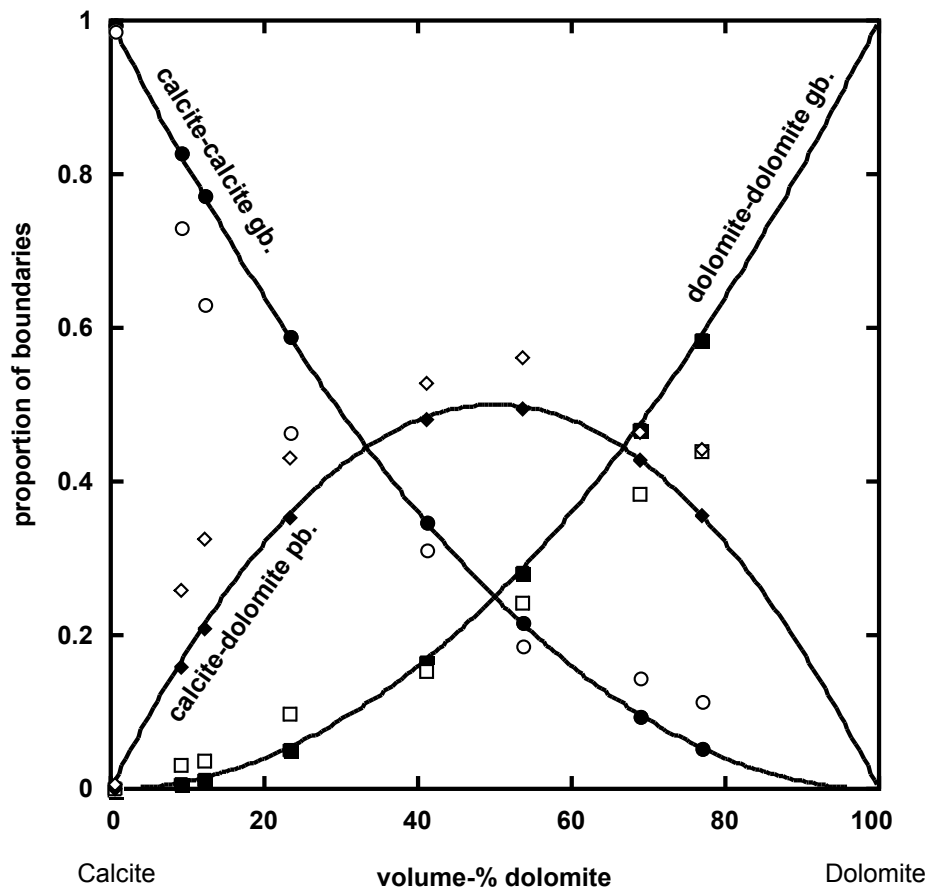


Fig. 4.15: Expected and observed proportion of calcite-calcite and dolomite-dolomite grain boundaries and calcite-dolomite phase boundaries. Expected proportions are shown by the solid lines and with filled symbols, observed proportions are shown with open symbols. For discussion see text. In addition to site 1 to 5 two other sites are plotted. These sites correspond to a dolomite volume proportion of 68% and 77%.

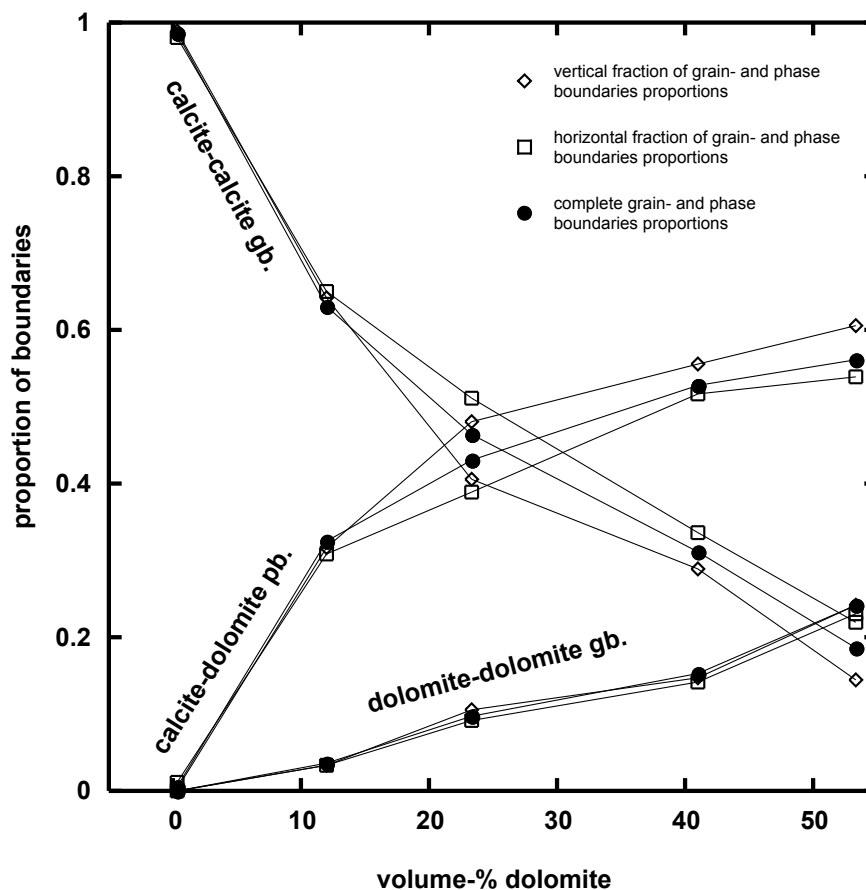


Fig. 4.16: Observed grain and phase boundaries of calcite and dolomite. Filled symbols represent proportions determined from the entire grain outline, open diamonds represent vertical boundaries, open squares horizontal boundaries. Note ranges from 0 to 50 vol-% dolomite, corresponding to the half of the horizontal axis of Fig. 4.15.

4.6.2 Deformation mechanism of the mixed calcite-dolomite layers

The grain size of calcite decreases with increasing dolomite volume proportion (Fig. 4.13a). This reduction can be explained by inhibited grain coarsening during dynamic recrystallization, related to the presence of dolomite. Because of this reason the microstructure of each layer is stabilized (Behrmann 1983, Kruse & Stünitz 1999, Herwegh 2000). Together with the decreasing grain size the calcite grains become less lobate (Fig. 4.13b), but maintain their moderate axial ratio. Grain flattening is usually interpreted to be the result of intra-crystalline deformation.

The microstructure of the mixed layers can be described as a fine-grained matrix composed of equiaxed grains with straight grain boundaries. A similar microstructure develops during experimental deformation of limestone (Schmid et al. 1977, Walker et al. 1990) and is interpreted to be the product of diffusion creep and grain boundary sliding. Also in nature fine-grained mylonites (e.g. Schmid et al. 1975) are believed to deform by these two mechanisms. In the analyzed sample the activity of grain boundary sliding may

be documented by the presence of secondary calcite, which appears along grain interfaces (Fig. 4.11b), indicating dilation between sliding particles. A similar observation was made by Busch & Van der Pluijm (1995) in mylonites from the Bancroft shear zone in Canada. They found bright luminescent calcite, which are located along calcite grain boundaries. On the basis of grain size, grain shape and texture they suggested diffusion creep and grain boundary sliding to be the dominant deformation mechanisms.

With increasing dolomite volume proportion the CPO of calcite becomes weaker. This tendency is represented by the decreasing J-index of the EBSD measurements (Fig. 4.13c). Weak textures are characteristic of diffusion creep dominated deformation (e.g. Schmid et al. 1977, Walker et al. 1990). Thus, the texture weakening and transition to a nearly random texture symmetry (Fig. 4.14) account for an increasing importance of diffusion creep as function of the increasing dolomite content.

In each calcite layer containing dolomite phase boundaries are more abundant and grain boundaries are less abundant than expected on the basis of random mixing (Fig. 4.15a). In layers containing less than 40 vol-% dolomite, calcite grain boundaries occur less frequently than expected, an observation, which is consistent with the detected larger amount of phase boundaries. Dolomite, however, shows in the same compositional interval more grain boundaries than theoretically expected. Since theoretical considerations (e.g. Kretz 1969) are based on equal volume proportions and equal particle sizes of the constituent phases, this discrepancy may be caused by the difference in grain size and volume proportion of calcite and dolomite. Above 60 vol-% dolomite more σ_{cc} and less σ_{dd} than expected were observed. Also, the difference in size and volume proportion of each phase may influence the number of grain- and phase boundaries. Between 40 to 60 vol-% dolomite both phases exhibit fewer grain boundaries than expected, which is consistent with the increase in observed phase boundaries. At this composition, where calcite and dolomite have the same grain size and approximately the same volume proportion, the above described influence of size and volume proportion is neutralized. The positive deviation of phase boundaries from the expected ones indicates that in all layers both phases tend to be dispersed and do not form aggregates of individual phases. Aggregation of individual phases occurs typically during dislocation creep dominated deformation of poly-phase materials, where interconnected layers of weak phases tend to develop (Jordan 1987, Handy 1990).

Bruhn et al. (1999) found during experimental deformation of calcite-anhydrite aggregates a significantly lower strength compared to the stress in the pure phases. They explained this phenomenon by the model of Chen (1983). After this model diffusion along phase boundaries is much faster than along grain boundaries of the individual phases. Thus, two-phase materials may deform much more rapidly or at much lower stresses than pure phases. Because of this reason Bruhn et al. (1999) suggested, that the number of phase boundaries has a significant influence on the rheology of their two-phase aggregates. A larger number of phase boundaries, related to a higher degree of mixing, i.e. dispersion of phases,

cause, therefore enhanced diffusion creep. The phase distribution of calcite and dolomite in the Carrara marble sample support the idea of the dominance of diffusion creep in the mixed layers.

The constant convex shape of dolomite crystals, their dispersed distribution and their preferred appearance at grain boundaries and triple junctions argue for heterogeneous nucleation of dolomite in voids, which probably opened during grain boundary sliding. Kruse & Stünitz (1999) suggested this mechanism for the formation of mixed plagioclase-hornblende layers in highly deformed gabbroic rocks. Their mixed layers deformed by granular flow, while the pure layers show evidence of dominant dislocation creep.

Combining the above arguments the variation of microstructure and texture suggest a change in dominant deformation mechanism from dislocation creep in the pure calcite layers to diffusion creep and grain boundary sliding in the mixed layers. This result is consistent to those from Olgaard (1990), Burlini & Kunze (2000) and Herwegh & Berger (submitted), who proposed a change of the dominant deformation mechanism of calcite from dislocation creep to diffusion creep as function of the second phase content.

4.6.3 The influence of annealing on the microfabric

Apart from site 5 (50 vol-% dolomite) the calcite grain size exceeds the typical grain size for rocks deforming by grain boundary sliding ($\sim 10 \mu\text{m}$) (Schmid 1981, Behrmann 1983, Heitzmann 1987). Therefore and because of the sensitivity of calcite to annealing, one could argue, that the observed grain size reduction is related to inhibited static recrystallization and grain growth, post-dating the deformation process. In the mixed layers grain growth is hindered by the pinning effect of the second phase particles. Assuming this process, the smallest calcite grain size in the mixed layers would approach most closely the initial, 'dynamic' grain size. However, Schmid et al. (1987) and Herwegh et al. (1998) showed that grain size and shape are rapidly modified by post-deformational processes; textures are much more long-lived. In the analyzed sample "dynamic" microstructures with lobate grain boundaries are preserved in the pure calcite layers, where annealing would have the greatest effect. Since no evidence of equilibrated microstructures (straight grain boundaries, 120° triple junctions) can be detected the influence of annealing post-dating the deformation is neglected.

4.6.4 Transition from dolomite veins to mixed calcite-dolomite layers

From the separated analysis of horizontal and vertical phase boundaries the following conclusions can be drawn: First, the fact that more vertical phase boundaries occur than horizontal ones may be a relict of the fracturing process of pre-existing dolomite veins (Panie Unit sample), which probably led to the formation of the calcite dolomite layers of

this sample. Dolomite clasts are fractured at a high angle to the shear plane, which cause the increase in vertical phase boundaries (Fig. 4.3e).

The sample from the Panie Unit, sample A and sample B represent three steps in a continuous deformation process. The meta-limestone (Panie Unit sample) shows only little evidence of brittle deformation and the structure of veins is preserved. Sample A is characterized by elongated dolomite clasts, which are fractured. The individual fragments are separated by calcite. Since the dolomite crystals of both samples are very similar in size, shape and internal structure it might be concluded that the Panie Unit sample represents the undeformed precursor of sample A. Further deformation leads to the complete disintegration of the dolomite clasts, so that a mixture of calcite and dolomite develops. The mixed layers of sample B represent the end product of the above described process. The constant size and equiaxed shape of the dolomite grains in the mixed layers indicate that the dolomite crystals are fractured to a critical size. The dolomite grain size can probably not fall below this critical value because the required stress would be too high to be supported by the rock. On the other hand it may reflect continuous heterogeneous nucleation of dolomite along calcite grain boundaries and triple junctions. The nucleation of small equiaxed grains between calcite leads to the dispersion and mixing of the two phases.

The process for the development of calcite-dolomite layers (sample B) from dolomite veins (Panie Unit sample) can be summarized as follows:

- 1) Late diagenetic growth leads to the formation of dispersed, calcite inclusion rich dolomite crystals (Fig. 4.3a).
- 2) Fragmentation of the calcite matrix and precipitation of dolomite in the fractures causes the formation of dolomite veins (Fig. 4.3c).
- 3) Fragmentation of the dolomite veins and precipitation of calcite in the opening fractures leads to the disintegration of the dolomite veins (Fig. 4.3e). Further fragmentation causes the break-up of the dolomite veins and the formation of elongated dolomite clasts (sample A) (Fig. 4.6a). The clasts fracture preferentially parallel to their cleavage planes, causing their disintegration into loosely packed dolomite rhombs (Fig. 4.6b).
- 4) Progressive deformation separates the individual fragments parallel to the shear direction and causes the opening of fractures, which are filled with calcite and dolomite precipitates (Fig. 4.6b).
- 5) The fragmentation continues until a critical size of $\sim 15 \mu\text{m}$ is reached (Fig. 4.9 and Fig. 4.10a). Further fragmentation would require stresses, which are probably too high to be maintained by the carbonate rock.
- 6) Continuous heterogeneous nucleation of dolomite in voids, which may open during grain boundary sliding, lead to a dispersion of calcite and dolomite.

A relict of this fragmentation process may be detected through the separated analysis of horizontal and vertical grain and phase boundaries (Fig. 4.16). The vertical fraction of phase boundaries is constantly higher than the fraction of horizontal phase boundaries. Considering the continuous fragmentation of dolomite clasts, the development of fractures at a high angle to the foliation plane cause an increase of vertical phase boundaries.

The smaller vertical fraction of calcite grain boundaries (Fig. 4.16) may reflect the slightly elongated shape of the calcite grains. Dolomite, in contrast, is less flattened and shows therefore almost no difference between the observed (o_{dd}) and the expected (p_{dd}) grain outline. This result is consistent with the idea of dolomite fragmentation. It indicates that the dolomite crystals fracture to an equiaxed shape. Alternatively it may reflect the process of heterogeneous nucleation of equiaxed dolomite grains in randomly distributed sites.

4.6.5 The position of the investigated sample in the deformation mechanism map

Ashby (1972) introduced the concept of the deformation mechanism map (DMM) in the material sciences; a concept, which was later also applied to minerals in the geosciences (e.g. for calcite Rutter 1974, Schmid et al. 1977, 1980, 1983, Frost & Ashby 1982, Van der Pluijm et al. 1991, Busch & Van der Pluijm 1995). In order to estimate the rheological conditions of the different layers of the analyzed sample a DMM was constructed. For the construction the following forms of flow laws for the different deformation mechanisms were used:

$$\text{Dislocation glide: } \dot{\epsilon} = A \exp\left(\frac{-H}{RT}\right) \exp\left(\frac{\sigma}{\sigma_0}\right), \quad (4.4)$$

$$\text{Dislocation creep: } \dot{\epsilon} = A \exp\left(\frac{-H}{RT}\right) \sigma^n, \quad (4.5)$$

$$\text{Diffusion creep: } \dot{\epsilon} = A \exp\left(\frac{-H}{RT}\right) \sigma^n d^b, \quad (4.6)$$

where the pre-exponential factor A is a material constant (for each flow law different), R is the gas constant (8.3144 J/mol K), H is the activation energy (in J/mol), T is the temperature in Kelvin, σ is the stress and σ_0 is a material constant in MPa, n is the stress exponent (typically for dislocation creep ≥ 3 and diffusion creep ~ 1), d the grain size in μm and b the grain size exponent (typically 2 -3).

The dislocation glide and dislocation creep field were calculated for a constant temperature of 366°C after the Carrara marble flow laws of Schmid et al. (1980). Since the rheological behaviour of a material is strongly dependent on its composition and grain size (Paterson 1987), the Carrara marble flow law was used. Carrara marble could not be deformed experimentally in the diffusion creep field, therefore the flow law of Solnhofen

limestone (Schmid et al. 1977, their regime 3) was selected to describe the field of grain size sensitivity. The parameters, which were used for the construction of the DMM, are presented in Table III.

Table III: Parameters used for calculation of the deformation mechanism map shown in Fig. 4.17.

| Flow regime | A | H (J/mol K) | n | b | σ_0 (MPa) | Material | Reference |
|-------------|-------------|-------------|-----|---|------------------|---------------------|---|
| exp. flow | $10^{5.8}$ | 259581.6 | - | - | 11.4 | Carrara marble | Rutter (1974) consistent with Schmid et al. (1980) |
| power law 1 | $10^{-4.5}$ | 376812 | 7.6 | - | - | Carrara marble | Schmid et al. (1980) |
| diff. creep | $10^{4.98}$ | 213526.8 | 1.7 | 3 | - | Solnhofen limestone | Schmid et al. (1977) |

The calculated DMM (Fig 4.17) is strictly valid only for pure calcite rocks with the same composition as the experimentally deformed Carrara marble or Solnhofen limestone. Therefore one might argue that flow laws derived from mono-mineralic rocks and hence calculated DMMs are not applicable to two-phase samples (Dresen et al. 1998). However, with the following considerations in mind mono-mineralic flows laws can be used to approximate the behaviour of two-phase rocks. Anderson (1972) pointed out that the diffusion of carbon and oxygen in dolomite is two orders of magnitude faster than in calcite. Moreover, Farver & Yund (1996) showed that in calcite-dolomite mixtures Ca is the species controlling diffusion, because Ca has the largest ionic radius of the constituent elements. Thus, diffusion is slowest in calcite and is rate-controlling in a calcite-dolomite mixture, so that the flow law for diffusion creep (Schmid et al. 1977) provides minimum strain rates. Therefore, as a first approximation to the rheological behaviour of the phase mixture the calcite flow laws for diffusion creep were applied.

The intersection of the grain size, calculated from the sectional areas, with the paleopiezometer of Rutter (1995) fix the position of the pure calcite layer in the deformation mechanism map. The grain size of pure calcite layers plot at the boundary between exponential flow (regime 1 in Schmid et al. 1980) and grain size sensitive creep (regime 3 in Schmid et al. 1977). This point is close to the triple junction of regime 1 (exponential flow), regime 2 (power law creep, $n = 7.6$) and regime 3 (regime 3, $n = 1.7$, $b = -3.0$). De Bresser et al. (1998, 2001) pointed out that the boundary region between the dislocation creep and diffusion creep field is a dynamic equilibrium between the two processes. Because of this reason dislocation creep and dynamic recrystallization may both contribute to the

deformation and the formation of a microstructure, even if the pure calcite layers are located outside the power law creep field.

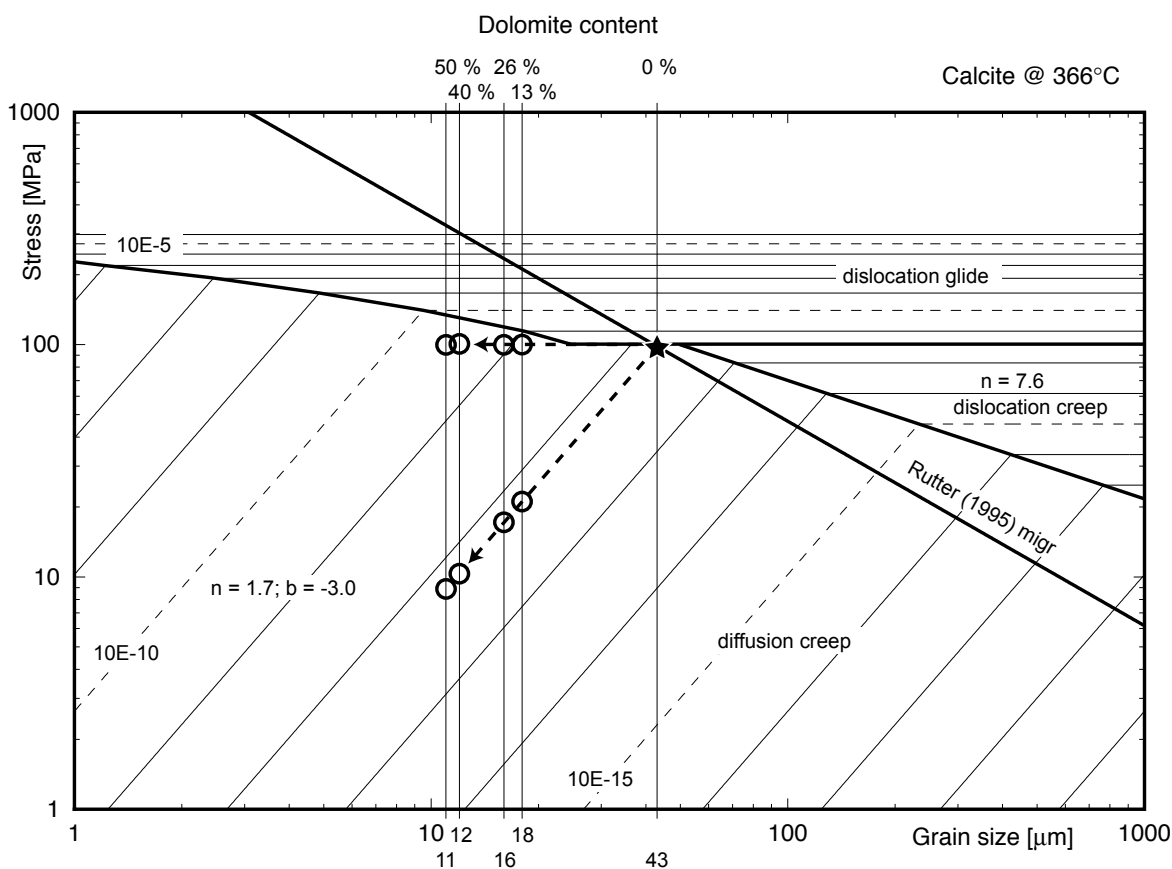


Fig. 4.17: Deformation mechanism map for calcite at 366°C, constructed from the flow laws for calcite from Schmid et al. (1977) (grain size sensitive flow, regime 3) and Schmid et al. (1980) (exponential flow, regime 1 and grain size insensitive flow, regime 2). Stress (n) exponent is indicated. The paleopiezometer of Rutter (1995) for grain boundary migration recrystallization is shown. The star indicates the intersection between the grain size (sectional size ($2D$)) of the pure calcite layer and the paleopiezometer. Note that the intersection is located in the boundary region of the three deformation regimes, for discussion see text. Two sets of circles and arrows indicate constant strain rate (higher stress values) and constant stress (lower stress values) conditions in the bulk sample.

From the results of the microstructural analysis it is concluded that the pure calcite layers of the sample was recrystallized dominantly by grain boundary migration recrystallization (fast migration of Urai et al. 1986). The application of the paleopiezometer of Rutter (1995) for migration recrystallization provides a stress of ~ 100 MPa for calcite in the pure layers (average sectional grain diameter 43 μm), corresponding to a strain rate of $\sim 10^{-12}$ s^{-1} . An increasing amount of dolomite leads to a reduction of calcite grain size. The application of these grain sizes to the piezometer for GBM yield unrealistic high stress values and the intersection of grain size and piezometer plot in the dislocation glide field. These inconsistencies indicate that dynamic recrystallization can be excluded as formation mechanism of the calcite grains in the mixed layers.

Starting from the position of the pure calcite layer in the DMM two endmembers of rheological behaviour can be considered; deformation at constant stress and deformation at constant strain rate (Schmid et al. 1983). Deformation under constant stress conditions would increase the strain rate from $\sim 10^{-12} \text{ s}^{-1}$ in the pure calcite layers to $\sim 5 \times 10^{-10} \text{ s}^{-1}$ in a layer composed to 50 vol-% of dolomite. At constant strain rate conditions calcite supports one order of magnitude less stress than the pure calcite layer. Both cases yield realistic geological strain rates and are consistent with experimental results (e.g. Bruhn et al. 1999), which showed that two-phase rocks deform either at lower stresses or at higher strain rates than their pure endmember phases. As a consequence natural deformation may localize into two-phase materials and accommodate therefore larger amounts of strain than mono-phase rocks.

4.7 Summary

A microstructural and textural analysis on two-phase carbonate rocks was carried out. The analyzed sample is derived from a Carrara marble shear zone from the Eastern Alpi Apuane close to the village of Arni. The sample is characterized by mm-scale layers composed to various volume proportions of calcite and dolomite. The mixed layers probably formed by continuous shearing of pre-existing dolomite veins. Samples, which may be similar to the starting material are found in the low grade metamorphic Panie Unit. In order to investigate the influence of dolomite on the deformation mechanism of calcite, five sites with 0 to 50 vol-% dolomite were analyzed. It became evident, that pure calcite layers deform dominantly by dislocation creep, as indicated by a GBM recrystallization microstructure and a basal $\langle a \rangle$ texture. With increasing dolomite content the texture becomes weaker and the orthorhombic symmetry of the basal $\langle a \rangle$ texture is increasingly randomized. Grain sizes get smaller and grain shapes less lobate, both arguing for an enhanced importance of diffusion creep at elevated second phase contents. The dispersed phase distribution and the appearance of dolomite at grain boundaries and triple junction suggest that grain boundary sliding contributes largely to the deformation of the mixed layers.

A constructed DMM for the determined deformation temperature and based on calcite flow laws were used to approximate the rheological behaviour of the pure and mixed layers. Two endmember types of rheological behaviour can be considered, constant stress and constant strain rate. Both endmembers yield realistic geological strain rates (10^{-10} to 10^{-12} s^{-1}), which are minimum values, because the presence of dolomite may cause an increase in strain rate. The presence of a second phase may lead to a change of the dominant deformation mechanism from dislocation creep in the pure calcite layers to diffusion creep in the mixed layers. The resulting decrease in flow stress or the increase in strain rate support the idea that the presence of a second phase causes the localization of deformation.

Chapter 5

Summary, Discussion and future work

The present study is concerned with deformation microstructures of naturally deformed Carrara marble from the Alpi Apuane. A large variety of dynamically recrystallized microstructures were found to be similar to those described by Molli et al. (1997) and Molli et al. (2000). In addition to statically recrystallized microstructures mainly two end members of ‘dynamic’ microstructures can be distinguished. These are grain boundary migration (GBM)-microstructures, with a coarse grain size, lobate grain boundaries and a preferred orientation of grain long axes and sub grain rotation (SGR)-microstructures characterized by coarse, lobate porphyroclasts embedded in a matrix of small, equiaxed recrystallized grains. The analyses of six shear zones sampled systematically across the Alpi Apuane reveals that D1 shear zones exhibit GBM-microstructures and D2 shear zones show SGR-microstructures. D1 microstructures correspond to type B1 after the classification of Molli et al. (2000) and D2 microstructures to type B2. Type A and type C microstructures in the sense of Molli et al. (2000) were not considered in this study.

On the scale of the Alpi Apuane distinct temperature gradients for D1 and D2 were detected. In the West D1 deformation occurred at higher temperatures (430°C) than D2 deformation (295°C), whereas in the East the deformation temperature of both events are the same (370°C). The regional temperature gradients obtained in the present study fit the temperature determination of ‘dynamic’ microstructures from D1 and D2 shear zones of Molli et al. (2000). This similarity supports the tectonic model suggested by Molli et al. (2000), in which the deformation in the Alpi Apuane is related to a west-directed subduction, nappe stacking and exhumation. Di Pisa et al. (1985) and Molli et al. (2000) determined temperatures from annealed marbles collected at various localities in the Alpi Apuane. They obtained a regional West to East temperature decrease from ~430 ° to ~370°C, which is similar to that of the D1 shear zones of this study. The fact that annealed and dynamic microstructures have formed at the same temperature indicates a simultaneous activity of annealing and deformation. It is therefore believed that the rock volume outside shear zones was annealed at the same time as deformation localized. Deformation and dynamic recrystallization must have continued until the temperature conditions were low enough to prevent a ‘static’ overprint, so that D1 deformation would have been active until the end of uplift and exhumation. A similar idea was proposed by Heitzmann (1987), who claims that dynamically recrystallized microstructures from the Central Alps are preserved today,

because deformation continued during uplift and exhumation. However, detailed structural field work in the Alpi Apuane carried out during this PhD-study confirms that D2 folds and shear zones clearly overprint the D1 deformation structures described by Carmignani et al. (1990, 1994) and Molli et al. (2000). Therefore, D1 cannot be active during the latest stages of deformation. An alternative explanation is related to the ionic exchange between calcite and dolomite. Below 500° C ionic exchange is very sluggish and can only be enhanced by dynamic recrystallization. Therefore, it can be concluded that the temperatures during D2 are much too low for the equilibration of calcite and dolomite, so that only dynamic recrystallization in the shear zones caused ionic equilibration and the resetting of the thermometer.

All D1 samples show a strong alignment of c-axes at a high angle to the S1 foliation plane. This is confirmed by CIP analyses, which yield pole figures with c-axes maxima perpendicular to S1 (D1 samples in Appendix C2) and by EBSD measurements, which additionally show a-axes girdle distributions parallel to S1 (Appendix C3). Considering easy slip conditions, this texture type can be explained in terms of basal <a> slip as dominant slip system (e.g. Schmid et al. 1987). Basal <a> slip is a common slip system in calcite, yet for a long time, it was considered of minor importance for the deformation of calcite (De Bresser 1991). Still, together with twinning textures (oblique c-axes maximum pointing toward the compression axis) basal <a> textures constitute, the typical texture types of natural calcite tectonites (Wenk 1985).

Recent studies of naturally and experimentally deformed calcite aggregates (e.g. Bestmann et al. 2000, Barnhoorn et al. 2004, Barnhoorn et al. in prep.) revealed an increasing importance of the basal <a> slip system with strain. Experimentally deformed Carrara marble to high strains ($\gamma < 50$, Barnhoorn et al. 2004) show the transition from e-twinning textures at low strains to basal <a> textures at high strains. The results of the microstructural and textural analysis of a mm-scale D2 shear zone from the Fondone area in the Alpi Apuane described in chapter 3, support the idea that textures do not only depend on P-T and strain rate conditions but vary as a function of accommodated strain.

The Fondone shear zone deforms the pre-existing S1 foliation. The protolith, which is a protomylonite with < 40 vol-% recrystallized grains (cf. chapter 3) is dominated by twinning with minor contributions of dynamic recrystallization. Towards the center of the shear zone it grades into a mylonite with a fine-grained recrystallized matrix. Behrmann (1983), Heitzmann (1987), Van der Pluijm (1991), Erskine et al. (1993) and Busch & Van der Pluijm (1995) described greenschist to amphibolite facies shear zones with similar microstructural features. These shear zones frequently display anastomosing structures, while strain markers are absent. As a consequence a direct relation of individual microstructural domains is unclear and absolute amounts of strain cannot be determined. The shear zone considered in this study, however, deforms the S1 foliation, which can be regarded as a passive marker and the development of microstructure and texture as a function of increasing shear strain

can be analyzed within a single thin section. The microstructure of individual sites along the S1 foliation shows increasing dynamic recrystallization from 0 to 100% with increasing $\dot{\gamma}$ from 0 to more than 20. The deformation temperature, determined by calcite-dolomite thermometry (mean value 325°C) stays constant both along S1 and parallel to the shear zone center.

The protolith next to this shear zone is characterized by a basal $\langle a \rangle$ texture of orthorhombic symmetry with respect to S1 and a monoclinic symmetry with respect to the shear plane. In the framework of the shear zone the c-axes maximum points towards the inferred σ_1 -direction, which is typical of mechanical twinning. However, the protolith texture probably formed during D1, because such textures are typical of D1 mylonites in the Alpi Apuane (Appendix C2). It is preserved, because textures can be very long lived (Rutter et al. 1994, Heilbronner & Tullis 2002) and may survive annealing and subsequent deformation phases, if dynamic recrystallization is absent. With increasing shear strain and increasing dynamic recrystallization the texture symmetry becomes orthorhombic with respect to the shear plane. Under simple shear and easy slip conditions, the formation of tilt wall boundaries during progressive SGR recrystallization leads to the formation of new grains with an orientation slightly rotated in the same sense as the overall shear. Consequently, with increasing strain the initially monoclinic texture becomes reoriented, so that in the center of the shear zone a basal $\langle a \rangle$ texture with orthorhombic symmetry is developed. Therefore it can be concluded that basal $\langle a \rangle$ slip is the dominant slip system at large shear strains. The c-axes maxima of the mylonite (cf. chapter 3 and sample 99-57 in Appendix C2) are slightly rotated towards the extension direction, which may indicate the continuation of the above described rotation process. Assuming this continued process, further SGR recrystallization transforms the basal $\langle a \rangle$ texture into a texture with a c-axes maximum (sub-) parallel to the extension direction. It may develop if the positive r-slip system becomes aligned to the shear plane and the shear direction. Barnhoorn et al. (2004), who used high strain torsion experiments to investigate the role of dynamic recrystallization on the mechanical behaviour and on the microfabric of experimentally deformed Carrara marble, found a transition from a twinning texture at low shear strains to a basal $\langle a \rangle$ texture at high shear strains. Consistent with the results of this study, the experimental study showed at very high shear strains ($\gamma \gg 20$) c-axes maxima, which are slightly rotated with the sense of the applied shear deformation. They proposed a balance of SGR- and GBM recrystallization to be the cause of the oblique tails in their c-axes pole figures. SGR recrystallization rotates the newly formed crystals away from the ideal easy slip orientation into a ‘hard’ crystallographic orientation and GBM recrystallization consumes those crystals unfavourably oriented, because of their higher dislocation density. As a consequence a further rotation of the texture is prevented and only a few grains are in a ‘hard’ orientation.

In nature such ‘forward’ rotated textures are found very rarely. Busch & Van der Pluijm (1995) found calcite mylonites from the Bancroft shear zone, Canada, with c-axes maxima

pointing towards the extension direction. They suggested that the slip plane of the basal <a> slip system must have rotated through the shear plane. However, it is possible that these textures formed by the same process as described above. Recently, a similar texture was also detected in calcite mylonites from the Western-Alps by Trullenque (pers. com., ongoing PhD study). The microstructural analyses of his samples reveal an increase of the rotation angle of the c-axes maximum as the finite strain increases. Samples, which accommodated the highest shear strains, exhibit a c-axes maximum inclined $\sim 45^\circ$ to the shear plane in the overall shear direction.

Schmid et al. (1987) proposed that elevated temperatures lead to GBM recrystallization and the development of a basal <a> texture, while at lower temperatures in the intracrystalline slip regime twinning and r- and f-slip are responsible for the formation of characteristic microstructures and textures. The strain of their experiments is always below $\gamma = 3$, so that the influence of strain on the formation of a microfabric could be investigated only to a limited extent. From the microstructures and textures of the natural shear zone of this study and those of the experimental study of Barnhoorn et al. (2004), however, it can be concluded, that strain is a major factor for the development of a microstructure and texture in calcite. At elevated temperatures dynamic recrystallization is more efficient (Barnhoorn et al. 2004) and requires lower strains to produce a given texture, than at lower temperatures.

Form the above the question arises, which are the most important factors leading to the localization of deformation and the formation of the Fondone shear zone. One possible solution is the presence of coarse-grained calcite, which appears repeatedly in the shear zone center (cf. Appendix C2). D2 shear zones (e.g. samples 98-19, 99-57, 2k-13 in Appendix C2) are frequently associated with such coarse-grained material, which are interpreted as relicts of pre-existing calcite veins. That such vein formation is prior to the ductile deformation can be deduced from the fact that the vein calcite is intensively mechanically twinned and shows evidence of twin boundary migration and beginning of SGR recrystallization. Assuming the shear deformation started with dislocation glide and twinning the coarse-grained calcite veins would have been deformed preferentially, because coarse-grained materials deform at lower flow stresses than fine-grained ones, as described by the Hall-Petch relationship (Nicolas & Poirier 1976). Kennedy & White (2001) investigated low temperature calcite shear zones, which are characterized by the cyclic introduction of coarse-grained calcite veins. With temperatures too low for the activation of dislocation creep (150° - 250°C), dislocation glide is the only deformation mechanism available for the accommodation of the bulk strain. Mechanical twinning and twin boundary migration lead to a reduction of grain size and thus to strain hardening owing to the Hall-Petch relationship. Decreasing permeability associated with mylonite development promotes the build-up of pore-fluid pressure, which in turn leads to the fragmentation of the rock and the renewed introduction of calcite veins. The sample discussed in this study only shows evidence of the first part of one of these cycles. Twinning reduces the calcite grain size and newly formed twin boundaries represent preferred sites of

dynamic recrystallization (Vernon 1981). Mechanical twinning is more efficient in coarse-grained materials (Schmid et al. 1981) and can accommodate only a limited amount of strain (~15%, Burkhard 1993). Because of this reason the initial vein calcite is after a certain amount of strain reduced to a size, where twinning is unfavourable. Since the temperature is high enough intracrystalline slip is abandoned in favour of dislocation creep and dynamic recrystallization.

In other shear zones of the Alpi Apuane, where coarse-grained precursors are absent, other mechanisms have to be operative to initiate localization. A number of field studies pointed out that deformation is concentrated in fine-grained poly-phase layers (e.g. Stünitz & Fitz Gerald 1993). Many natural calcite shear zones in Carrara marble are in fact associated with high volume percentages of dolomite. This suggests that the presence of dolomite may be related to the localization of deformation. In order to investigate the influence of dolomite on the deformation of calcite and to study the rheological behaviour of calcite-dolomite mixtures a layered calcite-dolomite shear zone was investigated (Arni shear zone, chapter 4). It turned out, that pure calcite layers deform dominantly by dislocation creep, as indicated by a 'dynamic' microstructure and a pronounced texture (CPO). The texture type is consistent with basal $\langle a \rangle$ slip arguing for large finite strains, as discussed above. With increasing dolomite content the calcite grain size decreases and the grains become less lobate, while dolomite maintains its small grain size and convex shape. At the same time the CPO of calcite weakens and become almost completely randomized. It is well documented in the literature that small grain sizes, equiaxed grains with straight boundaries and weak textures are characteristic of diffusion creep (e.g. Schmid et al. 1977, Walker et al. 1990).

In all layers dolomite seems to be undeformed and rheologically passive. Its contribution to the deformation of the rock is not entirely clear, however its presence probably causes the transition from a dislocation creep dominated deformation in the pure calcite layers to a diffusion creep dominated deformation in the mixed calcite-dolomite layers. Heterogeneous nucleation of dolomite in voids, which probably opened during grain boundary sliding, as proposed by Kruse & Stünitz (1999) for hornblende in plagioclase, leads to a dispersion of phases and an increase in the number of phase boundaries. An increasing fraction of phase boundaries (with respect to the total amount of grain boundaries) enhances diffusion and thus, the activity of diffusion creep (Bruhn et al. 1999).

The above-described transition from dislocation creep to diffusion creep is also already proposed by Herwegh & Berger (submitted) for impure limestones from the Helvetic Alps. They described variations in microstructure and texture as a function of grain size and volume fraction of the second phase and distinguished two microfabrics. The first one comprises microfabrics, which show no or only a weak dependence of calcite grain size and texture on second phase content and particle size ('second phase affected microfabric'). The second type of microfabrics is strongly controlled by the presence of the second phase ('second phase controlled microfabric'). Increasing second phase content and grain size

cause a decrease of calcite grain size, a weakening of the calcite texture and an increase of the fraction of phase boundaries.

A deformation mechanism map based on the flow laws for pure calcite (Schmid et al. 1977, Schmid et al. 1980) and the paleopiezometric determination of the flow stress (~ 100 MPa) indicate that the deformation of the pure calcite layers occurred at strain rates of ~ 10 - 12 s^{-1} . Because of the smaller grain size the calcite in the mixed layers must deform either at higher strain rates (up to $\sim 5 \times 10^{-10} \text{ s}^{-1}$) or at lower stresses (~ 10 MPa). Both higher strain rates and lower stress promote a localization of deformation into the mixed layers, so that the presence of a second phase indeed can cause localization.

At the end of this discussion a number of topics and questions can be raised, from which future projects may be developed. These topics, questions and unsolved problems are listed below; they concern the regional geology and the analysis of microstructures and textures of naturally deformed carbonate rocks.

1) Regional geology of the Alpi Apuane

In the present study the deformation temperatures were determined only for a few samples. The existing data set is incomplete and the understanding of the regional distribution of deformation and annealing temperatures remains limited. Thus, more temperature determinations on structurally well-constrained samples are desirable.

This study proposes, that D1a and D1b belong to a continuous deformation event rather than to be separated phases. Relative timing and the relationship of D1a and D1b to the annealing event are still unclear. Detailed microstructural analysis in connection with temperature determinations would give insight in these relationships.

A further important topic for the understanding of the Alpi Apuane structure is concerned with the up-right mega-antiform of the 'dome-structure' in the Eastern Alpi Apuane. It is believed to be related to the D2 deformation event. However, its internal structure and its relationship to the typical sub-horizontal D2 fold structures and shear zones is still unclear. Therefore, detailed structural field work in the 'Boana-', Monte Sumbra- and Monte Fiocca area can elucidate the meaning of the mega-antiform in the Alpi Apuane structure.

2) Microstructure, texture and deformation mechanism

The analysis of the calcite-dolomite shear zone in Carrara marble revealed that dolomite has a strong influence on the deformation mechanism of calcite. However, the deformation behaviour of dolomite remained unclear and it was suggested that dolomite is rheologically passive. Deformation experiments on calcite-dolomite mixtures are needed to arrive at a better understanding of the formation of the microstructure and texture in the individual phases. Theoretical and experimental work is needed to formulate flow

laws describing the rheological behaviour of a phase mixture deformation by dislocation creep and/or diffusion creep. The experimental results can be compared to those of natural shear zones from the Alpi Apuane, where calcite-dolomite marbles are frequently exposed. Examples of microstructures of natural calcite-dolomite shear zones are those of sample D1-E-1 (99-59, Appendix C2) and sample D1-E-2 (99-49, Appendix C2).

3) Annealing and diffusion

Carrara marble is well known for its annealed microfabric. The influence of annealing on the microstructure and texture is still not completely understood. Annealed marbles are characterized by 'foam-structures' with coarse grain sizes and straight grain boundaries with 120° triple junctions. Microscopically observations at higher magnifications reveal that the straight boundaries are formed by a staircase arrangement of individual grain boundary segments. The segments correspond to crystallographic low index planes with low surface energies. Detailed CIP and EBSD investigations could help to identify the preferred crystallographic planes. Grain boundary and volume diffusion are mechanisms by which ionic exchange is controlled. Calcite-dolomite thermometry is based on ionic exchange and temperature determinations from natural marbles yield frequently values, which are close to the limits of the analytical methods. The understanding of diffusion processes and rates is too limited, so that further experimental studies are required.



Acknowledgements

Many persons have contributed in a number of ways to this thesis and to all of them belong many thanks.

First of all I want to thank my supervisors Renée Heilbronner and Holger Stünitz for initiating this project and for numerous discussions on structural geology, rock deformation, image analysis and many more. From these discussions I learned very much, I am very grateful for this time!

I would also like to thank Giancarlo Molli, who introduced me to the Alpi Apuane geology, taught me structural geology in the field and supported me in all logistical concerns during my field work in Italy. Without his knowledge of the Alpi Apuane this thesis would have been impossible!

Many thanks also go to Marco Herwegh and Karsten Kunze for many very fruitful discussions and their continuous support and interest in my studies.

Special thanks go to Stefan Schmid, Bernhard Fügenschuh, Niko Froitzheim and Michael Stipp, for their decision to offer me this PhD-position. I also wish to thank Stefan Schmid for his interest in my thesis and a few but very fruitful and stimulating discussions.

Willi Tschudin prepared all the ultra-thin sections on which the major part of this thesis is based on. I know it took a long and sometimes frustrating time to develop the right technique, thanks a lot for your effort. Many thanks also belong to Hans-Ruedi Rüegg, who supplied and supported me in all mechanical concerns.

Auke Barnhoorn contributed significantly to this thesis, not just by many stimulating discussions during a number of EBSD session (he carried out all the measurements), but also during many hiking trips in the Alps and the Jura mountains. Thanks Auke, I really benefited a lot!

Special thanks go to Michael Stipp and Almar de Ronde, my room mates during the last four and a half years. I greatly benefited from discussions and suggestions from Michael and learned a lot from Almar's FORTRAN programming knowledge.

Furthermore, I like to thank Achim Reisdorf and Lukas Keller for our weakly meetings in the 'Langen Erlen'.

Many thanks go to all my colleagues and friends who supported me in this or that way during my time at the GPI. Thank you all for the common time.

Last but not least I would like to thank Simone Buser for supporting me in a non-scientific way and bearing me during stressful moments.



References

- Abbate, E., Balestrieri, M. L., Bigazzi, G., Norelli, P. & Quercioli, C. 1994. Fission-track dating and recent rapid denudation in the Northern Apennines, Italy. *Mem. Soc. Geol. Ital.* **48**, 579-585.
- Adams, B. L., Wright, S. I. & Kunze, K. 1993. Orientation imaging: the emergence of a new microscopy. *Metallurgical Transactions* **24A**(4), 819-830.
- Anderson, T. F. 1972. Self-Diffusion of Carbon and Oxygen in Dolomite. *Journal of Geophysical Research* **77**(5), 857-861.
- Anovitz, L. M. & Essene, E. J. 1987. Phase Equilibria in the System CaCO_3 - MgCO_3 - FeCO_3 . *Journal of Petrology* **28**(2), 389-414.
- Ashby, M. F. & Varell, R. A. 1977. Micromechanisms of flow and fracture, and their relevance to the rheology of the upper mantle. *Phil. Trans. Roy. Soc. Lond.* **288A**, 59-95.
- Barber, D. J. 1977. Defect microstructures in deformed and recovered dolomites. *Tectonophysics* **39**, 193-213.
- Barber, D. J. & Wenk, H.-R. 1979. Deformation Twinning in Calcite, Dolomite, and Other Rhombohedral Carbonates. *Physics and Chemistry of Minerals* **5**, 141-165.
- Barber, D. J., Heard, H. C. & Wenk, H.-R. 1981. Deformation of Dolomite Single Crystals from 20-80°C. *Physics and Chemistry of Minerals* **7**, 271-286.
- Barber, D. J. & Wenk, H.-R. 2001. Slip and dislocation behaviour in dolomite. *European Journal of Mineralogy* **13**, 221-243.
- Barnhoorn, A., 2003. Rheological and microstructural evolution of carbonate rocks during large. PhD-Thesis, ETH Zurich, 141 pp.
- Barnhoorn, A., Bystricky, M., Kunze, K. & Burlini, L. in prep. Post-deformational annealing of calcite rocks.
- Barnhoorn, A., Bystricky, M., Kunze, K. & Burlini, L. 2004. The role of recrystallization on the deformation behaviour of calcite rocks: Large strain torsion experiments on Carrara marble. *Journal of Structural Geology* **26**, 885-903.
- Behrmann, J. 1983. Microstructure and fabric transitions in calcite tectonites from the Sierra Alhamilla (Spain). *Geologische Rundschau* **72**(2), 605-618.
- Bestmann, M., Kunze, K. & Matthews, A. 2000. Evolution of a calcite marble shear zone complex on Thassos Island, Greece: microstructural and textural fabrics and their kinematic significance. *Journal of Structural Geology* **22**, 1789-1807.
- Bickle, M. J. & Powell, R. 1977. Calcite-Dolomite Geothermometry for Iron-Bearing Carbonates. *Contributions to Mineralogy and Petrology* **59**, 281-292.
- Boccaletti, M., Coli, M. & Gosso, G. 1982. Strutture di interferenza a scala megascopica nel settore Nord delle Alpi Apuane. *Memorie Società Geologica Italiana* **24**, 289-292.
- Bonatti, S. 1938. Studio petrografico delle Alpi Apuane. *Memorie Descrittive della Carta Geologica d'Italia* **26**, 116.
- Bouchez, J. L. 1977. Plastic deformation of quartzites at low temperature in an area of natural strain gradient. *Tectonophysics* **39**, 25-30.
- Bouchez, J. L. & Duval, P. 1982. The fabric of polycrystalline ice deformed in simple

- shear: experiments in torsion, natural deformation and geometrical interpretation. *Textures and Microstructures* **5**, 171-190.
- Bradley, F. 1999. *Marble quarrying*. Panorama, Pisa.
- Bruhn, D., Olgaard, D. L. & Dell'Angelo, L. N. 1999. Evidence for enhanced deformation in two-phase rocks: Experiments on the rheology of calcite-anhydrite aggregates. *Journal of Geophysical Research* **104**(B1), 707-724.
- Burg, J.-P. & Wilson, C. J. L. 1987. Deformation of two phase systems with contrasting rheologies. *Tectonophysics* **135**, 199-205.
- Burkhard, M. 1990. Ductile deformation mechanisms in micritic limestones naturally deformed at low temperatures (150–350°C). In: *Deformation Mechanisms, Rheology and Tectonics* (edited by Knipe, R. J. & Rutter, E. H.). *Geological Society of London Special Publication* **54** **54**, 241-257.
- Burkhard, M. 1993. Calcite twins, their geometry, appearance and significance as stress-strain markers and indicators of tectonic regime: a review. *Journal of Structural Geology* **15**(3-5), 351-368.
- Burlini, L. & Kunze, K. 2000. Fabric and Seismic Properties of Carrara Marble Mylonite. *Physics and Chemistry of the Earth* **25**(2), 133-139.
- Burrus, J. 1984. Contribution to a geodynamic synthesis of the Provençal basin (north-western) Mediterranean. *Mar. Geol.* **55**, 247-269.
- Busch, J. P. & Van der Pluijm, B. A. 1995. Calcite textures, microstructures and rheological properties of marble mylonites in the Bancroft shear zone, Ontario, Canada. *Journal of Structural Geology* **17**(5), 667-688.
- Carmignani, L., Giglia, G. & Kligfield, R. 1978. Structural evolution of the Apuane Alps: An example of continental margin deformation in the northern Apennines, Italy. *Journal of Geology* **86**, 487-504.
- Carmignani, L. & Giglia, G. 1979. Large scale reverse <<drag folds>> in the late alpine building of the Apuane Alps (N. Apennines). *Atti Soc. Toc. Sci. Mem.* **86**, 109-125.
- Carmignani, L. 1985. Carta geologico-strutturale delle Alpi Apuane, Foglio Nord, Litografia Artistica Cartografica, Firenze, scala 1:25.000.
- Carmignani, L., Gattiglio, M., Kalin, O. & Meccheri, M. 1987. Guida all'escursione sul complesso metamorfico delle Alpi Apuane, Carrara.
- Carmignani, L. & Kligfield, R. 1990. Crustal extension in the northern apennines: the transition from compression to extension in the Alpi Apuane core complex. *Tectonics* **9**(6), 1275-1303.
- Carmignani, L., Decandia, F. A., Fantozzi, P. L., Lazzarotto, A., Liotta, D. & Meccheri, M. 1994. Tertiary extensional tectonics in Tuscany (Northern Apennines, Italy). *Tectonophysics* **238**, 295-315.
- Casey, M., Kunze, K. & Olgaard, D. L. 1998. Texture of Solenhofen limestone deformed to high strains in torsion. *Journal of Structural Geology* **20**(2/3), 255-267.
- Chen, I.-W. 1983. Effects of boundary mobility and phase equilibrium on kinematic processes of multicomponent polyphase ceramics. In: *Character of Grain Boundaries* (edited by Yan, M. F. & Heuer, A. H.). Am. Ceram. Soc., Westville, Ohio, 224-235.
- Ciarapica, G. & Passeri, L. 1983. Coated Grains in Contrasted Environmental Situations: Norian and Lower Liassic of Northern Apennines. In: *Coated grains* (edited by Peryt, T. M.). Springer-Verlag, Berlin.
- Ciarapica, G. & Passeri, L. 1994. The Tuscan Nappe in Northern Apennines: Data, Doubts, Hypotheses. *Mem. Soc. Geol. It.* **48**, 7 - 22.
- Colacicchi, R., Passeri, L. & Piali, G. 1975. Evidence of Tidal Environment Deposition in

- the Calcare Massiccio formation (Central Apennines–Lower Lias).
- Coli, M. 1989. Litho-structural assemblage and deformation history of “Carrara marble”. *Bollettino della Società Geologica Italiana* **108**, 581-590.
- Covey-Crump, S. J. & Rutter, E. H. 1989. Thermally-induced grain growth of calcite marbles on Naxos Island, Greece. *Contributions to Mineralogy and Petrology* **101**, 69-86.
- Covey-Crump, S. J. 1997. The normal grain growth behaviour of nominally pure calcitic aggregates. *Contributions to Mineralogy and Petrology* **129**, 239-254.
- Covey-Crump, S. J. 1997. The high temperature static recovery and recrystallization behaviour of cold-worked Carrara marble. *Journal of Structural Geology* **19**(2), 225-241.
- Crisci, G. M., Leoni, L. & Sbrana, A. 1975. La formazione dei marmi delle Alpi Apuane (Toscana; studio petrografico, mineralogico e chimico). *Atti della Società Toscana die Scienza Naturali, Memorie, Serie A* **82**, 199-236.
- D’Albissin, M. 1963. Les traces de la déformation dans les roches calcaires. *Revue de géogr. physique et de géologie dynamique (fascicule supplémentaire)*, 174.
- De Bresser, H. 1989. Calcite c-axis textures along the Gavarnie thrust zone, Central Pyrenees. *Geol. Mijnbouw* **68**, 367-375.
- De Bresser, J. H. P. 1991. Intracrystalline deformation of calcite. Unpublished PhD thesis, University of Utrecht.
- De Bresser, J. H. P., Peach, C. J., Reijs, J. P. J. & Spiers, C. J. 1998. On dynamic recrystallization during solid state flow: effects of stress and temperature. *Geophysical Research Letters* **25**, 3457-3460.
- De Bresser, J. H. P., Ter Heege, J. H. & Spiers, C. J. 2001. Grain size reduction by dynamic recrystallization: can it result in major rheological weakening? *International Journal of Earth Sciences* **90**, 28-45.
- Deer, W. A., Howie, R. A. & Zussman, J. 1998. *An Introduction to the Rock-Forming Minerals*. Pearson Education Limited.
- Di Pisa, A., Franceschelli, M., Leoni, L. & Meccheri, M. 1985. Regional variations of the metamorphic temperatures across the Tuscanid 1 Unit and its implications on the alpine metamorphism (Apuan Alps, N-Tuscany). *Neues Jahrbuch für Mineralogie, Abhandlungen* **151**, 197-211.
- Di Sabatino, B., Giampaolo, C. & Negretti, G. 1977. Metamorfismo di “very low grade” ad altissimo pressione nella “Unità delle Panie”. *Per. Mineral.* **46**, 79-89.
- Dietrich, D. & Song, H. 1984. Calcite fabrics in a natural shear environment, the Helvetic nappes of western Switzerland. *Journal of Structural Geology* **6**(1/2), 19-32.
- Dingley, D. J. & Randle, V. 1992. Microtexture determination by electron back-scatter diffraction. *Journal of Material Science* **27**, 4545-4566.
- Dolci, E. 1988. Marmora Lunensia: Quarrying technology and archaeological use. In: *Classical Marble: Geochemistry, Technology, Trade* (edited by Herz, N. & Waelkens, M.), 77-84.
- Dresen, G., Evans, B. & Olgaard, D. L. 1998. Effect of quartz inclusions on plastic flow in marble. *Geophysical Research Letters* **25**(8), 1245-1248.
- Drury, M. R. & Humphreys, F. J. 1985. Large strain deformation studies using polycrystalline magnesium as a rock analogue; Part II, Dynamic recrystallisation mechanisms at high temperatures. In: *Experiments in solid state physics relevant to lithospheric dynamics* (edited by Gueguen, Y., Kern H.). Elsevier Amsterdam, Netherlands.
- Drury, M. R. & Urai, J. L. 1990. Deformation-related recrystallization processes.

- Tectonophysics* **172**(3-4), 235-253.
- Durand, E. & Comes, G. 1974. L'essai de torsion et la résistance au cisaillement des roches. In: *Advances in Rock Mechanics: Proceedings of the Third Congress of the International Society for Rock Mechanics National Academy of Sciences, Washington, D.C.*, Denver, Colorado Sept. 1-7, 1974, 226-232.
- Elter, P. 1975. Introduction à la géologie de l'Apennin septentrional. *Bulletin de la Société Géologique de France* **7**, 956-962.
- Erskine, B. G., Heidelbach, F. & Wenk, H.-R. 1993. Lattice preferred orientations and microstructures of deformed Cordilleran marbles: correlation of shear indicators and determination of strain path. *Journal of Geology* **15**(9/10), 1189-1205.
- Essene, E. J. 1982. Geologic thermometry and barometry. In: *Characterization of metamorphism through mineral equilibria* (edited by Ferry, J. M.) **10**. Mineralogical Society of America. Washington, DC, 153-206.
- Essene, E. J. 1983. Solid solutions and solvi among metamorphic carbonates with applications to geologic thermobarometry. In: *Carbonates; mineralogy and chemistry* (edited by Reeder, R. J.) **11**. Mineralogical Society of America. Washington, DC, 77-96.
- Farver, J. R. & Yund, R. A. 1996. Volume and grain boundary diffusion of calcium in natural and hot-pressed calcite aggregates. *Contributions to Mineralogy and Petrology* **123**, 77-91.
- Franceschelli, M., Leoni, L., Memmi, I. & Puxeddu, M. 1986. Regional distribution of Al-silicates and metamorphic zonation in the low-grade Verrucano metasediments from the Northern Apennines, Italy. *Journal of metamorphic Geology* **4**, 309-321.
- Franceschelli, M., Memmi, I., Carcangiu, I. & Gianelli, G. 1997. Prograde and retrograde chloritoid zoning in low temperature metamorphism, Alpi Apuane, Italy. *Schweizerische Mineralogische und Petrologische Mitteilungen* **77**, 41-50.
- Fredrich, J. T., Evans, B. & Wong, T. F. 1989. Micromechanics of the brittle to plastic transition in Carrara Marble. *Journal of Geophysical Research* **B 94**, 4129-4145.
- Frost, H. J. & Ashby, M. F. 1982. *Deformation mechanism-maps. The Plasticity and Creep of Metals and Ceramics*. Pergamon Press, Oxford.
- Giannini, E. & Lazzarotto, E. A. 1975. Tectonic Evolution of the Northern Apennines. In: *Geology of Italy* (edited by Squyres, C.). Tripoli.
- Giese, P., Reutter, K. J., Jacobshagen, V. & Nicolich, R. 1982. Explosion seismic crustal studies in the alpine mediterranean region and their implications to tectonic processes. In: *Alpine Mediterranean Geodynamics* (edited by H. Berkhemer, K. H.). *Geodyn. Ser. 7*. AGU, Washington D.C.
- Goetze, C. & Kohlstedt, D. L. 1977. The Dislocation Structure of Experimentally Deformed Marble. *Contributions to Mineralogy and Petrology* **59**, 293-306.
- Goldschmidt, J. R. & Heard, H. C. 1961. Subsolidus phase relations in the system CaCO_3 - MgCO_3 . *Journal of Geology* **69**(1), 45-74.
- Griggs, D. T., Turner, F. J., Borg, I. & Sosoka, J. 1951. Deformation of Yule marble, Part IV. *Geol. Soc. America Bull.* **62**, 1385-1406.
- Guillope, M. & Poirier, J.-P. 1979. Dynamic recrystallization during creep of single-crystalline halite; an experimental study. *Journal of Geophysical Research* **84**, 5557-5567.
- Handin, J. & Griggs, D. T. 1951. Deformation of Yule marble, Part II. *Geol. Soc. America Bull.* **62**, 863-885.
- Handin, J., Higgs, D. V. & O'Brien, J. K. 1960. *Torsion of Yule marble under confining pressure*. Rock Deformation, Vol.79

-
- Handy, M. R. 1990. The Solid-State Flow of Polymineralic Rocks. *Journal of Geophysical Research* **95**(B6), 8647-8661.
- Handy, M. R. 1992. Correction and Addition to “The Solid-State Flow of Polyphase Rocks”. *Journal of Geophysical Research* **97**(B2), 1897-1899.
- Harker, R. I. & Tuttle, O. F. 1955. Studies in the system CaO-MgO-CO₂; Part 1, The thermal dissociation of calcite, dolomite and magnesite; Part 2, Limits of solid solution along the binary join CaCO₃-MgCO₃. *American Journal of Science* **253**(4), 209-224.
- Heard, H. C. 1963. Effect of large strain rate in the experimental deformation of Yule marble. *Journal of Geology* **71**, 162-195.
- Heard, H. C. 1968. Steady-state flow in Yule marble at 500 degrees -800 degrees C. *Transactions - American Geophysical Union* **59**(1), 312.
- Heard, H. C. & Raleigh, C. B. 1972. Steady-state flow in marble at 500° to 800°C. *Geological Society of America Bulletin* **83**, 935-956.
- Heilbronner, R. & Bruhn, D. 1998. The influence of three-dimensional grain size distributions on the rheology of polyphase rocks. *Journal of Structural Geology* **20**(6), 695-705.
- Heilbronner, R. 2000. Automatic grain boundary detection and grain size analysis using polarization micrographs or orientation images. *Journal of Structural Geology* **22**, 969-981.
- Heilbronner, R. & Tullis, J. 2002. The effect of static annealing on microstructure and crystallographic preferred orientations of quartzites experimentally deformed in axial compression and shear. In: *Deformation Mechanisms, Rheology and Tectonics: Current Status and Future Perspectives* (edited by de Meer, S., Drury, M. R., de Bresser, J. H. P. & Pennock, G.). *Special Publication* **200**. Geological Society, London, 191-218.
- Heitzmann, P. 1987. Calcite mylonites in the Central Alpine “root zone”. *Tectonophysics* **135**, 207-215.
- Herwegh, M. & Handy, M. R. 1998. The origin of shape preferred orientations in mylonite: inferences from *in-situ* experiments on polycrystalline norcamphor. *Journal of Structural Geology* **20**(6), 681-694.
- Herwegh, M. 2000. A new technique to automatically quantify microstructures of fine grained carbonate mylonites: two-step etching combined with SEM imaging and image analysis. *Journal of Structural Geology* **22**, 391-400.
- Herwegh, M. & Kunze, K. 2002. The influence of nano-scale second-phase particles on deformation of fine grained calcite mylonites. *Journal of Structural Geology* **24**, 1463-1478.
- Herwegh, M., de Bresser, H. & Ter Heege, J. H. 2002. Composite Grain Size Sensitive and Grain Size Insensitive Flow of Naturally Deformed Calcite Mylonites: Evidence From Quantitative Microstructural Analysis. In: *AGU Fall Meeting 2002*, San Francisco.
- Herwegh, M. & Berger, A. submitted. Deformation mechanisms in Zener dragged systems and their microstructural energy balance.
- Hirth, G. & Tullis, J. 1992. Dislocation creep regimes in quartz aggregates. *Journal of Structural Geology* **14**(2), 145-159.
- Hirth, G., Teyssier, C. & Dunlap, W. J. 2001. An evaluation of quartzite flow laws based on comparisons between experimentally and naturally deformed rocks. *International Journal of Earth Sciences* **90**, 77-87.
- Ji, S., Wang, Z. & Wirth, R. 2001. Bulk flow strength of forsterite–enstatite composites as a

- function of forsterite content. *Tectonophysics* **341**, 69-93.
- Jolivet, L., Faccenna, C., Goffé, B., Mattei, M., Rossetti, F., Brunet, C., Storti, F., Funicello, R., Cadet, J., P., d'Agostino, N. & Parra, T. 1998. Midcrustal shear zones in postorogenic extension: Example from the northern Tyrrhenian Sea. *Journal of Geophysical Research* **103**(B6), 12,123 - 12,160.
- Jordan, P. G. 1987. The deformation behaviour of biminerale limestone-halite aggregates. *Tectonophysics* **135**, 185-197.
- Jordan, P. G. 1988. The rheology of polymineralic rocks-an approach. *Geologische Rundschau* **77**(1), 285-294.
- Kennedy, L. A. & White, J. C. 2001. Low-temperature recrystallization in calcite: Mechanisms and consequences. *Geology* **29**(11), 1027-1030.
- Kligfield, R. 1979. The Northern Apennines as a Collisional Orogen. *American Journal of Science* **279**, 676-691.
- Kligfield, R., Hunziker, J., Dallmeyer, R. D. & Schamel, S. 1986. Dating of deformation phases using K-Ar and $^{40}\text{Ar}/^{39}\text{Ar}$ techniques: results from the Northern Apennines. *Journal of Structural Geology* **8**(7), 781-798.
- Kretz, R. 1969. On the spatial distribution of crystals in rocks. *Lithos* **2**, 39-66.
- Kruse, R. & Stünitz, H. 1999. Deformation mechanisms and phase distribution in mafic high-temperature mylonites from the Jotun Nappe, southern Norway. *Tectonophysics* **303**, 223-249.
- Kunze, K., Wright, S. I., Adams, B. L. & Dingley, D. J. 1993. Advances in automatic EBSD single orientation measurements. *Textures and Microstructures* **20**, 41-54.
- Lafrance, B., White, J. C. & Williams, P. F. 1994. Natural calcite *c*-axis fabrics: an alternative interpretation. *Tectonophysics* **229**, 1-18.
- Law, R. D. 1990. Crystallographic fabrics: a selective review of their application to research in structural geology. In: *Deformation Mechanisms, Rheology and Tectonics* (edited by Knipe, R. J. & Rutter, E. H.) **54**. Geological Society Special Publication, 335-352.
- Leiss, B. & Barber, D. J. 1999. Mechanisms of dynamic recrystallization in naturally deformed dolomite inferred from EBSD analyses. *Tectonophysics* **303**, 51-69.
- Leiss, B. & Weiss, T. 2000. Fabric anisotropy and its influence on physical weathering of different types of Carrara marbles. *Journal of Structural Geology* **22**(11-12), 1731-1745.
- Leiss, B., Molli, G. & Oesterling, N. 2001. Temperature independent texture variations in Carrara Marble - new evidence from a calcite marble fold from the Alpi Apuane, Italy. In: *Deformation Mechanisms, Rheology and Tectonics*, International Conference Utrecht, Netherlands.
- Leiss, B. & Molli, G. 2003. 'High-temperature' texture in naturally deformed Carrara marble from the Alpi Apuane, Italy. *Journal of Structural Geology* **25**, 649-658.
- Lieberman, J. E. & Rice, J. M. 1986. Petrology of marble and peridotite in the Seiad ultramafic complex, northern California, USA. *Journal of metamorphic Geology* **4**, 179-199.
- Machel, H. G. & Burton, E. A. 1991. Factors Governing Cathodoluminescence in Calcite and Dolomite, and Their Implications for Studies of Carbonate Diagenesis. In: *Luminescence Microscopy: Quantitative and Qualitative Aspects* (edited by Baker, C. E. & Kopp, O. C.) - **SEPM Short Course 25**, 37-57.
- Machel, H. G., Mason, R. A., Mariano, A. N. & Mucci, A. 1991. Causes and Emission of Luminescence in Calcite and Dolomite. In: *Luminescence Microscopy: Quantitative and Qualitative Aspects* (edited by Baker, C. E. & Kopp, O. C.) - **SEPM Short**

Course 25, 9-25.

- Malavieille, J. 1982. Etude tectonique de la déformation ductile dans de grands chevauchements crustaux: Exemple des Alpes franco italiennes et de la Corse. Unpublished D. Sc. thesis, Montpellier.
- Mattauer, M., Faure, M. & Malavieille, J. 1981. Transverse lineation and large scale structures related to Alpine obduction in Corsica. *Journal of Structural Geology* **3**, 401-409.
- Matthews, A., Lieberman, J., Avigad, D. & Garfunkel, Z. 1999. Fluid-rock interaction and thermal evolution during thrusting of an Alpine metamorphic complex (Tinos island, Greece). *Contributions to Mineralogy and Petrology* **135**, 212-224.
- Means, W. D. 1983. Microstructure and micromotion in recrystallization flow of octochloropropane, a first look. *Geol. Rdschau*. **72**, 511-528.
- Means, W. D. 1995. Shear zones and rock history. *Tectonophysics* **247**, 157-160.
- Miller, J. K. & Folk, R. L. 1994. Petrographic, geochemical and structural constraints on the timing and distribution of postlithification dolomite in the Rhaetian Portoro ('Calcere Nero') of the Portovenere Area, La Spezia, Italy. *Spec. Publs. Int. Ass. Sediment.* **21**, 187-202.
- Molli, G., Heilbronner, R. & Wittensölner, V. 1997. Microstructures of naturally deformed marbles from the Alpi Apuane (NW Italy). In: *Deformation mechanisms in nature and experiment* (edited by Schmid, S. M., Stünitz, H. & Heilbronner, R.), Basel.
- Molli, G. & Heilbronner, R. 1999. Microstructures associated with static and dynamic recrystallization of Carrara marble (Alpi Apuane, NW Tuscany, Italy). *Geologie en Mijnbouw* **78**, 119-126.
- Molli, G., Conti, P., Giorgetti, G., Meccheri, M. & Oesterling, N. 2000. Microfabric study on the deformational and thermal history of the Alpi Apuane marbles (Carrara marbles), Italy. *Journal of Structural Geology* **22**, 1809-1825.
- Molli, G. 2002. Field Trip Eastern Liguria/Alpi Apuane (15-19 May 2002), Pisa, 58.
- Neumann, E.-R. 1969. Experimental recrystallization of dolomite and comparison of preferred orientation of calcite and dolomite in deformed rocks. *Journal of Geology* **77**, 426-438.
- Newman, J. & Mitra, G. 1994. Fluid-influenced deformation and recrystallization of dolomite at low temperatures along a natural fault zone, Mountain City window, Tennessee. *Geological Society of America Bulletin* **106**, 1267-1280.
- Nicolas, A. & Poirier, J. P. 1976. *Crystalline plasticity and solid state flow in metamorphic rocks*. John Wiley & Sons. London.
- Olgaard, D. A. & Evans, B. 1986. Effect of second-phase particles on grain-growth in calcite. *J. Am. Ceram. Soc.* **69**, C272-C277.
- Olgaard, D. L. & Evans, B. 1988. Grain growth in synthetic marbles with added mica and water. *Contributions to Mineralogy and Petrology* **100**, 246-260.
- Olgaard, D. L. 1990. The role of second phase in localizing deformation. In: *Deformation Mechanisms, Rheology and Tectonics* (edited by Knipe, R. J. & Rutter, E. H.) **54**. Geological Society of London Special Publication, 175-181.
- Ottavia, G. & Molli, G. 2000. Superimposed brittle structures in the late-orogenic extension of the Northern Apennine: results from the Carrara area (Alpi Apuane, NW Tuscany). *Terra Nova* **12**, 52-59.
- Panozzo, R. 1983. Two-dimensional analysis of shape-fabric using projections of digitized lines in a plane. *Tectonophysics* **95**, 279-294.
- Panozzo, R. & Hürlimann, H. 1983. A simple method for the quantitative discrimination of convex and convex-concave lines. *Microscopica Acta* **87(2)**, 169-176.

- Panozzo, R. 1984. Two-dimensional strain from the orientation of lines in a plane. *Journal of Structural Geology* **6**(1/2), 215-221.
- Panozzo Heilbronner, R. & Pauli, C. 1993. Integrated spatial and orientation analysis of quartz *c*-axis by computer-aided microscopy. *Journal of Structural Geology* **15**(3-5), 369-382.
- Passchier, C. W. & Trouw, R. A. J. 1998. *Microtectonics*. Springer, Berlin Heidelberg.
- Paterson, M. S. 1987. Problems in the extrapolation of laboratory rheological data. *Tectonophysics* **133**, 33-43.
- Paterson, M. S. & Olgaard, D. L. 2000. Rock deformation tests to large shear strains in torsion. *Journal of Structural Geology* **22**, 1341-1358.
- Pieri, M., Burlini, L., Kunze, K., Stretton, I. & Olgaard, D. L. 2001 a. Rheological and microstructural evolution of Carrara marble with high shear strain: results from high temperature torsion experiments. *Journal of Structural Geology* **23**, 1393-1413.
- Pieri, M., Kunze, K., Burlini, L., Stretton, I., Olgaard, D. L., Burg, J.-P. & Wenk, H.-R. 2001 b. Texture development of calcite by deformation and dynamic recrystallization at 1000 K during torsion experiments of marble to large strains. *Tectonophysics* **330**, 119-140.
- Platt, J. P. 1986. Dynamics of orogenic wedges and the uplift of high-pressure metamorphic rocks. *Geological Society of America Bulletin* **97**, 1037-1053.
- Poirier, J.-P. & Guillope, M. 1979. Deformation induced recrystallization of minerals. In: *Mecanismes de deformation des mineraux et des roches* (edited by Nicolas, A., Darot, M. & Willaime, C.). Masson, Paris, 67-74.
- Powell, R., Condliffe, D. M. & Condliffe, E. 1984. Calcite-dolomite geothermometry in the system CaCO_3 - MgCO_3 - FeCO_3 : an experimental study. *Journal of metamorphic Geology* **2**, 33-41.
- Principi, G. & Treves, B. 1984. Il sistema corso-apennino come prisma d'accrezione. Riflessi sul problema generale del limite Alpi-Apennino. *Mem. Soc. Geol. Ital.* **28**, 529-576.
- Ramsay, J. 1960. The deformation of early linear structures in areas of repeated folding. *Journal of Geology* **68**(1), 75-93.
- Ramsay, J. 1967. *Folding and fracturing of rocks*. McGraw-Hill, New York.
- Ramsay, J. & Graham, R. H. 1970. Strain variation in shear belts. *Canadian Journal of Earth Science* **7**, 786-813.
- Ramsay, J. G. 1981. Tectonics of the Helvetic Nappes. In: *Thrust and Nappe Tectonics* (edited by McClay, K. R. & Price, N. J.) **9**. Geological Society of London Special Publication, 293-309.
- Ratschbacher, L., Wenk, H.-R. & Sintubin, M. 1991. Calcite textures: examples from nappes with strain-path partitioning. *Journal of Structural Geology* **13**(4), 369-384.
- Rexin, E., Leiss, B. & Molli, G. 2000. Fold-Related Characterization of Carbonate Textures and Microstructures of the Carrara Syncline, Alpi Apuane, Italy. In: *Symposium Tektonik, Struktur- und Kristallingeologie*, Freiburg im Breisgau.
- Roger, J. J. W. & Bogy, R. F. 1958. A study of grain contacts in granitic rocks. *Science* **127**, 470-471.
- Ross, J. V., Bauer, S. J. & Hansen, F. D. 1987. Textural evolution of synthetic anhydrite-halite mylonites. *Tectonophysics* **140**, 307-326.
- Royden, L. H. 1993. Evolution of retreating subduction boundaries formed during continental collision. *Tectonics* **12**, 629-638.
- Rutter, E. H. 1972. The influence of interstitial water on the rheological behaviour of calcite rocks. *Tectonophysics* **14**(1), 13-33.

-
- Rutter, E. H. 1974. The influence of temperature, strain rate and interstitial water in the experimental deformation of calcite rocks. *Tectonophysics* **22**, 311-334.
- Rutter, E. H. 1984. The kinetics of grain coarsening in calcite rocks. In: *Sixth progress report of research supported by N.E.R.C., 1981-1984* (edited by Henderson, C. M. B.). *Progress in Experimental Petrology* **6**. Natural Environment Research Council. London, 245-249.
- Rutter, E. H., Casey, M. & Burlini, L. 1994. Preferred crystallographic orientation development during plastic and superplastic flow of calcite rocks. *Journal of Structural Geology* **16**(10), 1431-1446.
- Rutter, E. H. 1995. Experimental study of the influence of stress, temperature, and strain on the dynamic recrystallization of Carrara marble. *Journal of Geophysical Research* **100**(B12), 24,651-24,663.
- Schmid, S. M. 1975. The Glarus overthrust: Field evidence and mechanical modal. *Eclogae geol. Helv.* **68/2**, 247-280.
- Schmid, S. M. 1976. Rheological evidence for changes in the deformation mechanism of Solenhofen limestone towards low stresses. *Tectonophysics* **31**, T21-T28.
- Schmid, S. M., Boland, J. N. & Paterson, M. S. 1977. Superplastic flow in finegrained limestone. *Tectonophysics* **43**, 257-291.
- Schmid, S. M., Paterson, M., S. & Boland, J. N. 1980. High temperature flow and dynamic recrystallization in Carrara marble. *Tectonophysics* **65**, 245-280.
- Schmid, S. M. 1981. Laboratory experiments on rheology and deformation mechanisms in calcite rocks and their application to studies in the field. Unpublished Habilitationsschrift thesis, Eth Zürich.
- Schmid, S. M. 1983. Microfabric Studies as Indicators of Deformation Mechanisms and Flow Laws Operative in Mountain Building. In: *Mountain building processes* (edited by Hsü, K. J.). Academic Press, London, 95-110.
- Schmid, S. M., Panozzo, R. & Bauer, S. 1987. Simple shear experiments on calcite rocks: rheology and microstructure. *Journal of Structural Geology* **9**(5/6), 747-778.
- Schultz, H. 1996. Analyse der varistisch-apenninischen Deformationsgeschichte des paläozoischen Basements der Apuaner Alpen (Toskana, Italien). Berliner Geowissenschaftliche Abhandlungen, Reihe A: Geologie und Paläontologie 188.
- Serri, G., Innocenti, F. & Manetti, P. 1993. Geochemical and petrological evidence of the subduction of delaminated adriatic continental lithosphere in the genesis of the Neogene-Quaternary magmatism of central Italy. *Tectonophysics* **223**, 117-147.
- Sibson, R. H. 1977. Fault rocks and mechanisms. *Journal of the geological Society of London* **133**, 191-213.
- Siegesmund, S., Ullemeyer, K., Weiss, T. & Tschegg, E. K. 2000. Physical weathering of marbles caused by anisotropic thermal expansion. *International Journal of Earth Sciences* **89**, 170-182.
- Siegesmund, S., Weiss, T. & Vollbrecht, A. 2003. *Natural Stone, Weathering Phenomena, Conservation Strategies and Case Studies*. Geological Society Special Publication No. 205.
- Simpson, C. 1979. Oblique girdle patterns of quartz c-axes from a shear zone in the basement core of the Maggia Nappe (Ticino, Switzerland). *J. Struct. Geol.* **2**, 243-247.
- Stipp, M., Stünitz, H., Heilbronner, R. & Schmid, S. M. 2002. The Eastern Tonale fault zone: a "natural laboratory" for crystal plastic deformation of quartz over a temperature range from 250 to 700°C. *J. Struct. Geol.* **24**, 1861-1884.
- Stünitz, H. & Fitz Gerald, J. D. 1993. Deformation of granitoids at low metamorphic grade.

- II: Granular flow in albite-rich mylonites. *Tectonophysics* **221**, 299-324.
- Takahashi, M., Nagahama, H., Masuda, T. & Fujimura, A. 1998. Fractal analysis of experimentally, dynamically recrystallized quartz grains and its possible application as a strain rate meter. *Journal of Structural Geology* **20**(2/3), 269-275.
- Technisches Handbuch des Italienischen Marmors, Vol.1, 1982. *Der Marmor im Lauf der Jahrhunderte*. Fratelli Vallaridi, Mailand.
- Technisches Handbuch des Italienischen Marmors, Vol.2, 1982. *Der Marmor im Lauf der Jahrhunderte*. Fratelli Vallaridi, Mailand.
- Tullis, J. & Yund, R. A. 1981. Grain growth kinetics of quartz and calcite aggregates. *Journal of Geology* **90**(3), 301-318.
- Tullis, T. E., Horowitz, F. G. & Tullis, J. 1991. Flow laws of polyphase aggregates from end-member flow laws. *Journal of Geophysical Research* **86**(B5), 8081-8096.
- Tungatt, P. D. & Humphreys, F. J. 1981. An in-situ optical investigation of the deformation behaviour of sodium nitrate – an analogue for calcite. *Tectonophysics* **78**, 661-675.
- Turner, F. J., Griggs, D. T., Clark, R. H. & Dixon, R. H. 1956. Deformation of Yule marble, Part VII. *Geol. Soc. America Bull.* **67**, 1259-1294.
- Turner, F. J. 1962. “Compression” and “tension” axes determined from {1012} twinning in calcite. *Journal of Geophysical Research* **67**, 1660.
- Turner, F. J. & Weiss, L. E. 1963. *Structural analysis of metamorphic tectonites*. McGraw-Hill, New York.
- Underwood, E. E. 1970. *Quantitative Stereology*. Addison-Wesley, London.
- Urai, J. L., Means, W. D. & Lister, G. S. 1986. Dynamic recrystallization of minerals. In: *Geophysical Monograph* **36**, 161-199.
- Van der Pluijm, B. A. 1991. Marble mylonites in the Bancroft shear zone, Ontario, Canada: microstructures and deformation mechanisms. *Journal of Structural Geology* **13**(10), 1125-1135.
- Venables, J. A. & Harland, C. J. 1973. Electron back-scattering patterns-a new technique for obtaining crystallographic information in the scanning electron microscope. *Philosophical Magazine* **27**, 1193-1200.
- Vernon, R. H. 1981. Optical microstructure of partly recrystallized calcite in some naturally deformed marbles. *Tectonophysics* **78**, 601-612.
- von Karman, T. 1911. Festigkeitsversuche unter allseitigem Druck. *Zeitschrift des Vereins deutscher Ingenieure* **42**(55), 1749-1758.
- Walker, A. N., Rutter, E. H. & Brodie, K. H. 1990. Experimental study of grain-size sensitive flow of synthetic, hot-pressed calcite rocks. In: *Deformation Mechanisms, Rheology and Tectonics* (edited by Knipe, R. J. & Rutter, E. H.) **54**. Geological Society of London Special Publication, 259-284.
- Walker, G. & Burley, S. 1991. Luminescence Petrography and Spectroscopic Studies of Diagenetic Minerals. In: *Luminescence Microscopy: Quantitative and Qualitative Aspects* (edited by Baker, C. E. & Kopp, O. C.) - **SEPM Short Course** **25**, 83-96.
- Wenk, H.-R. & Shore, J., 1975. Preferred Orientation in Experimentally Deformed Dolomite. *Contrib Mineral Petrol*, **50**, 115-126.
- Wenk, H.-R. 1985. Carbonates. In: *Preferred orientation in deformed metals and rocks: an introduction to modern texture analysis* (edited by Wenk, H.-R.). Academic Press, London, 361-384.
- Wenk, H.-R. T., Van Houtte, P. & Wagner, F. 1986. Plastic Anisotropy and Texture Development in Calcite Polycrystals. *Journal of Geophysical Research* **91**(B3), 3861-3869.
- Wenk, H.-R., Takeshita, T., Bechler, E., Erskine, B. G. & Matthies, S. 1987. Pure shear and

-
- simple shear calcite textures. Comparison of experimental, theoretical and natural data. *Journal of Structural Geology* **9**(5/6), 731-745.
- White, S. H., Burrows, S. E., Carreras, J., Shaw, N. D. & Humphreys, F. J. 1980. On mylonites in ductile shear zones. *Journal of Structural Geology* **2**(1/2), 175-187.
- Wilson, C. J. L. 1981. Experimental folding and fabric development in multilayered ice. *Tectonophysics* **78**, 139-159.
- Zaccagna, D. 1932. Descrizione Geologica delle Alpi Apuane. *Memorie Descrittive della Carta Geologica d'Italia* **25**, 440.



Appendix A: Crystallography of calcite and dolomite

Calcite (CaCO_3) and dolomite ($\text{CaMg}(\text{CO}_3)_2$) are the most abundant minerals of the rock forming carbonates. More than 90 % of the naturally appearing carbonates are formed by calcite and dolomite. Both minerals are of trigonal symmetry; calcite has the space group R-3c and dolomite the space group R-3.

Calcite has a fairly simple structure, which can be described as a close packing of anion groups (CO_3^{2-}) with cations (Ca^{2+}) in octahedral interstices. Magnesite (MgCO_3), siderite (FeCO_3) and rhodochrosite (MnCO_3) have the same structure as calcite. In first approximation the calcite structure can be considered as the one of halite (NaCl), which was compressed parallel to one of the four triad axis (parallel to one of the body diagonals). Na^{2+} cations are replaced by Ca^{2+} ions and Cl^{2-} anions by CO_3^{2-} groups. The resulting face-centered rhombohedral cell has a lattice distance of a_{rh} 6.42 Å and an angle between the crystallographic directions of $\alpha = 101.92^\circ$. This morphologic pseudo cell (cleavage rhomb) contains 4 CaCO_3 , corresponding to the 4 NaCl in the cubic halite unit cell. The comparison to the NaCl cell, however, is not completely correct, because of the orientation of the CO_3^{2-} groups in the crystal lattice. The carbonate (CO_3^{2-}) groups are arranged in layers normal to the three fold inversion axis. The orientation of the CO_3^{2-} groups is constant in each layer; successive layers are characterized by a rotation of the CO_3^{2-} groups of 180° about the layer normal. A true face centered rhombohedral unit cell has an a_{rh} of 2×6.42 Å and an α of 101.92° and it contains 32 CaCO_3 . The rhombohedron with $\alpha = 101.92^\circ$ corresponds to cleavage rhomb of calcite, which has the Miller-Bravais index $\{10\text{-}11\}$. For the description of the calcite lattice a smaller rhombohedral cell (primitive cell), with 2 CaCO_3 and $a_{\text{rh}} = 6.37$ Å and $\alpha = 46.08^\circ$ can be chosen. Its faces correspond to $\{10\text{-}14\}$ in Miller-Bravais indices. In the case of calcite the anion layers alternate with layers of Ca^{2+} . In dolomite every second cation layer is composed of Ca^{2+} and Mg^{2+} , respectively.

Carbonates with cations larger than Ca^{2+} (e.g. Sr and Ba) crystallize in hexagonal-close-packing, because Ca^{2+} is near the limit of the 6-fold coordination (octahedral coordination). At elevated pressures (e.g. 100 MPa at 400 °C) the calcite structure breaks down to the aragonite structure, which crystallizes in 9-fold coordination.

The dolomite structure is similar to the one of calcite but has a slightly lower symmetry (space group R-3 instead of R-3c). It is best considered as a combination of layers of CaCO_3 and MgCO_3 . In agreement with calcite the cleavage of dolomite is index as $\{10\text{-}11\}$ (Miller-Bravais).

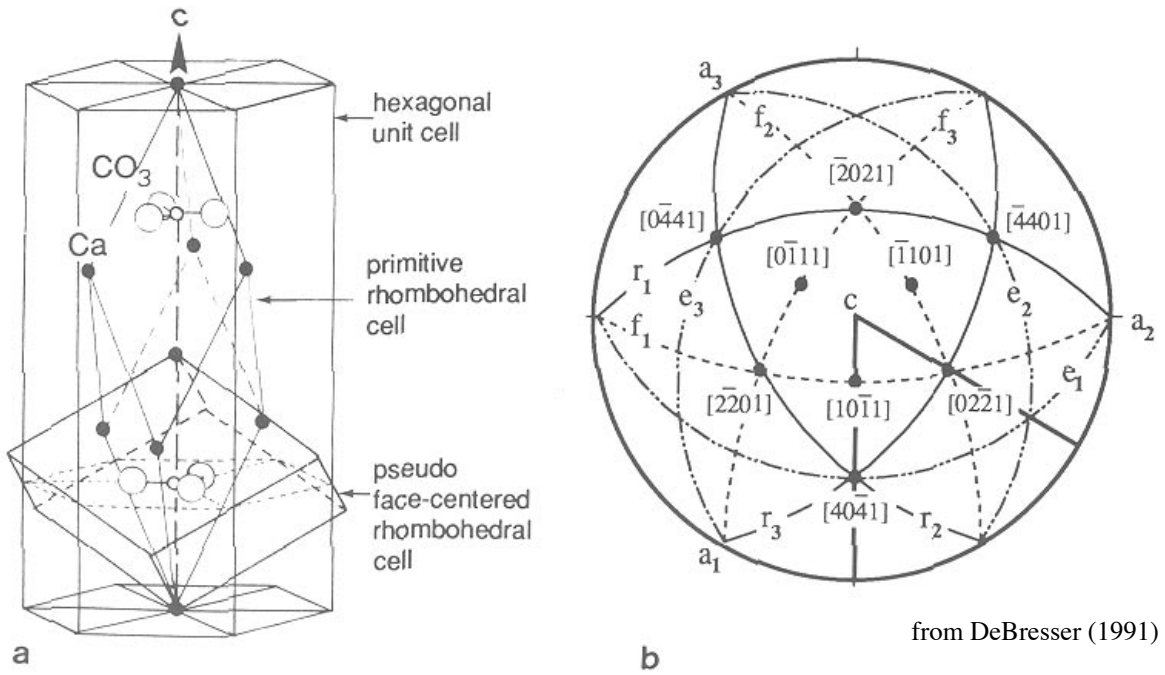
Aragonite is only stable at low temperatures and elevated pressures and it formed by some molluscs and in peculiar geochemical environments.

Calcite as well as dolomite are optically negative and a similar refractive index ($n_{\text{Cc}} = 1.486 - 1.658$; $n_{\text{Dol}} = 1.500 - 1.679$) and a similar birefringence ($\Delta n_{\text{Cc}} = 0.172$; $\Delta n_{\text{Dol}} = 0.177 - 0.185$).

NaN_3 is of the same structure as calcite and is used as analogue material for calcite in deformation experiments (Tungatt & Humphreys 1981).

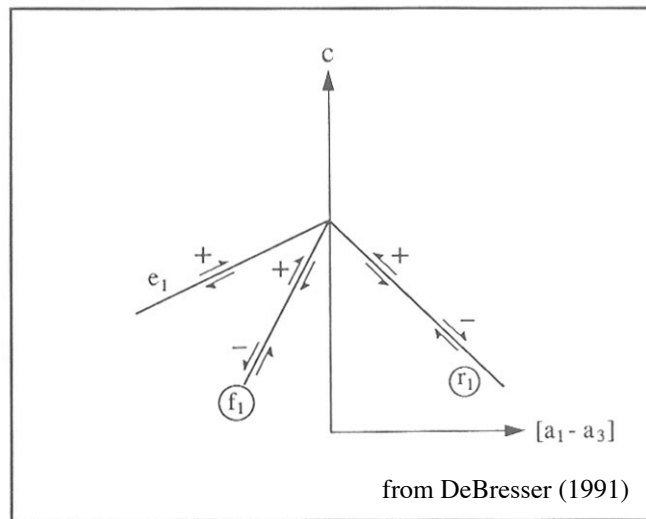
The following figures and tables are copied from Wenk (1985) and De Bresser (1991) and are intended to illustrate the crystallography of calcite and dolomite. Furthermore the most important Burgers vectors, slip systems and flow laws are listed.

Calcite: CaCO_3



from DeBresser (1991)

Structure of calcite (a) and stereographic projection (b) (upper hemisphere, equal angle projection). Shown are the elongated primitive rhombohedral cell (structural cell, containing 2 CaCO_3) and the pseudo-face-centered rhombohedral cell in relation to the hexagonal unit cell.



from DeBresser (1991)

Angular relationship between e-, r- and f-planes in calcite. The relative sense of slip on each plane is indicated.

| (planes) | hexagonal structural cell | hexagonal morphological cell | rhombohedral structural cell | rhombohedral morphological cell |
|----------------|---------------------------|------------------------------|------------------------------|---------------------------------|
| c | 0001 | 0001 | 111 | 111 |
| e ₁ | $\bar{1}018$ | $\bar{1}012$ | 233 | 011 |
| e ₂ | $\bar{1}\bar{1}08$ | $\bar{1}\bar{1}02$ | 323 | 101 |
| e ₃ | 01 $\bar{1}8$ | 01 $\bar{1}2$ | 332 | 110 |
| f ₁ | $\bar{1}012$ | $\bar{2}021$ | 011 | $\bar{1}\bar{1}1$ |
| f ₂ | $\bar{1}\bar{1}02$ | $\bar{2}\bar{2}01$ | 101 | $\bar{1}\bar{1}\bar{1}$ |
| f ₃ | 01 $\bar{1}2$ | 0 $\bar{2}\bar{2}1$ | 110 | $\bar{1}\bar{1}\bar{1}$ |
| r ₁ | 10 $\bar{1}4$ | 10 $\bar{1}1$ | 211 | 100 |
| r ₂ | $\bar{1}104$ | $\bar{1}101$ | 121 | 010 |
| r ₃ | 0 $\bar{1}14$ | 0 $\bar{1}11$ | 11 $\bar{2}$ | 001 |
| m ₁ | 10 $\bar{1}0$ | 10 $\bar{1}0$ | $\bar{2}\bar{1}\bar{1}$ | $\bar{2}\bar{1}\bar{1}$ |
| m ₂ | $\bar{1}100$ | $\bar{1}100$ | $\bar{1}\bar{2}\bar{1}$ | $\bar{1}\bar{2}\bar{1}$ |
| m ₃ | 0 $\bar{1}10$ | 0 $\bar{1}10$ | $\bar{1}\bar{1}\bar{2}$ | $\bar{1}\bar{1}\bar{2}$ |
| a ₁ | $\bar{2}\bar{1}\bar{1}0$ | $\bar{2}\bar{1}\bar{1}0$ | 1 $\bar{1}0$ | 1 $\bar{1}0$ |
| a ₂ | $\bar{1}\bar{2}\bar{1}0$ | $\bar{1}\bar{2}\bar{1}0$ | 01 $\bar{1}$ | 01 $\bar{1}$ |
| a ₃ | $\bar{1}\bar{1}\bar{2}0$ | $\bar{1}\bar{1}\bar{2}0$ | $\bar{1}01$ | $\bar{1}01$ |

| [intersections] | | | | |
|--------------------------------|---------------------|--------------------|-------------------------|-----|
| r ₁ :r ₂ | 0 $\bar{4}41$ | 0 $\bar{1}11$ | $\bar{1}\bar{1}3$ | 001 |
| r ₂ :r ₃ | 4041 | 10 $\bar{1}1$ | $\bar{3}\bar{1}\bar{1}$ | 100 |
| r ₁ :r ₃ | $\bar{4}401$ | $\bar{1}\bar{1}01$ | $\bar{1}\bar{3}\bar{1}$ | 010 |
| f ₁ :f ₂ | 0 $\bar{2}\bar{2}1$ | 01 $\bar{1}2$ | 11 $\bar{1}$ | 110 |
| f ₂ :f ₃ | $\bar{2}021$ | $\bar{1}012$ | $\bar{1}\bar{1}1$ | 011 |
| f ₁ :f ₃ | $\bar{2}\bar{2}01$ | $\bar{1}\bar{1}02$ | 1 $\bar{1}\bar{1}$ | 101 |
| a ₁ :f ₃ | 0 $\bar{1}11$ | 0 $\bar{1}14$ | 001 | 112 |
| a ₂ :f ₁ | 10 $\bar{1}1$ | 10 $\bar{1}4$ | 100 | 211 |
| a ₃ :f ₂ | $\bar{1}101$ | $\bar{1}104$ | 010 | 121 |

cell parameters:
 hexagonal structural cell: a = 4.99 Å, c = 17.06 Å
 hexagonal morphological cell: a = 19.96 Å, c = 17.06 Å
 rhombohedral structural cell: a_{RH} = 6.37 Å, α = 46.05°
 rhombohedral morphological cell: a_{RH} = 12.85 Å, α = 101.55°

Indices of the most important planes and directions in calcite, employing different unit cells. Indices for c and a axes as for planes, cell parameters after Deer et al. (1998).

from DeBresser (1991)

| Burgers vector direction | associated dislocations | material | reference |
|---|--|--|---|
| $\langle 2\bar{1}\bar{1}0 \rangle$ b ₁ | dipoles on r-plane | single crystal | Braillon et al. 1974, Braillon and Serughetti 1976b |
| $\langle \bar{2}021 \rangle$ b ₃ | dipoles dipoles on r free dislocs, dipoles, loops dislocation arrays // r | single crystal single crystal Solnhofen lmst Carrara marble | Braillon and Serughetti 1976b Braillon et al. 1978 Schmid et al. 1977 Schmid et al. 1980 |
| $\langle 2\bar{1}\bar{1}0 \rangle$ b ₁ $\langle 10\bar{1}1 \rangle$ b ₂ $\langle \bar{2}021 \rangle$ b ₃ | dislocation-reactions, nodes | Yule marble | Goetze and Kohlstedt 1977 |
| $\langle \bar{1}100 \rangle$ b ₄ | dislocations limiting planar (growth?) defects // c | single crystal | Braillon and Serughetti 1976a |
| $\langle 40\bar{4}1 \rangle$ b ₈ | dislocations in e-twin boundaries | single crystal | Braillon and Serughetti 1976b |

from DeBresser (1991)

Directions of Burger vectors in calcite reported in the literature. Number codes b_x after Goetze & Kohlstedt (1977).

| twinning systems: | experimental conditions | | | reference |
|-----------------------|-----------------------------|---|---------------------------|--|
| | temperature [°C] | strain rate [sec ⁻¹] | pressure [MPa] | |
| e* {1018}<4041> | 20-300 300-800 | 2.5x10 ⁻⁴ 2.5x10 ⁻⁴ | 500-1000 500 | Turner et al. 1954 Griggs et al. 1960 |
| r* {1014}<2021> * | 20 300 | torsion tests ? | 300 500 | Borg and Handin 1967 Weiss and Turner 1972 |
| f {1012}<1011> * | 300 ? | ? | 500 | Paterson and Turner 1970 |
| slip systems: | | | | |
| r {1014}<2021> | 20-400 300-600 25-500 | 2.5x10 ⁻⁴ 2.5x10 ⁻⁴ 4x10 ⁻¹ , 3x10 ⁻⁷ | 300-1000 500 500 | Turner et al. 1954 Griggs et al. 1960 Turner and Heard 1965 |
| r* {1014}<2021> | 300 460-550 350-650 | ? 1x10 ⁻⁴ 2.5x10 ⁻⁵ | 500 unconf. unconf. | Weiss and Turner 1972 Brailon & Serughetti 1976 Spiers and Wenk 1980 |
| f {1012}<2201><0221> | 20, (300?) 600-800 | 2.5x10 ⁻⁴ 2.5x10 ⁻⁴ | 500 500 | Turner et al. 1954 Griggs et al. 1960 |
| f* {1012}<2201><0221> | 575-650 | 2.5x10 ⁻⁵ | unconf. | Spiers and Wenk 1980 |
| a {1210}<2021> * | 300, 500 300 | ? 3.3x10 ⁻⁷ | 500 500 | Paterson and Turner 1970 Turner and Heard 1965a |
| c {0001}<1210> * | 800 300 | 2.5x10 ⁻⁴ 2.5x10 ⁻⁴ | 500 500 | Griggs et al. 1960 Turner and Orozco 1976 |
| m {1010}<1210> * | 550 | ? | ? | Thomas and Renshaw 1967 |

Slip and twinning system reported in the literature. System indicated by a * are of relative minor importance. Note that the basal a system is indicated by to be of minor importance. However, this study revealed that basal <a> is the dominant slip system at high strains in naturally shear zones.

from DeBresser (1991)

Empirical flow laws describing the mechanical behaviour of various experimentally deformed calcite rocks and microstructural observations. **a)** Heard 1963, Heard & Raleigh 1972, see also Rutter 1974: extension tests at temperatures 25-800°C, confining pressure 500 MPa, strain rate 10⁻¹ to 10⁻⁸ sec⁻¹. **b)** Rutter 1974: compression tests at temperatures 20-500°C, confining pressure 150 MPa and strain rates 6x10⁻⁴ to 5x10⁻⁶ sec⁻¹. **c)** Schmid et al. 1980: compression tests at temperatures 600-1050°C, confining pressure 300 MPa and strain rates 6x10⁻³ to 10⁻⁶ sec⁻¹. **d)** as b). **e)** Schmid 1976, Schmid et al. 1977: compression tests at 600-900°C, confining pressure 300 MPa and strain rates 7x10⁻³ to 10⁻⁶ sec⁻¹.

used empirical flow equations:

exponential: $\dot{\epsilon} = A' \cdot \exp(-Q/RT) \cdot \exp(\sigma/\sigma_0)$

power law: $\dot{\epsilon} = A \cdot \exp(-Q/RT) \cdot \sigma^n$

A, A', n and σ_0 are empirical constants, $\dot{\epsilon}$ is strain rate [sec⁻¹], σ is the flow stress [MPa], Q the apparent activation energy [kJ/mol], R the gas constant and T the absolute temperature.

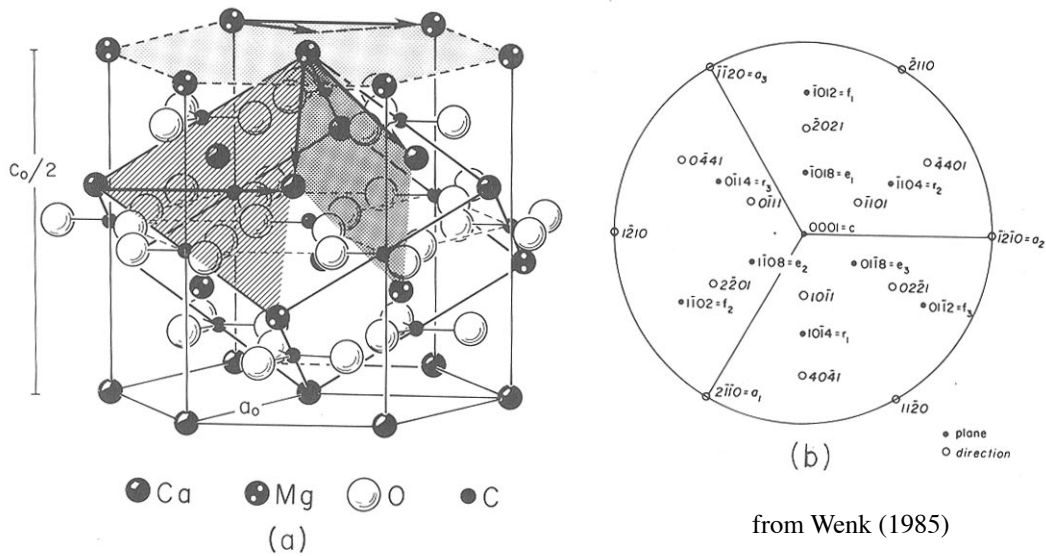
| material, refer. | LOG A' | σ_0 | Q | LOG A | n | |
|---|----------------|------------|-----|------------|------------|--------------------------|
| Yule marble, a) | l orientation: | 9.1 | 260 | -3.9 | 8.3 | at $\sigma > 110$ MPa |
| | | | 260 | | | at $\sigma < 110$ Mpa |
| | T orientation: | 13.8 | 239 | -3.6 | 7.7 | at $\sigma > 140$ MPa |
| | | | 256 | | | at $\sigma < 140$ MPa |
| Carrara marble regime 1, b): regime 2, c): regime 3, c): | 5.8 | 11.4 | 260 | 3.1 8.1 | 7.6 4.2 | at $\sigma > 100$ Mpa |
| | | | 420 | | | at $\sigma = 20-100$ MPa |
| | | | 428 | | | at $\sigma < 20$ MPa |
| Solnhofen lmst regime 1, d): regime 2, e): regime 3, e): | -0.12 | 16.0 | 197 | 3.4 4.4 | 4.7 1.7 | at $\sigma > 190$ MPa |
| | | | 298 | | | at $\sigma < 190$ MPa |
| | | | 214 | | | at $\sigma < 100-40$ MPa |

Yule marble, exponential regime: twinning, r-glide,
no subgrains, no polygonization
power law regime: polygonization, inter- and
intragranular recrystallization

Carrara marble, regime 1: predominant twinning, considerable slip movement, local
subgrain development and recrystallization, limited GBS
regime 2: absence or paucity of twinning, strong but variable sub-
grain development (core- and mantle structures)
regime 3: complete recrystallization by subgrain rotation mechanism,
exaggerated grain growth, more significant GBS

Solnhofen limestone, regime 1: flattened grains, unulose extinction, subgrains,
twinning insignificant
regime 2: as regime 1
regime 3: equiaxed grains, straight grain boundaries,
polygonal structure

Dolomite: $\text{CaMg}(\text{CO}_3)_2$



from Wenk (1985)

Structure of dolomite and stereographic projection (upper hemisphere, equal area projection). The most important slip plabnes (c light shading, t lined and f dark shading) and Burgers vectors are indicated.

| System | Burgers vector (if known) | Strain rate $-\log s^{-1}$ | Temperature (°C) | c.r.s.s. (MPa) | Reference |
|--|---|-------------------------------|---------------------|-------------------|-----------------------------|
| <i>Dolomite</i> | | | | | |
| slip | | | | | |
| *c (0001) $\langle 2\bar{1}10 \rangle$ | $\frac{1}{2}\langle 2\bar{1}10 \rangle$ | 5 | 25–700 | 50–130 | Barber <i>et al.</i> (1981) |
| *f- $\langle \bar{1}012 \rangle \langle 0\bar{2}2\bar{1} \rangle \langle \bar{2}20\bar{1} \rangle$ | $\frac{1}{2}\langle \bar{1}100 \rangle$ | 5 | 400–500 | 170–100 | Barber <i>et al.</i> (1981) |
| r- $\langle 10\bar{1}4 \rangle \langle 12\bar{1}0 \rangle$ | $\frac{1}{2}\langle 220\bar{1} \rangle$ | 5 | >500 | | Barber <i>et al.</i> (1981) |
| twinning | | | | | |
| *f $\langle \bar{1}012 \rangle \langle 10\bar{1}1 \rangle$ | | 5 | 150–500 | 90–100 | Barber <i>et al.</i> (1981) |

^a An asterisk denotes an important mechanism. All indices refer to $c = 17 \text{ \AA}$ structural unit cell.

Slip systems in dolomite

from Wenk (1985)



Appendix B: Methods

This Appendix summarises the methodical procedures, which are not described in the individual chapters of the thesis. The basic steps for the preparation of ultra-thin sections are listed in the first part of this Appendix. In the second part two manuals for the preparation of manually drawn grain boundary maps and the calculation of the equivalent grain diameter from sectional areas are given.

Preparation of ultra-thin sections with a thickness of $< 4\mu\text{m}$

In the following 15 steps the procedure of the preparation of ultra-thin sections with a thickness of less than $4\mu\text{m}$ is described. The procedure was developed and applied by the technical workshop of the Department of Earth Sciences of the University of Basel. Willi Tschudin carried out the main part of the work.

- 1) Cut samples to chips with a maximum edge length of 2 x 4 cm and grind the section- and rear side plan-parallel.
- 2) Open grain boundaries frequently result in the loss to cohesion, especially when cutting the sample with added water or cleaning the specimen from grinding powder by ultra-sonic. An Epoxy impregnation of the rock chips in high vacuum may help to overcome this problem.
- 3) Grind the section-surface with 600er corundum powder and mark the grinded surface by pencil hatches.
- 4) In order to close porosity, which opened during grinding, impregnate the sample chips by epoxy, again in high vacuum.
- 5) Put the sample chips with the grinded section-surface downward, in a plastic basin and fill the basin with epoxy. After epoxy hardened cut the sample chips out of the epoxy block with a leftover rim of 2 mm of epoxy. The epoxy rim protects the sample to be fractured and prevents fragments to leave the specimen during polishing, which would cause scratches on the polished surface.
- 6) Grind the section-surface with 600er and 1500er corundum powder on a grinding machine.
- 7) Excess epoxy at the edges of the sample chip are harder than calcite and result in non-homogeneous polishing and may lead to fracturing of the glass-slide. Therefore remove the epoxy rim manually.
- 8) Stick glass slide to the rear side of the sample chip (Sekundenkleber). The slide is necessary to mount the sample chip to a polishing machine.
- 9) Polish the section-surface with increasingly finegrained diamant paste (3, 1, 0.5, 0.25 μm) on a polishing machine.
- 10) Select equally thick glass-slides for the future ultra-thin sections. The variation in slide thickness should be less than 4-5 μm .

- 11) Stick the polished section surface on at 50° C with Hilquist adhesive to the glass-slide.
- 12) Remove the section from the sample chip with a diamant saw and grind the section on a grinding machine with 600er corundum powder to a thickness of 50 µm.
- 13) Grind the section manually, first with 800er to 25-30 µm thickness and than with 1500er corundum powder to 4 µm thickness. At this thickness the interference colors of calcite are of second order.
- 14) Polish the section automatically on a hard polishing disk with 3 µm diamant paste. Check the polishing every 5 min in reflected and polarized light. If necessary, correct the polishing manually with 3 –1.5 µm diamant paste.
- 15) Finish the polishing with 3-1.5 µm diamant paste until the entire section shows first order gray interference color.

Preparation of grain boundary maps

This manual illustrates in 10 steps how to produce a grain boundary map.

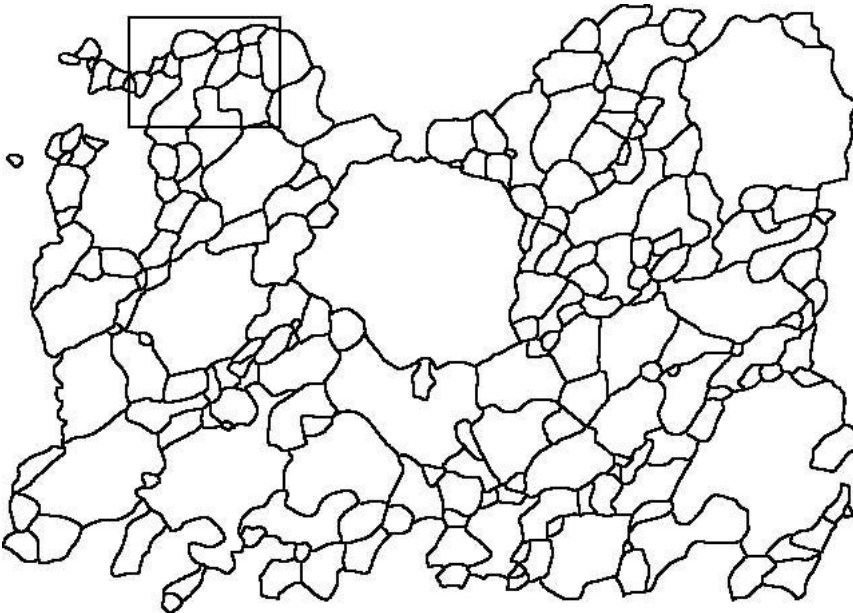
Step 1: Adobe Photoshop

This example is based on a digital orientation image calculated by CIP. If you do not have an orientation image, use a couple of digitally recorded micrographs with different orientations of the polarizers. Stacking these images in different layers past each other (Adobe Photoshop) is a quite good way to distinguish different grains. If you do not have the possibility to record digital images, you have to digitize a hand drawn grain boundary map.

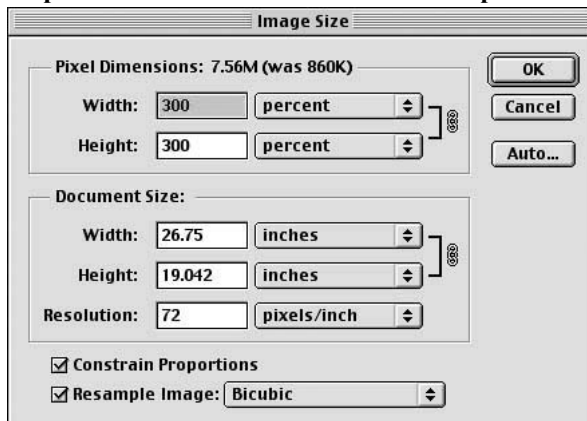


Step 2: Adobe Photoshop

Use Adobe Photoshop to prepare the grain boundary map. Set the pencil tool to a width of 2 pixel and start tracking the grain boundaries manually. You should draw the grain boundaries on a separate layer, otherwise you will have problems to export your grain boundary map.

Step 3: Adobe Photoshop

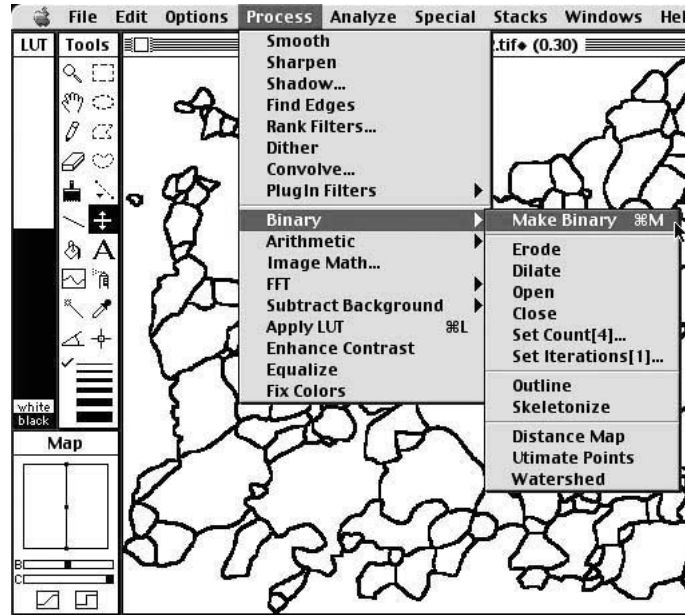
Check if all grain outlines are closed. If you finished drawing and checking the map, copy the layer containing the grain boundary map and save it as a tiff-file in gray scale mode.

Step 4: Adobe Photoshop

To enhance the resolution of the grain boundary map, set the pixel dimensions to 300% using the image size dialogue box in the image menu. Keep in mind that the size of the file increases extremely.

Step 5: NIH-Image

Open the grain boundary map in NIH-Image. To convert the image to a binary file choose Threshold from the Options menu or click into the “stair shaped” icon at the bottom right of the map window. After thresholding the image choose Make Binary from the Process menu or use apple-M on a Macintosh computer.



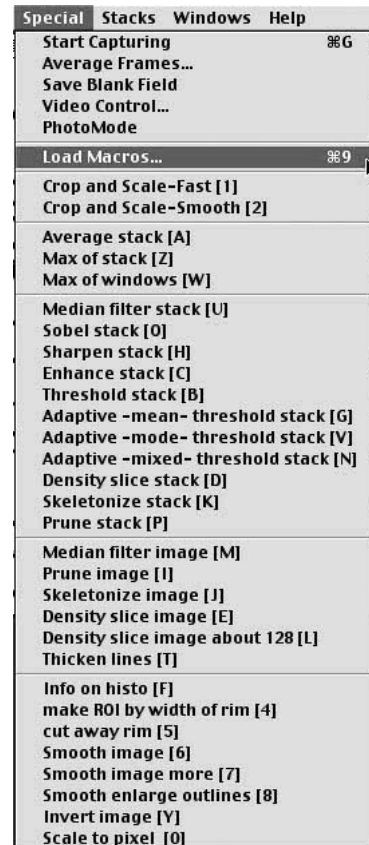
Step 6: NIH-Image

Load the Lazy Grain boundary macro (Heilbronner 2000) into NIH-Image by either choosing Load Macros... from the Special menu or using the apple-9 short-cut.

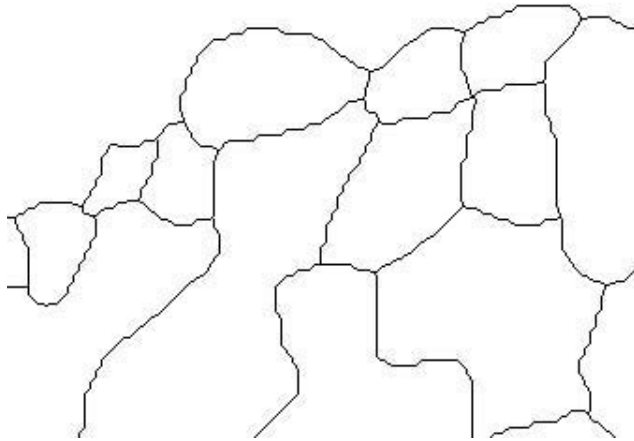
Now choose:

- 1) Skeletonize image [J];
- 2) Prune image [I], (optional, only if the grain boundary map show open boundaries;
- 3) Thicken lines [T];
- 4) Fill the rim of the map using the paint bucket tool ;
- 5) Invert image by either choosing Invert from the Edit menu or clicking on Invert image [Y] in the Lazy grain boundary macro.

Step 6 - 10 illustrate the procedure applied to the region indicated in Step 3 (rectangle at the upper left).

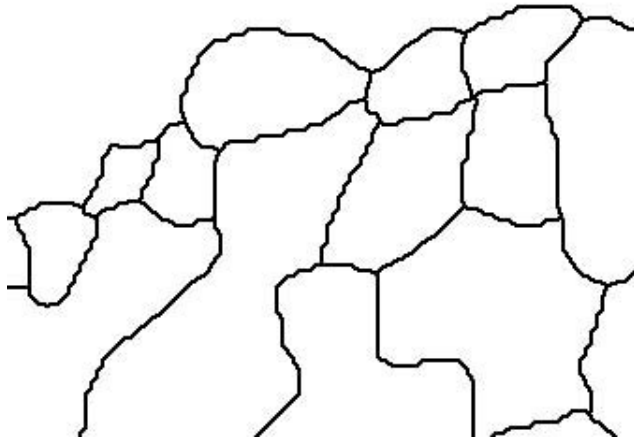


Step 7: NIH-Image



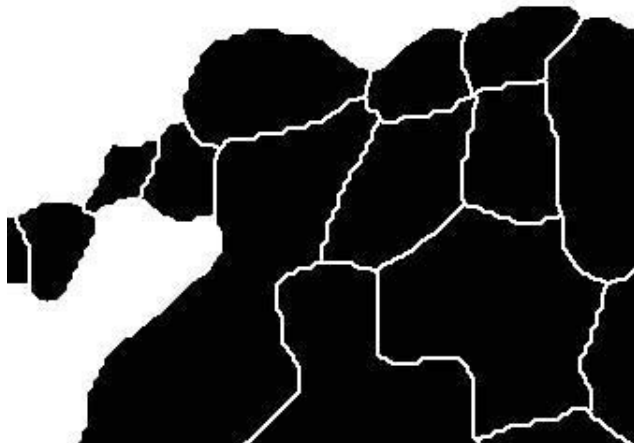
Skeletonize image [J]. The outline of the grains is set to 1 pixel width now.

Step 8: NIH-Image



Thicken lines [T]. The outline is thickened and set to two pixel width now.

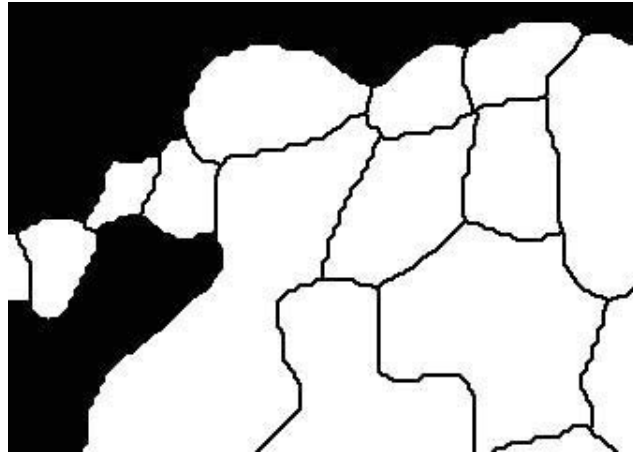
Step 9: NIH-Image



Fill the rim of the map using the paint bucket tool. Now, no grain touches the boundary of the image. Only “complete” grain boundaries are left.

Step 10: NIH-Image

Invert image by either choosing *Invert* from the *Edit* menu or clicking on *Invert image [Y]* in the *Lazy grain boundary* macro. The resulting file can be used as input for further analysis of: grain size, orientation of grain long axis (*PAROR*) and grain boundary orientation (*SURFOR*) and the grain shape (*PARIS*).

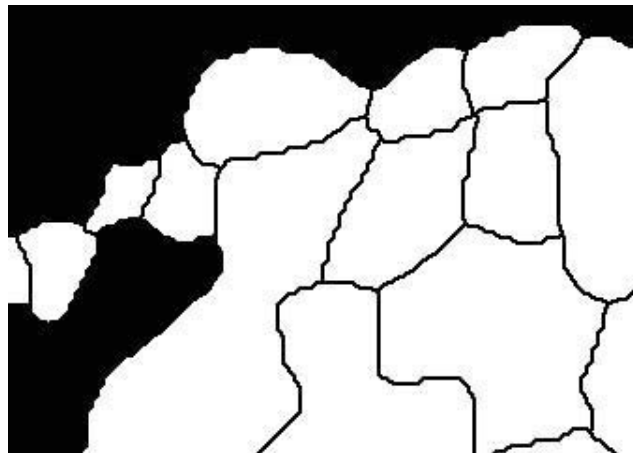


Calculating sectional grain sizes from grain boundary maps

This manual shows in 11 steps how to determine the cross sectional grain size (2D).

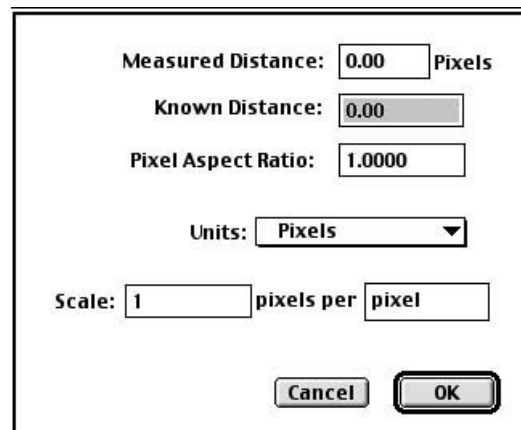
Step 1: NIH-Image

This grain boundary map were prepared in Step 1 – 10 in the previous “outline-manual”. Now we are going to calculate the sectional grain size distribution (2D) using NIH-Image. From the 2D grain size you can calculate the volume weighted grain size distribution using the program *StripStar* by Renée Heilbronner (Heilbronner & Bruhn 1998).

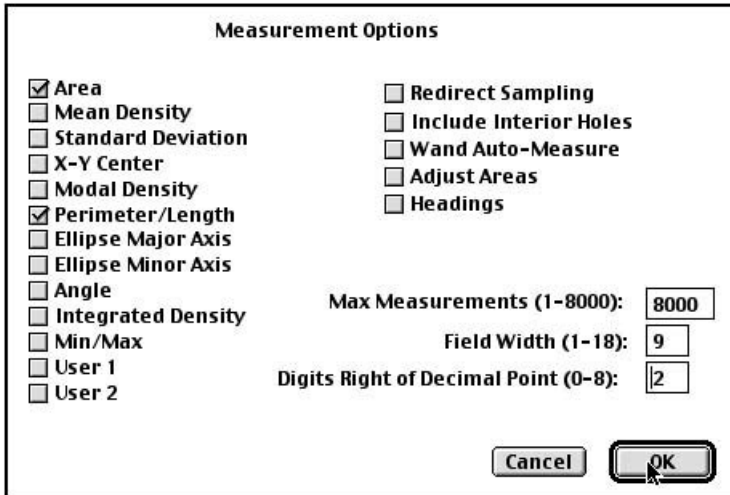


Step 2: NIH-Image

Choose *set scale* from the *analyze* menu and set the units to pixel and the scale to 1 pixel.

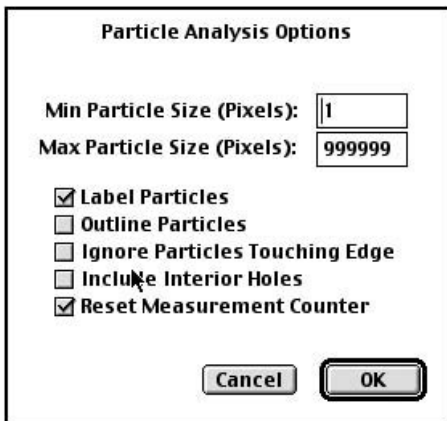


Step 3: NIH-Image



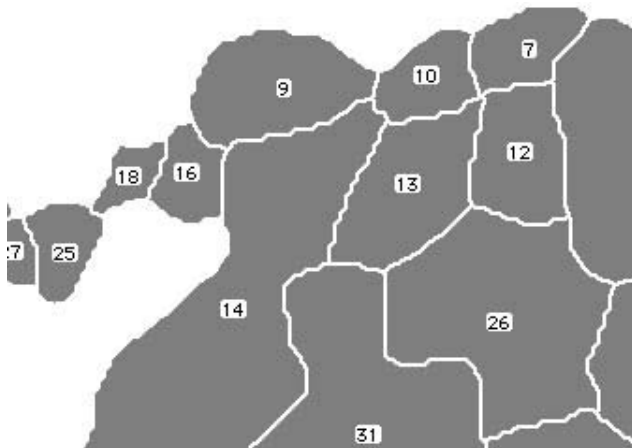
Choose options... from the analyze menu and check Area and Perimeter/Length. Set the maximum number of measurements to 8000.

Step 4: NIH-Image



Choose Analyze Particles... from the analyze menu and set the minimum particle size to 1 pixel and the maximum particle size to 999999. Check Label Particles and Reset Measurement Counter.

Step 5: NIH-Image

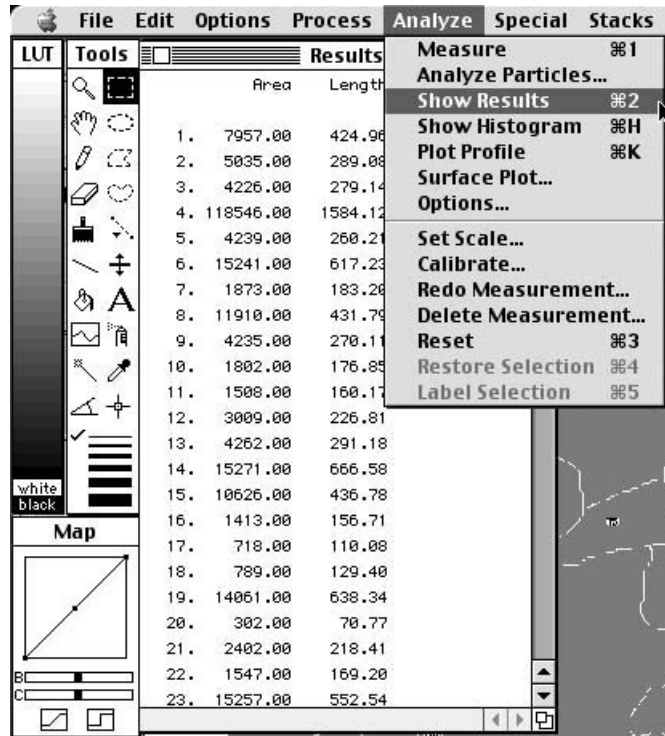


After NIH-Image measured the particles it labels each grain with an individual number. It is useful to save this image as separate file, because you can relate the numerical measurements to the particle appearance.

Step 6: NIH-Image

To see the result file choose Show Results from the analyze menu or type apple-2. The result text file appears on the screen and you have to save it as text file for the calculation of the grain sizes.

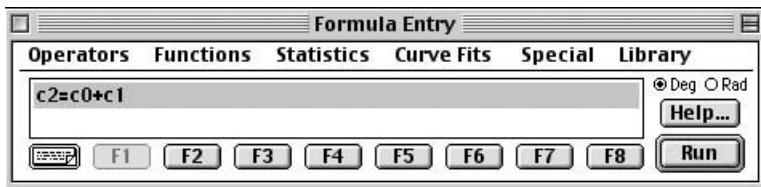
This is how the result file of our example looks like.



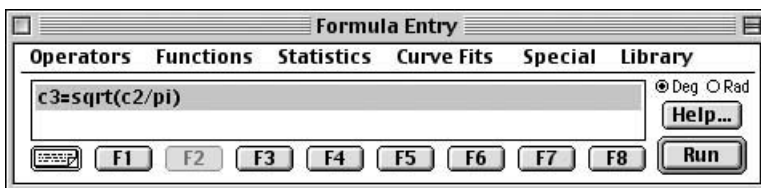
Step 7: Kalaida-Graph

Import the result file into a spreadsheet program like KalaidaGraph or Microsoft Excel. The Area (pixel) and the Length (pixel) should appear in column 0 and column 1, respectively. Calculate now:

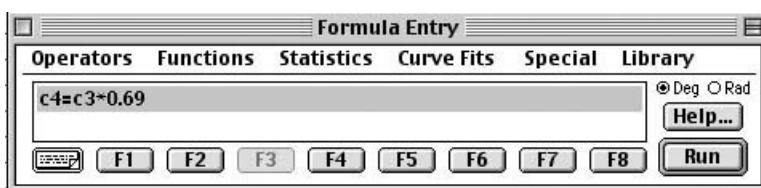
1) Corrected Area (pixel) = Area (pixel) + Length (pixel)



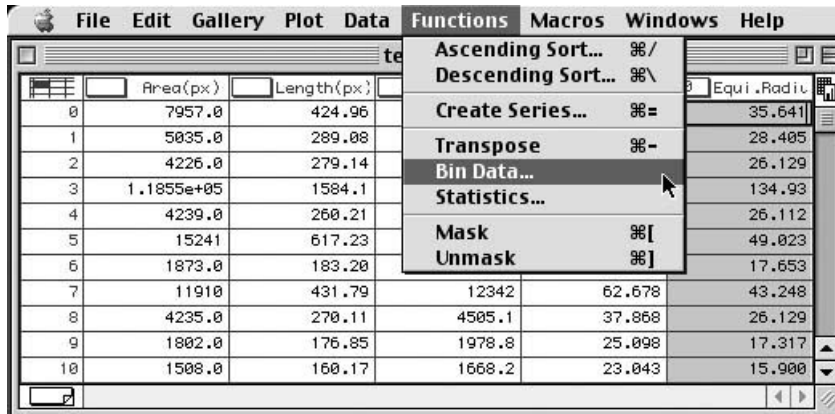
2) Equivalent Radius (pixel) = sqrt(Corrected Area (pixel) / pi)



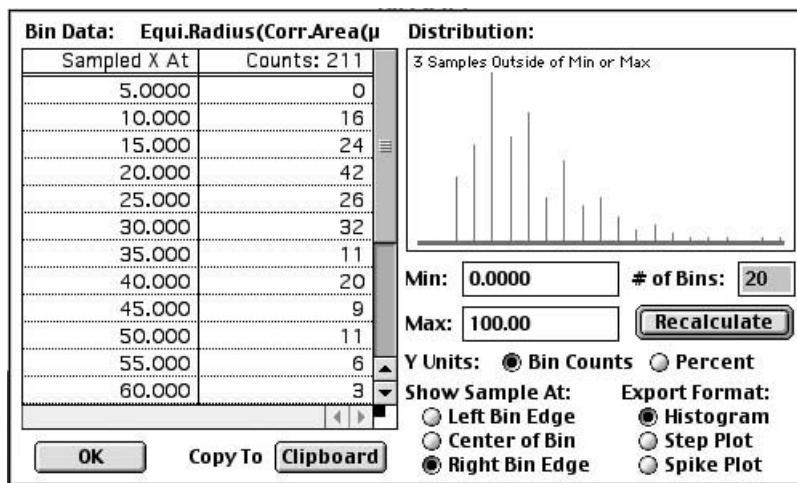
3) Equivalent Radius (µm) = Equivalent Radius (pixel) * Scale



An other way of calculating the cross-sectional grain size is to use the FORTRAN-program Grainsizer 1.0 (cf. Appendix D).

Step 8: Kalaida-Graph

To prepare the histogram of the 2D grain size choose Bin Data... from the Function menu. And go on as follows:



- Set # of Bins to 20, or any other number. However, we will use 20 bins for the calculation of the 3D grain size.

- Set difference of Max: to Min: to 100. In that way you obtain 5 μm steps for the radius and you can plot the grain size in 10 μm diameter steps. (optional)

- Set Y Units: to Bin Counts.
- Set Show sample at: Right Bin Edge. (optional)
- Set Export Format: to Histogram.
- To confirm the changes press the Recalculate button.
- Copy the Bin Data to the system clipboard by pressing the Clipboard button.

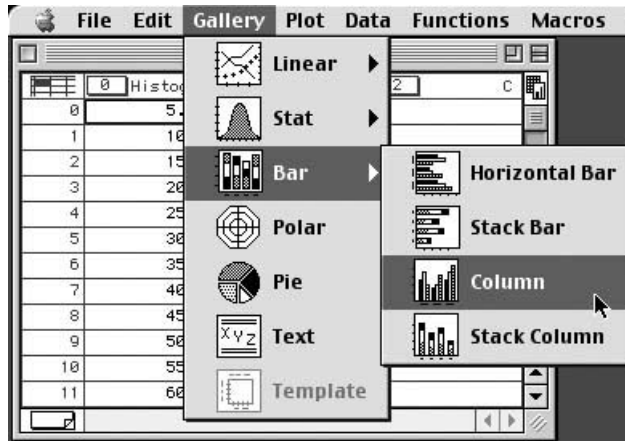
Step 9: Kalaida-Graph

| Histogram | Equi. Radii | Diameter(μ) |
|-----------|-------------|-------------|
| 5.0000 | 0.0000 | 10.000 |
| 10.000 | 16.000 | 20.000 |
| 15.000 | 24.000 | 30.000 |
| 20.000 | 42.000 | 40.000 |
| 25.000 | 26.000 | 50.000 |
| 30.000 | 32.000 | 60.000 |
| 35.000 | 11.000 | 70.000 |
| 40.000 | 20.000 | 80.000 |
| 45.000 | 9.0000 | 90.000 |
| 50.000 | 11.000 | 100.00 |
| 55.000 | 6.0000 | 110.00 |
| 60.000 | 3.0000 | 120.00 |

Create a new data file in your spreadsheet program and import the bin data. Present the grain size either as radius or as diameter.

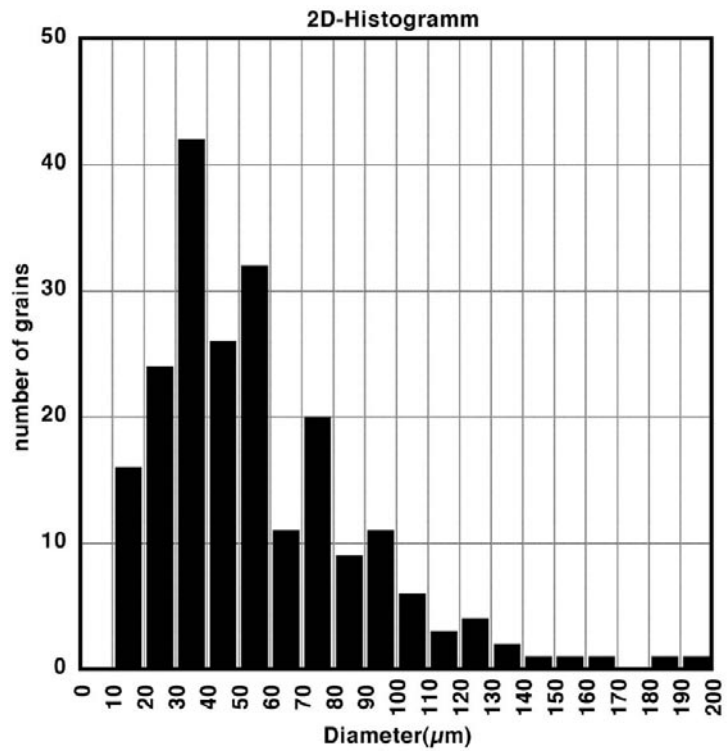
Step 10: Kalaida-Graph

By choosing Column from the Gallery menu you can create a histogram plot.



Step 11: Kalaida-Graph

This is the cross-sectional grain size distribution of the entire grain size map we prepared at the beginning.



Appendix C1: Thin sections and sample chips

This Appendix lists the samples from which ultra-thin sections were prepared. Only a few samples were analyzed in detail in this thesis, however, the other samples provided important information for the interpretation of the microstructures and textures. Six series of thin sections were prepared. The images of the sample chips are shown next and the locality, lithology and structural position. The sample chips were polished and scanned prior to the thin section preparation. The thin section series are listed in ascending order of their preparation year. The samples analyzed in detail (cf. chapter 2) are indicated in the images (boxes) and in the lists (bold text).

Abbreviations:

S1a = Foliation of early stage (D1a) of first deformation event

S1b = Foliation of late stage (D1b) of first deformation event

S2 = Foliation of second deformation event (D2)

SZ = Shear zone

D1-W = Analyzed D1-sample derived from the western Alpi Apuane

D1-E-1; D1-E-2 = Analyzed D1-samples derived from the eastern Alpi Apuane

D2-W = Analyzed D2-sample derived from the western Alpi Apuane

D2-C = Analyzed D2-sample derived from the central Alpi Apuane

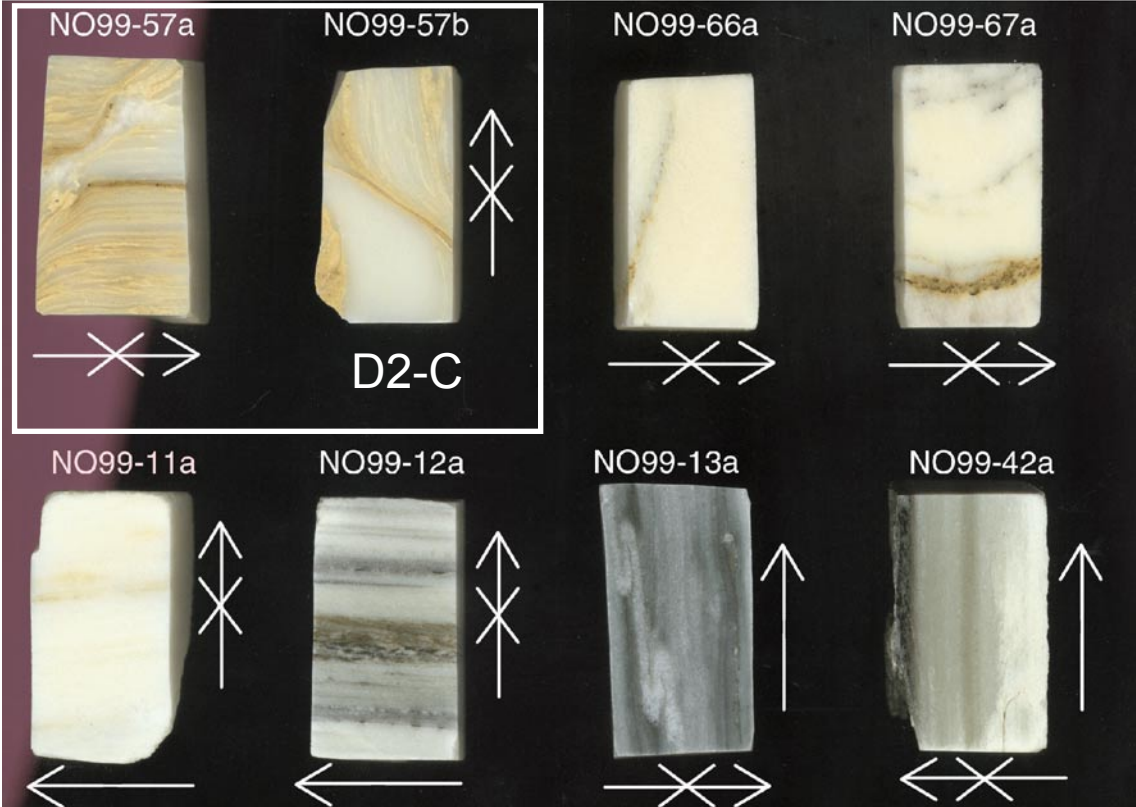
D2-E = Analyzed D2-sample derived from the eastern Alpi Apuane



Series 99-1

| Sample # | Locality | Lithology | Structure |
|---------------|--|---|--|
| 99-7a | Quarry 'La Rochetta', W-Alpi Apuane | Calcite marble of Massa Unit | Mylonites in contact to Massa thrust |
| 99-23a | SW quarry 'Cima di Gioia', W-Alip Apuane | grey-white marbles | S1 parallel |
| 99-32a | Canale di Calacatta, quarry 'Piastriccione', W-Alpi Apuane | 'Zebrino'-type of Carrara marble | Hinge of D2 fold in the inverted limb of Carrara syncline |
| 99-32b | Canale di Calacatta, quarry 'Piastriccione', W-Alpi Apuane | 'Zebrino'-type of Carrara marble | Limb of D2 fold in the inverted limb of Carrara syncline |
| 99-49a | Campo dell'Orzo, near Arni, E-Alpi Apuane | Calcite marble with dolomite rich layers | D1b shear zone |
| 99-50a | Campo dell'Orzo, near Arni, E-Alpi Apuane | Calcite marble with dolomite clasts | D1b shear zone |
| 99-55a | Ponti di Vara, quarry below the bridge, W-Alpi Apuane | white Carrara marble | Limb of D1b fold |
| 99-56a | Ponti di Vara, quarry below the bridge, W-Alpi Apuane | white Carrara marble | Hinge of D1b fold |
| 99-56b | Ponti di Vara, quarry below the bridge, W-Alpi Apuane | white Carrara marble | Hinge of D1b fold |
| 99-62a | Quarry 'Landi' near Arni, E-Alpi Apuane | Carrara marble | Limb of D1b fold |
| 99-63a | Quarry 'Landi' near Arni, E-Alpi Apuane | Carrara marble | Hinge of D1b fold |
| 99-68a | Quarry 'Landi' near Arni, E-Alpi Apuane | Carrara marble | D2 shear zone, outer part, (center = sample 2k-9 series 2000-1) |
| 99-69a | Quarry 'Landi' near Arni, E-Alpi Apuane | Carrara marble | D2 shear zone |

Series 99-2



Series 99-2

| Sample # | Locality | Lithology | Structure |
|-----------------|---|---|----------------------|
| 99-11a | Colonata valley, SW quarry 'Cima di Gioia' W-Alpi Apuane | white calcite marble in 'Zebrino'-type Carrara marble | S1 parallel |
| 99-12a | Colonata valley, SW quarry 'Cima di Gioia' W-Alpi Apuane | mixed calcite/ phyllosilicate marble in 'Zebrino'-type Carrara marble | S1 parallel |
| 99-13a | Colonata valley, SW quarry 'Cima di Gioia' W-Alpi Apuane | grey marble with folded calcite veins | S1 parallel |
| 99-42a | Ponti di Vara, quarry below the bridge | white marble with phyllosilicate rich layer | S1 parallel |
| 99-57a | 'Canale di Fondone', near Forno, Central Alpi Apuane | layered calcite/dolomite marble | D2 shear zone |
| 99-57b | 'Canale di Fondone', near Forno, Central Alpi Apuane | layered calcite/dolomite marble | D2 shear zone |
| 99-66a | quarry 'Landi', near Arni, E-Alpi Apuane | white calcite marble | Limb of D2 fold |
| 99-67a | quarry 'Landi', near Arni, E-Alpi Apuane | white calcite marble | Hinge of D2 fold |

Series 99-3



Series 99-3

| Sample # | Locality | Lithology | Structure |
|----------|---|--|--|
| 98-20a | Arni valley, near Arni, E-Alpi Apuane | white calcite marble | Hinge of D2 fold |
| 98-21a | Arni valley, near Arni, E-Alpi Apuane | white calcite marble | Limb of D2 fold |
| 98-22a | Arni valley, near Arni, E-Alpi Apuane | white calcite marble with phyllosilicate rich layers | D2 fold |
| 98-28a | quarry 'Coletino', Arni valley, E-Alpi Apuane | calcite marble with dolomite layers | D2 fold |
| 98-34a | upper part of Arni valley, E-Alpi Apuane | Cipollini | S2 in the prolongation of D2 marble fold |
| | | | |
| 99-14a | Colonata valley, SW quarry 'Cima di Gioia', W-Alpi Apuane | white Carrara marble | S1-parallel |
| 99-31a | Canale di Calacatta, W-Alpi Apuane | Cherty limestone | Hinge of D2 fold |
| 99-52a | Campo del' Orzo, near Arni, E-Alpi Apuane | white marble with dolomite rich layers | Limb of D1b fold |
| 99-54a | Campo del' Orzo, near Arni, E-Alpi Apuane | white marble with dolomite rich layers | Hinge of D1b fold |
| 99-54b | Campo del' Orzo, near Arni, E-Alpi Apuane | white marble with dolomite rich layers | Hinge of D1b fold |
| 99-61a | quarry 'Landi', near Arni, E-Alpi Apuane | calcite marble with phyllosilicate rich layers | D2 fold |
| 99-64a | quarry 'Landi', near Arni, E-Alpi Apuane | Cipollini | D1b fold, boudinaged quartz veins |
| 99-65a | quarry 'Landi', near Arni, E-Alpi Apuane | Cipollini | D1b fold, boudinaged quartz veins |
| 99-65b | quarry 'Landi', near Arni, E-Alpi Apuane | Cipollini | D1b fold, boudinaged quartz veins |
| 99-71a | lower part of Arni valley, near Arni, Eastern Alpi Apuane | calcite marble | Hinge of D2-folds |

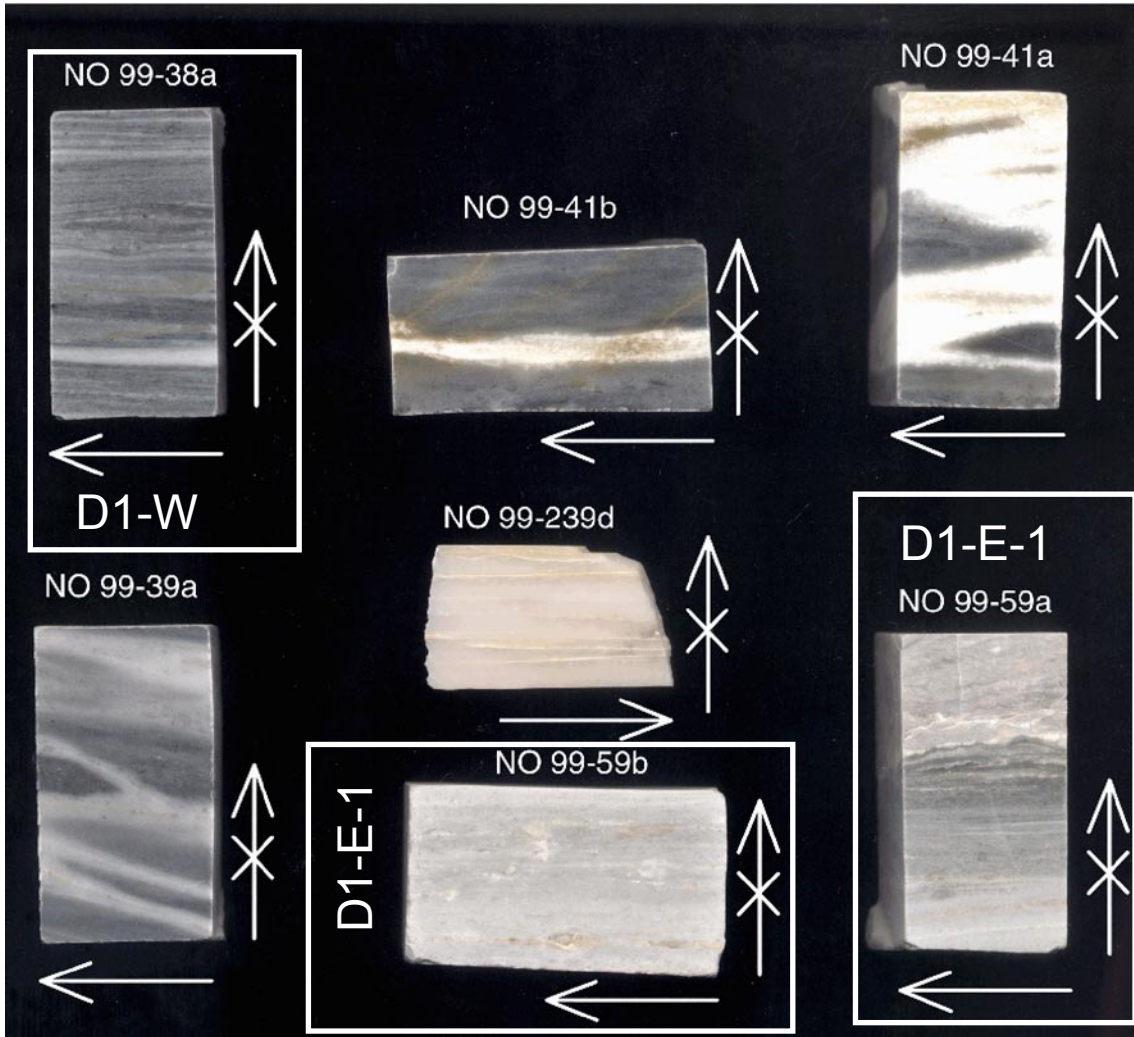
Series 2000-1



Series 2000-1

| Sample # | Locality | Lithology | Structure |
|--------------|--|---|--|
| 98-13a | quarry 'La Perla', near Collonata, W-Alpi Apuane | grey / white marble | D1b shear zone |
| 98-31a | Upper part of the Arni valley, N of quarry 'Faniello', E-Alpi Apuane | grey marble | parallel S1 |
| 98-35a | Upper part of the Ari valley, Passo Sella, E of Tunnel, E-Alpi Apuane | calcite-dolomite marble | parallel S1, with perturbation |
| 99-15a | N of Ponti di Vara, W-Alpi Apuane | 'Zebrino'-type of Carrara marble | parallel S1 |
| 99-17a | N of Ponti di Vara, W-Alpi Apuane | calcite-dolomite marble | parallel S1 |
| 99-22a | Collonata valley, road crossing toward quarry 'Cima di Gioia', W-Alpi Apuane | contact cherty limestone / Carrara marble | parallel S1, Strong L1 stretching lineation |
| 99-30a | Canale di Calacatta, W-Alpi Apuane | contact cherty limestone / 'Zebrino'-type of Carrara marble | parallel S1 |
| 99-37a | near Collonata, W-Alpi Apuane | grey / white marble | D1b shear zone |
| 99-45a | Campo dell'Orzo, near Arni, E-Alpi Apuane | calcite marble with dolomite rich layers | D1b Tambura thrust, overprinted by D2 fold, hinge |
| 99-46a | Campo dell'Orzo, near Arni, E-Alpi Apuane | calcite marble with dolomite rich layers | D1b Tambura thrust, overprinted by D2 fold, above hinge |
| 99-47a | Campo dell'Orzo, near Arni, E-Alpi Apuane | calcite marble with dolomite rich layers | D1b Tambura thrust, overprinted by D2 fold, below hinge |
| 2k-7a | quarry 'Vallini', W-Alpi Apuane | calcite marble | D2 shear zone |
| 2k-8a | quarry 'Vallini', W-Alpi Apuane | calcite marble | protolith of D2 shear zone |
| 2k9a | Quarry 'Landi' near Arni, E-Alpi Apuane | Carrara marble | D2 shear zone, center of shear zone, (outerpart = sample 99-68 series 99-1) |
| 2k-12a | Campo dell'Orzo, near Arni, E-Alpi Apuane | calcite marble with dolomite rich layers | Hinge of D1b folds with 'abnormal' NE dipping axial plane |
| 2k-13a | Campo dell'Orzo, near Arni, E-Alpi Apuane | calcite marble with dolomite rich layers | D2 shear zone |
| 2k-16a | Massa Unit | grey marble | S1 parallel |
| 2k-19a | Quarry 'Landi' near Arni, E-Alpi Apuane | Carrara marble | D2 shear zone |
| 2k-28a | Arni valley, near Arni, E-Alpi Apuane | calcite marble | Hinge of D2 fold |

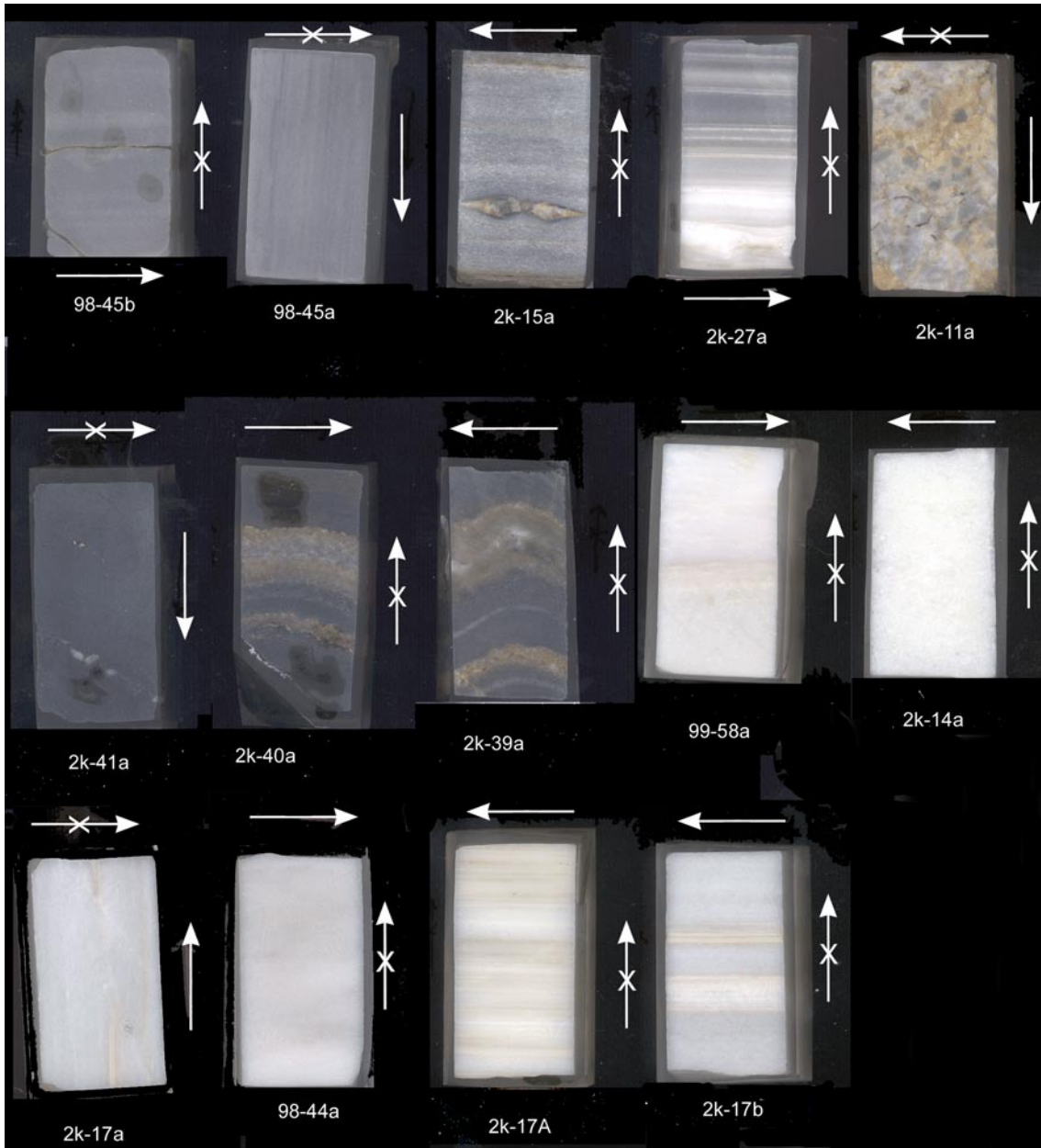
Series 2000-2



Series 2000-2

| Sample # | Locality | Lithology | Structure |
|-----------------|--|--|--|
| 99-38a | near Collonata, Western Alpi Apuane | grey /white marble | D1b shear zone, high strain zone |
| 99-39a | near Collonata, Western Alpi Apuane | grey /white marble | D1b shear zone, medium strain zone |
| 99-41a | near Collonata, Western Alpi Apuane | grey /white marble with chert layers | D1b shear zone, low strain zone and hinge of quartz D1b fold |
| 99-41b | near Collonata, Western Alpi Apuane | grey /white marble with chert layers | D1b shear zone, low strain zone and limb of quartz D1b fold |
| 99-59a | 'Via Vandelli', near Resceto, Central Alpi Apuane | calcite-dolomite marbles, from 'Marmolomitici' formation | D1b shear zone |
| 99-59b | 'Via Vandelli', near Resceto, Central Alpi Apuane | calcite-dolomite marbles, from 'Marmolomitici' formation | D1b shear zone |
| | | | |
| 99-239d | Base of 'Panie della Croze' SE-Alpi Apuane | metallime stone from Panie Unit, corresponding to Carrara marble | shear zone between Panie Unit and Apuane Unit |

Series 2001-1



Series 2001-1

| Sample # | Locality | Lithology | Structure |
|----------|--|---|--|
| 98-44a | Passo della Focolaccia, Central Alpi Apuane | white marble | parallel S1 |
| 98-45a | Passo della Focolaccia, Central Alpi Apuane | grey marble | parallel S1 |
| 98-45b | Passo della Focolaccia, Central Alpi Apuane | grey marble | parallel S1 |
| 99-58a | 'Canale di Fondone', near Forno, Central Alpi Apuane | layered calcite/dolomite marble | protolith of D2 shear zone (sample 99-57, Series 99-2) |
| 2k-11a | Campo dell'Orzo, near Arni, E-Alpi Apuane | cataclastic marble | D1b Tambura thrust |
| 2k-14a | Massa Unit | white phyllosilicate rich marble | S1 parallel |
| 2k-15a | Massa Unit | grey marble with pyrite clasts and strain fringes | S1 parallel |
| 2k-17A | Campo dell' Orzo, near Arni, E-Alpi Apuane | white marble with dolomite rich layers | D1b shear zone |
| 2k-17a | Campo dell' Orzo, near Arni, E-Alpi Apuane | white marble with dolomite rich layers | D1b shear zone |
| 2k-17b | Campo dell' Orzo, near Arni, E-Alpi Apuane | white marble with dolomite rich layers | D1b shear zone |
| 2k-27a | Upper part of the Arnie Valley, Passo Sella, E-Alpi Apuane | grey-white marble | parallel S1, strongly foliated |
| 2k-39a | Canale die Calacatta, W-Alpi Apuane | cherty limestone | Hinge of D2 fold |
| 2k-40a | Canale die Calacatta, W-Alpi Apuane | cherty limestone | Limb of D1 fold, overprinted by S2 |
| 2k-41a | Canale die Calacatta, W-Alpi Apuane | cherty limestone | S2 |

Appendix C2: CIP orientation maps, grain sizes and grain shapes

Samples analyzed by CIP and with respect to grain size and shape are listed in ascending order of their numbers. Locality, lithology, structural position and deformation phase are indicated, respectively. For each sample (if available) first an overview image in crossed polarized light is shown, followed by a CIP c-axes orientation image or microstructural images in crossed polarized light and volume weighted grain size histograms. The orientation of grain boundaries (SURFOR) and grain long axes (PAROR) are presented. Samples derived from D1 structures are shown at the beginning, samples from D2 at the end.

The following samples are listed:

D1:

98-02

98-03

98.05

99-38 = **D1-W**

99-49 = **D1-E-2**

99-59 = **D1-E-1**

2k-17A

M239 (from Giancarlo Molli, University of Pisa, Italy)

D2:

98-06a

98-06c

98-19 = 2k-7 = **D2-W**

99-57 = **D2-C**

99-68 = 2k-9 = **D2-E**

2k-13

Samples from the Helvetic nappes, Alps (from Marco Herwegh, Bern University, Switzerland)

DO 8

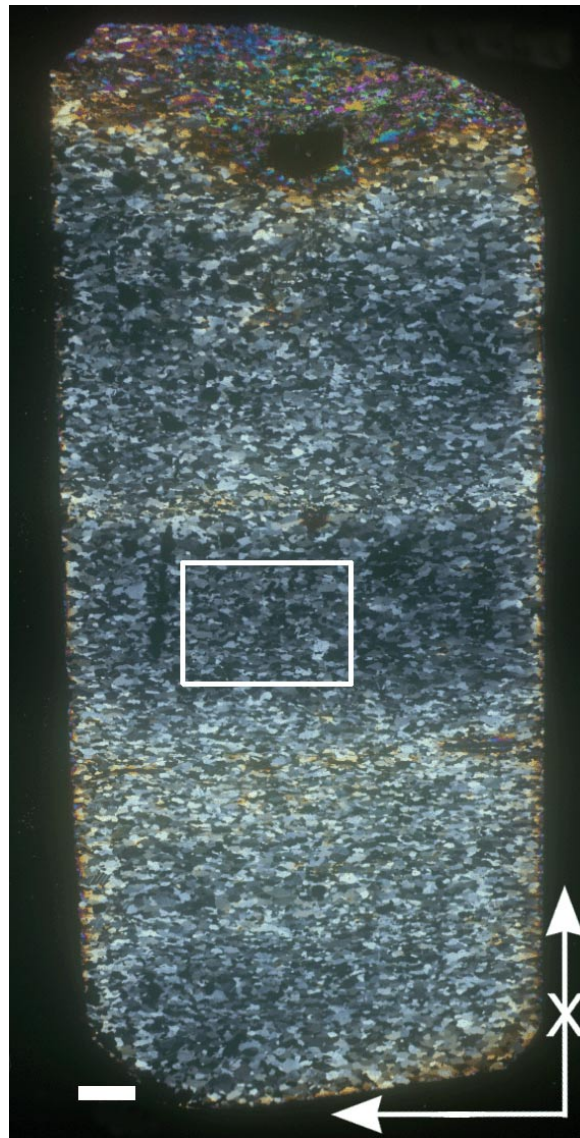
Ge 3

Sample: 98-02

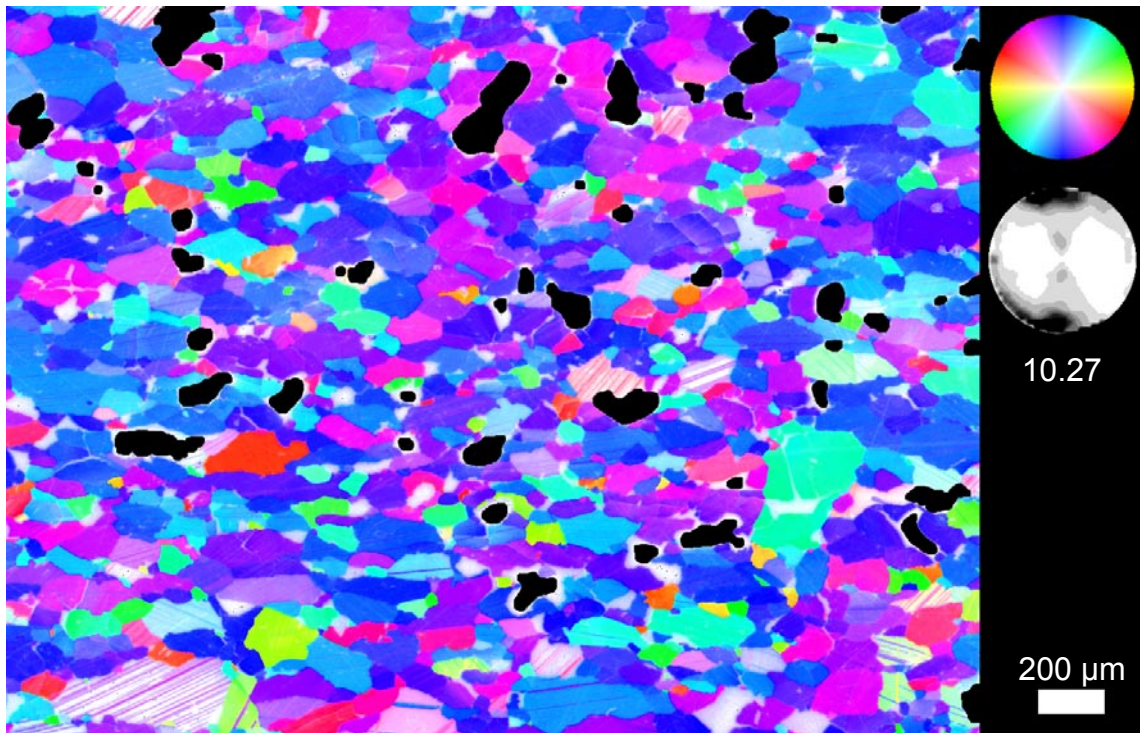
Locality: Eastern Alpi Apuane, close to the village of Arni.

Lithology: Carrara marble with layers of dolomite

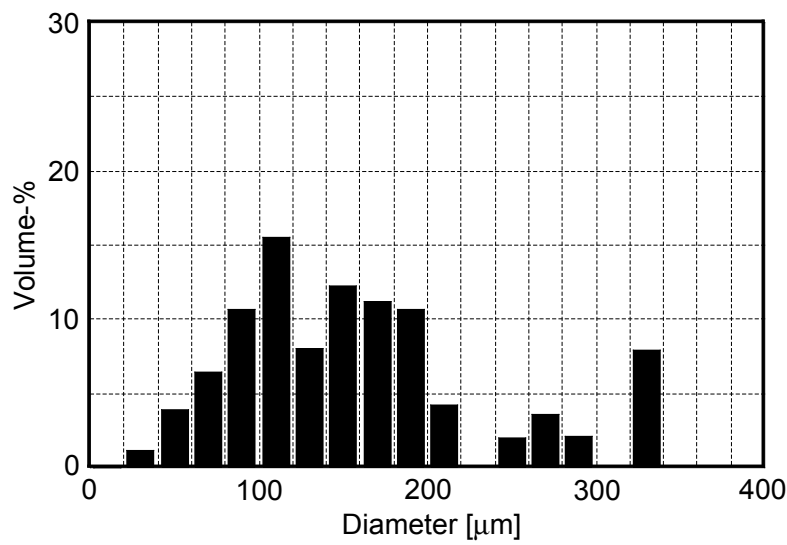
Structural position: Tambura thrust zone, D1b shear zone in the overturned limb of the Tambura anticline.



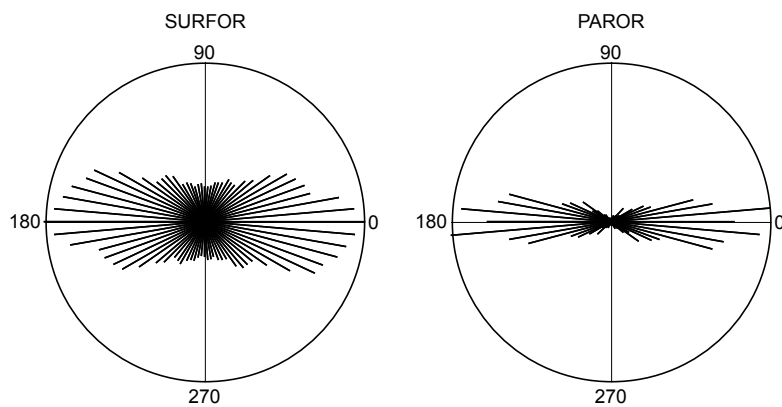
Overview of sample 98-02, crossed polarizers. The site investigated in detail is indicated. Crossed arrow points upward, East on the right-, West on the left-hand side. Scale bar is 1 mm.



CIP c-axis orientation image. The maximum of the polefigure is indicated.



Histogram of volume weighted grain size distribution.



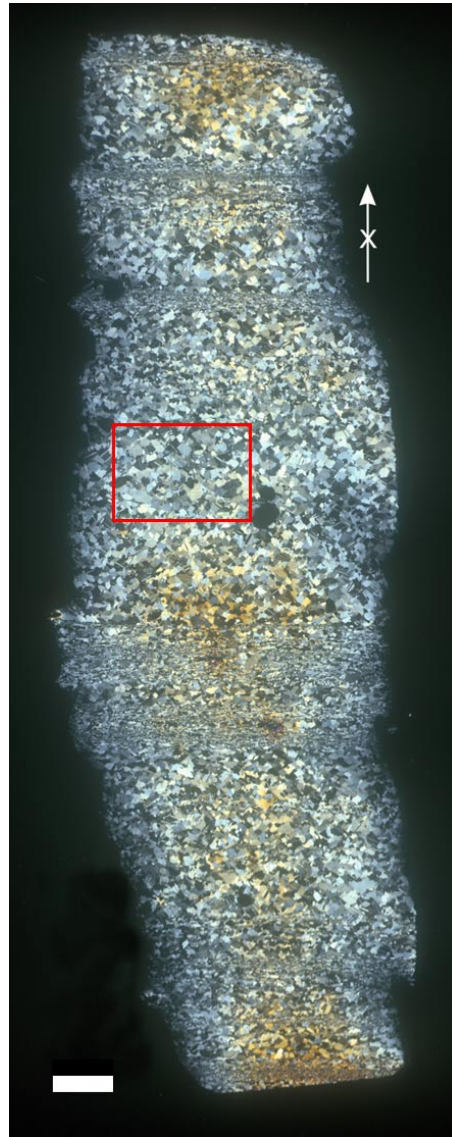
Rose diagrams of grain boundaries (SURFOR) and grain long axis (PAROR).

Sample: 98-03

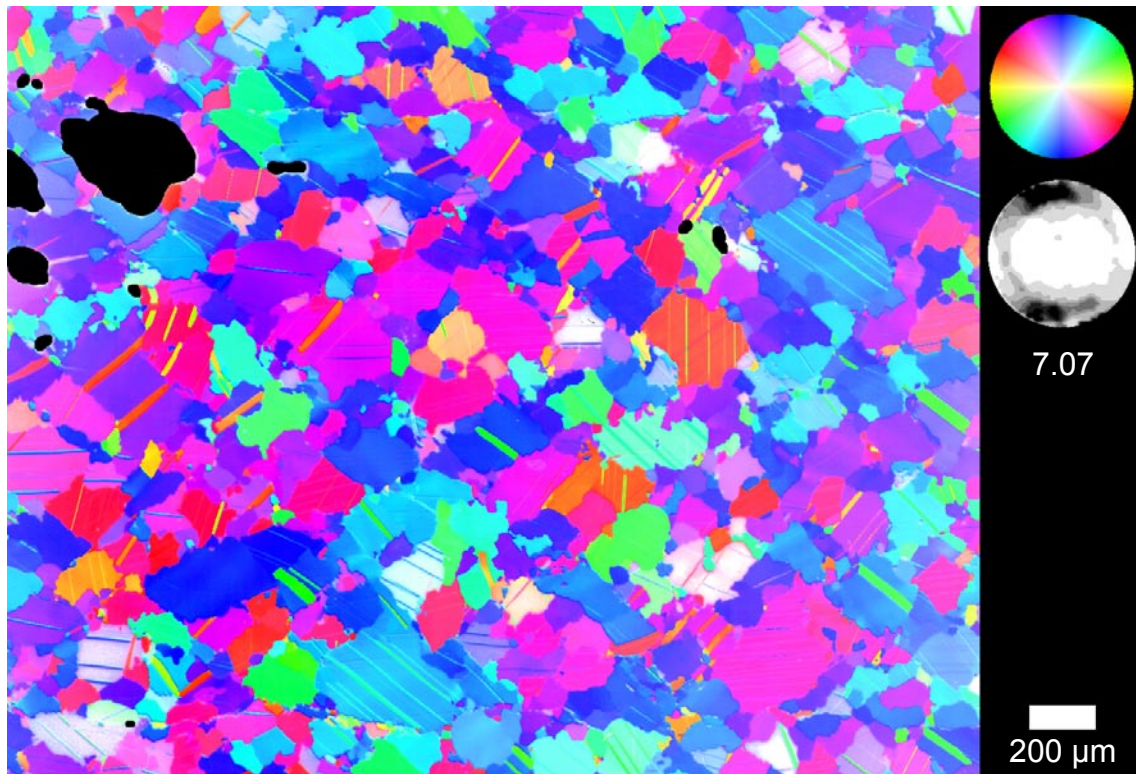
Locality: Eastern Alpi Apuane, close to the village of Arni.

Lithology: Carrara marble with layers of dolomite

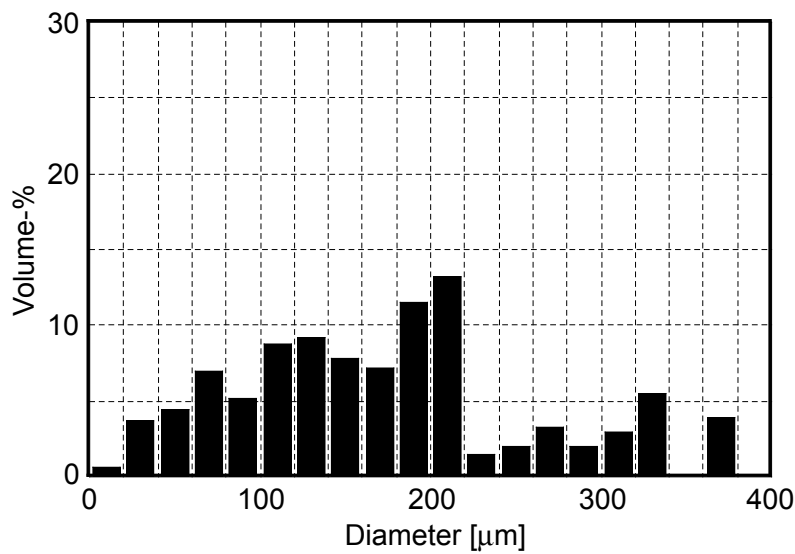
Structural position: Tambura thrust zone, D1b shear zone in the overturned limb of the Tambura anticline.



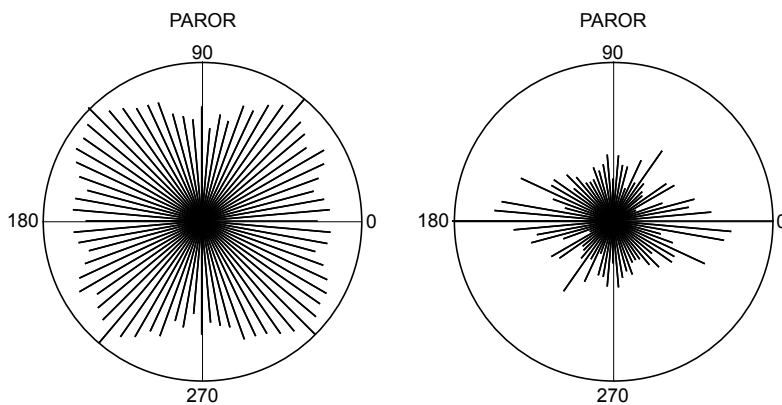
Overview of sample 98-02, crossed polarizers. The site investigated in detail is indicated. Crossed arrow points upward, East on the right-, West on the left hand side. Scale bar is 1 mm.



CIP c-axis orientation image. The maximum of the polefigure is indicated.



Histogram of volume weighted grain size distribution.



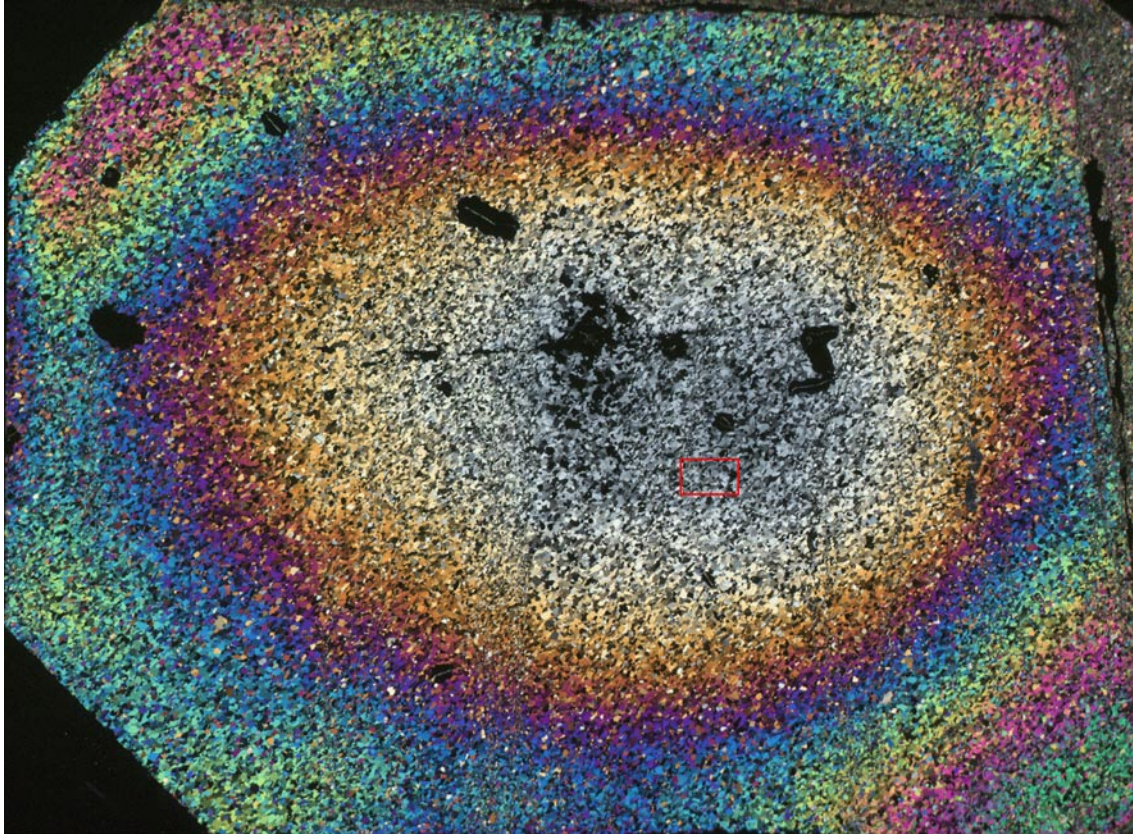
Rose diagrams of grain boundaries (SURFOR) and grain long axis (PAROR).

Sample: 98-05

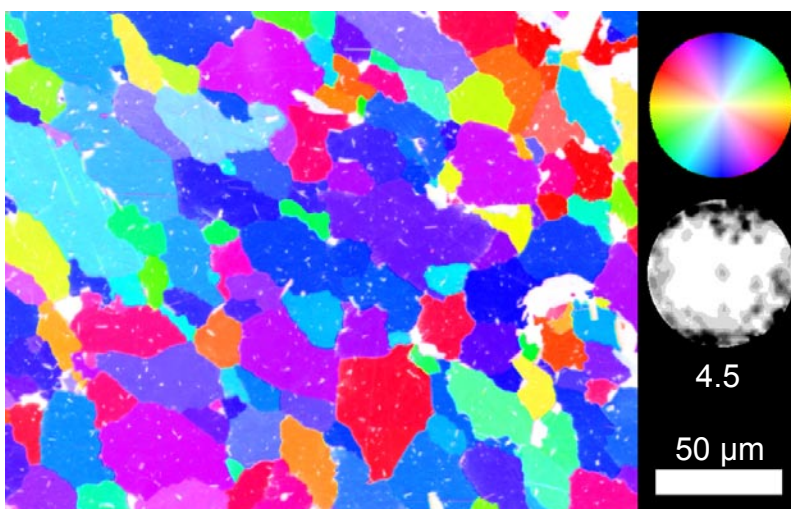
Locality: Eastern Alpi Apuane, close to the village of Arni.

Lithology: Carrara marble with layers of dolomite

Structural position: Tambura thrust zone, D1b shear zone in the overturned limb of the Tambura anticline.



Overview of sample 98-05, crossed polarizers. The gradient of the interference colors are due to a lower thickness of the section in the central part. Horizontal edge is ~2 cm. The area analyzed in detail is indicated.



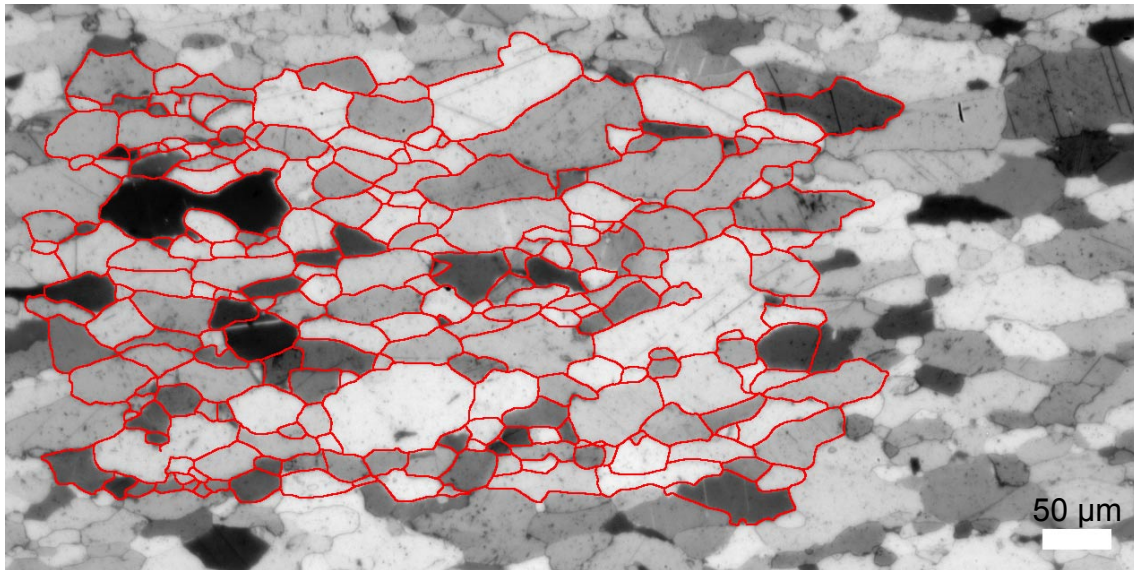
CIP c-axis orientation image. The maximum of the polefigure is indicated.

Sample: 99-38: D1-W

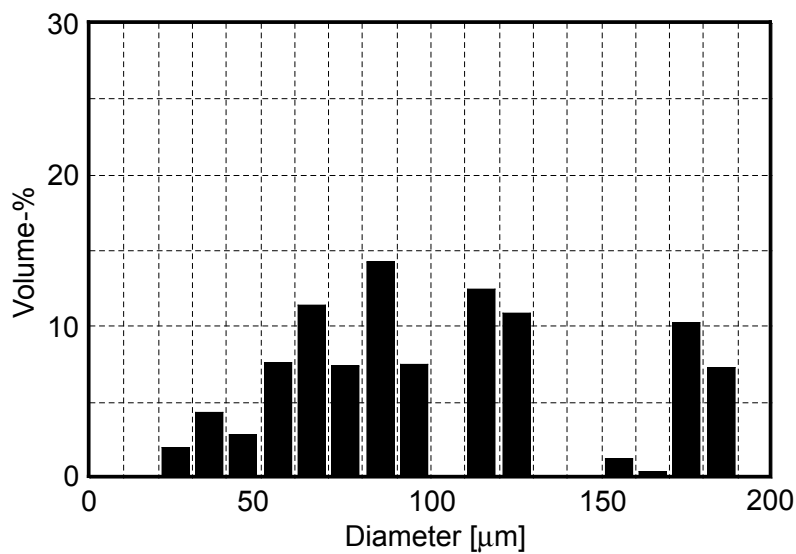
Locality: Western Alpi Apuane, normal limb of Vallini Syncline

Lithology: Carrara marble with layers of dolomite

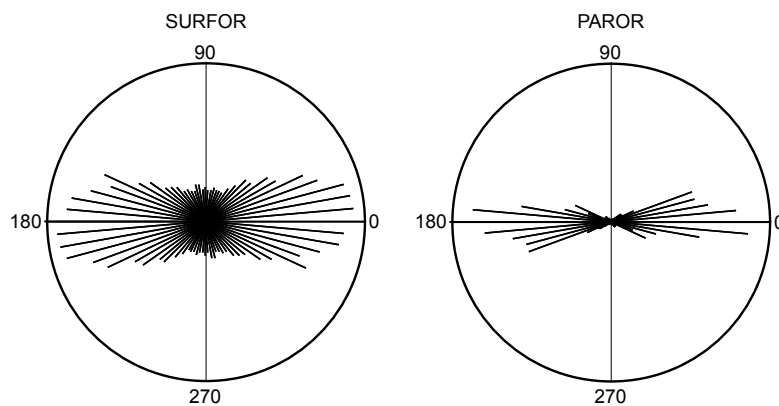
Structural position: D1b shear zone



Overview of sample 99-38, crossed polarized light. The grain boundary outline for the size and shape analysis is indicated in red. The scale (lower right) is 100 μm .



Histogram of volume weighted grain size distribution.



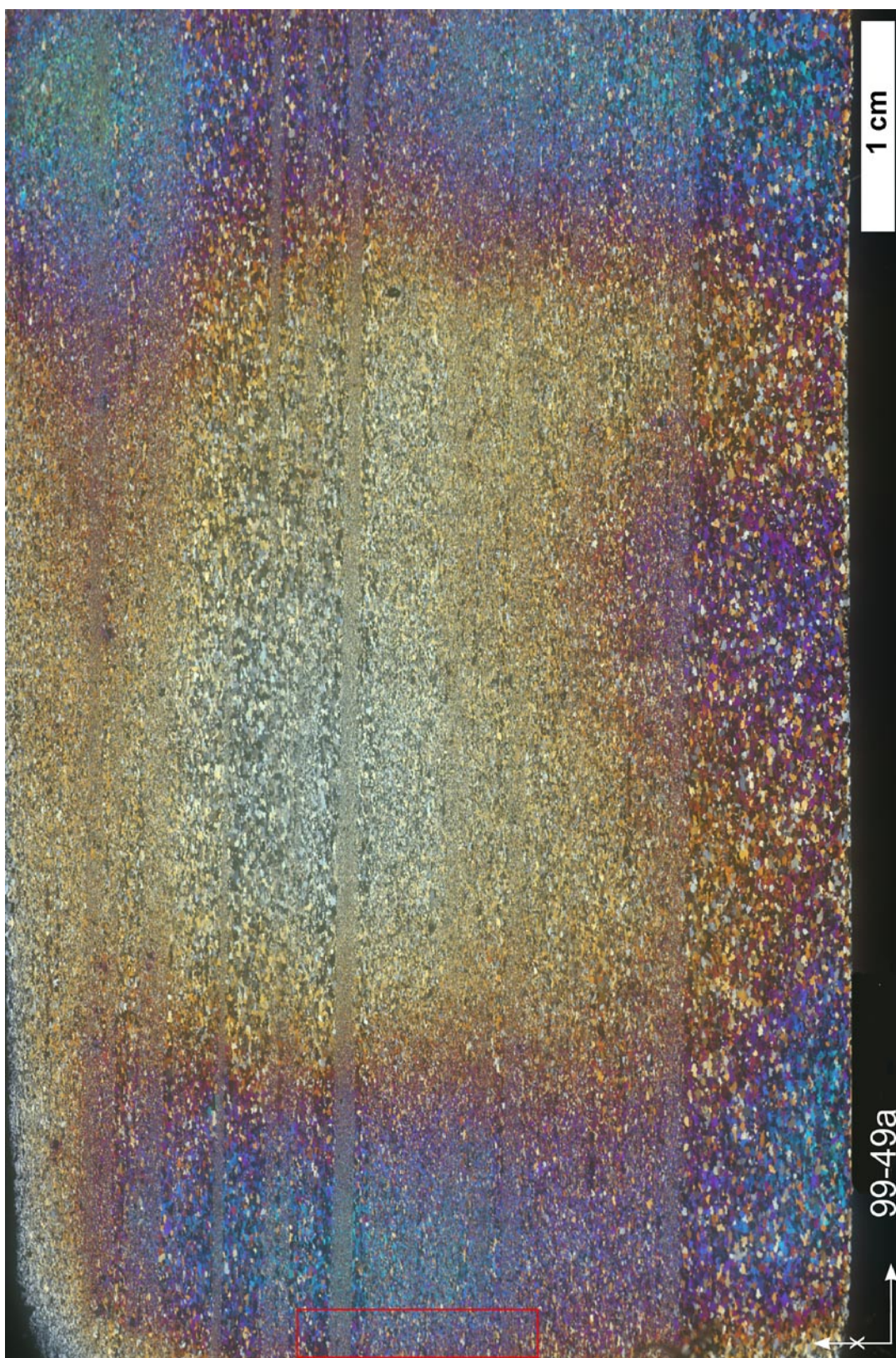
Rose diagrams of grain boundaries (SURFOR) and grain long axis (PAROR).

Sample: 99-49: D1-E-2

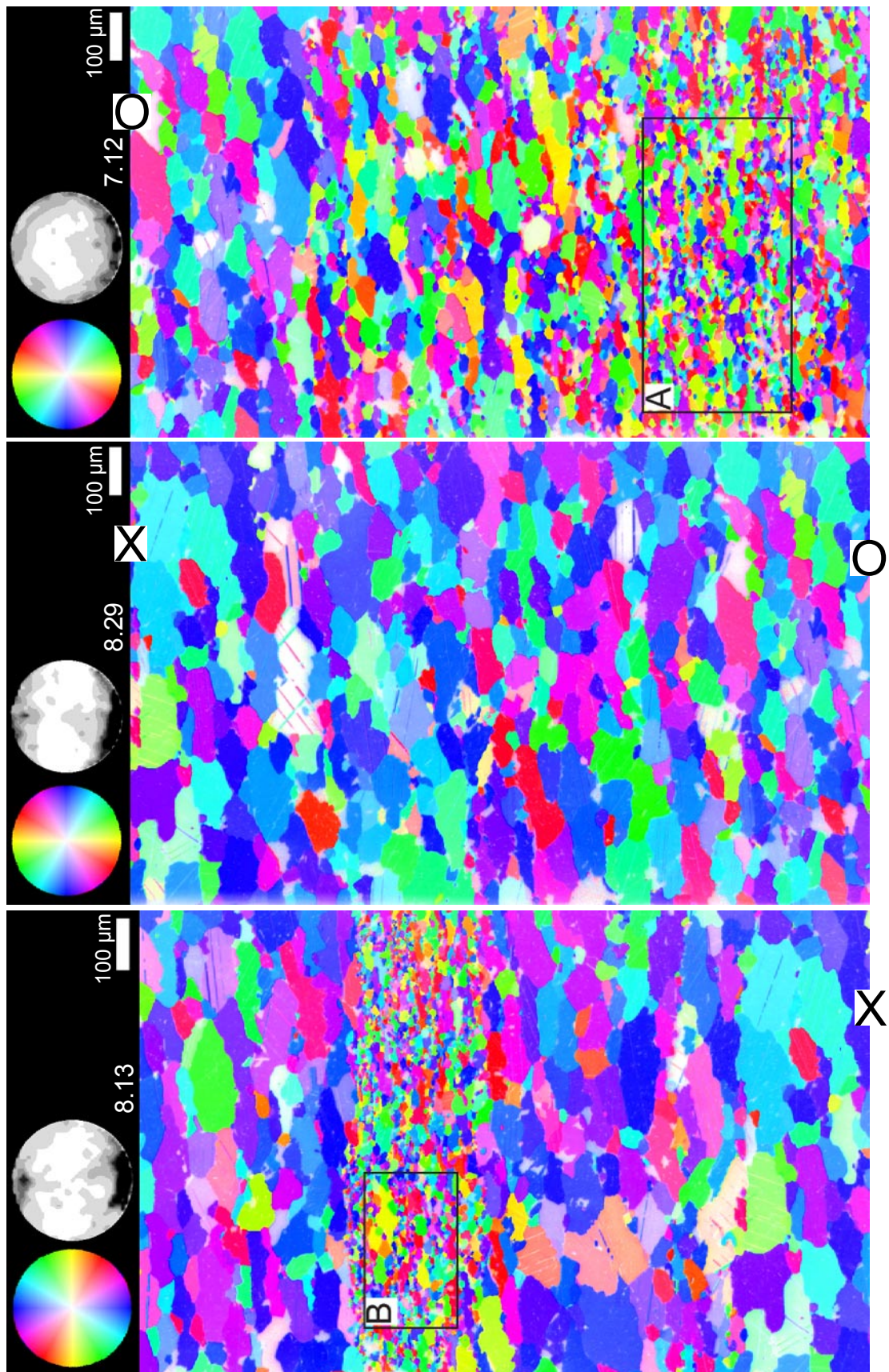
Locality: Eastern Alpi Apuane, close to the village of Arni.

Lithology: Carrara marble with layers of dolomite

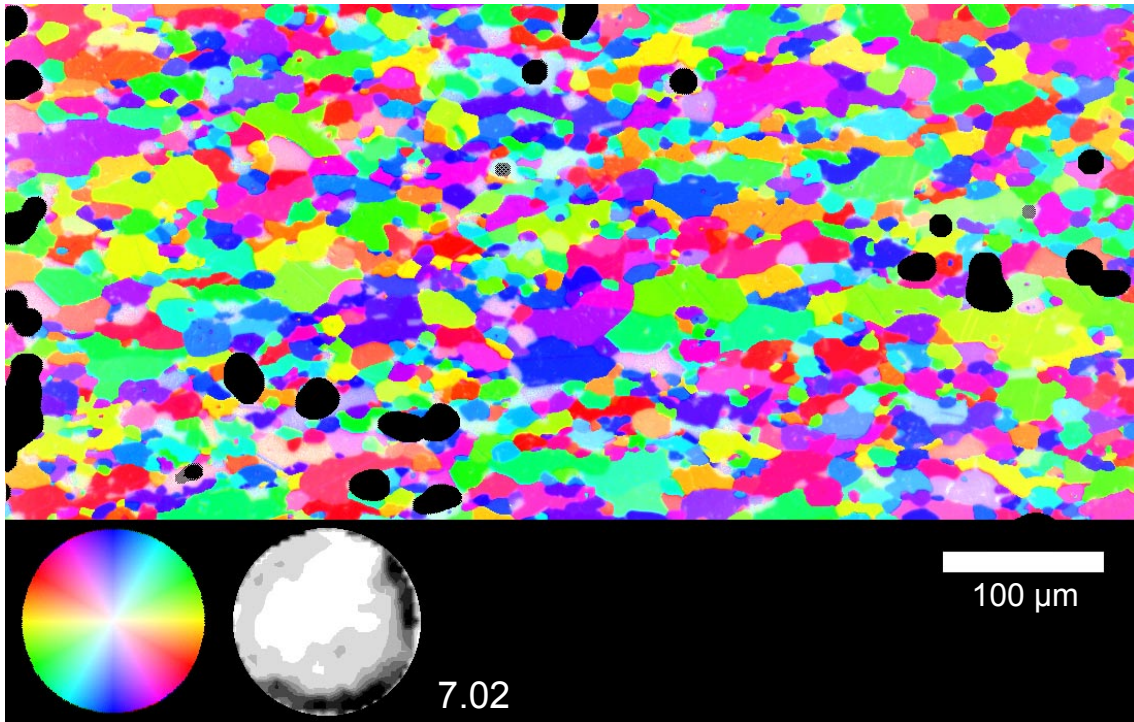
Structural position: Tambura thrust zone, D1b shear zone in the overturned limb of the Tambura anticline.



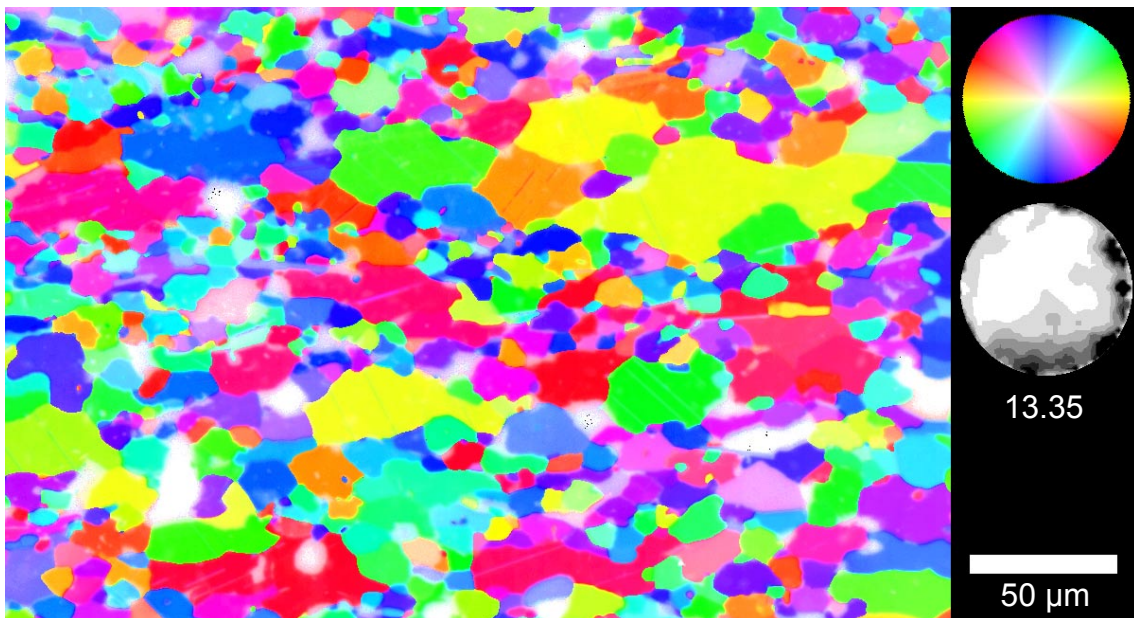
Overview image in crossed polarized light. The area, which is analyzed in detail (see next pages) is indicated.



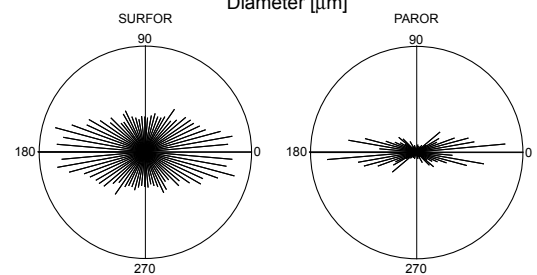
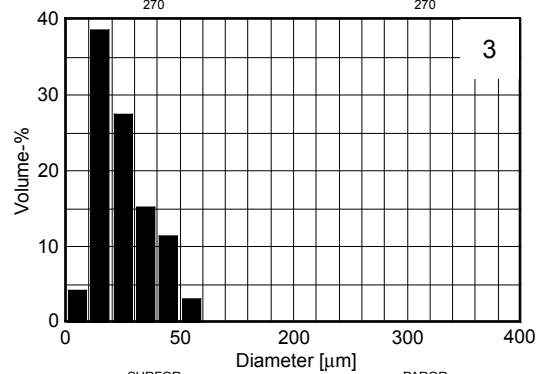
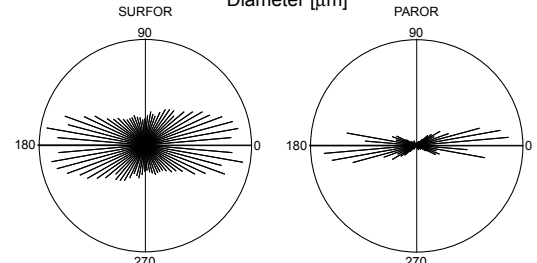
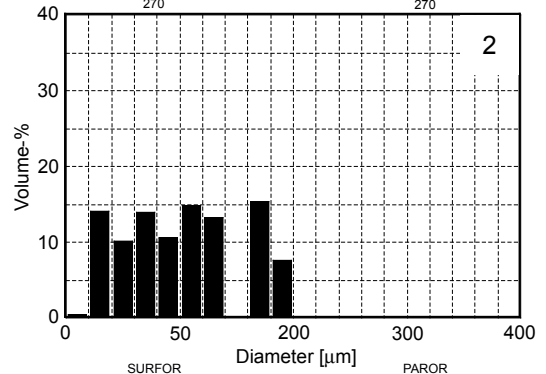
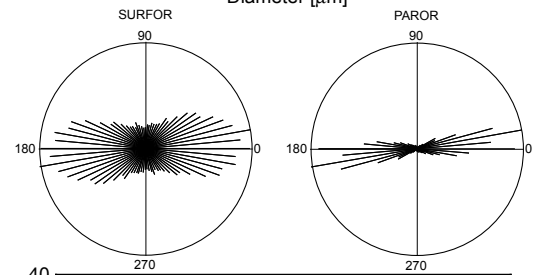
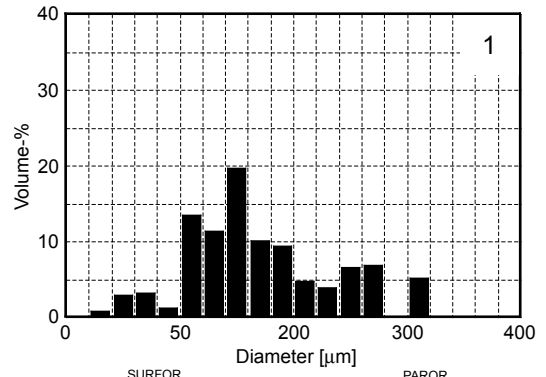
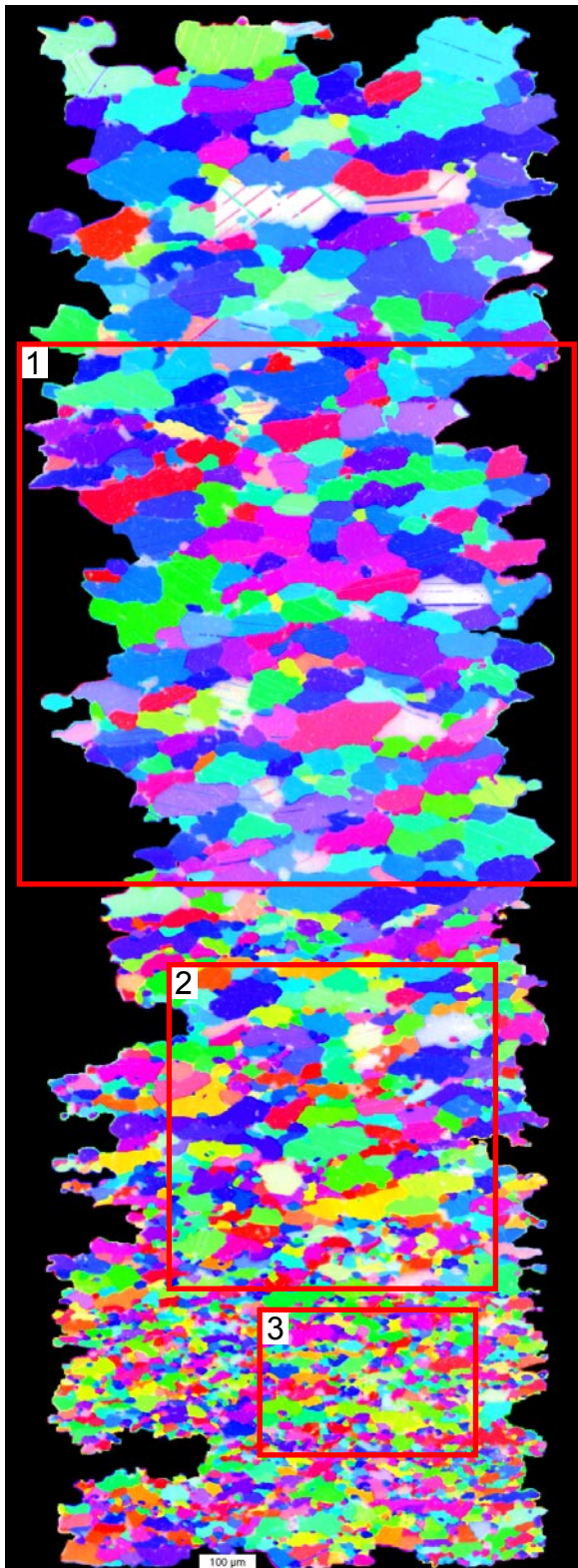
CIP c-axes orientation images of the area indicated in the overview image of the previous page. X and O indicate corresponding sites. The areas which were analyzed in detail are outlined (A and B). The maxima of the polefigures are indicated.



CIP c-axes orientation image of area A indicated on the previous page. The maximum of the polefigure is indicated. Note that calcite and dolomite influence the polefigure.

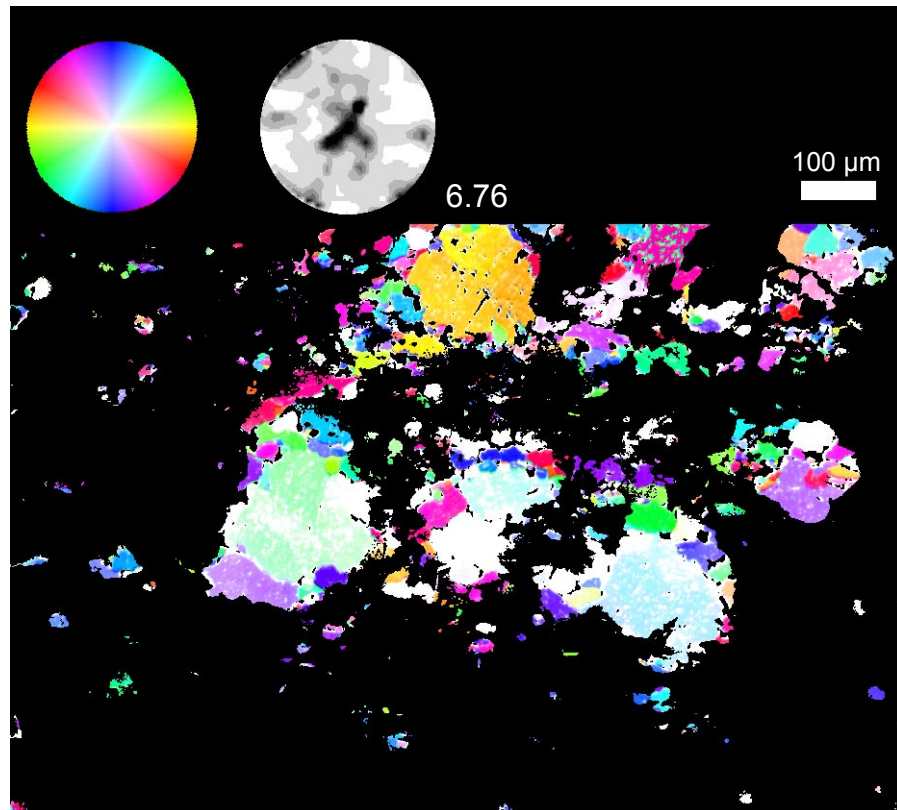


CIP c-axes orientation image of area B indicated on the previous page. The maximum of the polefigure is indicated. Note that calcite and dolomite influence the polefigure.

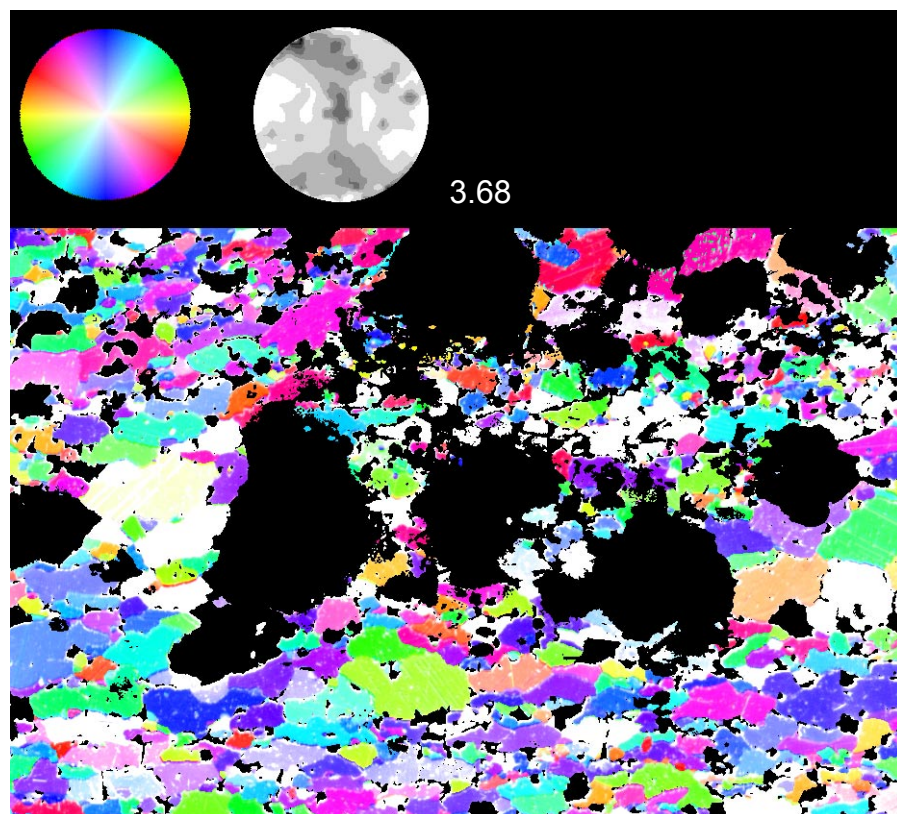


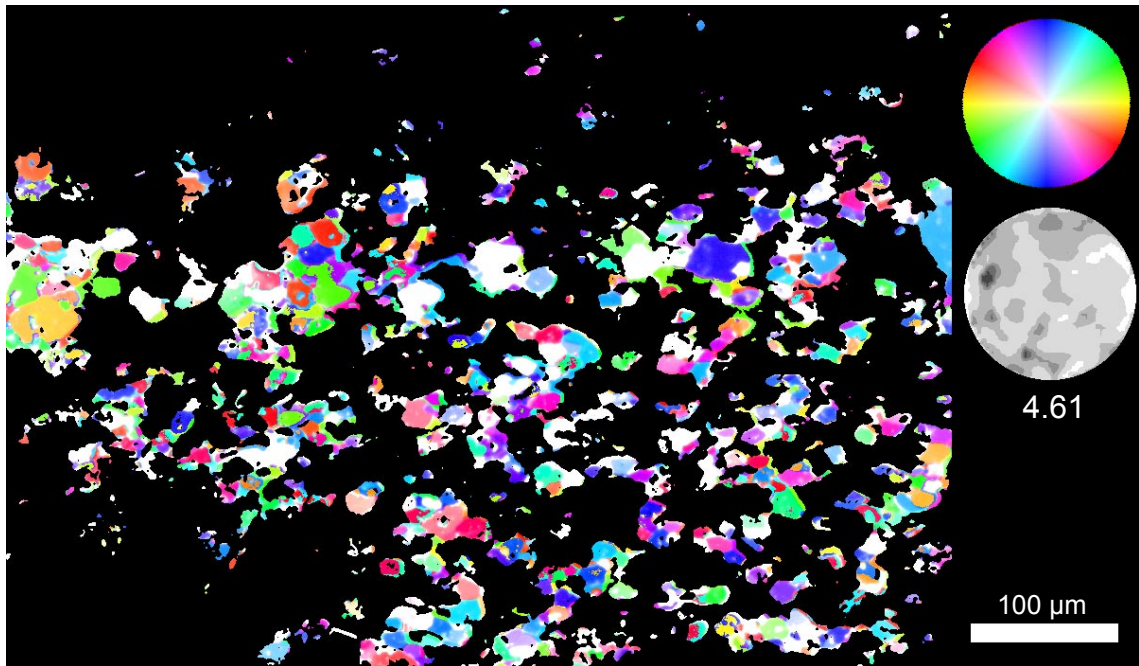
CIP c-axis orientation image (left) and grain size and shape analysis (right). The sites analyzed with respect to grain size and shape are indicated.

CIP c-axes orientation image of dolomite from a calcite-dolomite layer. The maximum of the polefigure is indicated. Calcite is masked using a CL image of the same area.



CIP c-axes orientation image of calcite of the same area as above. The maximum of the polefigure is indicated. Scale same as above. Dolomite is masked using the inverted mask file.





CIP c-axes orientation image of dolomite from a calcite-dolomite layer. The maximum of the polefigure is indicated. Calcite is masked using a CL image of the same area



CIP c-axes orientation image of calcite of the same area as above. The maximum of the polefigure is indicated. Scale same as above. Dolomite is masked using the inverted mask file.

Sample: 99-59: D1-E-1

Locality: Central Alpi Apuane, near the village Resceto

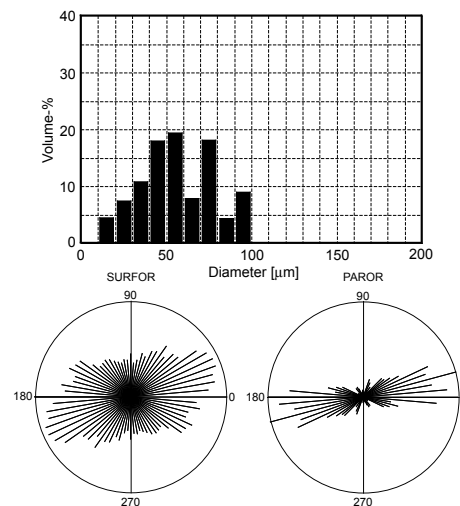
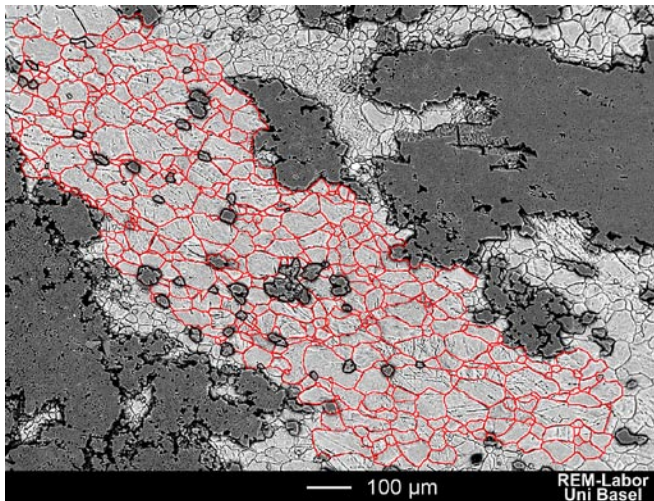
Lithology: Calcite/dolomite marble

Structural position: D1b shear zone

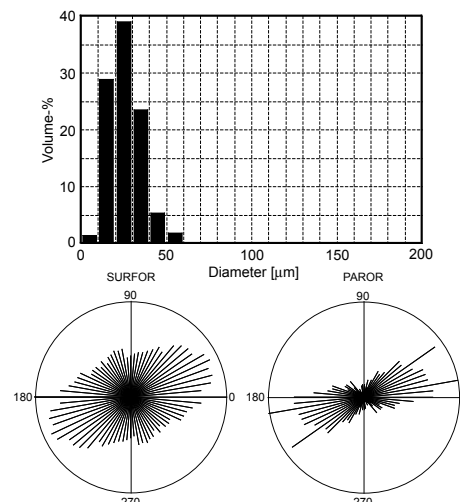
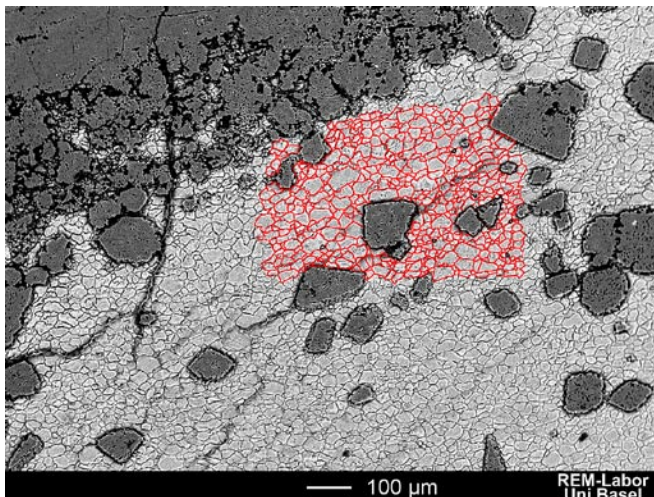
The marble of this locality is characterized by dispersed dolomite crystals and cm-scaled dolomite clasts in a calcite matrix. The five analyzed sites, shown on the following page are taken at different distances to a dolomite clast. Site 9 has the largest distance to the dolomite clast and site 1 is in direct contact with the clast. Site 0 represents a calcite inclusion inside the dolomite clast. The corresponding sample chip is shown in Appendix C1 (sample 99-59 a of series 2000-2). The upper part of the sample chip (light grey) represents the dolomite clast.

BSEM images of each site (dolomite is dark grey, calcite is light grey) and the grain outlines of the analyzed regions are shown on the left. The 3D-grain size distribution and PAROR- and SURFOR rose diagrams are depicted on the right.

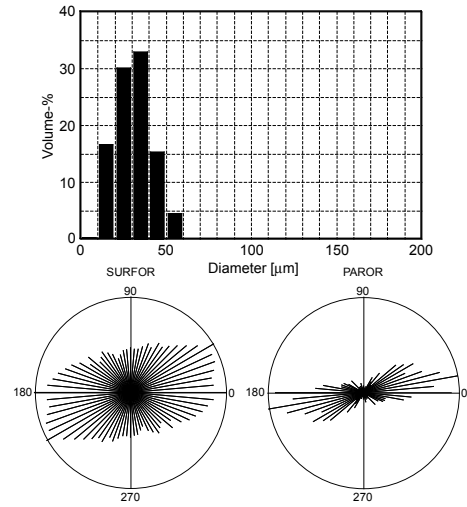
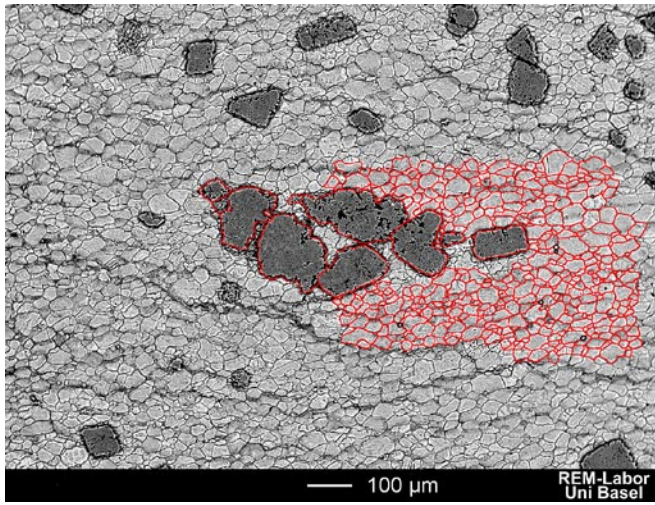
Site 0



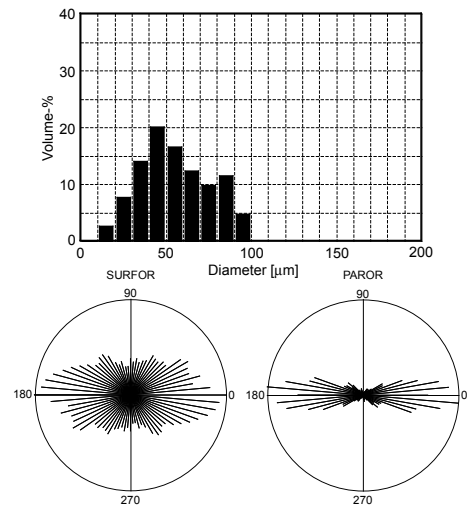
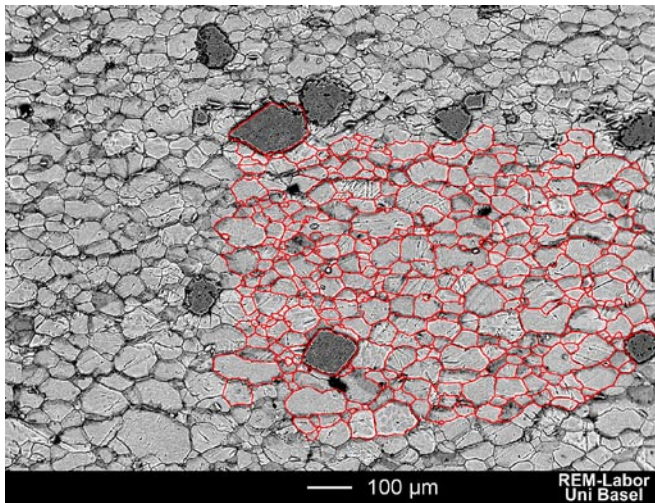
Site 1



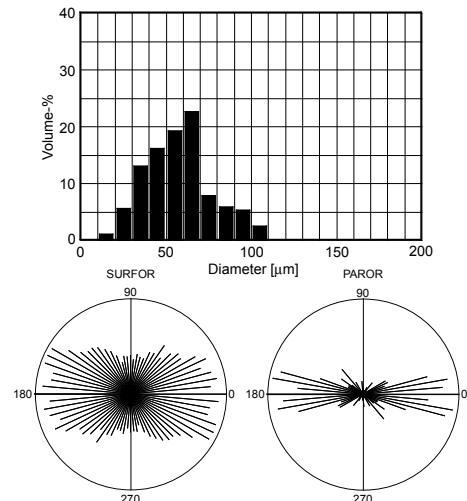
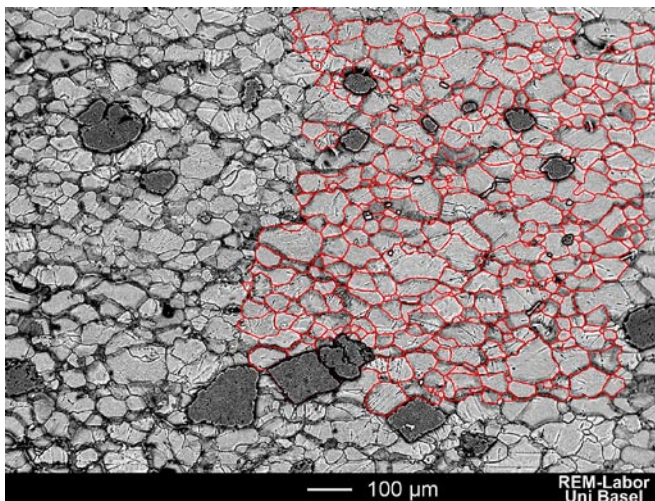
Site 3



Site 6



Site 9

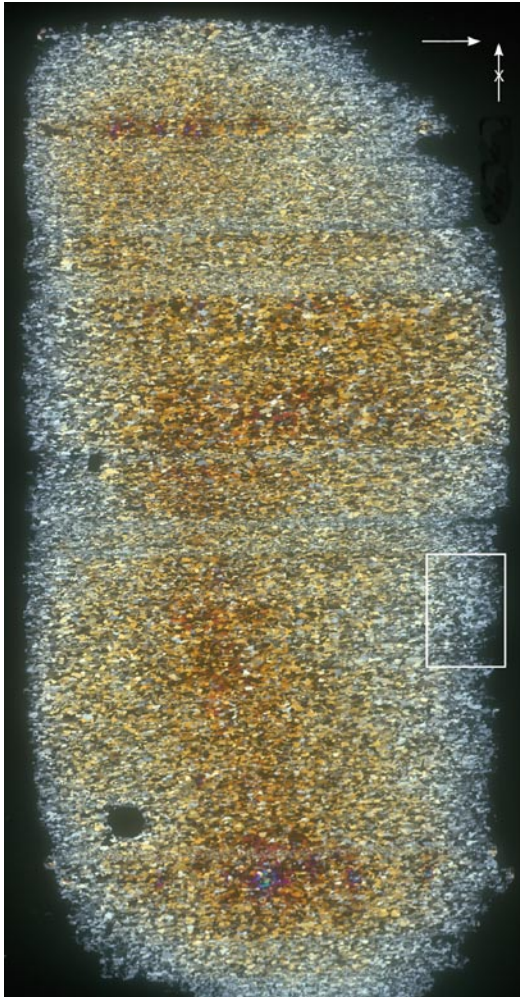


Sample: 2k-17A

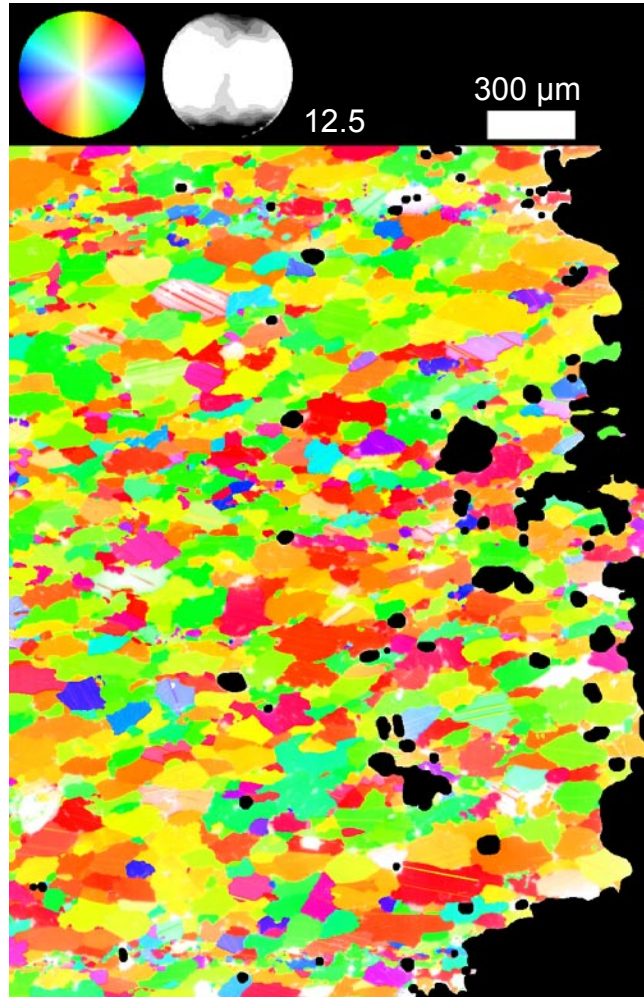
Locality: Eastern Alpi Apuane, close to the village of Arni.

Lithology: Carrara marble with layers of dolomite

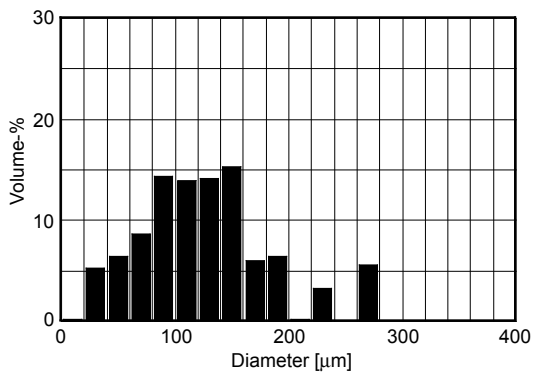
Structural position: Tambura thrust zone, D1b shear zone in the overturned limb of the Tambura anticline.



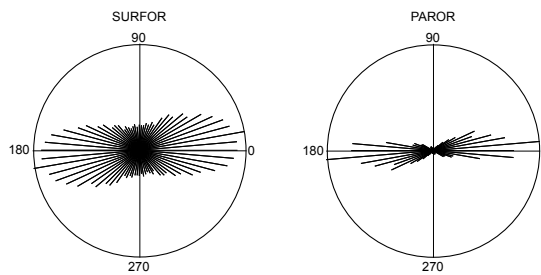
Overview of sample 2k-17A, cross polarized light. The investigated area is indicated. Crossed arrow points upward, East is on the right, West is on the left side.



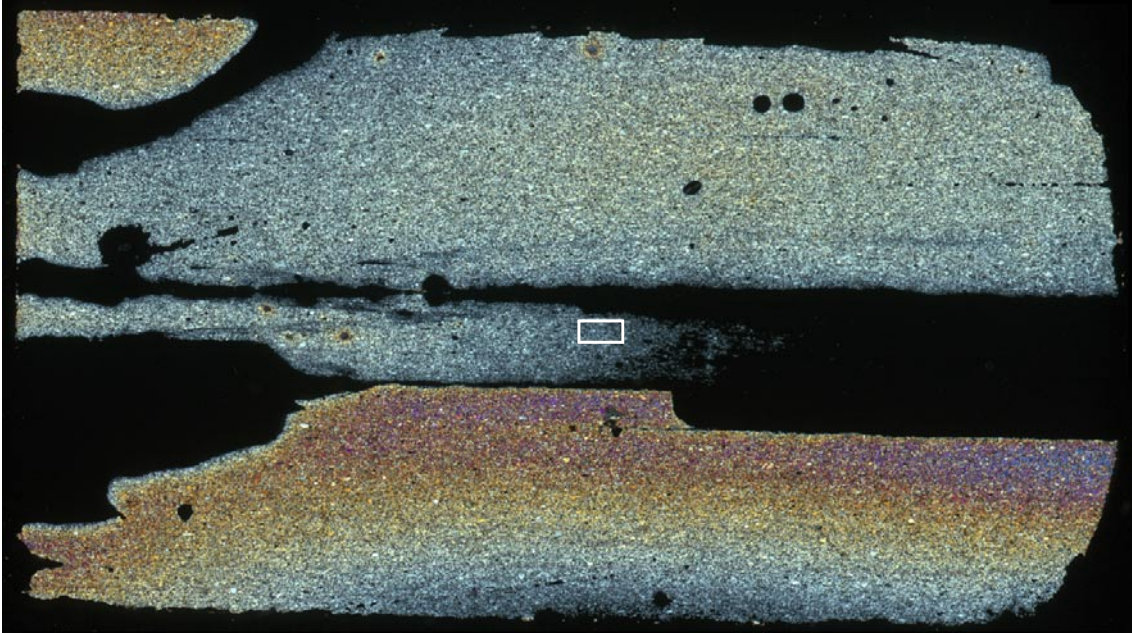
CIP c-axes orientation image. The maximum of the pole-figure is indicated.



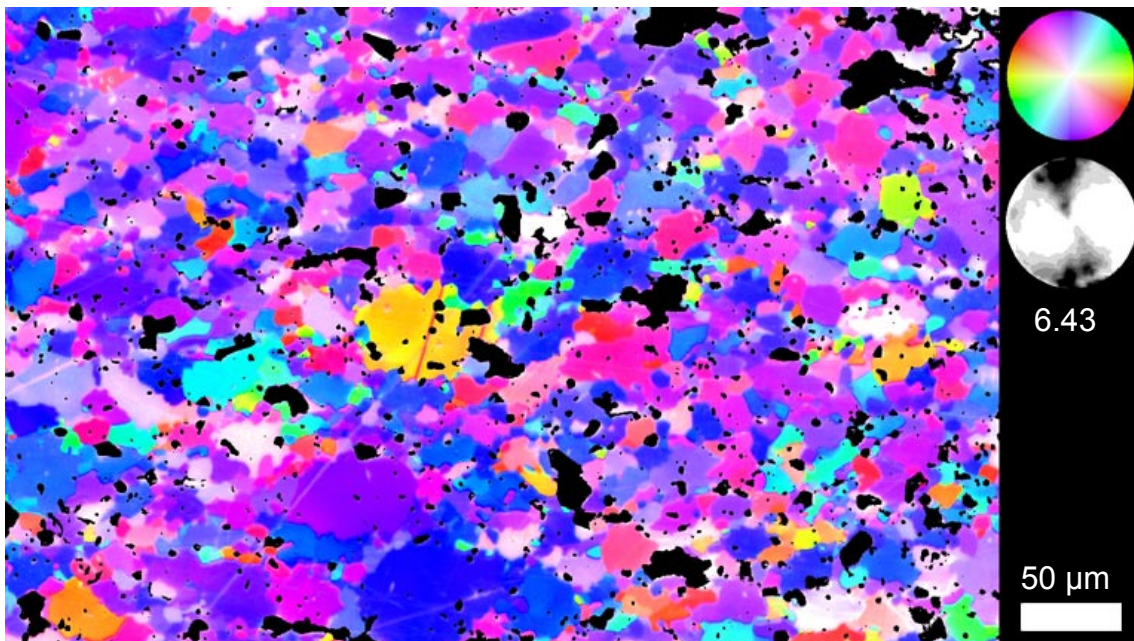
Histogram of volume weighted grain size distribution.



Rose diagrams of grain boundaries (SURFOR) and grain long axis (PAROR).

Sample: M 239 (from Giancarlo Molli, University of Pisa, Italy)**Locality:** Eastern Alpi Apuane, Panie Unit, Pania della Croche**Lithology:** Carrara marble**Structural position:** Tectonic contact Apuane Unit / Panie Unit

Overview image in crossed polarized light. The analyzed area is indicated.



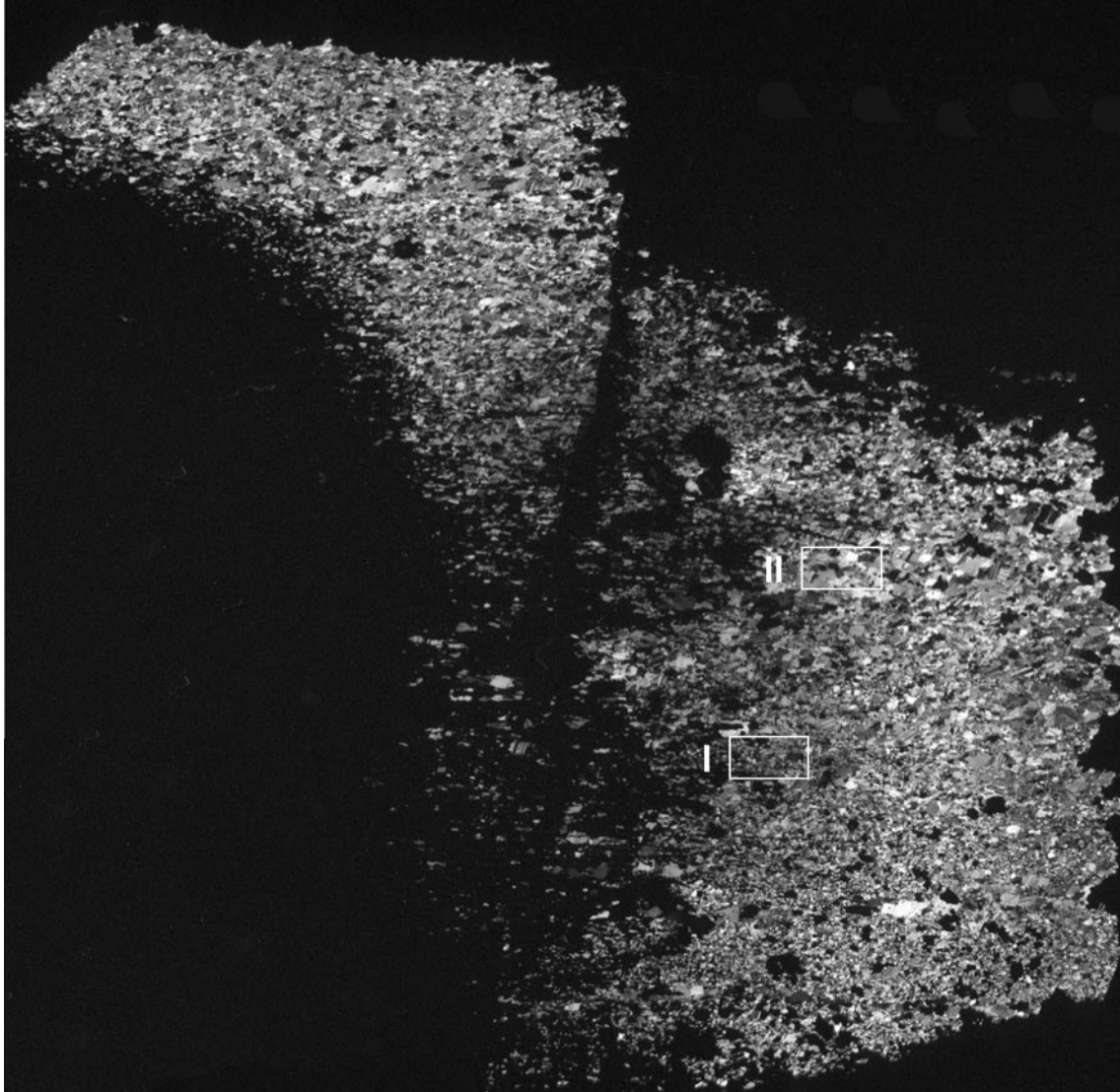
CIP c-axes orientation image of indicated area. The maximum of the polefigure is indicated.

Sample: 98-06a

Locality: Western Alpi Apuane, Quarry 'Vallini'

Lithology: Carrara marble

Structural position: D2 shear zone of millimeter scale

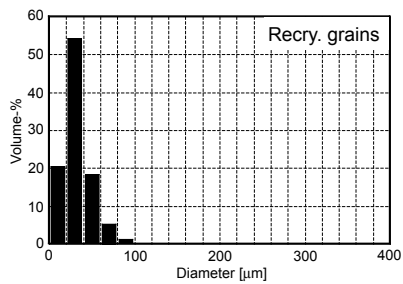
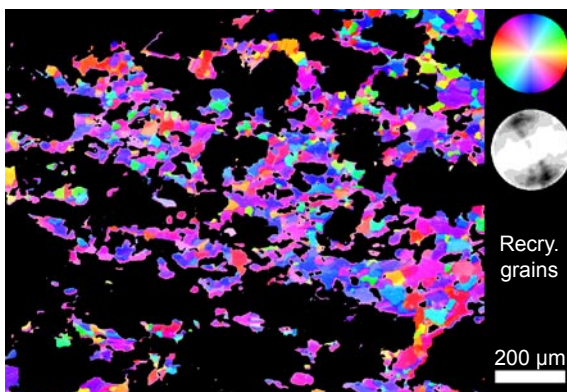
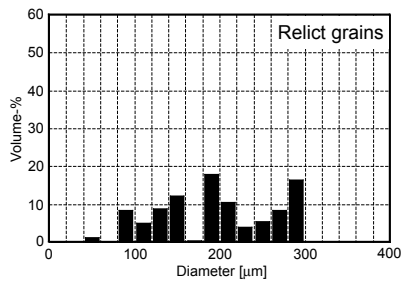
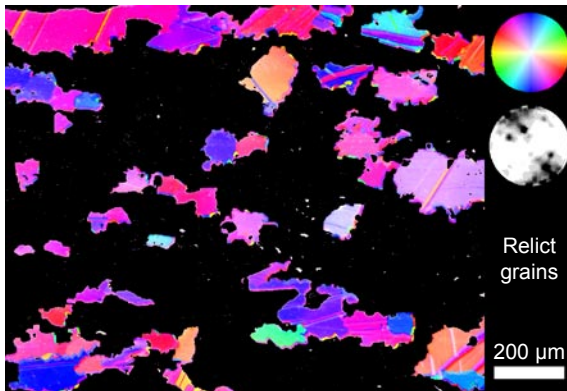
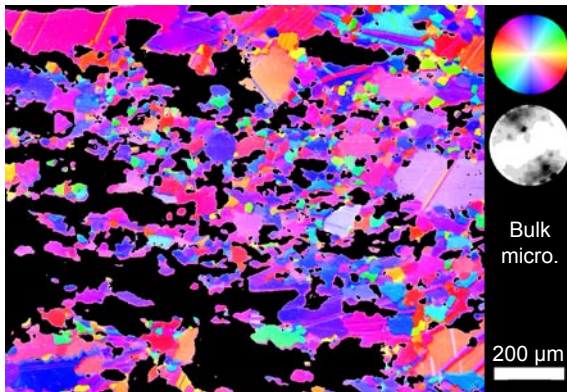


Overview image of sample 98-06a, crossed polarized light. Micrograph is in grayscale. Analyzed regions are I and II are indicated.

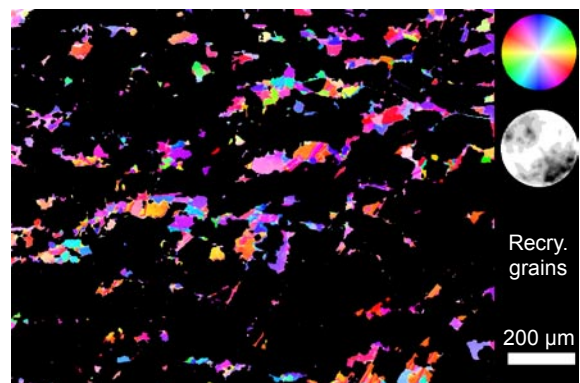
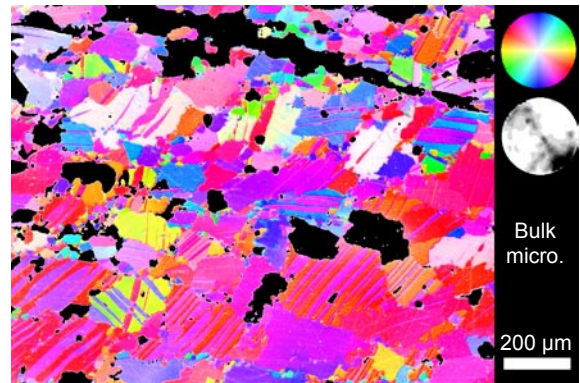
Following page:

CIP c-axes orientation images of region I and II. For each region the orientation image of the bulk microstructure (top row), the relict grains (middle row) and the recrystallized grains (bottom row) are shown.

98-06: Site I



98-06: Site II

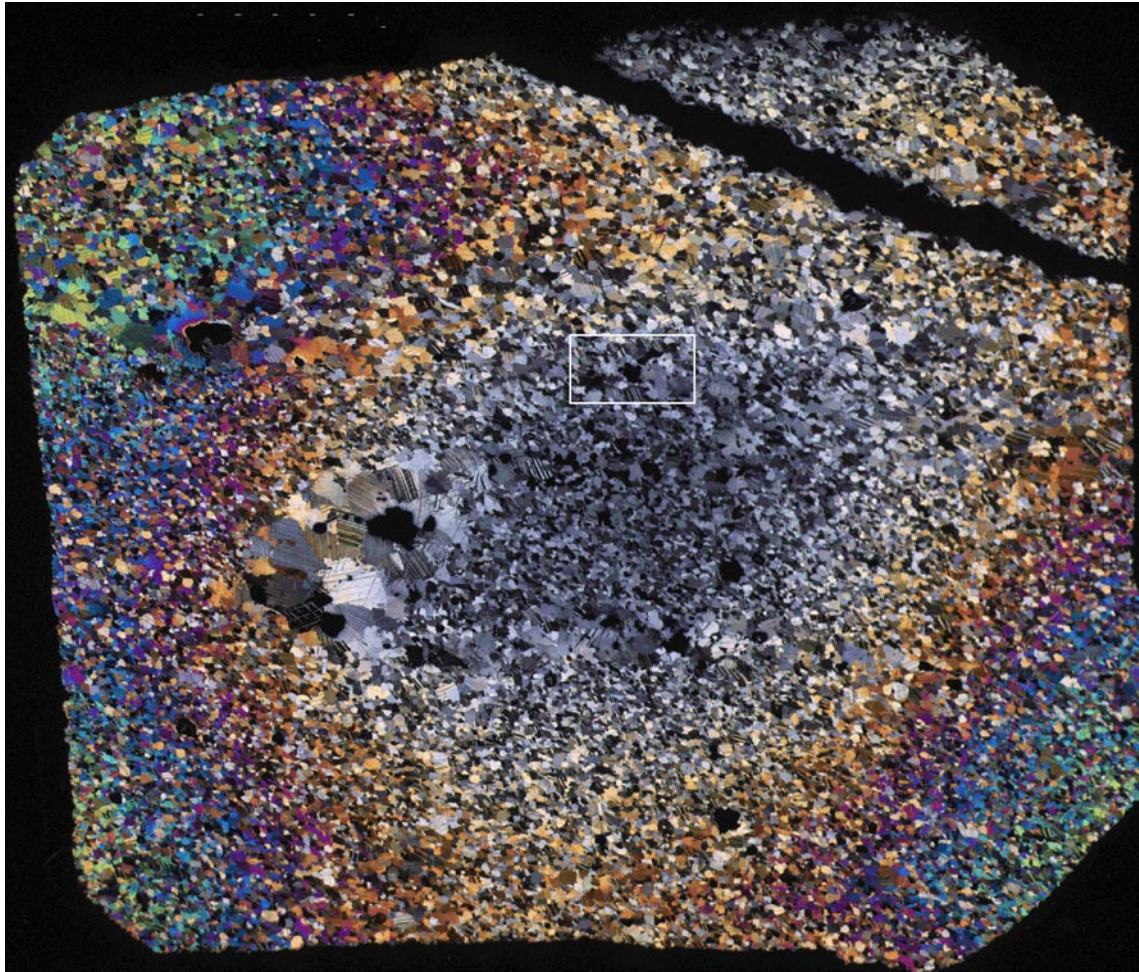


Sample: 98-06c

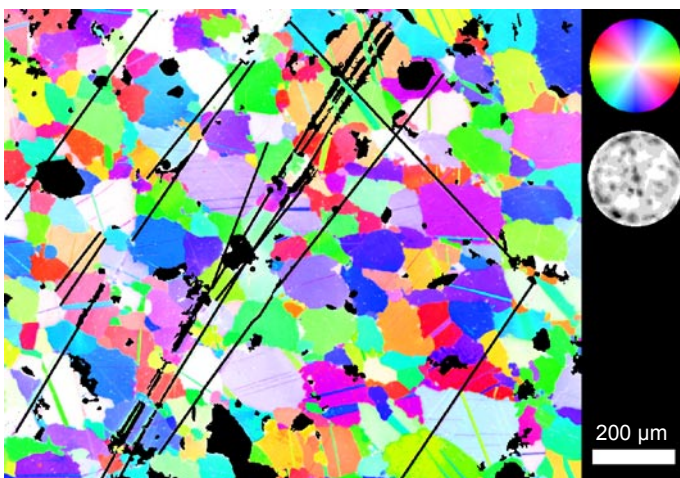
Locality: Western Alpi Apuane, Cava Vallini.

Lithology: Carrara marble

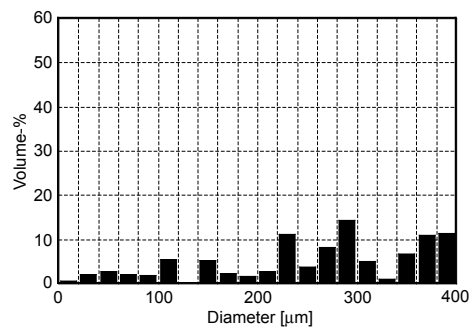
Structural position: Partially recrystallized marble, CIP from non-recrystallized domain.



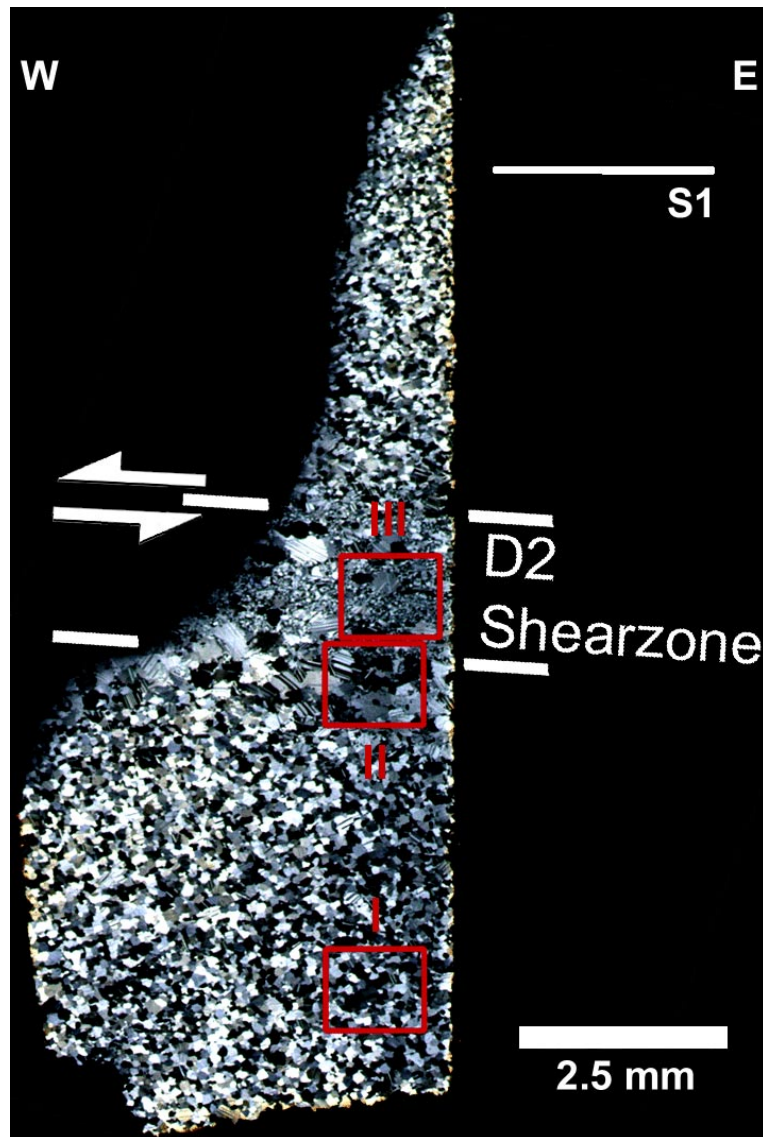
Overview of sample 98-06c, crossed polarizers. The gradient of the interference colors are due to a lower section thickness in the central part. Horizontal edge is ~2 cm.



CIP c-axes orientation image of indicated region. Black lines are scratches in the ultra-thin section.



Histogram of volume weighted grain size distribution.

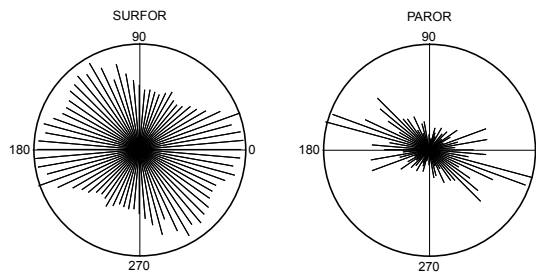
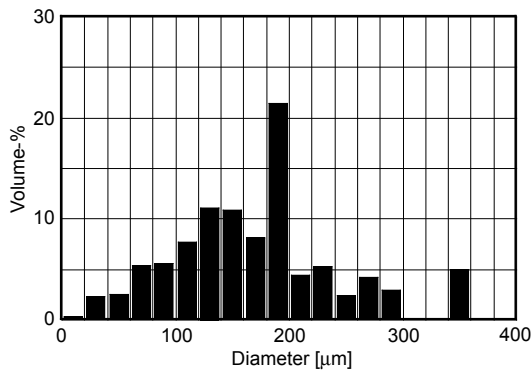
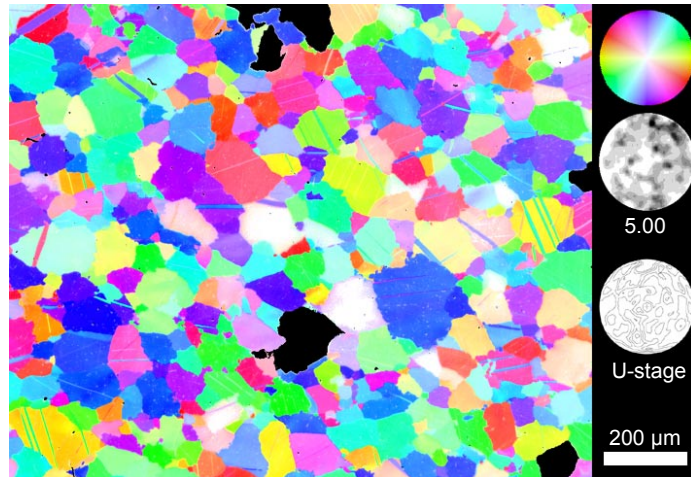
Sample: 98-19 = 2k-7 : D2-W**Locality:** Western Alpi Apuane, Cava Vallini.**Lithology:** Carrara marble**Structural position:** Microscale D2 shear zone

Overview of sample 98-19, crossed polarized light. Shear zone boundary, shear direction and orientation of S1 are indicated. The regions of three analyzed sites are indicated. Note that parallel to the fine recrystallized domain (site III) the grain size is larger (site II) than in the protolith (site I).

Sample 2k-7 comes from the same millimeterscale shear zone as sample 98-19. The microstructural characteristics of both specimen are similar.

98-19: Site I

CIP c-axes orientation image. The maximum of the polefigure is indicated. The second polefigure, below the CIP-polefigure is derived from U-stage measurements. Each grain of the region analyzed by CIP was also measured using the U-stage.

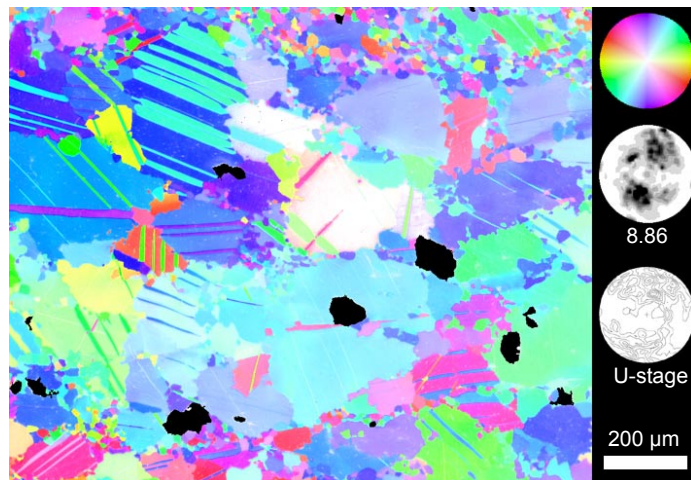


Rose diagrams of grain boundaries (SURFOR) and grain long axis (PAROR).

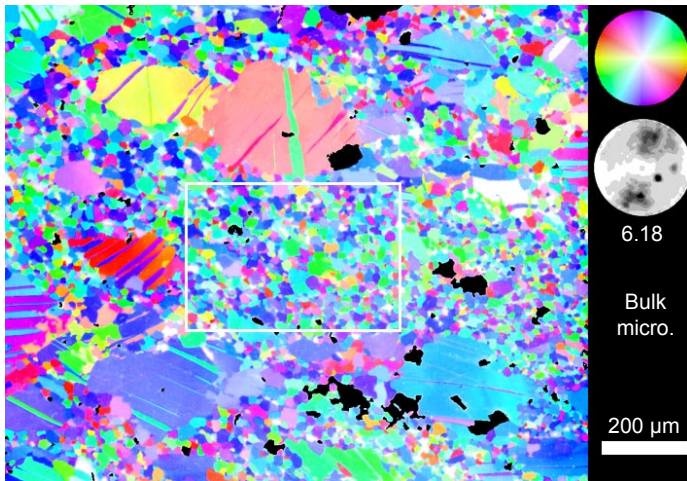
Histogram of volume weighted grain size distribution.

98-19: Site II

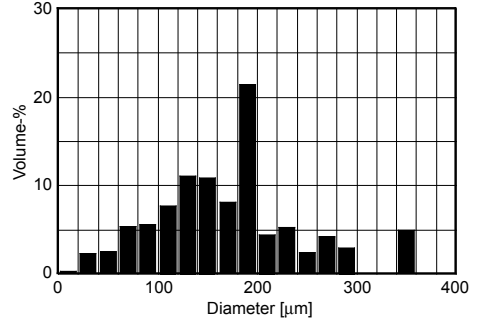
CIP c-axes orientation image. The maximum of the polefigure is indicated. The second polefigure, below the CIP-polefigure is derived from U-stage measurements. Each grain of the region analyzed by CIP was also measured using the U-stage.



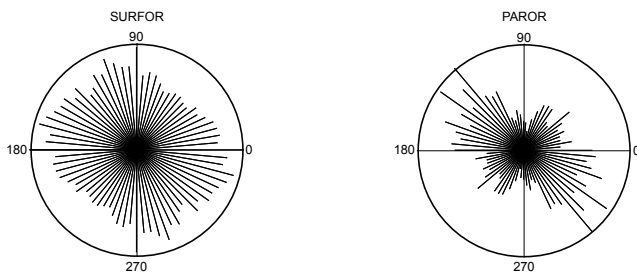
98-19: Site III



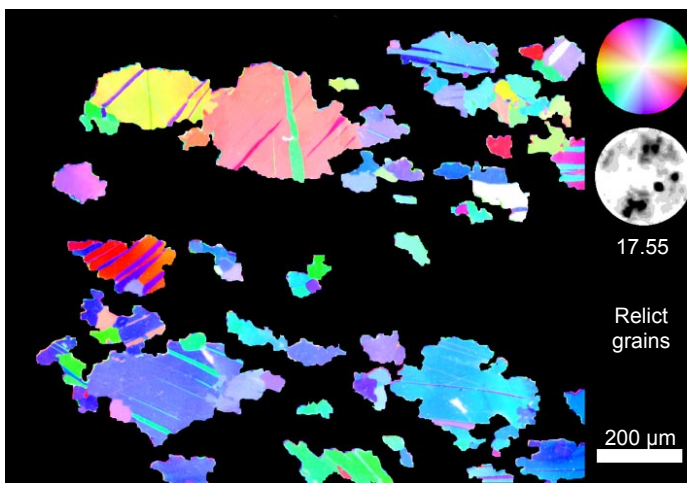
CIP c-axes orientation image of bulk microstructure. The maximum of the polefigure is indicated.



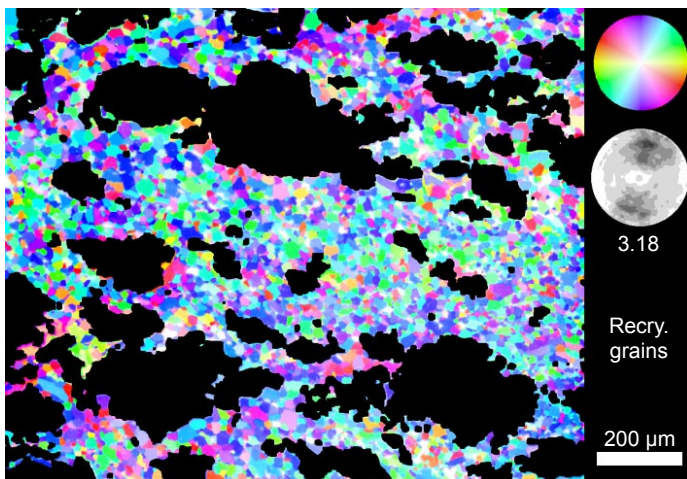
Histogram of volume weighted grain size distribution.



Rose diagrams of grain boundaries (SURFOR) and grain long axis (PAROR).

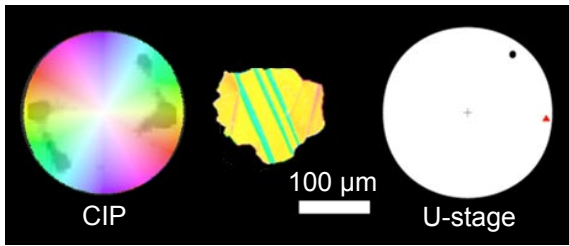


CIP c-axes orientation image of relict grains. The maximum of the polefigure is indicated.

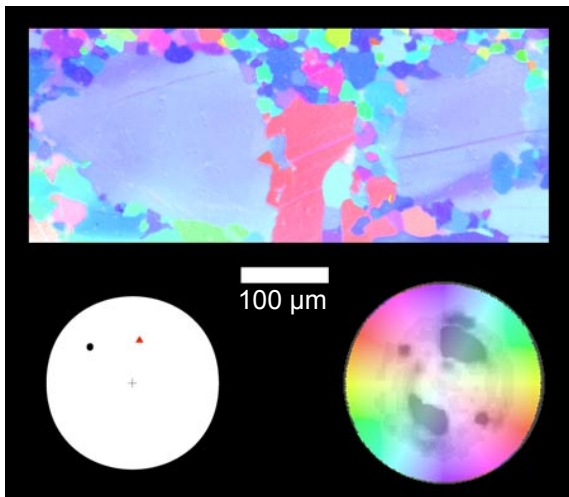


CIP c-axes orientation image of recrystallized grains. The maximum of the polefigure is indicated.

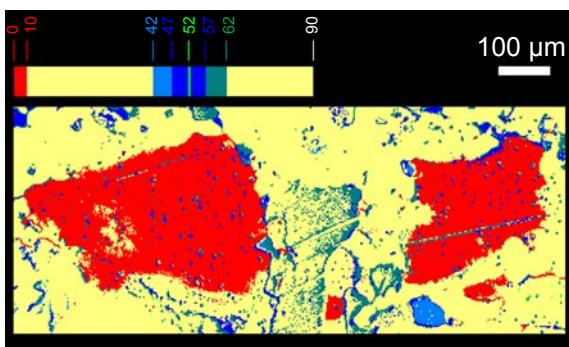
In order to check the quality of the CIP-measurements of calcite the following analysis was carried out. Individual twinned calcite grains were selected and analyzed by CIP and by U-stage. The corresponding twin and host grain orientations are depicted in CIP and U-stage polefigures. In the U-stage polefigures the host orientations are indicated by red triangles, those of twin lamellae by black dots.



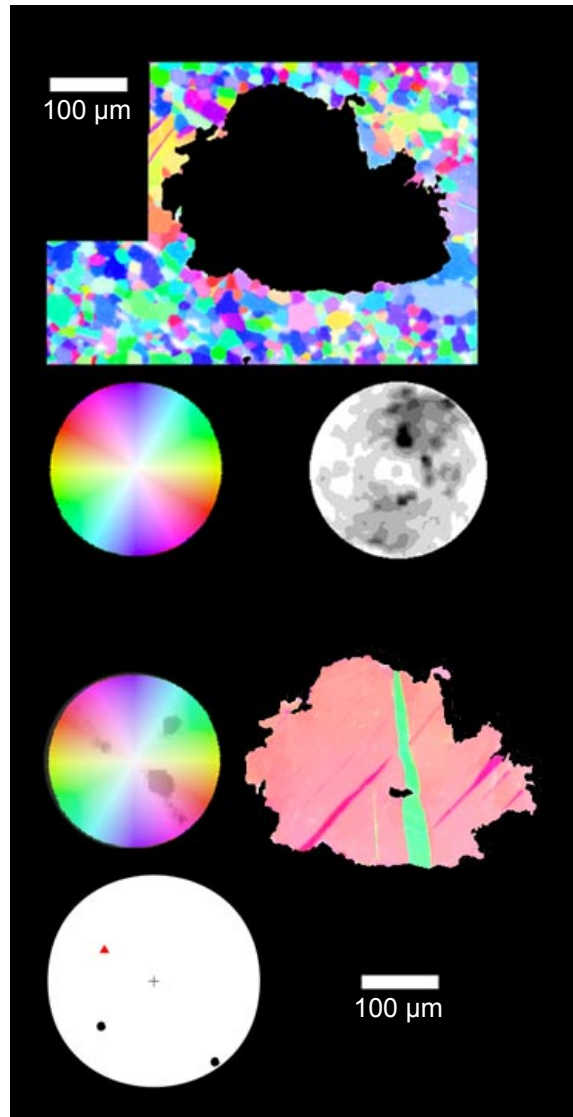
Color Look-UpTable (CLUT) and super-imposed CIP c-axes polefigure of the twinned grain (cf. sample 98-19, site I) are shown the left. The corresponding U-stage measurement of twinned and host domain is indicated on the right.



CLUT and super-imposed CIP c-axes polefigure of the twinned grain (cf. sample 98-19, site II) are shown the right. The corresponding U-stage measurement of twinned and host domain is indicated on the left.



Same area than above. The image is color-coded according to the CLUT indicated in the figure. Red domains include an angle less than 10° with the host domain, blue and green domains are at an angle close to the theoretical Twinning orientation (52° from host grain c-axis). Yellow areas have intermediate orientations.



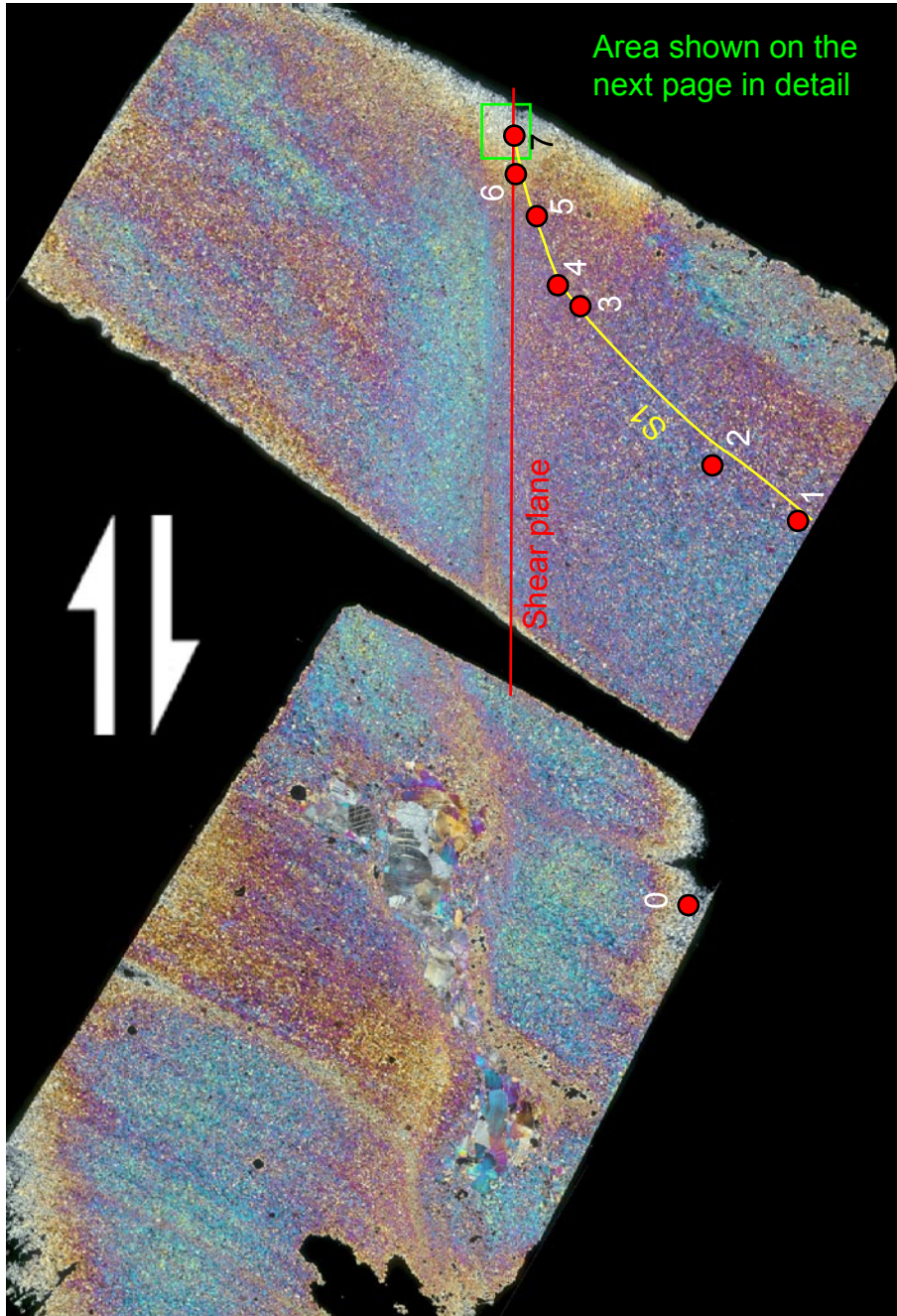
CIP-c-axes orientation image of twinned (bottom) grain (cf. sample 98-19, site III) and its surrounding recrystallized matrix (top).

Sample: 99-57: D2-C

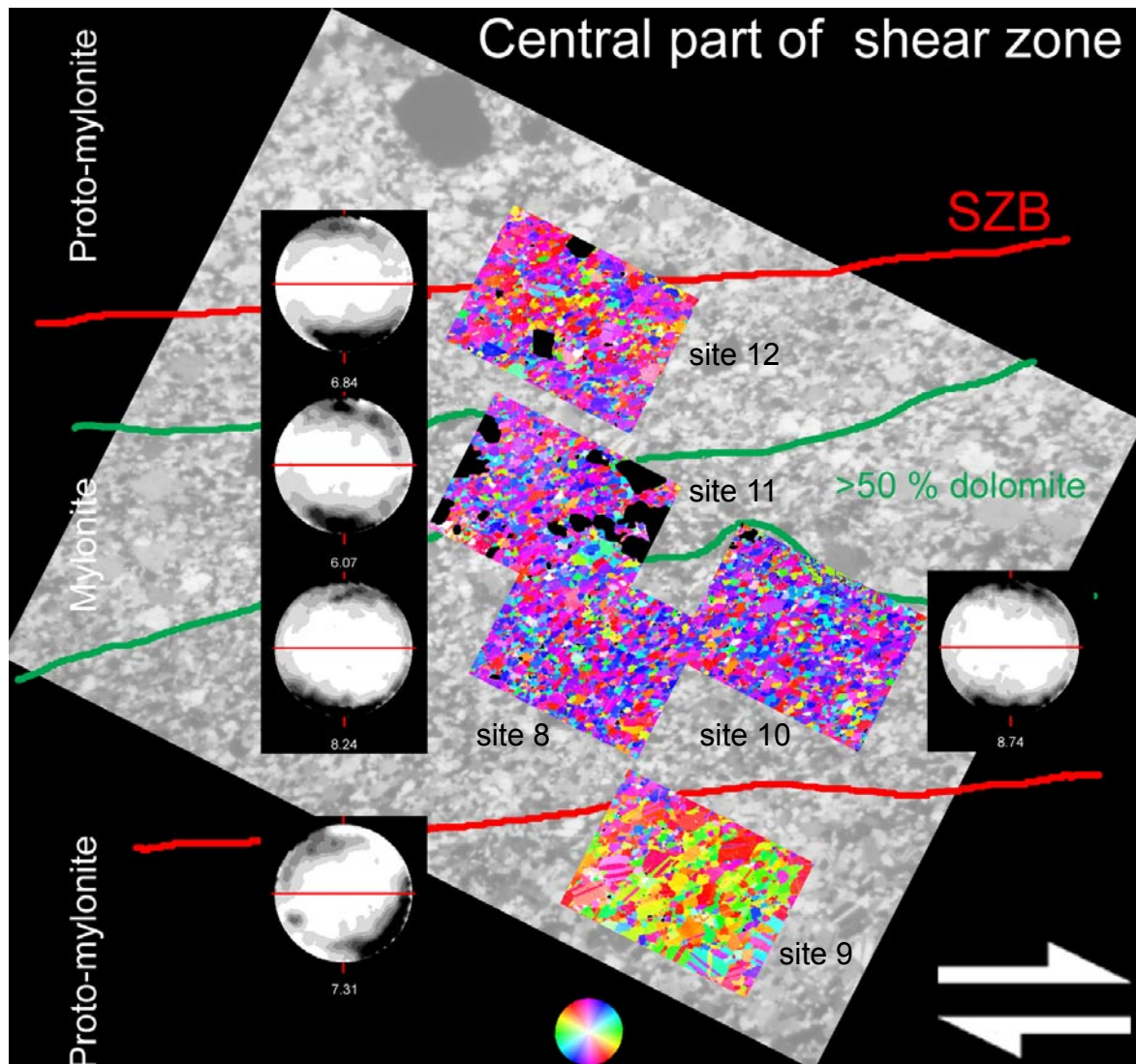
Locality: Central Alpi Apuane, close to the village of Forno.

Lithology: Carrara marble with layers of dolomite

Structural position: Rasori Antiform, refolded inverted limb of the Vinca-Forno anticline

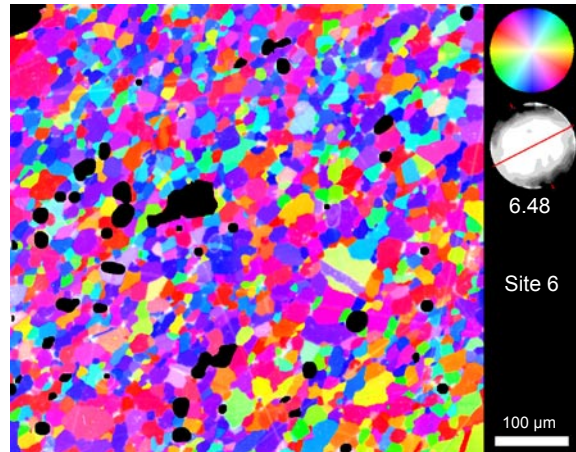
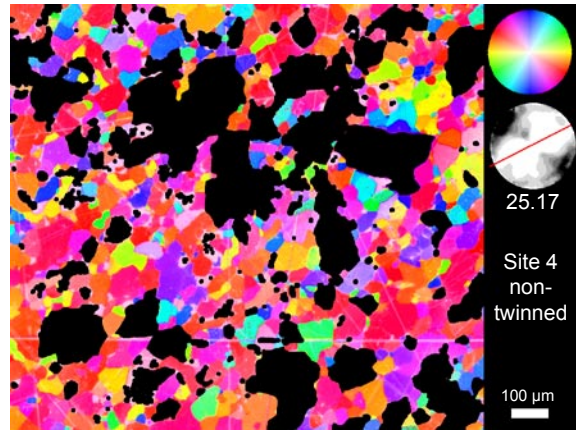
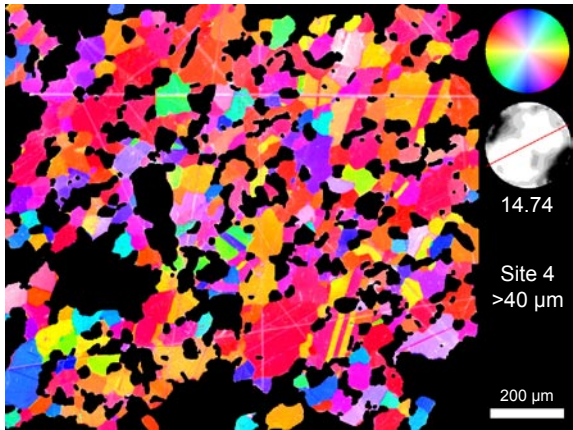
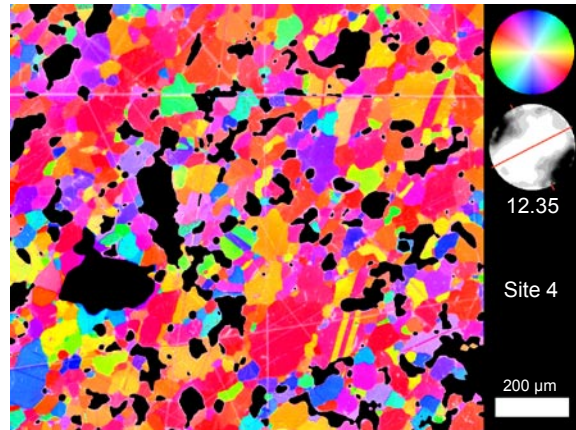


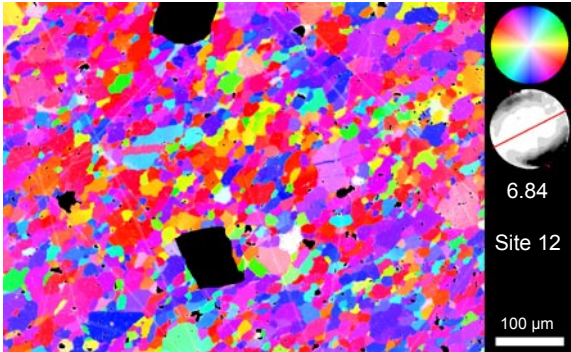
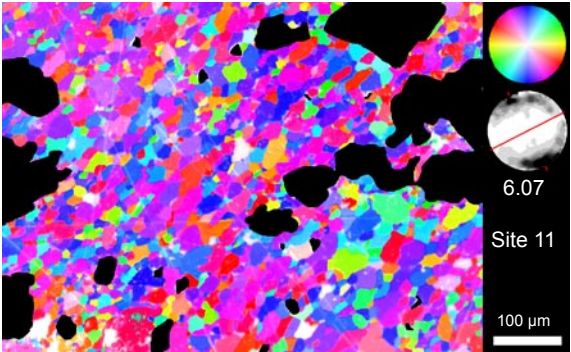
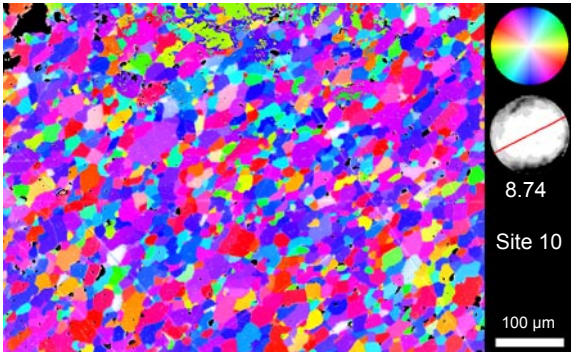
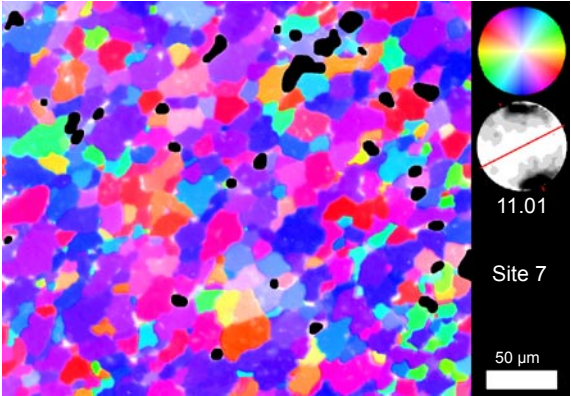
Overview of sample 99-57, crossed polarized light. The green square indicates the area shown on the next page in detail. Red dots represent sites investigated in detail, they are shown on the following pages. Shear plane and shear direction and trace of S1 foliation is indicated. Grain size and shape analysis are shown in chapter 3.

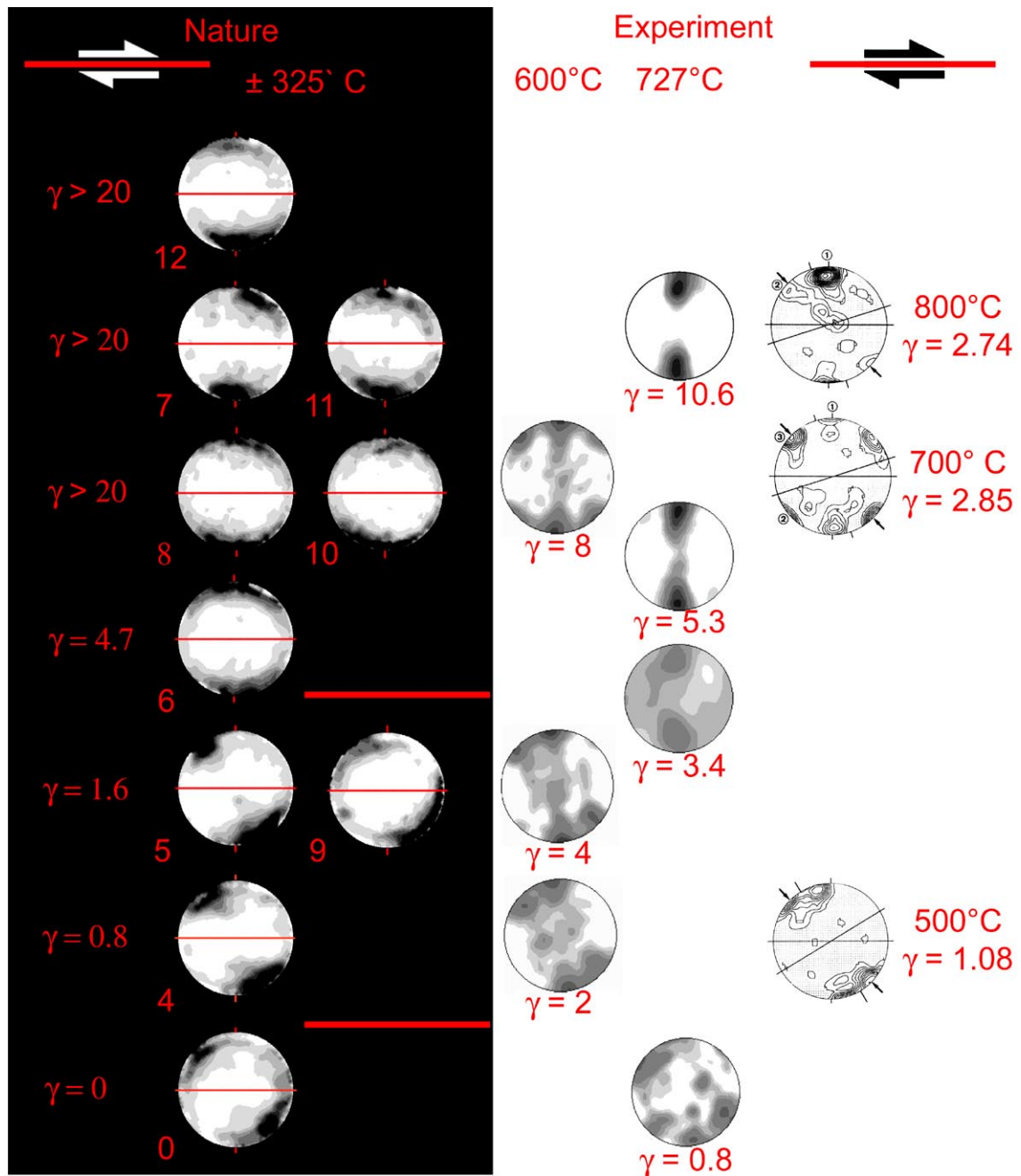


Overview of the center of the shear zone (site 8-12). Their position with respect to the shear zone is indicated on the previous page (green box) The c-axes pole figures determined from each site are shown. The maxima of the polefigures are, shear zone boundary (SZB), shear direction and high dolomite domain are indicated.

On the following pages individual CIP c-axes orientation images of site 0 to 12 are illustrated. Each orientation map is color coded according to the color look-up table (LUT) shown at the top left of each image. The c-axes polefigures corresponding to the shown areas are shown below the LUT. The maxima of the polefigures, site numbers and scales are indicated. The orientation of the shear plane (red line) is marked in each polefigure. Note that for site 4 the bulk microstructure and separated images for grains larger/smaller than $40\mu\text{m}$ and for twinned and untwinned grains are shown.







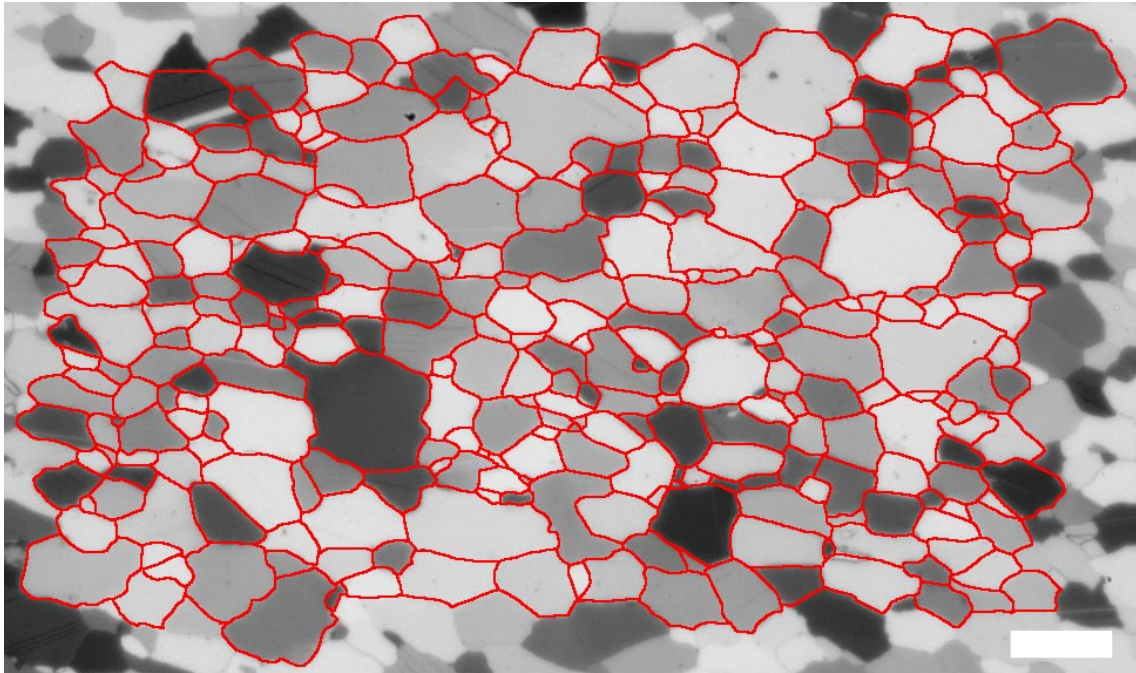
Compilation of polefigures across the natural shear zone (sample 99-57), left column and comparison to the experimental work of Barnhoorn (2003), middle column and of Schmid et al. 1987, right column. For the natural sample and the data of Barnhoorn is high shear strain at top of the figure. For the data of Schmid et al. the shear strain is approximately constant and the temperature increases towards the top. Since only the symmetry of polefigures are considered the maxima of the polefigures are not shown. Amount of shear strain, temperature and site numbers are indicated.

Sample: 99-68 = 2k-9: D2-E

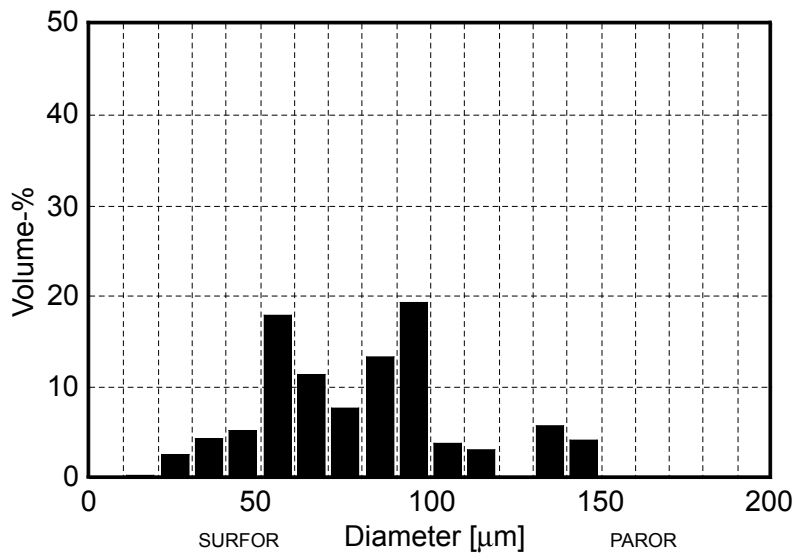
Locality: 'Cava Landi', Eastern Alpi Apuane, close to the village of Arni.

Lithology: Carrara marble

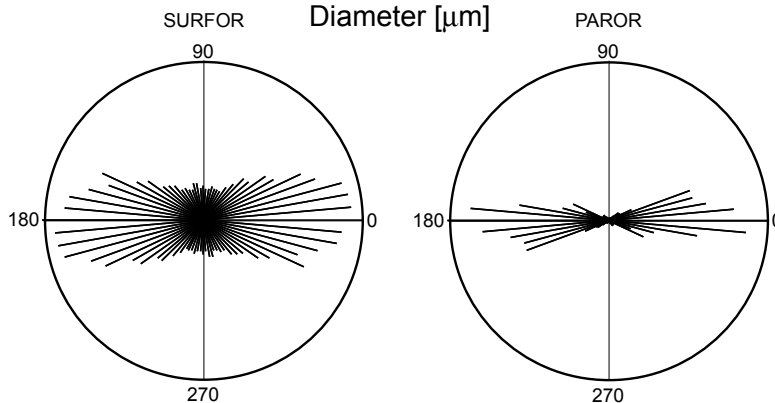
Structural position: Decimeter scale shear zone deforming s1 foliation.



Overview of sample 99-68, crossed polized light. The grain boundary outline for the size and shape analysis is indicated in red. The scale (lower right) is 100 μm .



Histogram of volume weighted grain size distribution.



Rose diagrams of grain boundaries (SURFOR) and grain long axis (PAROR).

Sample: 2k-13

Locality: Eastern Alpi Apuane, close to the village of Arni.

Lithology: Carrara marble with layers of dolomite

Structural position: Microscale shear zone cross-cutting mylonites of the Tambura thrusts

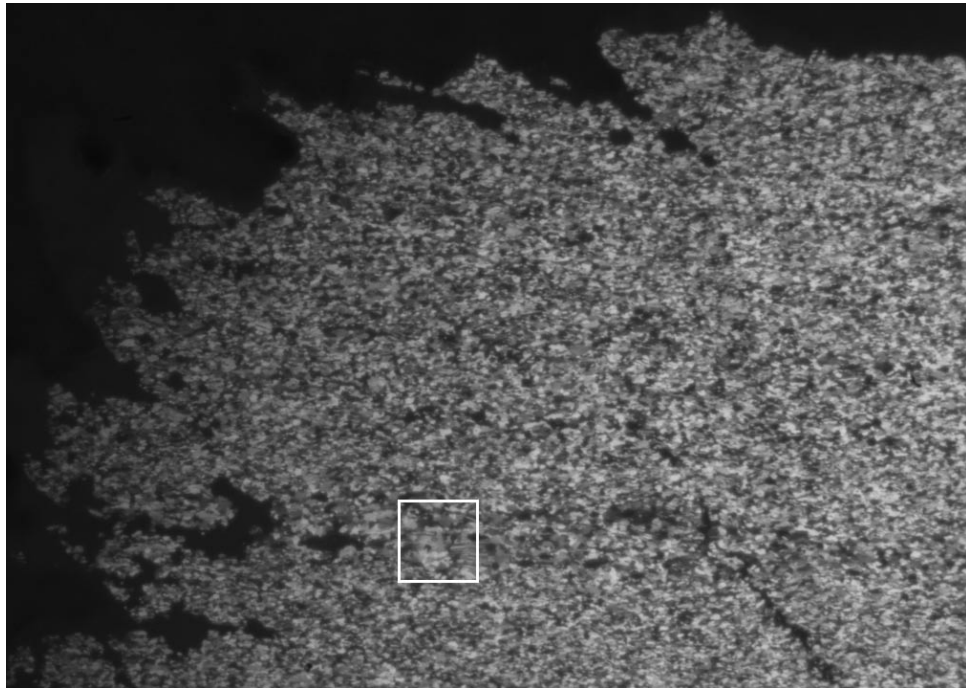


Sample:DO-8 (from Marco Herwegh, University of Bern, Switzerland)

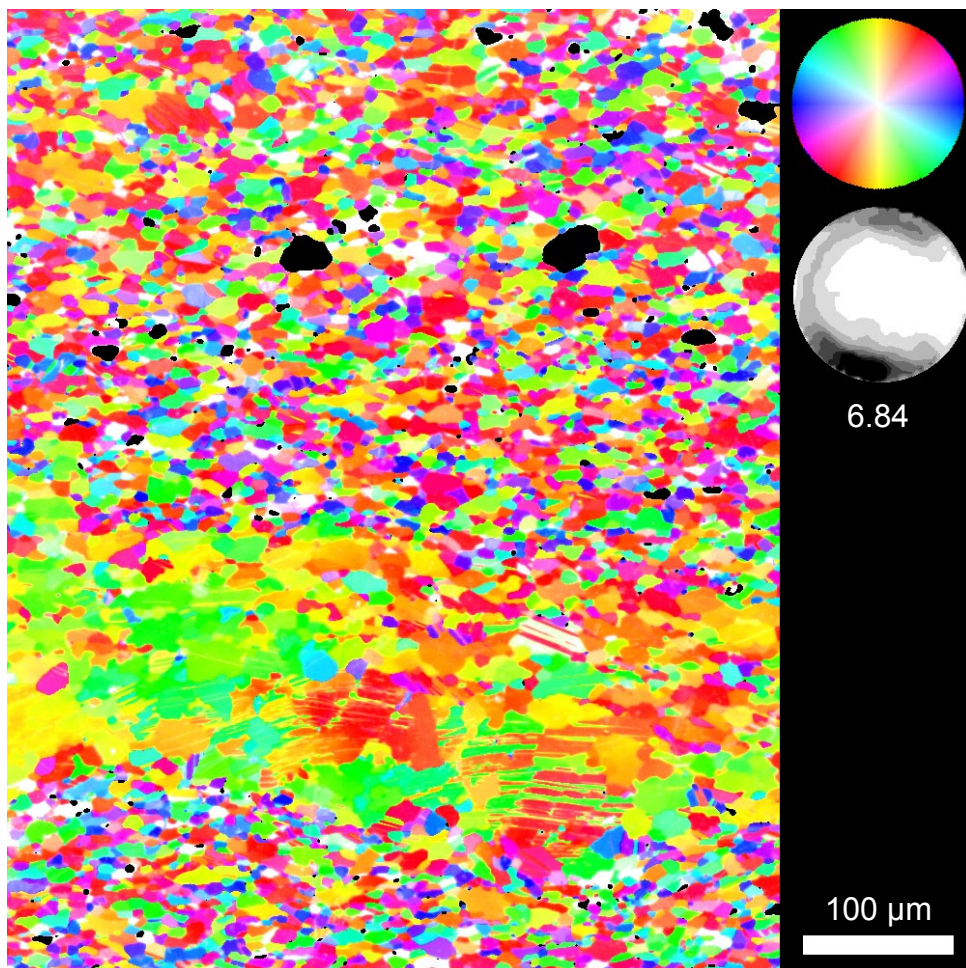
Locality: Basal thrust of Doldenhorn Nappe, Helvetic Alps (Herwegh & Kunze 2002)

Lithology: Meta-limestone

Structural position: Basal thrust of the Doldenhorn nappe, Helvetic Alps



Overview image in crossed polarized light. The analyzed area is outlined.



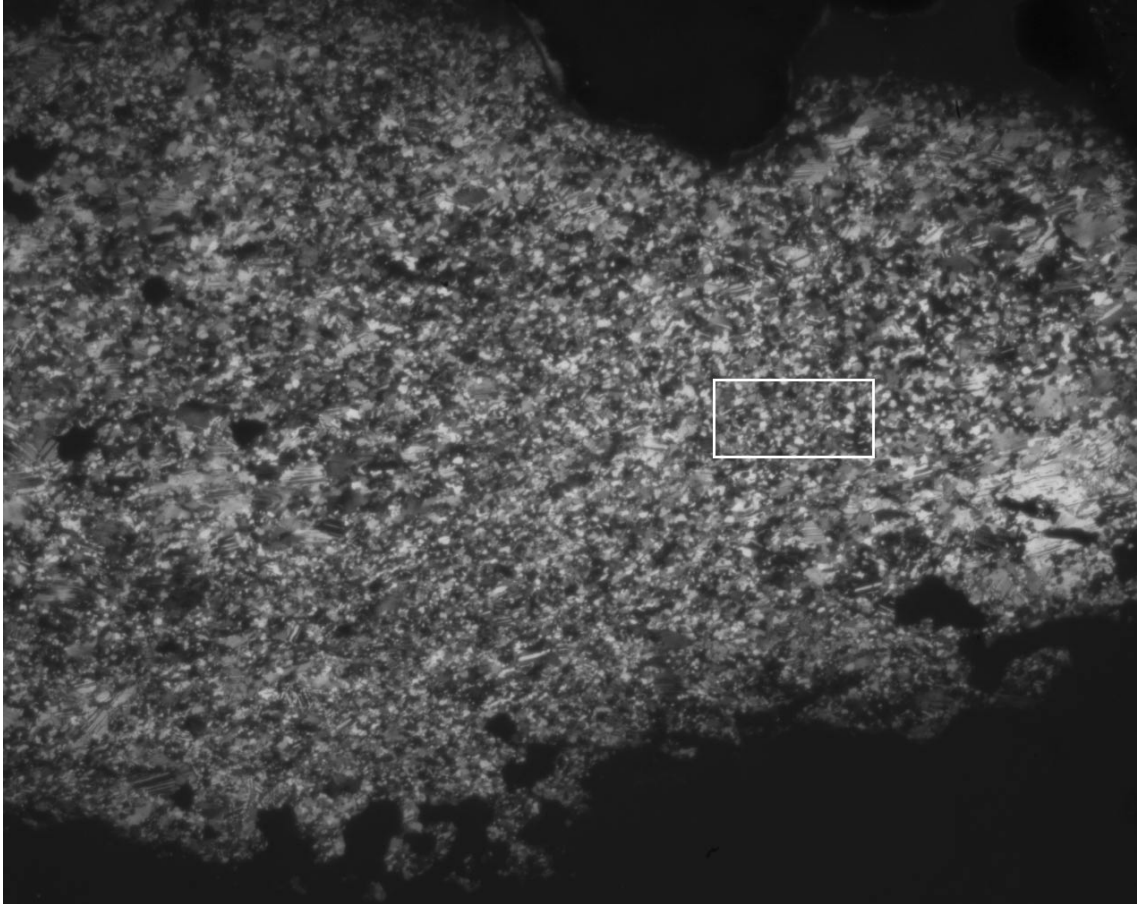
CIP c-axes orientation image of the area indicated in the overview image. The maximum of the polefigure is indicated.

Sample: Ge-3 (from Marco Herwegh, University of Bern, Switzerland)

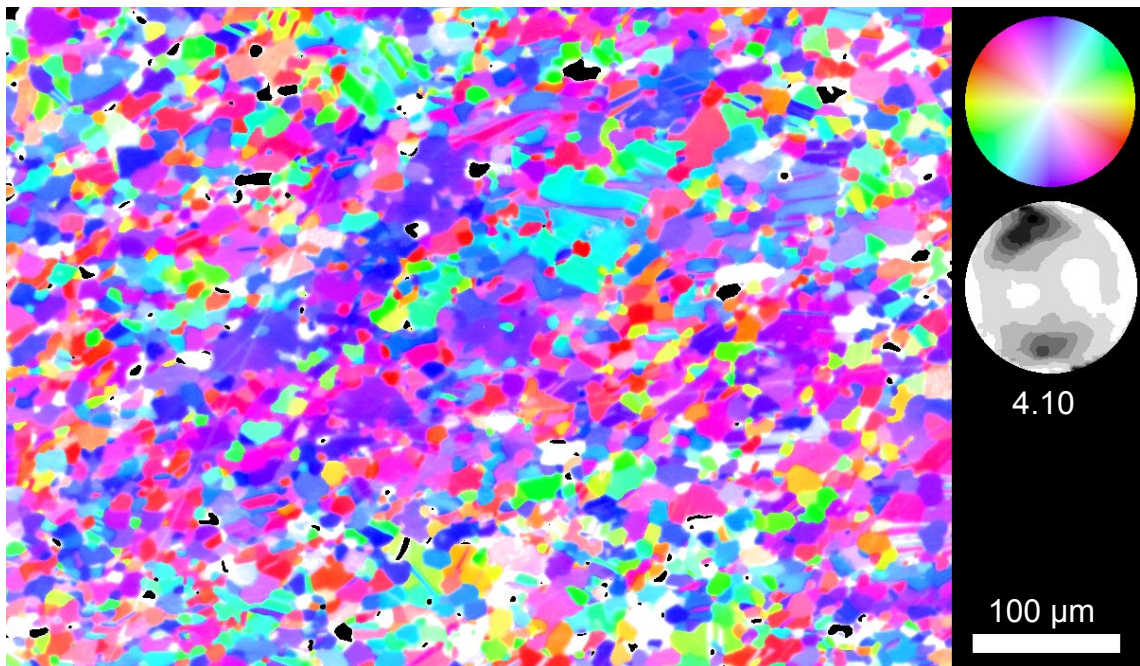
Locality: Basal thrust of Doldenhorn Nappe, Helvetic Alps (Herwegh & Kunze 2002)

Lithology: Meta-limestone

Structural position: Basal thrust of the Gellihorn nappe, Helvetic Alps



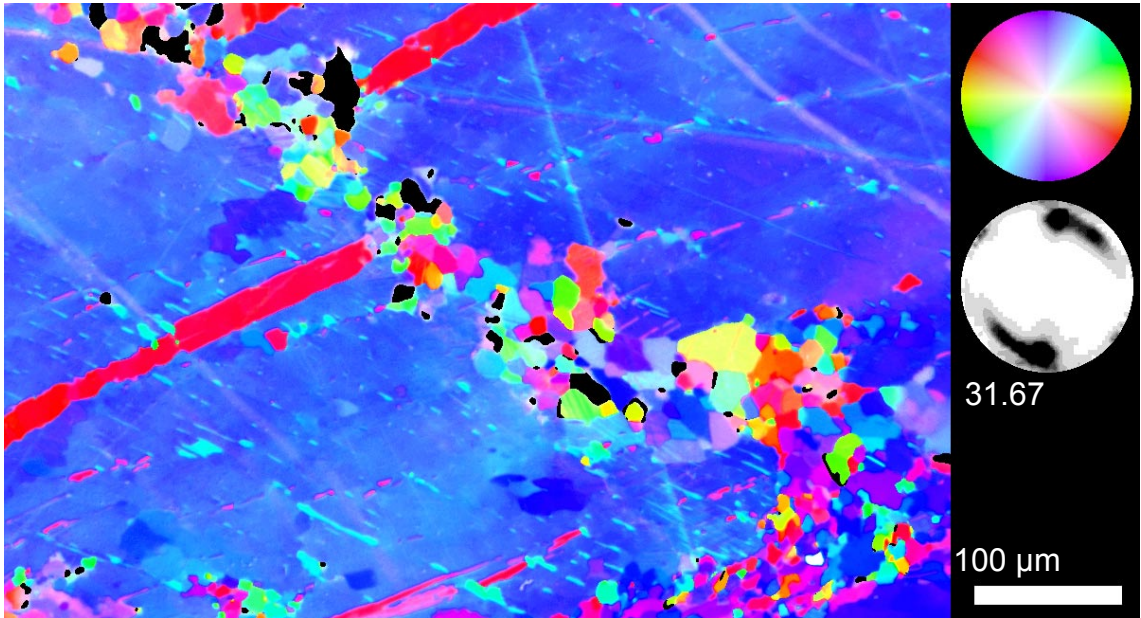
Overview image of area A in crossed polarized light. The analyzed area is outlined.



CIP c-axes orientation image of area A. The maximum of the polefigure is indicated.



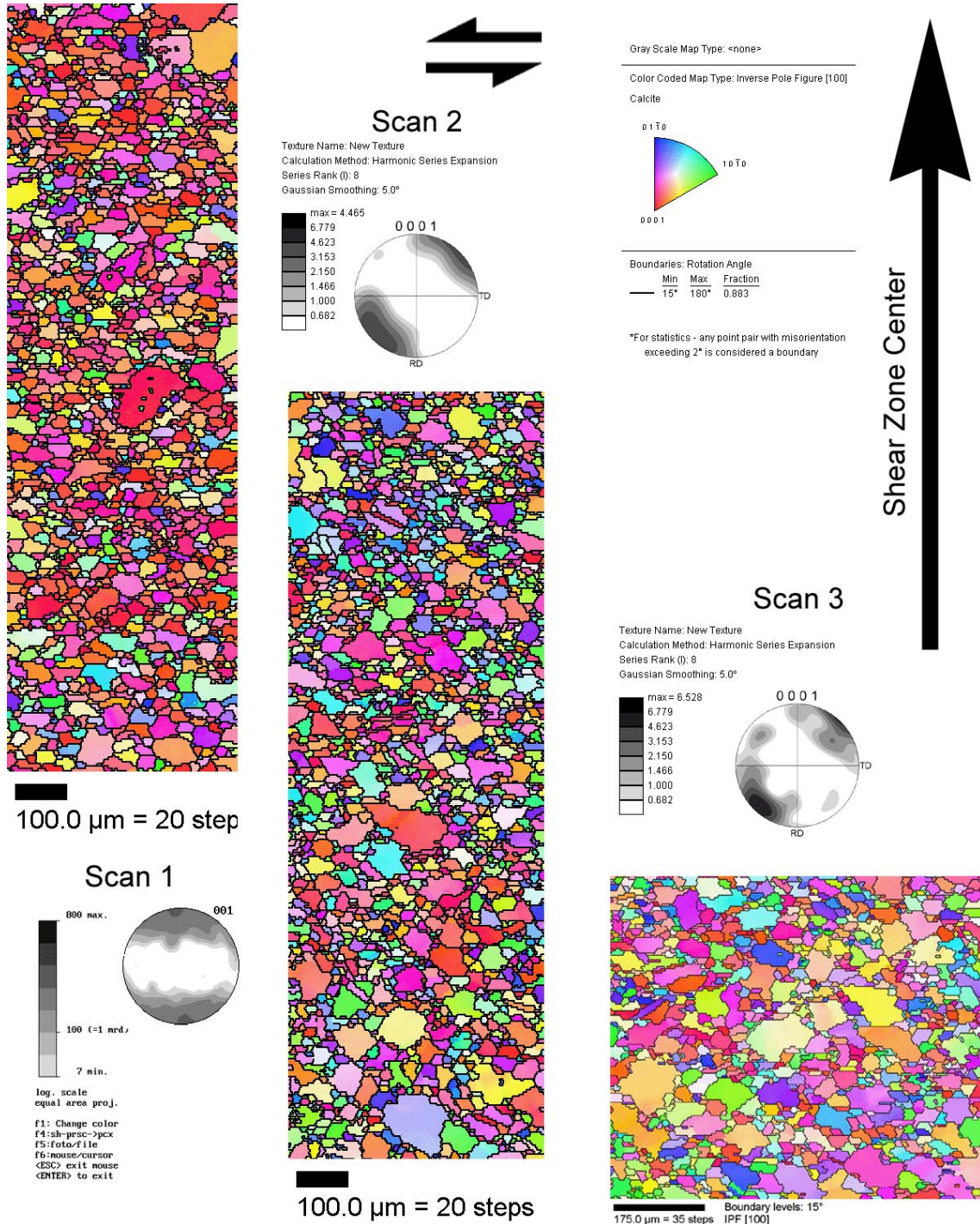
Overview image of area B in crossed polarized light. The analyzed area is outlined.



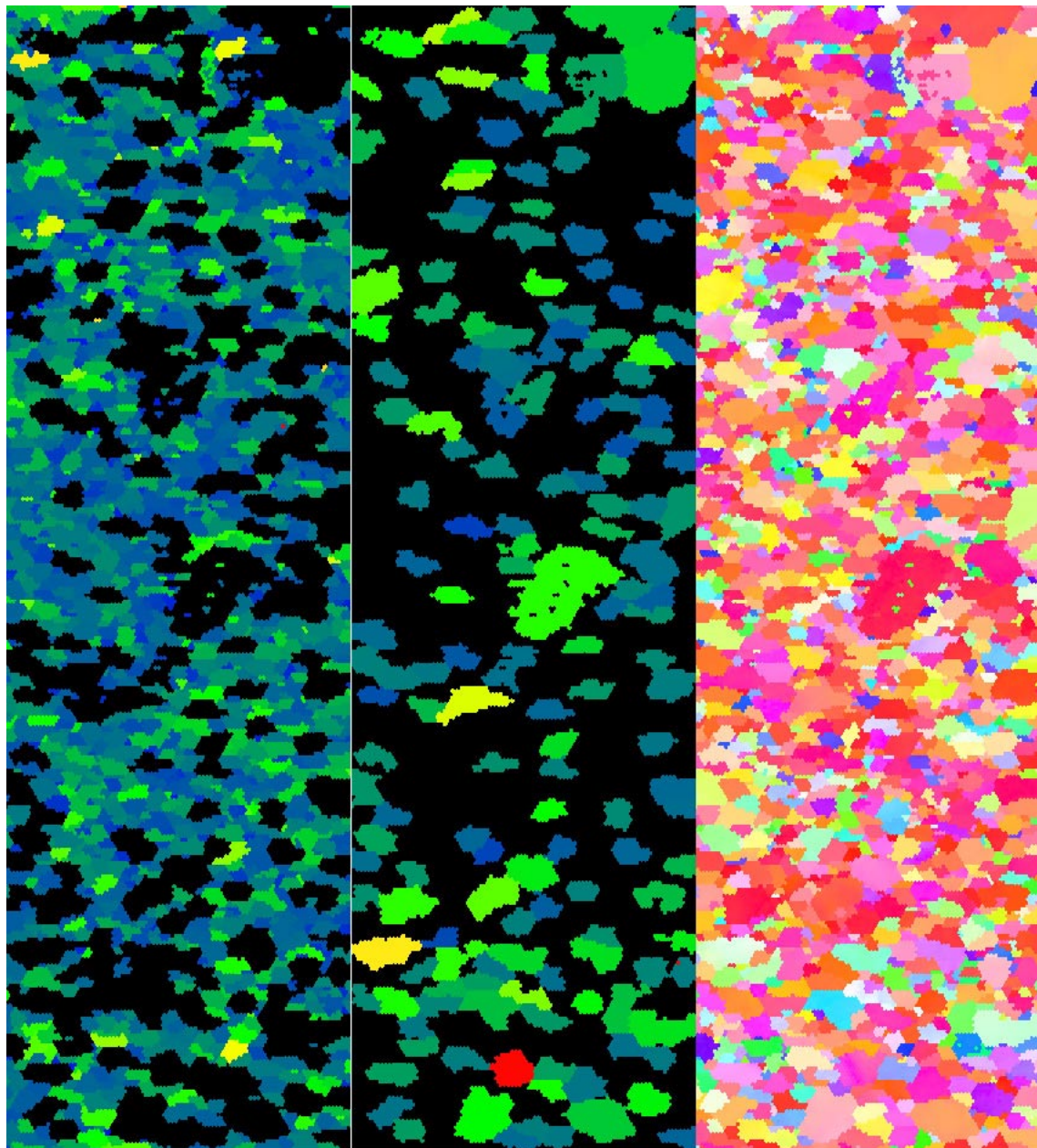
CIP c-axes orientation image of area B. The maximum of the polefigure is indicated. Note, the extremely strong maximum (31.67) of this sample is due to small sample statistics, since the largest part of the region is covered by a single grain.

Appendix C3: EBSD orientation maps and polfigures

This Appendix contains the EBSD orientation maps of sample D2-C and pole figures of sample D1-E-2 determined by EBSD (in collaboration with Auke Barnhoorn from the ETH Zurich). The filtering technique for the separation of calcite and dolomite patterns discussed in chapter 4 is illustrated here.



Overview of the relative position of the scan 1, 2 and 3 shown on the following pages. The c-axes orientation is colorcoded according to the Look-Up Table depicted at the upper right. The shear sense is top to left, opposite to the one indicated in chapter 3. C-axes pole figures derived from each map, their maxima and their contour intervals are indicated.



100.0 μm = 20 step

Scan 1

Color Coded Map Type: Inverse Pole Figure [100]
Calcite

Gray Scale Map Type: <none>

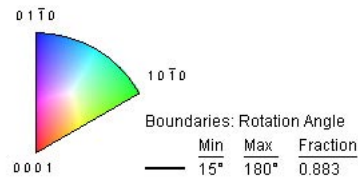
Gray Scale Map Type: <none>

Color Coded Map Type: Grain Orientation Spread

Color Coded Map Type: Grain Orientation Spread

| | Min | Max | Total Fraction | Partition Fraction |
|--|-----|-----|----------------|--------------------|
| | 0 | 7.5 | 0.619 | 1.000 |

| | Min | Max | Total Fraction | Partition Fraction |
|--|-----|-----|----------------|--------------------|
| | 0 | 7.5 | 0.372 | 1.000 |

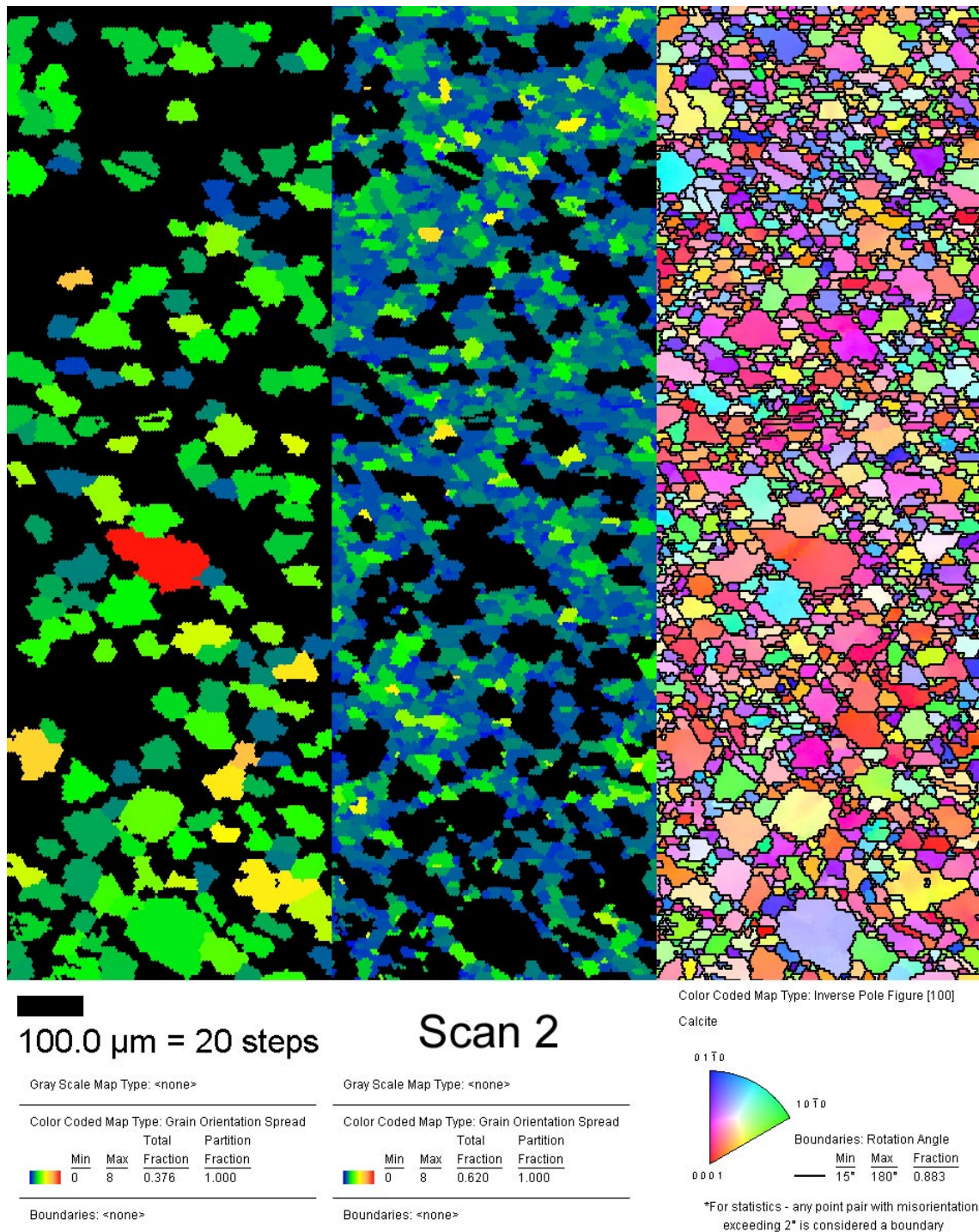


Boundaries: <none>

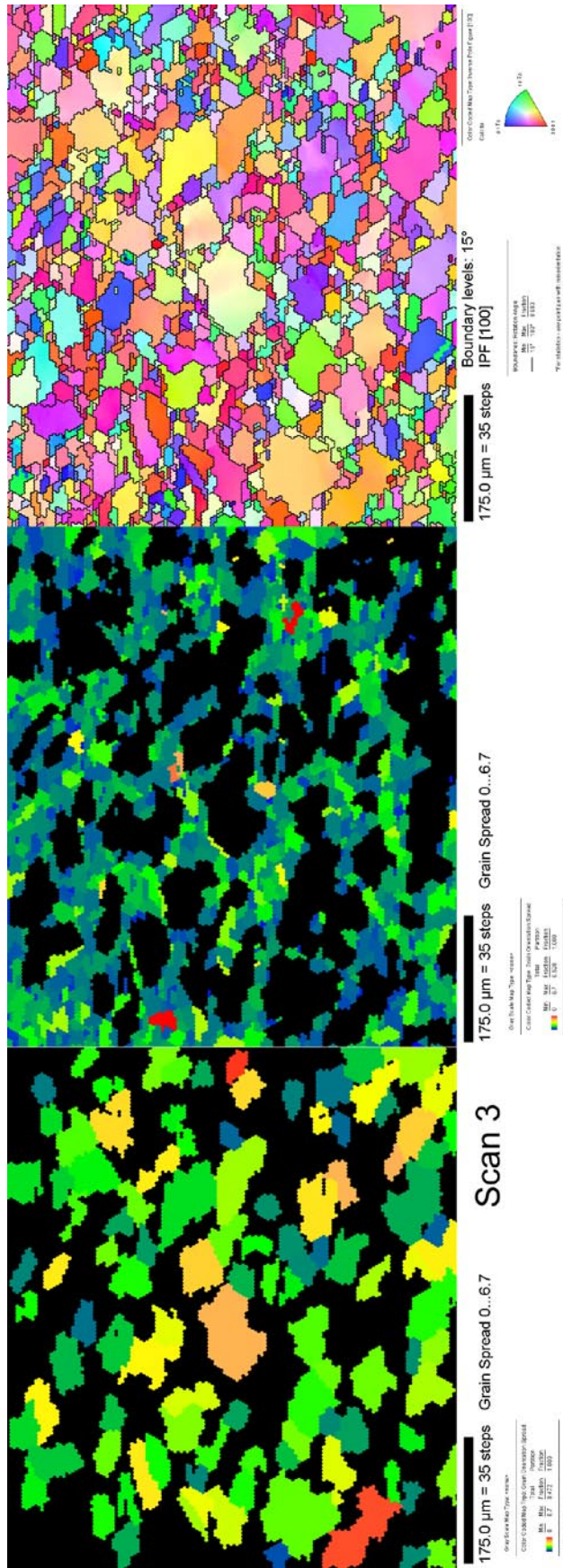
Boundaries: <none>

*For statistics - any point pair with misorientation exceeding 2° is considered a boundary

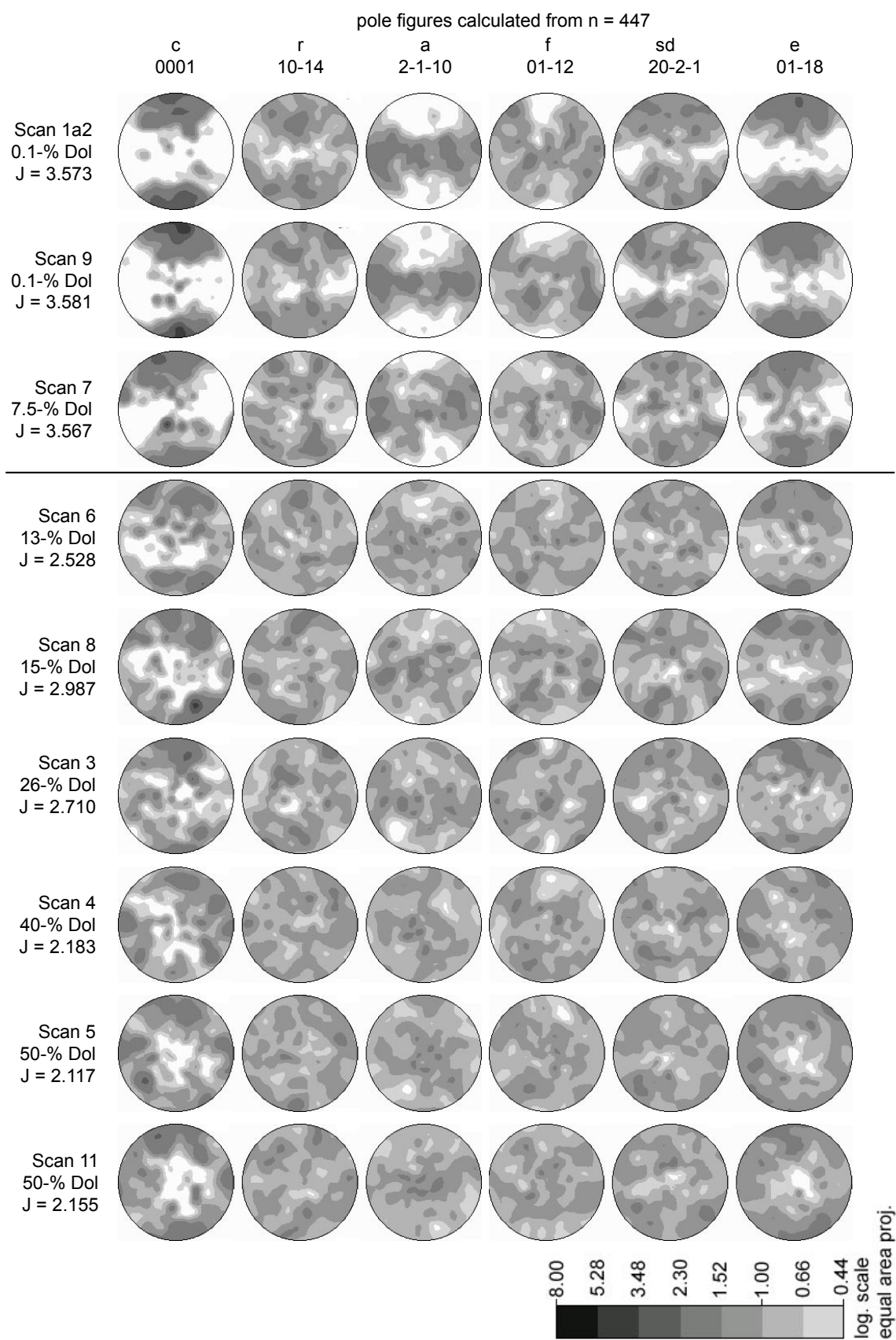
Scan 1: Orientation map of an area corresponding to the mylonite domain in sample **D2-Center (99-57)**. **Right:** crystallographic orientation map, colorcoding according to the Look-Up Table shown at the bottom right. Most grains are of reddish color indicating that their c-axis pointing upward. **Left and Middle:** orientation spread of recrystallized grains (diameter < 40 μm) and of porphyroclasts (diameter > 40 μm), respectively. The dominant blue color indicate that the recrystallized grain have a smaller orientation spread than the porphyroclasts, which may be related to a lesser internal deformation of the recrystallized grains. However, the spread is not grain size weighted.



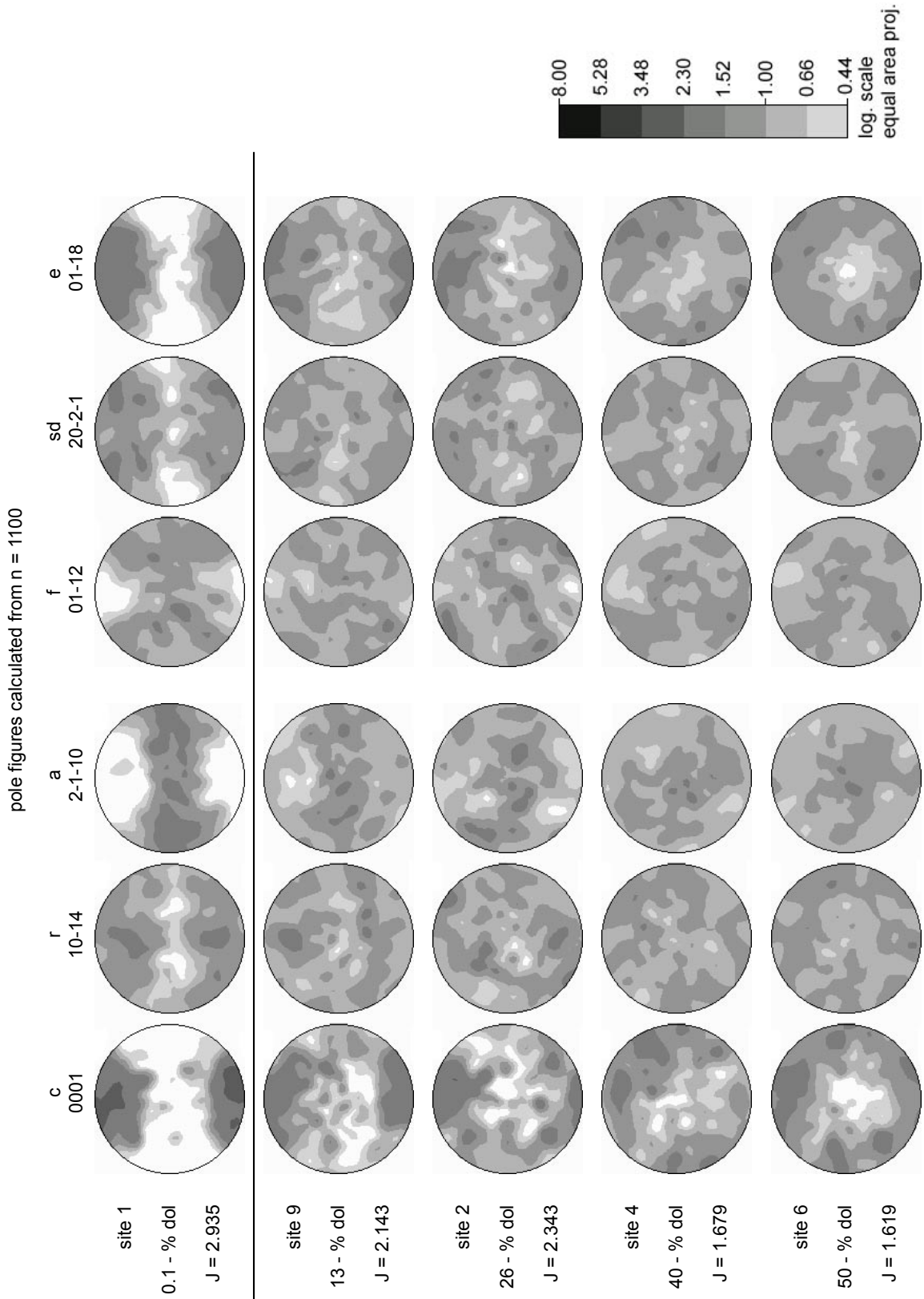
Scan 2: Orientation map of an area corresponding to the protomylonite domain in sample **D2-Center (99-57)**. **Right:** crystallographic orientation map, colorcoding according to the Look-Up Table shown at the bottom right. Most grains are of reddish color indicating that their c-axis pointing upward. Black lines indicate high angle grain boundaries with a misorientation of > 15°. **Left and Middle:** orientation spread of porphyroclasts (diameter > 40 μm) and of recrystallized grains (diameter < 40 μm), respectively. The dominant blue color indicate that the recrystallized grains have a smaller orientation spread than the porphyroclasts, which may be related to a lesser internal deformation of the recrystallized grains. However, the spread is not grain size weighted.



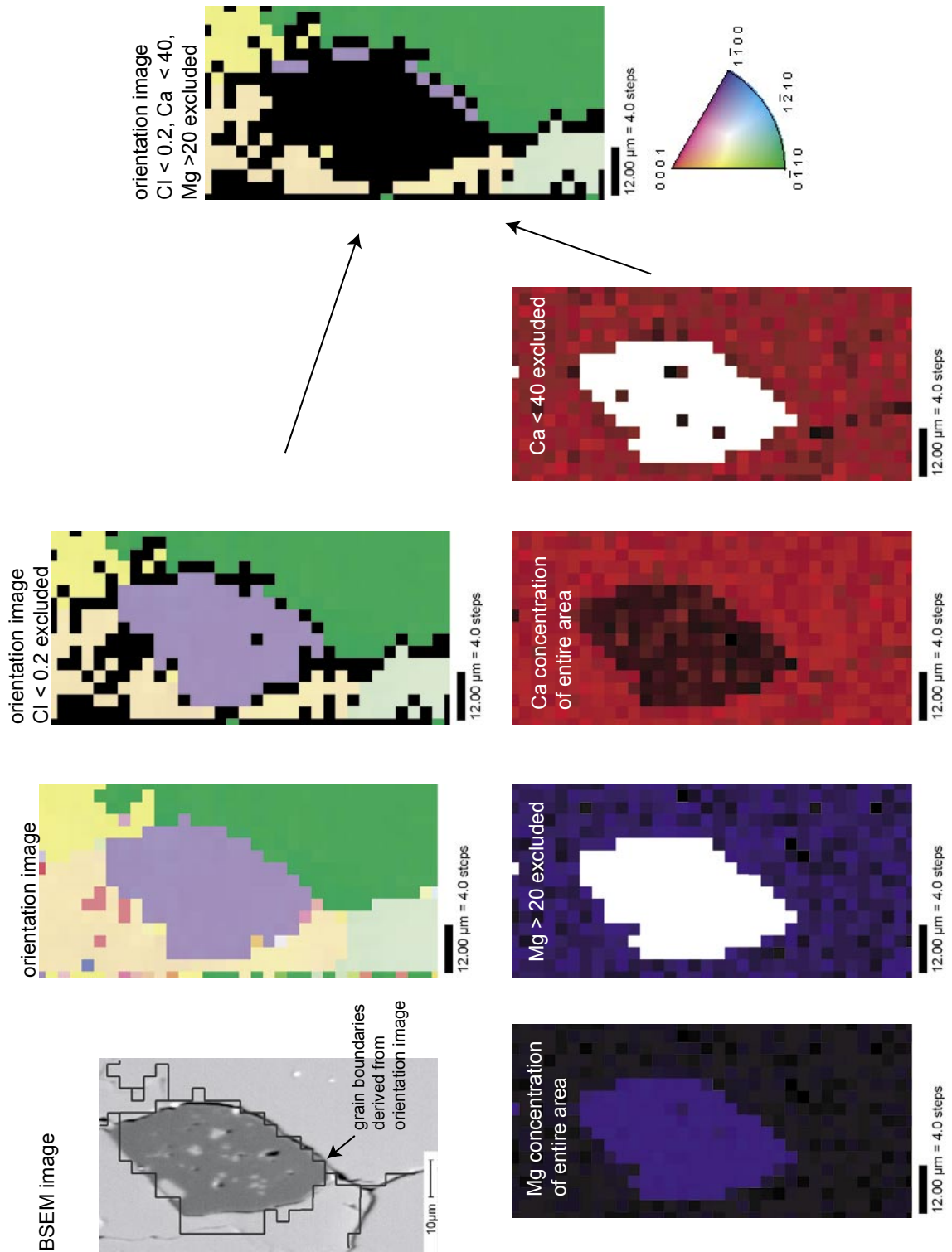
Scan 3: Orientation map of an area corresponding to the proctonite domain in sample **D2-Center (99-57)**. **Right:** crystallographic orientation map, color coding according to the Look-Up Table shown at the bottom right. Most grains are of reddish color indicating that their c-axis pointing upward. Black lines indicate high angle grain boundaries with a misorientation of > 15°. **Left and Middle:** orientation spread of porphyroclasts (diameter > 40 μm) and of recrystallized grains (diameter < 40 μm), respectively. The dominant blue color indicate that the recrystallized grain have a smaller orientation spread than the porphyroclasts, which may be relate to a lesser internal deformation of the recrystallized grains. However, the spread is not grain size weighted.



EBSB pole figures of sample D1-E-2 (99-49) determined from sites composed to different volume proportions of calcite and dolomite. The dolomite content increases from top to bottom. Dolomite content and texture index (J) are indicated on the left side. Textures are calculated on the basis of 445 measurements. Pole figures are contoured according to the scale at the bottom right.



Same as previous page, however, for each calculation 1100 measurements are used. Consequently, sites with less than 1100 measurements are not shown.



Filtering technique applied to mixed calcite-dolomite samples (cf. chapter 4), to exclude dolomite patterns. **Top row** show BSEM image (darkgray is dolomite, light gray is calcite), superimposed are the grain boundaries from the orientation map; orientation image of all measurements, and orientation image of measurements of confidence index (CI) < 0.2. Note that mainly measurements along grain boundaries are excluded.

Bottom row show the same area as in the top row, now colorcoded according to the magnesium (Mg = blue) and calcium content (Ca = red). Apart from measurements with more than 20 % Mg and less than 40 % Ca all dolomite measurements can be excluded (far right orientation map).

Appendix C4:

List of microstructural data

In this appendix the results of the microstructural analysis are listed. D1 samples are first shown, followed by D2 samples.

D1 - shear zones from the Western and Eastern Alpi Apuane

Samples form the D1b deformation phase

| Sample-Site | Micro-structure | Res. of Input 1 px = ? / μm | 2D-Mean | 2D-Median | 3D-Mode* | Grain size-distrib. | Res. of Input 1 px = ? / μm | b/a | A _{min} | A _{max} | Grain shape of complete microstructure α (A _{min}) [°] | B _{min} | α (B _{min}) [°] | PARIS [%] | Symmetry | Texture (CPO) max. of polif. | Temp. [°C] | Locality |
|-------------|------------------|-----------------------------|---------|-----------|-----------|---------------------|-----------------------------|--------|------------------|------------------|--|------------------|---------------------------|-----------|----------|------------------------------|------------|---|
| 98-2 | gbm-rx / anneal. | 1.22 | 81.29 | 71.90 | 110.00 | unimodal | 1.22 | 0.5543 | 0.6120 | 90 | 90 | 0.5929 | 90 | 3.27 | orthorh. | 10.27 | - | Lambura thrust, near Ami, E-Alpi Apuane |
| 98-3 | gbm-rx / anneal. | 1.22 | 30.63 | 20.75 | 130 / 310 | bimodal | 1.22 | 0.6310 | 0.9503 | 120-125 | 120-125 | 0.9297 | 115-120 | 4.63 | orthorh. | 7.07 | - | Lambura thrust, near Ami, E-Alpi Apuane |
| 99-38 | recrystallized | 1.28 | 53.90 | 47.88 | 85 / 175 | bimodal | 0.43 | 0.5188 | 0.5740 | 90 | 90 | 0.5503 | 85 | 3.13 | - | - | 420 | normal limb of Vallim syncline, W-Alpi Apuane |
| 99-59-0 | recrystallized | 0.99 | 31.92 | 27.70 | 55.00 | unimodal | 0.25 | 0.6112 | 0.7456 | 80 | 80 | 0.7189 | 80 | 3.31 | - | - | 395 | near Resceto, Central Alpi Apuane |
| 99-59-1 | recrystallized | 0.99 | 17.35 | 16.07 | 25.00 | unimodal | 0.25 | 0.6504 | 0.7911 | 70 | 70 | 0.7785 | 70 | 1.66 | - | - | 395 | near Resceto, Central Alpi Apuane |
| 99-59-3 | recrystallized | 0.99 | 21.04 | 19.46 | 35.00 | unimodal | 0.25 | 0.6354 | 0.7498 | 80 | 80 | 0.7366 | 80 | 1.59 | - | - | 395 | near Resceto, Central Alpi Apuane |
| 99-59-6 | recrystallized | 0.99 | 33.11 | 30.68 | 45 / 85 | bimodal | 0.25 | 0.6275 | 0.7203 | 90 | 90 | 0.6972 | 90 | 2.77 | - | - | 395 | near Resceto, Central Alpi Apuane |
| 99-59-9 | recrystallized | 0.99 | 37.27 | 34.73 | 65.00 | unimodal | 0.25 | 0.6182 | 0.7305 | 90 | 90 | 0.7040 | 95 | 3.83 | - | - | 395 | near Resceto, Central Alpi Apuane |
| 2k-17A | gbm-rx | 1.22 | 60.37 | 47.38 | 150.00 | unimodal | 1.22 | 0.5372 | 0.6084 | 85 | 85 | 0.5814 | 85 | 3.82 | orthorh. | 12.5 | - | Lambura thrust, near Ami, E-Alpi Apuane |

* center of class; if bimodal mode 1 / mode 2 arc indicated

— D1-E-1 — D1-W

D1 - shear zone from the Eastern Alpi Apuane

| Sample: | 99-49 | Location: | Tambura thrust, Arni | Deformation phase: | D1-East | Av. T (°C): | 365.54 Std. Dev.: | 19.58 | | | | | | | | |
|--------------|-----------------|----------------------------|----------------------|--------------------|----------|-----------------------|----------------------------|--------|--|--------------|--------------|-----------|----------|-----------------------|------------------|------------|
| Sample-Site | Micro-structure | Res. of Input I px = ? /µm | 2D-Mean | Grain diameter /µm | 3D-Mode* | Grain size - distrib. | Res. of Input I px = ? /µm | b/a | Grain shape of complete microstructure | α (Amin) [°] | α (Bmin) [°] | PARIS [%] | Symmetry | Texture (CPO) J-index | shear strain [ε] | Vol-% Dol. |
| 99-49-1-Cc | gbm-rex | 0.42 | 42.94 | 30.25 | 85-125 | broad | 0.42 | 0.5520 | 0.6599 | 0 | 0.6232 | 5 | 8.10 | orthorh. | const. | 99.58 |
| 99-49-1-Dol | - | 0.42 | 28.76 | 28.76 | 28.76 | unimodal | 0.42 | - | 0.9265 | 70 | - | - | 1.65 | - | - | 0.09 |
| 99-49-1-Rest | - | 0.42 | 4.73 | 3.75 | 5.00 | unimodal | 0.42 | 0.4968 | 0.5435 | 0 | 0.5310 | 0 | 0.09 | - | - | 0.32 |
| 99-49-9-Cc | - | 0.42 | 18.03 | 12.84 | 65.00 | broad | 0.42 | 0.5474 | 0.6549 | 0 | 0.6053 | 0 | 6.32 | orthorh. | const. | 86.17 |
| 99-49-9-Dol | - | 0.42 | 12.78 | 11.75 | 15.00 | unimodal | 0.42 | 0.6080 | 0.7297 | 0 | 0.7224 | 0 | 0.84 | - | - | 12.89 |
| 99-49-9-Rest | - | 0.42 | 3.94 | 3.42 | 5.00 | unimodal | 0.42 | 0.4640 | 0.6035 | 175 | 0.6041 | 0 | 0.25 | - | - | 0.95 |
| 99-49-2-Cc | - | 0.42 | 16.26 | 11.91 | 25.00 | unimodal | 0.42 | 0.5255 | 0.6106 | 0 | 0.5838 | 0 | 2.57 | orthorh./random | const. | 71.52 |
| 99-49-2-Dol | - | 0.42 | 15.35 | 14.45 | 15.00 | unimodal | 0.42 | 0.6374 | 0.7276 | 0 | 0.7250 | 0 | 2.46 | - | - | 25.90 |
| 99-49-2-Rest | - | 0.42 | 5.73 | 5.10 | 5.00 | unimodal | 0.42 | 0.5369 | 0.5472 | 0 | 0.5428 | 0 | 0.35 | - | - | 2.58 |
| 99-49-4-Cc | - | 0.42 | 11.93 | 9.44 | 25.00 | unimodal | 0.42 | 0.5415 | 0.6395 | 0 | 0.6050 | 0 | 4.78 | random | const. | 57.40 |
| 99-49-4-Dol | - | 0.42 | 13.60 | 13.19 | 15.00 | unimodal | 0.42 | 0.6196 | 0.7223 | 0 | 0.7213 | 0 | 1.74 | - | - | 40.01 |
| 99-49-4-Rest | - | 0.42 | 5.46 | 4.64 | 5.00 | unimodal | 0.42 | 0.5291 | 0.5644 | 5 | 0.5603 | 5 | 0.37 | - | - | 2.59 |
| 99-49-6-Cc | - | 0.42 | 10.75 | 8.72 | 15.00 | unimodal | 0.42 | 0.5415 | 0.6549 | 0 | 0.6197 | 0 | 4.38 | random | const. | 48.43 |
| 99-49-6-Dol | - | 0.42 | 12.44 | 11.39 | 15.00 | unimodal | 0.42 | 0.6257 | 0.7549 | 0 | 0.7560 | 0 | 2.50 | - | - | 50.14 |
| 99-49-6-Rest | - | 0.42 | 4.07 | 3.42 | 5.00 | unimodal | 0.42 | 0.5434 | 0.4750 | 0 | 0.4705 | 0 | 0.17 | - | - | 1.43 |

* center of class; if bimodal mode 1 / mode 2 are indicated

D2- shear zones from the Western, Central and Eastern Alpi Apuane

Samples from the D2 deformation phase

| Sample-Site | Micro-structure | Res. of Input 1 px = 2 μm | 2D-Mean | Grain diameter [μm] 2D-Median | 3D-Mode* | Grain size - distrib. | Res. of Input 1 px = 7 μm | b/a | Grain shape of complete microstructure α(Amb) [°] | Bin | α(Bin) [°] | PARIS [%] <40 μm | PARIS [%] >40 μm | Texture (CPO) Symmetry | max. of pol. | shear strain [PI] | Dist. from SZ [mm] | Vol-% recryst. | Temp [°C] | Locality | |
|-------------|-----------------|---------------------------|---------|-------------------------------|----------|-----------------------|---------------------------|--------|---|-----|------------|------------------|------------------|------------------------|--------------|-------------------|--------------------|----------------|-----------|----------|---|
| 99-57-0 | PM<40%: rex | 0.35 | 23.20 | 16.07 | 75.00 | unimodal | 0.35 | 0.6424 | 0.8864 | 43 | 0.8684 | 48 | 2.73 | 22.67 | monocl. | 5.76 | 0 | 14.7 | 33.12 | 325 | Casale di Frondese, Central Alpi Apuane |
| 99-57-1 | PM<40%: rex | 0.35 | 29.39 | 23.03 | 30 / 125 | bimodal | 0.35 | 0.6433 | 0.8715 | 13 | 0.8576 | 18 | 2.24 | 17.20 | - | - | 0 | 14.7 | 31.02 | 325 | " " |
| 99-57-2 | PM<40%: rex | 0.35 | 23.43 | 18.00 | 25.00 | unimodal | 0.35 | 0.6426 | 0.8541 | 8 | 0.8418 | 13 | 1.72 | 15.59 | - | - | 0.1 | 8.6 | 39.87 | 325 | " " |
| 99-57-3 | PM<40%: rex | 0.35 | 21.94 | 18.31 | 25.00 | unimodal | 0.35 | 0.6263 | 0.8082 | 13 | 0.7951 | 13 | 1.64 | 12.66 | - | - | 0.4 | 3.7 | 59.33 | 325 | " " |
| 99-57-4 | PM<40%: rex | 0.35 | 26.47 | 21.62 | 35.00 | unimodal | 0.35 | 0.6338 | 0.7996 | 13 | 0.7856 | 13 | 1.80 | 16.38 | monocl. | 12.35 | 0.8 | 2.3 | 43.09 | 325 | " " |
| 99-57-5 | PM<40%: rex | 0.35 | 20.34 | 16.61 | 25.00 | unimodal | 0.35 | 0.6333 | 0.8094 | 18 | 0.7895 | 18 | 1.36 | 15.67 | monocl. | 7.58 | 1.6 | 1.8 | 49.76 | 325 | " " |
| 99-57-6 | M<50%: rex | 0.35 | 14.91 | 13.35 | 20.00 | unimodal | 0.35 | 0.6424 | 0.8146 | 23 | 0.7995 | 23 | 1.74 | 12.79 | orthorh. | 6.48 | 4.7 | 1.1 | 88.11 | 325 | " " |
| 99-57-7 | M<50%: rex | 0.35 | 13.95 | 15.95 | 20.00 | unimodal | 0.35 | 0.6287 | 0.8108 | 8 | 0.7790 | 8 | 1.68 | - | monocl. | 11.01 | >20 | 0.6 | 100.00 | 325 | " " |
| 8 | M<50%: rex | - | - | - | - | - | - | - | - | - | - | - | - | - | monocl. | 8.24 | >20 | <0.6 | 100.00 | 325 | " " |
| 9 | M<50%: rex | - | - | - | - | - | - | - | - | - | - | - | - | monocl. | 8.87 | >20 | <0.6 | 100.00 | 325 | " " | |
| 10 | M<50%: rex | - | - | - | - | - | - | - | - | - | - | - | - | monocl. | 8.74 | >20 | <0.6 | 100.00 | 325 | " " | |
| 11 | M<50%: rex | - | - | - | - | - | - | - | - | - | - | - | - | monocl. | 6.07 | >20 | <0.6 | 100.00 | 325 | " " | |
| 12 | M<50%: rex | - | - | - | - | - | - | - | - | - | - | - | - | orthorh. | 6.84 | >20 | <0.6 | 100.00 | 325 | " " | |

D2-C

| Sample-Site | Micro-structure | Res. of Input 1 px = 2 μm | 2D-Mean | Grain diameter [μm] 2D-Median | 3D-Mode* | Grain size - distrib. | Res. of Input 1 px = 7 μm | b/a | Grain shape of complete microstructure α(Amb) [°] | Bin | α(Bin) [°] | PARIS [%] <40 μm | PARIS [%] >40 μm | Texture (CPO) Symmetry | max. of pol. | Temp [°C] | Locality |
|-------------|-----------------|---------------------------|---------|-------------------------------|---------------|-----------------------|---------------------------|--------|---|-----|------------|------------------|------------------|------------------------|--------------|-----------|---------------------------------|
| 2k-7-Am | annealed | 1.28 | 36.57 | 28.86 | 125.00 | unimodal | 0.64 | 0.6567 | 0.8558 | 105 | 0.8485 | 100 | 2.21 | random | 5 | 360 | quarry Vajllimi, W-Alpi Apuane' |
| 2k-7-SZ | rot-rsx | 1.23 | 16.04 | 14.60 | 25.00 | unimodal | 0.25 | 0.6860 | 0.9129 | 110 | 0.9072 | 110 | 1.60 | orthorh. | 5.42 | 295 | quarry Vajllimi, W-Alpi Apuane' |
| 2k-9 | recrystallized | 1.28 | 48.40 | 44.71 | 95 / 55 / 135 | trimodal | 0.43 | 0.6058 | 0.6948 | 100 | 0.6849 | 100 | 1.63 | - | - | 375 | quarry Landi, W-Alpi Apuane' |

* center of class; if bimodal mode 1 / mode 2 are indicated

M = Mylonite
PM = Proto-mylonite

D2-E D2-W

Appendix C5: Microprobe data and calculated temperatures

The results of microprobe measurements are listed in this appendix. The composition of co-existing calcite and dolomite is shown next to each other. Calcite-dolomite pairs are numbered and the calculated temperature after the approach of Anovitz & Essene (1987) is shown at the bottom of each column. Excluded measurements are highlighted in light gray. All measurements are on the basis of 6 oxygens. For each specimen the average temperature and standard deviation is indicated in the first row of the listing. Temperature histograms and the regional distribution of deformation temperatures are shown in chapter 2.

The following samples are listed:

D1:

99-38 = D1-W, Western Alpi Apuane

99-59 = D1-E1, Eastern Alpi Apuane

99-49 = D1-E2, Eastern Alpi Apuane

D2:

2k-7 = D2-W, Western Alpi Apuane

2k-7 (Annealed marble outside the shear zone), Western Alpi Apuane

99-57 = D2-C, Central Alpi Apuane

99-68 = D2-E, Eastern Alpi Apuane

2k-9 = D2-E, Eastern Alpi Apuane

Sample D1-W (99-38), Western Alpi Apuane.

| Sample: | 99-38 | Location: | 0 | Av. T (°C): | 402.08 | Std. Dev.: | 43.54 | Av. T (°C): selected: | 416.22 | Std. Dev.: selected: | 14.04 | |
|-------------------|-----------|-----------|-----------|-------------|-----------|------------|-----------|-----------------------|-----------|----------------------|-----------|-----------|
| Sample-Site | 1 | | 2 | | 3 | | 4 | | 5 | | 6 | |
| Mineral | Cc | Dol | Cc | Dol | Cc | Dol | Cc | Dol | Cc | Dol | Cc | Dol |
| Wt % | | | | | | | | | | | | |
| CaO | 54.08 | 30.24 | 51.36 | 30.19 | 55.75 | 29.20 | 56.40 | 29.63 | 53.57 | 29.89 | 54.00 | 30.46 |
| MgO | 0.98 | 20.54 | 1.12 | 20.47 | 0.91 | 20.59 | 1.03 | 20.30 | 1.13 | 20.76 | 1.13 | 22.02 |
| FeO | 0.23 | 0.92 | 0.19 | 0.90 | 0.07 | 0.04 | 0.01 | 0.34 | 0.00 | 0.26 | 0.05 | 0.76 |
| MnO | 0.00 | 0.00 | 0.12 | 0.08 | 0.06 | 0.01 | 0.06 | 0.00 | 0.06 | 0.00 | 0.00 | 0.00 |
| SrO | 0.00 | 0.00 | 0.07 | 0.00 | 0.00 | 0.18 | 0.15 | 0.08 | 0.00 | 0.00 | 0.00 | 0.00 |
| CO ₂ | 44.71 | 48.3 | 47.13 | 48.36 | 43.21 | 49.98 | 42.35 | 49.66 | 45.25 | 49.09 | 44.82 | 46.76 |
| Sum | 100.00 | 100.00 | 99.99 | 100.00 | 100.00 | 100.00 | 100.00 | 100.01 | 100.01 | 100.00 | 100.00 | 100.00 |
| # Ions | | | | | | | | | | | | |
| CaO | 1.913 | 0.994 | 1.778 | 0.992 | 2.000 | 0.945 | 2.040 | 0.962 | 1.885 | 0.974 | 1.908 | 1.011 |
| MgO | 0.048 | 0.939 | 0.054 | 0.935 | 0.046 | 0.927 | 0.052 | 0.917 | 0.055 | 0.942 | 0.056 | 1.016 |
| FeO | 0.006 | 0.024 | 0.005 | 0.023 | 0.002 | 0.001 | 0.000 | 0.009 | 0.000 | 0.007 | 0.001 | 0.020 |
| MnO | 0.000 | 0.000 | 0.003 | 0.002 | 0.002 | 0.000 | 0.002 | 0.000 | 0.002 | 0.000 | 0.000 | 0.000 |
| SrO | 0.000 | 0.000 | 0.001 | 0.000 | 0.000 | 0.003 | 0.003 | 0.001 | 0.000 | 0.000 | 0.000 | 0.000 |
| CO ₂ | 2.016 | 2.022 | 2.079 | 2.024 | 1.975 | 2.061 | 1.952 | 2.055 | 2.029 | 2.039 | 2.018 | 1.977 |
| Sum | 3.984 | 3.978 | 3.921 | 3.976 | 4.025 | 3.939 | 4.048 | 3.945 | 3.971 | 3.961 | 3.982 | 4.023 |
| Mol % | | | | | | | | | | | | |
| CaCO ₃ | 97.23 | 50.79 | 96.54 | 50.79 | 97.60 | 50.35 | 97.29 | 50.92 | 97.06 | 50.68 | 97.10 | 49.37 |
| MgCO ₃ | 2.45 | 48.01 | 2.93 | 47.92 | 2.22 | 49.41 | 2.47 | 48.55 | 2.85 | 48.98 | 2.83 | 49.67 |
| FeCO ₃ | 0.32 | 1.21 | 0.28 | 1.18 | 0.10 | 0.05 | 0.01 | 0.46 | 0.00 | 0.34 | 0.07 | 0.96 |
| MnCO ₃ | 0.00 | 0.00 | 0.18 | 0.11 | 0.08 | 0.01 | 0.08 | 0.00 | 0.09 | 0.00 | 0.00 | 0.00 |
| SrCO ₃ | 0.00 | 0.00 | 0.07 | 0.00 | 0.00 | 0.17 | 0.14 | 0.07 | 0.00 | 0.00 | 0.00 | 0.00 |
| XMg | 0.0245144 | 0.4800225 | 0.0292929 | 0.4791895 | 0.0221675 | 0.4940701 | 0.0247223 | 0.4854485 | 0.0284886 | 0.4897628 | 0.0282726 | 0.4966392 |
| XFe | 0.0032275 | 0.0120614 | 0.0027877 | 0.0118190 | 0.0009566 | 0.0005384 | 0.0001346 | 0.0045611 | 0.0000000 | 0.0034410 | 0.0007018 | 0.0096158 |
| T (°C) | 390.53 | | 424.66 | | 370.75 | | 392.16 | | 419.36 | | 417.92 | |
| Sample-Site | 7 | | 8 | | 9 | | 10 | | 11 | | 12 | |
| Mineral | Cc | Dol | Cc | Dol | Cc | Dol | Cc | Dol | Cc | Dol | Cc | Dol |
| Wt % | | | | | | | | | | | | |
| CaO | 55.05 | 30.59 | 54.79 | 29.85 | 56.89 | 29.70 | 54.69 | 29.16 | 53.32 | 30.14 | 55.06 | 29.86 |
| MgO | 1.14 | 22.24 | 1.23 | 23.21 | 1.54 | 23.06 | 0.62 | 23.14 | 1.17 | 22.41 | 1.15 | 22.26 |
| FeO | 0.03 | 0.63 | 0.17 | 1.23 | 0.14 | 1.04 | 0.04 | 0.31 | 0.18 | 0.44 | 0.12 | 0.61 |
| MnO | 0.19 | 0.07 | 0.00 | 0.00 | 0.00 | 0.04 | 0.11 | 0.07 | 0.04 | 0.04 | 0.09 | 0.12 |
| SrO | 0.02 | 0.00 | 0.00 | 0.02 | 0.00 | 0.00 | 0.00 | 0.00 | 0.00 | 0.00 | 0.04 | 0.16 |
| CO ₂ | 43.57 | 46.48 | 43.81 | 45.68 | 41.43 | 46.18 | 44.55 | 47.32 | 45.29 | 44.54 | 43.54 | 46.98 |
| Sum | 100.00 | 100.01 | 100.00 | 99.99 | 100.00 | 100.02 | 100.01 | 100.00 | 100.00 | 100.00 | 100.00 | 99.99 |
| # Ions | | | | | | | | | | | | |
| CaO | 1.968 | 1.017 | 1.954 | 0.998 | 2.072 | 0.988 | 1.939 | 0.960 | 1.876 | 1.021 | 1.969 | 0.988 |
| MgO | 0.057 | 1.028 | 0.061 | 1.079 | 0.078 | 1.068 | 0.030 | 1.060 | 0.057 | 1.056 | 0.057 | 1.025 |
| FeO | 0.001 | 0.016 | 0.005 | 0.032 | 0.004 | 0.027 | 0.001 | 0.008 | 0.005 | 0.012 | 0.003 | 0.016 |
| MnO | 0.006 | 0.002 | 0.000 | 0.000 | 0.000 | 0.001 | 0.003 | 0.002 | 0.001 | 0.066 | 0.003 | 0.003 |
| SrO | 0.000 | 0.000 | 0.000 | 0.000 | 0.000 | 0.000 | 0.000 | 0.000 | 0.000 | 0.000 | 0.001 | 0.003 |
| CO ₂ | 1.984 | 1.968 | 1.990 | 1.945 | 1.923 | 1.958 | 2.013 | 1.985 | 2.030 | 1.923 | 1.984 | 1.982 |
| Sum | 4.016 | 4.032 | 4.010 | 4.055 | 4.077 | 4.042 | 3.987 | 4.015 | 3.970 | 4.077 | 4.016 | 4.018 |
| Mol % | | | | | | | | | | | | |
| CaCO ₃ | 96.88 | 49.27 | 96.74 | 47.29 | 96.19 | 47.42 | 98.24 | 47.29 | 96.73 | 47.37 | 96.86 | 48.56 |
| MgCO ₃ | 2.79 | 49.85 | 3.02 | 51.17 | 3.62 | 51.23 | 1.55 | 52.22 | 2.95 | 49.02 | 2.82 | 50.37 |
| FeCO ₃ | 0.04 | 0.79 | 0.23 | 1.52 | 0.18 | 1.30 | 0.06 | 0.39 | 0.25 | 0.54 | 0.16 | 0.77 |
| MnCO ₃ | 0.26 | 0.09 | 0.00 | 0.00 | 0.00 | 0.05 | 0.16 | 0.09 | 0.06 | 0.37 | 0.13 | 0.15 |
| SrCO ₃ | 0.02 | 0.00 | 0.00 | 0.02 | 0.00 | 0.00 | 0.00 | 0.00 | 0.00 | 0.00 | 0.04 | 0.14 |
| XMg | 0.0279158 | 0.4984502 | 0.0302188 | 0.5116724 | 0.0362306 | 0.5123123 | 0.0154958 | 0.5222175 | 0.0295343 | 0.4901371 | 0.0281478 | 0.5036989 |
| XFe | 0.0004121 | 0.0079209 | 0.0023430 | 0.0152114 | 0.0018477 | 0.0129615 | 0.0005608 | 0.0039246 | 0.0025489 | 0.0053985 | 0.0016477 | 0.0077432 |
| T (°C) | 415.50 | | 430.56 | | 464.95 | | 293.55 | | 426.21 | | 417.07 | |
| Sample-Site | 13 | | 14 | | | | | | | | | |
| Mineral | Cc | Dol | Cc | Dol | | | | | | | | |
| Wt % | | | | | | | | | | | | |
| CaO | 54.11 | 31.33 | 56.34 | 30.22 | | | | | | | | |
| MgO | 1.21 | 23.19 | 0.78 | 22.72 | | | | | | | | |
| FeO | 0.04 | 0.44 | 0.00 | 0.18 | | | | | | | | |
| MnO | 0.00 | 0.04 | 0.07 | 0.09 | | | | | | | | |
| SrO | 0.00 | 0.00 | 0.13 | 0.02 | | | | | | | | |
| CO ₂ | 44.64 | 45.01 | 42.68 | 46.77 | | | | | | | | |
| Sum | 100.00 | 100.01 | 57.32 | 100.00 | | | | | | | | |
| # Ions | | | | | | | | | | | | |
| CaO | 1.914 | 1.052 | 2.032 | 1.000 | | | | | | | | |
| MgO | 0.060 | 1.083 | 0.039 | 1.047 | | | | | | | | |
| FeO | 0.001 | 0.012 | 0.000 | 0.005 | | | | | | | | |
| MnO | 0.000 | 0.001 | 0.002 | 0.002 | | | | | | | | |
| SrO | 0.000 | 0.000 | 0.003 | 0.000 | | | | | | | | |
| CO ₂ | 2.012 | 1.926 | 1.962 | 1.973 | | | | | | | | |
| Sum | 3.988 | 4.074 | 4.038 | 4.027 | | | | | | | | |
| Mol % | | | | | | | | | | | | |
| CaCO ₃ | 96.93 | 48.97 | 97.90 | 48.70 | | | | | | | | |
| MgCO ₃ | 3.02 | 50.44 | 1.89 | 50.95 | | | | | | | | |
| FeCO ₃ | 0.06 | 0.54 | 0.00 | 0.23 | | | | | | | | |
| MnCO ₃ | 0.00 | 0.05 | 0.10 | 0.11 | | | | | | | | |
| SrCO ₃ | 0.00 | 0.00 | 0.12 | 0.02 | | | | | | | | |
| XMg | 0.0298511 | 0.5043881 | 0.0188579 | 0.5094276 | | | | | | | | |
| XFe | 0.0005595 | 0.0053686 | 0.0000000 | 0.0022641 | | | | | | | | |
| T (°C) | 428.24 | | 337.60 | | | | | | | | | |

Sample D1-E1 (99-59), Eastern Alpi Apuane.

| Sample: | 99-59 | | Location: | 5 | | Av. T (°C): | | 350.25 | | selected: | | 394.05 | |
|-------------|-----------|-----------|-----------|-----------|------------|-------------|-----------|-----------|-----------|-----------|-----------|-----------|--|
| | | | | | Std. Dev.: | | 93.69 | | selected: | | 23.91 | | |
| Sample-Site | 1 | | 2 | | 3 | | 4 | | 5 | | 6 | | |
| Mineral | Cc | Dol | Cc | Dol | Cc | Dol | Cc | Dol | Cc | Dol | Cc | Dol | |
| Wt % | | | | | | | | | | | | | |
| CaO | 53.53 | 29.56 | 53.69 | 30.13 | 53.85 | 30.05 | 53.81 | 29.76 | 54.10 | 30.98 | 52.68 | 31.47 | |
| MgO | 0.90 | 21.37 | 1.02 | 22.76 | 0.63 | 22.12 | 1.07 | 23.34 | 0.38 | 22.73 | 0.77 | 22.72 | |
| FeO | 0.00 | 0.09 | 0.00 | 0.09 | 0.08 | 0.04 | 0.00 | 0.01 | 0.00 | 0.01 | 0.03 | 0.01 | |
| MnO | 0.00 | 0.00 | 0.05 | 0.18 | 0.02 | 0.00 | 0.00 | 0.04 | 0.00 | 0.07 | 0.20 | 0.04 | |
| SrO | 0.00 | 0.00 | 0.11 | 0.00 | 0.00 | 0.05 | 0.09 | 0.02 | 0.00 | 0.05 | 0.00 | 0.00 | |
| CO2 | 45.57 | 48.98 | 45.12 | 46.85 | 45.42 | 47.75 | 45.03 | 46.83 | 45.52 | 46.15 | 46.33 | 45.76 | |
| Sum | 100.00 | 100.00 | 99.99 | 100.01 | 100.00 | 100.01 | 100.00 | 100.00 | 100.00 | 99.99 | 100.01 | 100.00 | |
| # Ions | | | | | | | | | | | | | |
| CaO | 1.879 | 0.963 | 1.893 | 0.997 | 1.895 | 0.988 | 1.898 | 0.983 | 1.902 | 1.031 | 1.838 | 1.050 | |
| MgO | 0.044 | 0.968 | 0.050 | 1.047 | 0.031 | 1.011 | 0.052 | 1.073 | 0.019 | 1.052 | 0.037 | 1.055 | |
| FeO | 0.000 | 0.002 | 0.000 | 0.002 | 0.002 | 0.001 | 0.000 | 0.000 | 0.000 | 0.000 | 0.001 | 0.000 | |
| MnO | 0.000 | 0.000 | 0.001 | 0.005 | 0.000 | 0.000 | 0.000 | 0.001 | 0.000 | 0.002 | 0.005 | 0.001 | |
| SrO | 0.000 | 0.000 | 0.002 | 0.000 | 0.000 | 0.001 | 0.002 | 0.000 | 0.000 | 0.001 | 0.000 | 0.000 | |
| CO2 | 2.038 | 2.033 | 2.027 | 1.975 | 2.036 | 2.000 | 2.024 | 1.971 | 2.040 | 1.957 | 2.059 | 1.946 | |
| Sum | 3.962 | 3.967 | 3.973 | 4.025 | 3.964 | 4.000 | 3.976 | 4.029 | 3.960 | 4.043 | 3.941 | 4.054 | |
| Mol % | | | | | | | | | | | | | |
| CaCO3 | 97.71 | 49.79 | 97.25 | 48.59 | 98.26 | 49.35 | 97.22 | 47.78 | 99.03 | 49.41 | 97.68 | 49.85 | |
| MgCO3 | 2.29 | 50.09 | 2.57 | 51.07 | 1.60 | 50.55 | 2.69 | 52.14 | 0.97 | 50.45 | 1.99 | 50.08 | |
| FeCO3 | 0.00 | 0.12 | 0.00 | 0.11 | 0.11 | 0.05 | 0.00 | 0.01 | 0.00 | 0.01 | 0.04 | 0.01 | |
| MnCO3 | 0.00 | 0.00 | 0.07 | 0.23 | 0.03 | 0.00 | 0.00 | 0.05 | 0.00 | 0.09 | 0.29 | 0.05 | |
| SrCO3 | 0.00 | 0.00 | 0.11 | 0.00 | 0.00 | 0.04 | 0.09 | 0.02 | 0.00 | 0.04 | 0.00 | 0.00 | |
| XMg | 0.0228588 | 0.5008750 | 0.0257067 | 0.5106888 | 0.0159946 | 0.5054972 | 0.0268990 | 0.5213930 | 0.0096786 | 0.5044359 | 0.0198650 | 0.5008167 | |
| XFe | 0.0000000 | 0.0011834 | 0.0000000 | 0.0011329 | 0.0011394 | 0.0005128 | 0.0000000 | 0.0001253 | 0.0000000 | 0.0001245 | 0.0004342 | 0.0001237 | |
| Sample-Site | 7 | | 8 | | 9 | | 10 | | 11 | | 12 | | |
| Mineral | Cc | Dol | Cc | Dol | Cc | Dol | Cc | Dol | Cc | Dol | Cc | Dol | |
| Wt % | | | | | | | | | | | | | |
| CaO | 52.93 | 29.76 | 52.87 | 29.97 | 52.93 | 30.39 | 52.44 | 29.71 | 54.96 | 29.61 | 56.24 | 30.88 | |
| MgO | 0.83 | 22.78 | 0.91 | 23.05 | 0.69 | 22.71 | 1.01 | 23.58 | 0.31 | 22.99 | 0.48 | 22.34 | |
| FeO | 0.00 | 0.19 | 0.09 | 0.01 | 0.03 | 0.10 | 0.00 | 0.00 | 0.00 | 0.13 | 0.01 | 0.21 | |
| MnO | 0.00 | 0.18 | 0.09 | 0.00 | 0.11 | 0.00 | 0.00 | 0.07 | 0.00 | 0.09 | 0.09 | 0.00 | |
| SrO | 0.00 | 0.00 | 0.00 | 0.00 | 0.00 | 0.00 | 0.00 | 0.00 | 0.00 | 0.02 | 0.09 | 0.00 | |
| CO2 | 46.24 | 47.09 | 46.04 | 46.96 | 46.25 | 46.79 | 46.56 | 44.73 | 44.73 | 47.15 | 43.10 | 46.57 | |
| Sum | 100.00 | 100.00 | 100.00 | 99.99 | 100.01 | 99.99 | 100.01 | 100.00 | 100.00 | 99.99 | 100.01 | 100.00 | |
| # Ions | | | | | | | | | | | | | |
| CaO | 1.847 | 0.983 | 1.848 | 0.989 | 1.848 | 1.006 | 1.824 | 0.982 | 1.947 | 0.977 | 2.022 | 1.025 | |
| MgO | 0.040 | 1.046 | 0.044 | 1.059 | 0.034 | 1.046 | 0.049 | 1.085 | 0.015 | 1.055 | 0.024 | 1.031 | |
| FeO | 0.000 | 0.005 | 0.002 | 0.000 | 0.001 | 0.003 | 0.000 | 0.000 | 0.000 | 0.003 | 0.000 | 0.005 | |
| MnO | 0.000 | 0.005 | 0.002 | 0.000 | 0.003 | 0.000 | 0.000 | 0.002 | 0.000 | 0.002 | 0.003 | 0.000 | |
| SrO | 0.000 | 0.000 | 0.000 | 0.000 | 0.000 | 0.000 | 0.000 | 0.000 | 0.000 | 0.000 | 0.002 | 0.000 | |
| CO2 | 2.056 | 1.981 | 2.051 | 1.976 | 2.057 | 1.973 | 2.064 | 1.965 | 2.019 | 1.981 | 1.975 | 1.969 | |
| Sum | 3.944 | 4.019 | 3.949 | 4.024 | 3.943 | 4.027 | 3.936 | 4.035 | 3.981 | 4.019 | 4.025 | 4.031 | |
| Mol % | | | | | | | | | | | | | |
| CaCO3 | 97.86 | 48.19 | 97.41 | 48.30 | 98.02 | 48.96 | 97.39 | 47.48 | 99.22 | 47.92 | 98.61 | 49.70 | |
| MgCO3 | 2.14 | 51.34 | 2.33 | 51.69 | 1.78 | 50.91 | 2.61 | 52.44 | 0.78 | 51.78 | 1.17 | 50.04 | |
| FeCO3 | 0.00 | 0.24 | 0.13 | 0.01 | 0.04 | 0.13 | 0.00 | 0.00 | 0.00 | 0.16 | 0.01 | 0.26 | |
| MnCO3 | 0.00 | 0.23 | 0.13 | 0.00 | 0.16 | 0.00 | 0.00 | 0.09 | 0.00 | 0.12 | 0.12 | 0.00 | |
| SrCO3 | 0.00 | 0.00 | 0.00 | 0.00 | 0.00 | 0.00 | 0.00 | 0.00 | 0.00 | 0.02 | 0.09 | 0.00 | |
| XMg | 0.0213527 | 0.5133239 | 0.0233277 | 0.5168727 | 0.0177788 | 0.5091076 | 0.0260990 | 0.5243213 | 0.0077870 | 0.5177622 | 0.0117097 | 0.5003210 | |
| XFe | 0.0000000 | 0.0024018 | 0.0012943 | 0.0001258 | 0.0004336 | 0.0012576 | 0.0000000 | 0.0000000 | 0.0000000 | 0.0016424 | 0.0001369 | 0.0026383 | |
| T (°C) | 363.25 | | 380.84 | | 324.91 | | 402.62 | | 50.96 | | 217.70 | | |
| Sample-Site | 13 | | 14 | | 15 | | 16 | | 17 | | 18 | | |
| Mineral | Cc | Dol | Cc | Dol | Cc | Dol | Cc | Dol | Cc | Dol | Cc | Dol | |
| Wt % | | | | | | | | | | | | | |
| CaO | 53.21 | 32.35 | 51.92 | 32.31 | 54.27 | 32.23 | 51.76 | 30.01 | 53.43 | 29.85 | 54.94 | 30.20 | |
| MgO | 0.65 | 21.66 | 1.18 | 22.05 | 0.99 | 21.18 | 0.83 | 23.92 | 0.98 | 23.29 | 1.01 | 23.12 | |
| FeO | 0.00 | 0.08 | 0.18 | 0.00 | 0.03 | 0.00 | 0.68 | 0.13 | 0.00 | 0.04 | 0.00 | 0.05 | |
| MnO | 0.00 | 0.02 | 0.00 | 0.14 | 0.00 | 0.00 | 0.00 | 0.11 | 0.00 | 0.05 | 0.04 | 0.00 | |
| SrO | 0.00 | 0.00 | 0.00 | 0.05 | 0.00 | 0.02 | 0.00 | 0.02 | 0.00 | 0.07 | 0.11 | 0.12 | |
| CO2 | 46.14 | 45.89 | 46.72 | 45.45 | 44.71 | 46.56 | 46.73 | 45.81 | 45.60 | 46.71 | 43.91 | 46.50 | |
| Sum | 100.00 | 100.00 | 100.00 | 100.00 | 100.00 | 99.99 | 100.00 | 100.00 | 100.01 | 100.01 | 100.01 | 99.99 | |
| # Ions | | | | | | | | | | | | | |
| CaO | 1.860 | 1.081 | 1.803 | 1.083 | 1.920 | 1.072 | 1.800 | 0.999 | 1.875 | 0.987 | 1.958 | 1.001 | |
| MgO | 0.032 | 1.007 | 0.057 | 1.029 | 0.049 | 0.981 | 0.040 | 1.108 | 0.048 | 1.072 | 0.050 | 1.067 | |
| FeO | 0.000 | 0.002 | 0.005 | 0.000 | 0.001 | 0.000 | 0.019 | 0.003 | 0.000 | 0.001 | 0.000 | 0.001 | |
| MnO | 0.000 | 0.000 | 0.000 | 0.004 | 0.000 | 0.000 | 0.000 | 0.003 | 0.000 | 0.001 | 0.001 | 0.000 | |
| SrO | 0.000 | 0.000 | 0.000 | 0.001 | 0.000 | 0.000 | 0.000 | 0.000 | 0.000 | 0.001 | 0.002 | 0.002 | |
| CO2 | 2.054 | 1.954 | 2.067 | 1.942 | 2.015 | 1.973 | 2.071 | 1.943 | 2.039 | 1.969 | 1.994 | 1.964 | |
| Sum | 3.946 | 4.046 | 3.933 | 4.058 | 3.985 | 4.027 | 3.929 | 4.057 | 3.961 | 4.031 | 4.006 | 4.036 | |
| Mol % | | | | | | | | | | | | | |
| CaCO3 | 98.33 | 51.70 | 96.68 | 51.18 | 97.48 | 52.22 | 96.85 | 47.26 | 97.51 | 47.86 | 97.35 | 48.34 | |
| MgCO3 | 1.67 | 48.17 | 3.06 | 48.60 | 2.47 | 47.76 | 2.16 | 52.42 | 2.49 | 51.96 | 2.49 | 51.50 | |
| FeCO3 | 0.00 | 0.10 | 0.26 | 0.00 | 0.04 | 0.00 | 0.99 | 0.16 | 0.00 | 0.05 | 0.00 | 0.06 | |
| MnCO3 | 0.00 | 0.03 | 0.00 | 0.18 | 0.00 | 0.00 | 0.00 | 0.14 | 0.00 | 0.06 | 0.06 | 0.00 | |
| SrCO3 | 0.00 | 0.00 | 0.00 | 0.04 | 0.00 | 0.02 | 0.00 | 0.02 | 0.00 | 0.06 | 0.11 | 0.10 | |
| XMg | 0.0167129 | 0.4816944 | 0.0305731 | 0.4860011 | 0.0247433 | 0.4775480 | 0.0216081 | 0.5241997 | 0.0248856 | 0.5196185 | 0.0249008 | 0.5149274 | |
| XFe | 0.0000000 | 0.0009980 | 0.0026162 | 0.0000000 | 0.0004206 | 0.0000000 | 0.0099310 | 0.0015982 | 0.0000000 | 0.0005006 | 0.0000000 | 0.0006247 | |
| T (°C) | 311.14 | | 432.77 | | 392.33 | | 365.64 | | 393.44 | | 393.56 | | |

Appendix C5

| Sample-Site Mineral | 19 | | 20 | | 21 | | 22 | | 23 | |
|------------------------|-----------|-----------|-----------|-----------|-----------|-----------|-----------|-----------|-----------|-----------|
| | Cc | Dol |
| Wt % | | | | | | | | | | |
| CaO | 53.58 | 30.16 | 53.34 | 29.73 | 53.00 | 29.22 | 53.23 | 29.88 | 51.82 | 30.41 |
| MgO | 1.00 | 23.27 | 1.21 | 23.28 | 1.08 | 24.22 | 0.90 | 23.52 | 1.12 | 23.19 |
| FeO | 0.15 | 0.09 | 0.09 | 0.26 | 0.10 | 0.05 | 0.19 | 0.08 | 0.09 | 0.00 |
| MnO | 0.18 | 0.00 | 0.00 | 0.00 | 0.05 | 0.07 | 0.43 | 0.02 | 0.00 | 0.05 |
| SrO | 0.00 | 0.00 | 0.00 | 0.00 | 0.00 | 0.05 | 0.00 | 0.02 | 0.11 | 0.07 |
| CO ₂ | 45.08 | 46.48 | 45.35 | 46.73 | 45.76 | 46.39 | 45.24 | 46.48 | 46.86 | 46.27 |
| Sum | 99.99 | 100.00 | 99.99 | 100.00 | 99.99 | 100.00 | 99.99 | 100.00 | 100.00 | 99.99 |
| # Ions | | | | | | | | | | |
| CaO | 1.890 | 0.999 | 1.875 | 0.983 | 1.857 | 0.967 | 1.876 | 0.990 | 1.798 | 1.010 |
| MgO | 0.049 | 1.073 | 0.059 | 1.071 | 0.053 | 1.115 | 0.044 | 1.084 | 0.054 | 1.072 |
| FeO | 0.004 | 0.002 | 0.002 | 0.007 | 0.003 | 0.001 | 0.005 | 0.002 | 0.002 | 0.000 |
| MnO | 0.005 | 0.000 | 0.000 | 0.000 | 0.001 | 0.002 | 0.012 | 0.000 | 0.000 | 0.001 |
| SrO | 0.000 | 0.000 | 0.000 | 0.000 | 0.000 | 0.001 | 0.000 | 0.000 | 0.002 | 0.001 |
| CO ₂ | 2.026 | 1.963 | 2.032 | 1.969 | 2.043 | 1.957 | 2.031 | 1.962 | 2.072 | 1.958 |
| Sum | 3.974 | 4.037 | 3.968 | 4.031 | 3.957 | 4.043 | 3.969 | 4.038 | 3.928 | 4.042 |
| Mol % | | | | | | | | | | |
| CaCO ₃ | 97.01 | 48.17 | 96.82 | 47.70 | 97.03 | 46.35 | 96.83 | 47.66 | 96.84 | 48.46 |
| MgCO ₃ | 2.52 | 51.72 | 3.06 | 51.98 | 2.75 | 53.46 | 2.28 | 52.20 | 2.91 | 51.42 |
| FeCO ₃ | 0.21 | 0.11 | 0.13 | 0.33 | 0.14 | 0.06 | 0.27 | 0.10 | 0.13 | 0.00 |
| MnCO ₃ | 0.26 | 0.00 | 0.00 | 0.00 | 0.07 | 0.09 | 0.62 | 0.03 | 0.00 | 0.06 |
| SrCO ₃ | 0.00 | 0.00 | 0.00 | 0.00 | 0.00 | 0.04 | 0.00 | 0.02 | 0.11 | 0.06 |
| XMg | 0.0251924 | 0.5171507 | 0.0305586 | 0.5197255 | 0.0275119 | 0.5345663 | 0.0227805 | 0.5219840 | 0.0291239 | 0.5141750 |
| XFe | 0.0021199 | 0.0011220 | 0.0012751 | 0.0032562 | 0.0014290 | 0.0006191 | 0.0026979 | 0.0009960 | 0.0013129 | 0.0000000 |
| T (°C) | 395.81 | | 432.68 | | 412.72 | | 376.16 | | 423.56 | |

Sample D1-E2 (99-49), Eastern Alpi Apuane.

| Sample: | 99-49 | Location: | 10.5 | Av. T (°C): | 365.54 | Av. T (°C): selected: | 365.54 | | | | | |
|------------------------|-----------|-----------|-----------|-------------|-----------|-----------------------|-----------|-----------|-----------|-----------|-----------|-----------|
| | | | | Std. Dev.: | 19.58 | Std. Dev.: | 19.58 | | | | | |
| Sample-Site Mineral | 1 | | 2 | | 3 | | 4 | | 5 | | 6 | |
| Wt % | | | | | | | | | | | | |
| CaO | 52.99 | 29.32 | 53.05 | 29.89 | 52.82 | 29.67 | 52.69 | 29.44 | 54.76 | 29.53 | 57.88 | 29.52 |
| MgO | 0.86 | 20.97 | 1.00 | 19.90 | 0.82 | 20.19 | 0.87 | 20.66 | 0.76 | 20.65 | 0.80 | 20.66 |
| FeO | 0.00 | 0.07 | 0.10 | 0.03 | 0.04 | 0.53 | 0.12 | 0.05 | 0.05 | 0.12 | 0.08 | 0.05 |
| MnO | 0.00 | 0.01 | 0.00 | 0.00 | 0.01 | 0.00 | 0.11 | 0.03 | 0.03 | 0.00 | 0.00 | 0.01 |
| SrO | 0.15 | 0.00 | 0.00 | 0.00 | 0.07 | 0.00 | 0.02 | 0.00 | 0.07 | 0.00 | 0.00 | 0.00 |
| CO ₂ | 46.00 | 49.63 | 45.86 | 50.18 | 46.22 | 49.61 | 46.18 | 49.81 | 44.32 | 49.70 | 41.24 | 49.75 |
| Sum | 100.00 | 100.00 | 100.01 | 100.00 | 99.98 | 100.00 | 99.99 | 99.99 | 99.99 | 100.00 | 100.00 | 99.99 |
| # Ions | | | | | | | | | | | | |
| CaO | 1.854 | 0.951 | 1.857 | 0.967 | 1.844 | 0.964 | 1.841 | 0.954 | 1.946 | 0.958 | 2.115 | 0.957 |
| MgO | 0.042 | 0.946 | 0.049 | 0.896 | 0.040 | 0.913 | 0.042 | 0.931 | 0.037 | 0.932 | 0.041 | 0.932 |
| FeO | 0.000 | 0.002 | 0.003 | 0.001 | 0.001 | 0.013 | 0.003 | 0.001 | 0.002 | 0.003 | 0.002 | 0.001 |
| MnO | 0.000 | 0.000 | 0.000 | 0.000 | 0.000 | 0.000 | 0.003 | 0.001 | 0.001 | 0.000 | 0.000 | 0.000 |
| SrO | 0.003 | 0.000 | 0.000 | 0.000 | 0.001 | 0.000 | 0.000 | 0.000 | 0.001 | 0.000 | 0.000 | 0.000 |
| CO ₂ | 2.051 | 2.051 | 2.046 | 2.068 | 2.056 | 2.055 | 2.055 | 2.056 | 2.007 | 2.054 | 1.921 | 2.055 |
| Sum | 3.949 | 3.949 | 3.954 | 3.932 | 3.944 | 3.945 | 3.945 | 3.944 | 3.993 | 3.946 | 4.079 | 3.945 |
| Mol % | | | | | | | | | | | | |
| CaCO ₃ | 97.65 | 50.07 | 97.30 | 51.89 | 97.75 | 51.00 | 97.41 | 50.54 | 97.93 | 50.60 | 98.01 | 50.62 |
| MgCO ₃ | 2.21 | 49.83 | 2.55 | 48.07 | 2.11 | 48.29 | 2.24 | 49.35 | 1.89 | 49.24 | 1.89 | 49.30 |
| FeCO ₃ | 0.00 | 0.09 | 0.14 | 0.04 | 0.06 | 0.71 | 0.17 | 0.07 | 0.07 | 0.16 | 0.11 | 0.07 |
| MnCO ₃ | 0.00 | 0.01 | 0.00 | 0.00 | 0.01 | 0.00 | 0.16 | 0.04 | 0.04 | 0.00 | 0.00 | 0.01 |
| SrCO ₃ | 0.15 | 0.00 | 0.00 | 0.00 | 0.07 | 0.00 | 0.02 | 0.00 | 0.07 | 0.00 | 0.00 | 0.00 |
| XMg | 0.0220499 | 0.4982500 | 0.0255211 | 0.4806897 | 0.0211138 | 0.4828847 | 0.0223788 | 0.4935064 | 0.0189109 | 0.4923630 | 0.0188486 | 0.4929632 |
| XFe | 0.0000000 | 0.0009330 | 0.0014317 | 0.0004065 | 0.0005778 | 0.0071110 | 0.0017316 | 0.0006700 | 0.0006979 | 0.0016051 | 0.0010574 | 0.0006693 |
| T (°C) | 369.69 | | 398.31 | | 360.98 | | 372.64 | | 338.19 | | 337.49 | |
| Sample-Site Mineral | 7 | | 8 | | 9 | | 10 | | 11 | | 12 | |
| Wt % | | | | | | | | | | | | |
| CaO | 52.39 | 29.90 | 54.62 | 30.03 | 52.22 | 30.03 | 52.67 | 29.49 | 56.76 | 29.54 | 53.80 | 28.73 |
| MgO | 1.03 | 20.39 | 0.79 | 21.35 | 0.82 | 20.19 | 0.92 | 19.79 | 0.88 | 20.62 | 0.95 | 19.63 |
| FeO | 0.20 | 0.26 | 0.00 | 0.16 | 0.11 | 0.00 | 0.03 | 0.10 | 0.00 | 3.63 | 0.00 | 0.10 |
| MnO | 0.12 | 0.03 | 0.04 | 0.00 | 0.11 | 0.14 | 0.00 | 0.07 | 0.07 | 0.07 | 0.03 | 0.13 |
| SrO | 0.00 | 0.05 | 0.00 | 0.00 | 0.00 | 0.10 | 0.20 | 0.00 | 0.12 | 0.21 | 0.00 | 0.00 |
| CO ₂ | 46.25 | 49.38 | 44.55 | 48.46 | 46.75 | 49.54 | 46.18 | 50.55 | 42.17 | 45.93 | 45.23 | 51.42 |
| Sum | 99.99 | 100.01 | 100.00 | 100.00 | 100.01 | 100.00 | 100.00 | 100.00 | 100.00 | 100.00 | 100.01 | 100.01 |
| # Ions | | | | | | | | | | | | |
| CaO | 1.828 | 0.973 | 1.936 | 0.983 | 1.814 | 0.976 | 1.840 | 0.951 | 2.057 | 0.994 | 1.894 | 0.920 |
| MgO | 0.050 | 0.923 | 0.039 | 0.972 | 0.040 | 0.913 | 0.045 | 0.888 | 0.044 | 0.965 | 0.046 | 0.875 |
| FeO | 0.006 | 0.007 | 0.000 | 0.004 | 0.003 | 0.000 | 0.001 | 0.002 | 0.000 | 0.005 | 0.000 | 0.002 |
| MnO | 0.003 | 0.001 | 0.001 | 0.000 | 0.003 | 0.004 | 0.000 | 0.002 | 0.002 | 0.002 | 0.001 | 0.003 |
| SrO | 0.000 | 0.001 | 0.000 | 0.000 | 0.000 | 0.002 | 0.004 | 0.000 | 0.002 | 0.004 | 0.000 | 0.000 |
| CO ₂ | 2.056 | 2.048 | 2.012 | 2.021 | 2.070 | 2.052 | 2.055 | 2.078 | 1.947 | 1.970 | 2.029 | 2.099 |
| Sum | 3.944 | 3.952 | 3.988 | 3.979 | 3.930 | 3.948 | 3.945 | 3.922 | 4.053 | 4.030 | 3.971 | 3.901 |
| Mol % | | | | | | | | | | | | |
| CaCO ₃ | 96.89 | 51.09 | 97.97 | 50.16 | 97.55 | 51.52 | 97.39 | 51.59 | 97.69 | 48.24 | 97.56 | 51.10 |
| MgCO ₃ | 2.65 | 48.48 | 1.97 | 49.63 | 2.13 | 48.20 | 2.37 | 48.18 | 2.11 | 46.86 | 2.40 | 48.58 |
| FeCO ₃ | 0.29 | 0.35 | 0.00 | 0.21 | 0.16 | 0.00 | 0.04 | 0.14 | 0.00 | 4.63 | 0.00 | 0.14 |
| MnCO ₃ | 0.18 | 0.04 | 0.06 | 0.00 | 0.16 | 0.19 | 0.00 | 0.10 | 0.10 | 0.09 | 0.04 | 0.18 |
| SrCO ₃ | 0.00 | 0.05 | 0.00 | 0.00 | 0.00 | 0.09 | 0.20 | 0.00 | 0.11 | 0.19 | 0.00 | 0.00 |
| XMg | 0.0265032 | 0.4847658 | 0.0197164 | 0.4962532 | 0.0213126 | 0.4819643 | 0.0236694 | 0.4817382 | 0.0210728 | 0.4685482 | 0.0239698 | 0.4857915 |
| XFe | 0.0028869 | 0.0034677 | 0.0000000 | 0.0020863 | 0.0016038 | 0.0000000 | 0.0004330 | 0.0013656 | 0.0000000 | 0.0462721 | 0.0000000 | 0.0013883 |
| T (°C) | 405.57 | | 346.94 | | 362.87 | | 383.69 | | 360.58 | | 386.15 | |

| Sample-Site | 13 | | 14 | | 15 | | 16 | | 17 | |
|-------------------|-----------|-----------|-----------|-----------|-----------|-----------|-----------|-----------|-----------|-----------|
| Mineral | Cc | Dol |
| Wt % | | | | | | | | | | |
| CaO | 54.27 | 29.27 | 56.42 | 29.96 | 55.95 | 29.44 | 56.70 | 29.27 | 56.27 | 29.76 |
| MgO | 0.79 | 20.59 | 0.93 | 20.43 | 0.89 | 19.88 | 0.84 | 19.93 | 0.84 | 20.01 |
| FeO | 0.07 | 0.23 | 0.14 | 0.00 | 0.08 | 0.00 | 0.03 | 0.07 | 0.00 | 0.10 |
| MnO | 0.00 | 0.75 | 0.00 | 0.08 | 0.06 | 0.03 | 0.11 | 0.00 | 0.00 | 0.00 |
| SrO | 0.05 | 0.00 | 0.00 | 0.05 | 0.12 | 0.00 | 0.02 | 0.05 | 0.02 | 0.00 |
| CO ₂ | 44.82 | 49.15 | 42.51 | 49.47 | 42.90 | 50.66 | 42.30 | 50.68 | 42.87 | 50.14 |
| Sum | 100.00 | 99.99 | 100.00 | 99.99 | 100.00 | 100.01 | 100.00 | 100.00 | 100.00 | 100.01 |
| # Ions | | | | | | | | | | |
| CaO | 1.919 | 0.955 | 2.037 | 0.974 | 2.014 | 0.948 | 2.052 | 0.943 | 2.025 | 0.963 |
| MgO | 0.039 | 0.934 | 0.047 | 0.924 | 0.045 | 0.891 | 0.042 | 0.893 | 0.042 | 0.901 |
| FeO | 0.002 | 0.006 | 0.004 | 0.000 | 0.002 | 0.000 | 0.001 | 0.002 | 0.000 | 0.002 |
| MnO | 0.000 | 0.019 | 0.000 | 0.002 | 0.002 | 0.001 | 0.003 | 0.000 | 0.000 | 0.000 |
| SrO | 0.001 | 0.000 | 0.000 | 0.001 | 0.002 | 0.000 | 0.000 | 0.001 | 0.000 | 0.000 |
| CO ₂ | 2.020 | 2.043 | 1.956 | 2.049 | 1.968 | 2.080 | 1.951 | 2.081 | 1.966 | 2.067 |
| Sum | 3.980 | 3.957 | 4.044 | 3.951 | 4.032 | 3.920 | 4.049 | 3.919 | 4.034 | 3.933 |
| Mol % | | | | | | | | | | |
| CaCO ₃ | 97.87 | 49.87 | 97.57 | 51.23 | 97.54 | 51.53 | 97.78 | 51.27 | 97.95 | 51.59 |
| MgCO ₃ | 1.98 | 48.82 | 2.24 | 48.61 | 2.16 | 48.43 | 2.02 | 48.58 | 2.03 | 48.27 |
| FeCO ₃ | 0.10 | 0.31 | 0.19 | 0.00 | 0.11 | 0.00 | 0.04 | 0.10 | 0.00 | 0.14 |
| MnCO ₃ | 0.00 | 1.01 | 0.00 | 0.11 | 0.08 | 0.04 | 0.15 | 0.00 | 0.00 | 0.00 |
| SrCO ₃ | 0.05 | 0.00 | 0.00 | 0.05 | 0.11 | 0.00 | 0.02 | 0.05 | 0.02 | 0.00 |
| XMg | 0.0198230 | 0.4881279 | 0.0223785 | 0.4861135 | 0.0215878 | 0.4842209 | 0.0201547 | 0.4857997 | 0.0203443 | 0.4826958 |
| XFe | 0.0009853 | 0.0030588 | 0.0018898 | 0.0000000 | 0.0010886 | 0.0000000 | 0.0004038 | 0.0009572 | 0.0000000 | 0.0013532 |
| T (°C) | 348.06 | | 372.63 | | 365.45 | | 351.49 | | 353.41 | |

Sample D2-W (2k-7), Western Alpi Apuane.

| Sample: | 2k-7-SZ | | Location: | 0 | | Av. T (°C): | 333.80 | | Av. T (°C): selected: | 327.79 | | |
|-------------------|-----------|-----|-----------|-----|-----------|-------------|-----------|-----|-----------------------|-----------|-----------|-----|
| | | | | | | Std. Dev.: | 34.99 | | Std. Dev.: | selected: | | |
| | | | | | | | | | | 35.40 | | |
| Sample-Site | 1 | | 2 | | 3 | | 4 | | 5 | | 6 | |
| Mineral | Cc | Dol | Cc | Dol | Cc | Dol | Cc | Dol | Cc | Dol | Cc | Dol |
| Wt % | | | | | | | | | | | | |
| CaO | 57.44 | | 57.95 | | 58.18 | | 58.14 | | 58.25 | | 56.84 | |
| MgO | 1.01 | | 0.85 | | 0.79 | | 0.96 | | 0.88 | | 0.57 | |
| FeO | 0.49 | | 0.00 | | 0.41 | | 0.04 | | 0.20 | | 0.00 | |
| MnO | 0.06 | | 0.00 | | 0.00 | | 0.00 | | 0.00 | | 0.00 | |
| SrO | 0.00 | | 0.05 | | 0.00 | | 0.00 | | 0.00 | | 0.00 | |
| CO ₂ | 41.00 | | 41.15 | | 40.62 | | 40.86 | | 40.66 | | 42.59 | |
| Sum | 100.00 | | 100.00 | | 100.00 | | 100.00 | | 99.99 | | 100.00 | |
| # Ions | | | | | | | | | | | | |
| CaO | 2.105 | | 2.120 | | 2.140 | | 2.132 | | 2.141 | | 2.052 | |
| MgO | 0.052 | | 0.043 | | 0.040 | | 0.049 | | 0.045 | | 0.029 | |
| FeO | 0.014 | | 0.000 | | 0.012 | | 0.001 | | 0.006 | | 0.000 | |
| MnO | 0.002 | | 0.000 | | 0.000 | | 0.000 | | 0.000 | | 0.000 | |
| SrO | 0.000 | | 0.001 | | 0.000 | | 0.000 | | 0.000 | | 0.000 | |
| CO ₂ | 1.914 | | 1.918 | | 1.904 | | 1.909 | | 1.914 | | 1.959 | |
| Sum | 4.086 | | 4.082 | | 4.096 | | 4.091 | | 4.096 | | 4.041 | |
| Mol % | | | | | | | | | | | | |
| CaCO ₃ | 96.90 | | 97.95 | | 97.62 | | 97.70 | | 97.68 | | 98.62 | |
| MgCO ₃ | 2.37 | | 2.00 | | 1.84 | | 2.24 | | 2.05 | | 1.38 | |
| FeCO ₃ | 0.65 | | 0.00 | | 0.54 | | 0.05 | | 0.26 | | 0.00 | |
| MnCO ₃ | 0.08 | | 0.00 | | 0.00 | | 0.00 | | 0.00 | | 0.00 | |
| SrCO ₃ | 0.00 | | 0.05 | | 0.00 | | 0.00 | | 0.00 | | 0.00 | |
| XMg | 0.0237080 | | 0.0199910 | | 0.0184430 | | 0.0224470 | | 0.0205340 | | 0.0137610 | |
| XFe | 0.0064524 | | 0.0000000 | | 0.0053696 | | 0.0005247 | | 0.0026179 | | 0.0000000 | |
| T (°C) | 384.01 | | 349.81 | | 332.86 | | 373.24 | | 355.31 | | 263.78 | |
| Sample-Site | 7 | | 8 | | 9 | | 10 | | 11 | | 12 | |
| Mineral | Cc | Dol | Cc | Dol | Cc | Dol | Cc | Dol | Cc | Dol | Cc | Dol |
| Wt % | | | | | | | | | | | | |
| CaO | 56.66 | | 56.63 | | 56.88 | | 55.96 | | 57.33 | | 56.53 | |
| MgO | 0.87 | | 0.76 | | 0.86 | | 0.62 | | 0.59 | | 0.66 | |
| FeO | 0.00 | | 0.00 | | 0.00 | | 0.00 | | 0.00 | | 0.00 | |
| MnO | 0.00 | | 0.00 | | 0.17 | | 0.15 | | 0.04 | | 0.00 | |
| SrO | 0.00 | | 0.00 | | 0.05 | | 0.12 | | 0.02 | | 0.10 | |
| CO ₂ | 42.47 | | 42.61 | | 42.04 | | 43.14 | | 42.02 | | 42.72 | |
| Sum | 100.00 | | 100.00 | | 100.00 | | 99.99 | | 100.00 | | 100.01 | |
| # Ions | | | | | | | | | | | | |
| CaO | 2.047 | | 2.043 | | 2.064 | | 2.011 | | 2.081 | | 2.039 | |
| MgO | 0.044 | | 0.038 | | 0.043 | | 0.031 | | 0.030 | | 0.033 | |
| FeO | 0.000 | | 0.000 | | 0.000 | | 0.000 | | 0.000 | | 0.000 | |
| MnO | 0.000 | | 0.000 | | 0.005 | | 0.004 | | 0.001 | | 0.000 | |
| SrO | 0.000 | | 0.000 | | 0.001 | | 0.002 | | 0.000 | | 0.002 | |
| CO ₂ | 1.955 | | 1.959 | | 1.944 | | 1.976 | | 1.944 | | 1.963 | |
| Sum | 4.045 | | 4.041 | | 4.056 | | 4.024 | | 4.056 | | 4.037 | |
| Mol % | | | | | | | | | | | | |
| CaCO ₃ | 97.91 | | 98.17 | | 97.67 | | 98.16 | | 98.52 | | 98.31 | |
| MgCO ₃ | 2.09 | | 1.83 | | 2.05 | | 1.51 | | 1.41 | | 1.60 | |
| FeCO ₃ | 0.00 | | 0.00 | | 0.00 | | 0.00 | | 0.00 | | 0.00 | |
| MnCO ₃ | 0.00 | | 0.00 | | 0.23 | | 0.21 | | 0.05 | | 0.00 | |
| SrCO ₃ | 0.00 | | 0.00 | | 0.05 | | 0.11 | | 0.02 | | 0.09 | |
| XMg | 0.0209180 | | 0.0183310 | | 0.0205470 | | 0.0151330 | | 0.0141070 | | 0.0159700 | |
| XFe | 0.0000000 | | 0.0000000 | | 0.0000000 | | 0.0000000 | | 0.0000000 | | 0.0000000 | |
| T (°C) | 359.08 | | 331.54 | | 355.44 | | 287.83 | | 270.25 | | 300.67 | |

Appendix C5

| Sample-Site Mineral | 13 | | 14 | | 15 | | 16 | | 17 | | 18 | |
|------------------------|-----------|-----|-----------|-----|-----------|-----|-----------|-----|-----------|-----|-----------|-----|
| | Cc | Dol |
| Wt % | | | | | | | | | | | | |
| CaO | 57.28 | | 53.61 | | 53.06 | | 54.12 | | 51.77 | | 55.04 | |
| MgO | 0.81 | | 0.82 | | 0.82 | | 0.81 | | 0.75 | | 0.84 | |
| FeO | 0.37 | | 0.00 | | 1.26 | | 0.00 | | 0.30 | | 0.00 | |
| MnO | 0.00 | | 0.00 | | 0.23 | | 0.00 | | 0.14 | | 0.03 | |
| SrO | 0.05 | | 0.00 | | 0.00 | | 0.00 | | 0.07 | | 0.18 | |
| CO2 | 41.49 | | 45.57 | | 44.63 | | 45.07 | | 46.98 | | 43.91 | |
| Sum | 100.00 | | 100.00 | | 100.00 | | 100.00 | | 100.01 | | 100.00 | |
| # Ions | | | | | | | | | | | | |
| CaO | 2.090 | | 1.882 | | 1.883 | | 1.909 | | 1.796 | | 1.963 | |
| MgO | 0.041 | | 0.04 | | 0.041 | | 0.04 | | 0.036 | | 0.042 | |
| FeO | 0.010 | | 0 | | 0.035 | | 0 | | 0.008 | | 0 | |
| MnO | 0.000 | | 0 | | 0.006 | | 0 | | 0.004 | | 0.001 | |
| SrO | 0.001 | | 0 | | 0 | | 0 | | 0.001 | | 0.003 | |
| CO2 | 1.929 | | 2.039 | | 2.018 | | 2.026 | | 2.077 | | 1.996 | |
| Sum | 4.071 | | 3.961 | | 3.982 | | 3.974 | | 3.923 | | 4.004 | |
| Mol % | | | | | | | | | | | | |
| CaCO3 | 97.54 | | 97.92 | | 95.83 | | 97.96 | | 97.32 | | 97.71 | |
| MgCO3 | 1.92 | | 2.08 | | 2.06 | | 2.04 | | 1.96 | | 2.08 | |
| FeCO3 | 0.49 | | 0.00 | | 1.78 | | 0.00 | | 0.44 | | 0.00 | |
| MnCO3 | 0.00 | | 0.00 | | 0.33 | | 0.00 | | 0.21 | | 0.04 | |
| SrCO3 | 0.05 | | 0.00 | | 0.00 | | 0.00 | | 0.07 | | 0.17 | |
| XMg | 0.0191920 | | 0.0208400 | | 0.0206100 | | 0.0204000 | | 0.0196200 | | 0.0207500 | |
| XFe | 0.0049180 | | 0.0000000 | | 0.0177630 | | 0.0000000 | | 0.0044019 | | 0.0000000 | |
| T (°C) | 341.31 | | 358.32 | | 356.04 | | 353.97 | | 345.89 | | 357.44 | |

| Sample-Site Mineral | 19 | | 20 | | 21 | | 22 | | 23 | | 24 | |
|------------------------|-----------|-----|-----------|-----|-----------|-----|-----------|-----|-----------|-----|-----------|-----|
| | Cc | Dol |
| Wt % | | | | | | | | | | | | |
| CaO | 54.20 | | 54.92 | | 53.17 | | 52.72 | | 52.82 | | 53.94 | |
| MgO | 0.67 | | 0.59 | | 0.79 | | 0.82 | | 0.63 | | 0.76 | |
| FeO | 0.00 | | 0.00 | | 0.00 | | 0.00 | | 0.00 | | 0.00 | |
| MnO | 0.00 | | 0.00 | | 0.06 | | 0.00 | | 0.05 | | 0.03 | |
| SrO | 0.00 | | 0.00 | | 0.00 | | 0.04 | | 0.00 | | 0.00 | |
| CO2 | 45.13 | | 44.49 | | 45.98 | | 46.42 | | 46.50 | | 45.27 | |
| Sum | 100.00 | | 100.00 | | 100.00 | | 100.00 | | 100.00 | | 100.00 | |
| # Ions | | | | | | | | | | | | |
| CaO | 1.911 | | 1.948 | | 1.860 | | 1.837 | | 1.840 | | 1.900 | |
| MgO | 0.033 | | 0.029 | | 0.038 | | 0.040 | | 0.031 | | 0.037 | |
| FeO | 0.000 | | 0.000 | | 0.000 | | 0.000 | | 0.000 | | 0.000 | |
| MnO | 0.000 | | 0.000 | | 0.002 | | 0.000 | | 0.001 | | 0.001 | |
| SrO | 0.000 | | 0.000 | | 0.000 | | 0.001 | | 0.000 | | 0.000 | |
| CO2 | 2.028 | | 2.011 | | 2.050 | | 2.061 | | 2.064 | | 2.031 | |
| Sum | 3.972 | | 3.989 | | 3.950 | | 3.939 | | 3.936 | | 3.969 | |
| Mol % | | | | | | | | | | | | |
| CaCO3 | 98.31 | | 98.53 | | 97.89 | | 97.84 | | 98.29 | | 98.03 | |
| MgCO3 | 1.69 | | 1.47 | | 2.02 | | 2.12 | | 1.63 | | 1.92 | |
| FeCO3 | 0.00 | | 0.00 | | 0.00 | | 0.00 | | 0.00 | | 0.00 | |
| MnCO3 | 0.00 | | 0.00 | | 0.09 | | 0.00 | | 0.07 | | 0.04 | |
| SrCO3 | 0.00 | | 0.00 | | 0.00 | | 0.04 | | 0.00 | | 0.00 | |
| XMg | 0.0169100 | | 0.0147300 | | 0.0202400 | | 0.0211700 | | 0.0163100 | | 0.0192200 | |
| XFe | 0.0000000 | | 0.0000000 | | 0.0000000 | | 0.0000000 | | 0.0000000 | | 0.0000000 | |
| T (°C) | 313.78 | | 281.15 | | 352.33 | | 361.56 | | 305.60 | | 341.60 | |

| Sample-Site Mineral | 25 | | 26 | |
|------------------------|-----------|-----|-----------|-----|
| | Cc | Dol | Cc | Dol |
| Wt % | | | | |
| CaO | 52.55 | | 54.53 | |
| MgO | 0.55 | | 0.92 | |
| FeO | 0.19 | | 0.00 | |
| MnO | 0.14 | | 1.79 | |
| SrO | 0.00 | | 0.00 | |
| CO2 | 46.57 | | 42.76 | |
| Sum | 100.00 | | 100.00 | |
| # Ions | | | | |
| CaO | 1.831 | | 1.969 | |
| MgO | 0.027 | | 0.046 | |
| FeO | 0.005 | | 0.000 | |
| MnO | 0.004 | | 0.051 | |
| SrO | 0.000 | | 0.000 | |
| CO2 | 2.067 | | 1.967 | |
| Sum | 3.933 | | 4.033 | |
| Mol % | | | | |
| CaCO3 | 98.09 | | 95.29 | |
| MgCO3 | 1.43 | | 2.24 | |
| FeCO3 | 0.28 | | 0.00 | |
| MnCO3 | 0.21 | | 2.47 | |
| SrCO3 | 0.00 | | 0.00 | |
| XMg | 0.0142800 | | 0.0223700 | |
| XFe | 0.0027682 | | 0.0000000 | |
| T (°C) | 273.45 | | 372.55 | |

Sample D2-W (2k-7), Western Alpi Apuane. Annealed marble outside the shear zone

| Sample: | 2k-7-Ann | Location: | 0 | Av. T (°C): | 359.88 | Av. T (°C): selected: | 359.35 | | | | | |
|-------------------|---------------|-----------|---------------|-------------|---------------|-----------------------|---------------|-----|---------------|-----|---------------|-----|
| | | | | Std. Dev.: | 30.59 | Std. Dev.: selected: | 31.51 | | | | | |
| Sample-Site | 1 | | 2 | | 3 | | 4 | | 5 | | 6 | |
| Mineral | Cc | Dol | Cc | Dol | Cc | Dol | Cc | Dol | Cc | Dol | Cc | Dol |
| coarse vein | | | | | | | | | | | | |
| Wt % | | | | | | | | | | | | |
| CaO | 58.19 | | 56.92 | | 56.68 | | 56.45 | | 58.04 | | 51.91 | |
| MgO | 0.94 | | 0.75 | | 0.70 | | 0.79 | | 0.90 | | 0.81 | |
| FeO | 0.26 | | 0.01 | | 0.18 | | 0.00 | | 0.00 | | 0.23 | |
| MnO | 0.00 | | 0.00 | | 0.06 | | 0.00 | | 0.00 | | 0.00 | |
| SrO | 0.02 | | 0.19 | | 0.07 | | 0.00 | | 0.00 | | 0.00 | |
| CO ₂ | 40.59 | | 42.12 | | 42.31 | | 42.76 | | 41.06 | | 47.05 | |
| Sum | 100.00 | | 99.99 | | 100.00 | | 100.00 | | 100.00 | | 100.00 | |
| # Ions | | | | | | | | | | | | |
| CaO | 2.140 | | 2.065 | | 2.052 | | 2.034 | | 2.124 | | 2.140 | |
| MgO | 0.048 | | 0.038 | | 0.035 | | 0.040 | | 0.046 | | 0.039 | |
| FeO | 0.007 | | 0.000 | | 0.005 | | 0.000 | | 0.000 | | 0.006 | |
| MnO | 0.000 | | 0.000 | | 0.002 | | 0.000 | | 0.000 | | 0.000 | |
| SrO | 0.000 | | 0.004 | | 0.001 | | 0.000 | | 0.000 | | 0.000 | |
| CO ₂ | 1.902 | | 1.947 | | 1.952 | | 1.963 | | 1.915 | | 2.078 | |
| Sum | 4.098 | | 4.053 | | 4.048 | | 4.037 | | 4.085 | | 3.922 | |
| Mol % | | | | | | | | | | | | |
| CaCO ₃ | 97.45 | | 98.01 | | 97.93 | | 98.09 | | 97.89 | | 97.54 | |
| MgCO ₃ | 2.19 | | 1.80 | | 1.68 | | 1.91 | | 2.11 | | 2.12 | |
| FeCO ₃ | 0.34 | | 0.01 | | 0.24 | | 0.00 | | 0.00 | | 0.34 | |
| MnCO ₃ | 0.00 | | 0.00 | | 0.08 | | 0.00 | | 0.00 | | 0.00 | |
| SrCO ₃ | 0.02 | | 0.18 | | 0.07 | | 0.00 | | 0.00 | | 0.00 | |
| XMg | 0.0219040 | | 0.0179690 | | 0.0168280 | | 0.0191000 | | 0.0211200 | | 0.0211800 | |
| XFe | 0.0033987 | | 0.0001344 | | 0.0024274 | | 0.0000000 | | 0.0000000 | | 0.0033735 | |
| T (°C) | 368.36 | | 327.23 | | 312.69 | | 340.30 | | 361.04 | | 361.59 | |
| Sample-Site | 7 | | 8 | | 9 | | 10 | | 11 | | 12 | |
| Mineral | Cc | Dol | Cc | Dol | Cc | Dol | Cc | Dol | Cc | Dol | Cc | Dol |
| Wt % | | | | | | | | | | | | |
| CaO | 51.81 | | 52.92 | | 52.61 | | 55.46 | | 54.37 | | 54.53 | |
| MgO | 0.89 | | 1.12 | | 0.90 | | 0.90 | | 0.90 | | 0.85 | |
| FeO | 0.00 | | 0.12 | | 0.00 | | 0.00 | | 0.09 | | 0.09 | |
| MnO | 0.08 | | 0.00 | | 0.00 | | 0.00 | | 0.00 | | 0.00 | |
| SrO | 0.22 | | 0.00 | | 0.02 | | 0.00 | | 0.00 | | 0.00 | |
| CO ₂ | 46.99 | | 45.84 | | 46.46 | | 43.65 | | 44.64 | | 44.53 | |
| Sum | 99.99 | | 100.00 | | 99.99 | | 100.01 | | 100.00 | | 100.00 | |
| # Ions | | | | | | | | | | | | |
| CaO | 1.797 | | 1.853 | | 1.832 | | 1.981 | | 1.925 | | 1.933 | |
| MgO | 0.043 | | 0.054 | | 0.044 | | 0.045 | | 0.044 | | 0.042 | |
| FeO | 0.000 | | 0.003 | | 0.000 | | 0.000 | | 0.003 | | 0.003 | |
| MnO | 0.002 | | 0.000 | | 0.000 | | 0.000 | | 0.000 | | 0.000 | |
| SrO | 0.004 | | 0.000 | | 0.000 | | 0.000 | | 0.000 | | 0.000 | |
| CO ₂ | 2.077 | | 2.045 | | 2.062 | | 1.987 | | 2.014 | | 2.011 | |
| Sum | 3.923 | | 3.955 | | 3.938 | | 4.013 | | 3.986 | | 3.989 | |
| Mol % | | | | | | | | | | | | |
| CaCO ₃ | 97.33 | | 96.97 | | 97.66 | | 97.79 | | 97.63 | | 97.75 | |
| MgCO ₃ | 2.33 | | 2.86 | | 2.32 | | 2.21 | | 2.25 | | 2.12 | |
| FeCO ₃ | 0.00 | | 0.17 | | 0.00 | | 0.00 | | 0.13 | | 0.13 | |
| MnCO ₃ | 0.12 | | 0.00 | | 0.00 | | 0.00 | | 0.00 | | 0.00 | |
| SrCO ₃ | 0.22 | | 0.00 | | 0.02 | | 0.00 | | 0.00 | | 0.00 | |
| XMg | 0.0232600 | | 0.0285600 | | 0.0232400 | | 0.0220800 | | 0.0224900 | | 0.0212000 | |
| XFe | 0.0000000 | | 0.0017164 | | 0.0000000 | | 0.0000000 | | 0.0012614 | | 0.0012593 | |
| T (°C) | 380.30 | | 419.81 | | 380.14 | | 369.97 | | 373.58 | | 361.82 | |
| Sample-Site | 13 | | 14 | | 15 | | 16 | | 17 | | | |
| Mineral | Cc | Dol | Cc | Dol | Cc | Dol | Cc | Dol | Cc | Dol | | |
| coarse vein | | | | | | | | | | | | |
| Wt % | | | | | | | | | | | | |
| CaO | 52.12 | | 54.28 | | 52.65 | | 52.48 | | 53.65 | | | |
| MgO | 0.94 | | 0.87 | | 0.85 | | 0.80 | | 0.59 | | | |
| FeO | 0.00 | | 0.00 | | 0.24 | | 0.00 | | 0.00 | | | |
| MnO | 0.03 | | 0.00 | | 0.00 | | 3.03 | | 0.00 | | | |
| SrO | 0.00 | | 0.13 | | 0.07 | | 0.00 | | 0.00 | | | |
| CO ₂ | 46.91 | | 44.72 | | 46.20 | | 43.69 | | 45.76 | | | |
| Sum | 100.00 | | 100.00 | | 100.01 | | 100.00 | | 100.00 | | | |
| # Ions | | | | | | | | | | | | |
| CaO | 1.808 | | 1.921 | | 1.839 | | 1.882 | | 1.881 | | | |
| MgO | 0.046 | | 0.043 | | 0.041 | | 0.040 | | 0.029 | | | |
| FeO | 0.000 | | 0.000 | | 0.007 | | 0.000 | | 0.000 | | | |
| MnO | 0.001 | | 0.000 | | 0.000 | | 0.086 | | 0.000 | | | |
| SrO | 0.000 | | 0.003 | | 0.001 | | 0.000 | | 0.000 | | | |
| CO ₂ | 2.073 | | 2.017 | | 2.056 | | 1.996 | | 2.045 | | | |
| Sum | 3.927 | | 3.983 | | 3.944 | | 4.004 | | 3.955 | | | |
| Mol % | | | | | | | | | | | | |
| CaCO ₃ | 97.51 | | 97.69 | | 97.40 | | 93.73 | | 98.49 | | | |
| MgCO ₃ | 2.45 | | 2.18 | | 2.19 | | 1.99 | | 1.51 | | | |
| FeCO ₃ | 0.00 | | 0.00 | | 0.35 | | 0.00 | | 0.00 | | | |
| MnCO ₃ | 0.04 | | 0.00 | | 0.00 | | 4.28 | | 0.00 | | | |
| SrCO ₃ | 0.00 | | 0.13 | | 0.07 | | 0.00 | | 0.00 | | | |
| XMg | 0.0244700 | | 0.0217900 | | 0.0218800 | | 0.0198800 | | 0.0150700 | | | |
| XFe | 0.0000000 | | 0.0000000 | | 0.0034654 | | 0.0000000 | | 0.0000000 | | | |
| T (°C) | 390.17 | | 367.30 | | 368.13 | | 348.67 | | 286.83 | | | |

Sample D2-C (99-57), Central Alpi Apuane.

| Sample: | 99-57 | Location: | 3 | Av. T (°C): | 323.68 | selected: | 323.65 | | | | | |
|-------------|-----------|------------|-----------|-------------|-----------|-----------|-----------|-----------|-----------|-----------|-----------|-----------|
| Std. Dev.: | | Std. Dev.: | | selected: | 29.67 | selected: | 18.43 | | | | | |
| Sample-Site | 1 | | 2 | | 3 | | 4 | | 5 | | 6 | |
| Mineral | Cc | Dol | Cc | Dol | Cc | Dol | Cc | Dol | Cc | Dol | Cc | Dol |
| Wt % | | | | | | | | | | | | |
| CaO | 56.27 | 30.19 | 56.48 | 30.75 | 56.68 | 30.91 | 55.10 | 30.46 | 55.15 | 30.42 | 55.78 | 29.81 |
| MgO | 0.57 | 18.53 | 0.71 | 21.22 | 0.74 | 20.47 | 0.80 | 20.65 | 0.68 | 20.90 | 0.74 | 21.64 |
| FeO | 0.03 | 0.67 | 0.11 | 0.05 | 0.00 | 0.53 | 0.00 | 0.25 | 0.19 | 0.00 | 0.07 | 0.10 |
| MnO | 0.00 | 0.00 | 0.01 | 0.00 | 0.06 | 0.18 | 0.00 | 0.00 | 0.08 | 0.03 | 0.06 | 0.18 |
| SrO | 0.00 | 0.00 | 0.00 | 0.08 | 0.00 | 0.00 | 0.00 | 0.00 | 0.00 | 0.00 | 0.00 | 0.18 |
| CO2 | 43.14 | 50.61 | 42.69 | 47.90 | 42.52 | 47.90 | 44.10 | 48.65 | 43.90 | 48.66 | 43.35 | 48.08 |
| Sum | 100.01 | 100.00 | 100.00 | 100.00 | 100.00 | 99.99 | 100.00 | 100.01 | 100.00 | 100.01 | 100.00 | 99.99 |
| # Ions | | | | | | | | | | | | |
| CaO | 2.022 | 0.977 | 2.037 | 1.011 | 2.047 | 1.019 | 1.961 | 0.997 | 1.968 | 0.994 | 1.999 | 0.979 |
| MgO | 0.028 | 0.834 | 0.036 | 0.971 | 0.037 | 0.939 | 0.039 | 0.940 | 0.034 | 0.951 | 0.037 | 0.988 |
| FeO | 0.001 | 0.017 | 0.003 | 0.001 | 0.000 | 0.014 | 0.000 | 0.006 | 0.005 | 0.000 | 0.002 | 0.002 |
| MnO | 0.000 | 0.000 | 0.000 | 0.000 | 0.002 | 0.005 | 0.000 | 0.000 | 0.002 | 0.001 | 0.002 | 0.005 |
| SrO | 0.000 | 0.000 | 0.000 | 0.001 | 0.000 | 0.000 | 0.000 | 0.000 | 0.000 | 0.000 | 0.000 | 0.003 |
| CO2 | 1.975 | 2.086 | 1.962 | 2.007 | 1.957 | 2.012 | 2.000 | 2.029 | 1.996 | 2.027 | 1.980 | 2.011 |
| Sum | 4.025 | 3.914 | 4.038 | 3.993 | 4.043 | 3.988 | 4.000 | 3.971 | 4.004 | 3.973 | 4.020 | 3.989 |
| Mol % | | | | | | | | | | | | |
| CaCO3 | 98.57 | 53.43 | 98.12 | 50.94 | 98.13 | 51.56 | 98.02 | 51.29 | 97.94 | 51.10 | 98.01 | 49.48 |
| MgCO3 | 1.39 | 45.64 | 1.72 | 48.92 | 1.78 | 47.51 | 1.98 | 48.38 | 1.68 | 48.86 | 1.81 | 49.99 |
| FeCO3 | 0.04 | 0.93 | 0.15 | 0.06 | 0.00 | 0.69 | 0.00 | 0.33 | 0.26 | 0.00 | 0.10 | 0.13 |
| MnCO3 | 0.00 | 0.00 | 0.01 | 0.00 | 0.08 | 0.24 | 0.00 | 0.00 | 0.11 | 0.04 | 0.08 | 0.24 |
| SrCO3 | 0.00 | 0.00 | 0.00 | 0.07 | 0.00 | 0.00 | 0.00 | 0.00 | 0.00 | 0.00 | 0.00 | 0.16 |
| XMg | 0.0138929 | 0.4563648 | 0.0171623 | 0.4891738 | 0.0178270 | 0.4751109 | 0.0198017 | 0.4838114 | 0.0168032 | 0.4885464 | 0.0180918 | 0.4998510 |
| XFe | 0.0000000 | 0.0092568 | 0.0014916 | 0.0006466 | 0.0000000 | 0.0069008 | 0.0000000 | 0.0032858 | 0.0026338 | 0.0000000 | 0.0009601 | 0.0012958 |
| T (°C) | 266.28 | | 317.12 | | 325.50 | | 347.84 | | 312.37 | | 328.71 | |
| Sample-Site | 7 | | 8 | | 9 | | 10 | | 11 | | 12 | |
| Mineral | Cc | Dol | Cc | Dol | Cc | Dol | Cc | Dol | Cc | Dol | Cc | Dol |
| Wt % | | | | | | | | | | | | |
| CaO | 55.03 | 30.26 | 54.66 | 29.30 | 56.07 | 29.86 | 53.08 | 30.58 | 53.66 | 30.79 | 55.57 | 29.71 |
| MgO | 0.95 | 21.16 | 0.66 | 20.40 | 0.78 | 19.07 | 0.64 | 20.09 | 0.80 | 19.66 | 0.64 | 19.21 |
| FeO | 0.20 | 0.53 | 0.08 | 0.19 | 0.30 | 1.31 | 0.20 | 1.20 | 0.41 | 1.34 | 0.00 | 0.54 |
| MnO | 0.00 | 0.18 | 0.00 | 0.15 | 0.00 | 0.07 | 0.00 | 0.01 | 0.00 | 0.10 | 0.00 | 0.00 |
| SrO | 0.00 | 0.10 | 0.00 | 0.00 | 0.02 | 0.00 | 0.10 | 0.16 | 0.00 | 0.00 | 0.00 | 0.08 |
| CO2 | 43.82 | 47.76 | 44.60 | 49.96 | 42.82 | 49.69 | 45.98 | 47.96 | 45.13 | 48.11 | 43.79 | 50.46 |
| Sum | 100.00 | 99.99 | 100.00 | 100.00 | 99.99 | 100.00 | 100.00 | 100.00 | 100.00 | 100.00 | 100.00 | 100.00 |
| # Ions | | | | | | | | | | | | |
| CaO | 1.963 | 0.998 | 1.937 | 0.949 | 2.020 | 0.973 | 1.858 | 1.009 | 1.893 | 1.016 | 1.984 | 0.961 |
| MgO | 0.047 | 0.971 | 0.033 | 0.919 | 0.039 | 0.865 | 0.031 | 0.923 | 0.039 | 0.902 | 0.032 | 0.864 |
| FeO | 0.006 | 0.014 | 0.002 | 0.005 | 0.008 | 0.033 | 0.006 | 0.031 | 0.011 | 0.035 | 0.000 | 0.014 |
| MnO | 0.000 | 0.005 | 0.000 | 0.004 | 0.000 | 0.002 | 0.000 | 0.000 | 0.000 | 0.003 | 0.000 | 0.000 |
| SrO | 0.000 | 0.002 | 0.000 | 0.000 | 0.000 | 0.000 | 0.002 | 0.003 | 0.000 | 0.000 | 0.000 | 0.001 |
| CO2 | 1.992 | 2.006 | 2.014 | 2.062 | 1.966 | 2.064 | 2.052 | 2.017 | 2.028 | 2.022 | 1.992 | 2.080 |
| Sum | 4.008 | 3.994 | 3.986 | 3.938 | 4.034 | 3.936 | 3.948 | 3.983 | 3.972 | 3.978 | 4.008 | 3.920 |
| Mol % | | | | | | | | | | | | |
| CaCO3 | 97.38 | 50.17 | 98.24 | 50.56 | 97.68 | 51.95 | 97.97 | 51.34 | 97.40 | 51.95 | 98.42 | 52.21 |
| MgCO3 | 2.34 | 48.82 | 1.65 | 48.98 | 1.89 | 46.17 | 1.64 | 46.93 | 2.02 | 46.16 | 1.58 | 46.98 |
| FeCO3 | 0.28 | 0.69 | 0.11 | 0.26 | 0.41 | 1.78 | 0.29 | 1.57 | 0.58 | 1.76 | 0.00 | 0.74 |
| MnCO3 | 0.00 | 0.24 | 0.00 | 0.20 | 0.00 | 0.10 | 0.00 | 0.01 | 0.00 | 0.13 | 0.00 | 0.00 |
| SrCO3 | 0.00 | 0.09 | 0.00 | 0.00 | 0.02 | 0.00 | 0.10 | 0.15 | 0.00 | 0.00 | 0.00 | 0.08 |
| XMg | 0.0233919 | 0.4881603 | 0.0165045 | 0.4897984 | 0.0189074 | 0.4616862 | 0.0164356 | 0.4692937 | 0.0203502 | 0.4615308 | 0.0157720 | 0.4697201 |
| XFe | 0.0027626 | 0.0068591 | 0.0011223 | 0.0025591 | 0.0040795 | 0.0177916 | 0.0028813 | 0.0157251 | 0.0058079 | 0.0176469 | 0.0000000 | 0.0074072 |
| T (°C) | 381.38 | | 308.29 | | 338.15 | | 307.33 | | 353.47 | | 297.74 | |

Sample D2-E (99-68), Eastern Alpi Apuane.

| Sample: | 99-68 | | Location: | 12 | | Av. T (°C): | 297.60 | | Av. T (°C): selected: | 355.41 | | |
|---------------|---------------|-----|---------------|-----|---------------|-------------|-----------|-----|-----------------------|--------|----|-----|
| | | | | | | Std. Dev.: | 117.51 | | Std. Dev.: selected: | 25.66 | | |
| Sample-Site | 1 | | 2 | | 3 | | 4 | | 5 | | 6 | |
| Mineral | Cc | Dol | Cc | Dol | Cc | Dol | Cc | Dol | Cc | Dol | Cc | Dol |
| Wt % | | | | | | | | | | | | |
| CaO | 54.59 | | 30.54 | | 56.22 | | 56.98 | | 57.48 | | | |
| MgO | 0.93 | | 22.27 | | 0.37 | | 0.88 | | 0.76 | | | |
| FeO | 0.00 | | 0.08 | | 0.00 | | 0.12 | | 0.00 | | | |
| MnO | 0.20 | | 0.09 | | 0.00 | | 0.00 | | 0.00 | | | |
| SrO | 0.16 | | 0.00 | | 0.14 | | 0.00 | | 0.29 | | | |
| CO2 | 44.12 | | 47.02 | | 43.27 | | 42.02 | | 41.46 | | | |
| Sum | 100.00 | | 100.00 | | 100.00 | | 100.00 | | 99.99 | | | |
| # Ions | | | | | | | | | | | | |
| CaO | 1.943 | | 1.010 | | 2.019 | | 2.067 | | 2.098 | | | |
| MgO | 0.046 | | 1.024 | | 0.019 | | 0.044 | | 0.038 | | | |
| FeO | 0.000 | | 0.002 | | 0.000 | | 0.003 | | 0.000 | | | |
| MnO | 0.006 | | 0.002 | | 0.000 | | 0.000 | | 0.000 | | | |
| SrO | 0.003 | | 0.000 | | 0.003 | | 0.000 | | 0.006 | | | |
| CO2 | 2.001 | | 1.981 | | 1.980 | | 1.942 | | 1.929 | | | |
| Sum | 3.999 | | 4.019 | | 4.020 | | 4.058 | | 4.071 | | | |
| Mol % | | | | | | | | | | | | |
| CaCO3 | 97.26 | | 49.53 | | 98.96 | | 97.74 | | 97.93 | | | |
| MgCO3 | 2.31 | | 50.26 | | 0.91 | | 2.10 | | 1.80 | | | |
| FeCO3 | 0.00 | | 0.10 | | 0.00 | | 0.16 | | 0.00 | | | |
| MnCO3 | 0.28 | | 0.12 | | 0.00 | | 0.00 | | 0.00 | | | |
| SrCO3 | 0.15 | | 0.00 | | 0.13 | | 0.00 | | 0.27 | | | |
| XMg | 0.0230500 | | 0.0090620 | | 0.0210000 | | 0.0180200 | | 0.0180200 | | | |
| XFe | 0.0000000 | | 0.0000000 | | 0.0016067 | | 0.0000000 | | 0.0000000 | | | |
| T (°C) | 378.52 | | 124.16 | | 359.91 | | | | 327.80 | | | |

Sample D2-E (2k-9), Eastern Alpi Apuane. Center of shear zone in sample 99-68

| Sample: | 2k-9 | Location: | 12 | Av. T (°C): | 426.55 | Av. T (°C): selected: | 426.55 | | | | | |
|-------------|-----------|-----------|-----------|-------------|-----------|-----------------------|-----------|-----------|-----------|-----------|-----------|-----------|
| | | | | Std. Dev.: | 27.15 | Std. Dev.: selected: | 27.15 | | | | | |
| Sample-Site | 1 | | 2 | | 3 | | 4 | | 5 | | 6 | |
| Mineral | Cc | Dol | Cc | Dol | Cc | Dol | Cc | Dol | Cc | Dol | Cc | Dol |
| Wt % | | | | | | | | | | | | |
| CaO | 53.94 | | 52.10 | | 52.07 | | 53.31 | 29.35 | 56.38 | 41.49 | 53.49 | 30.09 |
| MgO | 0.72 | | 0.95 | | 0.75 | | 1.13 | 22.62 | 1.09 | 13.09 | 0.96 | 23.59 |
| FeO | 0.00 | | 0.00 | | 0.00 | | 0.00 | 0.19 | 0.00 | 0.00 | 0.04 | 0.12 |
| MnO | 0.00 | | 0.02 | | 0.00 | | 0.00 | 0.00 | 0.00 | 0.00 | 2.20 | 0.00 |
| SrO | 0.00 | | 0.00 | | 0.02 | | 0.05 | 0.00 | 0.00 | 0.14 | 0.00 | 0.07 |
| CO2 | 45.34 | | 46.94 | | 47.15 | | 45.52 | 47.84 | 42.53 | 45.29 | 43.31 | 46.13 |
| Sum | 100.00 | | 100.01 | | 99.99 | | 100.01 | 100.00 | 100.00 | 100.01 | 100.00 | 100.00 |
| # Ions | | | | | | | | | | | | |
| CaO | 1.898 | | 1.806 | | 1.803 | | 0.963 | 1.871 | 2.034 | 1.421 | 1.922 | 1.000 |
| MgO | 0.035 | | 0.046 | | 0.036 | | 1.033 | 0.055 | 0.055 | 0.624 | 0.048 | 1.090 |
| FeO | 0.000 | | 0.000 | | 0.000 | | 0.005 | 0.000 | 0.000 | 0.000 | 0.001 | 0.003 |
| MnO | 0.000 | | 0.000 | | 0.000 | | 0.000 | 0.000 | 0.000 | 0.000 | 0.063 | 0.000 |
| SrO | 0.000 | | 0.000 | | 0.000 | | 0.000 | 0.001 | 0.000 | 0.003 | 0.000 | 0.001 |
| CO2 | 2.033 | | 2.074 | | 2.080 | | 2.000 | 2.036 | 1.956 | 1.976 | 1.983 | 1.953 |
| Sum | 3.967 | | 3.926 | | 3.920 | | 4.000 | 3.964 | 4.044 | 4.024 | 4.017 | 4.047 |
| Mol % | | | | | | | | | | | | |
| CaCO3 | 98.18 | | 97.50 | | 98.02 | | 97.09 | 48.13 | 97.38 | 69.40 | 94.51 | 47.73 |
| MgCO3 | 1.82 | | 2.47 | | 1.96 | | 2.86 | 51.62 | 2.62 | 30.47 | 2.36 | 52.07 |
| FeCO3 | 0.00 | | 0.00 | | 0.00 | | 0.00 | 0.24 | 0.00 | 0.00 | 0.06 | 0.15 |
| MnCO3 | 0 | | 0.03 | | 0.00 | | 0.00 | 0.00 | 0.00 | 0.00 | 3.07 | 0.00 |
| SrCO3 | 0 | | 0.00 | | 0.02 | | 0.05 | 0.00 | 0.00 | 0.13 | 0.00 | 0.06 |
| XMg | 0.0229500 | | 0.0310800 | | 0.0247200 | | 0.0359400 | 0.5740780 | 0.0329100 | 0.3565030 | 0.0291300 | 0.5784590 |
| XFe | 0.0000000 | | 0.0000000 | | 0.0000000 | | 0.0000000 | 0.0027051 | 0.0000000 | 0.0000000 | 0.0006809 | 0.0016507 |
| T (°C) | 377.66 | | 435.89 | | 392.13 | | 463.44 | | 446.71 | | 423.60 | |

| Sample-Site | 7 | | 8 | | 9 | | 10 | | 11 | | 12 | |
|-------------|-----------|-----------|-----------|-----------|-----------|-----------|-----------|-----------|----|-----|----|-----|
| Mineral | Cc | Dol | Cc | Dol | Cc | Dol | Cc | Dol | Cc | Dol | Cc | Dol |
| Wt % | | | | | | | | | | | | |
| CaO | 52.01 | 29.17 | 52.93 | 30.71 | 52.17 | 29.45 | 52.62 | 29.49 | | | | |
| MgO | 0.89 | 23.05 | 0.87 | 22.50 | 1.08 | 23.22 | 0.92 | 22.13 | | | | |
| FeO | 0.28 | 0.00 | 0.00 | 0.00 | 0.00 | 0.12 | 0.09 | 0.16 | | | | |
| MnO | 0.00 | 0.00 | 0.17 | 0.00 | 0.00 | 0.09 | 0.00 | 0.00 | | | | |
| SrO | 0.11 | 0.00 | 0.09 | 0.05 | 0.00 | 0.00 | 0.00 | 0.00 | | | | |
| CO2 | 46.70 | 47.78 | 45.93 | 46.75 | 46.76 | 47.11 | 46.36 | 48.22 | | | | |
| Sum | 99.99 | 100.00 | 99.99 | 100.01 | 100.01 | 99.99 | 99.99 | 100.00 | | | | |
| # Ions | | | | | | | | | | | | |
| CaO | 1.808 | 0.956 | 1.853 | 1.017 | 1.811 | 0.971 | 1.834 | 0.966 | | | | |
| MgO | 0.043 | 1.052 | 0.043 | 1.037 | 0.052 | 1.065 | 0.045 | 1.008 | | | | |
| FeO | 0.008 | 0.000 | 0.000 | 0.000 | 0.000 | 0.003 | 0.003 | 0.004 | | | | |
| MnO | 0.000 | 0.000 | 0.005 | 0.000 | 0.000 | 0.002 | 0.000 | 0.000 | | | | |
| SrO | 0.002 | 0.000 | 0.002 | 0.001 | 0.000 | 0.000 | 0.000 | 0.000 | | | | |
| CO2 | 2.069 | 1.996 | 2.049 | 1.973 | 2.068 | 1.979 | 2.059 | 2.011 | | | | |
| Sum | 3.931 | 4.004 | 3.951 | 4.027 | 3.932 | 4.021 | 3.941 | 3.989 | | | | |
| Mol % | | | | | | | | | | | | |
| CaCO3 | 97.17 | 47.63 | 97.43 | 49.49 | 97.20 | 47.56 | 97.50 | 48.82 | | | | |
| MgCO3 | 2.31 | 52.37 | 2.23 | 50.46 | 2.80 | 52.18 | 2.37 | 50.98 | | | | |
| FeCO3 | 0.41 | 0.00 | 0.00 | 0.00 | 0.00 | 0.15 | 0.13 | 0.21 | | | | |
| MnCO3 | 0.00 | 0.00 | 0.25 | 0.00 | 0.00 | 0.11 | 0.00 | 0.00 | | | | |
| SrCO3 | 0.11 | 0.00 | 0.09 | 0.04 | 0.00 | 0.00 | 0.00 | 0.00 | | | | |
| XMg | 0.0290500 | 0.5817260 | 0.0279700 | 0.5629520 | 0.0351500 | 0.5792750 | 0.0298000 | 0.5677990 | | | | |
| XFe | 0.0051264 | 0.0000000 | 0.0000000 | 0.0000000 | 0.0000000 | 0.0016794 | 0.0016356 | 0.0023029 | | | | |
| T (°C) | 423.05 | | 415.89 | | 459.23 | | 427.94 | | | | | |

Appendix D: Program codes

This appendix contains the code, the file input, the screen dialog and the file output of three FORTRAN programs (Grainsizer, GraineX and Scasmoer), which were developed as tools for the microstructural analysis. These programs are considered as extension to the program package FABRIC 2.0, developed by Renée Heilbronner, which can be downloaded from: <http://www.unibas.ch/earth/micro...> One extra program (Tcalc) calculates calcite-dolomite temperatures from microprobe analysis using the approach of Anovitz & Essene (1987).

In addition to the FORTRAN programs the code of three GNU-plot (public domain software, <http://www.ucc.ie/gnuplot>) scripts are listed. The scripts plot deformation mechanism maps for calcite in stress-grain size and stress-temperature space. Moreover the stress at given grain sizes and given temperature or strain rate are calculated.

FORTRAN programs:

- Grainsizer:** Calculation of sectional areas from NIH-Image (public domain software: <http://rsb.info.nih.gov/nih-image/Default.html>) particle analysis.
- GraineX:** Separation of different grain size classes from vectorized grain boundary maps.
- Scasmoer:** Pre-processing of vectorized grain boundaries (grain coordinate files) for the use of SCASMO (part of program package FABRICS 2.0).
- Tcalc:** Calculation of calcite-dolomite temperatures from microprobe analysis. The temperature calculations are made after the approach of Anovitz & Essene (1987).

GNU-plot scripts:

- Data-script:** Contains parameters and constants of calcite and dolomite flow laws.
- Script 1.1:** Calculated and plots a deformation mechanism map in grain size – stress space for calcite after the flow laws contained in the ‘Data’ script.
- Script 2:** Calculated and plots a deformation mechanism map in temperature – stress space for calcite after the flow laws contained in the ‘Data’ script.

File input for Grainsizer 1.0

The input file contains the output data from the NIH-Image particle analysis. The first column contains the particle area (in pixel) and the second one the length of the particle outline (in pixel).

```
area (pixel)      length (pixel)
6057.00           397.69
2679.00           274.35
832.000           118.23
.
.
.
```

Screen dialog of Grainsizer 1.0

The following lines show the user interface of the program 'Grainsizer 1.0'. Bold text have to be typed by the user.

```
This program Grainsizer1.0
for the determination of grain sizes
from NIH-Image Gs-Files
Please enter Input-File-Name!
in.txt
Please enter Output-File-Name!
out.txt
Please enter Pixel-Scale. 1 px = ??? μm
0.42
Calculating Values

STOP
```

File output from Grainsizer 1.0

The equivalent radius in μm in the sevens column is highlighted.

```
Output file from Grainsizer 1.0.
The equivalent radius in μm in the sevens column is highlighted.
```

| Area(px) | Length (px) | Corr. Area(px) | Equi.Rad(Ar ea (px)) | Equi.Rad(Co rr Area(px)) | Equi. Length (px) | Equi.Rad(Co rr Area(μm)) | E.Length/ E.Rad(A) |
|----------|----------------|-------------------|----------------------------|--------------------------------|-------------------------|---|-----------------------|
| 6057.000 | 397.6900 | 6454.689 | 43.9090 | 45.3276 | 63.2943 | 19.0376 | 1.4415 |
| 2679.000 | 274.3500 | 2953.351 | 29.2019 | 30.6607 | 43.6642 | 12.8775 | 1.4952 |
| 832.0000 | 118.2300 | 950.2300 | 16.2737 | 17.3916 | 18.8169 | 7.3045 | 1.1563 |


```

Write(*,*) 'Extracting the Grain Size Range'
Write(*,*) ''
Write(*,*) 'Writing the Grain ID data to file'
Write(*,*) ''

Read(40,*) dum
40 Read(20,*,end=50) x,y

grainidl=grainid
grainsize1=grainsize

if (x.eq.9999) then
    grainid=y
    read(40,*,end=50) area, perimeter, term3, term4, term5, term6, grainsize
    totalpix=area+perimeter
else
    grainid=grainidl
    grainsize=grainsize1
endif

*----- Extracting the Grain Size Range and Writing the Grain ID data to file -----
Write (60,*) x,',',y,',',grainid,',',grainsize,',',totalpix

if (grainsize.ge.tmin.and.grainsize.le.tmax) then
    Write (80,*) x,',',y,',',grainid,',',grainsize,',',totalpix
    goto 40
else
    goto 40
endif

*----- Writing the SCASMO-Input-File for all grains -----
50 Write(*,*) 'Writing the SCASMO-Input-File for all grains'
Write(*,*) ''

rewind (unit=60)

Read (60,*) dum
Read (60,*) dum
45 Read (60,*,end=60) x,y,grainid,grainsize

if (x.eq.9999) then
    y=9999
    write(10,*) x,',',y
    goto 45
else
    write(10,*) x,',',y
    goto 45
endif

60 x=9999
y=9999

write (10,*) x,',',y

*----- Writing SCASMO-Input-File for extracted grains -----
70 Write(*,*) 'Writing the SCASMO-Input-File for extracted grains'
Write(*,*) ''

rewind (unit=80)

Read (80,*) dum
Read (80,*) dum
Read (80,*) dum
55 Read (80,*,end=80) x,y,grainid,grainsize

if (x.eq.9999) then
    y=9999
    write(30,*) x,',',y
    goto 55
else
    write(30,*) x,',',y
    goto 55
endif

80 x=9999
y=9999

write (30,*) x,',',y

*----- Ending the program -----
90 Write(*,*) ''
Write (*,*) 'Thank you for using GRAINEX'

close (unit=20)
close (unit=40)
close (unit=60)
close (unit=80)
close (unit=10)
close (unit=30)

stop
end

```

File input for Grainex 3.0

The program GrainEX needs the following input:

- 1) The equivalent radius in μm (= output from grainsizer, column 7)
- 2) Grain Coordinates from Ime d'Ouline or a digitizing tabled

The grain coordinate file has the following structure:

```

9999, 1           particle separator, number of particle
1798,1057        x-and y-coordinates
1804,1049
1810,1041
1816,1033
1822,1025
1829,1018
1837,1012
1846,1008
9999, 2           <- the coordinates of the second grain start here
2158,1054        <- x-and y-coordinates
.
.
.
.

```

Screen dialog of Grainex 3.0

The following lines show the user interface of the program 'GraineX 3.0'. Bold text have to be typed by the user.

```

This is the program GRAINEX3.0
for the Extraction of a certain Grain Size Range
from an ImedOuline / Tracking Coordinate-File and
a Grain Size-File.

```

The Output can be used for SCASMO.

Coordinate-File and Grain Size-File have to have the same number of lines and have to be saved as Text-Files.

Grain Sizes have to be located in the 7th Column in the Grain Size-File.

Grains have to be sorted in an ascending order.

```

Hello,
please enter Output-File-Name for the :
Complete Dataset
outall.txt
Extracted Data
out40_200.txt
Please enter File-Name for SCASMO-Input :
All Grains
scin.txt
Extracted Grains
scin40_200.txt
Please enter Coordinate-File-Name from ImedOuline or Tracking
out10.txt
Please enter Grain Size-File-Name
outgs.txt
Please enter a Grain Size Range ( $\mu\text{m}$ ) (min,max)
40,200

```

Please wait.....

Starting Grain ID comparison

Extracting the Grain Size Range

Writing the Grain ID data to file

Writing the SCASMO-Input-File for all grains

Writing the SCASMO-Input-File for extracted grains

Thank you for using GRAINEX

STOP

File output from GraineX 3.0

GraineX provides four output-files:

- 1) A text-file containing the x- and y-coordinates, the particle number, the grain size and the Total pixel(particle area + particle outline) of the entire data set.
- 2) A text-file containing the x- and y-coordinates modified for the use of SCASMO (program package FABRIC 2.0) similar to the output-file from the program Scasmoer
- 3) A text-file containing the x- and y-coordinates, the particle number, the grain size and the Total pixel(particle area + particle outline) of the selected grain size interval.
- 4) A text-file containing the x- and y-coordinates modified for the use of SCASMO (program package FABRIC 2.0) of the selected grain size interval.

The structure of the output-file for a selected grain size range is shown below:

```
Grainsize-range (µm): 40.00000 - 200.0000
x-coor , y-coor , Grain-ID , Grainsize , Total pixels
9999.000 , 9.000000 , 9.000000 , 43.23010 , 33283.18
1245.000 , 1020.000 , 9.000000 , 43.23010 , 33283.18
1254.000 , 1024.000 , 9.000000 , 43.23010 , 33283.18
. , . , . , . , .
. , . , . , . , .
```

FORTRAN code of the program: Scasmoer 1.0

```

*****
*
*
*       Scasmoer 1.0
*
* This program converts coordinate files derived from
* vectorization (Ime d'outline; Tracking) into input
* files for SCASMO 2.0.
*
*       Code in FORTRAN 77
*
*****

*----- Declaring files -----
      character coorfile*25, outshape*25

*----- Entering File-Names -----
      Write(*,*) 'Hello'
      Write(*,*) 'Please enter File-Name for SCASMO-Input for all grains : '
      Read (*,*) outshape

10      Write(*,*) 'Please enter Coordinate-File-Name from ImedOutline or Tracking'
      Read(*,*) coorfile

      goto 30

20      Write (*,*) 'OOOOPS, File not found!!! Please try again'
      goto 10

30      open (unit=20, file=coorfile, status='old', err = 20)
      open (unit=10, file=outshape, status='new')

      rewind (unit=20)
      rewind (unit=10)

*----- Starting Grain ID comparison -----

      Write(*,*) ''
      Write(*,*) ''
      Write(*,*) ''
      Write(*,*) 'Please wait.....'
      Write(*,*) ''

      Read (20,*) dum
      Read (20,*,end=60) x,y

      if (x.eq.9999) then
          y=9999
          write(10,*) x,',',y
          goto 40
      else
          write(10,*) x,',',y
          goto 40
      endif

60      x=9999
      y=9999

      write (10,*) x,',',y

*----- Ending the program -----

90      Write(*,*) ''
      Write(*,*) ''
      Write(*,*) ''
      Write (*,*) 'Thank you for using Scasmoer1.0'

      close (unit=20)
      close (unit=10)

      stop
      end

```

File input for Scasmoer 1.0

The data output from the automatic digitizing software Ime d'Ouline (by Christian Pauli) or from a digitalization table is required as input for the program Scasmoer. The structure of the input-file is shown below

```

9999, 1          <- particle separator, number of particle
1798,1057       <- x-and y-coordinates
1804,1049
1810,1041
1816,1033
1822,1025
1829,1018
1837,1012
1846,1008
9999, 2          <- the coordinates of the second grain start here
2158,1054       <- x-and y-coordinates
.
.
.

```

Screen dialog of Grainex 3.0

The following lines show the user interface of the program 'Scasmoer 1.0'. Bold text have to be typed by the user.

```

Hello
Please enter File-Name for SCASMO-Input for all grains :
test.scin
Please enter Coordinate-File-Name from ImedOuline or Tracking
test.out

```

Please wait.....

Thank you for using Scasmoer1.0

STOP

File output from Scasmoer 1.0

The output from Scasmoer is shown below.

It can be used as input for SCASMO, which is included in the program package FABRIC 2.0. The file contains x-and y-coordinates of the digitized particles, transformed for the use of SASMO.

```

1173.000 , 1047.000 <- x-and y-coordinates
1183.000 , 1045.000
1192.000 , 1041.000
1196.000 , 1032.000
1198.000 , 1022.000
1199.000 , 1012.000
9999.000 , 9999.000 <- end of the first particle
1561.000 , 1010.000
.
.
.

```

FORTRAN code of the program: Tcalc

```

*****
!
!
!           Tcalc
!
! This program calculates temperatures after the
!
!           program Tcalc
!
!
*****

! Declaring parametes and variables:
! -----
character (len=25) :: infile
character (len=25) :: outfile
character (len=25) :: dum

integer mID                ! MeasureID, number of measurement
integer n                  ! contiuous number
integer CD                  ! Calcite = 1; Dolomite = 2 : Specification of mineral in inputfile
integer y                  ! continuing or stopping program

real vCaO,vMgO,vFeO,vMnO,vSrO,vCO2    ! measurements from microprobe
real cCaO,cMgO,cFeO,cMnO,cSrO,cCO2    ! Molecular Weight
real oCaO,oMgO,oFeO,oMnO,oSrO,oCO2    ! moles cations
real sTot,cF                ! Sum of moles of cations, correctionfactor
real mCaO,mMgO,mFeO,mMnO,mSrO,mCO2    ! number of cations
real sE,xMg,XFe             ! Sum of cations, xMgCO3, xFeCO3

real A,B,C,D,E              ! parameters from T calculations after Anovitz & Essene '87
real aa,bb,cc,dd,ee,ff     ! parameters from Fe corr. T calculations after Anovitz & Essene '87
real tA                     ! Temperature after Anovitz & Essene '87

write (*,*)
write (*,*)"-----"
write (*,*)"This is the program: Tcalc . It calculates Calcite/Dolomite"
write (*,*)"temperatures after Anovitz & Essene '87."
write (*,*)"Measurements are corrected according to 6 oxygens."
write (*,*)
write (*,*)"-----"
write (*,*)"The input-file has to prepared as follows:"
write (*,*)"col 1 = ?,                i.e.: 234"
write (*,*)"col 2 = Measurement-ID,    i.e.: 22"
write (*,*)"col 3 = Cc (1) or Dol (2),  i.e.: 1"
write (*,*)"col 4 = CaO,                i.e.: 53.5"
write (*,*)"col 5 = MgO,                i.e.: 0.6"
write (*,*)"col 6 = FeO,                i.e.: 1.1"
write (*,*)"col 7 = MnO,                i.e.: 0.0"
write (*,*)"col 8 = SrO,                i.e.: 0.0"
write (*,*)"col 9 = CO2,                i.e.: 44.8"
write (*,*)"col 10 = ?,                i.e.: 100"
write (*,*)"The last row should be filled with 2."
write (*,*)
write (*,*)"-----"
write (*,*)"Prepare Input-file?"
write (*,*)"Type (1) to exit program. - Type (2) to continue program."

read (*,*) y
if(y.eq.1)then
  goto 310
else
  continue
endif

write (*,*)"-----"
write (*,*)"The following parameters are used:"
write (*,*)"CaO = 56.0794"
write (*,*)"MgO = 40.3044"
write (*,*)"FeO = 71.8464"
write (*,*)"MnO = 70.9374"
write (*,*)"SrO = 103.6294"
write (*,*)"CO2 = 44.009"
write (*,*)

! Loading input-file:
! -----
write (*,*)"-----"
write (*,*) "Please press RETURN to choose the input-file (after BaselTab) !"
read (*,*)
open (unit=20, file="", status='old')

! opening output-files:
! -----
write (*,*) "Please press RETURN to save the output-file !"
read (*,*)
open (unit=40, file="outfile", status='new')

```


Appendix D

```
write (*,*) n,mId,mCaO,mMgO,mFeO,mMnO,mSrO,mCO2,xMg,xFe,tA
write (40,*) n,"",mId,"",mCaO,"",mMgO,"",mFeO,"",mMnO,"",mSrO,"",mCO1,"",xMg,"",xFe,"",tA

n=n+1

goto 50

! This is the END
! -----
300      continue

write (*,*)
write (*,*)"-----"
write (*,*) "****Temperatures are calculated.***"
write (*,*)
write (*,*) "****Thanks for using Tcalc.***"
write (*,*)

close(unit=20)
close(unit=40)

310      continue
stop
write (*,*)

end
```

File input for Tcalc

A typical input file from the microprobe looks like this:

| x | mId | Cc/Dol | CaO | MgO | FeO | MnO | SrO | CO2 | total |
|--------|-----|--------|-------|------|------|------|------|-------|--------|
| 59.269 | 1 | 1 | 55.26 | 0.39 | 0.00 | 0.08 | 0.07 | 44.21 | 100.00 |
| 60.264 | 2 | 1 | 53.49 | 0.43 | 0.20 | 0.15 | 0.00 | 45.72 | 100.00 |
| 59.02 | 3 | 1 | 53.88 | 0.47 | 0.03 | 0.00 | 0.00 | 45.62 | 100.00 |
| 58.993 | 4 | 1 | 53.75 | 0.43 | 0.11 | 3.72 | 0.00 | 42.00 | 100.00 |
| 60.109 | 5 | 1 | 54.49 | 0.35 | 0.04 | 0.00 | 0.00 | 45.12 | 100.00 |
| 2 | 2 | 2 | 2 | 2 | 2 | 2 | 2 | 2 | 2 |

Screen dialog of Tcalc

The following lines show the user interface of the program 'Tcalc'. Bold text have to be typed by the user.

```
-----
This is the program: Tcalc . It calculates Calcite/Dolomite
temperatures after Anovitz & Essene '87.
Measurements are corrected according to 6 oxygens.

-----
The input-file has to be prepared as follows:
col 1 = ?,                i.e.: 234
col 2 = Measurement-ID,   i.e.: 22
col 3 = Cc (1) or Dol (2), i.e.: 1
col 4 = CaO,              i.e.: 53.5
col 5 = MgO,              i.e.: 0.6
col 6 = FeO,              i.e.: 1.1
col 7 = MnO,              i.e.: 0.0
col 8 = SrO,              i.e.: 0.0
col 9 = CO2,              i.e.: 44.8
col 10 = ?,               i.e.: 100
The last row should be filled with 2.

-----
Prepare Input-file?
Type (1) to exit program. - Type (2) to continue program.
2
-----
The following parameters are used:
CaO = 56.0794
MgO = 40.3044
FeO = 71.8464
MnO = 70.9374
SrO = 103.6294
CO2 = 44.009

-----
Please press RETURN to choose the input-file (after BaselTab) !

Please press RETURN to save the output-file !
```

```

n,mId,CaO,MgO,FeO,MnO,SrO,CO2,xMg,xFe,T
1, 1, 1.966, 1.931E-02, 0.0000000, 2.251E-03, 1.348E-03, 0.000000, 9.706E-03, 0.0000000, 152.387
2, 2, 1.878, 2.100E-02, 5.481E-03, 4.163E-03, 0.0000000, 0.000000, 1.100E-02, 2.871E-03, 197.751
3, 3, 1.892, 2.296E-02, 8.224E-04, 0.000E-03, 0.0000000, 0.000000, 1.198E-02, 4.292E-04, 224.858
.. .. ..
.. .. ..
.. ..

```

*****Temperatures are calculated.*****

*****Thanks for using Tcalc.*****

STOP
 Press **RETURN** to quit the program.

File output from Tcalc

| no | CaO | MgO | FeO | MnO | SrO | CO2 | xMg | xFe | T |
|----|--------|-------------|-------------|-------------|-------------|-----|-------------|-------------|----------------|
| 1 | 1.9668 | 1.93140E-02 | 0.00000 | 2.25100E-03 | 1.34827E-03 | 2 | 9.70676E-03 | 0.00000 | 152.387 |
| 2 | 1.8781 | 2.10074E-02 | 5.48128E-03 | 4.16364E-03 | 0.00000 | 2 | 1.10056E-02 | 2.87160E-03 | 197.751 |
| 3 | 1.8925 | 2.29697E-02 | 8.22483E-04 | 0.00000 | 0.00000 | 2 | 1.19865E-02 | 4.29206E-04 | 224.858 |
| 4 | 1.9615 | 2.18339E-02 | 3.13331E-03 | 0.10732 | 0.00000 | 1 | 1.04279E-02 | 1.49647E-03 | 179.158 |
| 5 | 1.9231 | 1.71880E-02 | 1.10195E-03 | 0.00000 | 0.00000 | 2 | 8.85301E-03 | 5.67584E-04 | 113.941 |

Code for GNU-plot script: Data

```

# ***** Data for Def.Mech.Map_Script 1.1 & 2 *****

#----- FLOW LAW Constants, Variables & Parameters -----

#--- Gas Constant in (cal/(mol K))
R=1.98

#--- Temperature in (K + 273 =°C)
T=370.0 + 273.0 # control label of plot in Def.Mech.Map_Script!!!    <== EDIT here !!!!

T1=200.0 + 273.0
T2=370.0 + 273.0
T3=350.0 + 273.0

#--- Strainrates in (1/s)
e4=10**(-4.0)
e5=10**(-5.0)
e6=10**(-6.0)
e7=10**(-7.0)
e8=10**(-8.0)
e9=10**(-9.0)
e10=10**(-10.0)
e11=10**(-11.0)
e12=10**(-12.0)
e13=10**(-13.0)
e14=10**(-14.0)
e15=10**(-15.0)
e16=10**(-16.0)
e17=10**(-17.0)
e18=10**(-18.0)
e19=10**(-19.0)
e20=10**(-20.0)

#--- log Strainrates in (1/s)
le4=-9.21
le6=-13.82
le8=-18.42
le10=-23.03
le12=-27.63
le14=-32.24
le16=-36.84
le18=-41.45
le20=-46.05

#----- Parameters of Flow Laws -----

#      Stress zero (s1) in (bar) for Regime1 of Schmid et al. (1980)
#      Activation energy (H#) (cal/mol)
#      A-parameter (A#)          ### In Heard (1976): MPa**1/n 1/s ###
#      Log (basis e) of A-parameter (lA#)
#      Stress exponent (n)
#      Grain size exponent (b)
#      Grain size (d)

##### CALCITE #####

#-----
# Regime1: Exponential law (Twinning)

#---Schmid et al. (1980) consistent with Rutter (1974) (Carrara marble)
s1=114.0
H1=62000.0          # 62000 ± 5800
A1=10**(5.8)
lA1=13.35

#---Rutter (1974) (Solnhofen limestone)
#s1=160.0
#H1=-47000.0
#A1=10**(-0.12)

#-----
# Regime2: Power law 1

#---Schmid et al. (1980) (Carrara marble)
n2=7.6              # 7.6 ± 0.8
H2=90000.0         # 100000 ± 10000
A2=10**(-4.5)     # -4.5 ± 0.4 for exponent

#---Schmid (1981) Habil (Carrara marble)
#n2=6.0
#H2=75000
#A2=10**(-5.5)

#---Schmid et al. (1977) (Solnhofen limestone)
#n2=4.7             # 4.7 ± 0.38
#H2=71000.0        # 71000 ± 6500
#A2=10**(-1.33)   # -1.33 ± 0.4 for exponent

```

```

#-----
# Regime3: Power law 2

#---Schmid et al. (1980) (Carrara marble)
n3=4.2 # 4.2 ± 0.4
H3=102000.0 # 102000 ± 11000.0
A3=10**(3.9) # 3.9 ± 0.2 for exponent

#---Schmid (1981) Habil (Carrara marble)
#n3=2.9
#H3=86000.0
#A3=10**(3.8)

#---Schmid et al. (1977) (Solnhofen limestone) without grain size dependence
#n3=1.7 # 1.7 ± 0.95
#H3=51000.0 # 51000 ± 1800.0
#A3=10**(2.7) # 2.7 ± 0.27 for exponent

#-----
# Regime4: Superplasticity

#---Schmid et al. (1977) (Solnhofen limestone)
n4=1.7
H4=51000.0
A4=10**(4.98) # 4.98 or 4.21
b4=-3.0 # -3.0 or -2.0

#-----
# Regime5: Grain size sensitive 1 (low stress: <250 bar); diffusion creep

#---Walker et al. (1990) (Synthetic calcite aggregates)
n5=1.67 # 1.67
H5=45380.72 # = 190000 J
A5=10**(4.93) # 4.93
b5=-1.87 # -1.87

#-----
# Regime6: Grain size sensitive 2 (high stress: 250-2500 bar); dislocation + diffusion creep

#---Walker et al. (1990) (Synthetic calcite aggregates)
n6=3.3 # 3.3
H6=45380.72 # = 190000 J
A6=10**(2.0) # 2.0
b6=-1.3 # -1.3

***** DOLOMITE *****

#---White & White (1980) from Heard (1976) (Crevola Dolomite)
nd1=9.0
Hd1=83596.0
Ad1=10**(-12.0)

#---Heard (1976) original data (Crevola Dolomite)
nd2=9.1 # 9.1 ± 0.9
Hd2=83200 # 83200 ± 6000
Ad2=10**(-12.9) # -12.9 ± 2.6

```

Code for GNU-plot script: Script 1.1

```

#-----
#
#                               Def.Mech.Map_Script 1.1
#
# This is the script 1.1 for GNUPLOT-3.7.1d. It calculates and plots
# calcite flow laws from Schmid et al. (1977, 1980) (Solnhofen limestone, Carrara
# marble),
# Rutter (1974) (Solnhofen limestone), Walker et al. (1990) (synthetic calcite)
# using the "data" input file.
# Stress is plotted as function of grain size, contour are iso-strain rate
# lines.
# The paleopiezometer of Rutter (1995) for migration recrystallization
# and of Schmid et al. (1980) for subgrain rotation are indicated.
#
#
#-----

#----- Loading Data file -----

load 'Data'

#----- Setting Graph options -----

set time
set samples 1000,1000
set key left bottom

# --- Title, Axes scale, label, ...
set logscale x; set xrange [1:1e4]          #<== EDIT here x-axis range
set logscale y; set yrange [1:1e4]        #<== EDIT here y-axis range

set title "Calcite @ 370°C"                #<== EDIT here T-label of plot
set xlabel "Grain size [µm]"
set ylabel "Stress [bar]"

#----- Setting the strain rate, T and grain sizes for calculations and screen output --

per=e12                                     #<== EDIT here strain rate
pt=370                                     #<== EDIT here temperature

gs1=42.918                                 #<== EDIT here grain size 1
gs2=18.030                                 #<== EDIT here grain size 2
gs3=16.262                                 #<== EDIT here grain size 3
gs4=11.932                                 #<== EDIT here grain size 4
gs5=10.750                                 #<== EDIT here grain size 5

#-- Plotting indicated grain sizes
# 0%-Dolomite
set arrow from gs1,1 to gs1,1e4

# 10-20%-Dolomite
set arrow from gs2,1 to gs2,1e4

# 20-30%-Dolomite
set arrow from gs3,1 to gs3,1e4

# 40%-Dolomite
set arrow from gs4,1 to gs4,1e4

# 40%-Dolomite
set arrow from gs5,1 to gs5,1e4

# set nokey                                #<== EDIT here legend yes or no?

#----- Calculating flow laws -----

# Regime1: Twinning
r1(x,er)=s1*(log(er)-log(A1)+(H1/(R*T)))

# Regime2: Power law 1
r2(x,er)=(er/(A2*exp(-H2/(R*T))))**(1/n2)

# Regime3: Power law 2
r3(x,er)=(er/(A3*exp(-H3/(R*T))))**(1/n3)

# Regime4: Superplasticity
r4(x,er)=(er/(A4*x**(b4)*exp(-H4/(R*T))))**(1/n4)

# Regime5: dislocation creep + diffusion
r5(x,er)=(er/(A5*x**(b5)*exp(-H5/(R*T))))**(1/n5)

# Regime6: diffusion creep
r6(x,er)=(er/(A6*x**(b6)*exp(-H6/(R*T))))**(1/n6)

#----- Calculating Minima -----

#---Setting r1 = 1000 bar
r1a(x,er)=r1(x,er) <= 1000 ? 1000 : r1(x,er)

```

```

#---Setting bounds of r5 (<250 bar)
r5a(x,er)=r5(x,er) <= 250 ? r5(x,er) : 1000000

#---Setting bounds of r6 (250 < r6 < 2500 bar)
r6a(x,er)=r6(x,er) <= 5000 ? r6(x,er) : 1000000

#--- calculating minima
test23(x,er)=r2(x,er) <= r3(x,er) ? r2(x,er) : r3(x,er)
test234(x,er)=test23(x,er) <= r4(x,er) ? test23(x,er) : r4(x,er)
test2341(x,er)=test234(x,er) <= r1a(x,er) ? test234(x,er) : r1a(x,er)

test56(x,er)=r5a(x,er) <= r6a(x,er) ? r5a(x,er) : r6a(x,er)
test2356(x,er)=test23(x,er) <= test56(x,er) ? test23(x,er) : test56(x,er)
test23561(x,er)=test2356(x,er) <= r1a(x,er) ? test2356(x,er) : r1a(x,er)

#----- Caclulating Paleopiezometer -----
# Schmid et al. (1980)
ps(x,er)=(10**3.67)*x**(-1.01)

# Rutter (1995)
prr(x)=(10**2.91)*x**(-0.88)*10.0
prm(x)=(10**3.43)*x**(-0.88)*10.0

# Twiss (1977)
pt(x,er)=(7.5*x**(-0.68))*100.0

#----- Printing Stress for given grain sizes to screen -----
print ""
print "----- Results for -----"
print "Calcite @ ",pt,"°C and strain rate of ",per
print "          ..DefMechMap...-...Rutter (1995) migr"
print "stress @ ",gs1," µm ",test2341(gs1,per)," , ",prm(gs1)," bar"
print "stress @ ",gs2," µm ",test2341(gs2,per)," , ",prm(gs2)," bar"
print "stress @ ",gs3," µm ",test2341(gs3,per)," , ",prm(gs3)," bar"
print "stress @ ",gs4," µm ",test2341(gs4,per)," , ",prm(gs4)," bar"
print "stress @ ",gs5," µm ",test2341(gs5,per)," , ",prm(gs5)," bar"

print "-----"

#----- Plotting Graph -----
plot test23561(x,e4) with l -1,\
    test23561(x,e5) with l 1,\
    test23561(x,e6) with l -1,\
    test23561(x,e7) with l -1,\
    test23561(x,e8) with l -1,\
    test23561(x,e9) with l -1,\
    test23561(x,e10) with l 1,\
    test23561(x,e11) with l -1,\
    test23561(x,e12) with l -1,\
    test23561(x,e13) with l -1,\
    test23561(x,e14) with l 1,\
    test23561(x,e15) with l -1,\
    test23561(x,e16) with l -1,\
    test23561(x,e17) with l -1,\
    test23561(x,e18) with l -1,\
    test23561(x,e19) with l -1,\
    test23561(x,e20) with l 1,\
    ps(x) with l -1,\
    prm(x) with l 1

#----- Creating output -----
#set terminal postscript eps
#set terminal postscript color
#set output "output.eps"
#replot

#<== EDIT here for writing eps-file

reset

```

Screen dialog of the Script 1.1 in GNUplot

The following lines show the user interface of the GNUplot script 'Script 1.1'. Bold text have to be typed by the user.

```

G N U P L O T
Macintosh version 3.7
patchlevel 1
last modified Fri Oct 22 18:00:00 BST 1999

Copyright (C) 1986 - 1993, 1998, 1999
Thomas Williams, Colin Kelley and many others

Type `help` to access the on-line reference manual

```

The gnuplot FAQ is available from
<http://www.ucc.ie/gnuplot/gnuplot-faq.html>

Send comments and requests for help to info-gnuplot@dartmouth.edu
 Send bugs, suggestions and mods to bug-gnuplot@dartmouth.edu

Terminal type set to 'pict'
 gnuplot> load's1.1'

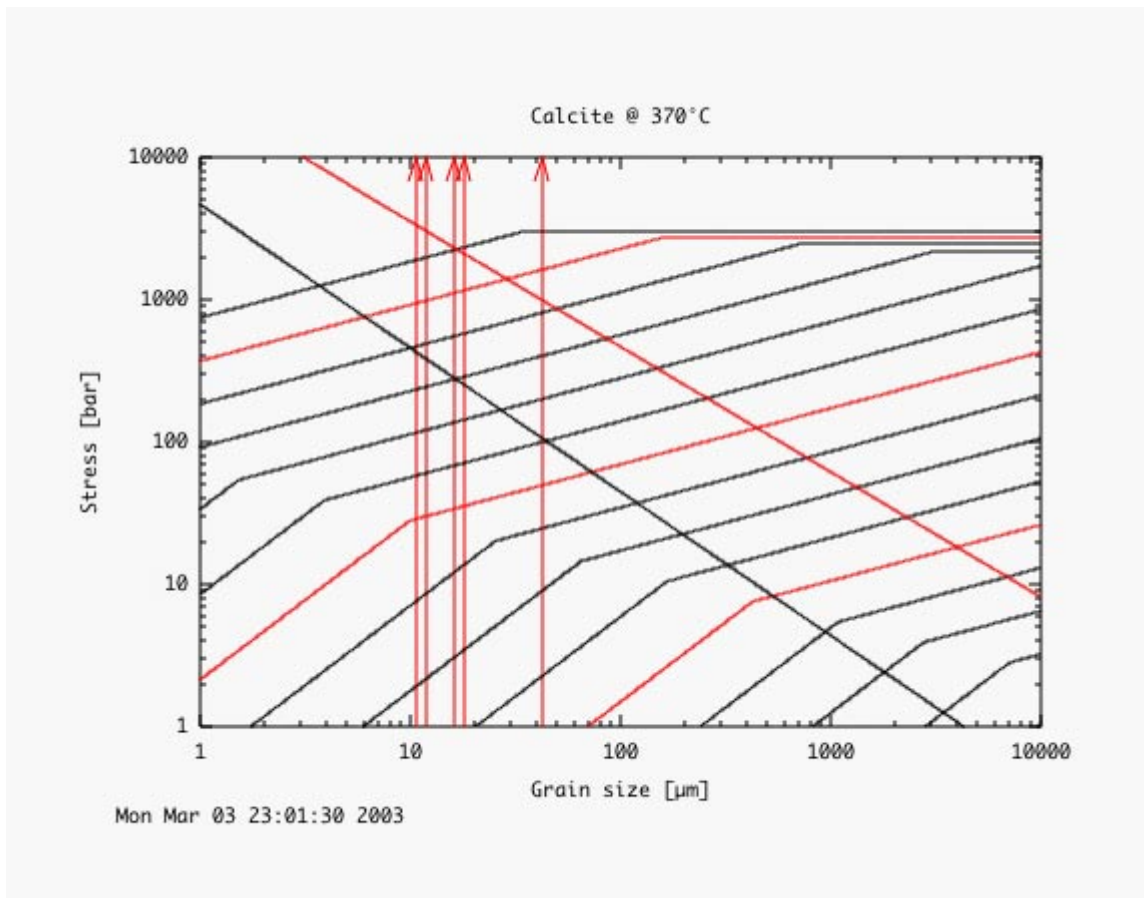
```
----- Results for -----
Calcite @ 370°C and strain rate of 1e-12
..DefMechMap.....Rutter (1995) migr
stress @ 42.918 µm 1000.0000000000 , 984.639517209622 bar
stress @ 18.03 µm 289.634635151551 , 2112.14515089525 bar
stress @ 16.262 µm 241.40888677583 , 2312.9535870694 bar
stress @ 11.932 µm 139.787920358299 , 3037.33255228472 bar
stress @ 10.75 µm 116.284018445919 , 3329.35842064448 bar
-----
```

Output from Script 1.1

The results contain the stresses determined for five different grain sizes.

- 1) from the flow law for a given strain rate (here 10e-12), and
- 2) from the intersection of the grain size with the paleopiezometer of migration recrystallization of Rutter (1995).

The calculated deformation mechanism map for a certain temperature (here 370°C) is shown below:



Code for GNU-plot script: Script 2.0

```

-----
#
#                               Def.Mech.Map_Script 2
#
# This is the script 2 for GNUPLOT-3.7.1d. It calculates and plots
# calcite and dolomite flow laws from Schmid et al. (1977, 1980) (Solnhofen limestone,
# Carrara marble), Rutter (1974) (Solnhofen limestone),
# Walker et al. (1990) (synthetic calcite) and Heard (1976) (Cervola dolomite)
# using the "data" input file.
# Stress is plotted as function of temperature
# The paleopiezometer of Rutter (1995) for migration recrystallization
# and of Schmid et al. (1980) for subgrain rotation are indicated.
#
#
-----

#----- Loading Data file -----

load 'Data'

#----- Setting Graph options -----

set time
set samples 1000,1000
set key left bottom

# --- Title, Axes scale, label,...
set xrange [100:1e3]          #<== EDIT here x-axis range
set logscale y; set yrange [1:1e5] #<== EDIT here y-axis range

pt=370                        #<== EDIT here temperature
per=e12                        #<== EDIT here strain rate

set title "Calcite @ 10e-10"   #<== EDIT here strain rate-label of plot
set xlabel "Temperature [°C]"
set ylabel "Stress [bar]"

# set nokey                    #<== EDIT here legend yes or no?

#----- Calculating flow laws as function (T) -----

***** CALCITE *****
# calculations on the basis of the flow laws of Schmid et al. (1977, 1980)

# Regime1: Twinning
r1(x,er)=s1*(log(er)-log(A1)+(H1/(R*(x+273))))

# Regime2: Power law 1
r2(x,er)=(er/(A2*exp(-H2/(R*(x+273)))))**(1/n2)

# Regime3: Power law 2
r3(x,er)=(er/(A3*exp(-H3/(R*(x+273)))))**(1/n3)

# Regime4: Superplasticity
r4(x,er)=(er/(A4*d4**(b4)*exp(-H4/(R*(x+273)))))**(1/n4)

***** DOLOMITE *****

rd1(x,er)=((er/(Ad1*exp(-Hd1/(R*(x+273)))))**(1/nd1))*10
rd2(x,er)=((er/(Ad2*exp(-Hd2/(R*(x+273)))))**(1/nd2))*10

#----- Calculating Minima -----

#--- Setting r1 = 1000 bar
r1a(x,er)=r1(x,er) <= 1000 ? 1000 : r1(x,er)

#--- calculating minima
test1a2(x,er)=r1a(x,er) <= r2(x,er) ? r1a(x,er) : r2(x,er)
test1a23(x,er)=test1a2(x,er) <= r3(x,er) ? test1a2(x,er) : r3(x,er)
#test2341(x,er)=test234(x,er) <= r1a(x,er) ? test234(x,er) : r1a(x,er)

#----- Calculating strength differences & printing values to screen -----

sdiff1=rd1(pt,per)-test1a23(pt,per)
sdiff2=rd2(pt,per)-test1a23(pt,per)

#--- Caclite -----
print ""
print "----- Results @ -----"
print "T = ",pt,"°C and Strain rate = ",per, " 1/s"
print "for : "
print "Calcite Strength = ",test1a23(pt,per)," bar"

#--- Dolomite -----
print "Dolomite Strength (Heard, 1976) = ",rd2(pt,per)," bar"
print "Dolomite Strength (White & White, 1980) = ",rd1(pt,per)," bar"

```

Appendix D

```
print ""
print "The Stress Difference Cc-Dol (Heard) is:  ",sdiff2," bar"
print "The Stress Difference Cc-Dol (White & White) is: ",sdiff1," bar"
print "-----"

#----- Plotting Graph -----

set arrow from pt,1 to pt,1e5

plot test1a23(x,per) with l -1,\
    rd2(x,per) with l 2
    # rd2(x,per) with l 3

#----- Creating output -----

#set terminal postscript eps          #<== EDIT here for writing eps-file
#set terminal postscript color       #<== EDIT here for writing eps-file
#set output "output.eps"            #<== EDIT here for writing eps-file
#replot                             #<== EDIT here for writing eps-file

reset
```

Screen dialog of the Script 2.0 in GNUplot

The following lines show the user interface of the GNUplot script 'Script 2.0'. Bold text have to be typed by the user.

```
GNU PLOT
Macintosh version 3.7
patchlevel 1
last modified Fri Oct 22 18:00:00 BST 1999

Copyright(C) 1986 - 1993, 1998, 1999
Thomas Williams, Colin Kelley and many others

Type `help` to access the on-line reference manual
The gnuplot FAQ is available from
<http://www.ucc.ie/gnuplot/gnuplot-faq.html>

Send comments and requests for help to <info-gnuplot@dartmouth.edu>
Send bugs, suggestions and mods to <bug-gnuplot@dartmouth.edu>

Terminal type set to 'pict'
gnuplot> load's2'

----- Results @ -----
T = 370°C and Strain rate = 1e-12 1/s
for :
Calcite Strength                = 1000 bar
Dolomite Strength (Heard, 1976) = 16508.9502284301 bar
Dolomite Strength (White & White, 1980) = 14739.4476849525 bar

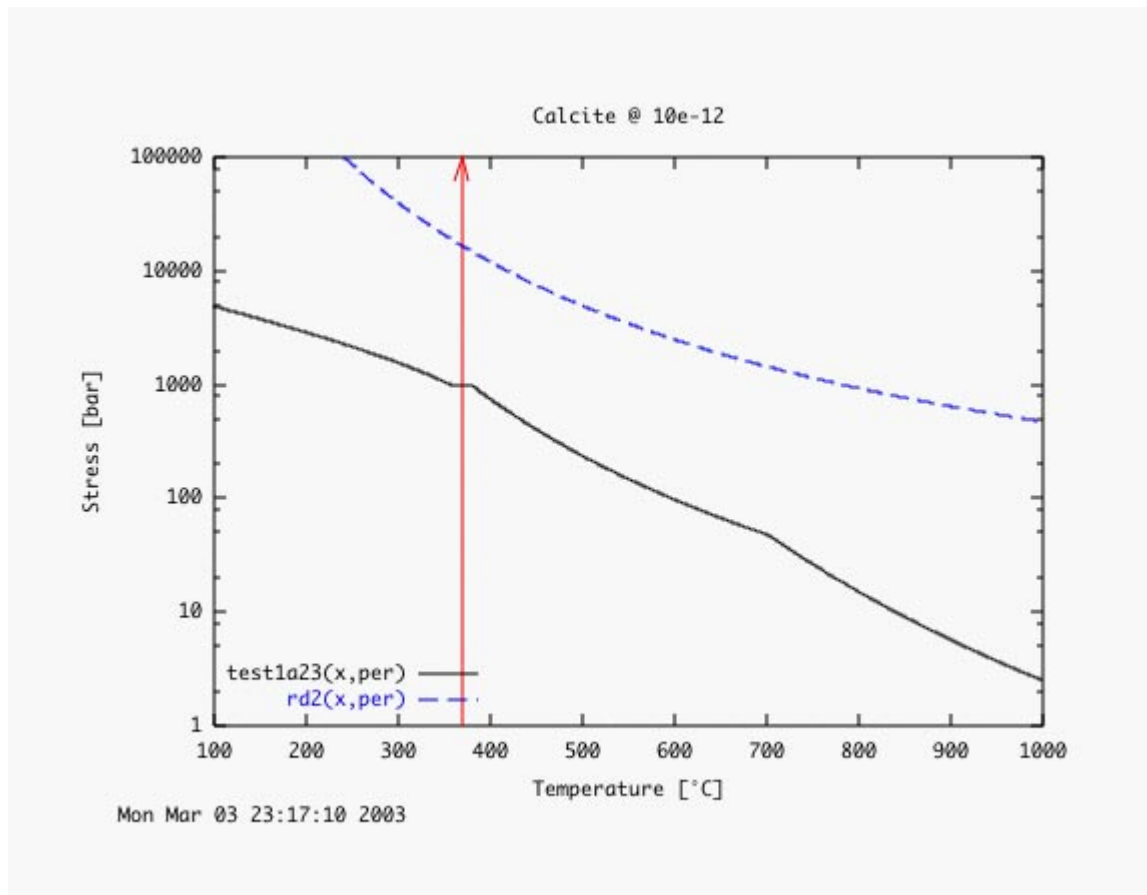
The Stress Difference Cc-Dol (Heard) is:      15508.9502284301 bar
The Stress Difference Cc-Dol (White & White) is: 13739.4476849525 bar
-----
```

Output from Script 1.1

The results are:

- 1) the stress of calcite and dolomite at a defined temperature (370°C) and strain rate (10e-12), and
- 2) the stress difference between calcite and dolomite for two different dolomite flow laws.

The calculated deformation mechanism map for a certain temperature (here 370°C) is shown below:





Appendix E: Posters

On the following pages five posters are shown, which were presented during the course of this PhD-thesis. The posters reflect the evolution of the different topics of the present study. At the beginning the microstructures and textures of pure calcite marble deformation were in the center of interest. The calibration of the CIP method and the comparison to experimental microstructures followed. The results presented at the DRT 2001 represent the extraction of the previous studies. During the last period of this thesis two-phase marbles came more and more into the center of interest as can be seen from the poster presented at the GRC conference.

Poster contributed to the International conference on Deformation Mechanisms, Rheology and Microstructures 1999, Neustadt an der Weinstrasse, Germany and to EUG X, 1999, Strassbourg, France.

Microstructures Related to Dynamic Overprint in Statically Recrystallized Carrara Marble

(Alpi Apuane, NW Italy)

N. Oesterling¹ (oesterling@basel.unibas.ch), R. Heilbrunner²

¹ Department of Earth Science, University of Basel, CH-4056 Basel, Switzerland ² Dipartimento Scienze della Terra, Università di Pisa, I-56126 Pisa, Italy

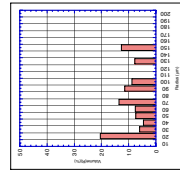
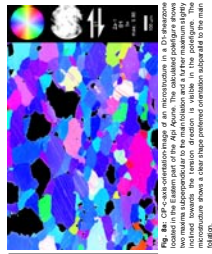
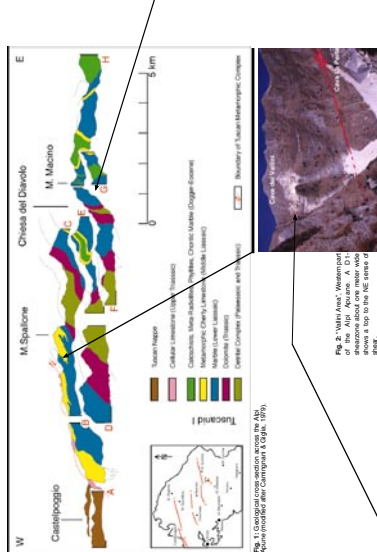
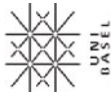
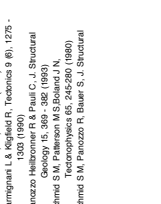
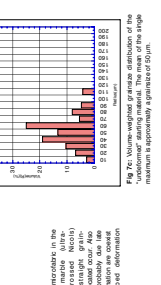
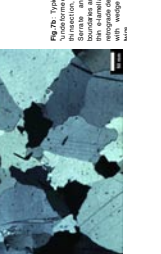
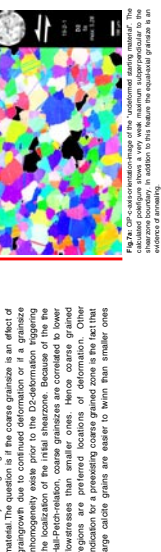
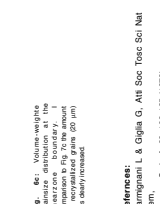
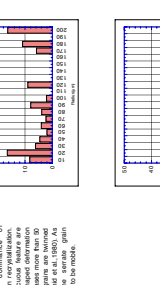
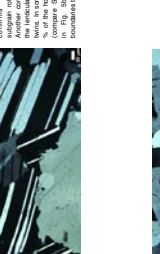
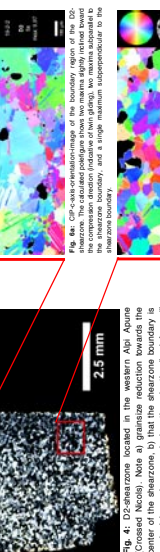
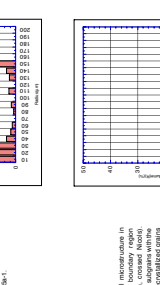
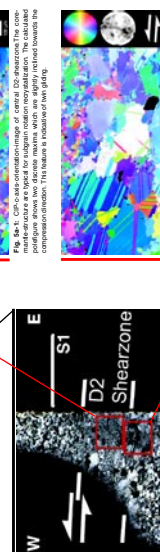
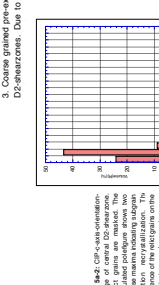
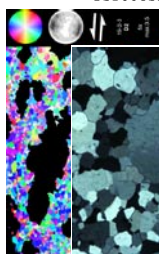


Fig. 1. Geological cross-section across the Alpi Apuane (after Camignani & Giglia, 1979).

Fig. 2. "White Area" (Western part of the Alpi Apuane, A-D) showing a top to the NE sense of shear.

Fig. 3. D2-shearzone with an estimated top to the SW, left sense of shear. The shearzone dips north 20° from the horizontal.

Fig. 4. D2-shearzone located in the western Alpi Apuane (Crosato Nocoli). Note a) grain size reduction towards the center of the shearzone. b) that the shearzone boundary is marked by a larger grain size than in the "undistorted" region. c) that the shearzone boundary is marked by a larger grain size than in the "undistorted" region. d) that the shearzone boundary is marked by a larger grain size than in the "undistorted" region.



Conclusions:

- Two deformation phases, D1 and D2, are distinguishable by their microstructures. The D1 deformation phase is characterized by a shape preferred orientation indicative of the D1-deformation phase. D2-microstructures show subgrain rotation recrystallization. The D2-microstructures are reflected by a bimodal grain size distribution.
- Transition from annealed to dynamically recrystallized marble is associated with a decrease in grain size and an increase in the volume fraction of recrystallized grains.
- Coarse grained pre-existing layers may have served as nucleation sites for D2-shearzones. Due to the high-P/low- T relation coarse grained regions are D2-shearzones.

Fig. 5a. Volume-weighted grain size distribution in the shearzone boundary. The distribution reflects a bimodal character with a peak at 100 μ m (shear zone) and a peak at 20 μ m (recrystallized grains). The volume fraction of recrystallized grains is 10%.

Fig. 5b. Volume-weighted grain size distribution in the shearzone boundary. The distribution reflects a bimodal character with a peak at 100 μ m (shear zone) and a peak at 20 μ m (recrystallized grains). The volume fraction of recrystallized grains is 10%.

Fig. 6a. Volume-weighted grain size distribution in the shearzone boundary. The distribution reflects a bimodal character with a peak at 100 μ m (shear zone) and a peak at 20 μ m (recrystallized grains). The volume fraction of recrystallized grains is 10%.

Fig. 6b. Volume-weighted grain size distribution in the shearzone boundary. The distribution reflects a bimodal character with a peak at 100 μ m (shear zone) and a peak at 20 μ m (recrystallized grains). The volume fraction of recrystallized grains is 10%.

Fig. 7a. Typical microstructure in the shearzone boundary region. The formation of subgrains within some annealed grains is associated with subgrain rotation recrystallization. The subgrain rotation recrystallization is associated with a decrease in grain size.

Fig. 7b. Typical microstructure in the shearzone boundary region. The formation of subgrains within some annealed grains is associated with subgrain rotation recrystallization. The subgrain rotation recrystallization is associated with a decrease in grain size.

Fig. 8a. D2-shearzone located in the western Alpi Apuane (Crosato Nocoli). Note a) grain size reduction towards the center of the shearzone. b) that the shearzone boundary is marked by a larger grain size than in the "undistorted" region. c) that the shearzone boundary is marked by a larger grain size than in the "undistorted" region. d) that the shearzone boundary is marked by a larger grain size than in the "undistorted" region.

Fig. 8b. D2-shearzone located in the western Alpi Apuane (Crosato Nocoli). Note a) grain size reduction towards the center of the shearzone. b) that the shearzone boundary is marked by a larger grain size than in the "undistorted" region. c) that the shearzone boundary is marked by a larger grain size than in the "undistorted" region. d) that the shearzone boundary is marked by a larger grain size than in the "undistorted" region.

Fig. 9a. D2-shearzone located in the western Alpi Apuane (Crosato Nocoli). Note a) grain size reduction towards the center of the shearzone. b) that the shearzone boundary is marked by a larger grain size than in the "undistorted" region. c) that the shearzone boundary is marked by a larger grain size than in the "undistorted" region. d) that the shearzone boundary is marked by a larger grain size than in the "undistorted" region.

Fig. 9b. D2-shearzone located in the western Alpi Apuane (Crosato Nocoli). Note a) grain size reduction towards the center of the shearzone. b) that the shearzone boundary is marked by a larger grain size than in the "undistorted" region. c) that the shearzone boundary is marked by a larger grain size than in the "undistorted" region. d) that the shearzone boundary is marked by a larger grain size than in the "undistorted" region.

Fig. 9c. D2-shearzone located in the western Alpi Apuane (Crosato Nocoli). Note a) grain size reduction towards the center of the shearzone. b) that the shearzone boundary is marked by a larger grain size than in the "undistorted" region. c) that the shearzone boundary is marked by a larger grain size than in the "undistorted" region. d) that the shearzone boundary is marked by a larger grain size than in the "undistorted" region.

Fig. 9d. D2-shearzone located in the western Alpi Apuane (Crosato Nocoli). Note a) grain size reduction towards the center of the shearzone. b) that the shearzone boundary is marked by a larger grain size than in the "undistorted" region. c) that the shearzone boundary is marked by a larger grain size than in the "undistorted" region. d) that the shearzone boundary is marked by a larger grain size than in the "undistorted" region.

Poster contributed to the International Conference on Textures and Physical Properties of Rocks, 1999, Göttingen, Germany.



Textures of Calcite-Mylonites in Carrara Marble. - Comparison of Computer Integrated Polarization Microscopy (CIP) and Universal Stage-Measurements.

Nils Oesterling¹ (Nils.Oesterling@unibas.ch), Renée Heilbronner¹ (renee.heilbronner@unibas.ch), Giancarlo Molli² (gmolli@dst.unipi.it)

1 Department of Earth Sciences, University of Basel, CH - 4056 Basel, Switzerland
 2 Dipartimento Scienze della Terra, Università di Pisa, I - 56126 Pisa, Italy

Introduction to the analysed microstructures:

Carrara marble is cropping out in the Alpi Apuane (NW-Appennine, Italy), which represent a large tectonic window (Carmignani & Kilgfield, 1990). In this study we analysed the microstructural variations of calcite mylonites found in post-thermal-peak shear zones in the marble. In contrast to the bulk of Carrara marble, which shows an annealed microstructure ($\pm 430^\circ\text{C}$), the shear zones are characterized by dynamic microstructures ($\pm 320^\circ\text{C}$, Molli et al. in press). Three different types of microstructures can be distinguished:

- 1) The host rock is characterized by isometric grain shape with a modal grain diameter of approximately 100 μm . Apart from slightly serrate grain boundaries and left-over-grains, which are indicative of grain boundary migration, this microstructure is interpreted as the result of an annealing process (Fig. C1).
- 2) The center of the shear zone shows a bimodal grain size distribution. Coarse, mechanically twinned relict grains (modal grain diameter 300 μm) are embedded in a matrix of recrystallized grains with a modal grain diameter of approximately 40 μm .

We interpret this core-mantle-structure as the product of subgrain rotation recrystallization (Fig. A1).

- 3) In the transition from the shear zone to the host rock a coarse grain zone (modal grain diameter 300 - 360 μm) of strongly twinned grains are visible. Along a few grain boundaries recrystallized grains (modal grain diameter 40 μm) and grain boundary migration structures, such as left-over-grains can be recognized. The grain size in this region and the size of large relict grains in the center of the shear zone are similar and about 200 μm larger than the

annealed grain size. We interpret this phenomenon as a pre-existing coarse grained vein which served as a site of preferred shear-initiation (Hall-Petch-relation) (Fig. B1).

E) How to Interpret CIP-textures:

For the interpretation of CIP polefigures it is important to consider the microstructure, the polefigure and the texture index together.

Example:
 The sample in Fig. C1 has a texture index of 5.00 times uniform, nevertheless the polefigure shows a random distribution of c-axis. This is due to small sample statistics, i.e., relatively large grain size. In contrast to the Fig. A1 shows a polefigure with a texture index of about 3 times uniform. Because of the much smaller grain size, a maximum of 3 times

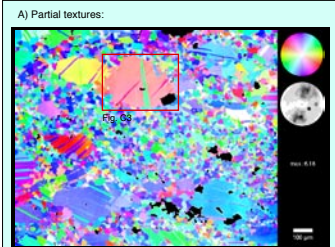


Figure A1 C-axis-orientation image (COI) of the central shear zone. In contrast to experimentally deformed marble (Schmid et al., 1987) the polefigure maxima of this naturally deformed marble are not located at the periphery but are shifted towards the centre.



Figure A2 COI where recrystallized grains are masked. The relict grains show a lattice preferred orientation, characterized by two broad maxima, which are shifted to the centre of the polefigure. Due to small sample statistics and a coarse grain size a high texture index is obtained (max=17.55).

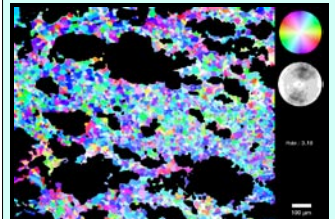
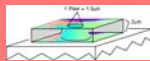


Figure A3 COI where relict grains are masked. The polefigure shows a broad grille with two weak maxima away from the periphery. In comparison to Fig. A2 the maxima are located at the same place. The c-axis-orientation distribution is more difficult than for the relict grains.

D) Ultra-thin-sections and analysed volume:



To record the input images for CIP an optical microscope with 5x-magnification and an numerical aperture (N.A.) of 0.15 was used. In order to obtain first order grey interference colours in calcite, as required by the CIP-method, ultra-thin-sections of approximately 2 μm thickness were prepared.

For objectives with N.A. = 0.15 the complete thickness of the analysed section is resolved optically, because the depth of focus clearly exceeds the thin-section thickness (Fig. D1).

Superposition of different grains, and resulting, distortion of orientation data, is unlikely, because the smallest grains have a mean diameter, which is about 20 times larger than the ultra-thin-section thickness. Three exceptions can be imagined:

- 1) Section parallel grain to grain contact within the volume of thin-section.
- 2) Strong lattice deformation, i.e. undulose extinction, perpendicular to the thin-section.
- 3) Oblique grain boundaries.

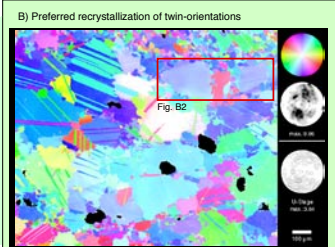
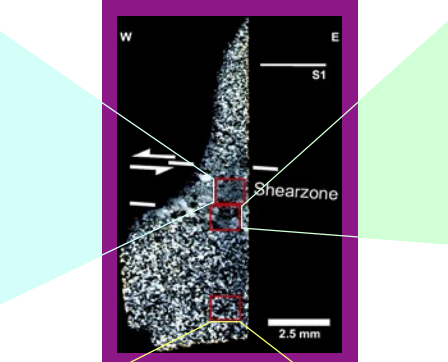


Figure B1 Coarse grain layer at the shear zone boundary. Recrystallization develops preferentially at twin boundaries; twin-orientations maybe preferred locations of recrystallization.

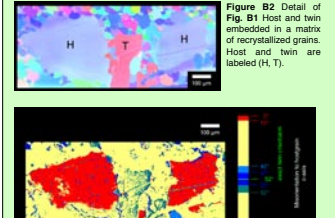


Figure B2 Detail of Fig. B1 Host and twin embedded in a matrix of recrystallized grains. Host and twin are labeled (H, T).

Figure B3 Color coded misorientation image (reference direction is the preferred orientation of the host grain). The host grain is shown in red, the twin orientation within a range of 20° in green and blue as shown in the lookup table. Note that the twin shows a misorientation of approximately $55^\circ - 60^\circ$ with respect to host grain. The recrystallized grains do not show any twin relation to either host or twin. This is compatible with grain boundary migration.

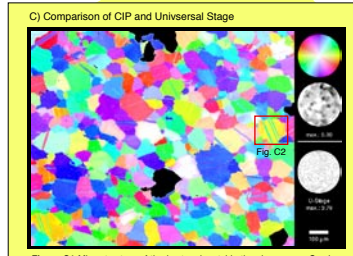


Figure C1 Microstructure of the host rock outside the shear zone. C-axis-polefigures determined by CIP as well as U-stage measurements show a random distribution. The weak maximum in the upper right is not statistically significant.

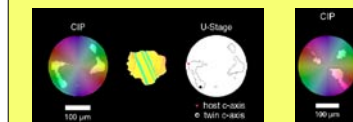


Figure C2 (Detail of Fig. C1) Comparison of single grain orientations determined by either CIP and U-Stage. The angle between host and twin are in both cases, i.e. CIP and U-Stage, identical.

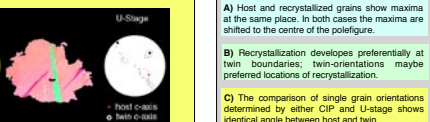


Figure C3 (Detail of Fig. A1) Comparison of single grain orientations determined by either CIP and U-Stage. The angle between host and twin are in both cases, i.e. CIP and U-Stage, identical.



Figure C4 CIP-inclination-image with orientation distribution of the selected grain. The grain does not display one single c-axis-orientation as would be measured by Universal-Stage, but a range of orientations. The modal value of the c-axis orientation range is identical to the Universal Stage measurement.

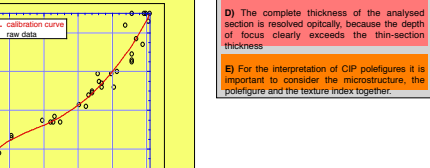


Figure C5 To calibrate the inclination-image about 40 c-axis were measured by the Universal-Stage, choosing a sample with a random c-axis distribution. To determine a valid calibration curve it is necessary to measure c-axis over the entire range of possible inclinations, i.e. $0^\circ - 90^\circ$. Using the U-Stage data a calibration curve can be determined to assign grey values to c-axis inclinations.

Conclusions:

- A) Host and recrystallized grains show maxima at the same place. In both cases the maxima are shifted to the centre of the polefigure.
- B) Recrystallization develops preferentially at twin boundaries; twin-orientations maybe preferred locations of recrystallization.
- C) The comparison of single grain orientations determined by either CIP and U-stage shows identical angle between host and twin. One single grain does not display one single c-axis-orientation as would be measured by Universal-Stage, but a range of orientations. The modal value of the c-axis orientation range is identical to the Universal Stage measurement.
- D) The complete thickness of the analysed section is resolved optically, because the depth of focus clearly exceeds the thin-section thickness.
- E) For the interpretation of CIP polefigures it is important to consider the microstructure, the polefigure and the texture index together.

References:

Carmignani L & Kilgfield R, Tectonics 9 (6), 1275 - 1303 (1990)
 Panzozzo Heilbronner R & Pauli C, J. Structural Geology 15, 369 - 382 (1993)
 Schmid, M.S., Panzozzo, R., Bauer, S., J. Structural Geology 9, 747 - 778 (1987)

Poster contributed to the Swiss Tectonics Group Meeting 17, 2000, Zurich, Switzerland.



Microstructure Analysis of Naturally and Experimentally Deformed Carrara Marble. – Correlation between Nature and Experiment.



Nils Oesterling (Nils.Oesterling@unibas.ch), Auke Barnhoorn (barnho@erdw.ethz.ch), Renée Heilbronner (Renee.Heilbronner@unibas.ch) and Luigi Burlini (luigi@erdw.ethz.ch)
 1. Geological-Palaeontological Institute, University of Basel, 4056 Basel, Switzerland; 2. Geological Institute, ETH - Zentrum, CH - 8092 Zurich, Switzerland

Introduction:

The aim of this study is the comparison of microstructures of naturally and experimentally deformed marbles in order better to understand the deformation processes occurring in the Earth's crust. Textures of naturally deformed marbles are difficult to interpret, for the following reasons: a) Shear direction and flattening plane are in contrast to experiment (Schmid et al., 1987); not easily identified in nature b) Natural textures may be the product of two distinct and overprinting deformation events. We chose Carrara marble because it is compositionally and microstructurally homogeneous, in some locations, it

shows a good equilibration microstructure, and has been extensively used as starting material for deformation experiments (Schmid et al., 1987; Rutter, 1998); in other locations, it shows dynamically recrystallised microstructures due to intensive deformation (Mölli et al., submitted; Oesterling et al., 1999). The latter allow us to investigate the textural development during progressive deformation in nature. Two types of deformation microstructures were observed in naturally deformed Carrara marble: 1) Grain boundary migration microstructures, with highly serrate grain boundaries, related to the first deformation

phase (D1), which occurred at 430°C in the West to 380°C in the East of the Alpi Apuane. 2) A core-mantle-microstructure typical of subgrain rotation recrystallisation in cases where deformation was accommodated by the development of shear zones (D2), which occurred at 320°C in the West to 380°C in the East of the Alpi Apuane. By way of experimental deformations, it is possible to reproduce the same microstructures in the laboratory. By varying one variable at a time (T, P, strain and strain rate) we can understand which parameter(s) determine(s) a specific feature in the fabric and microstructure.

Moreover, using a simple shear deformation technique (torsion), we can also study the microstructural evolution up to very large shear strain ($\gamma > 10$). The comparison will be performed through the analysis of the LPO and SPO by using both EBSD and CIP (Panzos Heilbronner & Pauli 1993) techniques. This will provide information on the complete crystallographic orientation of calcite grains and on the subfabrics. Comparative microstructural analysis of naturally and experimentally deformed Carrara marble provides a good basis for the investigation of the active deformation mechanisms of calcite during deformation.

Nature

Experiment

First deformation phase (D1): 380°C

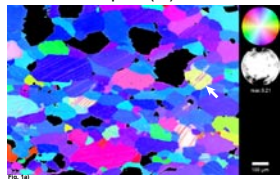


Fig. 1a) CIP c-axis orientation image of microstructure derived from the highly sheared limb of a regional scale fold. The temperature during deformation was estimated, using calcite - dolomite - thermometry, to 380°C. Different types of twins can be discovered in this microstructure. Twins with serrate boundaries (arrow) indicate a large deformation developed in a mm - cm scaled shear zone. The microstructure is characterised by a core-mantle-structure. Coarse, mechanically twinned relict grains ($d > 200\mu\text{m}$) are embedded in a matrix of fine recrystallised grains ($d = 30 - 40\mu\text{m}$). The polefigure is characterised by a pronounced maximum subperpendicular to the foliation plane and show serrate grain boundaries, which indicate grain boundary migration as dominant recrystallisation mechanism. The polefigure is characterised by a pronounced maximum subperpendicular to the foliation plane and show serrate grain boundaries, which indicate grain boundary migration as dominant recrystallisation mechanism. The polefigure is characterised by a pronounced maximum subperpendicular to the foliation plane and show serrate grain boundaries, which indicate grain boundary migration as dominant recrystallisation mechanism. The polefigure is characterised by a pronounced maximum subperpendicular to the foliation plane and show serrate grain boundaries, which indicate grain boundary migration as dominant recrystallisation mechanism.

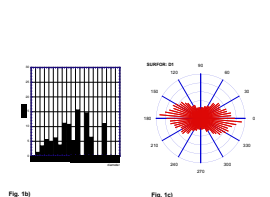


Fig. 1b) Volume weighted grain size distribution shows a modal grain diameter of 115 μm . Due to small sample statistics a irregular histogram is obtained.

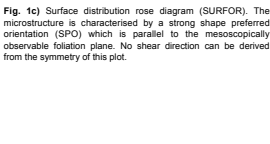


Fig. 1c) Surface distribution rose diagram (SURFOR). The microstructure is characterised by a strong shape preferred orientation (SPO) which is parallel to the mesoscopically observable foliation plane. No shear direction can be derived from the symmetry of this plot.

Second deformation phase (D2): 320°C



Fig. 2a) CIP c-axis orientation image (COI) of the microstructure developed in a mm - cm scaled shear zone. The microstructure is characterised by a core-mantle-structure. Coarse, mechanically twinned relict grains ($d > 200\mu\text{m}$) are embedded in a matrix of fine recrystallised grains ($d = 30 - 40\mu\text{m}$). The polefigure shows a pronounced c-axis maximum subperpendicular to the shear zone boundary. A similar polefigure is obtained in torsion experiments at 723°C and $\gamma = 2$ (Fig. 6b). Sense of shear cannot be inferred from this c-axis orientation distribution (compare Schmid et al., 1997).

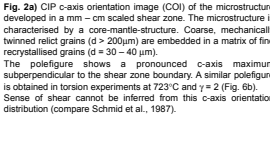


Fig. 2b) COI where recrystallised grains are masked. The different maxima in the polefigure can be related to the c-axis orientation of single relict grains. Due to small sample statistics and a coarse grain size a relatively high texture index of about 7 times uniform is obtained.

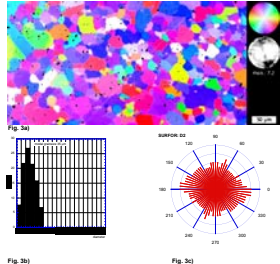


Fig. 2c) COI where relict grains are masked. The polefigure is characterised by a weak single maximum subperpendicular to the shear zone boundary. In comparison to the polefigure illustrated in Fig. 2b it is obvious that the c-axis orientation of the recrystallised grains is approximately the same as that of the relict grains. Therefore, it is likely that the new grains are developed by subgrain rotation recrystallization.

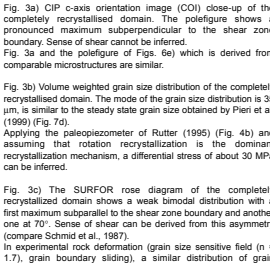


Fig. 3a) CIP c-axis orientation image (COI) close-up of the completely recrystallised domain. The polefigure shows a pronounced maximum subperpendicular to the shear zone boundary. Sense of shear cannot be inferred.

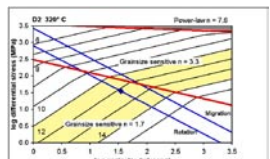


Fig. 3b) Volume weighted grain size distribution of the completely recrystallised domain. The mode of the grain size distribution is 35 μm , is similar to the steady state grain size obtained by Pieri et al. (1999) (Fig. 7d). Applying the paleopiezometer of Rutter (1995) (Fig. 4b) and assuming that rotation recrystallization is the dominant recrystallization mechanism, a differential stress of about 30 MPa can be inferred.



Fig. 3c) The SURFOR rose diagram of the completely recrystallized domain shows a weak bimodal distribution with a first maximum subparallel to the shear zone boundary and another one at 70°. Sense of shear can be derived from this asymmetry (compare Schmid et al., 1987). In experimental rock deformation (grain size sensitive field ($n = 1.7$), grain boundary sliding), a similar distribution of grain boundary surfaces was found in Solenhofen limestone.

Deformation mechanism maps:

The deformation mechanism maps have been constructed using data from Rutter (1974), Schmid et al. (1980) and Walker et al. (1990). All deformation mechanism maps are for amplification.

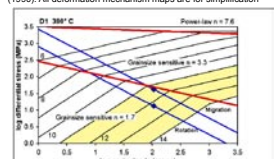


Fig. 4a) Deformation mechanism map constructed for a deformation temperature of 380°C, estimated by calcite - dolomite thermometry (Mölli et al., submitted). Assuming that the microstructure is a result of grainboundary migration recrystallisation and that, after deformation, the grain size has not been modified by grain growth, a differential stress of 30 MPa is obtained by the paleopiezometer of Rutter (1995). The data points plot in the boundary region between the grain size sensitive field with a stress exponent $n = 1.7$ and $n = 3.3$.

constructed for axial deformation, except for the 923 °C torsion experiment. The stresses have been converted to shear stresses.

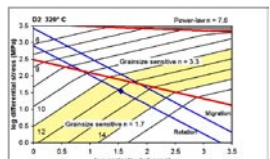


Fig. 4b) Deformation mechanism map constructed for a deformation temperature of 320°C estimated by calcite - dolomite thermometry (Mölli et al., submitted). According to the paleopiezometer of Rutter (1995), the recrystallized grain size of 35 μm yields a differential stress of 30 MPa. The corresponding strain rates lie in the range of 10^{-11} to 10^{-10} s $^{-1}$, which is geologically reasonable. The data point plots in the field of grain size sensitivity with a stress exponent $n = 1.7$, fairly close to the boundary to the grain size sensitive field with $n = 3.3$.

Axial deformation experiments:

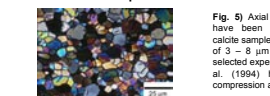


Fig. 5) Axial deformation experiments at 700 °C, 200 MPa confining pressure, have been performed on synthetic to strains of 31 %. Maximum reached calcite stresses is 28 MPa, which is primarily of 3 - 8 μm (Rutter et al., 1994). The controlled by the grainsize of the selected experiment (L28) from Rutter et al. (1994) has been performed in sections show equant grain shapes with compression at 700 °C, strainrate: 3×10^{-4} s $^{-1}$.

Torsion deformation experiments (Pieri et al. 1999):

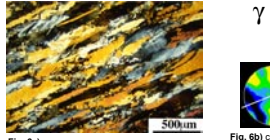


Fig. 6a) CIP c-axis orientation image of microstructure developed in a mm - cm scaled shear zone. The microstructure is characterised by a core-mantle-structure. Coarse, mechanically twinned relict grains ($d > 200\mu\text{m}$) are embedded in a matrix of fine recrystallised grains ($d = 30 - 40\mu\text{m}$). The polefigure shows a pronounced c-axis maximum subperpendicular to the shear zone boundary. A similar polefigure is obtained in torsion experiments at 723°C and $\gamma = 2$ (Fig. 6b). Sense of shear cannot be inferred from this c-axis orientation distribution (compare Schmid et al., 1997).

left-over grains ($d > 300\mu\text{m}$) for $\gamma = 2$. The completely recrystallised microstructure for $\gamma = 4.5$ shows a modal grain size 2 and 4.5, respectively, 300 MPa confining pressure and a of 30 μm . The amount of recrystallised grains increases with strainrate of 3×10^{-4} s $^{-1}$. Microstructural analyses show small shear strain. Both $\gamma = 2$ and 4.5 experiments show a strong c-axis equant recrystallised grains (grain diameter = 10 μm) and large maximum perpendicular to the foliation.

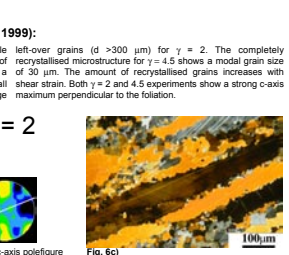


Fig. 6b) c-axis polefigure $\gamma = 2$. **Fig. 6c)** c-axis polefigure $\gamma = 5$. **Fig. 6d)** c-axis polefigure $\gamma = 4.5$.



Fig. 7a) CIP c-axis orientation image (COI) close-up of the completely recrystallised domain. The polefigure shows a pronounced maximum subperpendicular to the shear zone boundary. Sense of shear cannot be inferred.



Fig. 7b) COI where recrystallised grains are masked. The different maxima in the polefigure can be related to the c-axis orientation of single relict grains. Due to small sample statistics and a coarse grain size a relatively high texture index of about 7 times uniform is obtained.

Deformation mechanism maps

The deformation mechanism map for the axial deformation experiment on synthetic calcite show that the deformation occurred in the grainsize sensitive regime with the low stress exponent ($n = 1.7$), similar to the natural deformed Carrara

marble. The torsion experiments have been performed in the grainsize insensitive power law creep regime ($n = 7.6$). Final grain sizes of 30 μm shifted the deformation to the switch between grainsize insensitive and grainsize sensitive deformation.

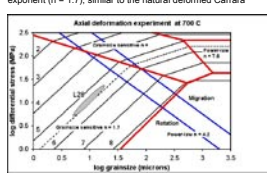


Fig. 8a) Deformation mechanism map for axial deformation experiments at 723 °C. The map shows log differential stress (MPa) vs log grain size (micrometers).

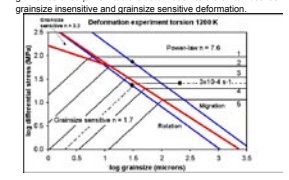


Fig. 8b) Deformation mechanism map for torsion experiments between 1200 °C. The map shows log differential stress (MPa) vs log grain size (micrometers).

Conclusions:

- 1) Microstructures and textures of naturally deformed Carrara marble (Fig. 2a - c) are similar to the microstructures and textures obtained by torsion experiments at 723°C and $\gamma = 2$ (Fig. 6a - c). In both cases core-mantle-structure are visible, indicative of subgrain rotation. The polefigures show c-axis maxima subperpendicular and inclined to the shear zone boundary, which can be related to the recrystallised and relict grains c-axis orientations, respectively.
- 2) The microstructures of the completely recrystallised domain in naturally deformed Carrara marble (Fig. 3a) can be correlated with microstructures produced in torsion experiments at 923°C and $\gamma = 5$ (Fig. 7a - c). However the polefigures are different.
- 3) Identical recrystallisation microstructures can be produced in different rheological regimes both in nature and experiment (Fig. 4 and Fig. 8).
- 4) Identical recrystallisation microstructures can also be obtained by imposing different deformation conditions (co-axial, shear and torsion) at different temperatures.
- 5) In naturally deformed samples better control on temperature, grainsize or strain rate is necessary to make a comparison with experimentally deformed samples.

References:

Oesterling, N., Barnhoorn, A., Heilbronner, R., & Burlini, L. (2000). Microstructures Related to Dynamic Overprint in Statistically Recrystallized Carrara Marble (Alpi Apuane, NW Italy) - Europ. Union of Geosciences, J. of Geology, 20(1), 289 - 301. April, 16, 2000, Strasbourg.
 Panzos Heilbronner, R., and Pauli, C. (1993). Integrated spatial and orientation analysis of quartz c-axis by computer-aided polarization microscopy. *J. Struct. Geol.* 15, 269 - 282.
 Pieri, M. (1999). Shear deformation of calcite: Kinetics and microstructural evolution of Carrara marble during dynamic recrystallization during torsion experiments. PhD Thesis ETH, Switzerland.
 Rutter, E.H. (1974). The influence of temperature, strain rate and interstitial water on the experimental deformation of calcite rocks. *Tectonophysics* 22, p. 311 - 324.
 Rutter, E.H., Cohen, J.L., and Keeler, S. (1986). Preferred crystallographic orientation during the shear of experimentally deformed calcite. *J. Struct. Geol.* 8, p. 1431 - 1446.
 Rutter, E.H. (1995). Experimental studies of the influence of stress, temperature and strain on the dynamic recrystallization of Carrara marble. *J. geophys. Res.* 100, p. 24651 - 24663.
 Schmid, S.M., Passchier, C.R., and Blue, G. (1993). Investigating the influence of finite strain on the rheological behaviour of marble. *J. Struct. Geol.* 15, p. 243 - 254.
 Schmid, S.M., Passchier, C.R., and Blue, G. (1993). Simple shear experiments on calcite rocks: rheology and microstructure. *J. Struct. Geol.* 15, p. 747 - 779.
 Walker, R.J., Rutter, E.H., and Hodges, K.V. (1990). Experimental study of grain-size sensitive flow of synthetic hot-pressed calcite rocks. In: Kröner, R.J. and Rutter, E.H. (eds) Deformation Mechanisms, rheology and tectonics, p. 285 - 298.

Poster contributed to the International conference on Deformation Mechanisms, Rheology and Tectonics 2001, Nordveijkerhoot, the Netherlands and to EUG XI, 2001, Strassbourg, France.

Late Stage Microstructural and Textural Evolution of Naturally Deformed Carrara Marble - A Comparison to Experimental Rock Deformation Data.

Nils Osterling¹ (nils.osterling@unibas.ch), Renée Heilbroner² (renee.heilbroner@unibas.ch), Hoiger Stunitz³ (hoiger.stunitz@unibas.ch) & Giancarlo Molli² (g.molli@dst.unipi.it)

¹ Department of Earth Sciences, University of Basel, CH-4056 Basel, Switzerland; ² Dipartimento di Scienze della Terra, Università di Pisa, I-56126 Pisa, Italy

Geological setting

The Carrara Marble is frequently used as starting material in experimental rock deformation and a lot of mechanical and microstructural data has been published. Microstructural and textural data of naturally deformed Carrara Marble can be compared with experimental data in order to evaluate whether experimental work is representative for the natural Carrara Marble. In this study we analyzed the progressive microstructural and textural evolution of a natural shear zone, which has formed during the second deformation event (D2) in the Apu-Aniene, Italy (Molli et al., 2000). The shear zone overprints a preexisting S1-main foliation, which is deflected into the shear zone. A schematic sketch of the Carrara Marble is shown in Fig. 1. The Carrara Marble is composed of calcic amphibole (Cpx), orthopyroxene (Opx), plagioclase (Pl), quartz (Qtz), and calcite (Cal). The shear zone is parallel to the sub-vertical foliation of the D2-deformation event.

Hand Specimen & Ultra-Thin-Section

The hand specimen shows a main foliation, which consists of this calcic amphibole, orthopyroxene, and plagioclase. The amphibole and orthopyroxene are oriented parallel to the shear zone. The plagioclase is oriented perpendicular to the shear zone. The calcite is oriented parallel to the shear zone. The ultra-thin section shows the same microstructural features at a higher resolution.

Microstructural Analysis

Fig. 5: Apparent grain size distribution of the shear zone. The grain size distribution is shown for different stages of deformation. The grain size increases from 100 μm to 270 μm. The PAFOR/SURFOR diagrams show the evolution of the microstructure from a single peak at 100-40 μm to a bimodal distribution with peaks at 100-40 μm and 270 μm.

Texture-Analysis

Fig. 10: The texture analysis shows changes in the local microstructure. The texture analysis is based on the PAFOR/SURFOR diagrams. The texture analysis shows a transition from a single peak at 100-40 μm to a bimodal distribution with peaks at 100-40 μm and 270 μm.

CIP-Analysis

Fig. 7: The CIP analysis shows the evolution of the microstructure. The CIP analysis is based on the PAFOR/SURFOR diagrams. The CIP analysis shows a transition from a single peak at 100-40 μm to a bimodal distribution with peaks at 100-40 μm and 270 μm.

Separated Analysis of Recryst. Grains and Porphyroclasts

Fig. 8: Porphyroclasts and recrystallized grains were analyzed separately. The separated analysis shows the evolution of the microstructure. The separated analysis is based on the PAFOR/SURFOR diagrams. The separated analysis shows a transition from a single peak at 100-40 μm to a bimodal distribution with peaks at 100-40 μm and 270 μm.

Experiments

Fig. 9: Experimental microstructures show the same development as the Carrara Marble. The experimental data is based on the PAFOR/SURFOR diagrams. The experimental data shows a transition from a single peak at 100-40 μm to a bimodal distribution with peaks at 100-40 μm and 270 μm.

Conclusions

1) The recrystallization mechanism dominates in the Carrara Marble. The recrystallization mechanism is based on the PAFOR/SURFOR diagrams. The recrystallization mechanism shows a transition from a single peak at 100-40 μm to a bimodal distribution with peaks at 100-40 μm and 270 μm.

Grain Size

Fig. 6: The PAFOR-factor (PAFOR-factor = 0.5% - 15% - 20%) is a shape factor. The grain size distribution is shown for different stages of deformation. The grain size increases from 100 μm to 270 μm.

Texture-Analysis

Fig. 11: The texture analysis shows changes in the local microstructure. The texture analysis is based on the PAFOR/SURFOR diagrams. The texture analysis shows a transition from a single peak at 100-40 μm to a bimodal distribution with peaks at 100-40 μm and 270 μm.

Grain Size

Fig. 12: The grain size distribution is shown for different stages of deformation. The grain size increases from 100 μm to 270 μm.

Texture-Analysis

Fig. 13: The texture analysis shows changes in the local microstructure. The texture analysis is based on the PAFOR/SURFOR diagrams. The texture analysis shows a transition from a single peak at 100-40 μm to a bimodal distribution with peaks at 100-40 μm and 270 μm.

Grain Size

Fig. 14: The grain size distribution is shown for different stages of deformation. The grain size increases from 100 μm to 270 μm.

Texture-Analysis

Fig. 15: The texture analysis shows changes in the local microstructure. The texture analysis is based on the PAFOR/SURFOR diagrams. The texture analysis shows a transition from a single peak at 100-40 μm to a bimodal distribution with peaks at 100-40 μm and 270 μm.

Poster contributed to the Gordon Research conference on Rock Deformation 2002, Barga, Italy.



The influence of dolomite content on the natural deformation behaviour of Carrara marble

Nils Oesterling (nils.oesterling@unibas.ch), Holger Stüdtz (holger.stuetztz@unibas.ch) & Renée Heilbronner (renee.heilbronner@unibas.ch)
 Department of Earth Sciences, University of Basel, Switzerland

Introduction

Besides the well known pure calcite Carrara marble a large amount of calcite-dolomite marbles are exposed in the Alps. The natural deformation behaviour of pure calcite marbles was investigated in this study we are analyzing the natural deformation behaviour of calcite-dolomite marbles, a rock type which can be frequently found in important regional scale tectonic zones. The influence of dolomite content on microstructural texture and the active deformation mechanism.

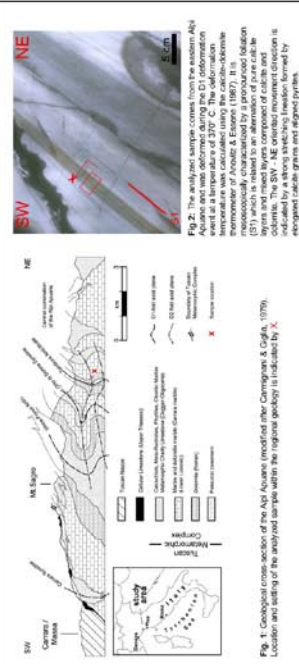


Fig. 1: Geological cross-section of the Aipi Aquifer (modified after Campana & Gagli, 1979). Location and setting of the analyzed sample within the regional geology is indicated by X.

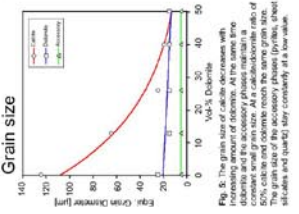


Fig. 2: The selected samples from the Aipi Aquifer. Calcite and dolomite content in the Aipi Aquifer and their deformation behaviour at a temperature of 370°C. The deformation mechanism is characterized by pronounced dislocation climb and secondary phase migration.

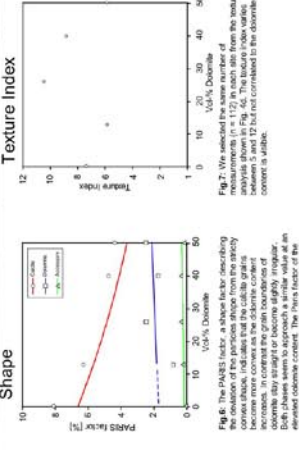


Fig. 3: The grain size distribution of the pure calcite and calcite-dolomite marbles. The grain size of the secondary phase (pyrite, sheet silicates and quartz) vary constantly with the calcite content.

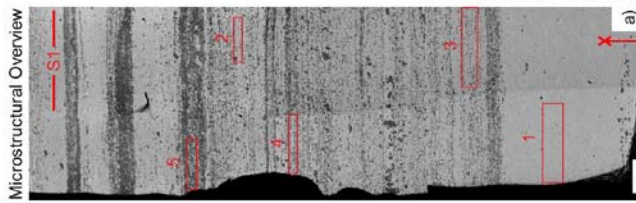


Fig. 3a: Back-scattered electron (BSE) image of a calcite-dolomite marble showing a layered microstructure. Red boxes 1-5 indicate different layers.

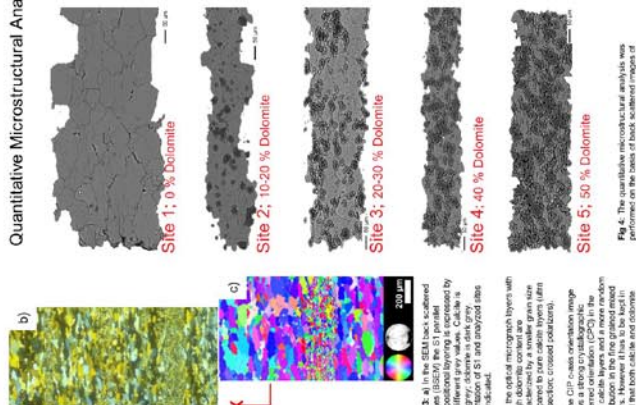


Fig. 3b: Quantitative microstructural analysis showing volume percentages of calcite and dolomite for five different sites (Site 1 to Site 5).

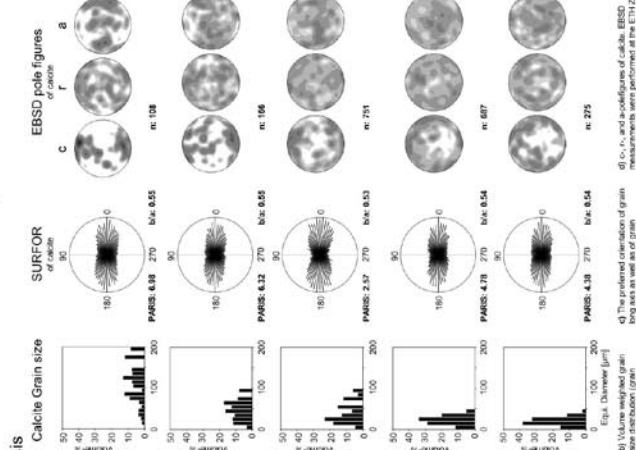


Fig. 3c: SURFOP and EBSD pole figures of calcite for five different sites, showing crystallographic orientation.

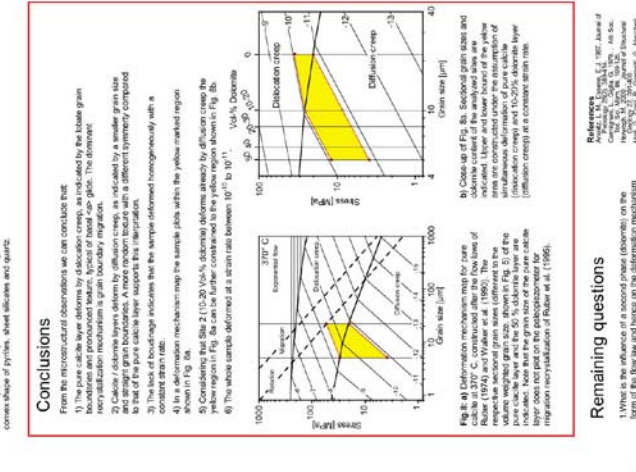


Fig. 3d: Deformation mechanism map for pure calcite at 370°C. The map shows the relationship between stress, grain size, and deformation rate, with regions for dislocation climb and diffusion creep.

Conclusions

- 1) The pure calcite layer deforms by dislocation climb, as indicated by the lobate grain boundaries and secondary phase migration.
- 2) Calcite/dolomite layers deform by diffusion creep, as indicated by a smaller grain size and straight grain boundaries. A more random texture with a different symmetry compared to the pure calcite layer is observed.
- 3) The lack of kink bands indicates that the sample deformed homogeneously with a constant strain rate.
- 4) In a deformation mechanism map the sample falls within the yellow marked region shown in Fig. 3d.
- 5) Considering Figs. 2, 3b, 3c, dolomite deformation by diffusion creep is the dominant mechanism in the calcite-dolomite marbles.
- 6) The calcite samples deformed at a strain rate between 10^{-11} to 10^{-12} s⁻¹.

Remaining questions

- 1. What is the influence of a second phase (dolomite) on the form of the flow law and hence on the deformation mechanism?
- 2. What is the relevant grain size (D, D₀) to use in the deformation mechanism map?
- 3. What is the influence of the grain size distribution on the relevant grain size?
- 4. What is the relative contribution of interoperative plasticity to the total of diffusion creep and dislocation climb?

References
 Campana, S. J., 1979. *Journal of Metamorphic Geology*, 1, 1-12.
 Heilbronner, R., 2000. *Journal of Structural Geology*, 22, 103-114.
 Oesterling, N., 2001. *Journal of Structural Geology*, 23, 103-114.
 Stüdtz, H., 1995. *Journal of Structural Geology*, 17, 103-114.
 Stüdtz, H., 1997. *Journal of Structural Geology*, 19, 103-114.
 Stüdtz, H., 1998. *Journal of Structural Geology*, 20, 103-114.



Curriculum Vitae

Name: Nils Oesterling
Date of birth: 23.10.1971
Nationality: german
Marital status: single



University education

August 1998 to April 2003 PhD-thesis at the Institute of Earth Sciences, Basel University, Switzerland, together with Prof. Dr. Renée Heilbronner and PD. Dr. Holger Stünitz. Title:
„Dynamic recrystallization and deformation mechanisms of naturally deformed Carrara marble.“
Abschluss: Dr. phil.nat.

October 1991 to Juni 1998 Studies of Geology at the Department of Geosciences, Ruhr-Universität Bochum, Germany, together with Prof. Dr. Bernhard Stöckhert. Title:
„Gefügeentwicklung und Hydrothermalsysteme im Umfeld kleiner Intrusivkörper am Rio Oro, Provinz Santa Cruz, Argentinien“
Abschluss: Dipl. Geologe

School education

1982 to 1991 Goetheschule Essen Städtisches Gymnasium, Essen

Professional experience

August 1998 to February 2003 Assistent at the Department of Earth Sciences, Basel University, Switzerland, with the following tasks:
Tutorials in Structural Geology, Interpretation of Geological Maps and Cross-Sections, Field Work and Digital Imageanalyse
Departemental Software- and Hardwaresupport, Network Administration, Website)
Organization of courses and conferenzen

June 1993 to May 1998 Freelancer at the Geological Department of the Ruhrlandmuseums Essen, Germany. Guide for exhibitions and field trips.

May 1995 to March 1998 Assistent at the Department of Geosciences of the Ruhr-Universität Bochum, Germany. Tutorials Interpretation of geological maps, organization of conferenzen, Interpretation of imageanalysis and massspectrometer data.

June 1996 to August 1996 Trainee at the BEB Erdgas und Erdöl GmbH, Hannover, Germany. Preparation of geological maps, Interpretation of 3D-seismic sections, Preparation of geological graphics and welldata
